MARTIN MARIETTA ENERGY SYSTEMS LIBRARIES

3 4456 0367321 9

ORNL/TM-12133

ornl

OAK RIDGE NATIONAL LABORATORY

MARTIN MARIETTA

Ceramic Technology Project Semiannual Progress Report for October 1991 Through March 1992

Prepared for
U.S. Department of Energy
Assistant Secretary for
Conservation and Renewable Energy
Office of Transportation Technologies
Materials Development Program

CERAMIC TECHNOLOGY FOR ADVANCED HEAT ENGINES

CERAMIC TECHNOLOGY PROJECT • DOE/ORNL •

OAK RIDGE NATIONAL LABORATORY
CENTRAL RESEARCH LIBRARY
CIRCULATION SECTION
4500N ROOM 175
LIBRARY LOAN COPY
DO NOT TRANSFER TO ANOTHER PERSON
If you wish someone else to see this report, send in name with report and the library will arrange a loan.
UCN-7969 (3 9-77)

MANAGED BY
MARTIN MARIETTA ENERGY SYSTEMS, INC.
FOR THE UNITED STATES
DEPARTMENT OF ENERGY

This report has been reproduced directly from the best available copy.

Available to DOE and DOE contractors from the Office of Scientific and Technical Information, P.O. Box 62, Oak Ridge, TN 37831; prices available from (615) 576-8401, FTS 626-8401.

Available to the public from the National Technical Information Service, U.S. Department of Commerce, 5285 Port Royal Rd., Springfield, VA 22161.

This report was prepared as an account of work sponsored by an agency of the United States Government. Neither the United States Government nor any agency thereof, nor any of their employees, makes any warranty, express or implied, or assumes any legal liability or responsibility for the accuracy, completeness, or usefulness of any information, apparatus, product, or process disclosed, or represents that its use would not infringe privately owned rights. Reference herein to any specific commercial product, process, or service by trade name, trademark, manufacturer, or otherwise, does not necessarily constitute or imply its endorsement, recommendation, or favoring by the United States Government or any agency thereof. The views and opinions of authors expressed herein do not necessarily state or reflect those of the United States Government or any agency thereof.

ORNL/TM-12133

Metals and Ceramics Division

CERAMIC TECHNOLOGY PROJECT SEMIANNUAL PROGRESS REPORT FOR OCTOBER 1991 THROUGH MARCH 1992

D. R. Johnson
Project Manager

Date Published: September 1992

NOTICE: This document contains information of a preliminary nature. It is subject to revision or correction and therefore does not represent a final report.

Prepared for
U.S. Department of Energy
Assistant Secretary for Conservation and Renewable Energy
Office of Transportation Technologies
Materials Development Program
EE 51 01 00 0

Prepared by the
OAK RIDGE NATIONAL LABORATORY
Oak Ridge, Tennessee 37831-6285
managed by
MARTIN MARIETTA ENERGY SYSTEMS, INC.
for the
U.S. DEPARTMENT OF ENERGY
under Contract DE-AC05-84OR21400

MARTIN MARIETTA ENERGY SYSTEMS LIBRARIES
3 4456 0367321 9

REPORTS PREVIOUSLY ISSUED

ORNL/TM-9325	Period March 1983-September 1983
ORNL/TM-9466	Period October 1983-March 1984
ORNL/TM-9497	Period April 1984-September 1984
ORNL/TM-9673	Period October 1984-March 1985
ORNL/TM-9947	Period April 1985-September 1985
ORNL/TM-10079	Period October 1985-March 1986
ORNL/TM-10308	Period April 1986-September 1986
ORNL/TM-10469	Period October 1986-March 1987
ORNL/TM-10705	Period April 1987-September 1987
ORNL/TM-10838	Period October 1987-March 1988
ORNL/TM-11116	Period April 1988-September 1988
ORNL/TM-11239	Period October 1988-March 1989
ORNL/TM-11489	Period April 1989-September 1989
ORNL/TM-11586	Period October 1989-March 1990
ORNL/TM-11719	Period April 1990-September 1990
ORNL/TM-11859	Period October 1990-March 1991
ORNL/TM-11984	Period April 1991-September 1991

Research sponsored by the U.S. Department of Energy, Assistant Secretary for Conservation and Renewable Energy, Office of Transportation Technologies, as part of the Ceramic Technology Project of the Materials Development Program, under contract DE-AC05-84OR21400 with Martin Marietta Energy Systems, Inc.

CONTENTS

SUMMARY 1

0.0 PROJECT MANAGEMENT AND COORDINATION 3

1.0 MATERIALS AND PROCESSING 5

INTRODUCTION 5

1.1 MONOLITHICS 7

1.1.1 Silicon Carbide 7

High Temperature Hexoloy SX Silicon Carbide (Carborundum) 7

1.1.2 Silicon Nitride 27

Improved Processing of Ceramic Composites (Southern Illinois University) 27

Characterization of Attrition Milled Silicon Nitride Powder (NIST) 30

Sintered Silicon Nitride (AMTL) 35

Microwave Sintering of Silicon Nitride (ORNL) . . . 44

Development of Microwave Processing of Silicon Nitride Components for Advanced Heat Engine Applications Reaction Bonded and Sintered Reaction Bonded Silicon Nitride (Norton) 60

Development of Microwave Processing of Silicon Nitride Components for Advanced Heat Engine Applications Microwave Annealing Si_3N_4 - *4 Wt%* Y_2O_3 (Norton) 62

Cost Effective Sintering of Silicon Nitride Ceramics (SIU-C) 65

Scalability Demonstration Program for Silicon Nitride by the Sullivan Process for Advanced Ceramics (Sullivan) 71

1.1.4 Processing of Monolithics 75

Improved Processing (Norton) 75

Improved Processing (ORNL) 114

Processing Science for Si_3N_4 Ceramics (University of California) 122

1.2 CERAMIC COMPOSITES 129

1.2.2 Silicon Nitride Matrix 129

Fabrication of SiC-AlN Composites (University of Michigan) 129

Optimization of Silicon Nitride Ceramics (University of Michigan) 145

Silicon Nitride with Elongated Grain Microstructures Exhibiting High Fracture Toughness (GCCD) 151

1.2.3 Oxide Matrix 158

Dispersion-Toughened Ceramic Composite (ORNL) . . . 158

1.3 THERMAL AND WEAR COATINGS 170

Fabrication and Testing of Corrosion-Resistant Coatings (ORNL) 170

Development of Adherent Ceramic Coatings to Reduce Contact Stress Damage of Ceramics (GTE) 175

Development of Adherent Coatings to Reduce Contact Stress Damage of Ceramics (Boston University) . . . 192

Wear-Resistant Coatings (Caterpillar) 196

Material Development of Thick Thermal Barrier Coating (TTBC) Systems (Caterpillar) 200

1.4 JOINING 203

1.4.1 Ceramic-Metal Joints 203

Joining of Ceramics for Heat Engine Applications (ORNL) 203

Analytical and Experimental Evaluation of Joining Silicon Nitride to Metal and Silicon Carbide to Metal for Advanced Heat Engine Applications (GTE) 207

1.4.2 Ceramic-Ceramic Joints 218

Analytical and Experimental Evaluation of Joining Silicon Carbide to Silicon Carbide and Silicon Nitride to Silicon Nitride for Advanced Heat Engine Applications (Norton) 218

2.0 MATERIALS DESIGN METHODOLOGY 231

INTRODUCTION 231

2.1 MODELING 233

2.1.1 Modeling 233

Microstructural Modeling of Cracks (University of Tennessee) 233

2.2 CONTACT INTERFACES 235

2.2.1 Static Interfaces 235

Elastic Properties and Adherence of Thin Films and Coatings (University of Tennessee) 235

2.2.2 Dynamic Interfaces 238

Studies of Dynamic Contact of Ceramics and Alloys for Advanced Heat Engines (Battelle) 238

Development of Standard Test Methods for Evaluating the Wear Performance of Ceramics (ORNL) 243

2.3 NEW CONCEPTS 247

Advanced Statistical Concepts of Fracture in Brittle Materials (GE) 247

3.0 DATA BASE AND LIFE PREDICTION 269

INTRODUCTION 269

3.1 STRUCTURAL QUALIFICATION 271

Microstructural Analysis of Structural Ceramics (NIST) 271

Mechanical Properties and Microstructural Characterization of Si_3N_4 Ceramics (ORNL) 282

Project Data Base (ORNL) 291

3.2 TIME-DEPENDENT BEHAVIOR 295

Fracture Behavior of Toughened Ceramics (ORNL) . . 295

Cyclic Fatigue of Toughened Ceramics (ORNL) 302

Rotor Data Base Generation (ORNL) 315

Toughened Ceramics Life Prediction (NASA Lewis Research Center) 325

Life Prediction Methodology (Allison) 352

Life Prediction Methodology (GAPD) 364

3.3 ENVIRONMENTAL EFFECTS 390

Environmental Effects in Toughened Ceramics (University of Dayton) 390

3.4 FRACTURE MECHANICS 398

Testing and Evaluation of Advanced Ceramics at High Temperature in Uniaxial Tension (North Carolina A&T State University) 398

Standard Tensile Test Development (NIST) 405

3.5 NONDESTRUCTIVE EVALUATION DEVELOPMENT 418

Nondestructive Characterization (ORNL) 418

NDE Standards for Advanced Ceramics (ORNL) 434

X-ray Computed Tomographic Imaging (ANL) 435

Nuclear Magnetic Resonance Imaging (ANL) 441

Physicochemical Characterization and Surface Modification of Silicon Nitride Ceramic Powders (University of Wisconsin-Madison) 449

4.0 TECHNOLOGY TRANSFER 451

4.1 TECHNOLOGY TRANSFER 451

4.1.1 Technology Transfer 451

Technology Transfer (ORNL) 451

IEA Annex II Management (ORNL) 452

Characterization of Ceramic Powders (NIST) 456

Ceramic Mechanical Property Test Method Development (NIST) 459

CERAMIC TECHNOLOGY PROJECT SEMIANNUAL PROGRESS REPORT FOR OCTOBER 1991 THROUGH MARCH 1992

SUMMARY

The Ceramic Technology Project was developed by the Department of Energy's Office of Transportation Systems (OTS) in Conservation and Renewable Energy. This project, part of the OTS's Materials Development Program, was developed to meet the ceramic technology requirements of the OTS's automotive technology programs.

Significant accomplishments in fabricating ceramic components for the Department of Energy (DOE), National Aeronautics and Space Administration (NASA), and Department of Defense (DoD) advanced heat engine programs have provided evidence that the operation of ceramic parts in high-temperature engine environments is feasible. However, these programs have also demonstrated that additional research is needed in materials and processing development, design methodology, and data base and life prediction before industry will have a sufficient technology base from which to produce reliable cost-effective ceramic engine components commercially.

An assessment of needs was completed, and a five-year project plan was developed with extensive input from private industry. In July 1990 the original plan was updated through the estimated completion of development in 1993. The objective of the project is to develop the industrial technology base required for reliable ceramics for application in advanced automotive heat engines. The project approach includes determining the mechanisms controlling reliability, improving processes for fabricating existing ceramics, developing new materials with increased reliability, and testing these materials in simulated engine environments to confirm reliability. Although this is a generic materials project, the focus is on the structural ceramics for advanced gas turbine and diesel engines, ceramic bearings and attachments, and ceramic coatings for thermal barrier and wear applications in these engines. This advanced materials technology is being developed in parallel and close coordination with the ongoing DOE and industry proof-of-concept engine development programs. To facilitate the rapid transfer of this technology to U.S. industry, the major portion of the work is being done in the ceramic industry, with technological support from government laboratories, other industrial laboratories, and universities.

This project is managed by ORNL for the Office of Transportation Technologies, Office of Transportation Materials, and is closely coordinated with complementary ceramics tasks funded by other DOE offices, NASA, DoD, and industry. A joint DOE and NASA technical plan has been established, with DOE focus on automotive applications and NASA focus on aerospace applications. A common work breakdown structure (WBS) was developed to facilitate coordination. The work described in this report is organized according to the following WBS project elements:

0.0 Management and Coordination

1.0 Materials and Processing

- 1.1 Monolithics
- 1.2 Ceramic Composites
- 1.3 Thermal and Wear Coatings
- 1.4 Joining

2.0 Materials Design Methodology

- 2.1 Modeling
- 2.2 Contact Interfaces
- 2.3 New Concepts

3.0 Data Base and Life Prediction

- 3.1 Structural Qualification
- 3.2 Time-Dependent Behavior
- 3.3 Environmental Effects
- 3.4 Fracture Mechanics
- 3.5 Nondestructive Evaluation Development

4.0 Technology Transfer

- 4.1 Technology Transfer

This report includes contributions from all currently active project participants. The contributions are arranged according to the work breakdown structure outline.

0.0 PROJECT MANAGEMENT AND COORDINATION

D. R. Johnson
Oak Ridge National Laboratory

Objective/scope

This task includes the technical management of the project in accordance with the project plans and management plan approved by the Department of Energy (DOE) Oak Ridge Field Office, and the Office of Transportation Technologies. This task includes preparation of annual field work proposals, initiation and management of subcontracts and interagency agreements, and management of ORNL technical tasks. Monthly management reports and bimonthly reports are provided to DOE; highlights and semiannual technical reports are provided to DOE and program participants. In addition, the program is coordinated with interfacing programs sponsored by other DOE offices and federal agencies, including the National Aeronautics and Space Administration (NASA) and the Department of Defense (DoD). This coordination is accomplished by participation in bimonthly DOE and NASA joint management meetings, annual interagency heat engine ceramics coordination meetings, DOE contractor coordination meetings, and DOE Energy Materials Coordinating Committee (EMaCC) meetings, as well as special coordination meetings.

1.0 MATERIALS AND PROCESSING

INTRODUCTION

This portion of the project is identified as project element 1.0 within the work breakdown structure (WBS). It contains four subelements: (1) Monolithics, (2) Ceramic Composites, (3) Thermal and Wear Coatings, and (4) Joining. Ceramic research conducted within the Monolithics subelement currently includes work activities on green state ceramic fabrication, characterization, and densification and on structural, mechanical, and physical properties of these ceramics. Research conducted within the Ceramic Composites subelement currently includes silicon carbide, silicon nitride, and oxide-based composites. Research conducted in the Thermal and Wear Coatings subelement is currently limited to oxide-base coatings and involves coating synthesis, characterization, and determination of the mechanical and physical properties of the coatings. Research conducted in the Joining subelement currently includes studies of processes to produce strong, stable joints between zirconia ceramics and iron-base alloys.

A major objective of the research in the Materials and Processing project element is to systematically advance the understanding of the relationships between ceramic raw materials such as powders and reactant gases, the processing variables involved in producing the ceramic materials, and the resultant microstructures and physical and mechanical properties of the ceramic materials. Success in meeting this objective will provide U.S. companies with new or improved ways for producing economical, highly reliable ceramic components for advanced heat engines.

1.1 MONOLITHICS

1.1.1 Silicon Carbide

High Temperature Hexoloy SX Silicon Carbide

K. Chia, G. V. Srinivasan, S. K. Lau (The Carborundum Company)

Introduction:

Hexoloy SX has been demonstrated to possess higher toughness and strength than Hexoloy SA®*.[1] Its toughness is about 50% to 100% higher than that of SA and its typical room temperature MOR value ranges between 620-915 MPa (90-133 ksi). Moreover, these are only preliminary data, it is believed that the mechanical properties can be further improved via proper optimization of composition, powder selection and processing conditions.

Scope and Objective:

The approach taken for this work is to first establish a complete mechanical property database and conduct detailed microstructural characterization on the first generation SX material currently available. After that, the emphasis will then be focused on the selection of a best SiC powder source and the optimization of processing conditions for this first generation material via a systematic designed experimental method. In parallel, a Carborundum in-house sponsored program with the objective of identifying a second generation additive composition with improved high temperature properties will also be conducted. Once this second generation composition is identified, the information will be fed into the current program. Then further experiments will be conducted to optimize the properties of this second generation SX material. Finally, the complete property database will then be established for the second generation composition.

The three major objectives for the current program are as follows: (1) to establish property database and conduct detailed characterization for the current best SX material, (2) to improve the processing conditions of that material via a designed experimental method, and (3) to develop a second generation SX material with improved properties.

Task 1 Objective: Complete Characterization of Generation I SX-SiC Material.

From previous internal work at Carborundum, a particular composition of Hexoloy SX, SX-G1 with 2 wt% total additive has been chosen for this task.

Experiments:

Sample Preparation: Two twenty pound batches of SiC powder were mixed with sintering additives, and spray dried into soft, flowable agglomerates. The powder was compacted into 63.5 mm square plates and subsequently isostatically pressed to 117 MPa. The green plates were pressureless sintered and post-treated to >99% theoretical density. The plates were then machined into flexural bars of size 3 x 4 x 48 mm. In fabricating the tensile specimens, green rods of length 216 mm and diameter 21 mm were isostatically pressed to 117 MPa. They were pressureless sintered to about 96% theoretical density. The density was enhanced to >99% by a post-treatment process. The dense rods were then machined into ORNL button-head type tensile specimens.

---

* Hexoloy SA, registered trade mark of Carborundum Company

Mechanical Properties Evaluation: Detailed microstructural and mechanical property characterizations were conducted on the samples fabricated. The mechanical properties evaluated included fracture toughness, flexural strength, tensile strength, dynamic fatigue, stress rupture and creep.

The fracture toughness (K_{IC}) was determined by the chevron notch technique. Chevron notches were cut in bars of size 3 x 4 x 48 mm which were subsequently fractured at a cross-head speed of 0.5 mm/min. in four-point bending. K_{IC} was evaluated using the fracture load from 5 samples each at RT, 1000, 1232 and 1370°C, respectively.

Flexural strength was evaluated on MIL STD 1942 bars (3 x 4 x 48 mm) in four-point bending at a cross-head speed of 0.5 mm/min. with 20 and 40 mm inner and outer spans. Flexural strength was evaluated for 20 bars each at RT, 1000, 1232 and 1370°C, respectively.

The strength of the SX-G1 samples was also determined in uniaxial tension. The specimens were machined according to the ORNL button-head tensile specimen specification. The specimens were then tested at a stressing rate of 11 MPa/sec. using self-aligning Instron Super Grip™ hydraulic couples in the load train to minimize specimen bending. The uniaxial tensile strengths were determined at room temperature, 1000, 1232 and 1370°C. These tension tests were carried out at the ORNL/HTML User Facility.

Dynamic Fatigue tests were conducted at 1232 and 1370°C in four-point bending using MIL STD. 1942 flexure bars. About 6 specimens were tested at each of three loading rates covering three orders of magnitude. Stress rupture experiments were also conducted at 1232 and 1370°C in four-point bending. The load-point deflection of each specimen was monitored during the testing.

Creep tests were conducted in uniaxial tension at 1260, 1370, and 1450°C. Strain rates were determined using extensometers at several temperatures ranging from 1260 to 1450°C, and at several stress levels ranging from 50 MPa to 250 MPa.

Extensive microstructural and fractographic analysis were conducted using both optical and scanning electron microscopy (SEM). When needed, scanning Auger electron microscopy (AEM) was also used to identify the chemistry of the fracture origin(s).

Results

Microstructural Characterization: The typical microstructure for a polished surface of SX-G1 sample is shown in Figure 1. The brighter regions in the backscattered SEM image is deduced to be YAG. XRD also revealed that the major second phase in the SX-G1 is YAG. An etched microstructure is shown in Figure 2. The SiC grains are equiaxed with a narrow grain size distribution. The average grain size is estimated to be 1.5 μm.

Toughness and Strength: The fracture toughness, K_{IC}, determined as a function of temperature is shown in Figure 3. The K_{IC} of SX-G1 decreases from 4.05 MPa $m^{1/2}$ at room temperature to 2.6 MPa $m^{1/2}$ at 1370°C. The K_{IC} for single phase α-SiC is also shown for comparison.[2] Note that the K_{IC} for α-SiC remains unchanged at all temperatures, while K_{IC} for SX-G1 decreases at elevated temperatures.

It has been proposed that the increase in toughness of SX relative to SA is due to a microcracking mechanism resulting from residual stresses developed by the coefficient of thermal expansion (CTE) mismatch between SiC and YAG.[3] At elevated temperatures, the residual stresses are reduced and a decrease in fracture toughness is expected. The observation that toughness decreases with increasing temperature is hence consistent with the proposed toughening mechanism in SX-SiC materials.

Figure 1. Microstructure from the polished surface.

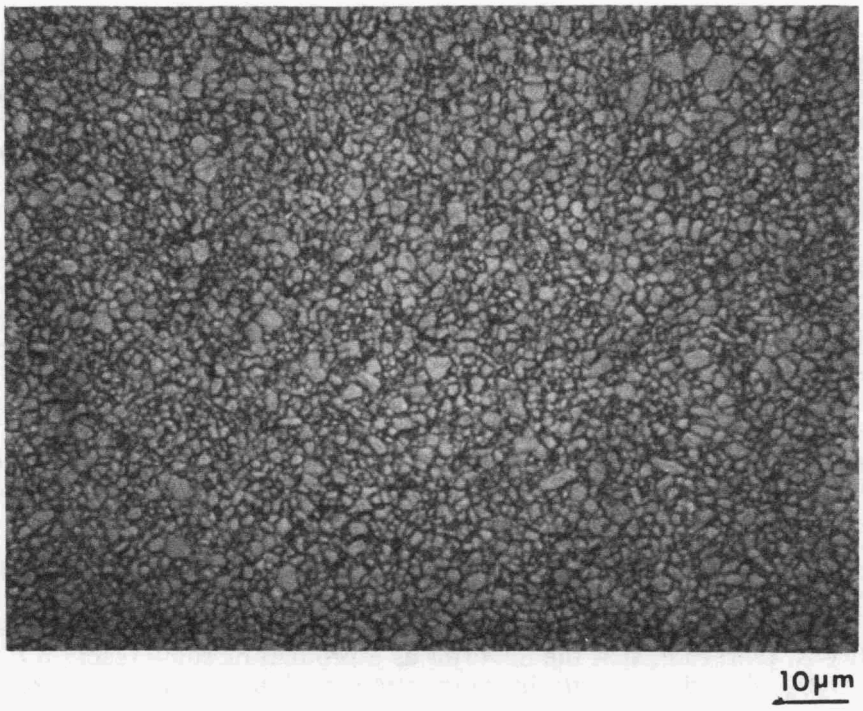

Figure 2. Microstructure from the etched surface.

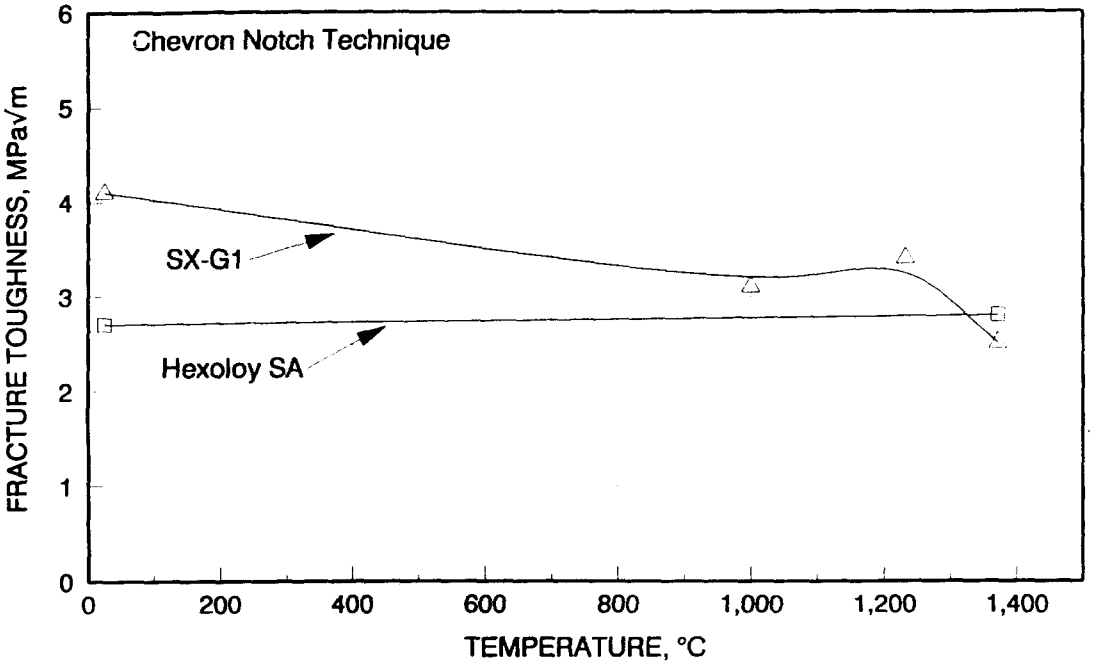

Figure 3. Fracture toughness of SiC materials as a function of temperature.

The strengths of SX-G1 measured from four-point bending and uniaxial tension at various temperatures are shown in Figure 4. Note that the uniaxial tensile strength variation with temperature is similar to that of the flexural strength. However, at a given temperature, the tensile strengths are consistently lower due to the larger effective volume of the button-head specimen. The strength decrease with an increase in temperature is consistent with the K_{1c} reduction at high temperature.

Strength Limiting Defects: Optical fractography was performed on all of the fractured specimens. Selected specimens were analyzed using SEM and scanning AEM. Figure 5 shows a fracture surface and failure origin from a typical flexure bar tested at room temperature. The same sample was examined in the Scanning Auger Electron microscope. Elemental mapping obtained from AEM suggest that the fracture origin consisted of elemental Si and Y-Al-O phases.

Similar volume flaws were identified as the strength limiting defects in all the tensile specimens tested at room temperature, 1000 and 1232°C. Figures 6 and 7 show typical fracture origins which are very similar to those observed in the flexural specimens.

It is interesting to note that although the strength limiting flaws are associated with the formation of elemental silicon and a nearby void area, the starting powder premix does not contain any significant amount of elemental Si to explain for the presence of Si in all the specimens. One possibility is, therefore, that the Si forms as a product of some reaction that occurs in the system $SiC-Al_2O_3-Y_2O_3$ during sintering as reported previously in the literature.[4]

The fracture behavior at 1370°C was different than that noted above. In the flexural tests, all the specimens failed from the surface. Figure 8 shows a typical fracture surface and failure origin. Note the appearance of a 'glassy phase' along the fracture origin. Elemental mapping of the 'glassy phase' was conducted in scanning AEM. The composition of the 'glassy' phase was deduced as $YAlSiO_x$. When the tensile specimens were tested at 1370°C and at higher stress rates (11 MPa/sec.), the failures were from a volume flaw as shown in Figure 9. This

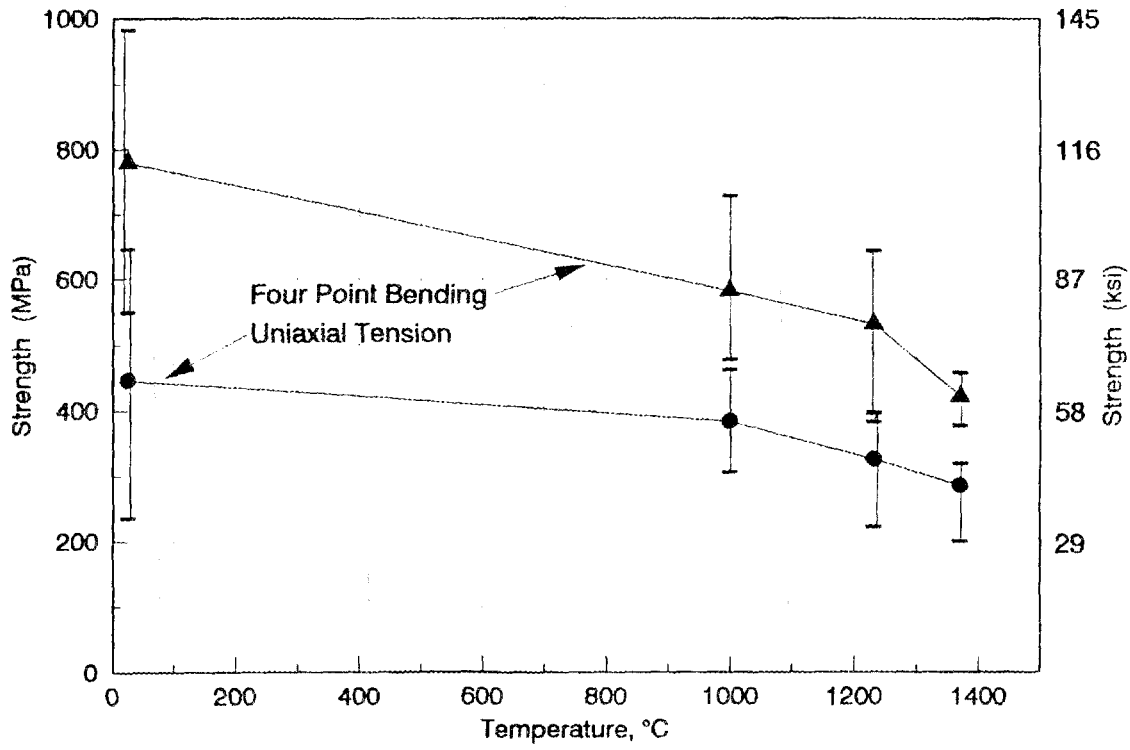

Figure 4. Flexure and tensile strength of SX-G1 as a function of temperature.

flaw is very similar to those shown in Figures 6 and 7. However, when the tensile specimens were tested at 1370°C under a lower stress rate (0.11 MPa/sec.), the failure originated from the surface, as shown in Figure 10. Such failure origins were very similar to the ones observed on the flexural specimens tested at 1370°C. The stress-strain plots for tension tests performed at 1370°C for various stress rates is shown in Figure 11. Note the non-linear behavior at lower stressing rates suggesting probable slow crack growth. The average strengths, Weibull modulus, and the defect type obtained from flexural tests, and tension tests are summarized in Tables 1a and 1b.

Fatigue Results: Dynamic fatigue experiments were done in four-point flexure at 1232 and 1370°C. Constant stress rates were used, which varied between 0.633 MPa/sec. to 63.3 MPa/sec. The average strengths measured at various stress rates are shown in Figure 12. The slow crack growth parameter is calculated using the relation:

$$\sigma_f \ \alpha \ \dot{\sigma}^{\frac{1}{N+1}}$$

where σ_f is the fracture strength, σ is the stressing rate and 'N' is the slow crack growth parameter. The slow crack growth parameter 'N' is calculated from the slope of the best fit regression line. At 1232°C there is very little reduction in strength at lower stress rates and hence a very high slow crack growth parameter of 51.6 was obtained. Also, the failures corresponded to volume defects, very similar to the defects observed in flexural bars used for strength evaluation, as shown in Figure 5. However, at 1370°C, there was a definite strength reduction at lower stress rates, indicative of slow crack growth (N=14.5). At 1370°C, all the specimens failed from surface flaws. The fracture origins were very similar to the one shown in Figure 8.

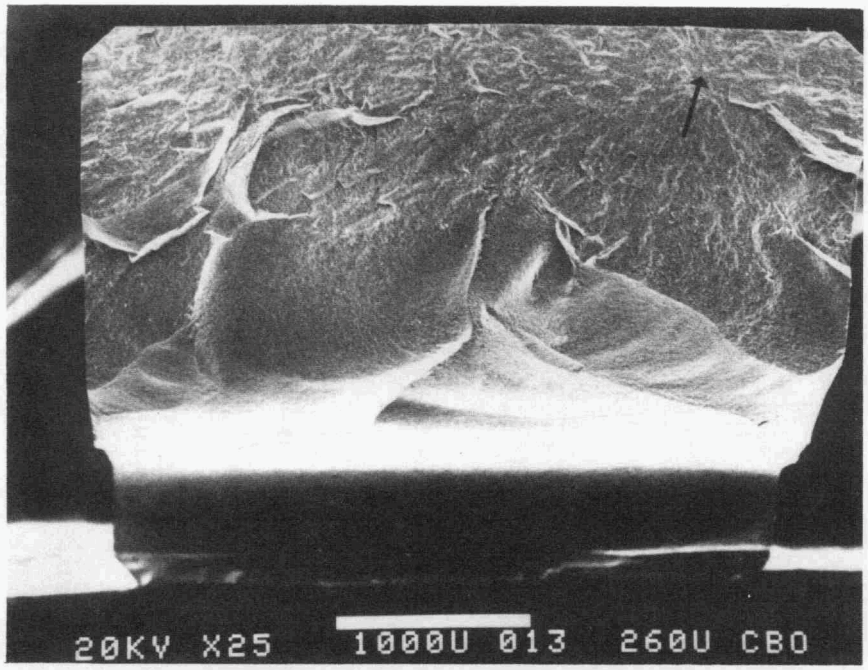

(a)

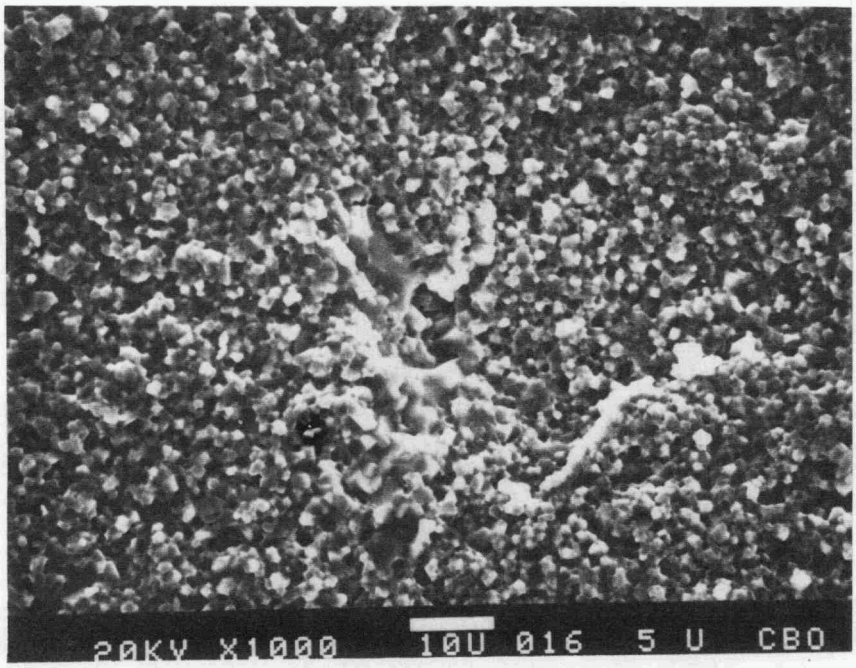

(b)

Figure 5. Fracture surface of a flexural bar tested at room temperature. Strength at Flaw = 786 MPa.

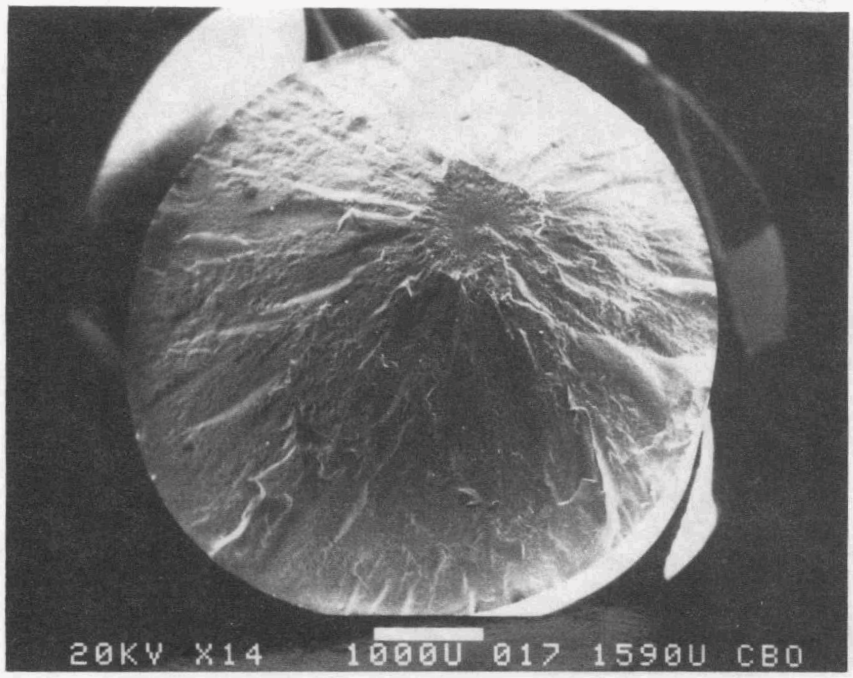

(a)

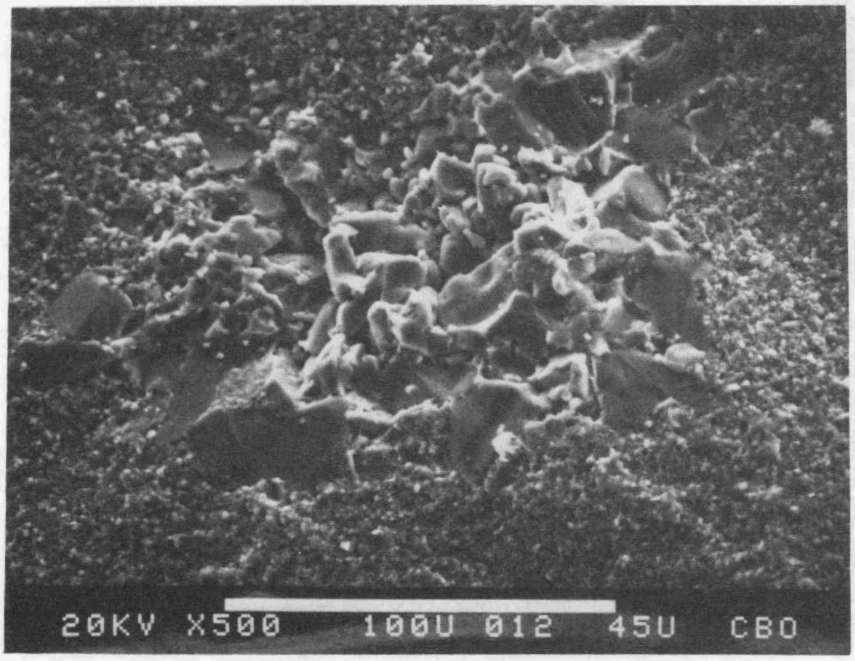

(b)

Figure 6. Fracture surface of a tensile specimen tested at room temperature. Tensile strength = 411 MPa.

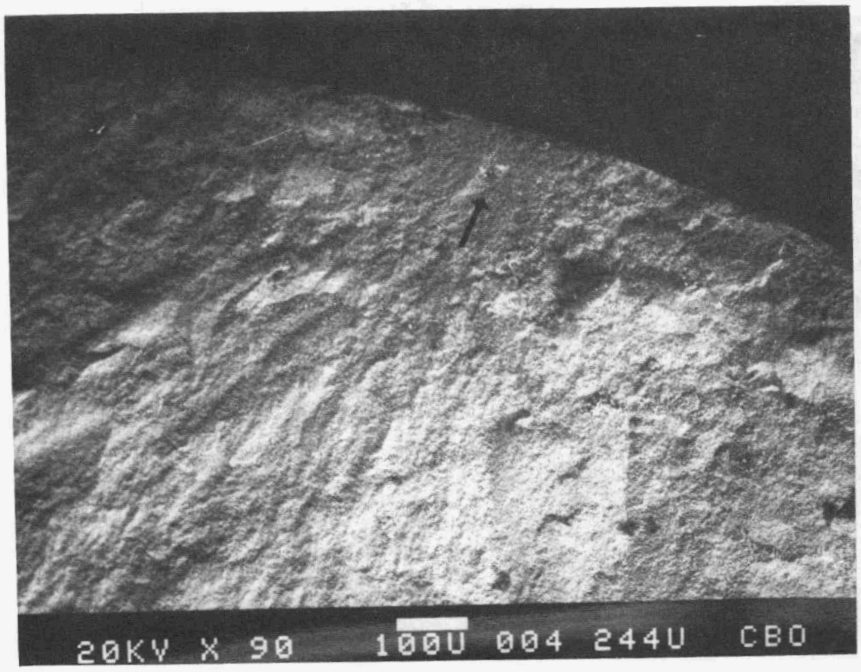

(a)

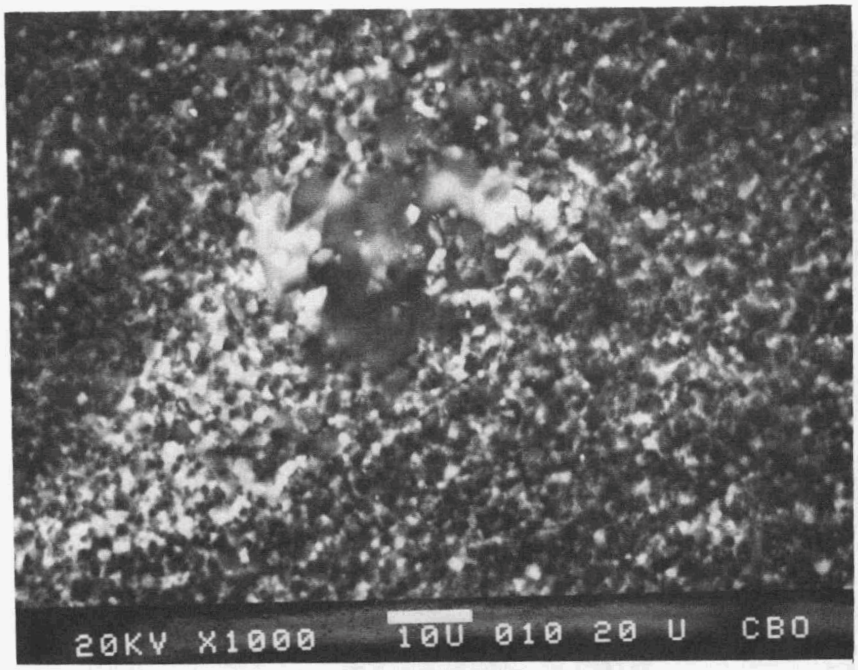

(b)

Figure 7. Fracture surface of a tensile specimen tested at room temperature. Tensile strength = 567 MPa.

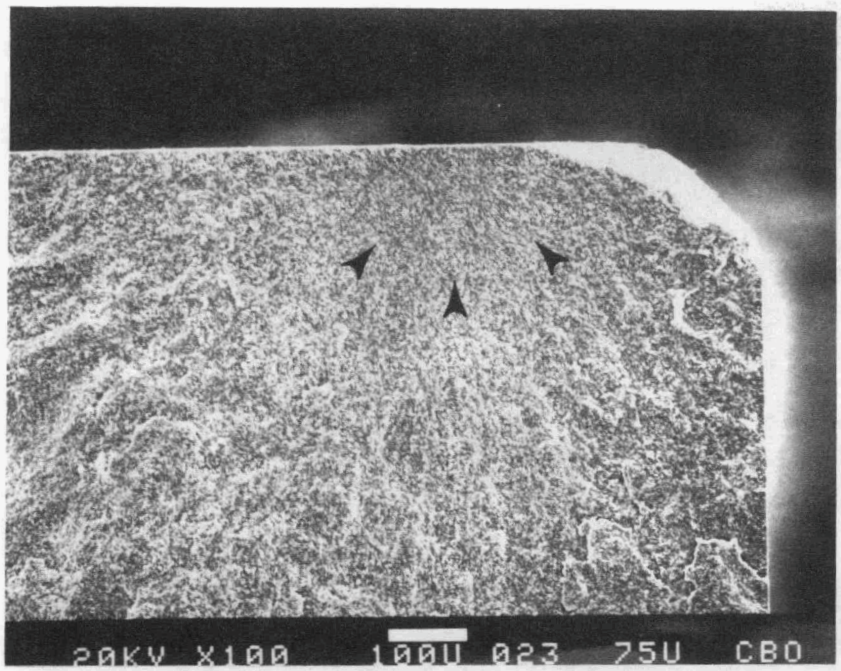

(a)

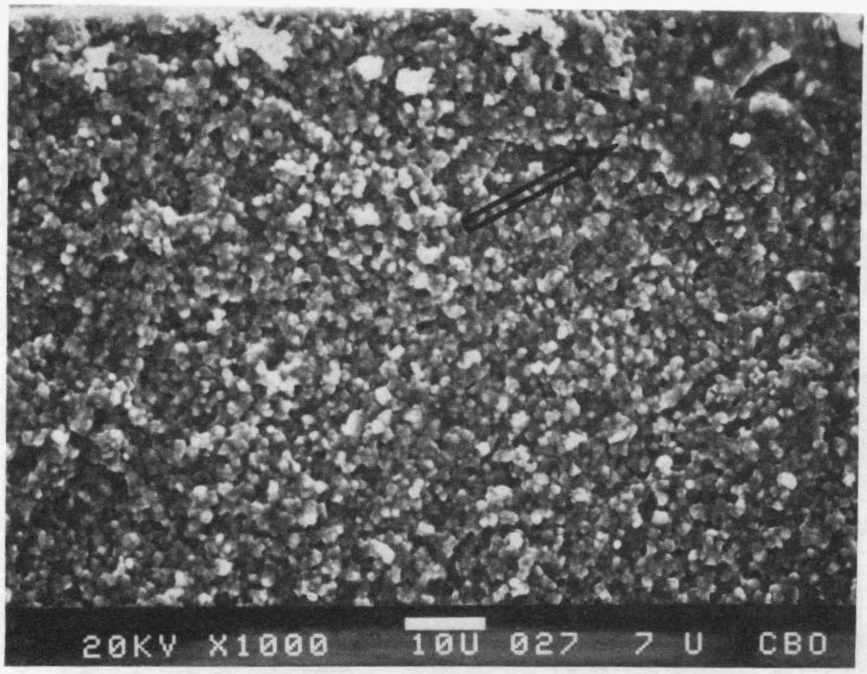

(b)

Figure 8. Fracture surface of a flexural bar tested at 1370°C. Flexural strength = 420 MPa.

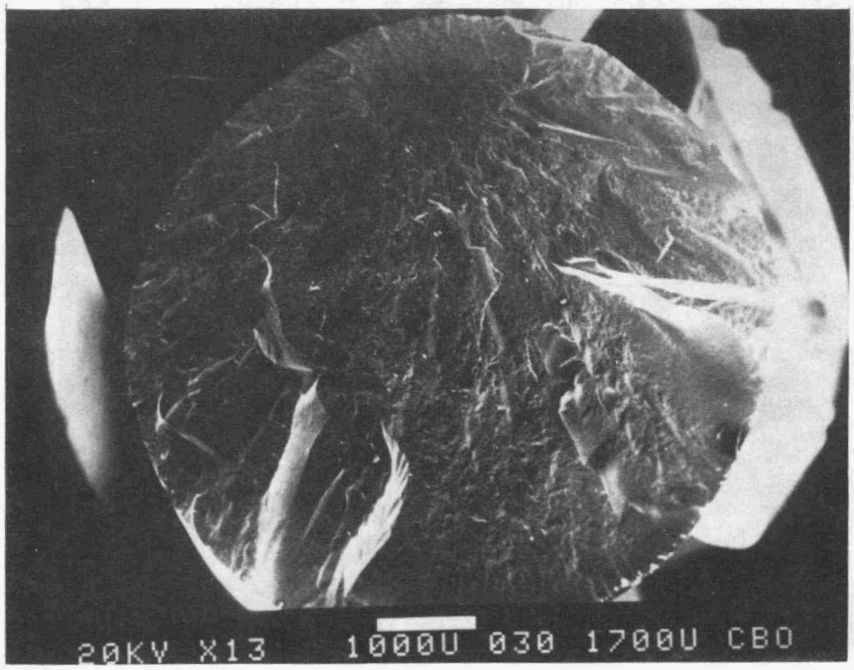

(a)

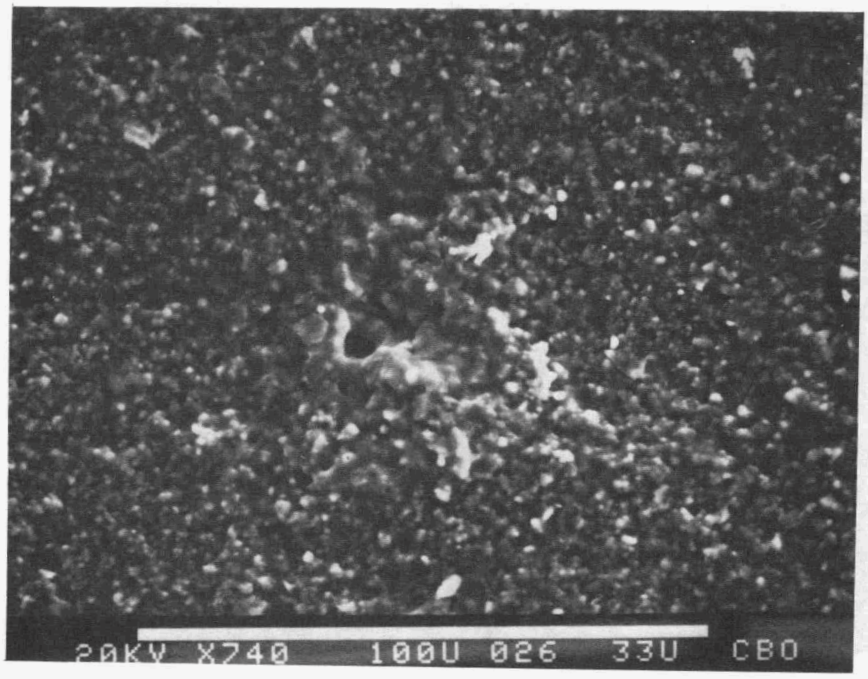

(b)

Figure 9. Fracture surface of a tensile specimen tested at 1370°C under a constant stress rate of 11 MPA/sec. Tensile strength = 309 MPa.

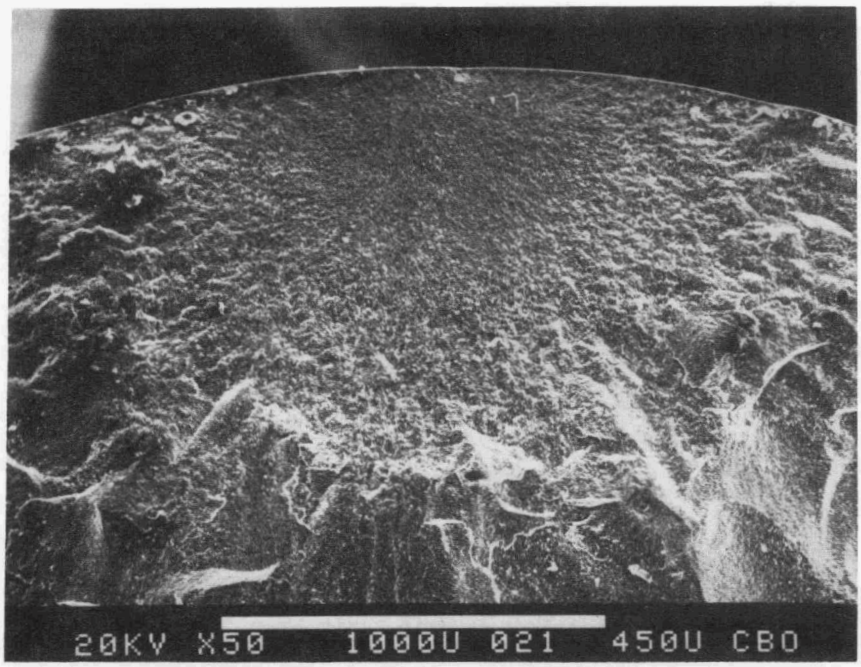

(a)

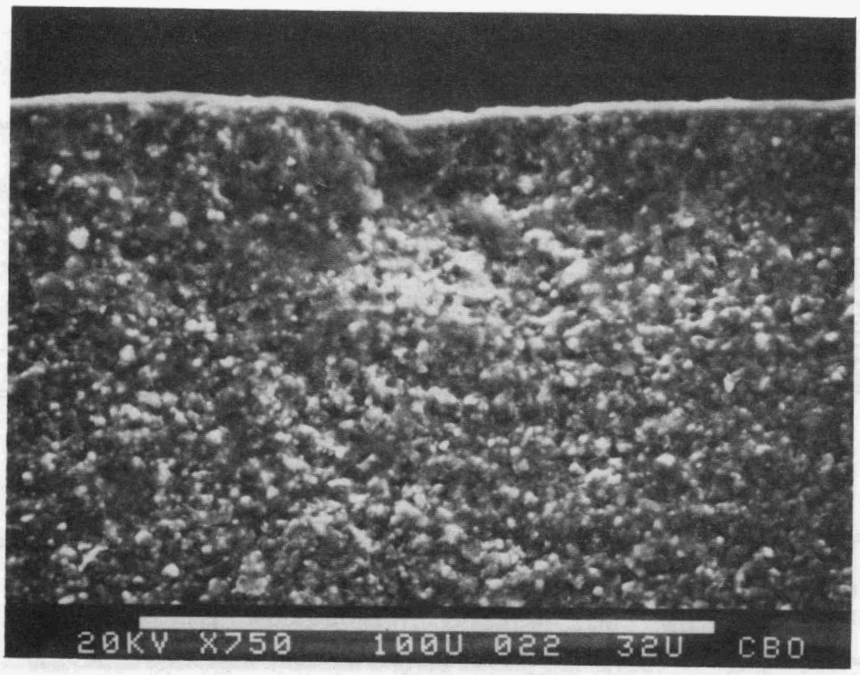

(b)

Figure 10. Fracture surface of a tensile specimen tested at 1370°C under a constant stressing rate of 0.11 MPa/sec. Tensile strength = 279 MPa.

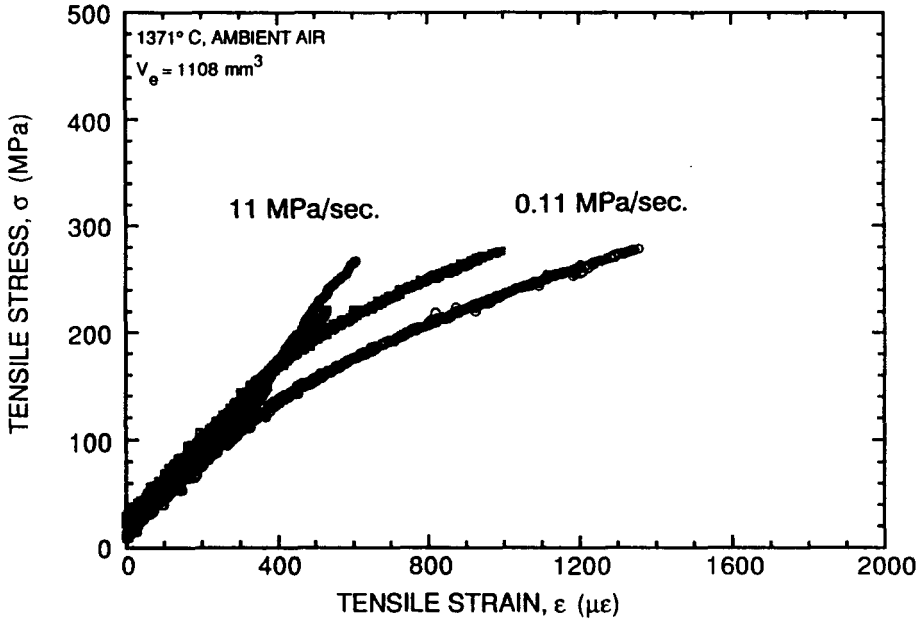

Figure 11. Stress-strain plots for tensile samples tested at 1370°C.

TABLE 1a
Flexure Data

Temp °C	MOR MPa (ksi)	Weibull Modulus	Flaw
RT	780 (113)	5.3	Volume defects, Si containing region
1000	580 (84)	8.2	"
1232	531 (77)	5.8	"
1370	421 (61)	10.3	Surface, glassy phase formation

TABLE 1b
Tensile Strength Data

Temp	# of Specimens	Stress Rate MPa/ sec	Ultimate Tensile Strength MPa (ksi)	Weibull Modulus	Flaw
RT	15	11	446 (64.7)	3.0	Volume defects, Si containing region
1000	8	11	384 (55.7)	6.5	"
1232	8	11	325 (47.2)	4.3	"
1370	6	11	286 (41.5)	4.5	"
	2	0.11	281 (40.8)	-	Surface, glassy phase formation

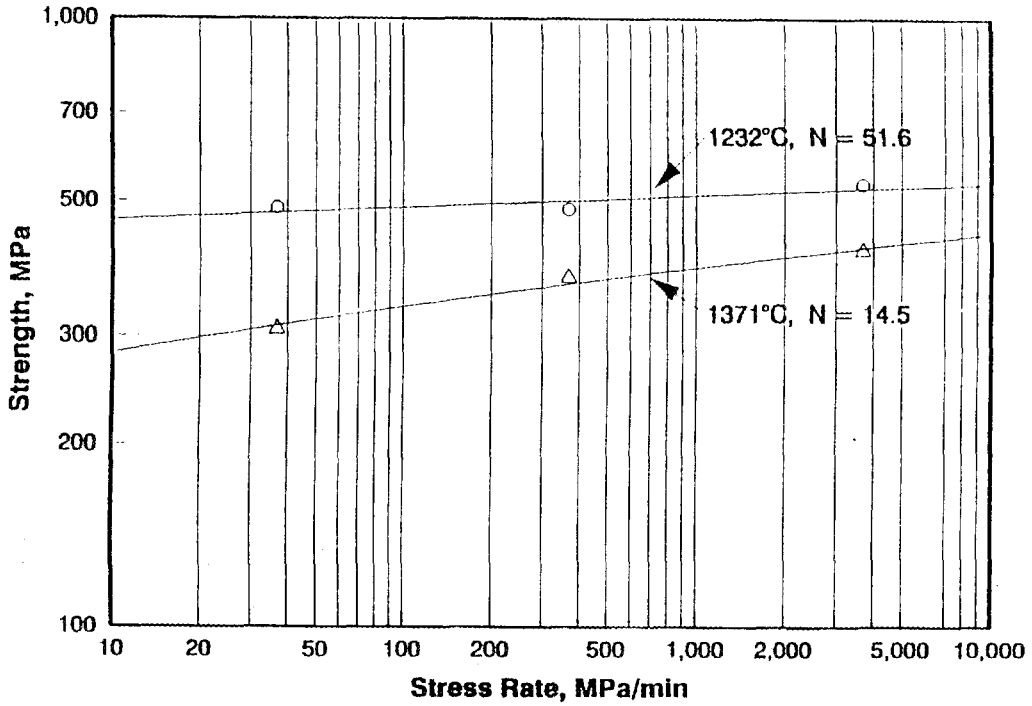

Figure 12. Dynamic fatigue behavior of SX-G1.

Stress rupture experiments were also conducted in four-point flexure at 1232 and 1370°C. The failure time for a given stress level was recorded and the applied stress vs failure time plot is shown in Figure 13. The slow crack growth parameter was estimated using the relation

$$t_f \ \alpha \ \sigma_{app.}^{N}$$

where t_f is the failure time, $\sigma_{app.}$ is the constant applied stress and 'N' is the slow crack growth parameter. The slow crack growth parameter was estimated as 75 at 1232°C. Again, a high value of N at 1232°C suggests very little or negligible slow crack growth or fatigue behavior. However, the fact that N decreased to 16.9 at 1370°C indicates that significant slow crack growth occurred at this temperature. These results are in good agreement with those obtained from the dynamic fatigue flexural results.

The slow crack growth here appears to be associated with the glass phase formation at the surface. Since the glass phase formation is associated with the tensile surface, this slow crack growth can be classified as environmentally induced slow crack growth.

Creep: Creep tests were carried out in uniaxial tension at 1260, 1370 and 1450°C. Very little or negligible deflection was recorded at 1260°C at stresses varying between 200 and 250 MPa. At 1370 and 1450°C measurable steady-state strain rates were obtained. Figure 14 shows a plot of steady-state strain rate vs applied stress at 1370 and 1450°C. A multiple lines regression analysis was used to determine the creep parameters from the generalized creep relation

$$\dot{\epsilon} \ \alpha \ \sigma^{n} \exp - \left(\frac{Q}{RT} \right)$$

where $\dot{\epsilon}$ is steady state strain rate, σ is the stress, and 'n' is stress exponent, Q is activation energy, R is gas constant, and T is the absolute temperature. The values of 'n' and 'Q' were estimated as 2.4 and 720 kJ/mol., respectively. Notice that the steady-state strain rates were between 10^{-9} and 2×10^{-8}/sec.

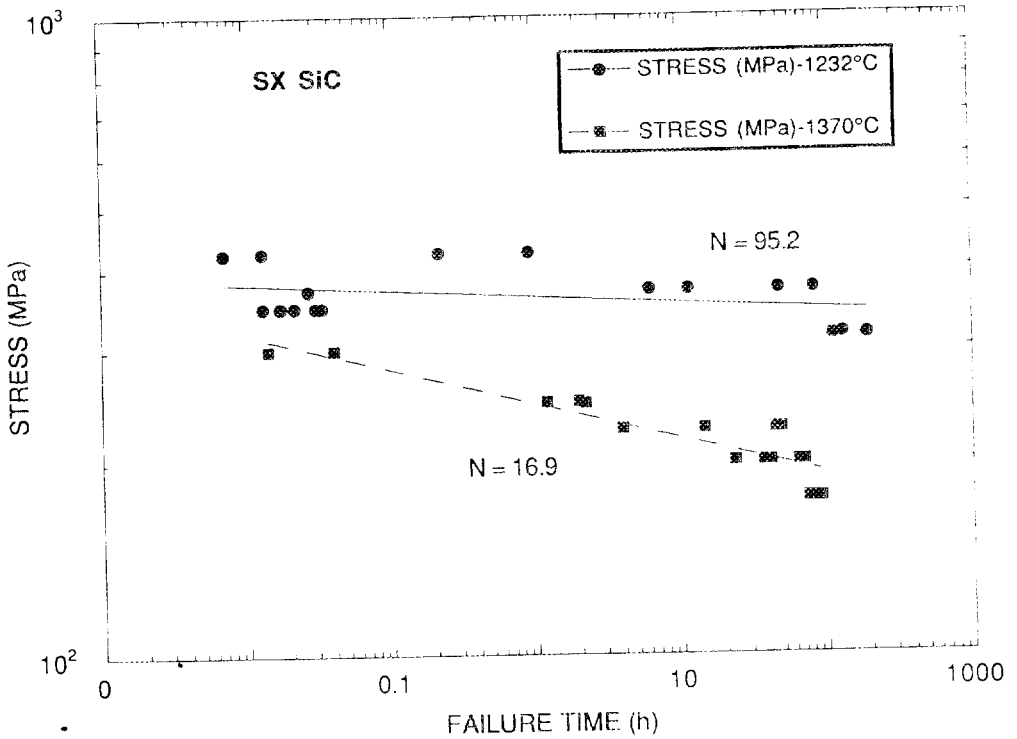

Figure 13. Stress rupture behavior of SX-G1.

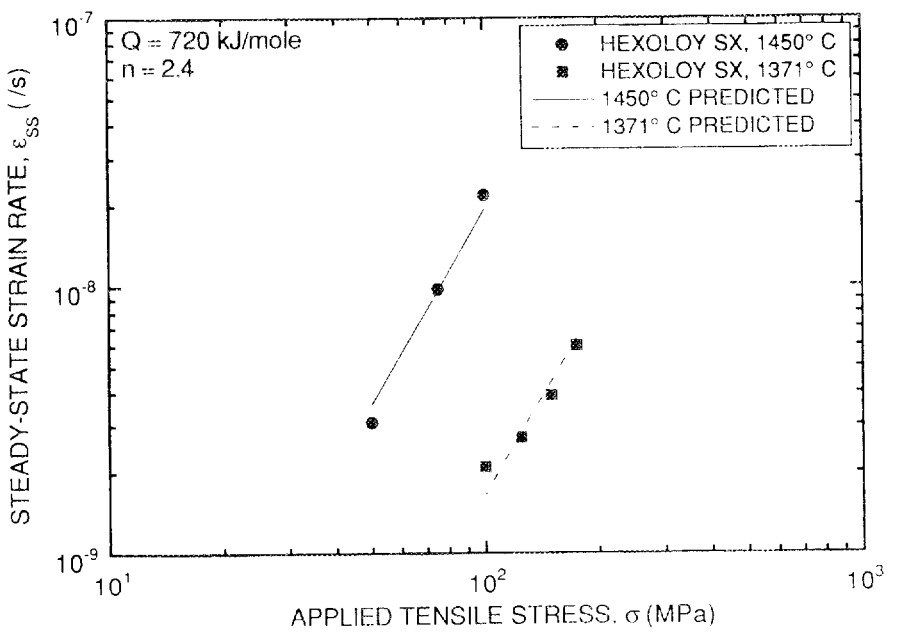

Figure 14. Strain rate vs. stress plots for SX-G1.

Summary of Task 1:

Extensive mechanical characterization on SX-Generation I composition has been completed with the following results:

- o A mean flexural strength value of 780 MPa has been obtained at room temperature.
- o Strength decreases at elevated temperatures, primarily due to reduction of K_{IC}.
- o The SX-G1 material appears to be susceptible to slow crack growth at 1370°C, while at 1252°C there was very little or negligible slow crack growth or fatigue behavior.
- o The SX-G1 material appears to possess good creep resistance, despite an oxide second phase in the material.

Task 2 Objective: SiC Powder Selection.

Experiments:

Five 2-1/2" square plates from each of the mixes made from SiC powder sources A, B, C, D, E and F were sintered and post-treated. The particle size distribution, surface area and sintered and final densities for these powders were reported in Table 2. Limited mechanical tests and fracture analysis were evaluated and the results were listed in Table 3.

Based on the sinterability and the mechanical strength data, powder A was selected for the remaining tasks.

Task 5 Objective: Development of an Improved Dispersion Process.

Experiments and Results:

For the Task 5 improved sintering aid distribution work, three approaches were explored. The first one was to use chemical precursor sintering aids. Three mixes were prepared with additives from chemical precursors. The total additive levels were 2 w/o, 2.5 w/o and 3.0 w/o. Sintered densities of 70%, 88% and 81% T.D. obtained were lower than controlled mix (95.5% T.D.). Chemical analysis for these 3 mixes showed relatively high free carbon contents (1.20 w/o, 1.15 w/o and 1.12 w/o). This was believed to be the cause of low sintered density.

The second approach was focused on improving premix uniformity by intensive grinding of sintering additives. Using the lab size attrition mill, the sintering additives were ground to a median size of 0.50 to 0.55 μm from an as-received size of between 3.0 to 4.9 μm.

With these grounded sintering additives. Three mixes were prepared with total additives of 2 w/o, 2.5 w/o and 3.0 w/o. Densities of 72%, 90% and 93% T.D. were obtained for these three mixes, again those densities were lower than the controlled mix.

High energy Turbomilling was the other technique investigated. Professor Wittmer of Southern Illinois University was retained as a consultant for this task. Using the Turbomill in his lab, high surface area mixes (up to 22.8 m^2/gm) were obtained. More significantly, green densities as high as 66% were achieved on filtered cakes. Samples were sintered and post-treated to high densities except the ones from WR5 mix was milled with sintered $Y\text{-}ZrO_2$ grinding media. It was suspected that contamination from $Y_2O_3\text{-}ZrO_2$ media wear was responsible for the poor sintering. It should also be noted that all these samples were prepared by a filter pressing technique without the use of any binder. As a result these filtered cake samples showed a lot of cracks after sintering.

Due to this cracking problem, only limited number of samples were obtained for MOR evaluation. These results are listed in Table 4. It can be seen that on the average, turbomilled SX samples showed higher MOR strengths than those of the traditionally prepared samples. A single all-time-high value of 1227 MPa has also been obtained.

TABLE 2

SiC POWDER AND SINTERING CHARACTERISTICS
FOR VARIOUS POWDER SOURCE WITH SX-G1 COMPOSITION

	As-Sintered Density % T.D.	Apparent Porosity v/o	Density After Post-Sinter Pressure Treatment % T.D.	Median Particle Size μm	90% of grains, ≤ x μm	% of grains ≤ 1 μm	Surface Area, BET m^2/gm
A	96.7	0.12	99.7	0.45	0.65	99.3	17.1
B	96.7	0.50	99.4	0.45	1.23	78.1	9.3
C	97.0	0.27	100.0	0.44	0.95	92.2	16.3
D	95.5	0.51	99.6	0.43	1.16	82.0	11.7
E	82.7	15.26	83.0	0.48	1.58	70.9	8.2
F	NA	NA	NA	NA	NA	NA	NA

Table 3
Task 2: Mechanical Properties for Various SiC Powder Sources

	Room Temperature				1371°C			
Powder Source	Toughness MPa.m1/2	MOR MPa	Weibull Modulus	Flaw*	MOR MPa	Weibull Modulus	Flaw	SCG Parameter
A	4.05	779	5.3	Volume, pools	420	10.3	SCG	14.5
B	4.43	627	4.5	Volume, pools	365	12.6	SCG	35
C	3.77	724	2.6	Volume, Agglm. Surface, Mach.	352	2.9	SCG	17.3
D	3.87	496	6.3	Volume, Voids	269	7.2	SCG & Voids	9
E	–	–	–	–	–	–	–	–
F	4.25	648	4	Volume, pools	338	15.4	SCG	63.4

*SGC – Slow Crack Growth

TABLE 4

Turbomilling Results

	Milled Time (hour)	Grind Media	Surface Area m^2/g	Post-Sinter Density g/cc	MOR R.T. MPa	# of samples
WR1	2	SiC	22.0	3.224	804	2
WR2	2	SiC	20.5	cracked	NA	
WR3	1	SiC	18.6	3.226	969	3
WR4	4	SiC	22.8	3.226	1231	1
WR5	0.5	$Y\text{-}ZrO_2$	NM*	cannot be densified	NM	
WR6	4	SiC	NM	3.220	903**	4
SX-G1+	NA***	SiC	16.0	3.22	779	20

*Not measured.
**Average strength 131 ksi, highest individual strength is 170 ksi.
***Not applied.
+Conventional process.

To eliminate the cracking problem, a sixth turbomilled batch duplicating mix WR4 was prepared. Instead of using filter-caking with no added binder, this time spray drying with an added binder was used. It was found that the cracking problem was indeed resolved. The average strength of the samples fabricated from the spray drying route was 903 MPa, with a highest single value of 1172 MPa. Nevertheless, the sinterability was not consistent, because a second plate processed the same way was found to exhibit a very low density (<95% T.D.). However, based on the exceptional mechanical properties achieved, turbomilling was chosen as the processing technique for the rest of the tasks for further study.

Task 3 Objective: To optimize the current SX-G1 material through an experiment design methodology.

The experimental plan for Task 3 has been established based on a design experimental approach to optimize the furnacing and post-treatment conditions for SX-G1. The experimental variables chosen included sintering temperature, post treatment temperature and pressure. The responses to be monitored included sintered and post-treatment density, room and high temperature MOR and K_{1c} as well as dynamic fatigue at 1232°C. Concurrence of the ORNL technical monitor was obtained. Five powder mixes were prepared by turbomilling at South Illinois University using a new batch of SiC grit as grinding media.

Sintered densities for these five mixes were between 90 to 94% T.D., as compared to >95% for the earlier turbomilled samples. After post-treatment, the densities obtained were in the range of 92 to 97%, still below full density. To understand the reason for this low density, particle size analysis for these 5 mixes were conducted. Larger particles (≥ 1 μm) were detected with a Horiba analyzer. BET surface area measurements of these turbomilled mixes were

between 16.0 to 17.2 m^2/g as compared to >20 m^2/g obtained on earlier turbomilled samples. Both results indicated the presence of large particles which are believed to be coming from wearing of SiC grit grinding media.

Review of powder processing data also confirmed that there was about 250 grams of media wear from the grinding grit for each 1500 gm batch mix. Such excessive wear of grinding media can have significant effect on retarding the sintering kinetics.

Earlier Task 5 turbomilled sintered samples were also revisited for analysis of fractured surfaces. In one set of the samples that densified poorly, excess grit concentration was observed on both etched microstructure and fractured surfaces. In another set that densified well and exhibited strengths in excess of 896 MPa (as high as 1227 MPa), fracture analysis revealed no obvious fracture origin but no evidence of Si pools nor large grits was found. In other plates that also densified well but with somewhat lower strengths (ranging from 620 to 896 MPa), occasional grits were found and they were also determined to be strength limiting defects. An example of the microstructure with the large grits is shown in Figure 15.

These results reveal that although turbomilling has shown the potential of achieving exceptionally high mechanical properties, processing reproducibility is a major issue. These results were reported to ORNL in a review meeting held on April 2 at Carborundum.

Plan: Inconsistent sintering due to excessive and nonuniform wear of SiC grit media is a major current issue. Several approaches are being investigated to determine whether and how this problem can be solved.

Travel

G.V. Srinivasan travelled to Oak Ridge to conduct tensile testing, stress rupture and creep experiments at HTML/ORNL during October to December of 1991.

Publications

"Mechanical properties Evaluation of Generation I SX-SiC," G.V. Srinivasan, K.Y. Chia, S.K. Lau, R.S. Storm, M.K. Ferber and M.G. Jenkins. Accepted for presentation/publication at the ASME/IGTI Annual meeting at Cologne, Germany, June 1992.

Acknowledgement

The authors wish to acknowledge the valuable assistance provided by Dr. M.K. Ferber and Dr. M.G. Jenkins of HTML/ORNL in conducting the stress rupture, and uniaxial tension tests at HTML.

References:

1. Chia, K.Y., and S.K. Lau, "High Toughness Silicon Carbide," Ceramic Engg. and Science Proceedings, 12 [9-10], pp. 1845-1861 (1991).

2. Seshadri, S.G., and M. Srinivasan; unpublished work, 1980-1981.

3. Evans, A.G., Presentation at 92nd Annual Meeting of the Amer. Ceram. Soc., (1990).

4. Omori, M., and H. Takei, "Preparation of Pressureless-Sintered $SiC-Y_2O_3-Al_2O_3$," J. Mater. Sci., 23, pp. 3744-49 (1988).

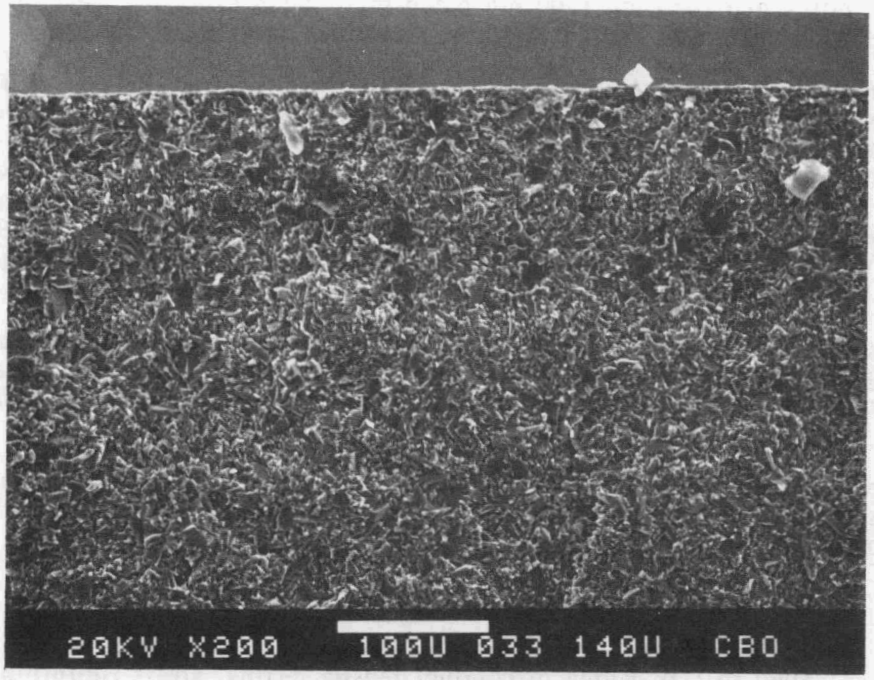

Figure 15. Poor densification due to excess concentration of grits.

1.1.2 Silicon Nitride

Improved Processing of Ceramic Composites

D. E. Wittmer (Associate Professor, Southern Illinois University at Carbondale, Carbondale, IL 62901)

Objective/Scope

The purpose of this work is to continue the investigation of the turbomilling process as a means of improved processing for SiC whisker-ceramic matrix composites and dispersion of matrix powders prior to composite processing.

Technical Progress

Phase II is divided into 4 major tasks:

Task 1. Beneficiation of SiC whiskers.
Task 2. Development of aspect ratio reduction parameters.
Task 3. Dispersion Trials and ß-Si_3N_4 Seed Development
Task 4. Development of ß-Si_3N_4 Seed
Task 5. Development of Self-Reinforced Si_3N_4 with Reduced Sintering Aids
Task 6. Final Report

Task 1. Beneficiation of SiC whiskers

Task 1 was completed ahead of schedule as reported previously.

Task 2. Development of aspect ratio reduction parameters.

Task 2 was completed as reported previously.

Task 3. Dispersion Trials and ß-Si_3N_4 Seed Development

Task 3 was completed as reported previously.

Task 4. Development of ß-Si_3N_4 Seed

Task 4 was completed Completed as reported previously.

Task 5. Development of Self-Reinforced Si_3N_4 with Reduced Sintering Aids

Task 5 was completed during this reporting period. During this reporting period work has continued on the preparation and property measurement for A2Y6 and A4Y6 compositions with the addition of 5 wt.% ß-Si_3N_4 seed produced as part of Task 4. Several discs processed by turbomilling and pressure casting have been isopressed and sintered. Some of these discs have been sent off for machining into test bars, while others are being held until the room temperature flexural strength measurements have been completed. Because of delays in completion of this task, a no cost extension extend the contract to March 31, 1992.

The 4-pt flexural strength of 10 standard 3X4X45 mm bars averaged 1.15+/-.07 GPa and the fracture toughness for 8 test bars (40 indentations) was 11.5 to 13.1 MPa-$m^{1/2}$ by the Cook and Lawn controlled flaw method and 7.7 to 7.9 MPa-$m^{1/2}$ by the Chantikul, et al. strength method. Data determined previously was 958-1075 MPa for the 4-pt flexural strength for the baseline A4Y6-Si_3N_4 (6 bars) and 875-988 MPa for the seeded A4Y6-Si_3N_4 (6 bars). Fracture toughness, using the Lawn and Cook modified indentation method was found to be 8-10 MPa-$m^{1/2}$ for the baseline Si_3N_4 (4 bars) and 10-13 MPa-$m^{1/2}$ for the seeded Si_3N_4 (4 bars). This recent data shows some improvement over the previously reported data and supports earlier conclusions that ß-Si_3N_4 seeding of Si_3N_4 compositions containing low amounts of sintering aids can provide for enhanced toughening. Materials have been submitted to AMTL for high-temperature flexural strength and possibly creep rupture testing.

A rough draft final report was submitted and is presently being reviewed.

Status of Milestones

1. Run Beneficiation Trials and Report in Bimonthly	Completed
2. Run Aspect Ratio Reduction Trials and Report in Bimonthly	Completed
3. Run Matrix Dispersion and Report in Bimonthly	Completed
4. Develop ß-Si_3N_4 Seed and Report in Bimonthly	Completed
5. Develop Self-Reinforced Si_3N_4 with Reduced Sintering Aids and Report in Bimonthly	Completed
6. Rough Draft of Final Report to Contract Monitor	Completed

Publications

D. E. Wittmer, T. E. Paulson and D. Doshi, Southern Illinois University Carbondale, IL and C. W. Miller, Jr., Centorr Furnaces/Vacuum Industries, Inc., Nashua, NH, "Improved Processing and Cost Effective Sintering of Si_3N_4 ," Contractor's Coordination Meeting, October 27-31, 1991, Dearborn, MI.

D. H. Doshi, "Microstructural Development of Si_3N_4 ," Thesis for Master of Science in Mechanical Engineering, Dept. of Mechanical Engineering and Energy Processes, Southern Illinois University, Carbondale, IL, October (1991).

D. E. Wittmer, D. Doshi and T. E. Paulson, "Development of β-Si_3N_4 for Self-Reinforced Composites," Ceramic Engineering and Science Proceedings (to be published in **13** [9-10] (1992).

Presentations

D. E. Wittmer*, T. E. Paulson and D. Doshi, Southern Illinois University Carbondale, IL and C. W. Miller, Jr., Centorr Furnaces/Vacuum Industries, Inc., Nashua, NH, "Improved Processing and Cost Effective Sintering of Si_3N_4 ," Contractor's Coordination Meeting, October 27-31, 1991, Dearborn, MI.

D. E. Wittmer, D. Doshi and T. E. Paulson, "Development of β-Si_3N_4 for Self-Reinforced Composites," Presented at the 16th Annual Conference on Composites and Advanced Ceramics, Cocoa Beach, FL, Jan. 7-10, 1992. 16th Annual Conference on Composites and Advanced Ceramics, Cocoa Beach, FL, Jan. 7-10, 1992.

Characterization of Attrition Milled Silicon Nitride Powder

S. G. Malghan and D. B. Minor
(National Institute of Standards and Technology)

Objective/Scope

Currently, the starting materials in the manufacture of silicon nitride ceramic components are fine powders. These fine sized powders tend to form agglomerates due to the van der Waals attractive forces. For improved reliability in the manufacture of ceramic components, the agglomerates in the powders should be eliminated since they form defects. In addition, the powders should have an appropriate range of size distribution and specific surface area for achieving a near-theoretical density of the ceramic after densification. These factors necessitate the use of powder milling as one of the major powder processing unit operations. Therefore, milling of powders is an integral unit operation in the manufacture of silicon nitride components for advanced energy applications. The production and use of these powders require the use of efficient milling techniques and understanding of characteristics of the milled powders in a given environment. High energy attrition milling appears to offer significant advantages over conventional tumbling and vibratory mills.

The major objectives of this project are: 1. establish repeatability of particle size distribution and other relevant characteristics of slurries milled in a high energy agitation mill (HEAM); 2. determine processing and densification characteristics of powders milled in HEAM; and 3. compare properties of powder, and resulting ceramic obtained by milling in the HEAM vs. vibratory ball mill in a collaborative project with Norton Company.

Technical Progress

In the past three years, this project has accomplished the following:

1. Extensive data were obtained on the physical, bulk chemical and surface chemical properties of the milled powder which established the feasibility and merits of the HEAM.

2. Interrelationships were established between parameters of the HEAM and resulting physical and chemical properties of the Ube silicon nitride powder.

3. A predictive model of the HEAM system was developed for process simulation and evaluation. Using the model parameters, particle size distributions were simulated for a number of different milling conditions.

The data and understanding developed until now have established the superior characteristics of the HEAM (fast milling kinetics,

flexible modification of particle and powder morphology, ability to control the level of impurities, ability to prepare high density suspensions, and elimination of separate mixing and sintering-aid unit operations). However, a need exists to obtain data on the repeatability of the powder characteristics produced from the HEAM and evaluation of the powder in relation to that produced by conventional methods.

In the current program, the following four tasks are addressed:

1. Repeatability of Powder Properties - A series of statistically designed milling tests are being conducted in which repeatability of the milling system with respect to the properties of milled powders will be examined. The specific properties included for evaluation are; median and interquartile range of particle size distribution, specific surface area, isoelectric point, acoustophoretic mobility, and concentration of oxygen and carbon. The milling experiments will be carried out under fixed experimental conditions.

2. Processing of Powders Milled in HEAM - A number of advantages in terms of powder properties obtained from the HEAM have been established. However, a need exists to demonstrate the beneficial effects of these powders by processing and densification. The processing of these powders constitutes colloidal mode of sintering-aids addition by utilizing electrostatic interactions between oppositely charged Si_3N_4 and Y_2O_3 particles in an aqueous suspension. The suspension densities will be maintained at a high level. The purpose of these steps is to increase homogeneity of sintering-aids at low water content of the slurries. The powders processed in this manner will be pressure cast. The green bodies produced in this manner will be characterized for density, porosity, and homogeneity of sintering-aid and binder distribution. Finally, selected samples of green bodies will be densified for evaluation of microstructure.

3. Comparison of Milled Powder Properties - This effort will be carried out in collaboration with Norton Company in conjunction with the DOE-ORNL contract on processing for reliability. Milling of powders will be conducted at NIST and Norton Company with an objective to obtain the same particle size distribution and interquartile range. The Y_2O_3 addition will be carried out by co-milling and under optimum pH conditions of electrostatic attraction. The resulting slurries will be pressure cast and the green body will be densified by hot isostatic pressing. The dense ceramics will be evaluated to identify differences in the microstructural and mechanical properties.

4. Simulation Model Refinement - Using the milling data developed in these tests, the simulation model will be refined in terms of parameters improvement and incorporation of energy consumption in

the breakage rate function. This refinement will increase the model capability in terms of scale-up, off-line simulation and process control for intelligent processing.

During this period, milling experiments were conducted to evaluate the effects of weight ratio of SNE-5 and SNE-10 in the starting feed, milling at pH 5.8 in the presence of Y_2O_3 and time of yttria addition. The primary purpose of these experiments was to develop a standardized procedure for obtaining high density suspensions without sacrificing homogeneity and milling kinetics.

In the initial experiments with 60/40 weight % mixture of SNE-5/SNE-10 Ube powders, the purpose was to test the feasibility of milling at pH 5.8 ± 0.2. Milling tests were conducted in the presence of 4% (weight) Y_2O_3 powder in aqueous suspension of 55% volume (V) solids and 150 ppm (based on solids weight) polyacrylate surfactant. These parameters were selected based on milling of SNE-3/SNE-5 under the above mentioned milling conditions, except for pH 9.0 and absence of Y_2O_3. However, acoustophoresis and surfactant adsorption measurements had indicated that a pH of 5.8 was the most appropriate for achieving strong repulsion due to electrostatic and electrosteric interaction. At pH 5.8, silicon nitride particles carry a net negative surface charge; whereas, the yttria particles carry a net positive surface charge. By milling at pH 5.8, homogeneous mixing of silicon nitride and yttria can take place due to electrostatic attraction between oppositely charged particles. During milling, however, we were unable to increase solids loading beyond 35% V of slurry. Extensive agglomeration was found to inhibit further loading of solids into the slurry and pumping of this slurry through the mill became difficult. Data on particle size distribution and specific surface area of powders obtained in one of the milling experiments were presented in December 1991 report. The d_{50} of starting powder is approximately 1.2 μm. However, the powders analyzed from milling experiments exhibited d_{50} values as large as 2.3 μm even after milling for 160 min. The measured size distributions were certainly those of agglomerates resulting from interaction of silicon nitride and yttria particles in the presence of a polyacrylate dispersant. Even the specific surface areas of the powders that were obtained from milling slurries at various intervals were affected. It appears that extensive agglomeration had taken place under these conditions of slurry preparation. The increase of specific surface area of milled powders after milling for 60 min. is probably due to deagglomeration of agglomerates produced during slurry preparation. Another experiment was attempted by increasing the slurry pH to 6.8 ± 0.2. No improvement in solids loading was obtained.

At this stage, the milling experiments were discontinued, and silicon nitride and yttria powders were examined separately in aqueous suspensions in order to identify appropriate dispersion parameters. These experiments included settling studies and agglomerate size distribution at different pH and dispersant concentration in the slurry. These results showed that the concentration (100 to 500 ppm) of polyacrylate dispersant (Daxad 32) had very little influence on the d_{50}

of both powders at pH 9.0. Since one of our objectives is to use a minimum concentration of the dispersant, settling experiments were conducted at 100 ± 15 ppm at different pH of the suspensions. These data for SNE-5/SNE-10 mixture clearly demonstrated that the suspensions were highly stable only at pH 9.0; whereas, extensive settling was observed at lower pH. The agglomerate size distribution was found to be larger at lower pH values.

Second activity was to evaluate potential for high density suspensions preparation. Since the particle size distribution of Y_2O_3 is much coarser than that of silicon nitride, two alternatives were examined in which the Y_2O_3 was added either at t = 0 min. or t = 45 min., where t is milling time. In these experiments, the total milling time was 160 min., and milling was carried out at pH = 9.0 in the presence of 150 ppm Darvan C. At this pH, silicon nitride particles carry a strong net negative charge; whereas, the Y_2O_3 particles are expected to carry a weak positive charge, assuming that very small concentration of polyacrylate ions is available for adsorption of Y_2O_3 particles. In this experiment, a solids loading of 51% V (76% by weight) was easily achieved at about 45 min. of milling time. The rate of increase of specific surface area appears to be a linear function of milling time. In our studies, the measurement of agglomerate size is emphasized more than that of viscosity. These data indicate that the decrease of median size is fairly rapid in the initial period. However, at longer milling times, due to crowding effect of particles, the milling rate decreases. However, the median size continues to decrease. Further evidence of this was obtained by observing the entire size distribution of samples taken at milling times 0 through 160 min. We found that the size distribution did not expand in the fine end of size distribution curve, indicating that extreme fine sizes were not produced, while deagglomeration was more dominant. A sample of the milled slurry was cast and the resulting green body was studied by electron microscopy for Y_2O_3 distribution. These data showed that the distribution was highly uniform.

Subsequently, experiments were conducted to examine the impact of starting with a well-dispersed Y_2O_3 suspension to which silicon nitride powder was added. Therefore, Y_2O_3 was added at the initial period right after the addition of dispersant to pH-adjusted distilled water. The resulting slurry of Y_2O_3 thickened, and caused difficulty in the addition of silicon nitride powder to 51% V. Normal time to add the required weight of silicon nitride powder in the absence of Y_2O_3 is about 20 minutes. In this experiment, the time required was 45 min., which indicates that the Y_2O_3 particles may have formed agglomerates as a result of electrostatic interaction with polyacrylate ions. Subsequent addition of silicon nitride powder to the agglomerated slurry of Y_2O_3 could have induced more agglomerates to form. However, powders milled in this experiment exhibited the highest specific surface area, 15.1 m^2/g. We are studying the cause of this behavior. In a subsequent experiment, Y_2O_3 was added after milling silicon nitride for 20 min., and the entire powder addition was completed within 30 min. The final solids content in this experiment was 51% V. Final specific surface

area after milling for 160 min. was 10.9 m^2/g, which is much lower than that of the previous experiment where Y_2O_3 was added at t = 0 min. The difference in the specific surface area was accompanied by a slight decrease in particle size distribution in a test where Y_2O_3 was added at t = 0 min. One possible explanation for this is precipitation of some type of a complex between Y_2O_3 and/or Y^{3+} ions and polymethacrylate ion. This complex could have formed at the beginning of the milling test. An indirect proof of this type of interaction is seen in the higher surface area of powder samples obtained at various milling times when Y_2O_3 was added at t = 0 min.

Based on these and additional tests conducted in this series, an experimental procedure has been developed. This procedure consists of fixing all the parameters of powder, mixing, milling, and dispersion so that repeatability of the milling procedure can be established. Currently tests are in progress to assess repeatability.

Status of Milestones

On target.

Communications/Visits

None

Publications

None

Sintered Silicon Nitride

J. Mangels (Ceradyne Inc.)
G. E. Gazza (Army Materials Technology Laboratory)

Objective/Scope

The program is currently conducted on contract to Ceradyne Inc. with support from AMTL. The contract has the overall objective of developing scale-up processing conditions for a silicon nitride material having the general composition 85.8m/o Si_3N_4-4.73m/o Y_2O_3-9.47m/o SiO_2-1.0m/o Mo_2C and characterizing the properties of this composition with the goal of producing complex components for testing in related heat engine programs. The first task of the program will concentrate on processing studies and data base generation while the second task will focus on producing and characterizing engine components.

Technical Highlights

I. Sintering of Matrix 4 (mix 6 & 7) Compositions

Matrix 4 billets 4" x 4" x 1/2" in size were isopressed from the Matrix 4 powders (with 0 and 1 mol% Mo_2C) to be used for mechanical testing of the material after sintering. A processing temperature of 1850C for 5 hours was chosen for both compositions based on results from previous runs. A total of four sintering runs were conducted, MTL 23-26. MTL run 23 was performed on half billets in two different packing powders (with 0 and 2% SiO_2 additions) in order to establish which of the packing powders should be used as well as to verify the sinterability of larger samples. Since samples of both compositions sintered to density only in 0% SiO_2 packing powder (Table 1), it was chosen for all the remaining runs.

Densities: Full size billets sintered in MTL runs 24-26 all reached density irrespective of composition. Billet densities for mix 6 were 3.258 ± 0.003 g/cu.cm and for mix 7, 3.278 ± 0.006 g/cu.cm. About 50% of the billets experienced shrinkage induced cracking that originated from the billet edges and extended radially into the billet for up to approximately 1/2 in. Cracks were observed on samples of both compositions. It is believed that this problem could be overcome by slowing down the heating rate in the last 100C temperature range and by changing the way the parts are loaded in the sintering furnace.

Weight losses of billets with no Mo_2C ranged from 1-2%. Billets with Mo2C had losses of 1.5-3.6%. These values are typically lower than for smaller samples which were used in previous Matrix 4 sintering runs.

Samples were found to contain $Y_2Si_2O_7$ (card #22-1103) as a second phase irrespective of which composition was used. Molybdenum carbide or silicides were not detectable on XRD.

Surfaces of polished samples were examined and were similar to surfaces observed in Matrix 4 on smaller samples. In general, mix 7 samples (containing 1 mol% Mo_2C) appeared to contain more pores and have a larger average pore size than samples from mix 6.

TABLE 1. Characterization of sintered samples of mix 6 (0% Mo_2C) and mix 7 (1m/o Mo_2C) for run MTL 23

Temperature-1850C time-5 hrs.
Packing powders: (1) 0% SiO_2 (2) 2% SiO_2
parts: rods and half billets crucible: graphite

Parts	mix 6		mix 7	
packing powd.	(1)	(2)	(1)	(2)
wt. loss (%)				
half-billet	1.600	0.400	2.100	1.300
rod	1.000	0.700	2.600	2.200
density				
half billet	3.257	3.119	3.286	3.068
rod	3.259	3.230	3.294	3.271
% Theor.	0.999	0.957	0.999	0.933
	1.000	0.991	1.001	0.994
Phase compos.				
half billet	a-$Y_2Si_2O_7$		a-$Y_2Si_2O_7$	
Hardness (kg/sq.mm)	1388		1373	
Toughness ($MPam^{1/2}$)	5.5		7.6	

Hardness and Toughness: Material from runs MTL 23-26 had hardnesses in the 1380 kg/sq.mm range (Table 1). These values are lower than in previous Matrix 4 sintering runs. Toughness values remained in the range of 5.5-8.0 $MPam^{1/2}$.

II. Sintering of Matrix 5 and 6 Compositions

Matrix 5-Sintering: The Matrix 5 sintering experiments continued. Experiments at 1875C showed consistent densities (>99.3%) for compositions with and without Mo_2C additions. The microstructure exhibited 10-30um porosity and was not improved from the previous reporting period. The phase composition was beta-silicon nitride with either a nitrogen apatite phase (usually referred to as H phase) or $Y_{4.67}(SiO_4)_3O$.

Matrix 5-Preoxidation and Sintering: Samples from Matrix 5 were pre-oxidized in air at 900C in an attempt to increase the amount of SiO_2 in the body. The samples containing Mo_2C cracked and discolored. The samples without Mo_2C gained 0.13% in weight. The sintered densities of these samples were lower than the standard samples (3.25 vs 3.27g/cc).

TiOxide Powder: A powder batch was prepared and supplied by TiOxide Chemicals, Ltd. (Billingham, England by Dr. Anthony Jones) prepared to the following composition:

87.5w/o Si_3N_4-4.67w/o SiO_2-7.8w/oY_2O_3

TiOxide Chemicals was selected because their processing techniques seemed most likely to produce homogeneously mixed powder. TiOxide Chemicals was isopressed and sintered at 1875C. The density was 3.267g/cc. The microstructure contains uniformly dispersed 6-12um porosity. The phase composition is beta-silicon nitride + Y_2SiO_5.

III. Matrices 5 and 6-Composition and Nitriding

Table 2 presents an overview of the material composition variations made in Matrices 5 and 6. Matrix 5, studied in previous reports, varied only the amount of Mo_2C (Mixes 10 and 11, 0 and 1.48w/o Mo_2C, respectively). Matrix 6 was designed to determine the effects of varying three different additives (SiO_2, Y_2O_3, and Al_2O_3) at two concentration levels on the density, weight loss, and phase composition using an L_4 (2^3) orthogonal array. The Mo_2C content was kept constant at a level of only 0.2%. SiO_2 and Y_2O_3 were varied in order to assure that the final sintered composition will be in the Si_3N_4-$Y_2Si_2O_7$-Si_2N_2O phase field. Al_2O_3 was added in an attempt to reduce weight losses due to SiO volatilization by forming a glassy phase and so reducing the SiO activity. The amount of Al_2O_3 was kept low (1.0w/o) in order to reduce the amount of alumina-containing second phase with a low melting temperature.

Mix 16 was made in two versions (A and B) using different sources of SiO_2; (A) Cab-O-Sil and (B) Elchem Fumed Silica.

Table 2. Composition and Theoretical Density of Matrix 5 and 6.

Composition	Matrix 5			Matrix 6		
	mix 10	mix 11	mix 16	mix 17	mix 18	mix 19
Si_3N_4	88.0	86.56	88.0	90.8	85.0	89.8
Y_2O_3	7.8	7.81	7.8	4.0	7.8	4.0
Al_2O_3	0.0	0.00	0.0	1.0	1.0	0.0
SiO_2	4.2	4.14	4.0	4.0	6.0	6.0
Mo_2C	0.0	1.48	0.2	0.2	0.2	0.2
Theor.Dens. (g/cc)	3.266	3.290	3.278	3.238	3.28	3.228

Table 3 summarizes the nitriding of Matrix 5 and 6 compositions. All of the compositions nitrided with a higher than 98% conversion in two nitriding runs.

Sintering

Sintering experiments of compositions from Matrices 5 and 6 were performed at 1900C, a temperature which was found to give reproducible densities for mixes 10 and 11. Time at sintering temperature and high pressure (1500 psi) was increased from 1 to 2 and 3 hours in order to reduce the amount of residual porosity in the samples. The time at

Table 3. Nitriding Data on Matrix 5 and 6 Compositions

Nitriding Data	Matrix 5			Matrix 6		
	mix 10	mix 11	mix 16	mix 17	mix 18	mix 19
Theoretical Nitriding Wt. Gain	1.542	1.529	1.542	1.568	1.514	1.559
Actual Wt. Gain-Nitrid.I	1.52	1.51	1.521	1.536	1.490	1.522
Actual Wt. Gain-Nitrid.II	1.51	1.51	1.520	1.544	1.492	1.534
Avg. Yield (% conversion)	98.25	98.8	98.61	98.21	98.48	98.01

sintering temperature and low pressure was kept constant at 5 hours. The MTL 41 run was conducted at 1910C, a 5/3 schedule, and in addition, a 1200C, 2 hour hold was added to the run on cooldown.

Figure 1 shows the relative densities of Matrix 5 and 6 compositions as a function of the Mix number. Densities of samples from both nitriding runs are presented, e.g., 17 and 17II represents mix 17, samples from first and second nitriding runs. Mixes 10, 11, and 18 were the only ones that consistently reached densities of 99.3% theoretical in all runs. Also, the sintering behavior of these compositions did not appear to be affected by the batch-to-batch nitriding variations.

Weight Losses

Weight losses in Matrix 5 and 6 compositions are presented in Figure 2. Quest software analysis of the Matrix 6 weight losses (using a L_4 (2^3) experimental matrix) shows that the major contribution to the sintering weight loss comes from the amounts of SiO_2 and Y_2O_3 (Table 4). As expected, a higher level of SiO_2 increases the sintering weight losses. However, increasing the levels of Y_2O_3 and Al_2O_3 both decrease them. Figure 2 also shows that nitriding has an effect on the sintering weight losses of most compositions. Nitriding run II consistently produced a slightly lower weight loss than the first run. MTL 40 and MTL 41 runs has lower weight losses than in MTL 39 due to an effective increase in the amount of packing powder in the first two runs.

Microstructure

Some 10-30um pores were present in Mixes 10 and 11 samples. Mix 18 samples were found to have the best microstructure of all the mixes. When compared to microstructures obtained previously by using the Si_3N_4 powder route, an improvement in the general microstructure as well as pore size reduction can be found in all samples. Table 5 contains secondary phases identified in the samples, i.e., Mixes 10, 11, and 18.

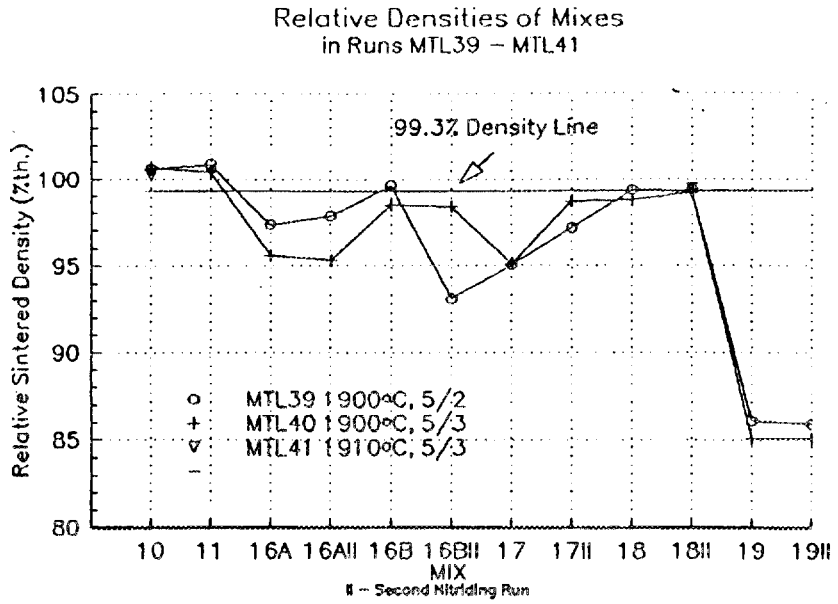

Figure 1 Relative Densities of Mixes from Matrices 5 and 6. Roman numeral II after the Mix number signifies the second nitriding run on the mix.

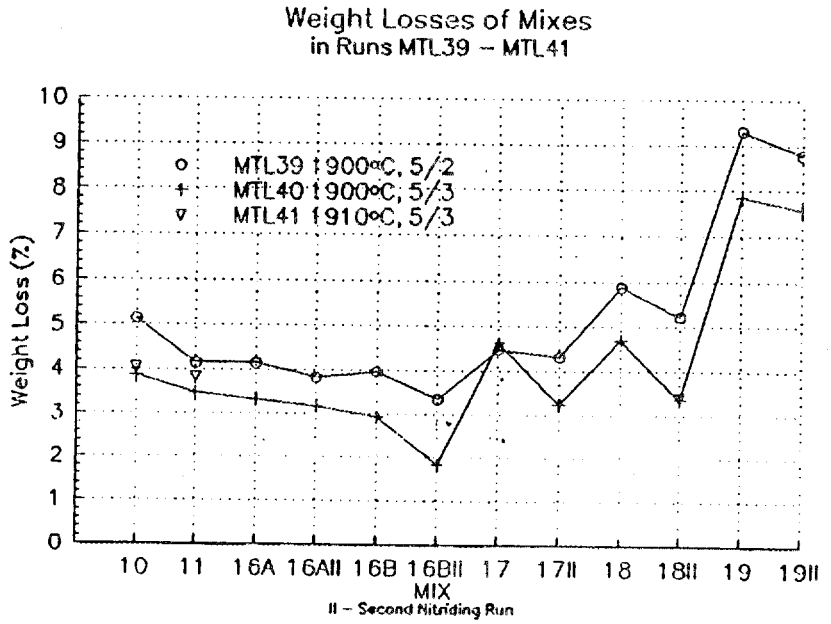

Figure 2 Sintering weight losses of Matrix 5 and 6 samples in MTL39-41 runs.

Table 4. ANOVA Table-Percent and Sign of Factor Contributions to the Sintering Weight Loss (Computations used signal to noise ratio of the test results with two repetitions).

Factors	Contribution to Weight Loss (%)	Sign of Contribution
SiO_2	60.78	positive*
Y_2O_3	32.10	negative
Al_2O_3	7.12	negative

* positive sign indicates that an increase in additive amount will increase the weight loss

Table 5. Secondary Phases in Mixes 10, 11, and 18

Run No.		Mix 10	Mix 11	Mix 12
40	phase	H	H	$Y_2Si_2O_7$
	ratio	0.16	0.25	0.08
41	phase	H	$Y_2Si_2O_7$ or $Y_{4.67}(SiO_4)_3O$	$Y_2Si_2O_7$
	ratio	0.23	0.33	0.20

Only Mix 18 consisitently contained $Y_2Si_2O_7$ as the second phase. The amount of second phase (expressed as the ratio of 100% peaks of the second and beta-Si_3N_4 phases) is significantly higher in MTL 41 than MTL 40 due to a 1200C hold on cooling that was added to the sintering cycle for MTL 41.

Mechanical Properties

Hardness and Toughness: Table 6 summarizes hardness and toughness data of Mixes 10, 11, and 18 in the most recent runs. Due to its high additive content, Mix 18 has a lower hardness than mixes 10 and 11.

Sintered rods from SRBSN Matrix 5 (Mixes 10 and 11) and Matrix 6 (Mix 18), using MTL 41 sintering cycle, have been sent for machining into size B MOR bars to evaluate their room temperature strengths.

Table 6. Hardness and Toughness of Mixes 10, 11, and 18

Sintering Run	Hardness (kg/mm^2) Mix			Toughness (MPa m°) Mix		
	10	11	18	10	11	18
MTL 39	1436	1473	1366	7.1	8.8	6.8
MTL 40	1399	1421	1358	6.3	9.0	8.8

RT Strength - Mixes 10, 11, and 18

Table 7 summarizes the strength data using size B MOR bars made from Mix 10, 11 (Matrix 5), and 18 (Matrix 6) compositions. Bars were made from material sintered in MTL run 41 at 1910C. In Table 7, present strength data is compared to the strengths obtained for Mixes 6 and 7 (reported previously) which have essentially the same composition as Mixes 10 and 11, respectively. Present Mix 10, 11, and 18 materials were produced using the SSN (sintered silicon nitride route). Table 7 also includes the strength of an SRBSN material with no silica additions (Mix 15). A significant improvement in strength was made in Mix 11 SRBSN material over Mix 7. The Weibull modulus was increased by nearly a factor of three, from 6.3 to 18. The high Weibull modulus suggests a uniform flaw population in the Mix 11 material.

Mix 10 material had essentially the same mean and characteristic strength as Mix 6. The Weibull modulus of Mix 10 is 2.8 times greater than determined for Mix 6.

Mix 18 material had the highest average and characteristic strength of the materials investigated but it's Weibull modulus was only 3.8.

Mix 15 material was employed as a control. This material was processed at the same time as Mixes 10, 11, and 18. It's composition was similar to the Mix 18 but had no SiO_2 additions. As can be seen, this material has a strength well above 700 MPa with a high Weibull modulus of 26.

Fracture Origins

Fracture surfaces of broken MOR bars were examined and fracture origins were identified wherever possible. Table 8 lists individual bar strengths of Mixes 10, 11, and 18 and indicates the nature of the fracture origins.

It was observed that porosity is still strength limiting for the Mix 10 material, which does not contain Mo_2C. Although the porosity size variation has been reduced compared to Mix 6, the average size appears to be approximately the same (assuming that the fractrue toughness is also similar, which measurements support). Optical comparisons of microstructure of Mix 10 (and other silica containing mixes) to Si_3N_4 materials that do not contain silica as an additive, e.g., Mix 15, indicate that the Mix 10 porosity, which is concentrated in the interior of the sample, is a result of SiO_2 vaporization as SiO. This gas evolution occurs during and after the sample has reached the closed pore stage, and it's pressure in the pores counteracts the external pressure applied during the sintering cycle.

As observed optically, exaggerated grain growth appears to be strength limiting for the Mix 11 samples sintered at 1910C. The higher strength of Mix 11 indicates that the pore size in this material is finer than in Mix 10 and/or that it's fracture toughness is higher.

For Mix 18 bars, pores were found to be fracture origins in most low strength samples. Since Mix 18 contained 6% SiO_2 (versus 4% in Mixes 10 and 11) and 1% Al_2O_3 (versus none in Mixes 10 and 11), the presence of Al_2O_3 appears to have minimized pore formation by promoting chemical bonding with some of the SiO_2. This composition appears to have a

Table 7. RT Strength Comparison of Mix 10, 11, and 18 Materials to Previous Results

Mix No.	6	10	7	11	18	15
Production Rte.	SSN	SRBSN	SSN	SRBSN	SRBSN	SRBSN
Xmean (MPa)	420.00	435.17	408.28	518.62	532.41	757.24
Xcharact (MPa)	468.28	459.31	437.24	534.48	588.28	773.10
1e0 (MPa)	137.24	57.24	72.41	35.86	155.17	35.17
Weibull Mod.	3.2	9.1•3.0	6.3	18•6.0	3.8•2.0	26.7•9
# of bars	15	15	15	15	8	15

Table 8. Fracture Origins and Individual Bar Strengths from Mix 10, 11, and 18 Materials.

bar #	Mix 10		Mix 11		Mix 18	
	Strength (MPa)	Fracture Origin	Strength (MPa)	Fracture Origin	Strength (MPa)	Fracture Origin
1	342.98	pore surface	518.46	grain subsurface	700.25	
2	479.58	--	463.05	--	634.06	--
3	460.64	--	439.56	--	429.24	--
4	432.24	--	425.54	--	371.24	pore
5	440.10	--	541.28	--	674.32	--
6	366.56	--	508.37	--	424.82	pore
7	481.02	--	553.21	--	660.49	--
8	399.96	pore	528.83	--	391.52	--
9	372.04	--	565.75	--		
10	460.94	--	508.75	--		
11	462.95	--	510.43	--		
12	507.62	pore	539.71	--		
13	364.21	--	550.34	large grain		
14	457.73	--	482.61	large grain		
15	514.45	pore	546.89	--		

bimodal flaw size distribution with samples falling into two strength groups, i.e., 634-700 Mpa and 371-429 MPa.

Based on presented data, further improvements in strength could be made either by eliminating exaggerated grain growth of the current Mix 11 composition by limiting the time at temperature during sintering (experiments are in progress) or further reducing the amount of porosity of Mix 18 by reducing the amount of added SiO_2. Both approaches are being considered.

IV. Established Milestones

(A) Establish powder processing approach for preparing selected composition. Determine preferred sintering conditions. Generate data base for room temperature and high temperature properties.
July 1991

(B) Fabricate, inspect, and make components available for engine testing in a gas turbine ceramic component development/evaluation program.
July 1992

V. Status of Milestones

The program is behind schedule due to various technical difficulties involving processing of selected compositions. A revised schedule is proposed with processing experiments continuing through May 92, material characterization experiments beginning in July 92, and Task I being completed at the end of August 92. Task II would start in August and be completed at the end of December 92. It appears that sufficient funds currently remain in the contract to permit the revised schedule.

Microwave Sintering of Silicon Nitride

T. N. Tiegs, J. O. Kiggans, P. A. Menchhofer, K. Ploetz, and D. Coffey
(Oak Ridge National Laboratory)

Objective/scope

The objective of this research element is to identify those aspects of microwave processing of silicon nitride that might (1) accelerate densification, (2) permit sintering to high density with much lower levels of sintering aids, (3) lower the sintering temperature, or (4) produce unique microstructures. The investigation of microstructure development is being done on dense silicon nitride materials annealed in the microwave furnace. The sintering of silicon nitride involves two approaches. The first approach comprises heating of silicon nitride and sialon powder compositions in the 2.45- or 28-GHz units. The second approach deals with using reaction-bonded silicon nitride as the starting material and is done entirely in the 2.45-GHz microwave furnace.

Technical highlights

Microstructure development

Microstructural changes occurring during the annealing of silicon nitride materials have been previously reported. Significant grain growth; depending on the intergranular phase composition and the annealing conditions, has been observed.

Rods of a commercial silicon nitride (PY6 from GTE Laboratories, Waltham, Massachusetts) were microwave annealed at 1500°C for 10 h and have been tensile creep tested at 1370°C at ORNL. Those results showed essentially no difference between the as-fabricated and microwave-annealed materials. Obviously, the anneal conditions used were not appropriate for this composition in either time or temperature (or both) to change the microstructure significantly. The PY6 contains nominally 6% Y_2O_3 as a sintering aid and was glass-encapsulated hot-isostatically pressed (HIP) to high density. It is considered a very refractory composition having a eutectic temperature for the Y-Si-O-N system of ~ 1500°C. Additional annealing runs are planned at higher temperatures where liquid formation in the intergranular phases is prevalent.

Previous work on microwave annealing of silicon nitride showed enhanced grain growth and improved creep resistance for materials annealed at temperatures of 1200 to 1500°C. However, the anneal times were on the order of 20 h to achieve these properties. The objective of the present work was to determine if higher temperatures, but shorter anneal times; could be employed to produce the desired microstructures. The anneal time was therefore reduced to 2 h and the temperature increased to 1800°C.

It is well documented that significant decomposition of Si_3N_4 occurs at temperatures > 1800°C. Thus, nearly all earlier studies concerned with microstructural development at elevated temperatures used nitrogen overpressure to inhibit the decomposition.[1-6] In some cases, the nitrogen was used at high enough pressures to aid in densification. Consequently, the 1800°C anneal

temperature was the highest temperature that was considered to be appropriate in the microwave cavity at 0.1 MPa (1 atm) N_2 pressure.

Four compositions were annealed: two hot-pressed and two sintered materials as shown in Table 1. The hot-pressed materials had refractory grain-boundary phases that would densify only with pressure assistance or at very high temperatures and nitrogen overpressures. They represented materials that would have good properties at high temperatures and would have high cost. The sintered materials were densified at 1 atm and represented more cost-effective silicon nitride materials.

Table 1. Summary of materials annealed in the 2.45-GHz microwave furnace at 1800°C for 2 h.

Composition	Densification Method	Densification Parameters (Temperature/ Time, °C/min)	Initial Density (% T. D.)
Si_3N_4-8% Y_2O_3-4% SiO_2	HIP	1800/90	98.4
Si_3N_4-11% La_2O_3-4% SiO_2	HIP	1800/90	98.7
Si_3N_4-12% Y_2O_3-4% Al_2O_3	Sintered	1700/60	96.8
Si_3N_4-11% La_2O_3-3% Al_2O_3	Sintered	1700/60	98.2

As shown in Fig. 1, the coupling behavior of the various compositions was dependent on the type of grain-boundary phase. The relaxation was observed in the same temperature range as the eutectic liquid temperature for each combination of sintering additives. Weight losses were also observed to be a function of the grain-boundary chemistry as shown in Fig. 2. The losses are believed due to SiO volatilization and can result in compositional shifts in the chemistry of the intergranular phases. Changes in the measured densities were observed as indicated in Fig. 3. The materials with highly refractory grain-boundary phases showed increases in the densities, whereas the materials with the less refractory phases showed density decreases. The reasons for these differences are unknown at the present time.

Examination of fracture surfaces revealed significant grain growth in the materials with the less refractory grain-boundary phases (Figs. 4 and 5). No significant changes in grain size were evident in the materials with the highly refractory additives (Figs. 6 and 7).

ORNL-DWG 92-11906

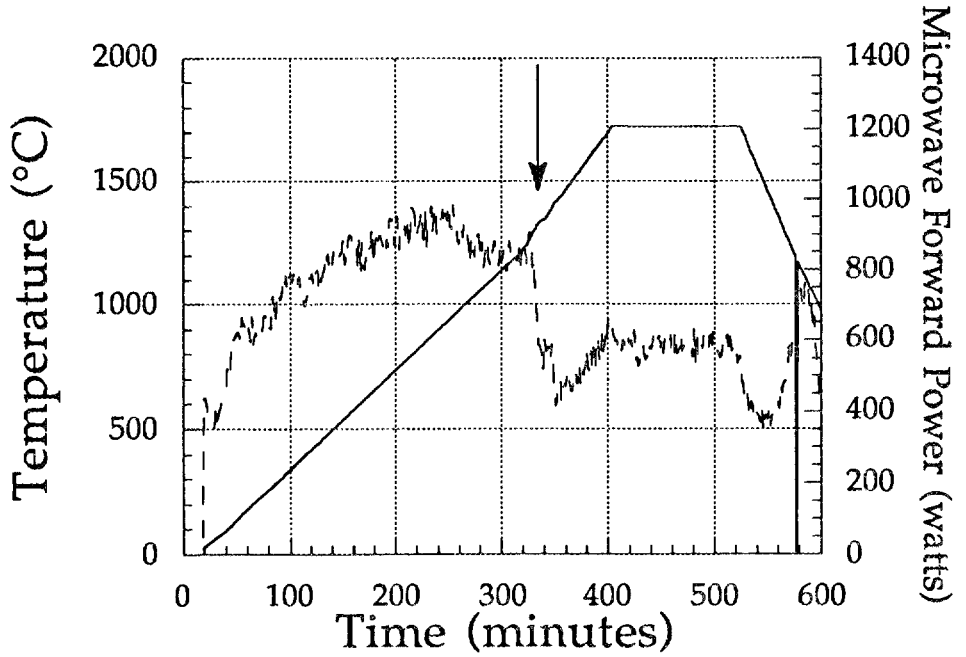

(a)

ORNL-DWG 92-11907

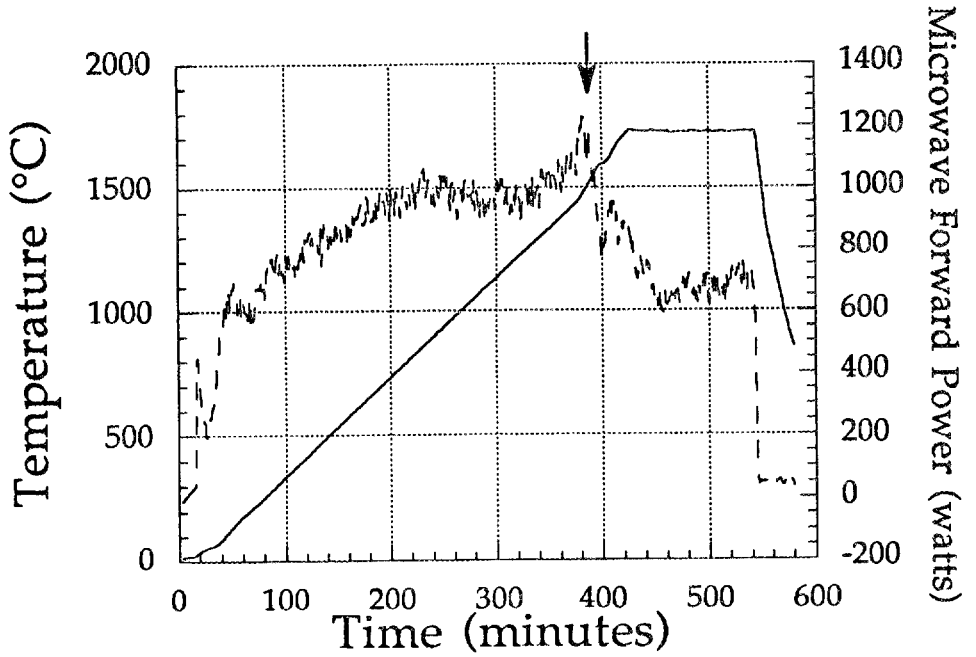

(b)

Fig. 1. Time-temperature-power curves for microwave annealing of dense silicon nitride showing differences in coupling behavior: (*a*) Si_3N_4-12 Y_2O_3-4% Al_2O_3, eutectic temperature ~ 1280°C and (*b*) Si_3N_4-8 Y_2O_3-4% SiO_2, eutectic temperature ~ 1500°C.

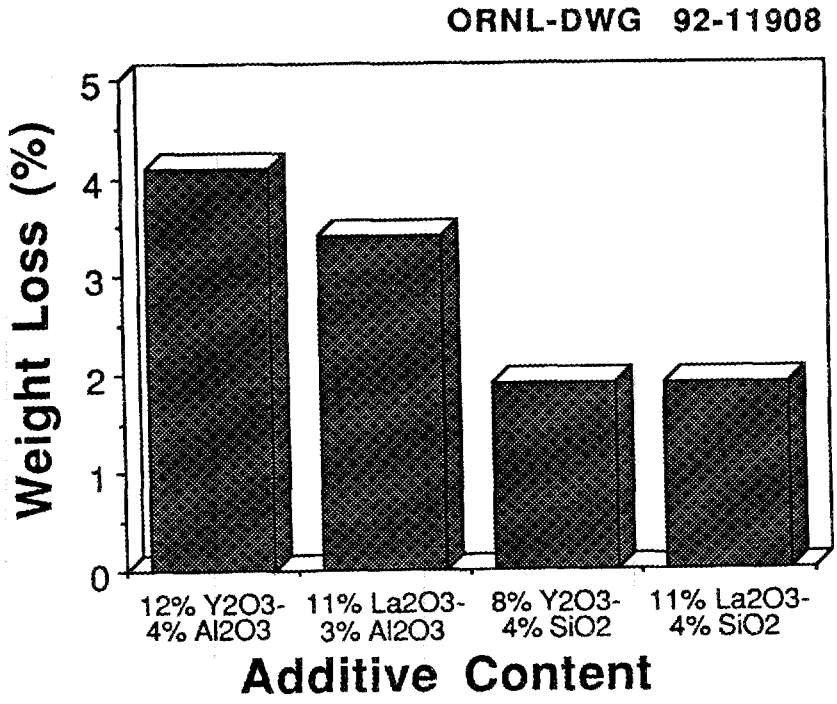

Fig. 2. Weight losses associated with microwave annealing of dense silicon nitride. Losses are believed due to SiO volatilization and can result in compositional shifts in chemistry of intergranular phases. Annealed for 2 h at 1800°C in 2.45-GHz cavity.

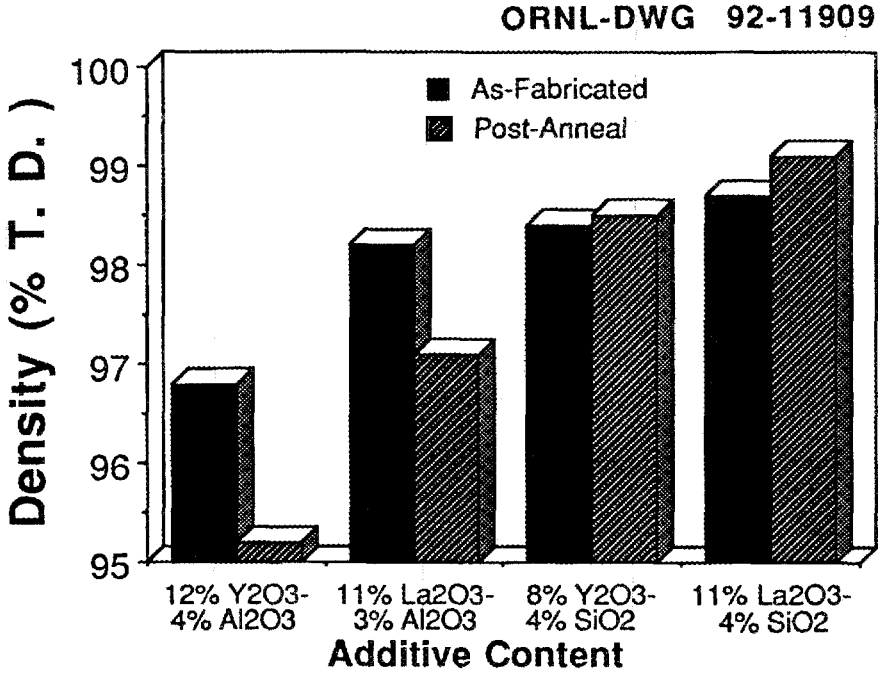

Fig. 3. Changes in density during high-temperature microwave annealing of dense silicon nitride. Annealed for 2 h at 1800°C in 2.45-GHz cavity.

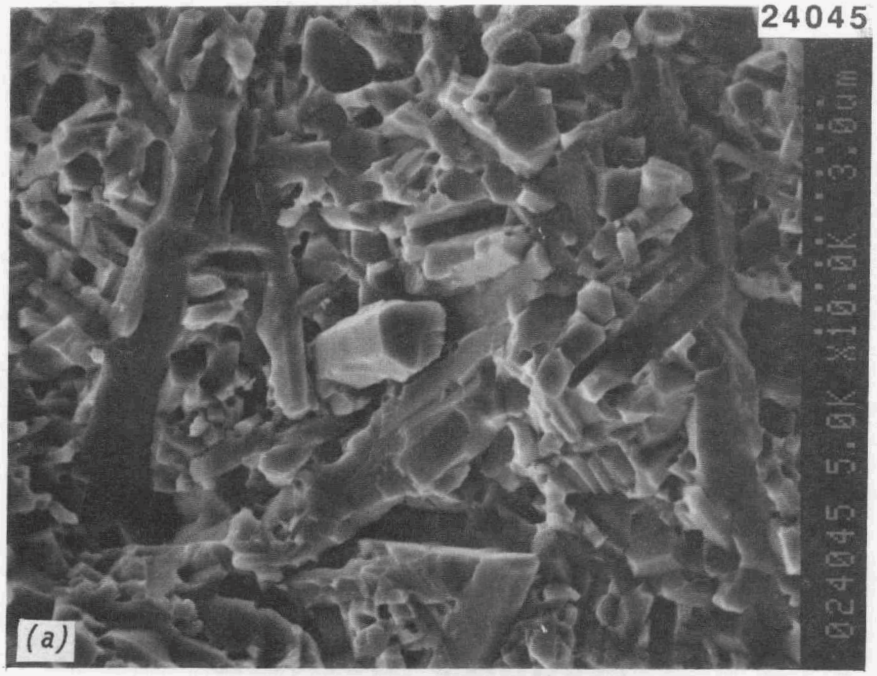

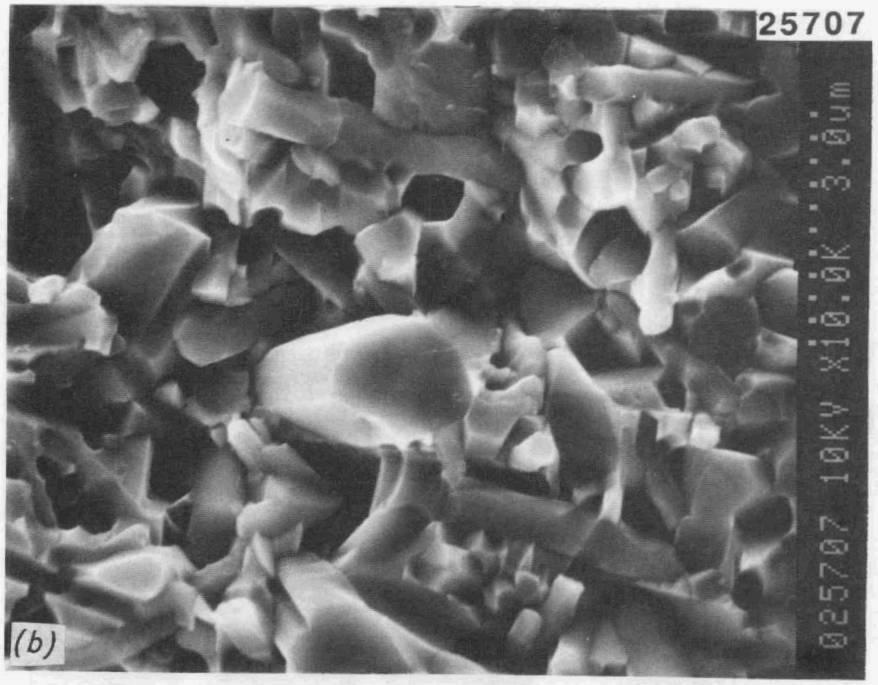

Fig. 4. Fracture surfaces of dense Si_3N_4-12 Y_2O_3-4% Al_2O_3: (*a*) as-fabricated and (*b*) after microwave annealing at 1800°C for 2 h in 2.45-GHz cavity.

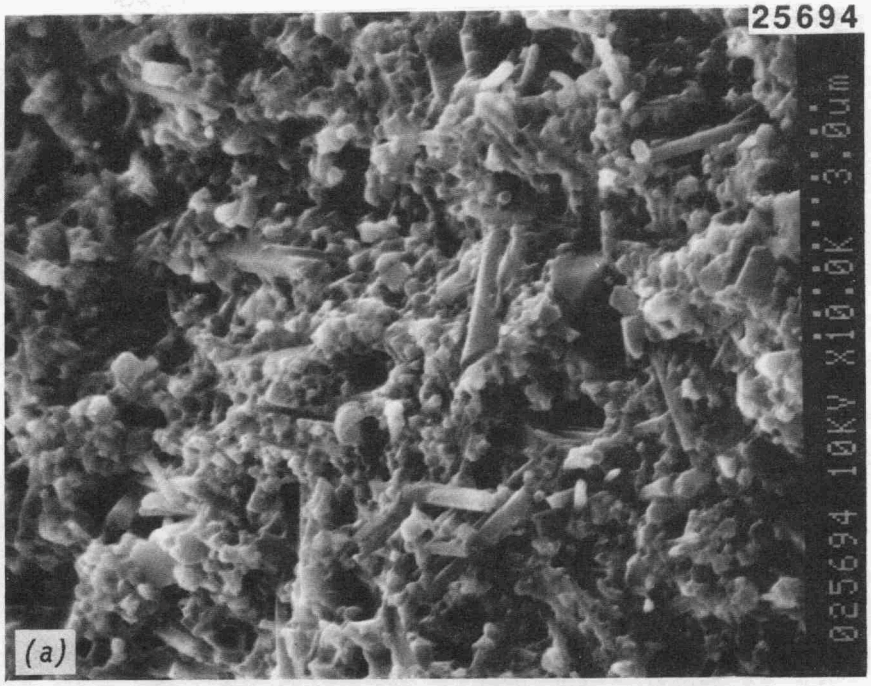

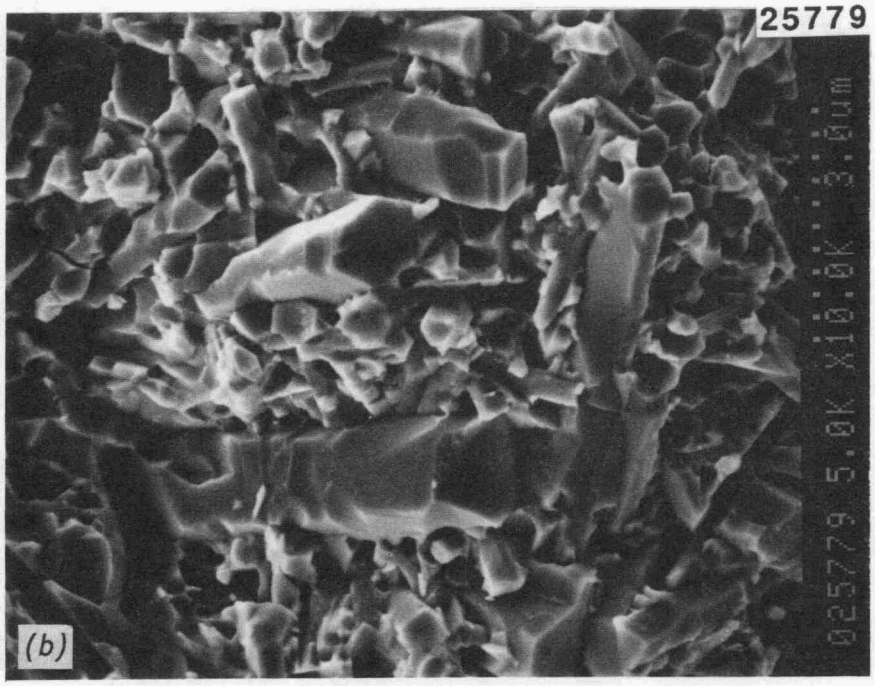

Fig. 5. Fracture surfaces of dense Si_3N_4-11 % La_2O_3-3% Al_2O_3: (*a*) as-fabricated and (*b*) after microwave annealing at 1800°C for 2 h in 2.45-GHz cavity.

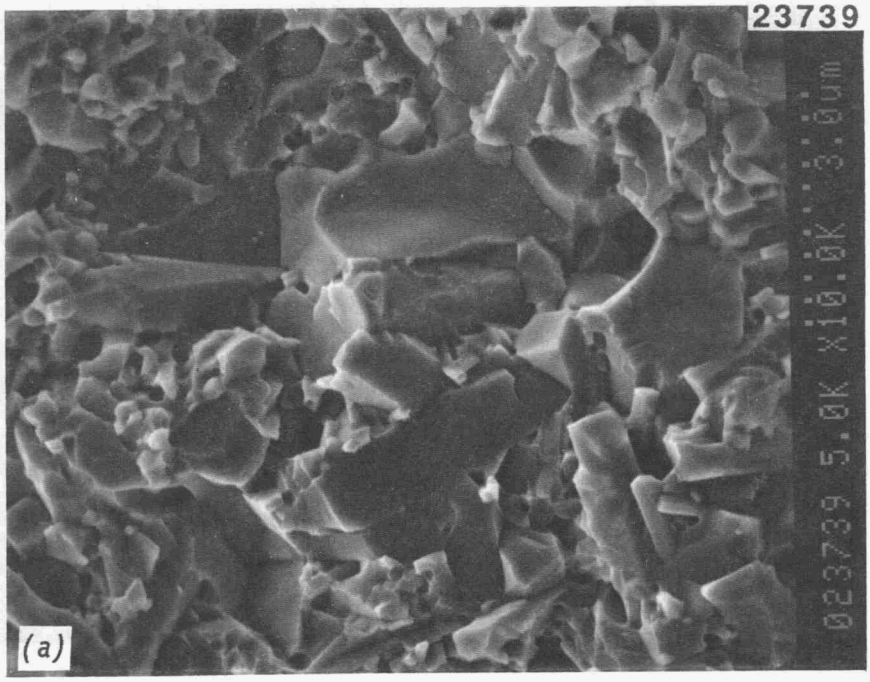

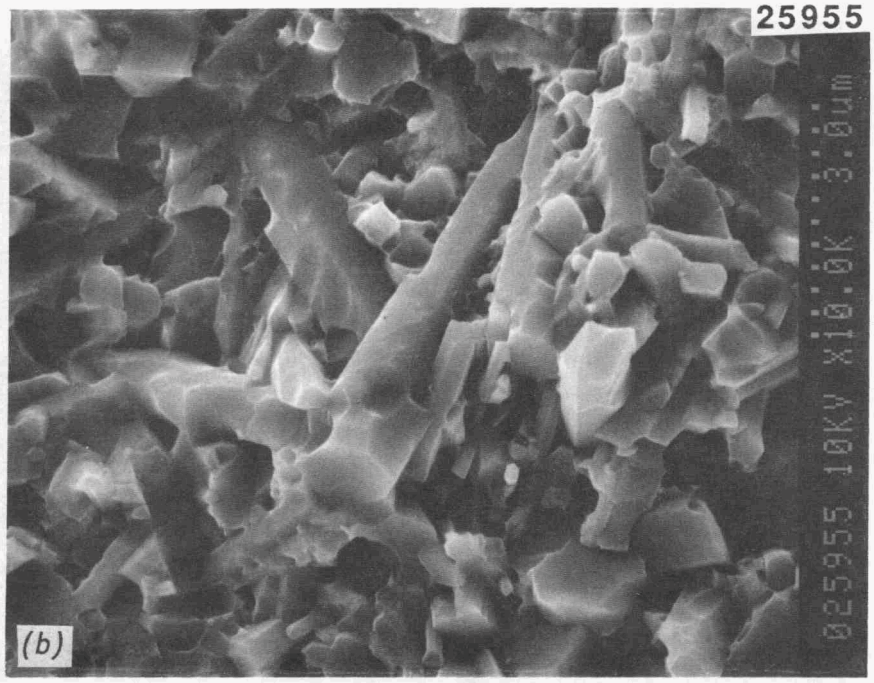

Fig. 6. Fracture surfaces of dense Si_3N_4-8% Y_2O_3-4% SiO_2: (*a*) as-fabricated and (*b*) after microwave annealing at 1800°C for 2 h in 2.45-GHz cavity.

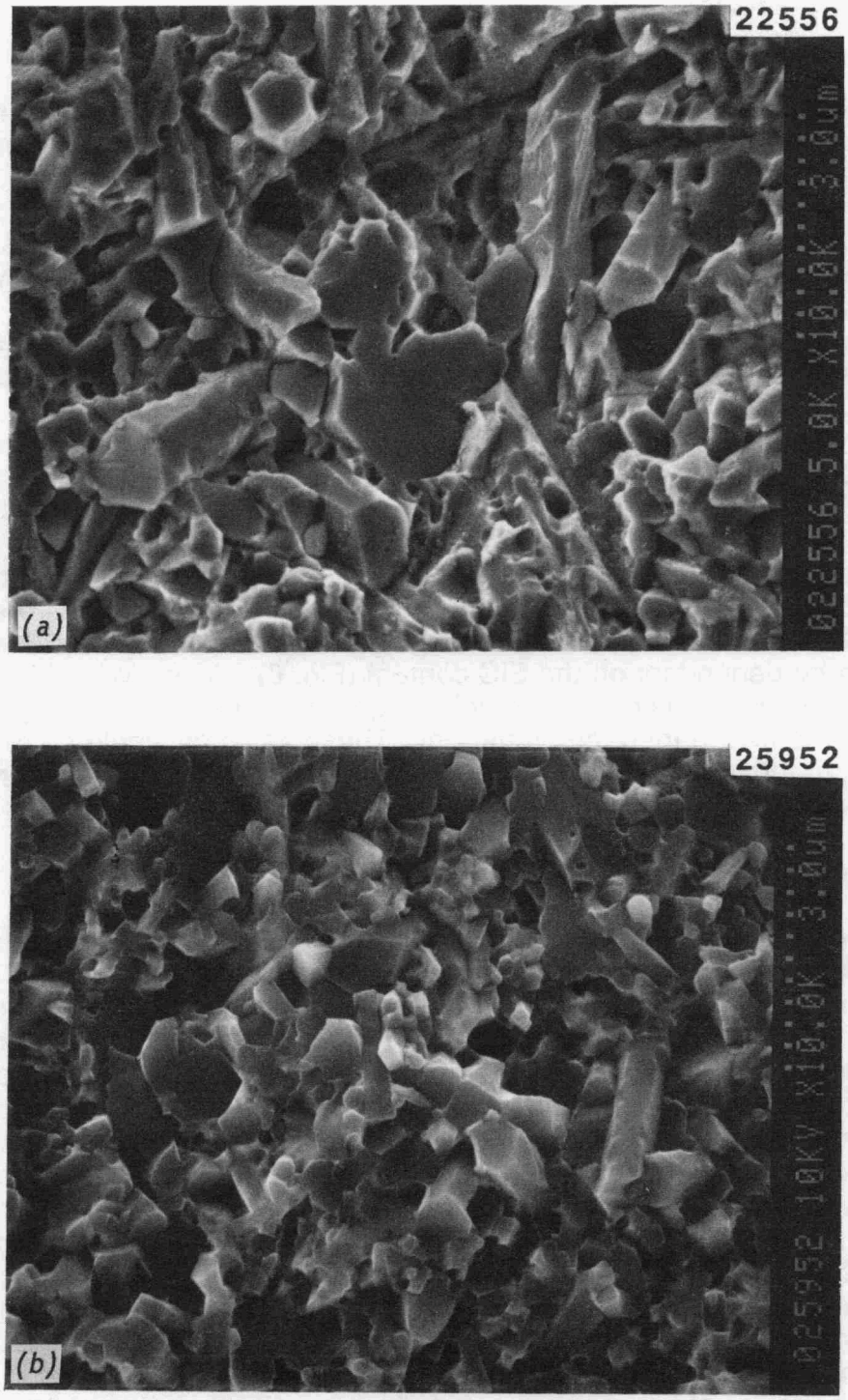

Fig. 7. Fracture surfaces of dense Si_3N_4-11% La_2O_3-4% SiO_2: (*a*) as-fabricated and (*b*) after microwave annealing at 1800°C for 2 h in 2.45-GHz cavity.

Sintering

In the last reporting period, several specimens of silicon nitride materials were fabricated and sintered in the 2.45-GHz microwave furnace. Compositions ranged from Si_3N_4-12% Y_2O_3-4% Al_2O_3 to Si_3N_4-9% Y_2O_3-3% Al_2O_3. The results showed only minor improvements in the densification behavior and mechanical properties as compared to conventionally heated materials.

Additional runs have been made in which the sintering was followed by a grain-growth cycle (1500°C for 10 h) and then an intergranular phase crystallization step. The composition used was Si_3N_4-9% Y_2O_3-3% Al_2O_3. Samples are currently being machined into test bars for mechanical property evaluation.

SiC grit has been routinely added to the packing powders surrounding the samples during sintering to aid in heating uniformity. Concentrations have ranged from 2 to 8% and little difference was noted between samples at these low concentrations. In an attempt to allow sintering of samples in the microwave with low additive contents where sample heating uniformity is the major problem, several runs were made with SiC grit concentrations up to 50%. The heating profiles were interesting in that the relaxation in the coupling behavior was observed to be dependent on the SiC content (Fig. 8). As shown, at high SiC contents, no relaxation is observed indicating that the sample is being heated primarily by the heat generated by the grit. These samples would be expected to be identical to those sintered by conventional heating. The samples are being machined into test specimens.

Sintered Reaction-Bonded Silicon Nitride

In the last reporting period, several specimens of silicon materials were fabricated, nitrided, and sintered in the 2.45-GHz microwave furnace. These materials are significantly less expensive than other materials fabricated exclusively from high-purity silicon nitride powders. In addition, sintering of the reaction-bonded silicon nitride (RBSN) in the microwave is a one-step process as compared to conventional processing where nitridation and sintering occur as two steps. Compositions were nominally Si_3N_4-9% La_2O_3-3% Al_2O_3 and were fabricated with two different grades of silicon as shown in Table 2. A cost comparison is shown in Fig. 9. The compositions were fabricated as plates and fired in the microwave furnace between either SiC or BN plates. The nitridation cycle was 20 h to 1400°C, followed by 1 h at the sintering temperature of 1750°C. As shown in Table 3, high densities were obtained in the higher purity materials. Samples were also sintered at 1800°C and, as shown in Fig. 10, higher densities were obtained.

The behavior of the reaction-bonded silicon nitride during sintering was slightly different than sintering of compacts fabricated exclusively with Si_3N_4 powder. The relaxation normally observed at temperatures of 1200 to 1300°C was shifted to higher temperatures of ~ 1400°C with the RBSN (Fig. 11). This relaxation is associated with formation of liquid phases caused by the reaction of the sintering additives and the SiO_2 on the surface of the silicon nitride particles. However, during the nitridation process, these sintering additives tend to form crystalline

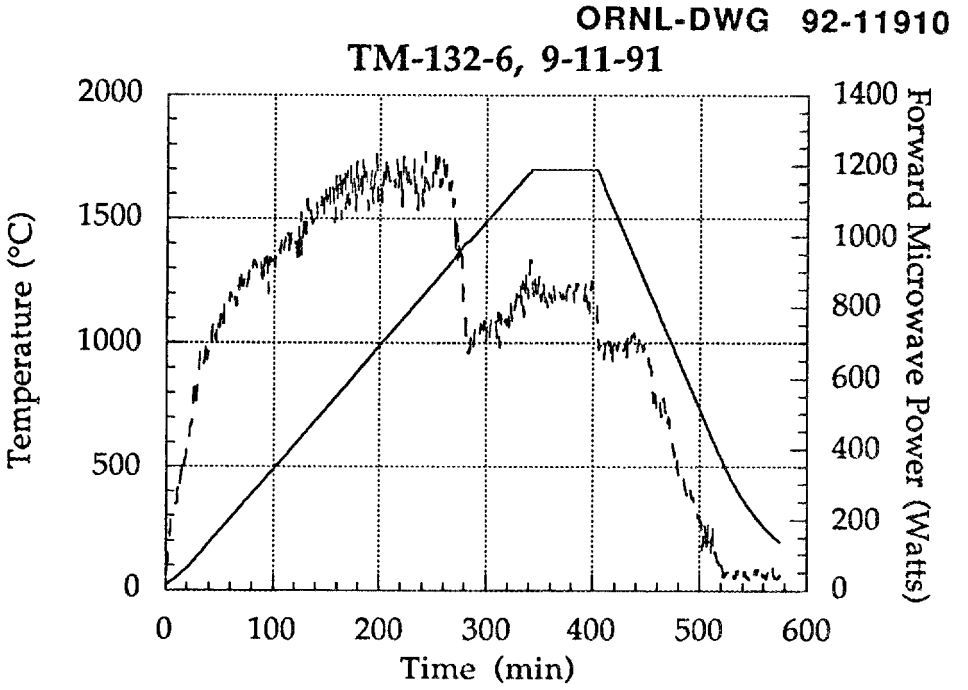

(a)

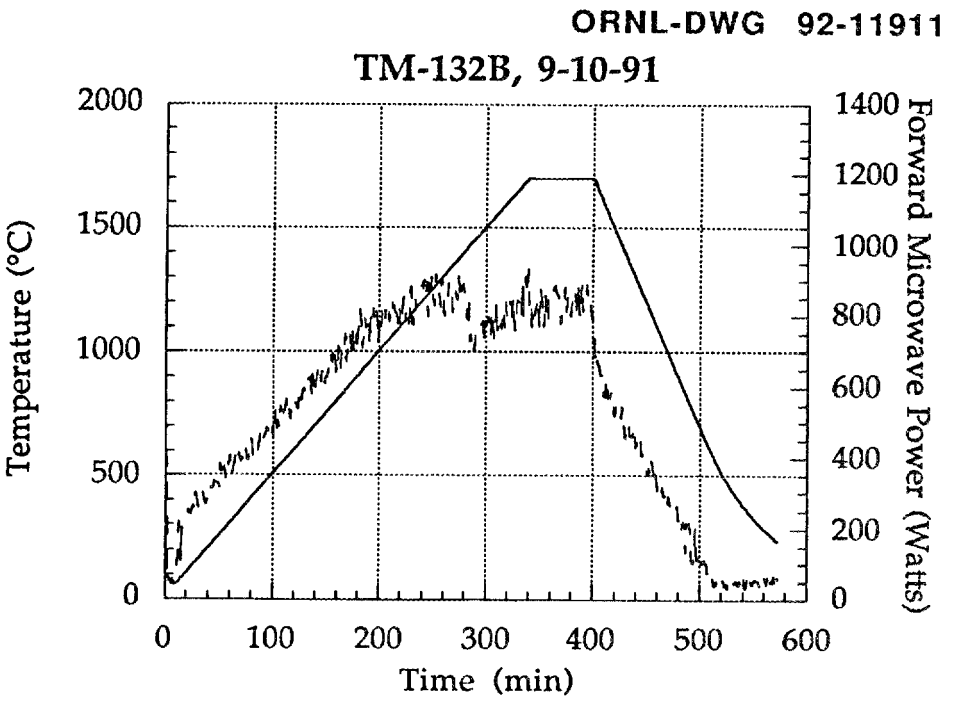

(b)

Fig. 8. Temperature and forward microwave power profiles during sintering of Si_3N_4-9% Y_2O_3-3% Al_2O_3 with different SiC grit contents in the packing powder: (*a*) 8% grit, (*b*) 24% grit, and (*c*) 50% grit. Relaxation during coupling to the silicon nitride samples is characterized by a decrease in power at ~ 1350°C.

ORNL-DWG 92-11912

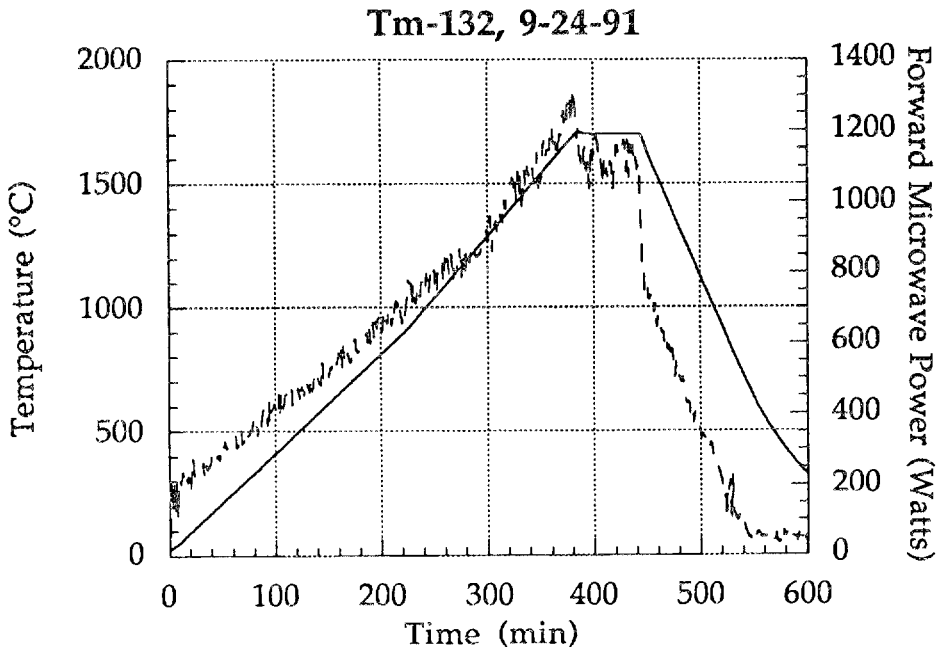

(c)

Fig. 8 Continued

Table 2. Compositions of sintered reaction-bonded silicon nitride materials

Sample No.	Silicon Purity (wt. %)	Mean Particle Size (μm)	Additive Content* (wt. %)	a-Si_3N_4 Content (wt. %)	Material Cost - ($/lb) As-Fabricated†	Material Cost - ($/lb) As-Sintered**
TM-136	< 0.5[a]	3.4	11.5.% R. E.[c]	5[d]	4.06	2.90
TM-137	< 0.05[b]	4.2	11.5 % La2O3[g]	10[e]	8.83	6.42
TM-132	N. A.	< 0.5	9% Y2O3[h]	>98[f]	41.76	41.76

*All compositions contain the same molar content of sintering additives.

†Material cost based on purchase price in 10-kg lots. Cost will decrease at larger quantities.

**Assumes a yield of 58% from nitridation of silicon.

[a]Elkem Metals Co., Buffalo, New York; Grade Metallurgical Si.

[b]Elkem Metals Co., Buffalo, New York; Grade Si-HQ.

[c]Molycorp, White Plains, New York; Grade 5232, Rare earth mixture (< 1% CeO_2). This composition also contains 0.5 wt. % Fe_2O_3 as a nitridation aid.

[d]Starck, Berlin, Germany; Grade S1 Si_3N_4.

[e]Starck, Berlin, Germany; Grade LC-10N Si_3N_4.

[f]Ube Industries, Japan; Grade E-10 Si_3N_4.

[g]Molycorp, White Plains, New York; Grade 5205, > 99.9% La_2O_3.

[h]Molycorp, White Plains, New York; Grade 5600, > 99.9% Y2O3.

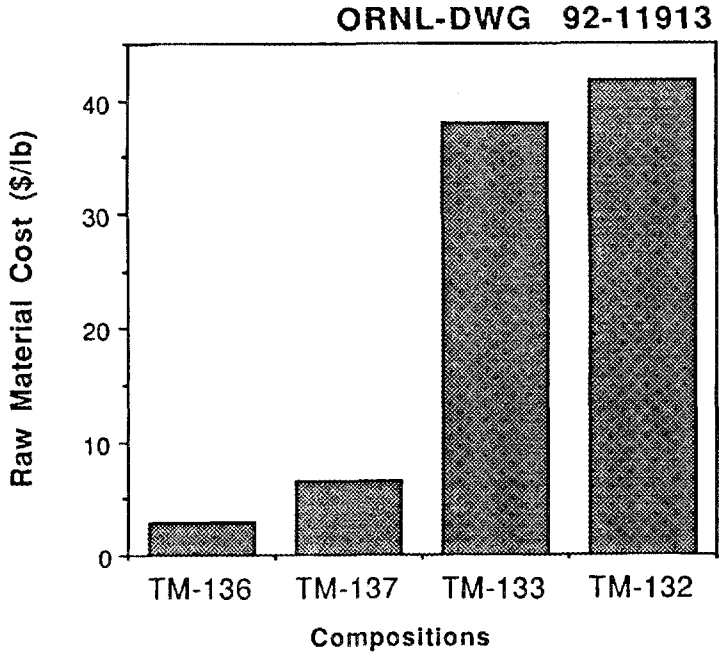

Fig. 9. Raw material cost comparisons between RBSN (TM-136 and TM-137) and materials fabricated with high-purity silicon nitride powders (TM-133 and TM-132). TM-136 and TM-137 are nominally Si_3N_4-11% La_2O_3-3% Al_2O_3 and used different grades of silicon and additive powders; TM-133 is nominally Si_3N_4-11% La_2O_3-3% Al_2O_3 and used high-purity starting silicon nitride and additive powders; TM-132 is nominally Si_3N_4-8% Y_2O_3-3% Al_2O_3 and used high-purity starting silicon nitride and additive powders.

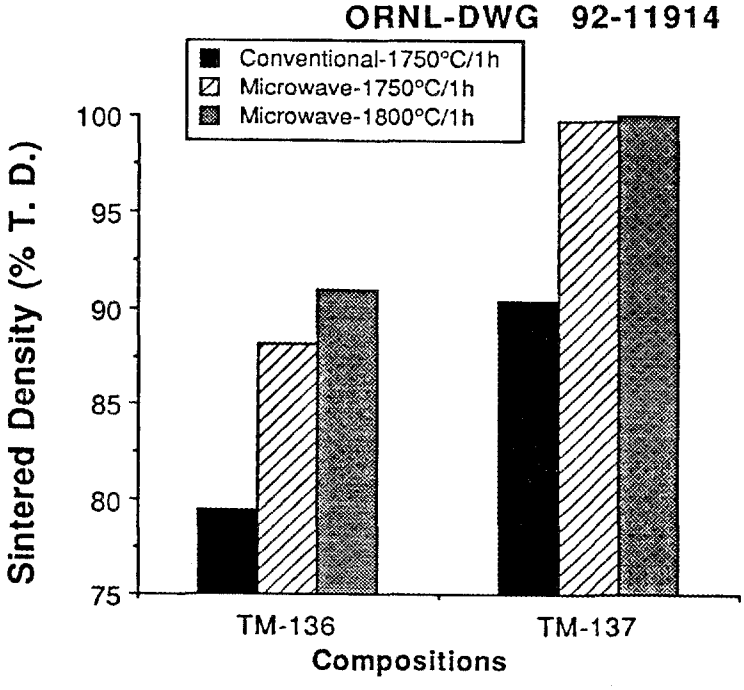

Fig. 10. Densification behavior of sintered RBSN materials.

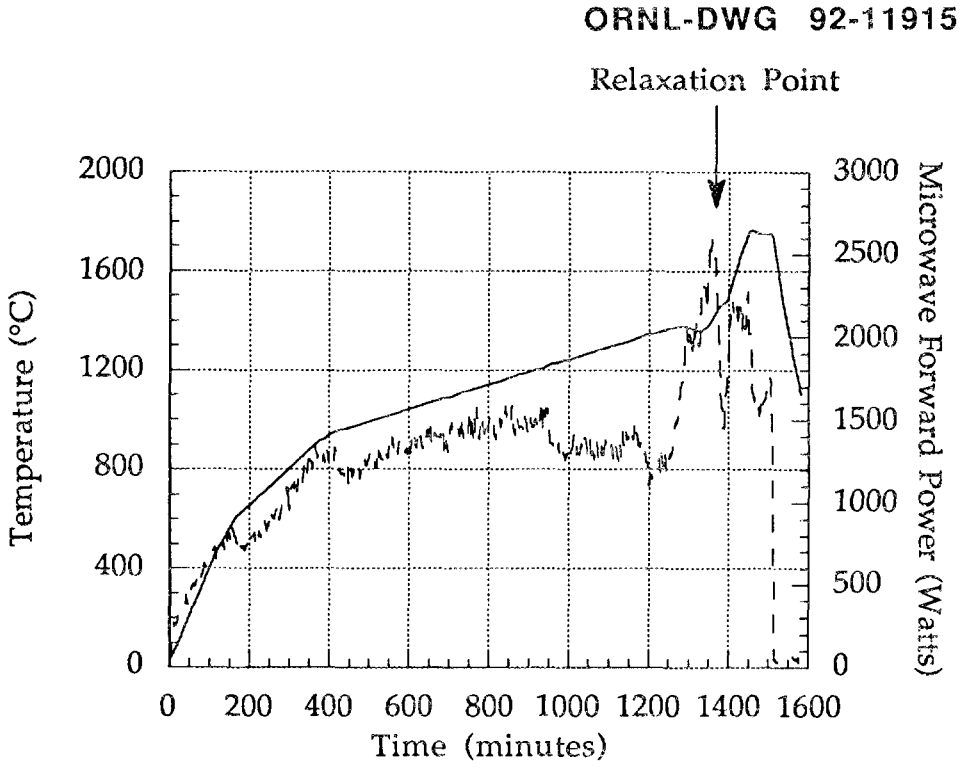

Fig. 11. Relaxation behavior of RBSN during sintering in the 2.45-GHz cavity. Composition is nominally Si_3N_4-11 % La_2O_3-3% Al_2O_3.

phases with the silicon nitride.[7,8] The result is that liquid formation is inhibited and doesn't occur with the RBSN until the higher temperatures are reached.

Mechanical property testing showed the flexural strength of the materials microwave sintered at 1800°C to be ~ 480 MPa and relatively constant up to 800°C (Fig. 12). At temperatures > 800°C, some reduction in flexural strength was observed. Large standard deviations were associated with the strength measurements. Examination of fracture surfaces showed these materials to contain agglomerates introduced into the samples during aging of the slurries. Elimination of these defects would tend to increase the average strengths.

Oxidation testing of the materials microwave sintered at 1800°C showed increased weight gains as compared to materials fabricated with high-purity powders (Fig. 13).

Cooperative Research and Development Agreements

Three Cooperative Research and Development Agreements (CRADAs) have been started in the area of microwave processing of silicon nitride. The first CRADA is with Garrett Ceramic Components/Allied-Signal and will anneal specimens of silicon nitride with high additive contents (> 5 %). Compositions include AS-44, GN-10, and AS-700. In a second CRADA with Norton, we will microwave anneal silicon nitride having additive contents less than 5%. Most of the

phases with the silicon nitride.[7,8] The result is that liquid formation is inhibited and doesn't occur with the RBSN until the higher temperatures are reached.

Mechanical property testing showed the flexural strength of the materials microwave sintered at 1800°C to be ~ 480 MPa and relatively constant up to 800°C (Fig. 12). At temperatures > 800°C, some reduction in flexural strength was observed. Large standard deviations were associated with the strength measurements. Examination of fracture surfaces showed these materials to contain agglomerates introduced into the samples during aging of the slurries. Elimination of these defects would tend to increase the average strengths.

Oxidation testing of the materials microwave sintered at 1800°C showed increased weight gains as compared to materials fabricated with high-purity powders (Fig. 13).

Cooperative Research and Development Agreements

Three Cooperative Research and Development Agreements (CRADAs) have been started in the area of microwave processing of silicon nitride. The first CRADA is with Garrett Ceramic Components/Allied-Signal and will anneal specimens of silicon nitride with high additive contents (> 5 %). Compositions include AS-44, GN-10, and AS-700. In a second CRADA with Norton, we will microwave anneal silicon nitride having additive contents less than 5%. Most of the work will be involved with NT-154 with a range of a-phase contents. Norton is also involved in the third CRADA where RBSN will be fabricated in the microwave. The results will be directly compared to their materials fabricated by conventional heating.

Specimens of AS-44 silicon nitride from Garrett Ceramic Components/ Allied-Signal have been annealed. Conditions used were 1600 to 1800°C for times of 2 to 10 h. The samples have been machined into test specimens and are currently being tested for mechanical properties. Initial results showed only minor changes due to the microwave annealing.

Samples of Norton NT-154 with high a-phase contents have been annealed in the last reporting period. The conditions are reported in a following section.

Samples of Norton RBSN have been fabricated. The status of the work is reported in a following section.

References

1. Y. Tajima, K. Urashima, M. Watanabe, and Y. Matsuo, "Fracture Toughness and Microstructural Evaluation of Silicon Nitride Ceramics," pp. 1034-1041 in *Ceramic Transactions, Ceramic Powder Science, II,* B., ed. G. L. Messing, E. R. Fuller, Jr., and H. Hausner. American Ceramic Society, Westerville, Ohio, 1988.

2. G. Wötting, B. Kanka, and G. Ziegler, "Microstructural Development, Microstructural Characterization and Relation to Mechanical Properties of Dense Silicon Nitride," pp. 83-96 in *Non-Oxide Technical and Engineering Ceramics*, ed. S. Hampshire, Elsevier Applied Science, London, 1986.

ORNL-DWG 92-11916

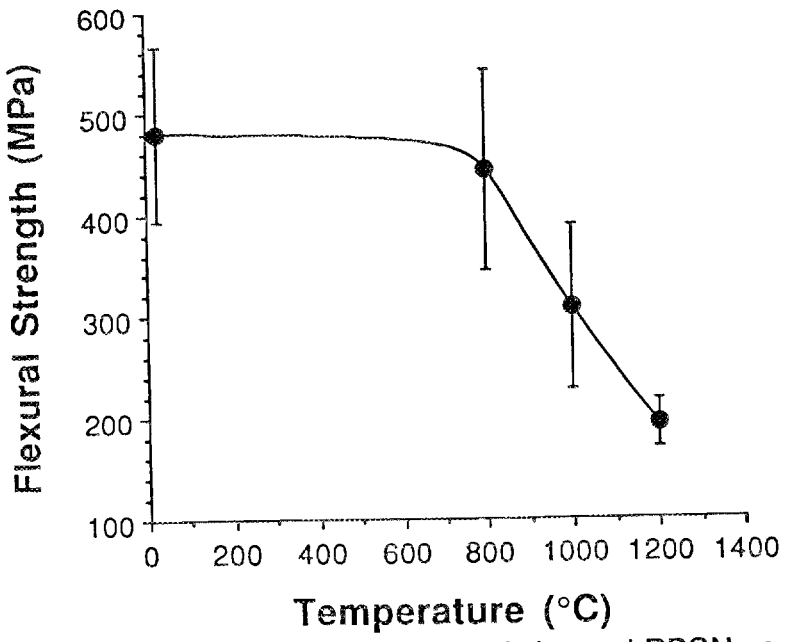

Fig. 12. Flexural strength of sintered RBSN as a function of temperature. The sample was composition TM-137 (Si_3N_4-11% La_2O_3-3% Al_2O_3) sintered at 1800°C.

ORNL-DWG 92-11917

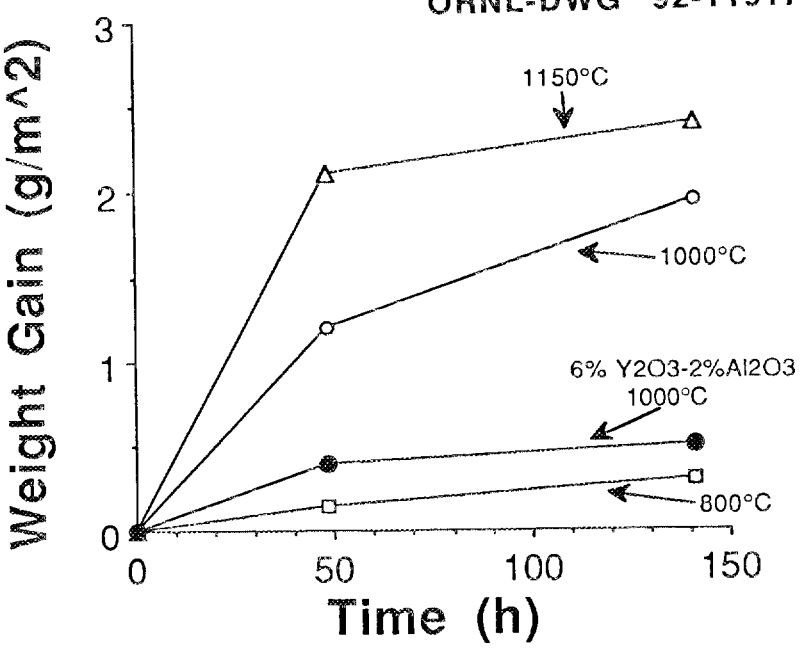

Fig. 13. Oxidation behavior of sintered RBSN as a function of temperature. The sample was composition TM-137 (Si_3N_4-11% La_2O_3-3% Al_2O_3) sintered at 1800°C. For comparison, a silicon nitride with Si_3N_4-6% Y_2O_3-2% Al_2O_3 and fabricated with high-purity starting powders is also shown.

3. M. B. Trigg and E. Tani, "Effect of Fabrication Routes and Heat Treatments on the Microstructure of Silicon Nitride-Based Materials," pp. 593-97 in *Mater. Sci. Forum*, Vol. 34-36, ed. C. C. Sorrell and B. Ben-Nissan, Trans. Tech. Pub., Switzerland, 1988.

4. G. Ziegler and G. Wötting, "Post-treatment of Pre-sintered Silicon Nitride by Hot Isostatic Pressing," *Int. J. High Technol. Ceram.* **1**, 31-58 (1985).

5. G. Wötting and G. Ziegler, "Microstructural Development of Sintered, Hot-Pressed and Hot-Isostatic-Pressed Silicon Nitride," pp. 412-24 in *Proceedings of the International Symposium on Ceramic Components for Engines*, KTK Science Publishers, Tokyo, Japan, 1984.

6. K. P. Plucknett and M. B. Lewis, "Hot Isostatic Pressing of Sintered Si_3N_4 Ceramics," *Ceram. Eng. Sci. Proc.* **12**(7-8), pp. 1327-1344 (1991).

7. H. Kleebe and G. Ziegler, "Influence of Crystalline Secondary Phases on the Densification Behavior of Reaction-Bonded Silicon Nitride During Postsintering Under increased Nitrogen Pressure," *J. Am. Ceram. Soc.* **72**(12),2314-2317 (1989).

8. P. L. Antona, A. Giachello, and P. C. Martinengo, "Nitridation of Silicon in the Presence of Oxides," pp. 753-66 in *Ceramic Powders*, ed. P. Vincenzini, Elsevier Science Publishers, Amsterdam, 1983.

Status of milestones

All milestones are on schedule.

Publications

None.

Development of Microwave Processing of Silicon Nitride Components for Advanced Heat Engine Applications Reaction Bonded and Sintered Reaction Bonded Silicon Nitride

C. A. Willkens (Saint-Gobain/Norton Industrial Ceramics Corporation)

Objective/Scope

Microwave processing offers potential advantages, such as decreased nitriding and sintering times, nitriding of larger cross-sections and unique microstructures, as compared to traditional sintering techniques. This CRADA project will apply Microwave processing technology developed at ORNL to unfired reaction bonded silicon nitride (RBSN) and sintered reaction bonded silicon nitride (SRBSN) materials processed at NRDC. Powder compacts produced at NRDC will be brought to ORNL for microwave nitriding and sintering studies. The properties of microwave nitrided and/or sintered silicon nitride will be directly compared against same lot materials traditionally "fired" at NRDC.

Technical Progress

Baseline tiles of RBSN precursor (unnitrided) have been fabricated. The tiles were presintered and surface ground in order to provide strength to survive transport to ORNL for microwave nitriding. A similar set of tiles will be nitrided in a standard cycle at NRDC. A second iteration, having a higher density, is being processed.

Pressureless sintered silicon nitride compositions, previously made at NRDC using the conventional powder process route, were reviewed for potential transfer to the SRBSN

process. Several compositions (A, B and C) were chosen for screening evaluation. The unmodified RBSN nitriding cycle resulted in relatively low alpha content for the pressureless SRBSN compositions, necessitating adjustment of the nitride cycle. The modified nitride cycle resulted in an acceptable alpha content. A standard pressureless sinter cycle resulted in >97% density for Compositions A and B. Composition C did not densify well, and this has been attributed to a low as-nitrided oxygen content. A modification to Composition C to compensate for the low oxygen is in process. Composition B appears to be suitable for further study and, if mechanical properties are acceptable, the remaining as-nitrided tiles will be sent to ORNL for microwave sintering.

Status of Milestones

On Schedule

Publications

None

Development of Microwave Processing of Silicon Nitride Components for Advanced Heat Engine Applications Microwave Annealing Si_3N_4 - 4 Wt% Y_2O_3

R. L. Yeckley (Saint-Gobain/Norton Industrial Ceramics Corporation)

Objective/Scope

The purpose of the annealing trials is to improve the fracture toughness and creep resistance of HIP silicon nitride with 4% yttria by promoting growth of elongated grains.

Technical Progress

HIPing of Silicon Nitride - Twenty slip cast silicon nitride tile were densified by glass encapsulation HIPing. The HIP conditions achieved high density while retaining high alpha contents. The high alpha contents may be necessary for grain growth to occur during microwave annealing of silicon nitrides with low additive contents.

Annealing Trials - The annealing trials have been completed. Two tile were annealed at each microwave condition in Table 1. The tile were buried in silicon nitride powder during the annealing trials. The HIP silicon nitride did not couple well below 1100°C. Because of the poor coupling, deviations of 50°C occurred during the heating cycle of the first annealing trial. In subsequent runs, the microwave power was set at 1500 watts until the samples reached 900°C. Then power was increased to 2000 watts untilthe samples reached 1150°C. Above 1150°C the furnace was computer controlled. Figure 1 shows the time-temperature-power curves for microwave anneal MW3. The improved coupling above 1100°C is evident by the reduced power required to continue the heating cycle and maintain the soak temperature.

Table 1. Microwave Annealing Conditions.

Trial	Temperature (C^o)	Time (hr)
MW1	1738	0.5
MW2	1507	6.7
MW3	1650	5.25
MW4	1738	1.4
MW5	1650	10
MW6	1773	6.7
MW7	1562	1.4

Status of Milestones

On Schedule

Publications

None

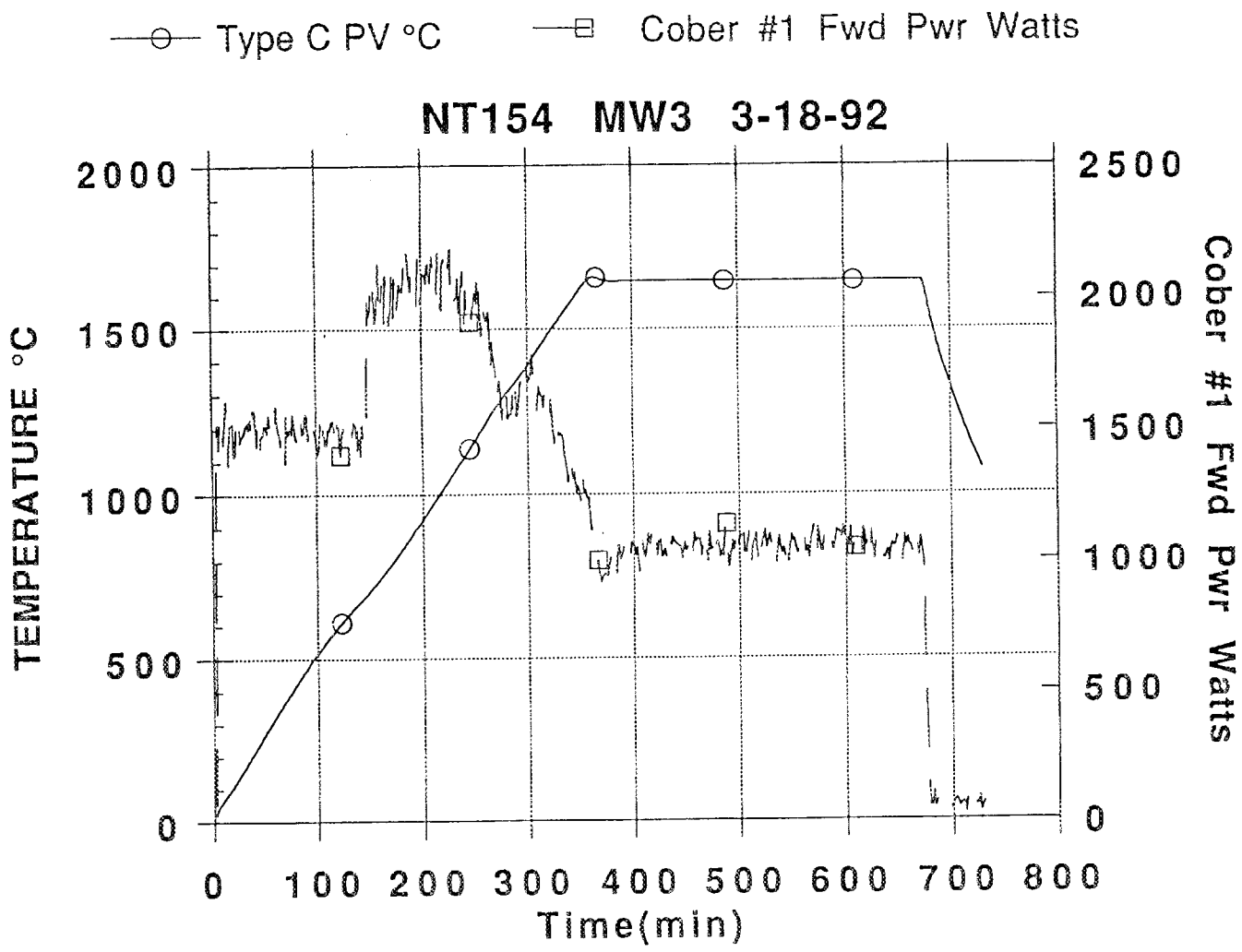

FIGURE 1. Time-Temperature-Power Curves for Microwave Annealing of HIP Si_3N_4

Cost Effective Sintering of Silicon Nitride Ceramics (SIU-C)

D. E. Wittmer (Associate Professor, Southern Illinois University
at Carbondale, Carbondale, IL 62901

Objective/Scope

The purpose of this work is to investigate the potential of cost effective sintering of Si_3N_4 through the development of continuous sintering techniques and the use of lower cost Si_3N_4 powders and sintering aids.

Technical Highlights

The project research goals for Phase I are divided into 4 major tasks:

Task 1. Conduct economic comparisons of continuous sintering with batch sintering.

Task 2. Assess the effects of heating rate on densification, microstructure and properties.

Task 3. Determine feasibility of using lower cost Si_3N_4 powders.

Task 4. Determine feasibility of using alternate materials and furnace design to improve loading and throughput.

Task 5. Final Report.

Task 1. Conduct economic comparisons of continuous sintering with batch sintering.

A simple economic model was developed through the use of a spreadsheet program to allow for comparative analyses of the costs involved with continuous sintering and batch sintering. The size of the belt and belt speed control the throughput for continuous sintering, while the size of the furnace chamber and sintering cycle time (loading, sintering, cooling, and unloading) control the throughput for the batch furnace. Some assumptions in the cost modelling are based on requiring several batch furnaces to match the throughput for the belt furnace; where the capital cost of the batch furnaces is directly related to the number of furnaces, but the capital cost of the belt furnace is related to the size of the hot zone. In other words, the cost of doubling the length of the hot zone for the belt furnace may only increase the

capital cost of the belt furnace by 40%. Similar assumptions were made for increasing the furnace capacity by improvements in belt design or materials. Assumptions were made of a 98% yield for the belt furnace compared with 90% and 70% yields from the batch furnace. The preliminary results from this economic model are given in Table I.

Table I. Results of Economic Comparisons for Continuous and Batch Sintering

Economic Consideration	Belt Furnace Per Part Cost/Per Kg Cost	Batch Furnace Per Part Cost/Per Kg Cost
No Modifications	$1.35/$13.48	$9.98/$99.80 (90%) $12.83/$128.33 (70%)
Modify Belt Design	$0.68/$6.74	$9.98/$99.80 (90%) $12.83/$128.33 (70%)
Modify Belt Material	$0.55/$5.47	$9.98/$99.80 (90%) $12.83/$128.33 (70%)
Modify Hot Zone & Belt	$0.32/$3.18	$9.98/$99.80 (90%) $12.83/$128.33 (70%)

These results demonstrate that sintering cost can be reduced significantly for the belt furnace ($13.48/kg to $3.18/kg), but would remain constant for the batch furnace ($99.80/kg @ 90% and $128.33/kg @ 70%). Additional refinement of this model is warranted to better reflect the true cost of sintering based on scaling of furnace and throughput, material costs, and overhead rates.

Task 2. Assess the effects of heating rate on densification, microstructure and properties.

Several batches of Si_3N_4 containing sintering aids were processed by turbomilling and pressure casting. The techniques used were developed as part of subcontract 19X-SA796C, WBS Element 1.1.1.6 Improved Processing of Ceramics Composites (SIU-C), and the details have been reported in previous reports. The Si_3N_4 compositions and formulations prepared included:

- A4Y13--4 wt.% Al_2O_3 (Ceralox), 13 wt.% Y_2O_3 (Starck) and 83 wt.% Si_3N_4 (2 batches using Starck LC-10 and Ube E-10)

- A4Y13--4 wt.% Al_2O_3 (Ceralox), 13 wt.% Y_2O_3 (Starck) and 83 wt.% Si_3N_4 (Ube E-10) containing 5 wt. % ß-Si_3N_4 seed.

- A4Y6--4 wt.% Al_2O_3 (Ceralox), 6 wt.% Y_2O_3 (Starck) and 90 wt.% Si_3N_4 (3 batches using Starck LC-10, Starck LC-12SX and Ube E-10)

- A4L6--4 wt.% Al_2O_3 (Ceralox), 6 wt.% La_2O_3 (Molycorp) and 90 wt.% Si_3N_4 (3 batches using Starck LC-10, Starck LC-12SX and Ube E-10)

- A2Y8--2 wt.% Al_2O_3 (Ceralox), 8 wt.% Y_2O_3 (Starck) and 90 wt.% Si_3N_4 (3 batches using Starck LC-10, Starck LC-12SX and Ube E-10)

- A6L8--2 wt.% Al_2O_3 (Ceralox), 8 wt.% La_2O_3 (Molycorp) and 90 wt.% Si_3N_4 (3 batches using Starck LC-10, Starck LC-12SX and Ube E-10)

- A4Y6L7-4 wt.% Al_2O_3 (Ceralox), 6 wt.% Y_2O_3 (Starck) 7 wt.% La_2O_3 (Molycorp) and 83 wt.% Si_3N_4 (Ube E-10)

During this reporting period, several Si_3N_4 formulations were sintered in the belt furnace at 1675, 1750, 1775, 1800, and 1850°C for 90 min. with poor to excellent density results. Compositions sintered at 1800°C and above were severely decomposed and reacted with the Mo boat material. This was anticipated due to the lack of N_2 over-pressure to retard the Si_3N_4 decomposition. At lower temperatures most of the compositions sintered with very good to excellent results. In order to eliminated cracking due to thermal shock, it was necessary to run the belt furnace with the first hot-zone off for compositions with lower sintering aid additions.

Some disks were selected from those runs which produced high sintered densities. These disks were machined into standard test bars or the faces were machined parallel to determine the extent of surface reactions. Table II shows the results from density measurements and flexural testing. Specimens for fracture toughness measurements and microstructural evaluations are presently being prepared.

Also as part of this task, several samples of Norton Co. NT-451, provided by Norton/TRW, Salem, NH, were successfully sintered to greater than the target density in separate belt furnace runs. The effect of continuous sintering on the microstructure and properties is being examined by Norton/TRW.

Table II. Density and Flexural Strength Results for Some Selected Sintering Trials

Sample ID	Composition	Sintering Conditions	Density (%TD)	Flexural Strength (MPa)
9-1	A2Y8-E10	Belt Furnace 1625/90 min. 1st Zone Off	3.07 (94%)	880
20-5	A4Y6L7-E10	N_2 Overpressure 1750/240 min.	3.30 (99.1%)	972
20-9	A4Y6L7-E10	Belt Furnace 1625/90 min. 1st Zone Off	3.28 (99.4%)	974
23-6	A4Y13-E10 5% ß-Seed	Belt Furnace 1625/90 min. 1st Zone Off	3.32 (99.5%)	929
24-10	A4Y13-E10	Belt Furnace 1625/90 min. 1st Zone Off	3.32 (99.5%)	918
23-1	A4Y13-E10 5% ß-Seed	Belt Furnace 1725/90 min.	3.32 (99.5%)	915
24-2	A4Y13-E10	Belt Furnace 1725/90 min.	3.32 (99.5)	1084

Task 3. Determine Feasibility of Using Lower Cost Si_3N_4 Powders.

This task was initiated through the use of 3 commercially available Si_3N_4 powders as part of Task 2. These 3 Si_3N_4 powders have a range of purity and cost, with the LC-10 being the lower cost and purity and Ube E-10 being the higher in cost and purity. Formulations prepared from both LC-10 and E-10 were sintered to high densities in the belt furnace, however those prepared from

the E-10 Si_3N_4 had somewhat higher densities for the same sintering conditions.

Another source of Si_3N_4 having low purity and cost from Performance Ceramics, Peninsula, OH is presently being evaluated in the A4Y13 formulation. The concept of using lower purity and cost rare earth oxide sintering aids is also being explored. This work should be continued.

Task 4. Determine feasibility of using alternate materials and furnace design to improve loading and throughput.

Initially the use of alternate construction materials and design of the belt were investigated to improve the loading and part throughput. The impact of improving the loading and throughput on the per part cost were incorporated as part of the input in the economic modelling in Task 1. A change in the belt design was tested which allowed for at least double the load capacity of the previous design. In addition, alternate setter and crucible materials were investigated as a means of improving heating uniformity and reducing the reactions between the Si_3N_4 parts and the setter. These modifications were tested successfully in Task 2.

Also, the construction materials for the furnace elements and belt are a major issue in determining both the load capacity and operating costs for a continuous sintering furnace. Several options have been considered which need to be addressed by further research.

Due to the demonstrated potential of continuous sintering for compositions with reduced sintering aids, additional funding was requested for the following tasks: 1) refine economic model and design for a chosen furnace, 2) continue the evaluation of sintering parameters on properties of selected Si_3N_4 composition, 3) continue evaluation of low cost Si_3N_4 powders.

Given the success of this additional research, it is anticipated that Phase II would involve the design, construction and testing of a pilot scale belt furnace with improved load bearing capacity for specific heat engine component, 3) sintering of parts provided by industrial partner(s) and 4) continued evaluation of sintering parameters on properties of selected Si_3N_4 composition, and Phase III would involve conducting pilot scale production of heat engine components, and the assessment of properties, production yields and manufacturing costs related to continuous sintering of actual heat engine component(s).

Status of Milestones

1.	Conduct economic comparisons of continuous sintering with batch sintering.	Completed
2.	Assess the effects of heating rate on	On Schedule

densification, microstructure and properties.

3.	Determine feasibility of using lower cost Si_3N_4 powders.	On Schedule
4.	Determine feasibility of using alternate materials and furnace design to improve load and throughput.	Completed
5.	Final Report	On Schedule

Publications

D. E. Wittmer, T. E. Paulson and D. Doshi, Southern Illinois University Carbondale, IL and C. W. Miller, Jr., Centorr Furnaces/Vacuum Industries, Inc., Nashua, NH, "Improved Processing and Cost Effective Sintering of Si_3N_4 ," DOE's Contractor's Coordination Meeting, October 27-31, 1991, Dearborn, MI.

D. E. Wittmer,D. E., Paulson, T. E. and Miller, C. W. Jr., "Continuous Sintering of Si_3N_4 in a Controlled Atmosphere Belt Furnace," Ceramic Engineering and Science Proceedings (to be published in **13** [9-10] (1992).

Presentations

D. E. Wittmer*, T. E. Paulson and D. Doshi, Southern Illinois University Carbondale, IL and C. W. Miller, Jr., Centorr Furnaces/Vacuum Industries, Inc., Nashua, NH, "Improved Processing and Cost Effective Sintering of Si_3N_4 ," Contractor's Coordination Meeting, October 27-31, 1991, Dearborn, MI.

D. E. Wittmer, T. E. Paulson, and C.W. Miller, Jr., "Continuous Sintering of Si_3N_4 in a Controlled Atmosphere Belt Furnace," Presented at the 16th Annual Conference on Composites and Advanced Ceramics, Cocoa Beach, FL, Jan. 7-10, 1992.

Scalability Demonstration Program for Silicon Nitride by the Sullivan™ Process for Advanced Ceramics - Thomas M. Sullivan (Sullivan Mining Corporation)

Approach

The purpose of this effort is to demonstrate the scalability of the Sullivan™ Process for making silicon nitride; to develop unique high and low temperature versions of silicon nitride; to determine the net-shape capability of the process; and to characterize the microstructural, mechanical, tribological, and physical properties of the Sullivan™ Process silicon nitride.

Background

Automobile engines and gas turbines have many components that will perform better if made from ceramics. However, ceramics must be manufacturable in very high volumes for costs comparable to mass-produced steel assemblies. The economic impact of ceramic engines components to the United States will be substantial, energy savings will be economically important, and emissions to the environment will be reduced.

Chrysler Corporation has been developing an experimental ceramic cam follower since 1984. Chrysler originally discussed the application with twenty-one domestic and foreign sources of high performance ceramics, and received pro forma cost analyses and process capability assessments from eighteen of these suppliers. Ten sources sent sample rollers for evaluation. Chrysler concluded that "Sullivan Mining Corporation was the only source to supply silicon nitride material which met our (Chrysler) requirements for mechanical performance, high volume process capability, and pro forma cost in automotive volumes." The Sullivan™ Process rollers were made using bench top laboratory equipment. Advantages must now be demonstrated on an expanded laboratory scale and pilot scale.

Objectives/Scope

Sullivan™ Process capability shall be demonstrated on a commercial scale for both a low temperature and a high temperature silicon nitride. Work shall include construction of a pilot scale system, mass flow calculation, and cost analysis. High and low temperature silicon nitride processing shall be optimized. Process capability for net shaping shall be evaluated with respect to tensile bars. Material shall be examined by NDE methods and be evaluated at the High Temperature Materials Laboratory.

Technical Progress

MOR Bar Casting - The minimum content of catalyst derivatives are anticipated to result in minimum high temperature creep. It was therefore decided to use the minimum amount of catalyst for high temperature silicon nitride. Changes in catalyst content and type, however, not only modify the thermal profile at high temperature, but alter the low temperature casting of the material as well.

A statistical Design of Experiments (DOE) developed by Chrysler Corporation using RS\1 Discover software (BBN Software Products Division, Bolt, Beranek, and Newman, Inc., Cambridge, MA) was used to define the parameters for casting. This DOE software emphasizes the importance of interactions between factors. The matrix that was developed had sixteen factors and six interactions. Two values were selected for each factor. Factors included reactant viscosity, reactant rate, catalyst material, entrainer concentration, critical temperature, critical pressure, critical time, drain rate, curing temperature, curing rate, control gas pressure, maximum heating rate, maximum temperature, soak time, step down temperature, and time at the step down temperature.

Results of the experiments indicated that casting temperatures beyond T + 5°C were detrimental to part formation. Lower ramp rates were beneficial as compared to the low temperature silicon nitride composition. Eight bars were finally cast in Run #91112205 with acceptable shape, density, and precision using the selected high temperature composition. Parts were made within 0.001 inch of the net shape.

Low-temp Microstructure Refinement -Refining the microstructure of silicon nitride composition for low temperature focused on a uniform distribution of constituents and process control. Controlling the solvolysis of undesirable concentrates like iron compounds at temperatures below solidification enables the removal of many impurities in the solvent. Changes in temperature of less than 1°C can have order-of-magnitude impacts on solvolysis. Refining microstructure is, therefore, in large measure, a matter of refining process control.

Process equipment was run after incorporating changes in metering valve location and adjustment, pre-heating and post-heating valves and outlet lines, tuning electrical regulators,

adjusting valve actuators, and changing the operating program. Twenty-four process system runs were conducted. Many runs were aborted because of excessive pressure gradients. Process iteration, however, identified a particular combination of process control program and equipment configuration which results in the optimum level of control. Unfortunately, changes in the material produced were minimal in comparison to previously produced material.

Heat-Cycle Acicular Microstructure - Changing the heat cycle to develop a pronounced acicular microstructure was tried in Run #91102404. At T_M - 250°C for 20 minutes, whisker-like grains were formed in areas of low density. Efforts to form acicular grain shapes in dense parts was unsuccessful using high temperature heat treatment.

Acicular grains appear to be formed by a vapor-liquid-solid mechanism which is most pronounced in areas with high concentrations of catalyst derivatives. Since catalyst derivatives represent a particularly small weight fraction of a part, formation of significant acicular grain shape content by means of heat cycle alone without mechanical pressure or large additive levels appears unlikely.

High Temperature Microstructure Refinement - An acicular grain shape is particularly advantageous for high temperature applications. Low oxynitride levels are a concomitant of the Sullivan™ Process and conducive to low creep in the 1450-1550°C temperature region of interest. It was therefore decided to eliminate any Ziegler catalyst derivatives to reduce creep and to form an acicular grain shape by chemical means using inorganic polymers.

Acicular grains were easily and economically formed in a two stage process in which 1) grains were formed from silanes, and 2) were densified by supercritical processing. Analysis of the material by EDS indicated large amounts of oxygen. Neutron Absorption Analysis (NAA) indicated a 5.5 wt. % oxygen level. Since only 1.1 wt. % of the oxygen could be attributed to oxygen in the silane, the system was checked again for leaks. A small leak was found. The run was replicated. NAA is currently being conducted to verify the oxygen level.

Supercritical ammonia solutions abstract oxygen from metal or ceramic surfaces. Abstracted oxygen is added to silicon nitride while the material is in an intermediate, highly reactive "getter" state.

The chemicals used for making acicular grain shape silicon nitride are very aggressive. Stainless steel and corrosion resistant alloys such as Hastelloy C are dissolved in a matter of minutes. A variety of alloy and metals were tested in order to identify optimum materials of construction. Coupons made from three different transition metals were found to be compatible.

Molds for making bars are being made from two of the transition metals, though obtaining material to make molds turned became protracted, determining the materials of construction experimentally on a small scale was important before finally committing to much larger scale equipment.

14" Process System - Detailed blueprints for finishing the 14" pressure vessel were completed and distributed for quotation. The vessel will be lined with a corrosion resistant transition metal to permit combining the two step process used to make acicular grain shaped ceramics in a single step.

The 14" process system will incorporate a cryogenic system to remove moisture from the metal surfaces of the interior. This is particularly important because of the very large surface area of multiple cavity molds and the hygroscopic nature of the chemical process. Special double seal designs will also be used to maintain the integrity of the seal during supercritical conditions.

An automated system is being designed to install and remove gang molds from the pressure vessel. The system will include tracks that index with the mold connections inside the autoclave. Mold connections will be made outside the pressure vessel.

Components are being acquired and assembled in preparation for the arrival of long lead time components. The basic cryogenic system has been acquired and is in the process of being assembled.

Status of Milestones

Critical milestones are on schedule.

1.1.4 Processing of Monolithics

Improved Processing

V. K. Pujari, D. M. Tracey, M. R. Foley, A. K. Garg, N.I. Paille,
P. J. Pelletier, L.C. Sales, C. A. Willkens, R. L. Yeckley (Norton Company)

OBJECTIVE/SCOPE

The goals of the program are to develop and demonstrate significant improvements in processing methods, process controls, and nondestructive evaluation (NDE) which can be commercially implemented to produce high-reliability silicon nitride components for advanced heat engine applications at temperatures to 1370°C. Achievement of these goals shall be sought by:

- The use of silicon nitride - 4% yttria composition which is consolidated by glass encapsulated HIP'ing.
- The generation of baseline data from an initial process route involving injection molding.
- Fabrication of tensile test bars by colloidal techniques - injection molding and colloidal consolidation.
- Identification of (critical) flaw populations through NDE and fractographic analysis.
- Correlation of measured tensile strength with flaw populations and process parameters.
- Minimization of these flaws through innovative improvements in process methods and controls.

The quantitative program goals are: 1) mean RT tensile strength of 900 MPa and Weibull modulus of 20, 2) mean 1370°C fast fracture tensile strength of 500 MPa, and 3) mean 1230°C tensile stress rupture life of 100 hours at 350 MPa.

TECHNICAL PROGRESS

The technical progress against the major tasks described in the statement of work is summarized in the following. The major tasks are: 1) Material Selection and Characterization; 2) Material Processing and Process Control; 3) Development and Application of NDE; 4) Property Testing and Microstructural Evaluation; 5) Reporting; 6) Quality Assurance.

Process optimization efforts continued during the reporting period according to the Stage II experimental plan which involves processing 16 iterations of buttonhead tensile bars. The iterations serve as factorial designed experiments based on control variables established in Stage I of the Program. The outcomes of successive iterations relative to targeted mechanical properties are used to establish the optimum control variable combinations/levels for the final process demonstration of Stage III (5/1/92 - 9/30/92). Current technical highlights are as follows:

- Development and scaleup of the aqueous based powder processing methodology has been completed for production of NCX-5102 silicon nitride slurry used in the closed loop colloidal consolidation facility. SPC has been implemented for chemical and physical property control. SOP (Standard Operating Procedures) and control charts involving all key parameters have been established for the aqueous powder processing.

- Iron contamination has been eliminated from the powder processing and colloidal consolidation equipment through judicious selection of construction material and refinement of the filtration process. Casting iteration data verified the successful elimination of iron inclusions from the powder processing and casting equipment.

- Programmed pressure profile casting methodology has been completed using an automated, multi-station casting apparatus configured for rapid and efficient casting batches. A developmental in-process feedback control system based upon ultrasonic monitoring has been demonstrated for assuring precision green parts and high yields.

- An optimized HIP densification process has been developed and implemented as SOP for tensile bar iterations. The process provides an excellent toughness, fine-grain/high aspect ratio microstructure. Furthermore, the process has been refined to provide high loadings and excellent yields.

- Various NDE methods (RT, UT, CT, NMR, LDP, XRD) were successfully utilized in the above developments and have been incorporated in process control SOP. Recommendations on NDE for detection of flaws below 50 μm were made (in accordance to a 12/31/91 milestone). These included microradiography with geometric enlargement, radiograph high resolution digital display and computed x-ray microtomography.

- A tensile testing calibration study was conducted using a set of strain gaged buttonhead tensile specimens which established the range of bending imposed with the SOP. Strain gage data indicate an acceptable level of bending at fracture using the straight collet/"SuperGrip" system.

- Experiments involving heat treatments after HIP'ing (crystallization) and after machining (oxidation) were conducted. The post-HIP crystallization was found to significantly enhance the 1370°C fast fracture strength. The post-machining oxidation treatment was found to enhance both the room and elevated temperature tensile strengths.

TASK 1 MATERIAL SELECTION AND CHARACTERIZATION

Materials at each stage of processing are being analyzed according to established standard operating procedures (SOP). Statistical Process Control (SPC) charts are being developed for all key process parameters during Stage II for overall process monitoring purposes.

TASK 2 MATERIALS PROCESSING AND PROCESS CONTROL

i) Powder Processing

The iron inclusion failure origins first observed in Iteration O tensile rods increased in frequency through Iteration X. To eliminate these failure origins several changes were made to the process including adding a pre-mill filtration and magnetic separation step to remove any iron inclusions in the as-received powder prior to being milled to a submicron size. Additional microfocus x-ray radiography had shown the starting Ube Si_3N_4 powder to have significant degree of metallic contamination. Ten (10) out of 15 samples (30 g each) were found to contain either one or two high density inclusions from 25 to 200 microns in size. All materials of construction for the process equipment were reviewed and changed to non-metallic materials. These steps resulted in a significant decrease in metallic inclusions as detected in the rods by microfocus x-ray and the virtual elimination of metallic inclusion failure origins during tensile testing, as discussed in Task 4.

Lot E silicon nitride powder was received from Ube Chemical. The particle size of the silicon nitride was found to have enough variation to necessitate considerable adjustment in milling parameters from previous lots. Figure 1 shows the surface area of the three grades of Ube silicon nitride powder. Milling time has varied by as much as 93% in order to achieve a consistent milled average particle size.

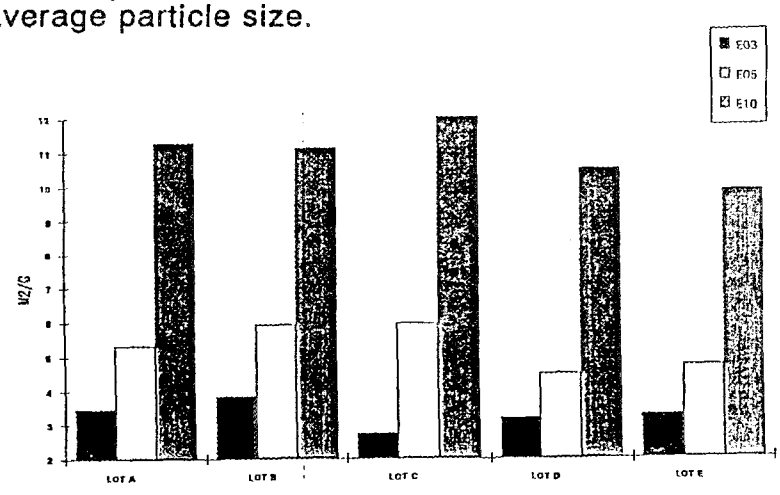

Figure 1: Ube Si_3N_4 Surface Area

Table 1: Process Control Charts

Original	Additional
Oxygen	D_{10}, D_{90}
Surface Area	pH
Yttria	Viscosity
D_{50}	Acoustic Mobility
Fracture Toughness	Conductivity
	Specific Gravity
	Packing Density (CIP'd)

Five batches (CO26-CO30) were prepared for colloidal consolidation studies during the period. Additional control charts were initiated as shown by Table 1 in response to a significant decrease in cast density for batch CO30. The lower cast density resulted in unacceptable warpage during HIP'ing. The low cast density is attributed to a narrower particle size distribution, even though the average particle size was within specification. This resulted in a lower packing density as measured on CIP'd control samples (Figure 2). The narrow particle size distribution was caused by variation in the starting Ube silicon nitride powder particle size distribution for Lot E as compared to prior lots. Efforts to compensate by adjusting the milling parameters (solids content, time) were only partly successful in re-establishing the milled particle size distribution and packing density. Therefore, the Lot E silicon nitride power will be replaced.

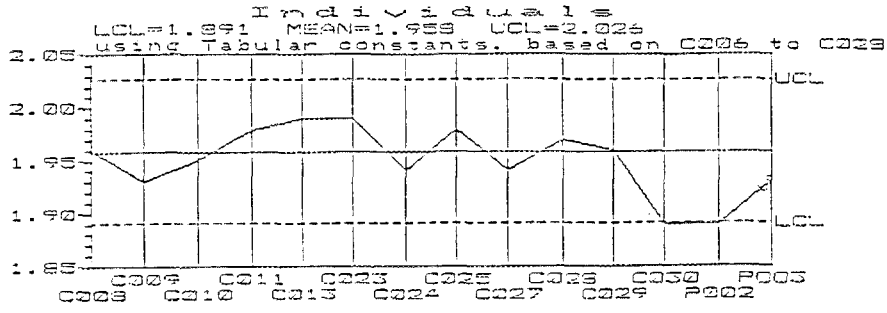

Figure 2: CIP'd Packing Density (g/cc)

ii) Colloidal Consolidation

Seven (7) casting iterations were performed during the reporting period. The first four of these (XXX, X, Y, and Z) served to monitor progress in the milling and casting equipment modification efforts. These modifications were developed in response to NDE and fractography data on the nature of the strength impairing defects associated with these unit operations. The last three iterations (AA, AB, and AC) were cast to provide samples for concurrent studies in HIP'ing and machining.

Incremental modifications were made on the pressure cast operating procedure and the new casting machine so as to achieve more reproducible cast pieces. These modifications have taken the form of: 1) more uniform slurry flow, 2) tighter control on pressure profile reproductions from one cast to the next, 3) better mold treatment and handling procedures, 4) elimination of all metallic components to eliminate metal inclusions in the cast part, and 5) modifications in the design of the equipment to reduce the incidence of voids. One of the most significant changes made was to automate the pressure application which results in duplication of the pressure profile throughout the casting campaign. The effect of these changes may be quantified by the successively smaller confidence intervals shown in Figure 3. The figure shows the 99.73% confidence intervals (3-sigma) on the average weight of the as-cast tensile rods. Figure 4 shows the relationship between the as-cast weight and the pre-sintered weight of the tensile rods for Iterations Y, Z and AA. The pre-sintered weights very closely follow the as-cast rod weights with an extremely high degree of correlation ($r2 > 0.95$). Any deviation from the regression line can be explained by a proportional deviation in rod length measured at the pre-sintered stage (r2 increase to .99). As all rods were cast in the same size cavity, the difference in pre-sintered lengths is the result of differing amounts of ceramic powder cast in the mold. Since the density differences of the dried cast pieces are negligible (standard deviation $< 0.3\%$), this implies that controlling as-cast weights of the tensile rods will result in control of dimensional variation in the end product. Effort is under way to further reduce the observed variations in the as-cast weight. Exceptions to this trend reflect variations in the casting time, for various batches. For example Iteration Y represents different casting times which resulted in parts which were not fully cast and therefore of varying weights. This problem can be addressed by the use of in-situ monitoring of casting which will be covered in the section on Development and Application of NDE, Task 3.

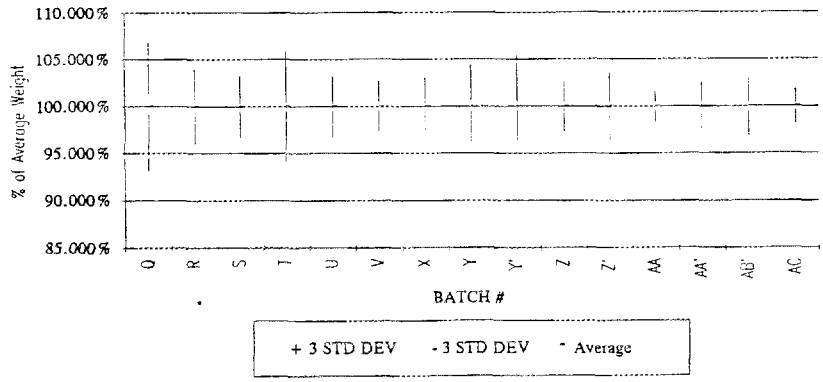

Figure 3: Confidence Intervals on As-Cast Tensile Rod Weights

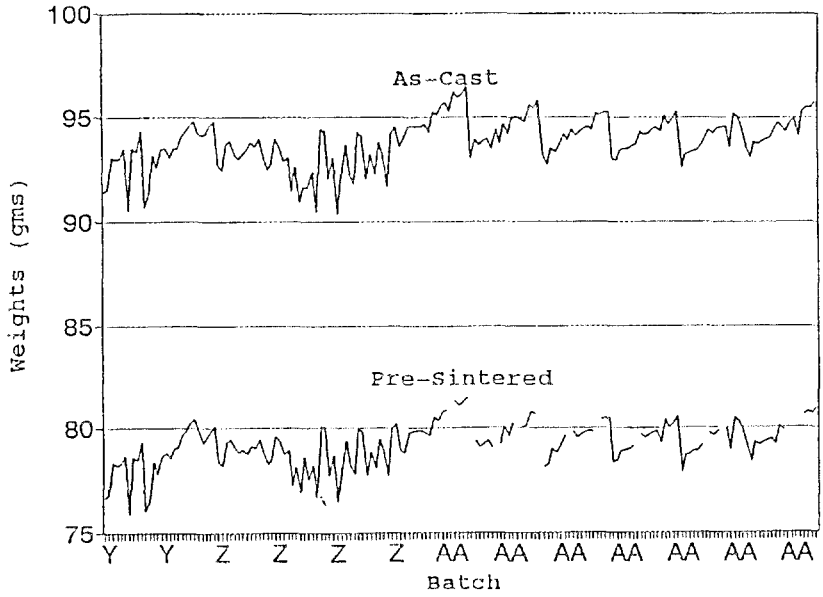

Figure 4: As-Cast and Pre-Sintered Weights for Iteration Y, Z & AA

The effect of different lots of raw materials, (e.g. D and E) is evident when comparing molding batches AA with Batches AB' and AC. The lower solids content slips made with Lot E powder gave more variability. The AB' as distinct from AB indicates a mold design variation which also results in increased variability.

iii) Hot Isostatic Processing

Reproducible densification behavior during HIP with consistent toughness is an important requirement for attaining

stated strength and Weibul Modulus objectives. The tensile strength depends both on the flaw size and the toughness as described by well known Griffith's equation.

Therefore, a change in toughness value will result in shifting of the strength distribution. As a result a HIP experimental matrix was designed to examine the correlation of toughness with HIP parameters and microstructure.

The first step of the matrix was to densify the tile at HIP conditions which achieved full density while retaining a high percentage of alpha silicon nitride. Subsequently the tiles were sintered at one of three temperatures, three soak times and one of two pressures. The first HIP step allowed investigation of pressures and temperatures that were sufficient to density the material but may affect grain development during the α to β transformation.

The range of times and temperatures selected resulted in significant microstructural variation. The resultant average grain size ranged from 0.5 microns to 1.68 microns.

These changes in microstructure due to the variation in above parameters resulted in difference in fracture toughness. Within the range studied, the pressure was found to have insignificant effect on the microstructure.

Generally, the toughness of silicon nitride is dependent on the β silicon nitride aspect ratio as shown in Figure 5. The micrographs in Figure 5 compare a high toughness microstructure with that of a low toughness microstructure. The high toughness material has a finer grain size with higher aspect ratio grains. Because of this dependence, the apparent aspect ratio measured from micrographs was correlated to toughness values. The measurements were taken from 2.5KX micrographs similar to those shown in Figure 5. Lines were randomly drawn across the photomicrograph. Rectangular grains touching the lines were measured.

The average aspect ratios for high and low toughness microstructures were measured to be 10 and 4 respectively. The aspect ratio was correlated with toughness by determining a aspect frequency. The aspect frequency is the number of grains with an aspect ratio greater than 4 divided by the length of lines transversed on the micrographs. The plot in Figure 6 shows a very strong dependence of toughness on the aspect frequency.

Five HIP runs (using tiles cast from milled powder batches CO29 an CO30) were conducted using the two step process and the measured toughness values are shown in Table 2. Each toughness value in Table 2 is an average of 5 separate measurements on each tile. Slightly lower K_{IC} for batch CO30 tiles is suspected to be due to the excessive crystallization of the intergranular phase. As shown in Table 2, two stage HIP process results in higher α-phase content in the microstructure. Higher α-content is expected to improve hardness as measured by Knoop or Vicker indenter. Hardness and strength values are currently being measured on these tiles and will be reported in the next report.

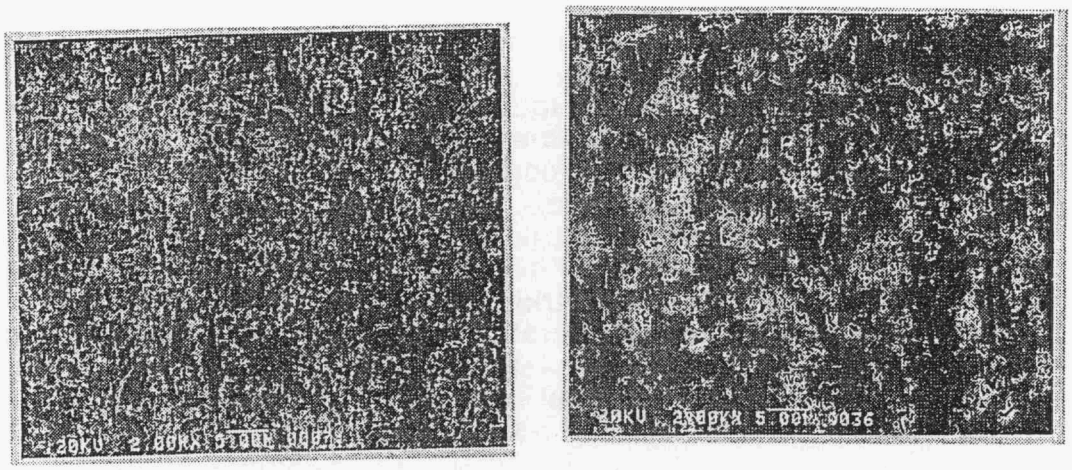

K = 6.26 MPa m1/2 K = 5.75 MPa m1/2

Figure 5: The finer microstructure (left) has a toughness of 6.26 MPa√m. The coarser microstructure has a toughness of 5.75 MPa√m. The coarser structure was densified at a higher temperature with the same soak time.

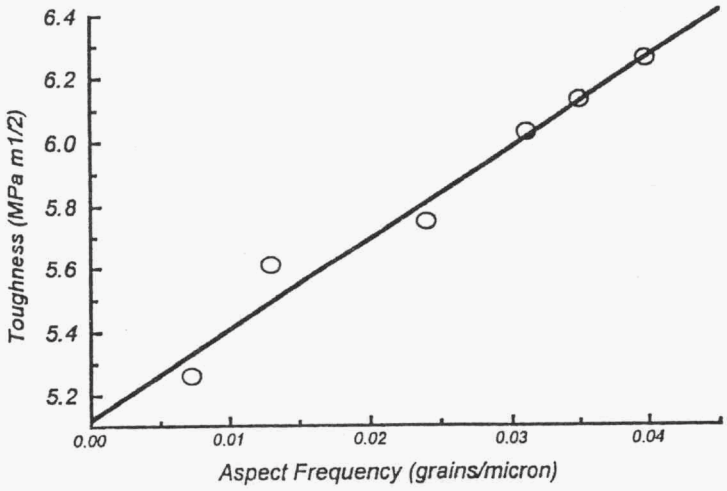

Figure 6: Toughness exhibits a strong dependence on aspect frequency.

Table 2: Summary of Fracture Toughness Values from the Two Stage HIP Cycle.

Batch	HIP	K_{IC} MPa $m^{1/2}$	α - Si_3N_4 %
CO29	a	6.46	23
C029	a	6.2	22.5
CO29	b	6.4	22.6
C029	b	6.43	21.5
C029	c	6.24	-
C029	c	6.1	-
C030	d	5.9	-
C030	d	5.7	-
C030	e	6.4	-
C030	e	6.2	-
C030	e	6.2	-

iv) Process Control

Process control procedures and charts have been continuously revised and updated during Stage II of the program. This has been done so as to:

1) reduce the set of charts to those which can most efficiently discriminate between product which does and does not meet specification,
2) tighten control limits (by increasing the sample size) where specifications do not allow for deviation (low process capability index Cpk),
3) loosen control limits (by decreasing sample size) where specification limits were broad compared to control limits,
4) consolidate multiple control charts/decision criteria into go/no-go charts.

Control charts have been written into Standard Operating Procedures (SOP) which will be followed in Stage III of the program. One of the go/no-go charts used in the pressure casting unit operation is shown in Figure 7. Cast thickness squared is plotted versus time in this chart and the slope is compared to an UCL which serves as a pass/fail test. Each slurry batch is evaluated by this casting rate test prior to NSF bar iteration casting by the following

procedure:

* A fixed volume of slip is cast at constant pressure on an established porous material.
* The thickness of the cast is monitored at fixed time increments.
* Thickness^2 vs. time of cast is plotted for the slurry.
* The slope of the line is estimated using linear regression.
* If the slope of the line is found to be greater than specification, the slip is rejected.

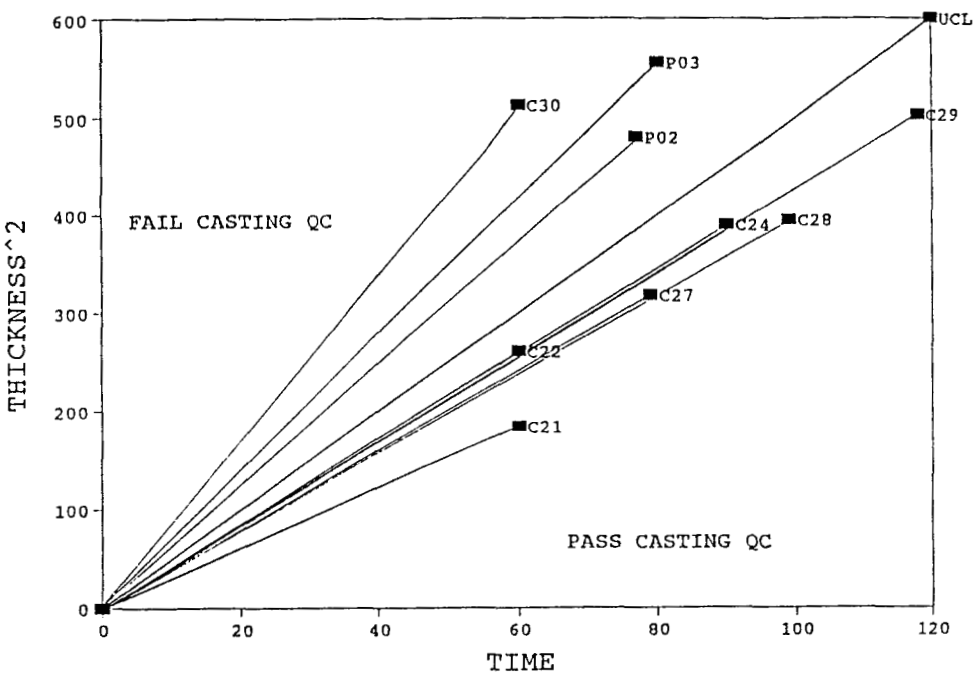

Figure 7: Puck-casting QC for Slurry

The importance of this casting rate measure is shown by examining the effect of the slope with respect to the total indicated run-out (TIR), Figure 8. TIR is a measure of the amount of warpage or bending of the tensile rod and determines the yield during the densification stage, as the greater the runout, the less likely it is to obtain a machinable rod. Runout also has a bearing on the tensile strength, as it determines the amount of removal of the relatively low density reaction layer during the machining process, Figure 9.

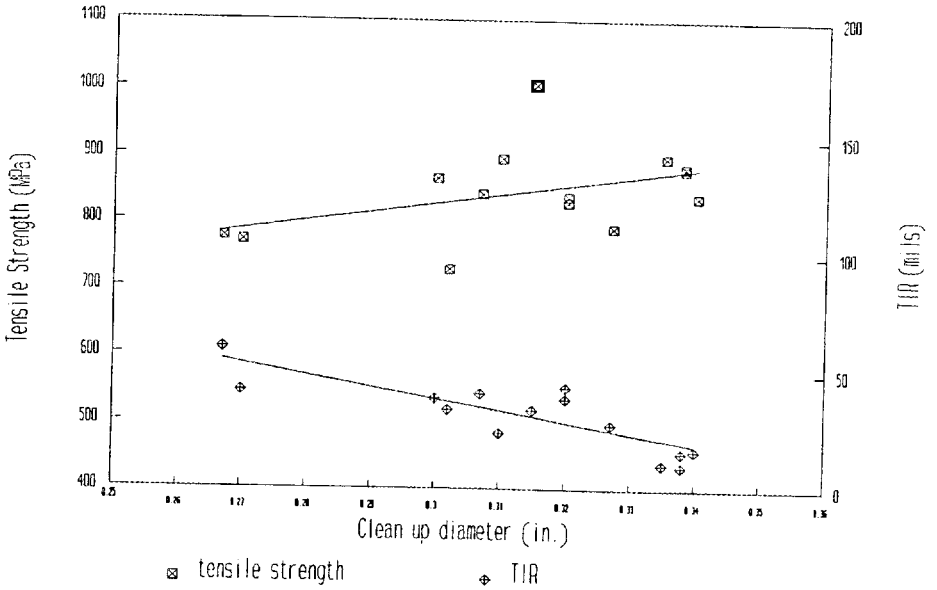

Figure 8: Regression of Average HIP'ed Runout on Casting Rate

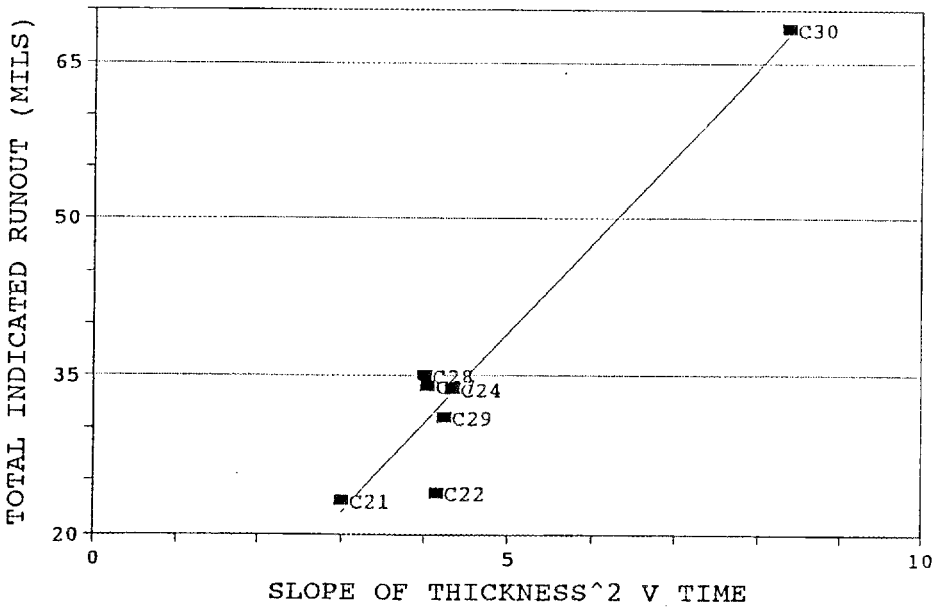

Figure 9: RT Strength - Runout Correlation

TASK 3: DEVELOPMENT AND APPLICATION OF NDE

i) Microfocus X-ray Radiography

Specimens from all stages of processing have been examined by MFX radiography in order to monitor and control the process. This includes all steps from the starting powder to the final machined NSF bar. The machined NSF bars are also examined for strength impairing flaws for correlation with fractographic analysis data and the development of a strength/Weibull prediction model.

a) MFX of As-Received Si_3N_4 Powder

Lot E Ube powder was evaluated for the presence of inclusions. Three samples of each powder size (E10, E05, E03) were examined. No indications of iron inclusions were found in the nine samples examined.

Earlier, Lot D Ube powder was examined by MFX X-ray. A total of fifteen 30 g samples were tested for the presence of metallic inclusions from the E03 powder size. Ten samples were found to have high density inclusions, as mentioned in Task 2.

b) MFX of Colloidal Suspensions

During the reporting period, four colloidal suspensions (CO27, CO28, CO29, CO30) were evaluated for the presence of agglomerates and inclusions. The evaluations were performed during the period that the casting operation was being conducted so that unessential aging issues were avoided. No indications of these two types of defects were found in the 6 samples evaluated for slips CO27-CO29. Two agglomerates were detected in one of the CO30 samples. The sensitivity limit in these evaluations was 25μm.

c) Strength-Flaw Correlation

A number of NSF bars from Iterations T, V and X failed from inclusions during tensile testing, corresponding to the metallic contamination that has previously been discussed. Radiographs of those specimens which failed in the gauge length were used to establish a possible relationship between inclusion size and NSF bar strength. Fracture mechanics suggests the relationship

$$\sigma_f = C \frac{K_{IC}}{\sqrt{a}} \qquad (1)$$

where the constant c represents the geometrical features of the defect with dominant dimension a. In this case, a is taken as one-half the largest inclusion dimension perpendicular to the tensile axis which is apparent in the radiograph. A penny shaped crack would have a value of 0.89 for the constant c.

Given the flaw size from the radiograph, a predicted value of σ_f was computed for each specimen using equation (1) and this was compared to the actual test strength. A value of 6.2 MPa√m was used for K_{IC} in this computation. The value considered to be the best choice for the constant c was that value which gave a regression line which best approximated the predicted = actual line, Figure 10. As can be seen, although there is considerable scatter in the data, the regression line with c = 0.65 corresponds almost exactly to the 45° line in this plot. The value of 0.65 suggests that the effect of an inclusion in Si_3N_4 is more severe than a penny shaped crack of equivalent dimension.

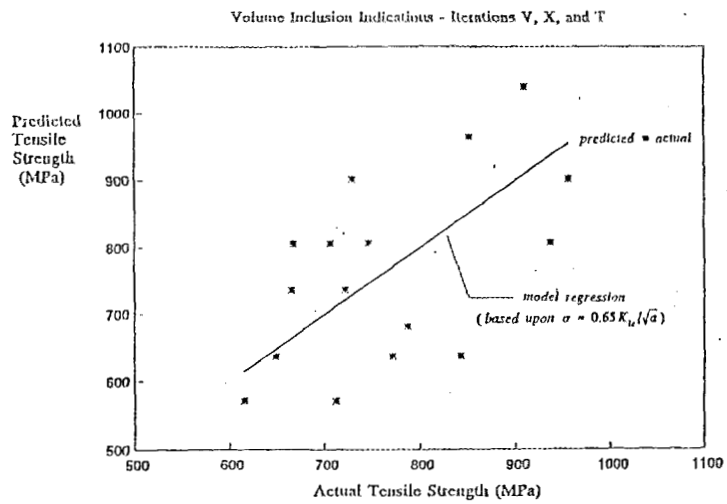

Figure 10: Predicted vs. Actual Tensile Strength

d. <u>Iteration Data</u>

Presintered NSF bars from iterations S, T, U, V, X, Y, Z and AA were radiographed at 9x in the gauge area. MFX was used to establish casting controls as they relate to air entrapment and the resultant void defects. Figure 11, which represents the # voids for each presintered sample of Batch Y, illustrates how MFX is used to monitor the casting process. Significant improvement has been realized as can be seen in the plot of # voids/sample for iterations V through AA. After the installation of the automated casting unit which commenced at Batch X, Figure 12 shows the great

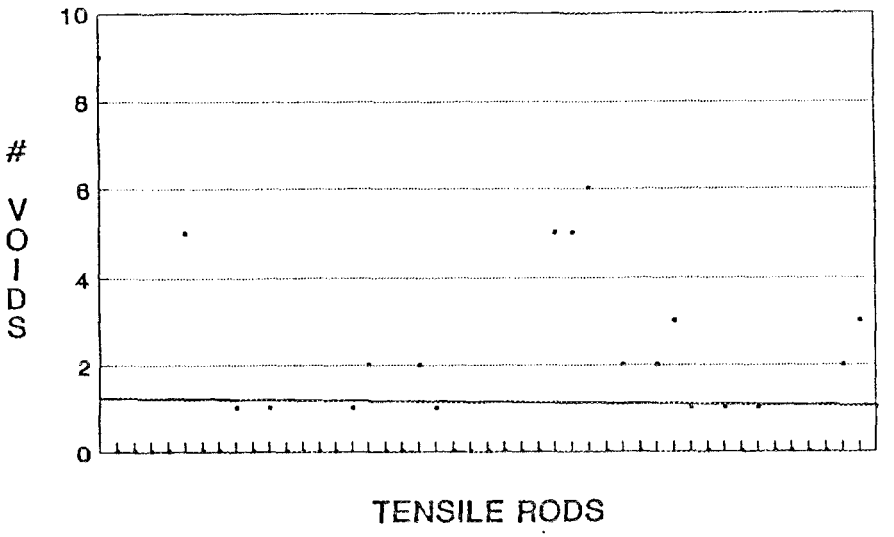

Figure 11: Batch Y Presintered Frequency of Voids

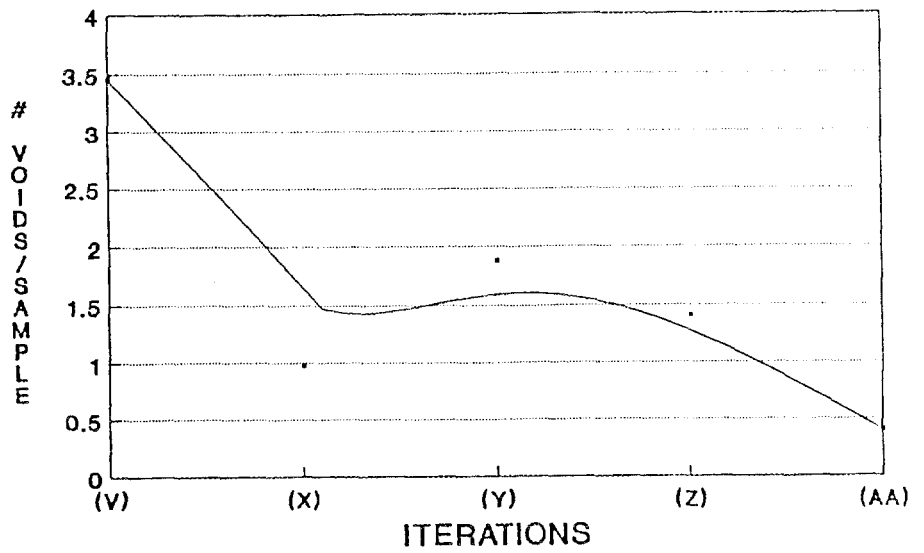

Figure 12: Microfocus X-ray Flaw Detection of Voids in Green Tensile Rods

improvement in void frequency from a level of 3.5 to 1.5 voids/sample. The 1.5 voids/sample level of Iterations X, Y and Z has been reduced to a .5 level for the most recent iteration AA.

HIP'ed tensile specimens from Iterations V, X, Y and Z were evaluated at 10x in the gage area during this reporting period. The number of HIP'ed bars examined for the iteration above were 65, 19, 52, and 77 respectively. The inclusion flaw populations for iterations T-Z are plotted in Figure 13 in the form of # inclusions/sample and % rods with inclusions. After Batch T was processed, iron contamination was discovered in the milling and casting equipment. The iron contamination was associated with the wear and corrosion of the metallic components. At that point, replacement components were redesigned with organic materials to circumvent the problem. As can be seen in the graph, the metallic contamination has been decreased drastically. Whereas more than 50% of Iteration T rods were found to contain metallic inclusions, only 7% of Iteration Z samples were found to have these defects. The final sources of contamination were addressed at the end of Iteration Z. The major flaw population that has now been identified in the last two iterations by both LDP and MFX is microporosity. The microporosity is present in small clusters of $\simeq$ 20μm. Figure 14 is a photograph of a HIP'ed rod after LDP testing. The white areas on the surface of the sample are the clusters of porosity.

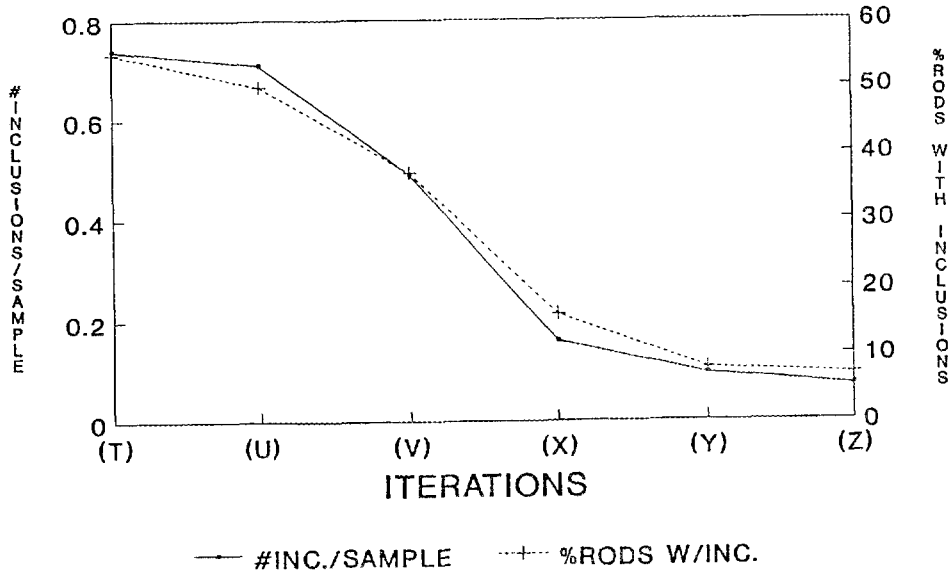

Figure 13: Microfocus X-ray Flaw Detection of Inclusions in HIP'ed Rods

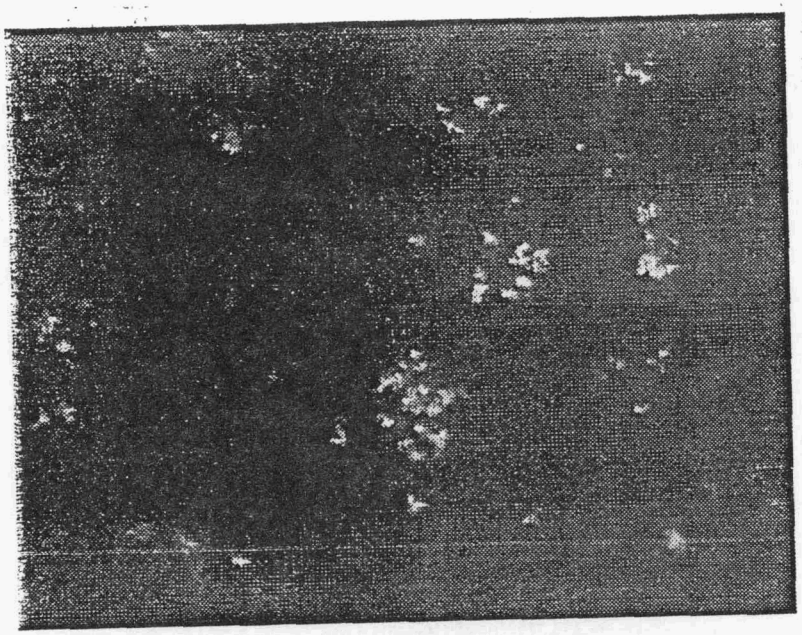

Figure 14: HIP'ed Rod After LDP Testing

e. NDE/SEM Identification of Flaw

As-cast tensile rods from a recent batch were MFX to monitor the casting process. One rod was found to have high density inclusions right at the surface. The areas containing the flaw were mapped using the radiograph and examined using SEM/EDS. Figure 15 shows the results of EDS analysis and it suggests that the high density areas are calcium and sulfur. From this data, it was concluded that calcium sulfate debris, the mold material, had leached out into the slip of the mold cavity. The combination of using NDE/SEM together is very useful in identifying flaws in order to solve process problems. The identification of these $CASO_4$ particles in tensile rods was an isolated case and atypical of the process.

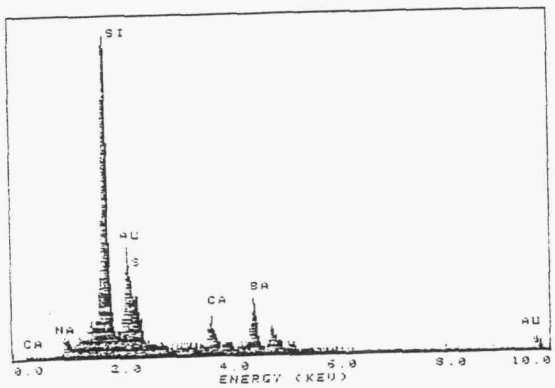

Figure 15: SEM/EDS Map of Fractured Origin

ii) Ultrasonics (Precision Acoustics Devices, Inc.)

a) Examination of Surface Cracks

A technique to detect surface flaws 150 μm and below has been developed and verified using indented cylindrical specimens. Indentation loads of 40 kg, 30 kg, and 20 kg were used to generate controlled surface flaws for UT examination.

As shown in Figure 16, a 100 MHz transducer was employed and appropriately focussed below the surface (instead of at the surface) to eliminate the longitudinal wave component of the signal. The signal thus received is mainly due to the surface wave interaction with the median crack. A typical UT (C-scan) image obtained from a 20 kg indented specimen is shown in Figure 16. The width of the trailing edge of the scan represents the width of the median crack as shown. The leading edge of the signal is caused by the interaction between multiple reflections received from the crack surface.

Based upon the strength of the signal, it is anticipated that a sub surface flaw in the vicinity of 40 μm may be detected. Efforts are now underway to utilize this technique to examine finish machined NSF bars prior to testing.

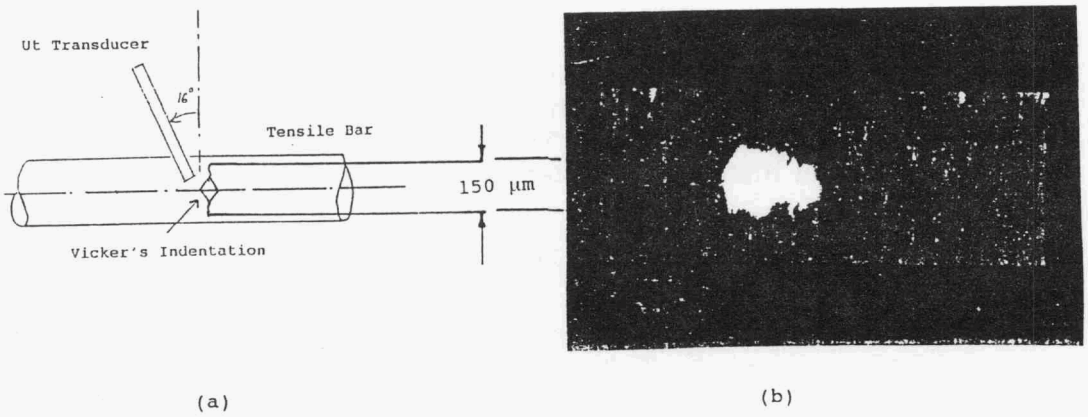

Figure 16: Ultrasonic Examination of Surface Crack (20 kg Indented Specimen)
a. Schematic Drawing Showing Test Configuration
b. C-Scan of 150 μm Indented Surface Flaw

b) Ultrasonic Monitoring of the Casting Process

Ultrasonic Characterization of the Ceramic Suspension

The ultrasonic impedances of a column of ceramic suspension and the saturated cast body were established for baseline data needed in the process monitoring. The liquid column measured 25 mm in diameter x 198 mm high. Two 1.5 MHz UT transducers, (one at each end of the liquid column or cast body) were placed to measure time of flight and signal amplitude (attenuation). The measured values of the transmission velocity and the attenuation for the ceramic suspension and the cast body are compiled in Table 3.

Table 3: Ultrasonic Characteristics of Casting Systems

Materials	UT PROPERTIES	
	Velocity (m/sec)	Attenuation (db/mm)
Water	1500	0.0
Slip (70W% solids)	1385	0.154
Cast Green Saturated Bar	1516	0.094

As expected, the attenuation in the ceramic suspension is greater than that measured in pure water. The cast body on the other hand measures velocity similar to that in water as all its pores are fully saturated. For a similar reason the impedance in the cast body is also lower than that measured in the suspension. The ultrasonic characteristics of the slurry and the cast body established from these experiments are used to interpret the wave forms during in-situ monitoring of the casting process.

In-Situ Monitoring of the Filtration Process

Casting experiments were performed in a two piece plaster mold. The mold cavity shape was that of a button head tensile bar. Figure 17 shows a schematic drawing of the mold cavity along with the location of the UT transducers. Two transducers (1.5 MHz), one at each end of the mold cavity, were placed such that their active faces were flush with the end of the cast tensile bar button heads. The transducers were fixtured in the mold to a) assure positive

contact with the cast bar throughout the experimentation and b) prevent being pushed out of the mold under the applied suspension pressure. The mold cavity was fed from two gates located at the two ends of the bar near the button heads.

The mold cavity was pressurized with the suspension at 0.14 MPa (20 psi) and the casting process was monitored by the attenuation of the ultrasonic signal. The ultrasonic signal was transmitted from one end and received at the other end of the mold cavity. Both the amplitude and the time of flight were monitored throughout the experimentation using a personal computer. A computer algorithm was designed to acquire maximum signal amplitude and the corresponding time of flight at regular time intervals.

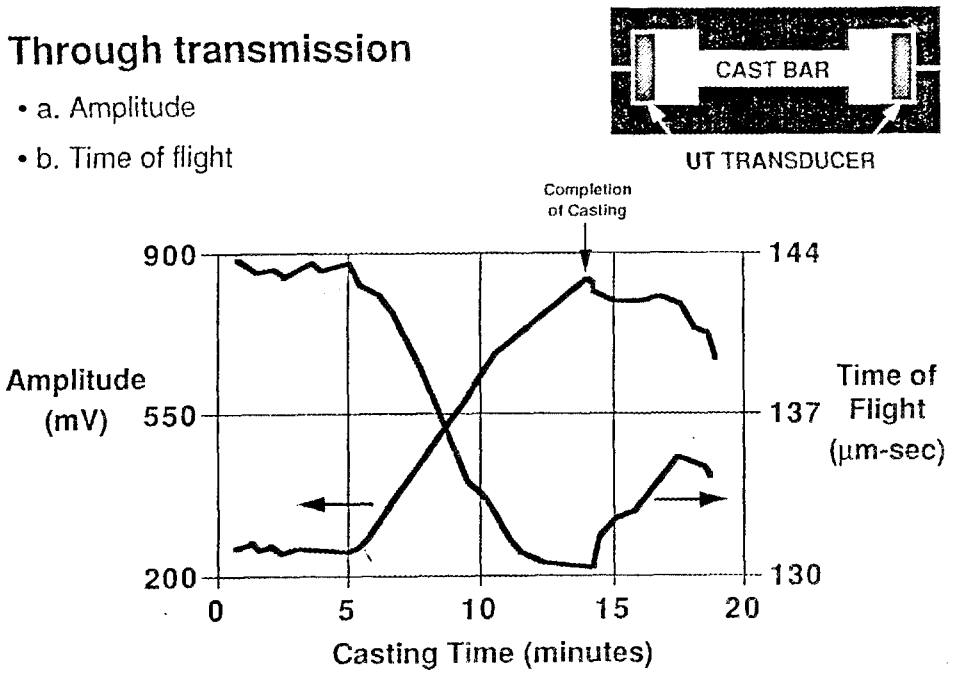

Figure 17: In-Situ Monitoring of Tensile Bar Casting by Ultrasonic Imaging

The amplitude and the corresponding time of flight for the transmission through the cast layer as a function of casting time are also plotted in Figure 17. It can be seen from Figure 17 that as the casting proceeds, the cast layer thickness increases causing the received signal amplitude to increase while simultaneously time of flight to decrease. This trend continues until the completion of the casting process. At this point the amplitude and the time of flight achieve their highest and lowest values respectively. This may be

explained by the fact that at this point the cavity is completely filled with the powder and the interstitial spaces are fully saturated with the liquid (water) providing highest conductance path for the UT signal. Beyond this point, the suspension supply to the cavity ceases due to the casting of the gate. However, because of the continued drainage of the pore fluid through the plaster mold, water content in the cast body decreases causing precipitous drop in the UT signal amplitude. At this point the cast body should be removed from the mold. If, on the other hand, the drainage process is allowed to continue (overcasting condition), the cast part begins to shrink non-uniformly inside the mold resulting in undesirable cracking specially in the transition regions (as would be the case for a turbocharger rotor casting).

Typical wave forms of the received signal as a function of the casting time are shown in Figure 18. In the beginning ($t=t_1$) the signal is transmitted through the suspension only and a single peak appears on the oscilloscope screen. As the casting progresses ($t=t_2$), the signal is transmitted both through the suspension and the cast layer and two separate peaks appear. With further progress in casting ($t=t_3$, t_4), more and more signal is carried through the cast layer and hence signal amplitude corresponding to cast layer increases at the cost of suspension peak amplitude. With increasing signal amplitude the corresponding time of flight decreases simultaneously. Finally, with further increase in the casting time ($t=t_5$) suspension peak disappears leaving a strong cast layer signal peak.

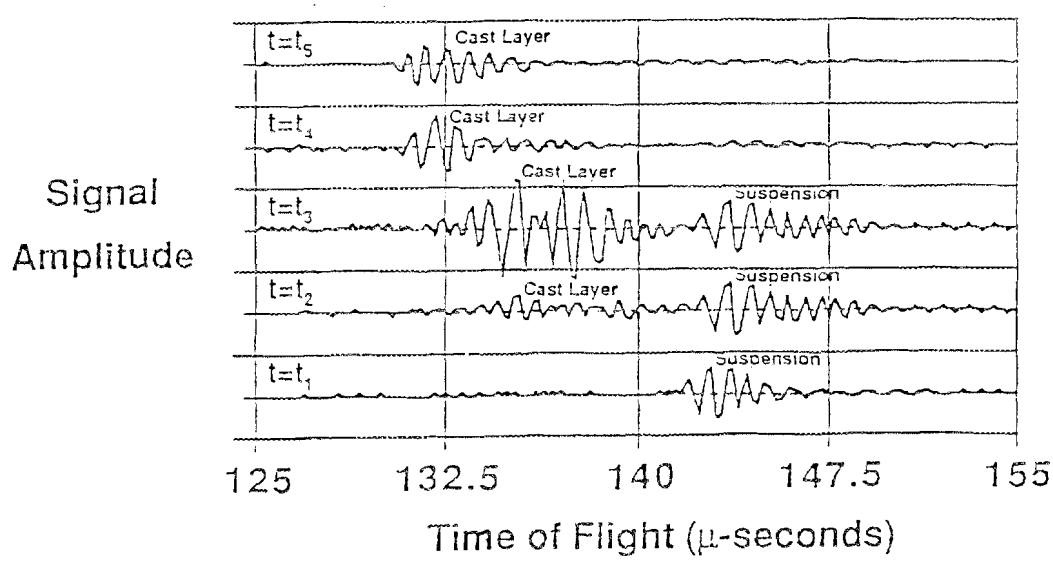

Figure 18: UT Signal Characteristics as a Function of Casting Time ($t=t_1$ to t_5)

The results have been reproduced for various applied pressures and suspension concentrations thus providing a simple and yet effective way to monitor and control the casting process.

Comparison of Casting Rate Prediction From Ultrasonic and Physical Measurements

The measured cast thickness vs. time data is plotted in Figure 19 alongside the UT amplitude data from Figure 17. Both these data correspond to the casting experiments performed at a fixed applied pressure of 0.14 MPa (20 psi). The casting kinetics data from physical measurement, (curve A, Figure 19) and that obtained from ultrasonic evaluation (curve B, Figure 19) seem to be in a reasonably good agreement suggesting that the UT amplitude could be utilized as a feedback signal to adjust the applied pressure and hence control the casting rate. A system may be designed incorporating the above knowledge base to develop intelligent processing methodology.

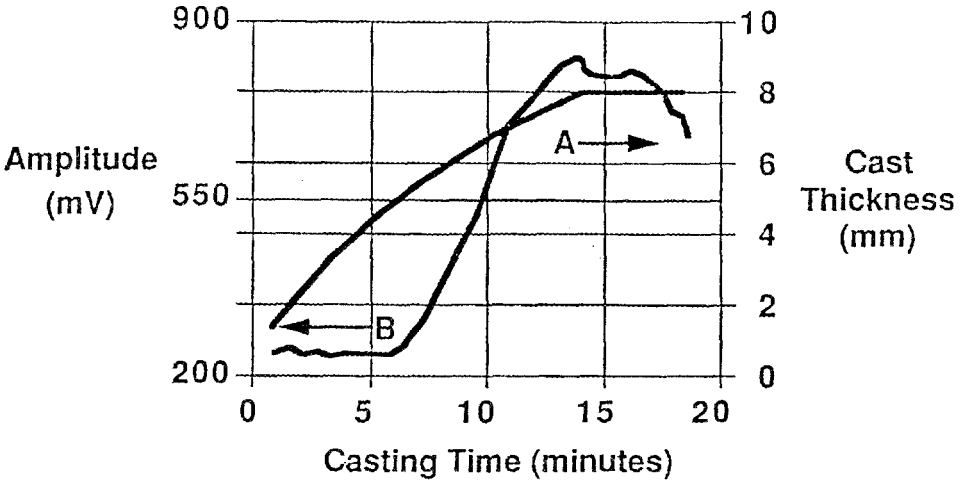

Figure 19: Comparison of Casting Rate Prediction from Ultrasonic (B) and Physical Measurement (A)

iii) NMR Spectroscopy - Argonne National Laboratory

Standard NMR methods of analysis were developed to evaluate the aging effects of freshly prepared batch milled slurries with surfactant. The results of two of the NMR methods (i.e. T_1 and T_2 measurements) were reported earlier (July-August 1991). A third standard NMR method designed to monitor the adsorption of the surfactant in Si_3N_4 slurried with heavy water, D_2O, has been developed. Optimization of this method to monitor adsorption of the

aqueous ammonium polyacrylate is currently underway. Initiation of a study designed to monitor the adsorption of surfactant in a Si_3N_4 slurry (containing 37.5 wt% solids), prepared by milling the powder in D_2O, will follow immediately.

The method development involved standardization of integrated signal intensity from methyl protons in a standard solution of the surfactant against the signal from an analytically prepared aqueous NMR reference standard which was chosen to be 3 - (Trimethylsilyl) propionic-2,2,3,3-d_4 acid, sodium salt (TSP).

Two primary considerations were the focus in the development of this method. The first was identification of a proton NMR resonance suitably distant from other spectral lines, and with sufficient relative intensity, for quantitation of the surfactant concentration in D_2O solution. The signal from the methyl group, appearing as a doublet, in the surfactant was chosen for this surfactant at 2% concentration in D_2O. This signal with chemical shift δ = 1.14 ppm is well removed from the reference signal δ = 0.0 ppm, other signals arising from the surfactant δ = 3.5 - 3.9 ppm, and especially from the residual H_2O signal at ca. 4.86 ppm.

The second consideration was the generation of a calibration line for quantitation of the surfactant in D_2O solution. The ratio of the integrated signal intensities of methyl protons to TSP reference protons was determined as a function of concentration (0.08-2.0 wt%) in D_2O. These data are plotted in Figure 20. A good linear correlation was found (slope = 1.48, y-intercept = 0.03, correlation coefficient = 0.99997); and the maximum experimental error (10%) was found at the lowest concentration (0.08%), where the signal-to-noise ratio was the poorest. This error can be reduced in future determinations by extending the signal averaging with a concomitant increase in signal-to-noise.

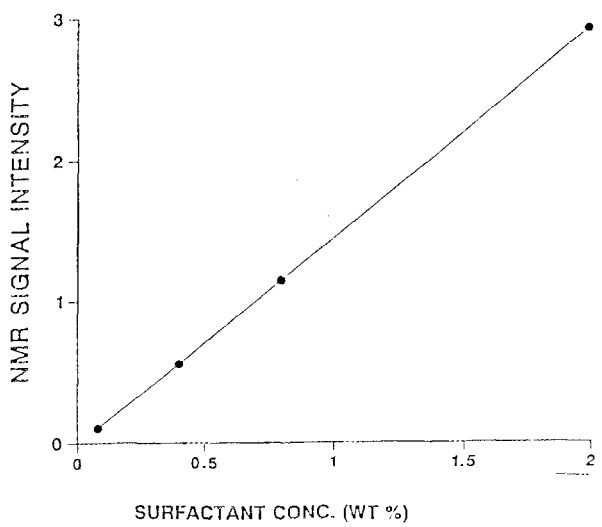

Figure 20: Calibration Line for NMR Signal Intensity vs. Non-Aqueous Surfactant Concentration in D_2O Solution.

The optimization of this method applied to quantitation of the aqueous ammonium polyacrylate concentration in D_2O is currently underway. The same NMR method used to generate the calibration lines will be used to monitor the adsorption of surfactant in a Si_3N_4 slurry (containing 37.5 wt% solids), prepared by milling the powder in D_2O. The first study will determine adsorption as a function of time, and the second study will determine adsorption as a function of initial surfactant concentration. Both studies will employ samples of supernatant liquid obtained by centrifugation of the slurry so that the NMR experimental conditions will be identical with those used in generating the calibration lines.

iv) Milestone on Detection of flaws Below 50 μm

Three approaches have been evaluated to effectively detect flaws in the size range below 50 μm in 6 mm diameter Si_3N_4 samples. Two involve film micro-radiography and the other is computed x-ray microtomography. Geometric enlargement (to 30X) is a standard option of the microfocus system that is being utilized in this processing improvement program. An enlargement of 10X is SOP for HIP'ed bars and this provides a field of view which includes the gage length of the bars. This SOP provides a factor of 10 improvement over the 200 μm resolution which is customary in visual radiographic analysis. Thus 20 μm resolution over a 40 mm height is routinely attainable.

State-of-the-art radiograph film digitization systems have been evaluated with reference to the subject milestone. This technology addresses the need for automation in the analysis of film and also improved detection probability. Image processing of digital representations at high resolution have been found to provide dramatic advantage over the traditional visual film reading evaluation. A commercially available system which provides a 2560x2048 pixel, 12-bit display of a laser-scanner (50 μm spot size/12-bit) digital image has been found to provide the necessary resolution with the use of on-screen zooming and gray level windowing.

The computed microtomography technique has been evaluated using a commercially available turnkey laboratory system. The manufacturer claims a 25 μm resolution. A HIP'ed tensile bar processed with 20 μm FeAl seeds was used to evaluate the system. Tomographs were generated which indicated microstructural features of a size representative of the seeds, indicating the potential for sub 50 μm flaw detection. It is clear however that considerable effort and expense would generally be required to evaluate the entire gage length of an NSF bar, due to the exceedingly small slice thickness which is required at this flaw size range. On the other hand, evaluations to establish typical microstructural patterns could be profitably pursued since then only a limited number of slices would be necessary.

TASK 4: PROPERTY TESTING AND MICROSTRUCTURAL EVALUATION

i) Effects of Heat Treatment on Tensile Strength

Iteration V specimens were used to evaluate the effects of post-HIP and post-machining heat treatments on room and elevated temperature tensile strength. The post-HIP treatment is conducted prior to machining to crystallize the secondary phases present after densification. The post-machining treatment is performed to anneal and oxidize (blunt) surface and near surface flaws caused by the grinding process. A total of 63 room temperature and 13 elevated temperature (1370°C) tensile tests were conducted on specimens which comprised the 2x2 experimental matrix.

The mean tensile strength values for the room temperature tests are summarized in Figure 21. A 10% strength improvement can be associated with the oxidation treatment (731-808 MPa). The data suggest that crystallization has an insignificant effect on the room temperature strength (774-765 MPa). While the oxidation treatment appears to have a significant effect on the character of the surface flaw population, apparently crystallization does not influence the room temperature strength limiting volume defects. There is a small interaction of the two treatments which is also displayed in Figure 21.

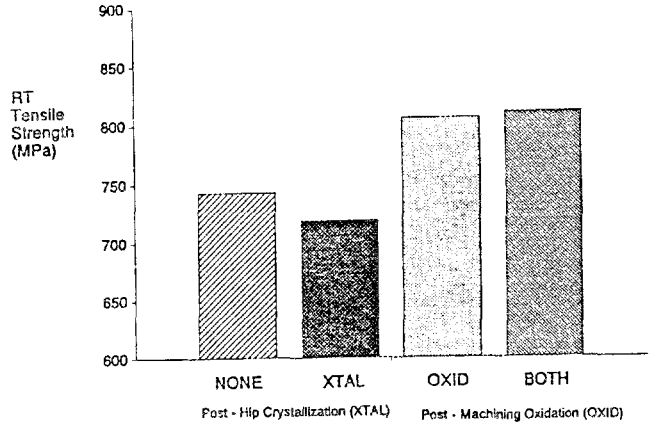

Figure 21: Mean Room Temperature Tensile Stength as a Function of Heat Treatment Condition

The elevated temperature strength data are summarized in Figure 22. Each treatment can be seen to have a significant positive effect on the 1370°C tensile strength. Crystallization accounted for an 18% strength enhancement (393-462 MPa), while oxidation separately provided a 16% increase in strength (396-460 MPa). The interaction of the two treatments on high temperature strength is also plotted in Figure 22.

The average strength improved by 9% (743-811 MPa) at room temperature and a very significant 38% (347-480 MPa) at 1370°C when specimens were processed with both the post-HIP and post-machining heat treatments. These results clearly suggest that the two heat treatments be included as SOP to assure achievement of both the 900 MPa room temperature and 500 MPa 1370°C strength targets of the program.

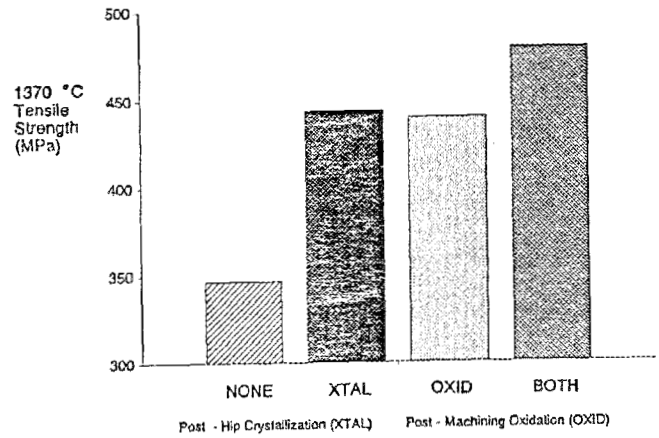

Figure 22: Mean Elevated Temperature Tensile Strength as a Function of Heat Treatment Condition

ii) <u>Room Temperature Tensile Testing of Iterations XXX, X, Y and Z</u>

Room temperature tensile tests were performed on a total of 135 specimens from Iterations XXX, X, Y and Z. Iteration XXX specimens were from 1 densification run, Iteration X and Y specimens were from 2 densification runs each and Iteration Z specimens were from three densification runs. Results are summarized in Table 4. The mean strength shows significant improvement from Iteration XXX to Iteration Z. All bars were formed using the new casting machine but starting with Iteration Y a new filter was installed in the closed loop system to minimize inclusions. The Weibull distributions are plotted in Figure 23. The Weibull Modulus for each iteration was approximately equal to 9. However, as shown in Figure 23, one can see the strength improvement from Iteration XXX to Z. The Weibull moduli are lower than those found in previous Iterations (e.g. 13 for Iteration N) due to the control variable levels set for these particular designed experiments.

Table 4: Stage II RT Tensile Strength Data: Iterations XXX - Z

Batch	Mean Strength (MPa)	Std. Dev. (MPa)	Characteristic Strength (MPa)	Weibull Modulus m	No. of Specimens
XXX	707	88	746	9.0	25
X	771	105	816	8.5	18
Y	847	103	892	9.4	45
Z	878	108	924	9.4	47

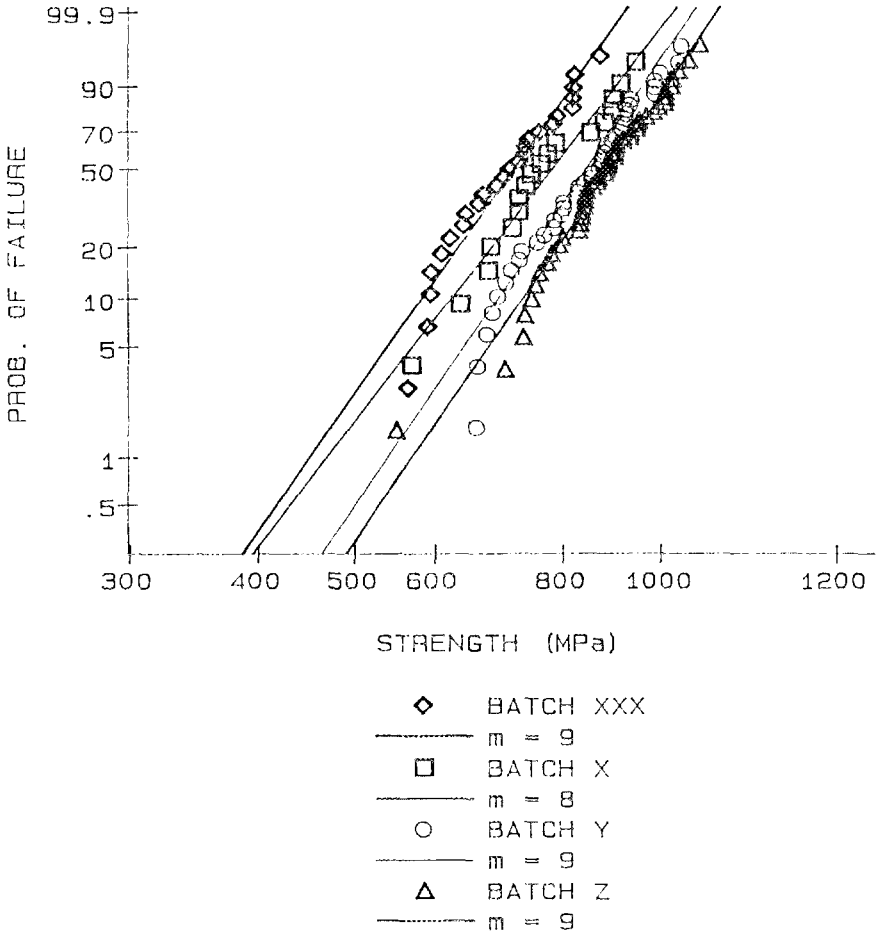

Figure 23: Weibull Analysis for Stage II Batches XXX, X, Y and Z

Optical and SEM fractography were performed on all specimens and the results are summarized in Table 5. There is a significant shift from volume failures to surface failures with the elimination of iron contamination from Iteration XXX up to Iteration Z. The flaw type "G", glass impurity, was found to be related to our post-machining heat treatment and steps have been taken to eliminate this source of failures. The predominate flaw origin is now related to machining. The other significant flaw type "A/P", zones of microporosity, occurs in the volume and may be related to the two step densification process. Examples of specific flaw types are discussed below.

iii) Iteration Z Heat Treatment Tensile Strength Results

The majority of Iteration Z specimens (32 of 47) intended for RT fast fracture testing was given a post-machining heat treatment. Previous tests from Iteration V demonstrated a significant (10%) improvement in strength related to this oxidation heat treatment. To verify this effect, a group of 15 Iteration Z specimens were tested in an as-machined state. The results showed the same trend as found for Iteration V. The mean strength of the 15 specimens was found to be 834 MPa, 7% lower than the 891 MPa mean strength of the oxidized Iteration Z specimens.

Table 5: Stage II Fractography Summary: Batches XXX - Z

Batch	Location		Flaw Type (%)					Size Range (μm)
	% V	% S	I	A/P	M	G	U	
XXX	68	32	72	0	20	0	8	>100
X	29	71	41	6	24	12	17	15-50
Y	2	98	0	2	28	68	2	10-80
Z	29	71	0	40	45	9	6	5-65

V = volume
S = surface

I = iron inclusions
A/P = agglomerates and/or microporosity
M = machining damage
G = glass impurity at surface
U = unknown

iv) Iteration Z 1370°C Tensile Strength Results

Tensile tests were performed on 14 specimens from Iteration Z at 1370°C in air. No heat treatments were performed prior to

testing. The mean strength was 357± 22 MPa with a characteristic strength of 367 MPa and a Weibull Modulus of 19. Fractography results show no iron contamination and all failures occurred at the surface apparently at sites of machining damage.

v) Strain Gaging of Tensile Specimens

Specimens from Iterations XXX, X and Y were strain gaged prior to testing, to study bending during testing and to determine what, if any, effect bending has on strength and reliability data. Each specimen had four gages mounted around the center of the gage section and located every 90°. The amount of bending is calculated per ASTM Standard E 602 - 81, Reference 1, in the following manner:

$$\%\,bending = \frac{[(\Delta g_{1,3})^2 + (\Delta g_{2,4})^2)]^{1/2}}{g_0} x100 \tag{2}$$

where

$$\Delta g_{1,3} = \frac{(g_1 - g_0) - (g_3 - g_0)}{2} = \frac{(g_1 - g_3)}{2} \tag{3}$$

$$\Delta g_{2,4} = \frac{(g_2 - g_0) - (g_4 - g_0)}{2} = \frac{(g_2 - g_4)}{2} \tag{4}$$

$$g_0 = \frac{(g_1 + g_2 + g_3 + g_4)}{4} \tag{5}$$

and g_1, g_2, g_3, and g_4 are the strain gage readings in units of strain.

A Daytronic System 10 DataPAC was used to monitor and record the strain and load data. Iteration XXX tensile specimens were strained gaged and the load-bend data was recorded without any realignment. The % bending at failure was < 5.5% for all but 24 of 25 specimens with one at 12.5%. This shows that overall the test system is in very good alignment.

As part of the experiment 50% of the specimens (predetermined randomly) from Iteration X were to be realigned if

the % bending at a preload of 1500 lbs. was > 10%. The realignment involves unloading the specimen, twisting the grip/collet load train assembly and reloading the specimen. Load-displacement curves have a "knee" in the curve at about 1250 lbs where the copper collets deform into the buttonhead radius. Therefore the preload was chosen to be higher than 1250 lbs to monitor the "preload" bending. If after two preloads the % bending was not below 10%, the specimen was tested to failure.

Figure 24 shows representative load-bend curves for specimens with no realignment while Figure 25 show curves for three specimens that were realigned (only four specimens required realignment). A typical curve shows an increase in bending during initial load up but as the collets seat themselves the bending begins to decrease. The figures show that the range of % bending at the preload level (1500 lbs) is 4 to 16%, and in all cases the bending at failure is ≤6%. For two of the specimens for which realignment took place, the best % bending achieved at the preload was 12% (Figure 25), but still resulted in low (2%) bending at failure. However, as shown in Figure 26, and consistent with the decreasing bending level after preload, there appears to be a trend that the higher strength specimens experience a lower % bending at failure. Also noteworthy is that the specimens that had a realignment performed have a lower % bending at failure than those without a realignment.

In an attempt to determine the effect bending has on the Weibull Modulus, 23 specimens from Iteration Y (out of 45) were strain gaged and tested to failure. The average and maximum strains were recorded for each specimen. Two Weibull Moduli were calculated. The first modulus was determined from the standard fracture stress of each specimen (load/area) and was equal to 10.04. A second or predicted fracture stress was determined as the product of the maximum strain times Young's Modulus (310 GPa). A Weibull analysis was performed using the predicted strengths giving a value of 10.27. For practical purposes the difference (2.2%) is negligible. It is therefore concluded that 100% strain gaging is not required for our purposes. However, a periodic sampling using strain gaged specimens to check load train alignment will be conducted.

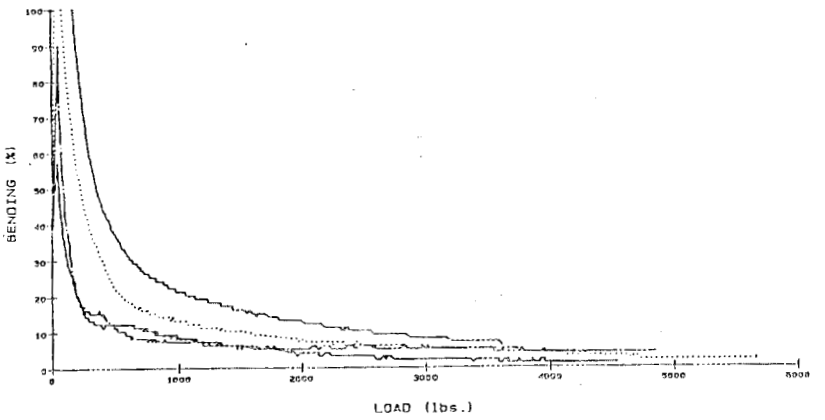

Figure 24 : Load vs. Bending for Batch X With No Realignment

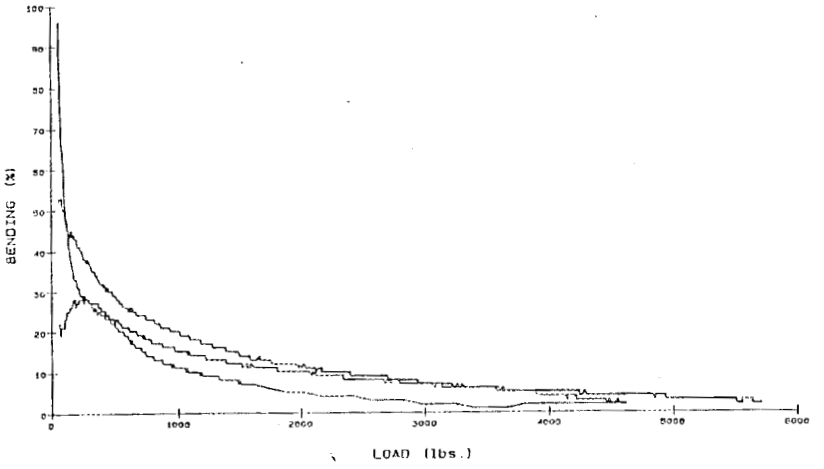

Figure 25 : Load vs. Bending for Batch X With Realignment

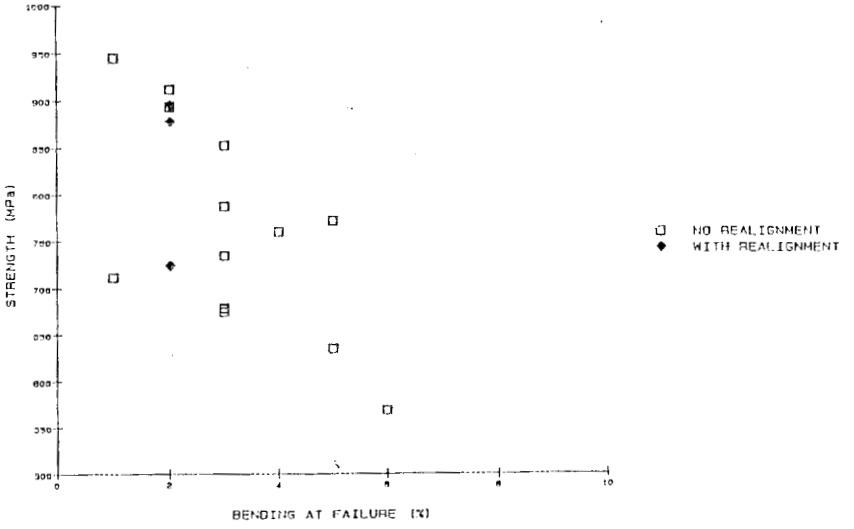

Figure 26 : Strength vs. Bending for Batch X

vi) Stage II Tensile Strength Data Summary

The Stage II experimental plan involves 16 NSF bar iterations with 10 control variables and one MLP iteration. The iteration schedule spans the 15 month period 2/1/91 to 4/30/92. Tensile data have been obtained for specimens from iterations N through Z. These data are summarized in Figure 27. The doublets for Batches V and Z are from the oxidation treatment experiments while for O the 3 values correspond to the 3 machining procedures employed.

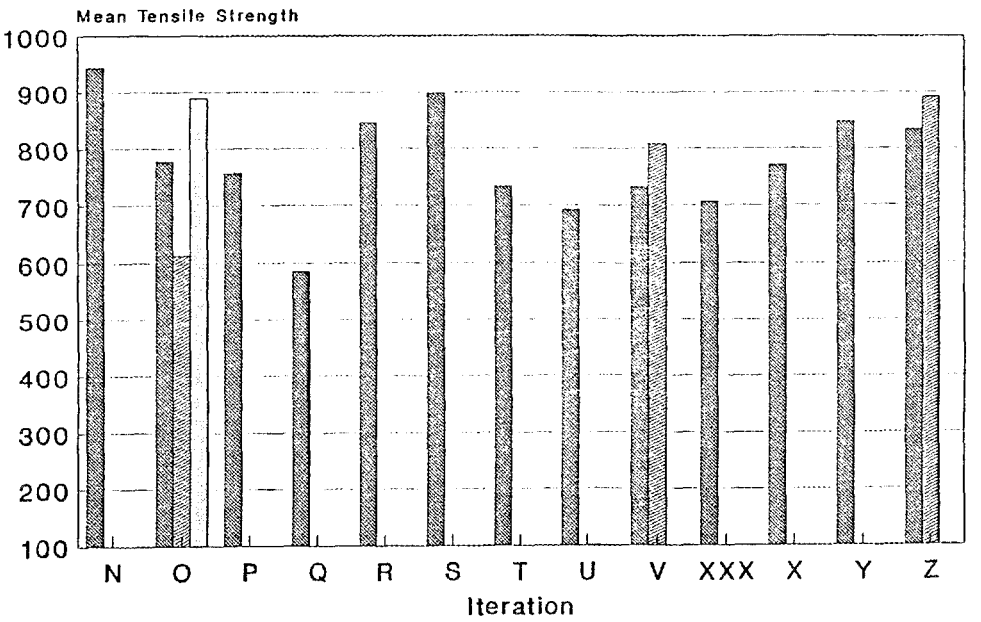

Figure 27: Mean Tensile Strengths from Stage II Iterations

vii) Censored Weibull Statistics for Stage II

Extensive optical and SEM fractography have shown several types of failure origins (e.g. metallic inclusions, agglomerates, machining damage) throughout Stage II. Figure 28 shows a tensile strength distribution for all specimens tested in Stage II. Within that distribution, no less than 8 flaw types have been observed, namely, iron inclusions, agglomerates, porosity, glass impurities, several types of machining damage and unknown flaws. Censored Weibull distributions were generated for each specific flaw type and are shown on Figure 29. Weibull Moduli range from 6 for inclusions to 24 for machining damage relative to Iteration "O". All sources of flaws have been identified with many already eliminated or minimized, as shown above for Iteration Z. Figures 30-33 show micrographs of some of the flaw types analyzed. Included are major

machining damage, standard machining damage, Si-rich glass regions and zone of microporosity. It is apparent from Iteration Z data that surface flaws related to machining are the major strength and reliability limiting defects. The remaining Stage II experiments are concentrating on machining effects.

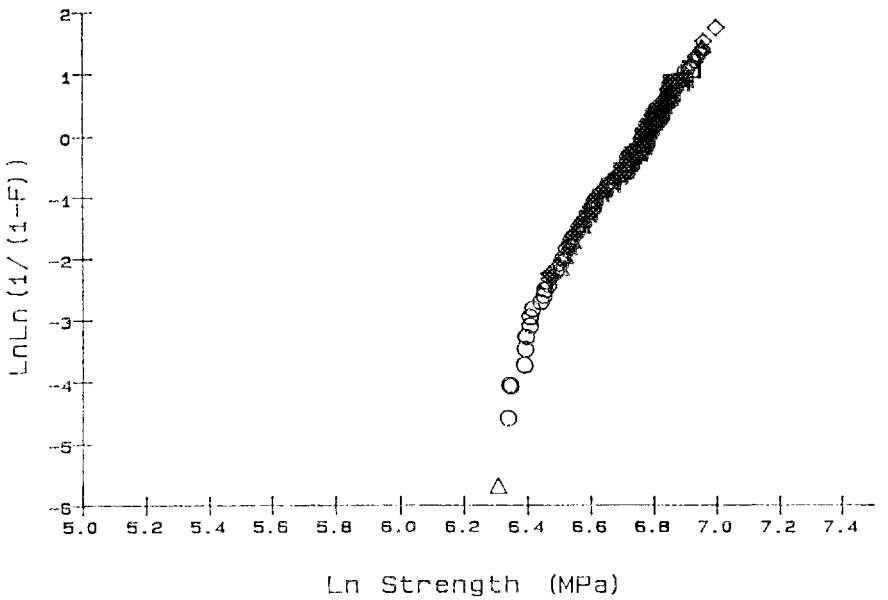

Figure 28: Weibull Plot of Strength Data for Stage II: Uncensored

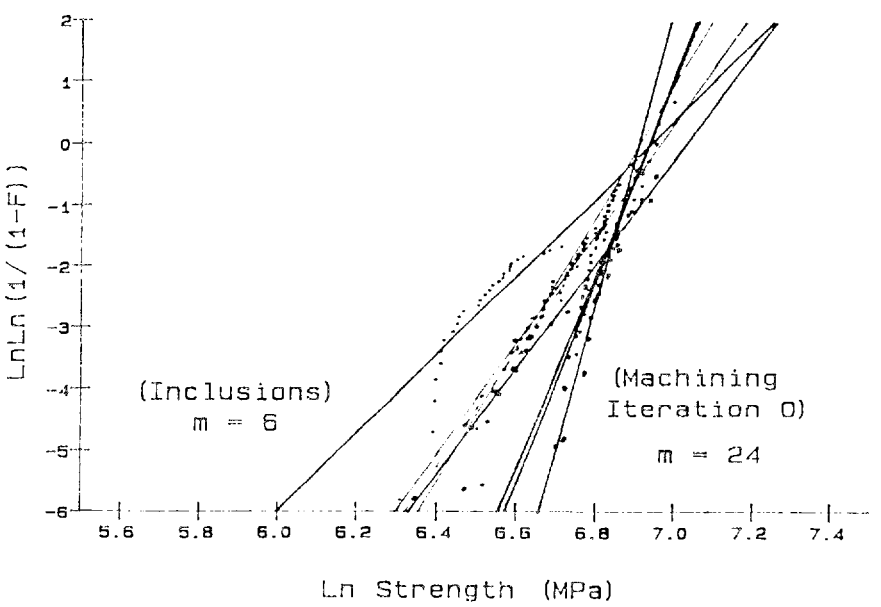

Figure 29: Weibull Plot of Strength Data for Stage II: Censored

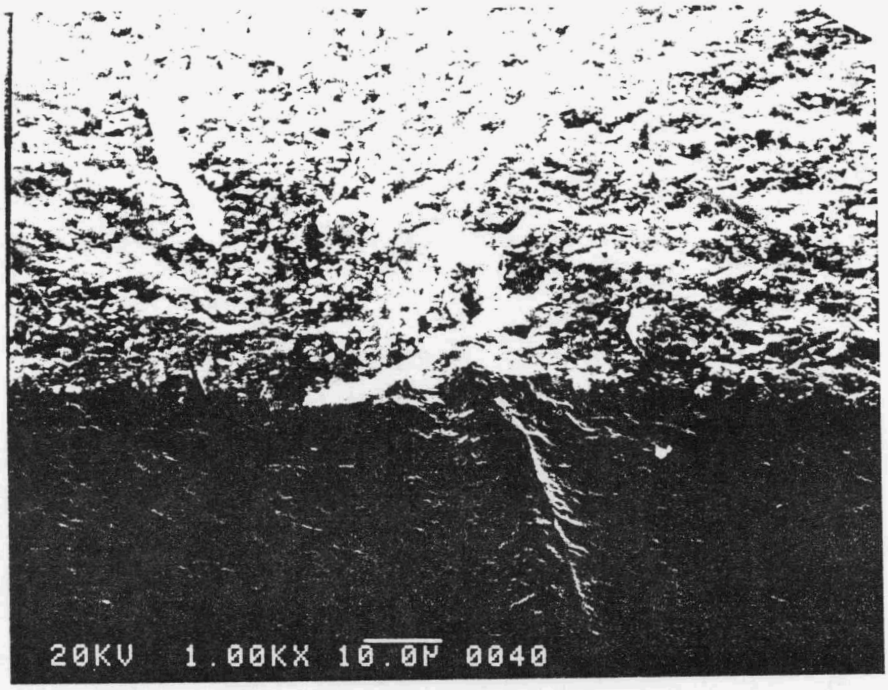

Figure 30a: SEM of the failure origin of specimen V-28 fractured at RT (σ_f = 685 MPa) showing severe machining damage (Type MD).

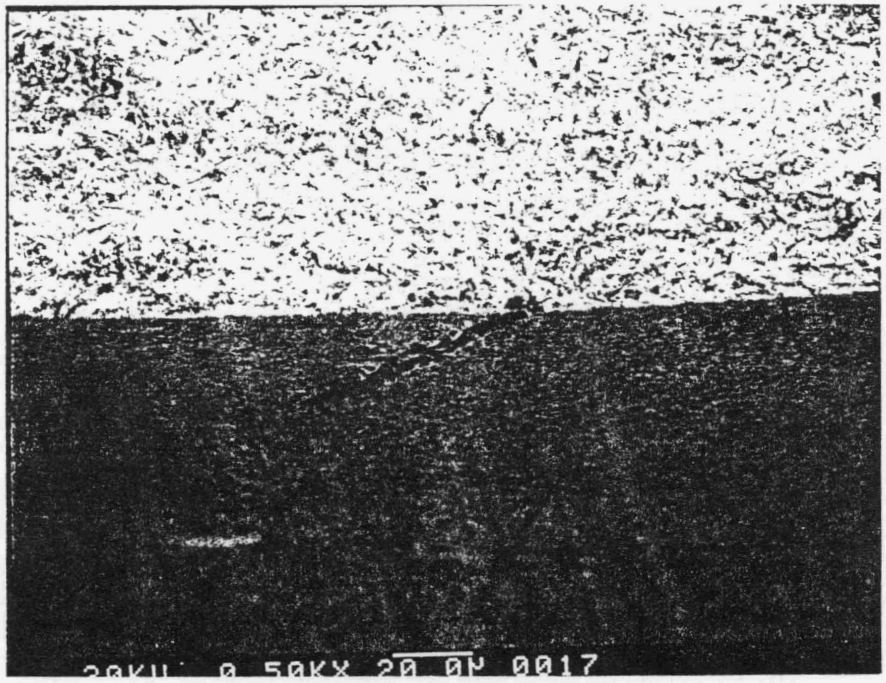

Figure 30b: SEM of the failure origin of specimen Z-13 fractured at RT (σ_f = 731 MPa) showing severe machining damage (Type MD).

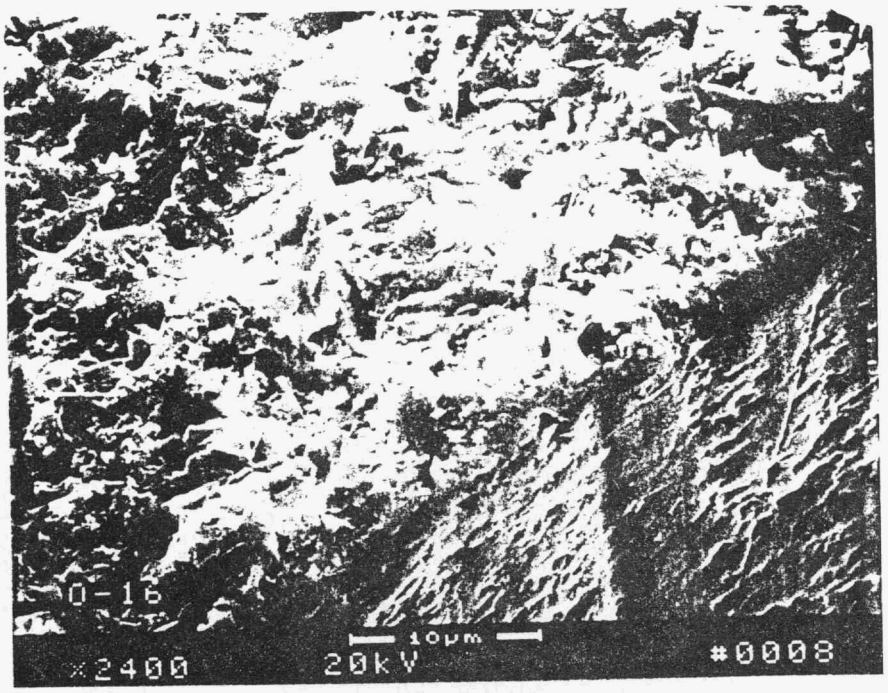

Figure 31a: SEM of the failure origin of specimen O-16 fractured at RT (σ_f = 884 MPa) showing a 5 μm wide machining groove surrounded by a 45 μm semi-circular sub-surface crack (Type MO).

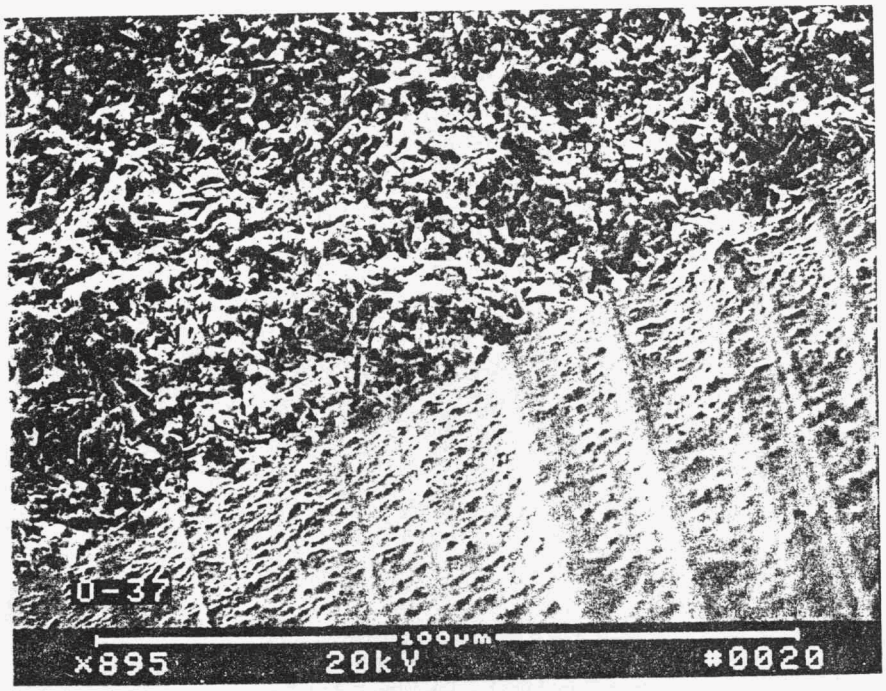

Figure 31b: SEM of the failure origin of specimen O-37 fractured at RT (σ_f = 894 MPa) showing a 10 μm wide machining groove surrounded by a 25 μm semi-circular sub-surface crack (Type MO).

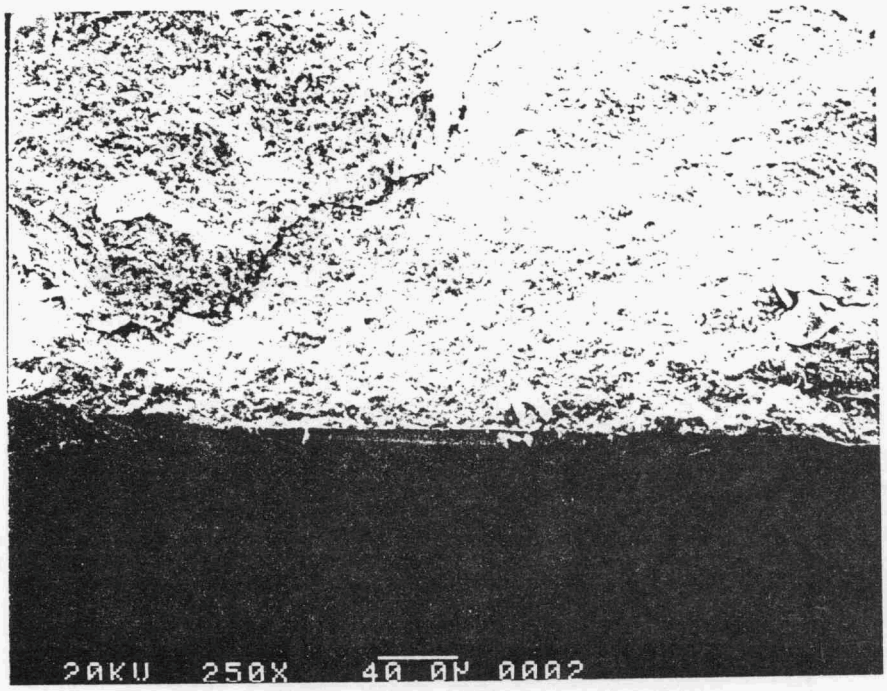

Figure 32a: SEM of specimen Y-9 fractured at RT (σ_f = 682 MPa) showing a glass impurity from oxidation (Type G).

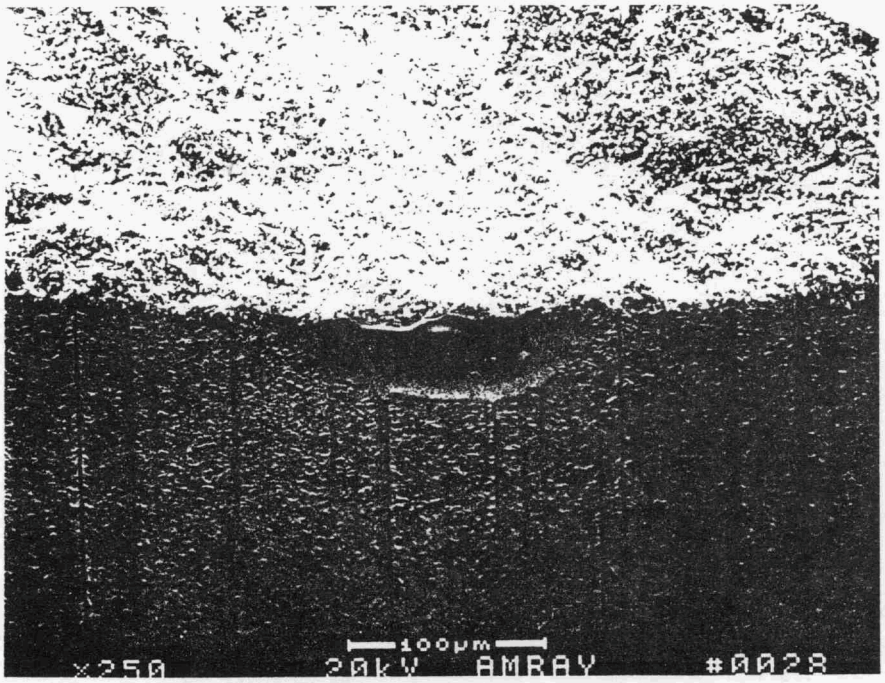

Figure 32b: SEM specimen Y-57 fractured at RT (σ_f = 921 MPa) showing a glass impurity (Type G).

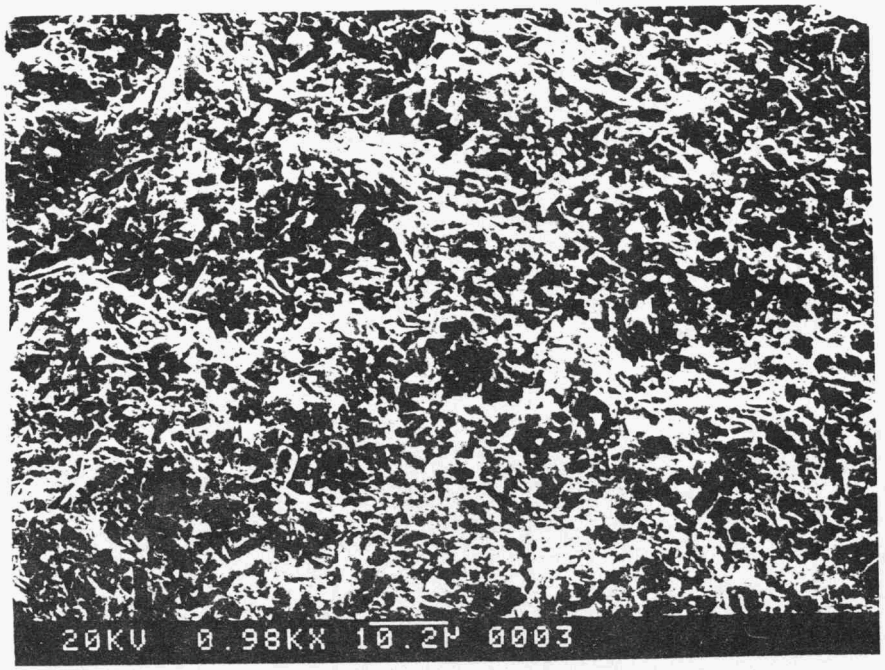

Figure 33a: SEM of specimen Z-12 fractured at RT (σ_f = 1025 MPa) showing a volume defect containing microvoids (Type V).

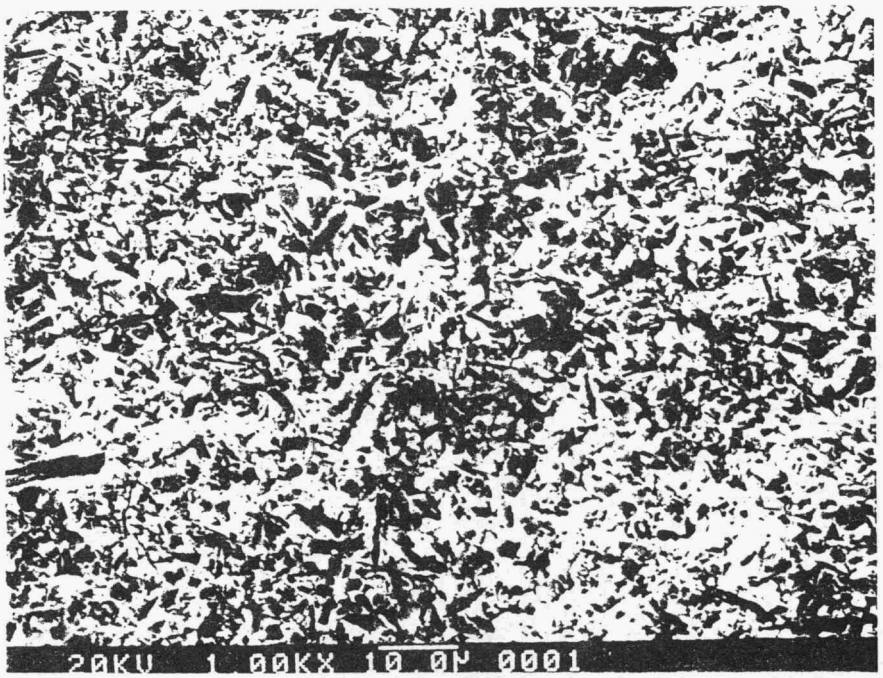

Figure 33b: SEM of specimen Z-33 fractured at RT (σ_f = 1040 MPa) showing a volume defect containing microvoids (Type V).

viii) Strength-Flaw Correlation

A limited amount of fractography data was quantitatively analyzed during the reporting period to establish relationships between strength and flaw size. Data for specimens which failed from agglomerates in the baseline pressure casting iteration are plotted in Figure 34. Strength is plotted as a function of $1/\sqrt{a}$, following the fracture mechanics equation (1) which was discussed in Task 3. There were seven agglomerate failure origins in the iteration ranging in size (radius) from a = 15 to 50 μm. The plot illustrates the strength variation (roughly 400-1000 Mpa) which corresponds to this agglomerate size range. The predicted strength-flaw size relationship suggested by the penny shaped crack model, using K_{IC} - 4.67 MPa√m (average for the 7 specimens), falls above the regression line. This suggests that agglomerates have a more detrimental effect on strength than penny shaped cracks.

A similar representation of strength-flaw data is plotted in Figure 35 for Iteration O machining damage related surface flaw failures. The maximum depth of the surface flaw (not the surface length) is plotted as the dimension a. There is excellent agreement between the regression line and the semi-circular surface crack fracture mechanics prediction, (c = 1.11, Reference 2). This prediction was developed using the iteration average K_{IC} value of 5.35 MPa√m. The prediction following from the long surface crack model (c = 1.55) can be seen to fall significantly below the actual data.

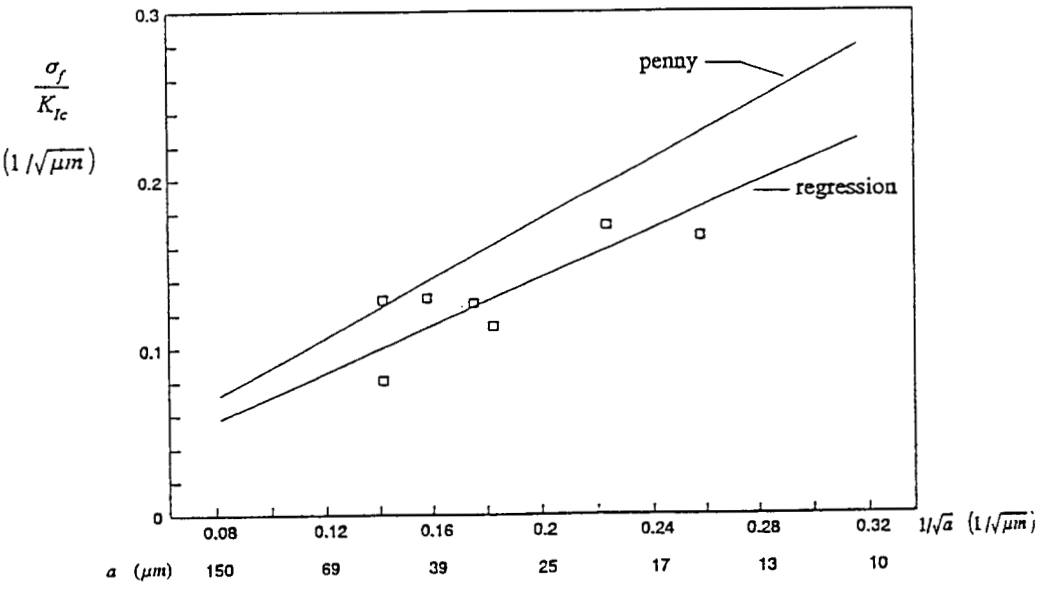

Volume Agglomerate Failure Origins
Baseline Pressure Casting Iteration

Figure 34: Strength - Flaw Correlation

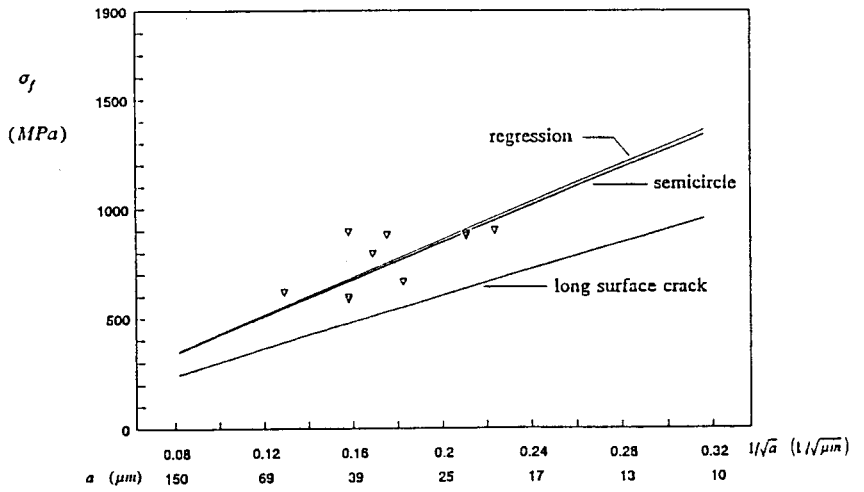

Machining Damage Failure Origins
Pressure Casting - Iteration O

Figure 35: Strength - Flaw Correlation

References

1. "Sharp-Notch Tension Testing with Cylindrical Specimens," American Society for Testing and Materials, E602-81, 1989

2. D.M. Tracey, "3D Elastic Singularity Element for Evaluation of K Along an Arbitrary Crack Front," Int'l J. Fracture, 9, 1973, pp. 340-343.

Status of Milestones

All Milestones are on schedule. Milestone #114116, (evaluate other promising NDE technologies for detection of flaws below 50 μm and recommend implementation to processing steps) completed on schedule on 12/31/91.

Publications

1. "Reliability Improvement of High Strength Silicon Nitride Through Process Optimization and Control", by V.K. Pujari et al, presented at ATD CCM, Dearborn, MI, October 28, 1991 by V.K. Pujari.

2. "Precision Casting Process Control by Ultrasonic Technique", by V.K. Pujari, L.C. Sales, J.S. Wang and J. Fraser, presented at the 16th Annual Conference on Composites and Advanced Ceramics, Cocoa Beach, FL, January 8-10, 1992 by V.K. Pujari. This paper received the ACS Engineering Ceramic Division Technical Presentation First Prize.

3. "Tensile Testing in the Development of Processing Methods for High Strength/High Reliability Silicon Nitride", by M.R. Foley and V.K. Pujari was presented as a poster paper at the 16th Annual Conference on Composites and Advanced Ceramics, Cocoa Beach, FL, January 8-10, 1992 by M.R. Foley. This paper received the ACS Engineering Ceramic Division Best Poster Award.

Improved Processing

S. D. Nunn and O. O. Omatete (Oak Ridge National Laboratory)

Objective/scope

To determine and develop the reliability of selected advanced ceramic processing methods. This program is to be conducted on a scale that will permit the potential for manufacturing use of candidate processes to be evaluated. The emphasis is on silicon nitride. Issues of practically; safety, hygiene, and environmental issues; and in-process testing methods are to be addressed in addition to technical feasibility. The methodology includes selection of candidate processes and evaluation of their range of applicability to various kinds of commercially available ceramic powders.

Technical highlights

I. Silicon Nitride Gelcasting

Repair of the gas-pressure sintering furnace has been completed. However, thermocouple life continues to be a problem for firing runs involving moderately long times (up to 2 h) at high temperatures.

Silicon-nitride samples containing 8.4 wt % La_2O_3 and 2 wt % Al_2O_3 were gelcast to evaluate the effects of using an alternative rare-earth sintering aid in the gelcasting process. The composition is comparable in terms of mol. % additive to 6 wt % Y_2O_3 and 2 wt % Al_2O_3. The gelcasting slurry contained 50 vol % ceramic powder and was very fluid before the addition of the cross-linking and accelerating agents.

Samples of the gelcast material were sintered for 4 h at 1750 or at 1850°C under 0.2 MPa (2 atm) overpressure of nitrogen. The sintered densities were 95.2% and 96.6%, respectively. The material fired at 1850°C formed some free silicon metal on the surface.

Additional samples were fired using a two-step, gas-pressure sintering cycle. The firing conditions were 2 h at 1850°C under 0.4 MPa N_2 pressure followed by 2 h at either 1900 or 1950°C under 2 MPa (300 psi) N_2 pressure. The sample fired to 1900°C had a density of 99.2% and a weight loss of 1.6%. The sample fired to 1950°C had a lower sintered density of 98.7%, probably due to decomposition as indicated by the higher weight loss of 2.68%.

Examination of sliced sections of the fired samples showed the presence of large flaws that appear to be the result of localized non-uniform shrinkage during densification. This was probably caused by spot gelation during the addition of the cross-linker and accelerator to the slurry, which resulted in inhomogeneities in the cast parts. The processing procedure is being examined to try to eliminate this type of flaw.

II. Alternate Gelcasting Systems

Experiments are continuing with alternate gelcasting systems other than those based on the polymerization of acrylamide. Several systems have been examined. We had shown earlier that the monofunctional (one double bond) monomers, acrylic acid and methacrylic acid, combined with the multifunctional (at least two double bonds) cross-linking monomers, diallylamine and triallylamine, produced usable gels. However, the ionic nature of the acidic monofunctional monomers limited the solids loading attainable in the system. Further search has shown that a system using methacrylamide (MAM) monomer and poly(ethylene glycol) dimethacrylate (PEGDMA) as the crossliner is very promising for gel casting. Parts have been successfully cast and sintered in this new system. The chemistry is being studied in order to define more precisely its compatibility with both alumina and silicon-nitride ceramics.

III. Alumina Gelcast Specimen Testing

A set of specimens was tensile tested. The results of these tests show relatively low tensile strengths and considerable variability, the average strength being 192 ± 66 MPa. As previously reported for other samples, the low strengths resulted from the presence of large pores that act as critical flaws. The pores were formed by air bubbles that were trapped during casting of the slurry.

IV. Collaborative Research Agreement Between Garrett Ceramic Components (GCC) and Oak Ridge National Laboratory (ORNL) [CRA-89-002].

The objective of this work is for GCC and ORNL to perform a collaborative research program to examine the gelcasting process for fabrication of ceramic components using GCC's GN-10 silicon-nitride material. This program will investigate whether the process exhibits advantages over slipcasting, pressure slip casting, or injection molding in terms of the resultant material properties, part quality, and shape-forming ability. The applicability of the process to GN-10 complex-shaped parts, such as turbocharger rotors and advanced gas turbine rotors, will be examined.

A. ORNL Technical Progress

Twenty-two square-cross-section bars cut from a gelcast silicon-nitride plate have been tested for uniaxial tensile strength. The plate, which wa fabricated of GCC GN-10 material, was cast at ORNL and then glass-encapsulation hot-isostatically pressed (HIPed) by GCC. The test bars had a nominal 6 by 6 mm cross section and were chamfered before being mounted in the grips for tensile testing. The material had an average fracture strength of 334.3 MPa (48.5 ksi) with a standard deviation of 31.3 MPa (4.5 ksi). The calculated Weibull modulus was 11.0 for this group of samples. A Weibull plot for this material is shown in Fig. 1.

Optical examination of the fracture surfaces indicated that the fracture origins were at internal process-related flaws. These appear to be primary pores that were filled by the sintering aid glass during HIPing. This resulted in inclusion particles that acted as critical flaws. Five of the 22 specimens were selected for

ORNL-DWG 92-11874

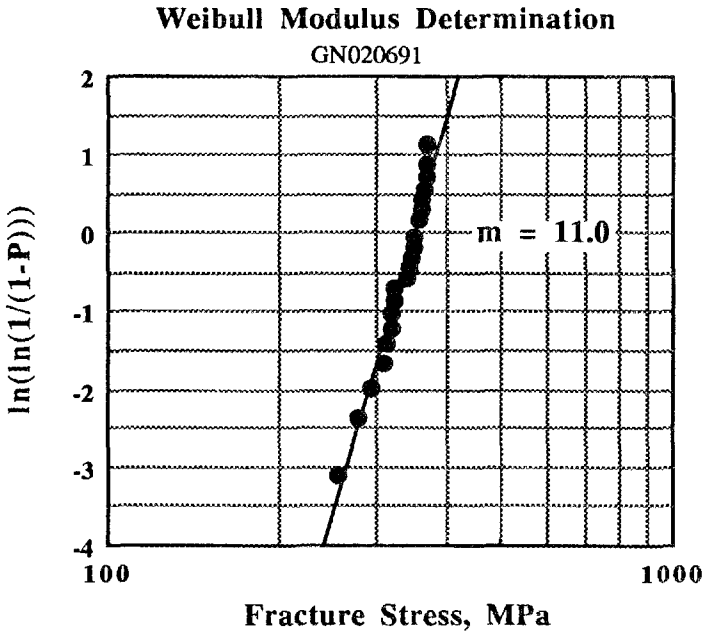

Fig. 1. Weibull plot of the fracture stress determined in tensile testing of gelcast and HIPed GN-10 silicon nitride. The average fracture strength was 334.3 ± 31.3 MPa and the calculated Weibull modulus was 11.0.

scanning electron microscopy/energy-dispersive spectroscopy (SEM/EDS) analysis of the fracture surfaces. An example of the type of flaw that was observed in the samples is shown in the SEM micrographs in Fig. 2.

The EDS analysis (Fig. 3) showed that the inclusions contained silicon, yttrium, and oxygen which would indicate formation of one of the yttrium silicate phases in the Y-Si-O-N system. The results were similar for all of the samples that were examined. No nitrogen was detectable in the inclusions. The source of the trace amount of calcium in the EDS spectrum is unknown at this time. The particles had a coarse, crystalline appearance [as shown in Fig. 2(b)] and probably formed when the sintering aid liquid was forced into open pores in the sample during the HIPing operation.

Preliminary examination of gelcast silicon-nitride turbocharger rotors by computed X-ray tomography was described in the Oct. - Nov. 1991 bimonthly report under W.B.S. Element 3.5 (Nondestructive Evaluation Development) and showed the potential benefit of this technique for screening out parts that contain defects. Numerous flaws were detected in the rotors. Evaluation of the results is continuing, including plans to correlate detected flaws in the images with actual flaws in the sectioned parts.

026215

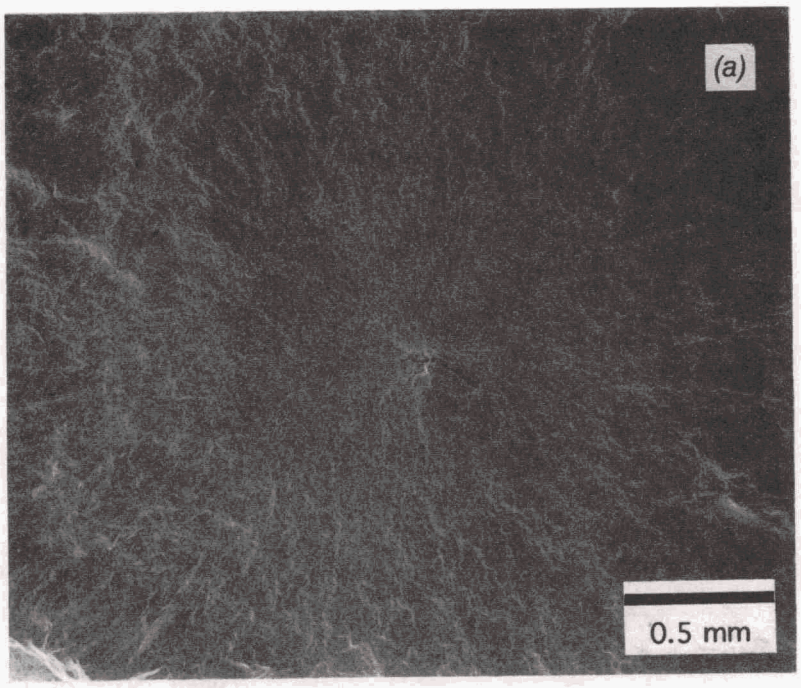

026214

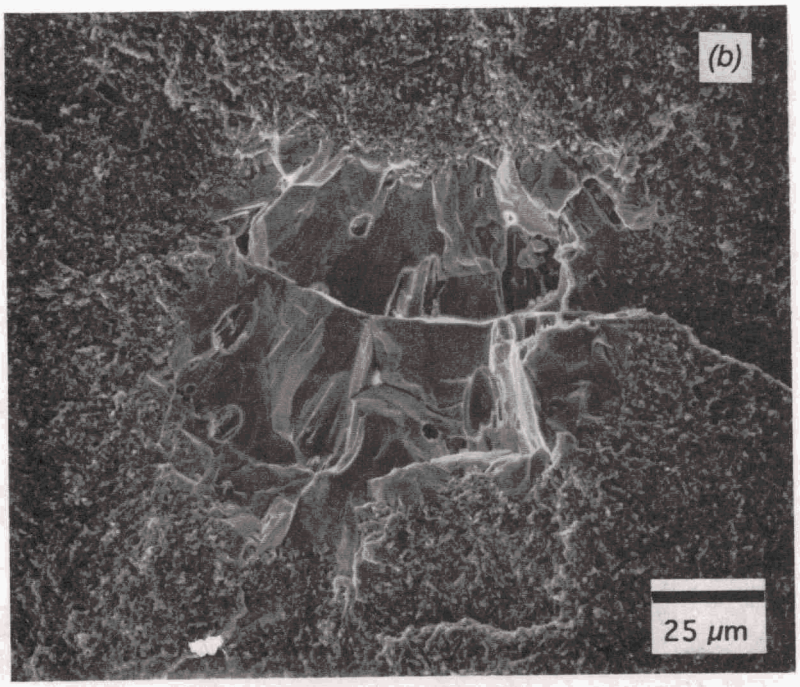

Fig. 2. SEM micrographs of a typical fracture origin found in the tensile-tested specimens of gelcast and HIPed GN-10 silicon nitride: (*a*) low-magnification view showing the critical flaw and the surrounding fracture mirror and (*b*) higher magnification view showing the inclusion particle, which acted as the critical flaw.

ORNL-DWG 92-11875

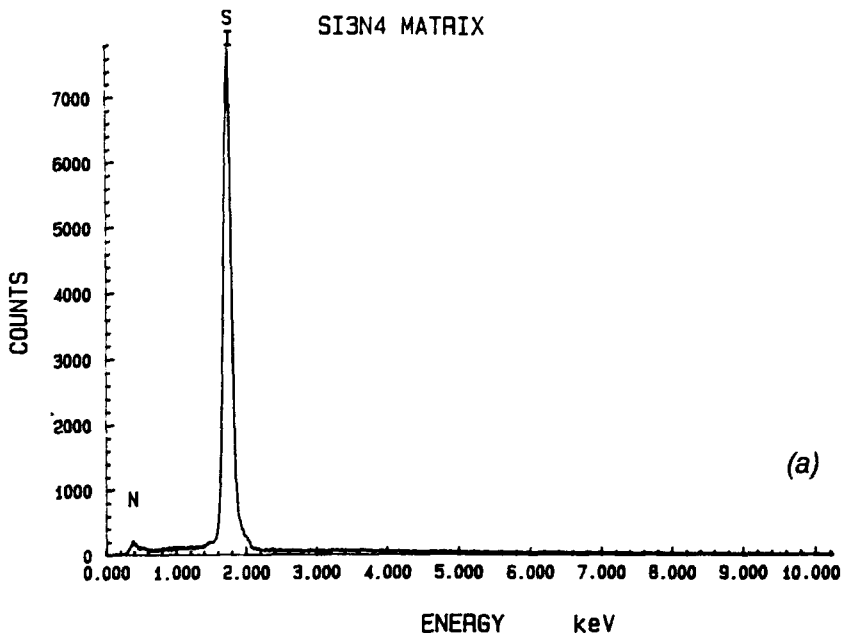

ORNL-DWG 92-11876

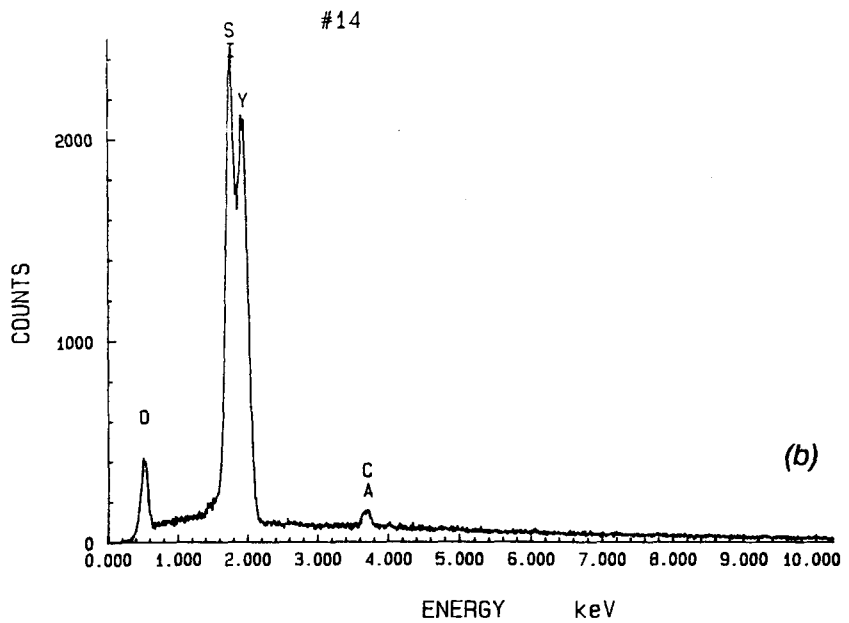

Fig. 3. Typical EDS spectra collected from the fracture surfaces of the tensile-tested specimens of gelcast and HIPed GN-10 silicon nitride: (*a*) bulk analysis of the sample showing the silicon and nitrogen peaks and (*b*) spectrum of an inclusion particle showing the presence of silicon, yttrium, oxygen, and a trace amount of calcium.

B. Technical Progress Summary From GCC for This Period

Room- and high-temperature 4-pt. flexure testing were conducted on silicon-nitride samples that were gelcast at ORNL with GN-10 composition powder provided by GCC. The gelcast plates were densified by glass-encapsulation HIPing at GCC. Samples for fracture testing were machined from the HIPed plates.

At all of the test temperatures (room temperature, 2200°F, and 2500°F), the strengths of the ORNL gelcast specimens were low when compared to standard slip-cast GN-10, as shown by the values listed in Table 1. The Weibull modulus (maximum likelihood method) for the room-temperature test samples is shown in the table and plotted in Fig. 4. ORNL has suggested that the lower strengths may be attributed to defects that result from trapped air bubbles in the gelcast plates. Fractography of the room-temperature test samples revealed that the failure origins were primarily at agglomerates and/or internal porosity.

Table 1. GCC four-point flexure test results

Sample ID	Description	Number of samples	Fracture strength MPa (ksi)	Standard deviation MPa (ksi)	Weibull modulus
			Room Temperature		
GN081490	ORNL gelcast	15	692.9 (100.5)	80.7 (11.7)	9.6
GN-112990	ORNL gelcast	15	545.4 (79.1)	71.7 (10.4)	9.1
GN-10 STD	Typical GN-10		896 (130)		20
91A-007A	GCC gelcast	15	852.2 (123.6)	53.8 (7.8)	27
S910032-4	Slip-cast control	10	902.6 (130.9)	64.1 (9.3)	21
			1204°C (2200°F)		
GN081490	ORNL gelcast	3	537.1 (77.9)	9.7 (1.4)	
GN112990	ORNL gelcast	4	442.7 (64.2)	26.9 (3.9)	
GN-10 STD	Typical GN-10		690 (100)		
91A-007A	GCC gelcast	3	558.5 (81.0)	31.7 (4.6)	
S910032-4	Slip-cast control	2	565.4 (82.0)	9.7 (1.4)	
			1371°C (2500°F)		
GN081490	ORNL gelcast	3	353.0 (51.2)	20.7 (3.0)	
GN112990	ORNL gelcast	4	342.0 (49.6)	26.9 (3.9)	
GN-10 STD	Typical GN-10		483 (70)		
91A-007A	GCC gelcast	3	412.3 (59.8)	6.9 (2.2)	
S910032-4	Slip-cast control	2	394.4 (57.2)	11.0 (1.6)	

ORNL-DWG 92-11877

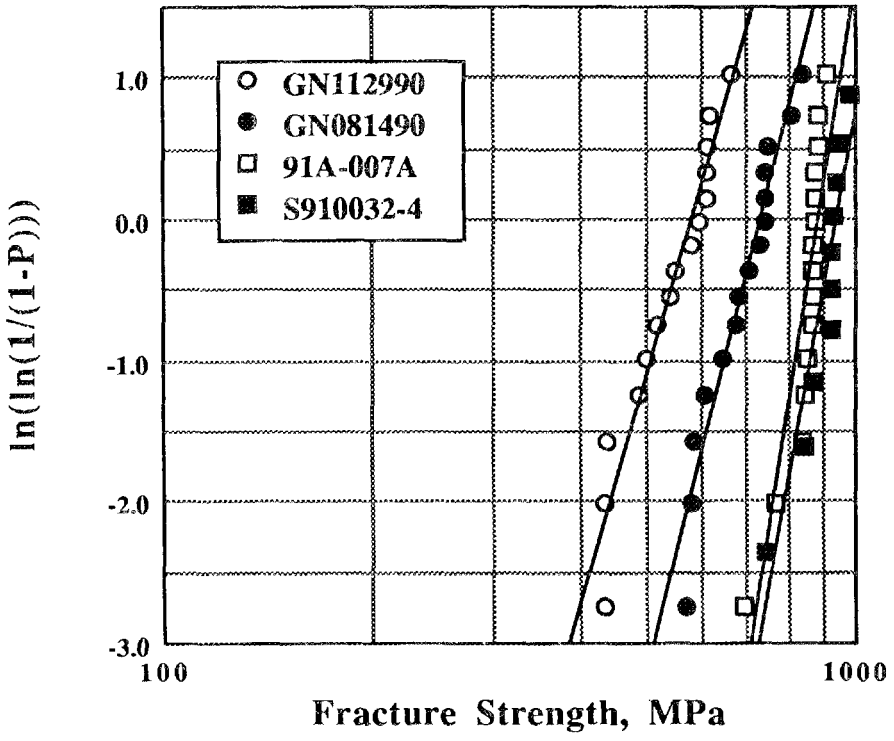

Fig. 4. Weibull plot of the modulus of rupture test data. Samples GN112990 and GN081490 were gelcast at ORNL and HIPed at GCC. Sample 91A-007A was gelcast and HIPed by GCC. Sample S910032-4 was slip cast and HIPed by GCC.

GCC also conducted mechanical testing at room and high temperature on samples fabricated in-house. GN-10 composition test bars, which were gelcast at GCC, were processed through mechanical testing along with slip-cast bars that were used as a control group. Strengths of the GCC gelcast and the control test bars were nearly identical at all of the test temperatures as shown by the data in Table 1. However, the high-temperature strengths of both groups of samples were lower than the typical GN-10 slip-cast data. The high-temperature test fixture is being evaluated as a possible explanation for this discrepancy.

The data from the GCC gelcast material reinforced the concept of the technology transfer, i.e., with ORNL's technology and GCC's processing experience, a potentially viable process can be developed for producing complex-shaped parts.

C. Activities Planned by GCC During Next Reporting Period

This activity was designed to report the technical progress during the course of development of the acrylamide gelcasting system for use with the Garrett GN-10 silicon-nitride composition. This stage of the collaborative research agreement

has been completed. Due to the changes anticipated for continuing work on the current Cooperative Research and Development Agreement (CRADA), this activity will be modified as necessary.

Status of milestones

Milestone 114207 is now overdue. R. A. Strehlow is completing work on a draft report of work completed under the collaborative research agreement with Garrett.

Publications and presentations

None.

Processing Science for Si_3N_4 Ceramics. F.F. Lange, D.S. Pearson (University of California, Santa Barbara)

Objective/scope.

We are trying to increase the understanding of the role of interparticle forces in the processing of ceramics. The effects of electrolyte addition and pH changes on the rheological properties of dispersions, the kinetics of pressure filtration, and the mechanical properties and microstructure of the resulting bodies will be compared to each other and to existing models of interparticle forces (*i.e.* DLVO theory).

Technical progress.

We are formulating a new processing paradigm. The current paradigm is based on producing slurries with long-range repulsive forces. We propose that strong, short-range repulsive forces produce better slurries and green bodies. Unlike long-range repulsive forces which permit particle segregation, short-range repulsive forces prevent particle segregation by permitting particles to weakly agglomerate without surface/surface contact. We are examining two silicon nitride systems with short-range repulsive forces: one aqueous and the other non-aqueous.

This short-range repulsive force can be tailored to create a shear-thinning slurry where particles can be separated and mixed at high shear rates and the mixing frozen in place when no shear is applied. The green bodies formed from these weakly agglomerated slurries are plastic when saturated and dry without cracking.

We are exploring two approaches to forming these short range forces: using salts in aqueous systems; and using short hydrocarbons in non-aqueous systems.

Aqueous systems.

Alumina slurries have shown improved processing when salt is added[1] and we have attempted to determine if this effect occurs in silicon nitride. In alumina, the viscosity of the slurry is increased by the addition of salt while the green body remains plastic with little effect on the green-density. In silicon nitride, we see something similar to the alumina; however, the effect is not nearly as pronounced. The viscosity of slurries increases substantially, but the density of green bodies decreases

significantly and the green bodies are not plastic.

To circumvent this problem we are modifying the surface of silicon nitride powder by hydrolyzing aluminum isopropoxide to form a surface coating following the work of Liden *et al.* (2) With this surface coating which doubles as a sintering aid, we expect more alumina-like behavior.

Sample Preparation.

Dried silicon nitride powder and aluminum isopropoxide dissolved in dry hexane are mixed together in a flask. The alkoxide reacts with the hydroxyl groups on the silicon nitride surface. After a short time for reaction, the powder is then washed by repeated centrifugation and additions of fresh hexane, and finally dried.

Results.

Zeta potential measurements indicate an isoelectric point of pH~9 for the reacted silicon nitride powder similar to the isoelectric point of alumina which is pH~8. This is comparable with the behavior of unmodified silicon nitride which has an isoelectric point of pH~5, see figure 1.

Figure 1

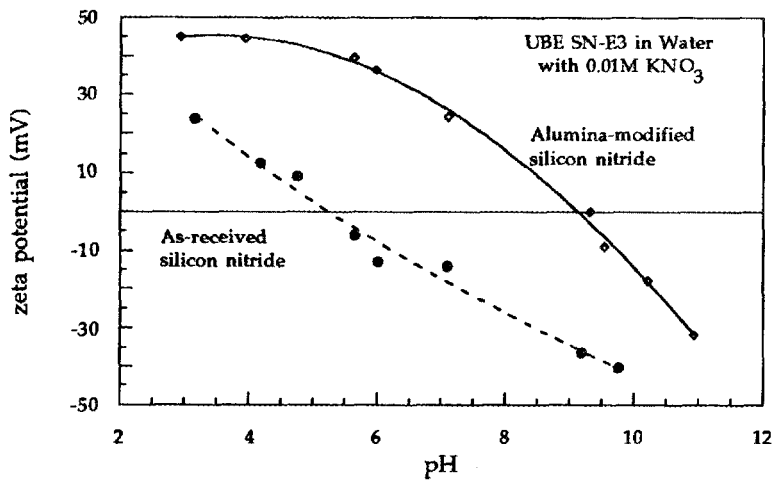

Figure 1. Zeta potential from electrophoretic mobility measurements for as-recieved and alumina-treated silicon nitride powder.

Sedigraph experiments showed that alumina modification did not promote agglomeration, *i.e.*, the reaction procedure did not

change the particle size distribution of the silicon nitride powder. To study the packing density, we dispersed the modified powders in water at pH 4 and filter pressed these slurries into pellets. Because the densities of these pellets were lower than expected, we made zeta potential measurements on washed samples of the modified powder which showed that the isoelectric point was nearly identical to that of unmodified silicon nitride.

To prevent this washing off of the alumina "layer," we heated the modified silicon nitride powder to 600 C (no hold time). This improved the packing behavior of modified silicon nitride. Packing density measurements on filter pressed bodies made from the heat-treated, modified silicon nitride slurry dispersed at pH 4 showed densities of 63% compared to 58% for filter pressed bodies mad from an unmodified silicon nitride at pH 2. The packing density of bodies made from heated-treated, modified silicon nitride showed similar improvement. For example, a modified silicon nitride slurry with 2 M NH_4Cl at pH4 produced bodies with a green density of 56%, compared to 51% for unmodified silicon nitride with 0.5 M NH_4Cl at pH 2.

Discussion.

The packing density of modified silicon nitride slurries is very encouraging. We are currently producing more modified silicon nitride to confirm these results. We expect that the packing density of salt added slurries will depend on the salt concentration. Methodical experiments are currently under way to determine the effect of the salt on the interparticle forces.

Nonaqueous systems

We are expanding the range of molecular weights of the molecules which we are reacting with the surface. The rheology of these reacted particles is similar to that observed earlier. We have examined the properties of the alkylated surface on a two additional batches of UBE E3 powder. All batches show the same effect: greatly reduced viscosities and increased densities relative to the non-alkylated, as-received material. However the extent of the effect varies from batch to batch.

Sample Preparation.

The physisorbed samples were prepared by adding 0.2, 1, or 5% by weight octadecanol to silicon nitride powder (UBE SNE-3).

Dodecane was added to this mixture in a 4:1 volume ratio and these mixtures shaken for 1 day and then tumbled for 2 more to permit the system to equilibrate.

The chemisorbed sample was prepared by reacting the powder with excess octadecanol for 2 h at 200°C as previously described. The excess octadecanol was washed from the powder by repeated centrifugation and addition of isopropanol. After 4 washings, the isopropanol remaining in the centrifugate was evaporated to leave a dry powder. This dried powder was then mixed with dodecane in the 4:1 ratio to produce a 20 vol% slurry which was shaken for 24 h.

These slurries were used to form pellets by pressure filtration. A 25 mm diameter press was filled with about 12 cc of the slurry (enough to produce a pellet around 1 cm tall) and pressed using a simple hydraulic press. Initially, the press moved quite freely as liquid was forced through the filter. When the press stopped moving, the pressure was raised to 500 kg load (*ca.* 100 MPa pressure) and held for 10 minutes.

Some of the physisorbed samples were held 1 day after they had been pressed to permit them to age, others were tested immediately on removal. The chemisorbed were all tested immediately because aging did not appear to be significant for the aged, physisorbed samples.

The samples were tested in compression by applying an 2% axial strain in a relatively quick ramp (1 mm/min) and then holding the strain constant while monitoring the load with a personal computer. This computer also controlled the application of the strain. Some of the samples were subjected to repeated loadings.

Results.

The 0.2% and 1.0% physisorbed slurries were both very lumpy with a clear supernatent always present. The 5.0%physisorbed and chemisorbed slurries resembled a thick cream and had no clear supernatent unless they had stood for some time (minutes). All of the pellets were easily removed from the pressure filtration die and had a nice surface finish. The volume fraction of silicon nitride in the pellets was determined from the formula:

$$F(Si_3N_4) = \frac{\left(\rho_{total} - \rho_{liquid}\right)}{\left(\rho(Si_3N_4) - \rho_{liquid}\right)}$$

where ρ_{total} is experimentally determined from the pellet and $\rho(Si_3N_4)$ is the density of silicon nitride (3.2g/ml) and ρ_{liquid} is the density of dodecane (0.749g/ml). All of the physisorbed had a particle volume fraction of 0.45, while the chemisorbed were slightly higher at 0.49.

The step-strain tests on the pellets showed that increasing the amount of octadecanol added to the physisorbed samples decreased the peak stress and the long-time stress (figure 2a). The chemisorbed sample was similar to the 5% physisorbed octadecanol sample (figure 2b). For the samples which had multiple step-strain applications, the first step-strain was consistently lower than subsequent step-strain applications (figure 2c).

Discussion.

The low density of these pellets was probably due to the quick pressing procedure used. We have produced samples with very high densities (60 vol%), these were pressed very slowly. The results here are internally consistent and will be extended to higher density pellets in the future.

The step-strain experiments show that the physisorbed alcohol works nearly as well as the chemisorbed alcohol if the concentration is high (this is similar to rheology results reported earlier). Aging of the physisorbed samples under sealed conditions did not have a large effect on the physical properties of the pellets. These samples were not exposed to moisture and, as we saw during our rheological studies, moisture may have a strong effect on physisorbed samples.

Conclusions.

We have demonstrated that short-range repulsion can be achieved with silicon nitride in both aqueous and non-aqueous systems. These short-range forces increase the density and plasticity of green bodies.

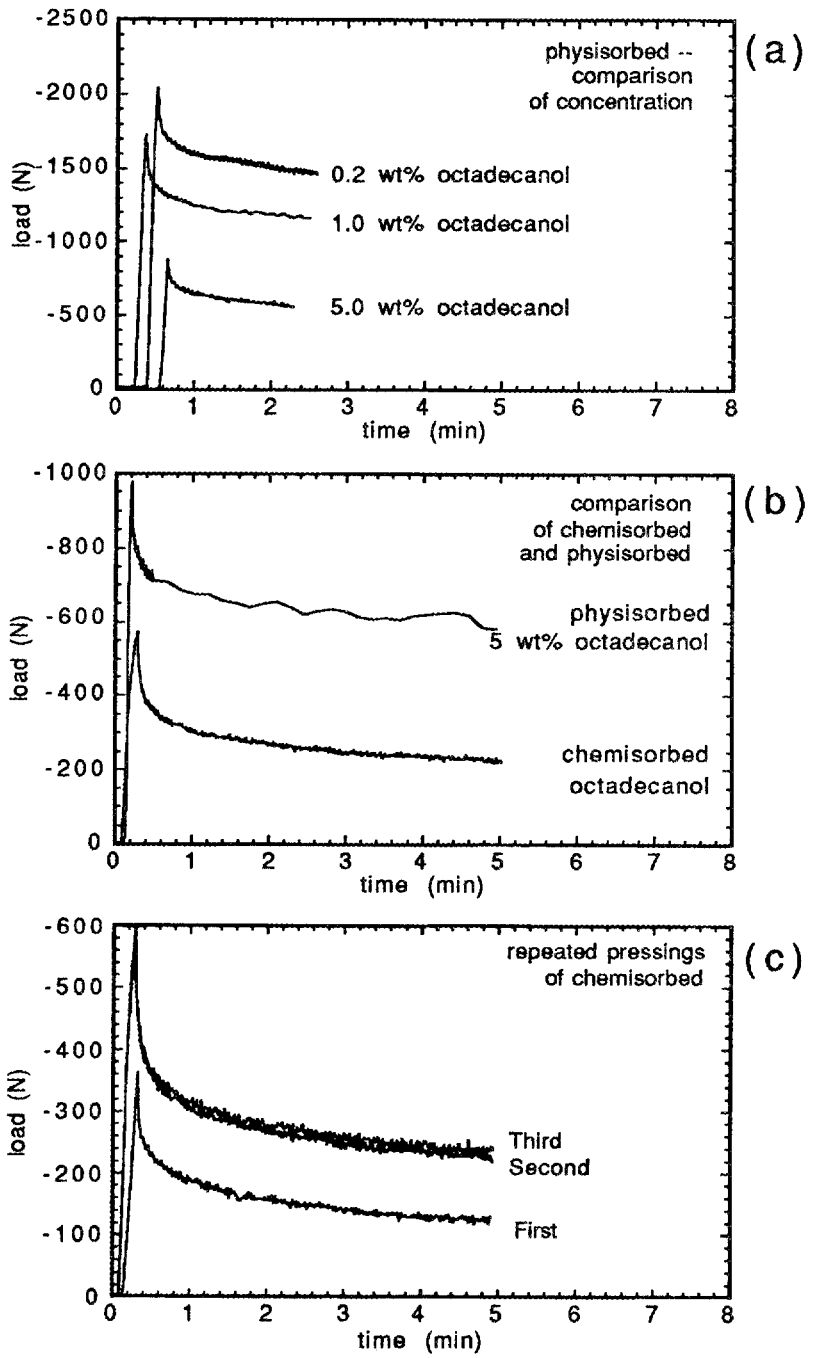

Figure 2. Rheology of green bodies:
(a) amount of physisorbed material.
(b) comparison of a physisorbed with a chemisorbed. sample
(c) repeate pressings for chemisorbed samples

Status of milestones

114401	Survey rheological characteristics of slurries produced under a variety of pH/electrolyte conditions. Develop methodologies for characterization of slurry rheological properties and green body mechanical properties.	ok
114402	Status report on testing procedures and preliminary results.	ok
114403	Determine effect of pH/electrolyte conditions on green body properties including processing rates, mechanical properties, and density.	ok
114404	Status report on green body properties and processing relationships.	ok
114405	Explore other means to modify interparticle interactions (surface modification).	ok
114406	Status report on polymer effects.	1 May 92
114407	Examine flaw populations in sintered bodies.	1 Oct 92
114408	Final report on colloidal processing.	1 Nov 92

Publications

T. Kramer, F.F. Lange, and D. Pearson, "Colloidal Processing of Silicon Nitride: Rheology of Alkylated Powders" to be published.

Erik P. Luther, Thomas M. Kramer, Fred F. Lange and Dale S. Pearson, "Development of Short Range Repulsive Potentials in Aqueous Colloidal Processing of Silicon Nitride" to be published.

References

(1) B.V. Velamakanni, J.C. Chang, F.F. Lange, D.S. Pearson, "New Method for Efficient Colloidal Particle Packing via Modulation of Repulsive Lubricating Hydration Forces", Langmuir **6**, p.1323 (1990).

(2) E. Liden, L. Bergstrom, M Persson and R. Carlsson, "Surface Modification of Silicon Nitride and Silicon Carbide", accepted by J. Europ. Ceram. Soc.

1.2 CERAMIC COMPOSITES

1.2.2 Silicon Nitride Matrix

FABRICATION OF SiC-AlN COMPOSITES

G. E. Hilmas and T. Y. Tien
(The University of Michigan)

Objective/Scope

The goal of this project is to obtain dense SiC-AlN composites containing AlN-polytypoid phases(s) as a dispersed second phase. AlN-polytypoids (8H, 15R, 12H, 21R and 27R) form as elongated rod-like or platelet-like grains and are stable at high temperatures potentially producing an in-situ reinforcement phase in advanced composites. Hot-pressing was selected for this study to optimize densification at high temperatures.

Technical Progress

1.0 INTRODUCTION

The transformation of β-SiC (3C) at high temperature to one or more of the α-SiC polytypes (2H, 4H, 6H, 15R, etc.) has been investigated extensively with the results showing that the transformation and the resulting α-polytype formed is strongly dependent on the polytypic make-up of the starting SiC powder, the sintering temperature, and the amount and type of additives used [1,2]. Small additions of Al, B, and C or BeO β-SiC (3C) have predominantly resulted in transformation to the 4H-polytype of α-SiC [3]. While small additions of only B and C to β-SiC have produced transformations to the 6H-polytype [4]. Strongly affected by the present research is the finding by several authors that β-SiC (3C) preferentially transforms to α-SiC (2H) in the presence of AlN (2H). This can occur over a broad range of SiC-AlN mixtures, in the range of 35 to 100 weight percent AlN, accompanied by an extensive 2H solid-solution above 2050 °C [5,6].

Often overlooked in the study of SiC is the difficulty in readily determining the overall SiC-polytype phase content from bulk analytical methods like X-ray diffraction. The multitude of possible transformations, the presence of many of the polytypes during high temperature forming and ultimately the overlap of their diffraction peaks makes quantification rigorous. The accepted method to accomplish this goal has been to utilize the experimentally calculated and measured single-crystal data, and thus quantified x-ray intensity equations of Ruska et al. [7]. Unfortunately, their results do not allow for the presence of the 2H-polytype of α-SiC which is present in our material. But, the

calculations are relatively straightforward, permitting the 2H-polytype to be added to their results.

The atomic positions for the 2H-polytype of SiC (space group - $P6_3mc$) were obtained from Wyckoff [8]. In line with the calculations of Ruska et al., atomic scattering factors were calculated using Si^{2+} and C^{2-} which were calculated by linear extrapolation from tabulated data for Si^0, Si^{3+} and C^0, C^{2+} [9]. The x-ray intensities are then calculated from the following equation:

$$I_n = m[F]^2 * LP/V^2$$

where I_n is the intensity normalized to the unit cell volume-V, m is the multiplicity, F is the structure factor and LP is the Lorentz-polarization factor. Table 1 shows the factors and resultant x-ray intensities for the 2H-polytype for the reflections in the range of 0.266 to 0.217 nm. These intensities were then normalized to the strongest diffraction line or I_{100} for pure 3C-SiC. Table 2 outlines the final equations for quantifying the amount of SiC-polytypes utilizing the new calculated data for 2H-SiC and the calculated and measured data for 15R, 6H, 4H and 3C from Ruska et al..

2.0 EXPERIMENTAL

2.1 X-ray Diffraction

In order to fully understand the formation of SiC polytypes it is necessary to follow the solid-state transformation among the polytypes during the hot-pressing cycle. SiC:AlN:Al_2O_3 compositions BS90, BS80, BS70, BS60 and BS50 were prepared by hot-pressing at 1700, 1800, 1900, and 2000 °C for 1 hour hold times and 2100 °C for times of 1, 2 and 5 hours (See Table 3 for the starting compositions). The samples were then ground into 3mm x 3mm x 10mm bars and crushed into a fine powder using a vibratory WC ball and mortar. These powder samples were then evaluated by x-ray diffraction. A 60 rpm motor was added to the x-ray stage to rotate the samples. Along with using a fine powder, the rotation of the sample helps to eliminate any disparity between calculated and observed x-ray intensities due to both extinction and preferred orientation. The range scanned was 32° to 45° 2θ, and the low rpm motor required scan rates to be slowed to 1°/minute.

2.2 Analytical Electron Microscopy

TEM specimens were prepared from compositions in this series that were hot-pressed for 1, 2, and 5 hours at 2100 °C. Analytical electron microscopy was then performed to more accurately determine the grain shape, grain morphology and chemical

Table 1. Calculated X-ray Intensities for the 2H-Polytype of α-SiC

h k l	d(nm)	F	(F/V)	m	L.P.	I_n
1 0 0	0.2669	14.21	0.3436	6	21.20	15.016
0 0 2	0.2515	20.88	0.5049	6	18.56	9.461
1 0 1	0.2357	12.38	0.2993	12	16.00	17.204

Table 2. Equations for Calculating SiC-Polytypes X-ray Peak Intensities

15R†		6H†		4H†		2H		3C†		Peak	d (nm)
3.2a			+	9.9c	+	39.4d			=	A	0.266
11.2a	+	19.4b							=	B	0.263
26.0a			+	38.9c					=	C	0.257
31.1a	+	59.2b	+	25.1c	+	24.8d	+	100.0e	=	D	0.251
		18.1b	+	34.1c	+	45.1d			=	E	0.235
2.4a	+	6.5b					+	13.1e	=	F	0.217

† Calculated and measured data taken from reference [7].

Table 3. Compositions of β-SiC:AlN:Al_2O_3 Series

Sample Code	Volume % β-SiC	Volume % 3AlN:1Al_2O_3
BS50	50	50
BS60	60	40
BS70	70	30
BS80	80	20
BS90	90	10

content of the grains for each composition. The specimens were ultrasonically cut into 3 mm discs from 1 mm thick sections of the hot-pressed billets. The discs were then mechanically ground and polished down to a final thickness of 100 μm, dimpled to a 20 μm center thickness and ion milled to electron transparency using 6 kV Ar^+ ions. This report is a summary of preliminary AEM results for all of the compositions.

3.0 Results and Discussion

3.1 X-ray Diffraction

The data for the BS series samples is shown graphically in figures 1 - 5. For each composition, (A) represents an overall plot of volume% SiC-polytype versus hot-pressing temperature, including 2 and 5 hours at 2100 °C; and (B) represents changes in the SiC-polytype phase content with time, plotted in minutes at 2100 °C. The data clearly shows that the transformation to the high temperature SiC-polytype is compositionally dependent.

Figure 1 shows composition BS90 transforming almost exclusively to the 6H-polytype in the range of 1900 - 2100 °C with only slight amounts of the 2H-polytype. In figure 2, the BS80 composition also transformed to the 6H-polytype, but with an intermediate development of the 15R-polytype which achieved a maximum of ~20 vol.% at 1900 °C before being consumed to form 6H. The amount of the 6H polytype actually decreased slightly for longer times at 2100 °C. The BS70 composition, figure 3, seems to be in strong competition between forming the 2H- and 6H-polytypes. While the sample still retains some 3C-SiC after 5 hours at 2100 °C, only the amount of 2H-polytype is increasing for times longer than 1 hour at 2100 °C. Compositions BS60 and BS50 are similar, both transforming more rapidly to the 2H-polytype. Both compositions exhibit an intermediate development of a 6H-polytype with a maximum occurring at 2000 °C for BS60 and 1800 °C for BS50. The 6H-polytype is subsequently consumed to form more of the 2H-polytype at higher temperatures. Appreciable amounts of the 4H-polytype are starting to form along with 2H above 2000 °C, only to be slowly consumed along with more 3C-SiC to form the 2H-polytype.

The results of this investigation emphasize the composition and additive dependence to the polytypism in the SiC matrix phase. For compositions BS90 and BS80, having 10 - 20 vol.% $3AlN:1Al_2O_3$, the preferred SiC-polytype is 6H. Larger additions of 30 - 50 vol.% $3AlN:1Al_2O_3$ resulted in competition between forming the 6H- and the 2H-polytype, with the 2H-polytype predominating at higher temperatures, longer times, and an increasing percentage of AlN and Al_2O_3 additives.

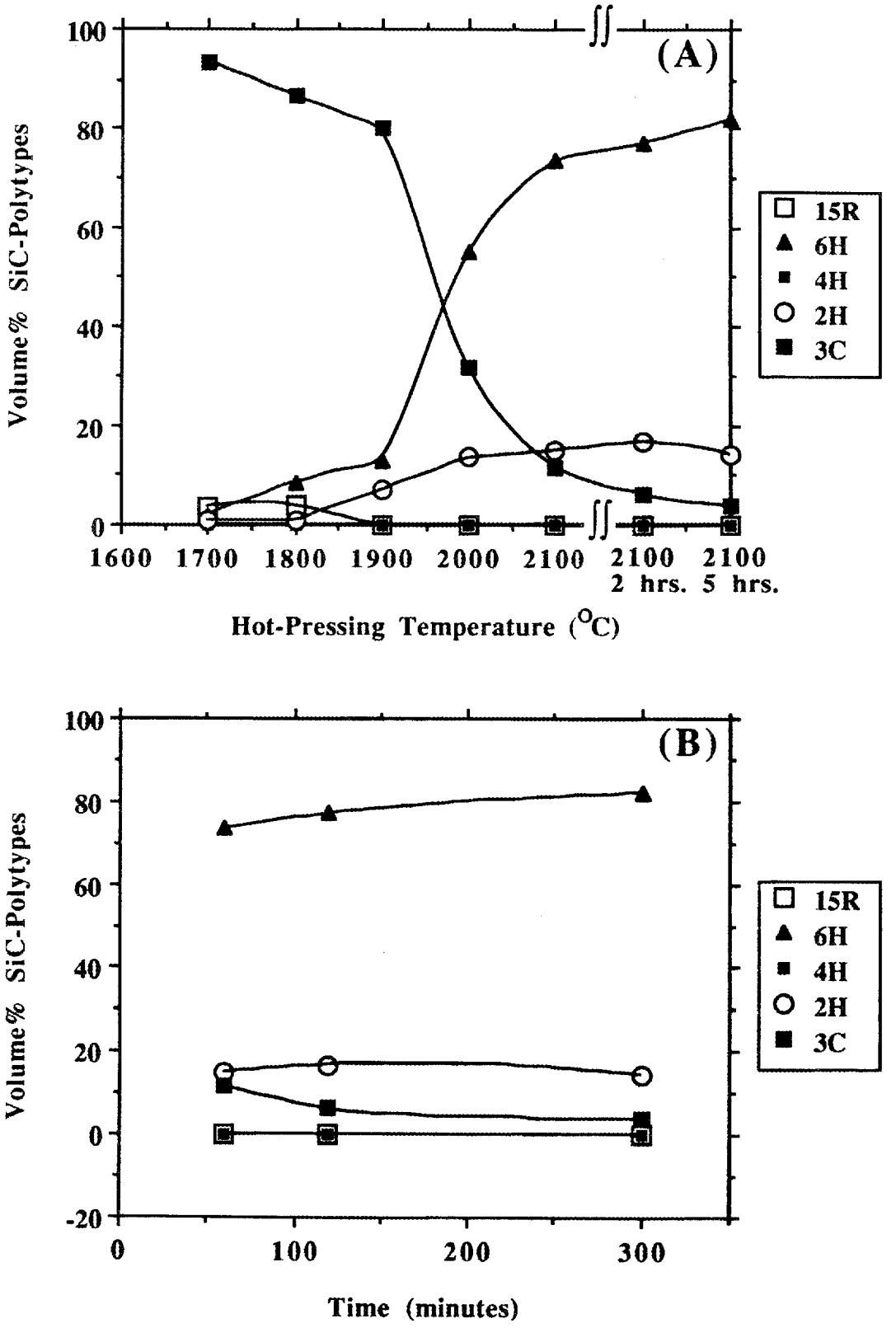

Figure 1. Composition BS90: (A) Plot of Volume% SiC-Polytype vs. Hot-pressing Temperature for 1 hour hold times up to 2100 °C, and 2100 °C for 2 and 5 hours. (B) Plot of Volume% SiC-Polytypes vs. Time at 2100 °C in minutes.

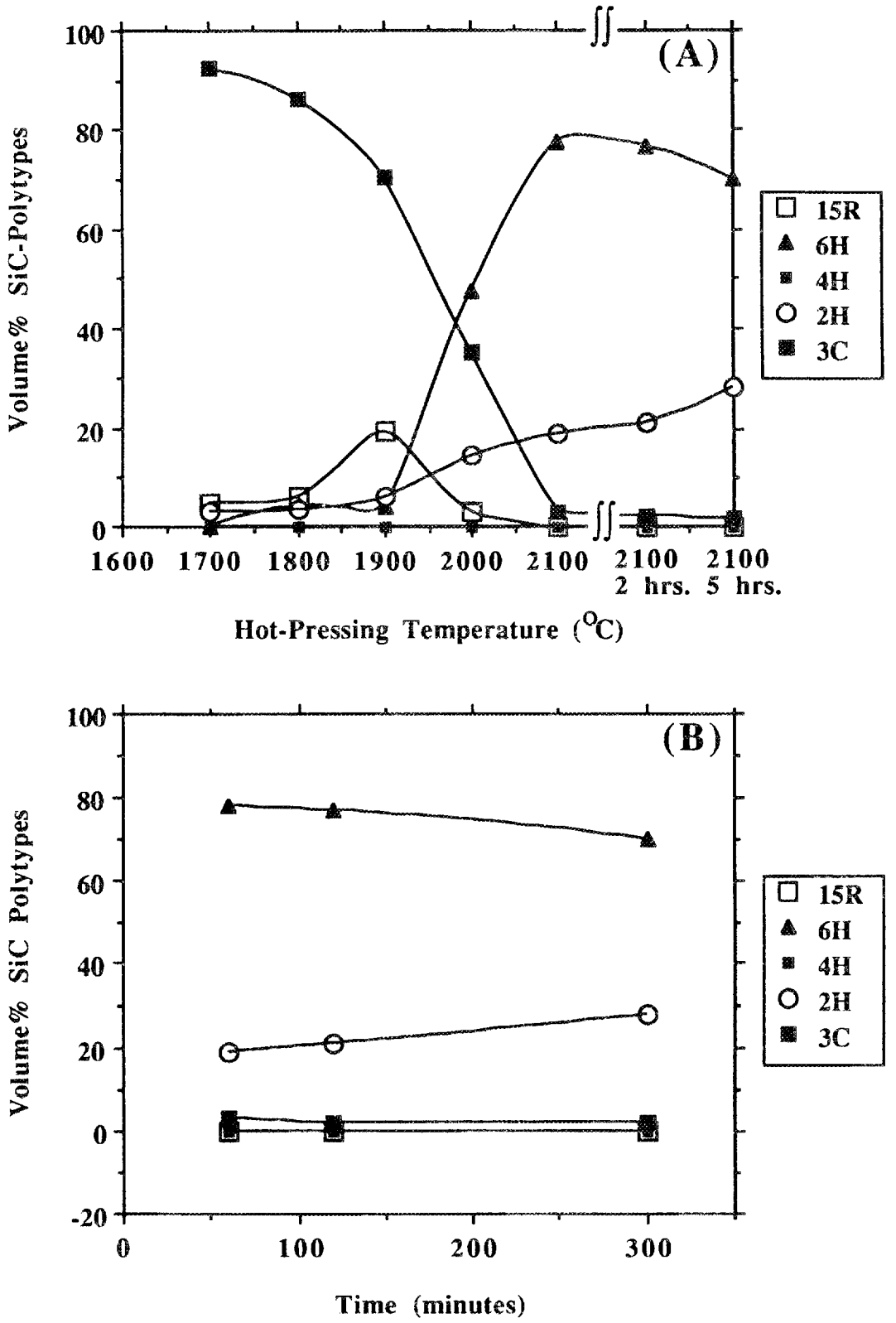

Figure 2. Composition BS80: (A) Plot of Volume% SiC-Polytype vs. Hot-pressing Temperature for 1 hour hold times up to 2100 °C, and 2100 °C for 2 and 5 hours. (B) Plot of Volume% SiC-Polytypes vs. Time at 2100 °C in minutes.

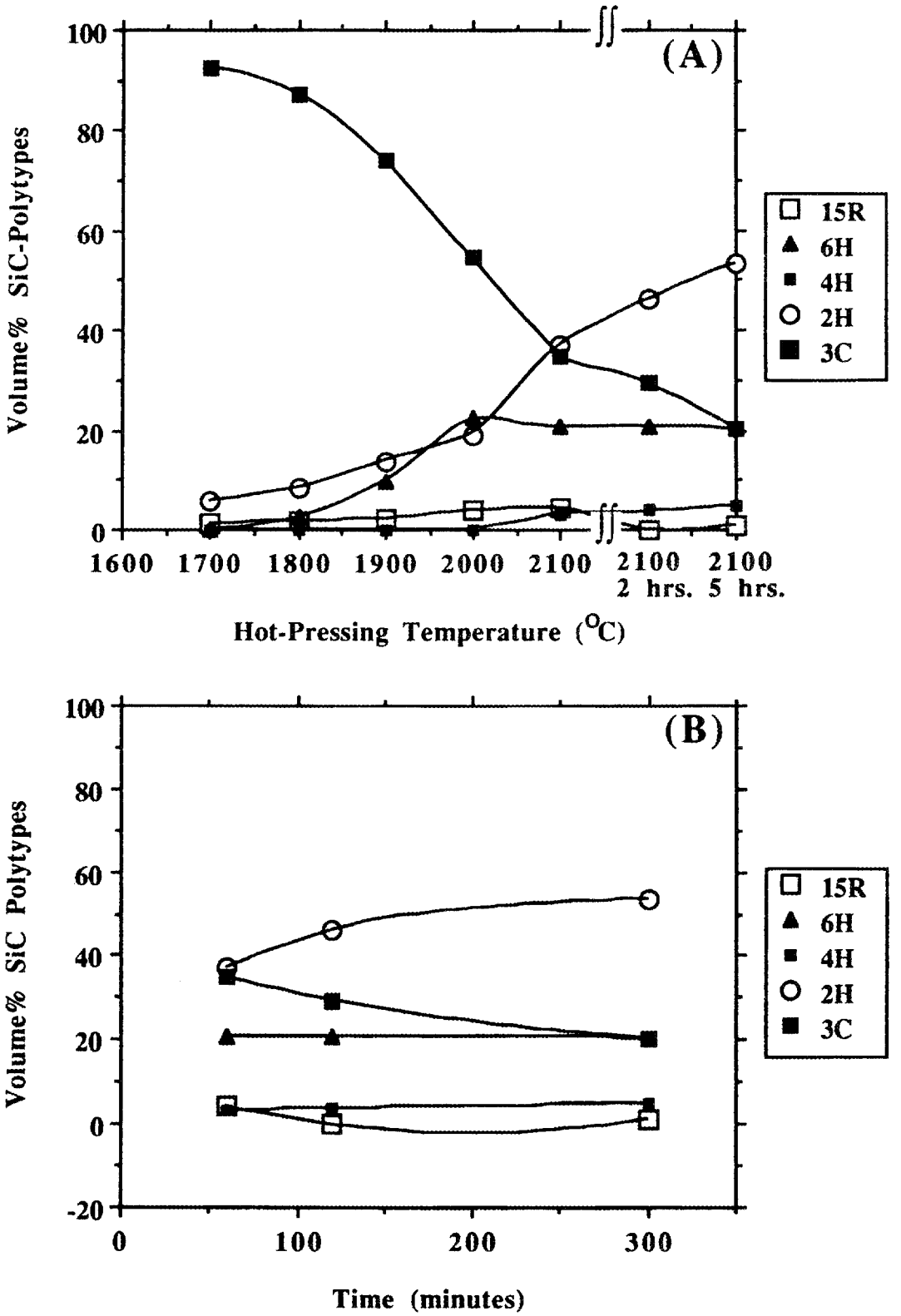

Figure 3. Composition BS70: (A) Plot of Volume% SiC-Polytype vs. Hot-pressing Temperature for 1 hour hold times up to 2100 °C, and 2100 °C for 2 and 5 hours. (B) Plot of Volume% SiC-Polytypes vs. Time at 2100 °C in minutes.

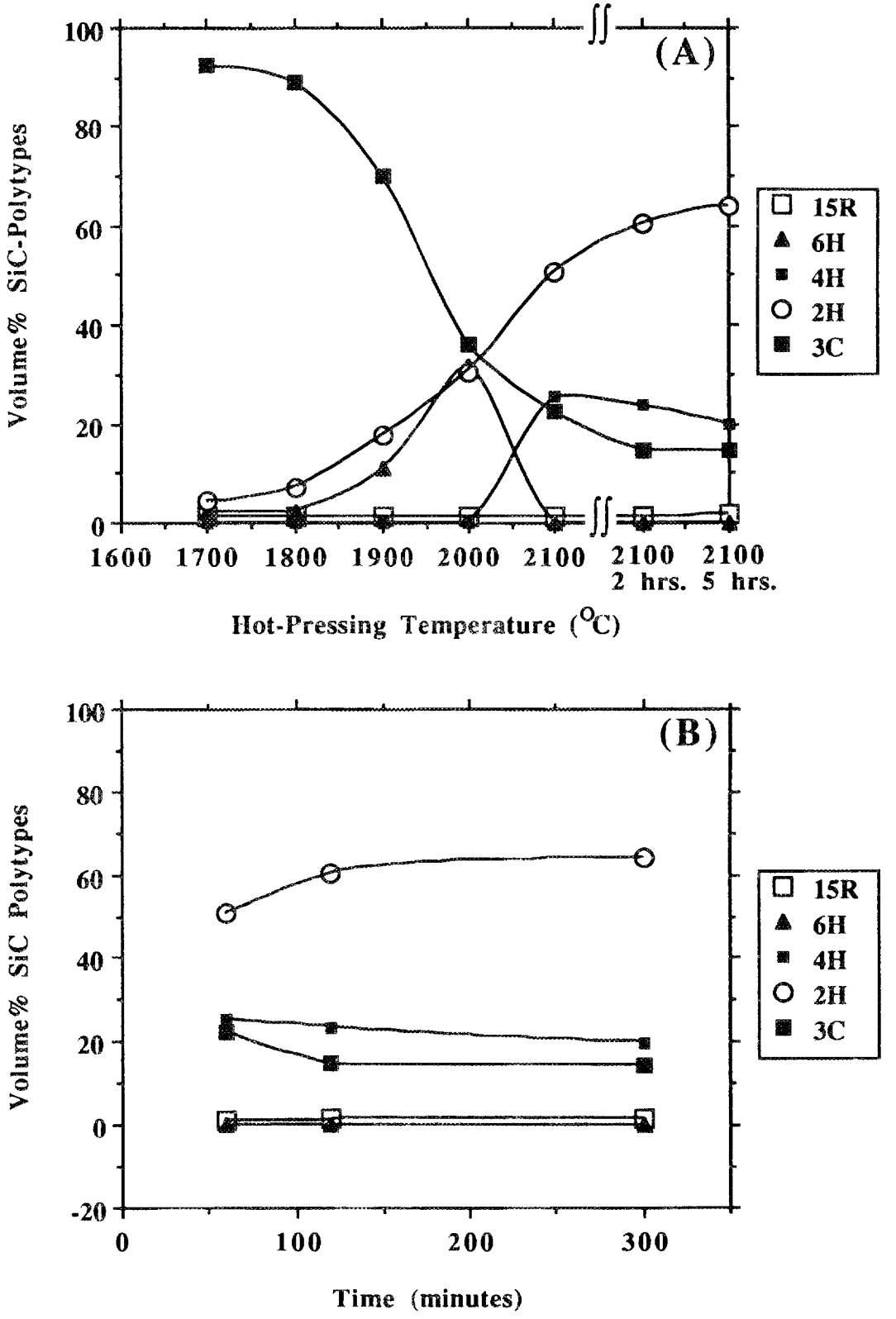

Figure 4. Composition BS60: (A) Plot of Volume% SiC-Polytype vs. Hot-pressing Temperature for 1 hour hold times up to 2100 °C, and 2100 °C for 2 and 5 hours. (B) Plot of Volume% SiC-Polytypes vs. Time at 2100 °C in minutes.

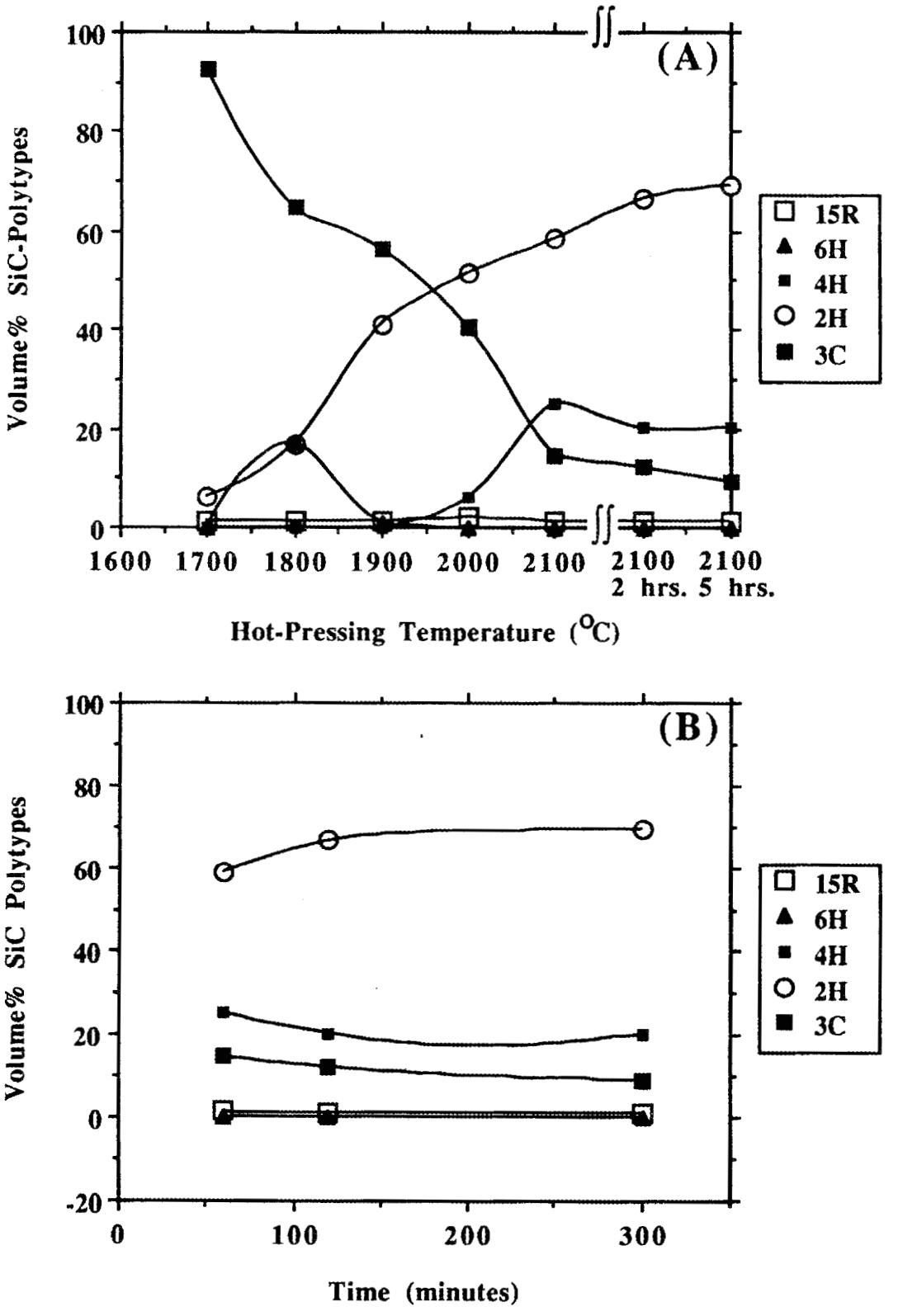

Figure 5. Composition BS50: (A) Plot of Volume% SiC-Polytype vs. Hot-pressing Temperature for 1 hour hold times up to 2100 °C, and 2100 °C for 2 and 5 hours. (B) Plot of Volume% SiC-Polytypes vs. Time at 2100 °C in minutes.

3.2 Analytical Electron Microscopy

Figure 6 shows a bright-field image of the general microstructure of composition BS90 which has transformed almost exclusively to the 6H-polytype. This 6H SiC-polytype has grown into an elongated "platelet-like" morphology with a grain size ranging from ~2 to 20 μm in length. Figure 7 is a bright-field image of the general microstructure of the BS80 composition which has also transformed primarily to the 6H-polytype. Although not close to the size of the 6H-grains in the BS90 composition, these grains have also grown elongated and range in length from ~1 to 5 μm. It should be noted that both the BS90 and BS80 compositions also contain 2H SiC-polytype grains, ~15 and 30 vol.%, respectively according to XRD results. These grains are equiaxed and typically <1 μm in size. The microstructure of the BS70 composition, figure 8, shows a majority of equiaxed 2H-polytype grains with ~20 vol.% of elongated 6H-polytype grains. The 2H grains range in diameter from 0.2 to 2 μm, while the 6H grains are 1 to 4 μm in length. Compositions BS60 and BS50 are similar, both transforming almost exclusively to the 2H-polytype. Figure 9, from the BS60 composition, is a representative bright-field image of the general microstructure of both compositions. These equiaxed 2H-polytype grains range from 0.2 to 2 μm in diameter. Some β-SiC (3C) grains are also found in all five of the compositions which remain as untransformed or partially transformed from the starting powder.

There is not enough room in a report like this to detail all of the analytical results from all of the compositions. To summarize, a bright-field image of a of 6H-polytype grain from the BS80 composition is shown in figure 10 along with a selected area diffraction pattern and an EDS spectrum showing that the grain contains Si, Al, O and C. This 6H-grain is representative of all 6H-grains in both the BS90 and BS80 compositions in that they all contain Al and O. There are no pure (Si and C, only) 6H-polytype grains in these compositions. A bright-field image of a 2H-polytype grain from the BS60 composition is shown in figure 11 along with a selected area diffraction pattern and an EDS spectrum showing a grain content of Si, Al, N, and C. This grain is representative of the 2H-grains present in all five of the compositions. All of the 2H-polytype grains are a 2H solid-solution, there are no pure 2H-grains (Si and C, only). In terms of grain boundary phase content, there is no presence of a grain boundary phase at the two-grain interfaces at the limits of the resolution of the equipment being used (~10 Å). There is a crystalline grain boundary phase which can be found in all of the compositions located at some three-grain and multi-grain junctions as shown in figure 12 with an EDS spectrum (taken from composition BS80). EDS shows that the phase is high in Al and O with

Figure 6. TEM image of the microstructure of composition BS90.

Figure 7. TEM image of the microstructure of composition BS80.

Figure 8. TEM image of the microstructure of composition BS70.

Figure 9. TEM image of a representative microstructure of compositions BS60 and BS50 (from composition BS60).

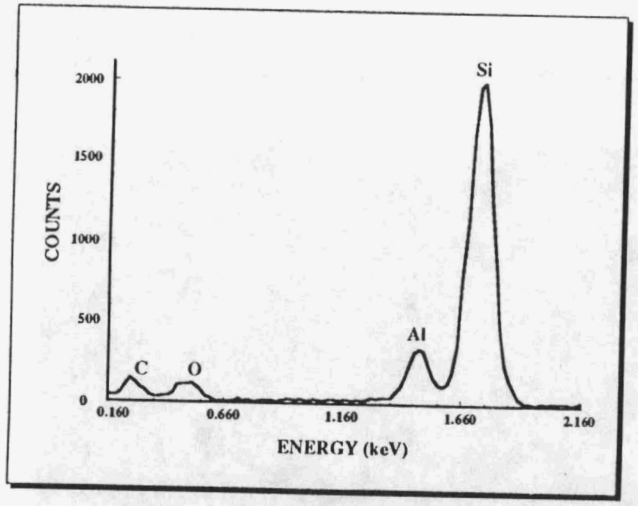

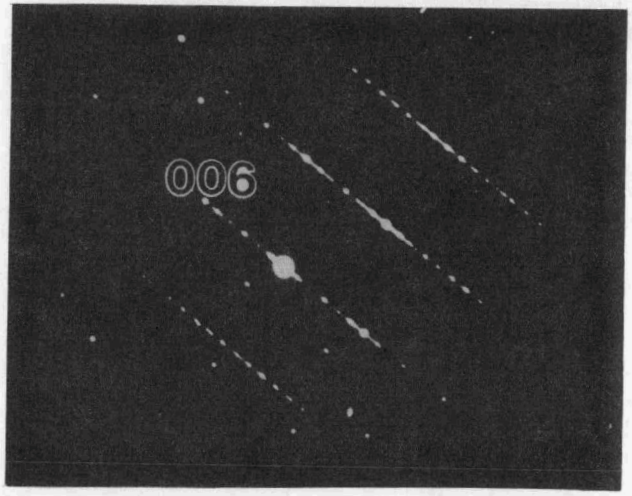

Figure 10. TEM image, selected area diffraction pattern and an EDS spectrum from an elongated 6H-polytype grain (Taken from composition BS80).

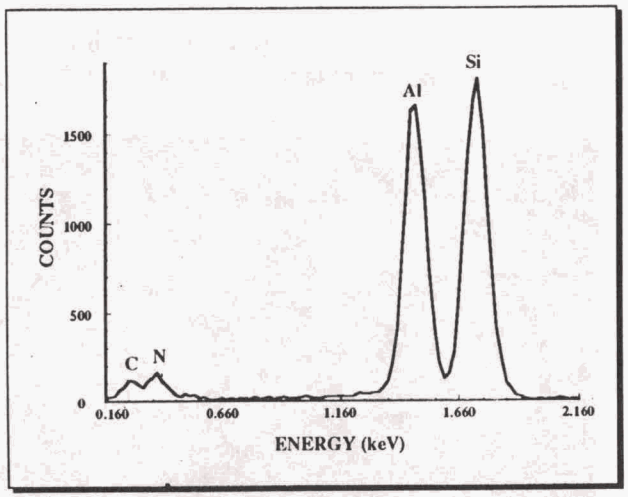

Figure 11. TEM image, selected area diffraction pattern and an EDS spectrum from an equiaxed 2H-polytype grain (Taken from composition BS60).

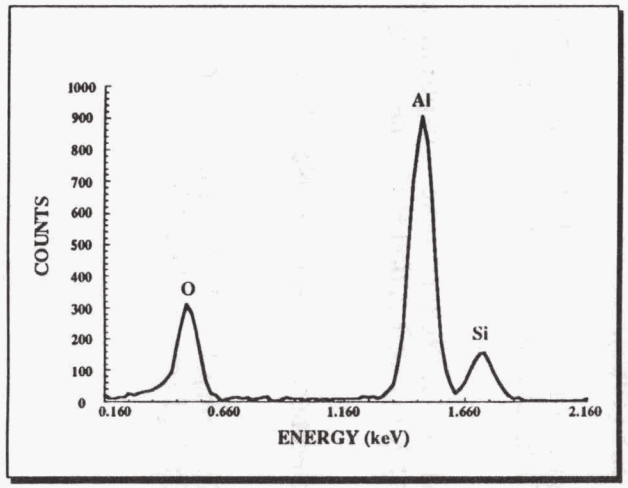

Figure 12. TEM image and an EDS spectrum from the grain boundary phase located at some three-grain and multi-grain junctions in all five of the compositions (Taken from composition BS80).

some Si and maybe some N. This phase remains unidentified by selected area electron diffraction and EDS.

Status of Milestones

On Schedule.

Publications

None.

References

[1] S. S. Shinozaki and K. R. Kinsman, "Evolution of Microstructure in Polycrystalline Silicon Carbide," Proceedings of Crystalline Ceramics, edited by Hayne Palmer III, R. F. Davis and T. M. Hare, pp. 641, 1978.

[2] Y. Tajima and W. D. Kingery, "Solid solubility of Aluminum and Boron in Silicon Carbide," *Comm. Am. Ceram. Soc.*, **65** [2], C27-C29 (1982).

[3] S. S. Shinozaki, J. Hangas, K. Maeda and A. Soeta, "Enhanced Formation of 4H Polytype in Silicon Carbide Materials," Proceedings of the Silicon Carbide 1987 Symposium held in Columbus, OH, August 1987, edited by J. D. Cawley and C. E. Semler (The American Ceramic Society), pp. 113-121, 1989.

[4] R. M. Williams, B. N. Juterbock, C. R. Peters and T. J. Whalen, "Forming and Sintering Behavior of B- and C-Doped α- and β-SiC," *Comm. Am. Ceram. Soc.*, **67** [4], C62-C64 (1984).

[5] R. Ruh and A. Zangvil, "Composition and Properties of Hot-Pressed SiC-AlN Solid Solutions," *J. Am. Ceram. Soc.*, **65** [5] 260-265 (1982).

[6] W. Rafaniello, "Fabrication and Characterization of Silicon Carbide Alloys: The Silicon Carbide-Aluminum Nitride System"; A PhD dissertation, The University of Utah, June, 1984.

[7] J. Ruska, L. J. Gauckler , J. Lorenz and H. U. Rexer, "The Quantitative Calculation of SiC Polytypes from Measurements of X-ray Diffraction Peak Intensities," *J. Mat. Sci.*, **14**, 2013-2017 (1979).

[8] R. Wyckoff, "Crystal Structures," Vol. 1, 2nd edition (Interscience, New York), pp. 113-120, 1963.

[9] "International Tables for X-ray Crystallography," Vol. 3, edited by C. H. MacGillavry and G. D. Rieck (Kynmoch Press, Birmingham), pp. 202-203, 1962.

Optimization of Silicon Nitride Ceramics

K. R. Lai and T. Y. Tien (Department of Materials Science and Engineering, The University of Michigan)

Objective/scope

To develop processing methods to optimize strength, fracture toughness and creep resistance of monolithic silicon nitride ceramics. Silicon nitride ceramics with acicular grains will have higher strength and toughness and better creep resistance. The fiber-like structure can be obtained by sintering the silicon nitride ceramics at high temperature under a nitrogen over-pressure. The mechanical properties can further be improved by controlling the composition and grain boundary phase(s). The major goal of this project is to develop monolithic silicon nitride ceramics with optimum mechanical properties and to understand their mechanisms.

Technical progress

It was reported in the literature that silicon nitride powders with high α content are prepared versus those with a low α content and are being used as starting materials. It was believed that the acicular β-Si_3N_4 grains grow only on the preexisting β nuclei. To verify this concept, starting powder with different β–Si_3N_4 contents were used as starting materials.

Fine β-Si_3N_4 powder was obtained by converting the Ube SN-E10 powder (β = 5%) to 100% β phase by heating the powder at 1900°C for 1 hr under 20 atm N_2 pressure. XRD results (Fig. 1) show only β-Si_3N_4 phase present in the fine powder. Powder agglomerates were then attrition milled for 2 hours using iso-propyl alcohol and high purity Si_3N_4 grinding media. A diluted suspension (< 0.4%) was placed in a beaker of iso-propyl alcohol. After settling, the upper part of the suspension was removed with a pipette to obtain β-Si_3N_4 powder with a particle size < 0.6 μm. The settling time t and sedimentation height h were determined according to Stoke's law.[3]

β-Si_3N_4 powder was then added to the SN-E10 to prepare powder mixtures with different fractions of β-Si_3N_4. 10 wt% $Y_3Al_5O_{12}$ was added as a sintering aid. Powder compacts were then sintered at 1800°C under 10 atm N_2 pressure. Grain size was determined using the disintegration method.

Fig. 2 shows microstructures of monoliths sintered from the powders consisting of various β contents. Grain sizes and morphologies for these specimens are almost the same. The measured grain lengths and

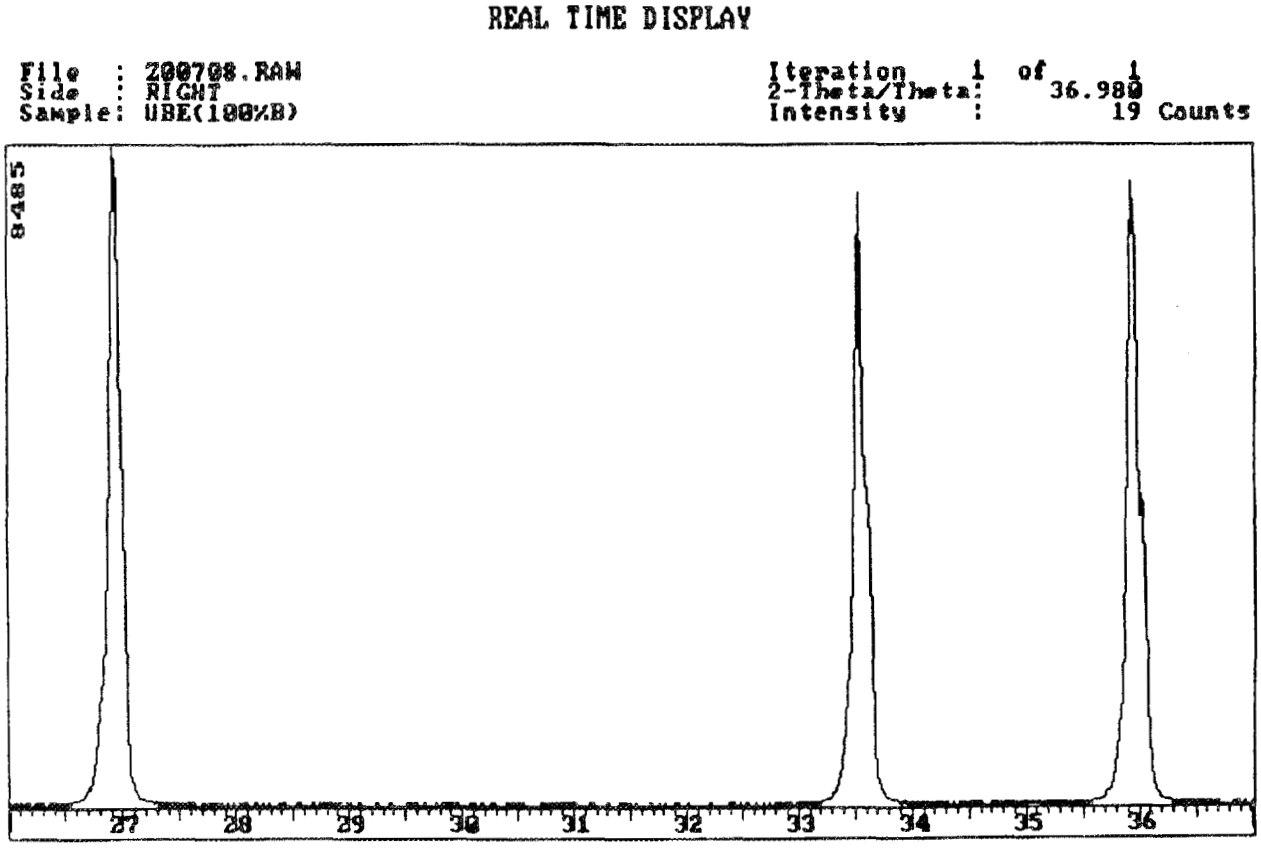

Fig. 1 Only β-Si_3N_4 phase presents in powder mixture of Ube SN-E10 after being converted at 1900°C for 1 hr. under 20 atm N_2 pressure.

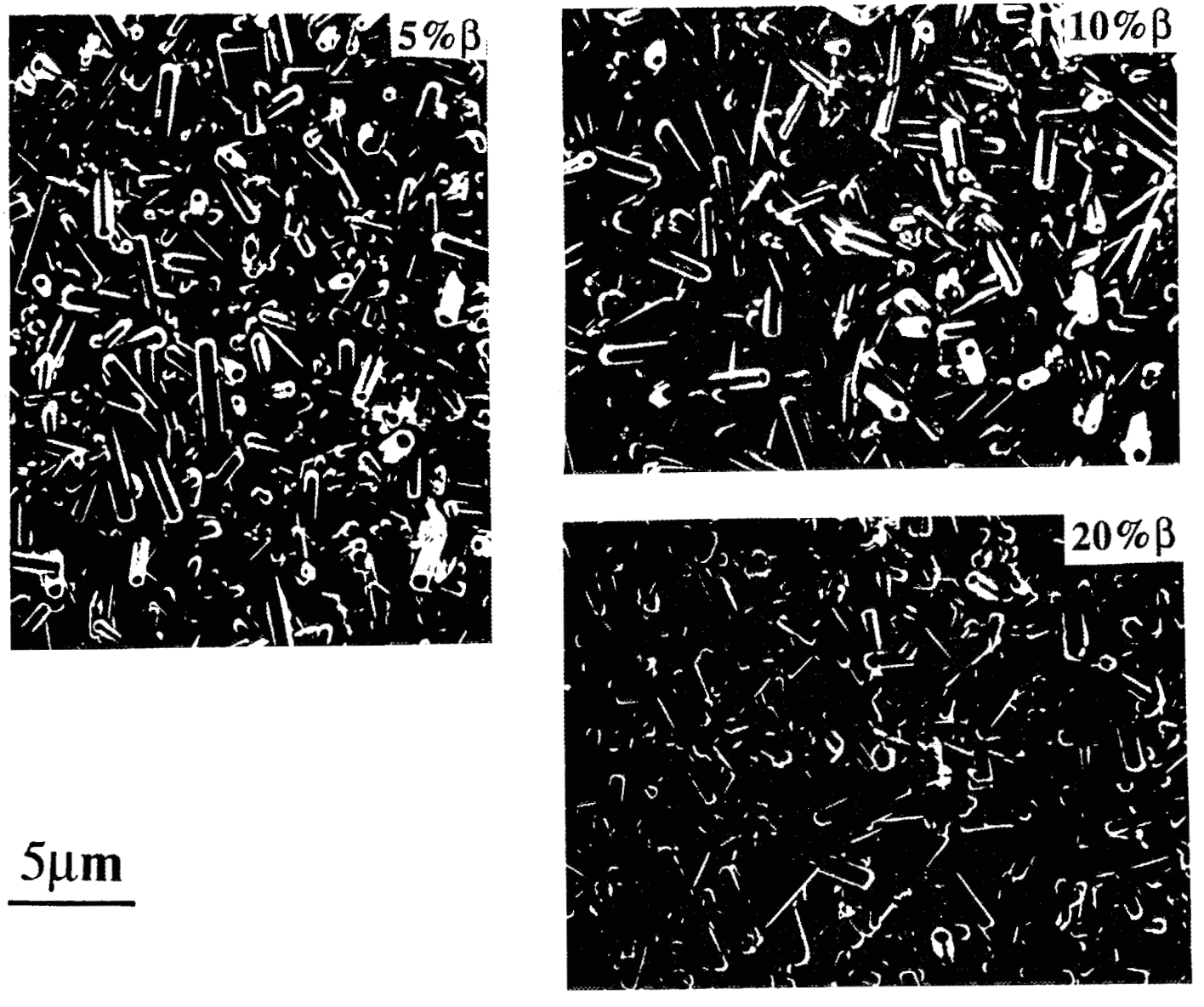

Fig. 2 Microstructures of β-Si_3N_4 Ceramics sintered from powders consisting various β contents. Specimens were sintered at 1800°C for 1 hr. under 10 atm N_2 pressure.

widths of the specimens are shown in Fig. 3. The growth exponents approximately equal 3 and 5 for length and width directions, respectively.

Grain length, width and aspect ratio can be further illustrated in Fig. 4. It is very clear that the grain size and aspect ratio appear to be nearly invariant despite the change in β content in the powder mixtures.

References

1. J. L. Iskoe and F. F. Lange, "Development of Microstructure and Mechanical Properties During Hot Pressing of Si_3N_4." in Ceramic Microstructure '76. pp. 669-78. Edited by R. M. Fulrath and J. A. Pask. Westview Press. Boulder, Colo., 1977.

2. D. D. Lee, S. L. Kang, G. Petzow, and D. N. Yoon, "Effect of α to β (β') Phase Transition on the Sintering of Silicon Nitride Ceramics." *J. Am. Ceram. Soc.* **73** [3] 767-69 (1990)

3.J. S. Reed in Introduction to the Principles of Ceramic Processing. pp. 87-89. John Wiley & Sons, New York, 1988

Status of milestones

On Schedule.

Publications

None.

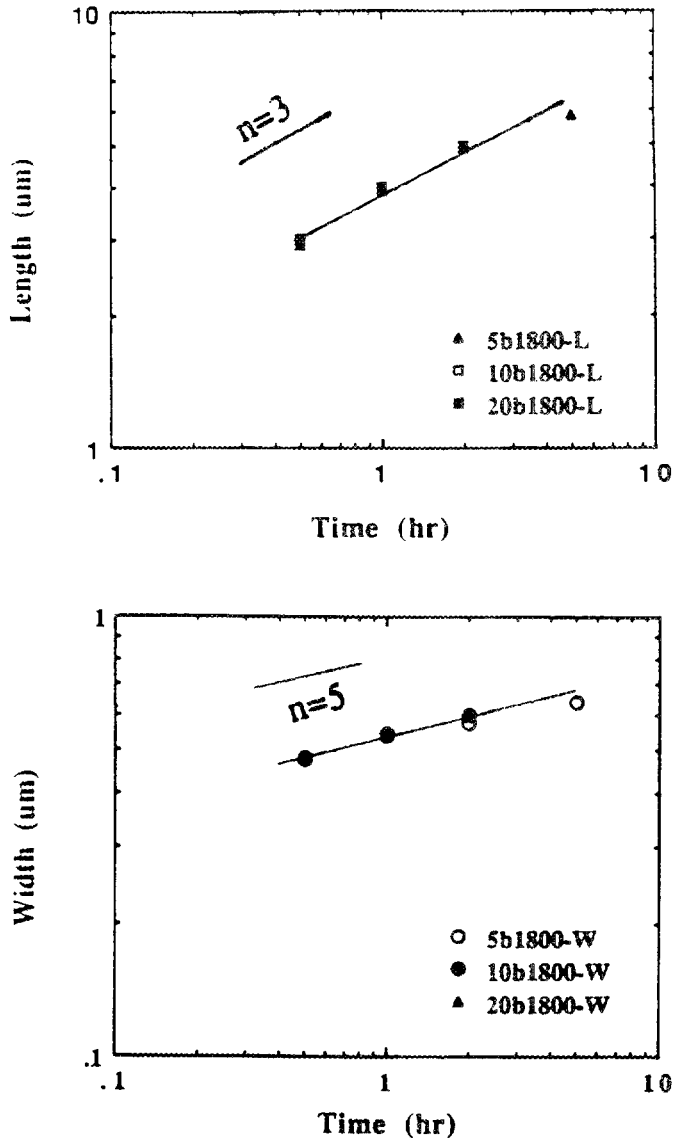

Fig. 3 Grain growth of β-Si_3N_4 grains in ceramics sintered from powders consisting various β contents.

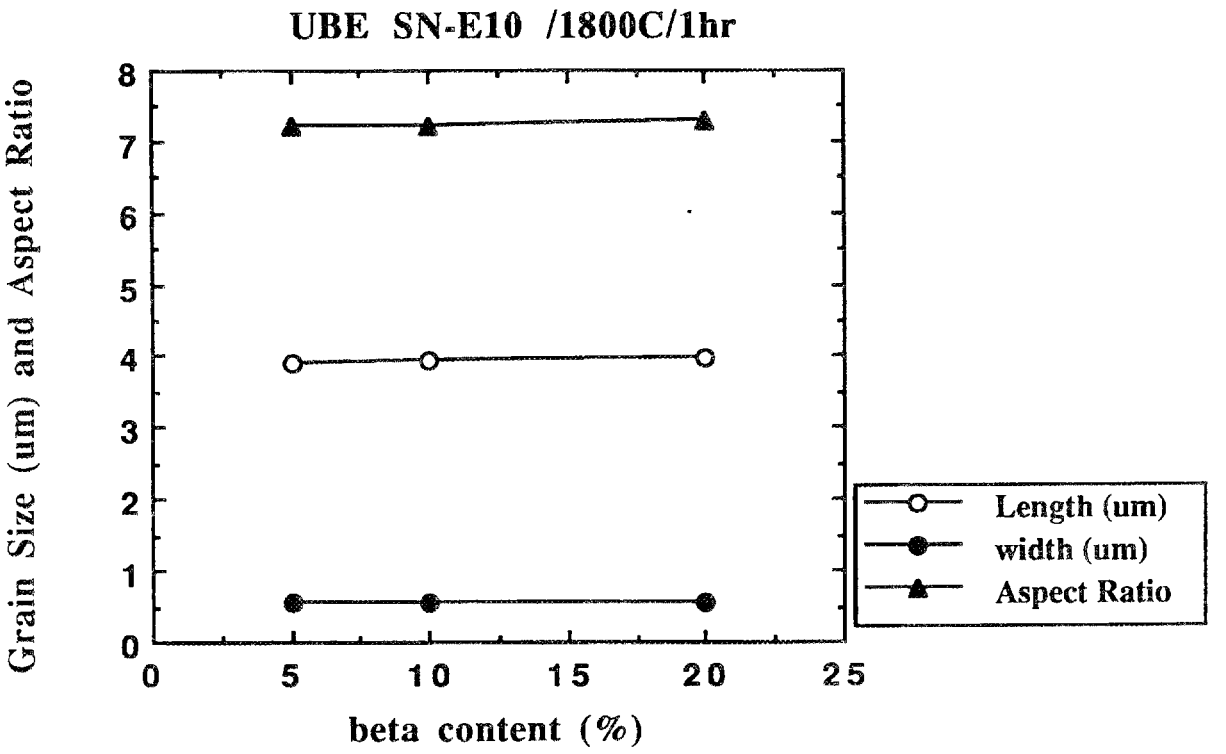

Fig. 4 An alternative figure shows the invariance of aspect ratio, grain length and width among the Si_3N_4 ceramics sintered from powders consisting various β contents.

Silicon Nitride with Elongated Grain Microstructures Exhibiting High Fracture Toughness - J. Pollinger and H. Yeh (Garrett Ceramic Components), C-W. Li and J. Yamanis (Allied-Signal Research & Technology)

Objective/scope

The objective of this program is to develop compositions and processes to obtain high fracture toughness and strength for silicon nitride (Si_3N_4) based ceramic materials through microstructure control. Resulting microstructures will have elongated grains that will promote crack bridging and deflection toughening mechanisms. These types of materials, known as *in-situ* reinforced (ISR) Si_3N_4, are intended for application in advanced heat engine components. A significant amount of the improved mechanical properties must be retained to elevated temperatures. The properties should not substantially degrade over time and would thus allow the material to survive stress under extended exposures at high and moderate temperatures in oxidizing environments. The mechanical property goals of the program are listed below:

Modulus of Rupture at 25°C*	900 MPa (130 ksi)
1200°C*	630 MPa (90 ksi)
1400°C*	490 MPa (70 ksi)
Stress Rupture at 1000°C#	630 MPa (90 ksi)
1200°C#	490 MPa (70 ksi)
Weibull Modulus+	20
Fracture Toughness, K_{Ic} at room temperature**	10 MPa$\sqrt{m}$
Maximum Use Temperature	1400°C

The technical effort is divided into two stages. The first stage shall be a refinement stage (Tasks 1 and 2), and shall focus on the effects and interactions of the chemical composition and thermal processing variables on microstructure, mechanical behavior, and oxidation resistance. In parallel, the effects of green processing on the required amount of sintering aids, room temperature strength, Weibull statistics, and critical flaws shall be assessed. The goal for this stage shall be to identify conditions which improve the baseline material and to map composition-processing-property relationships. The second stage shall be an optimization stage (Tasks 3, 4 and 5) and shall focus on the development of ISR Si_3N_4 with optimized microstructure and properties which meet or exceed the property goals and on the establishment of composition-processing-property correlations. In addition, a simulated engine component shall be fabricated in order to demonstrate process feasibility.

---

*Four point flexure using Department of Defense MIL-STD-1942 (size B) test specification.

#Stress at which sample shall survive 100 h at 1000°C.

**Measured by Chevron notch method.

+As determined by maximum likelihood method.

The technical effort was initiated in February 1992. Only Task 1 - Composition and Process Development was conducted in this reporting period.

Technical progress

TASK 1 - Composition and Process Development

The objective of this task is to determine the relationships among the variables that control the microstructural development in the proposed ISR Si_3N_4 compositions. The focus is directed to the refinement of the baseline material (AS-800) and processes which have already been developed at Allied-Signal prior to the start of this program. The AS-800 Si_3N_4 baseline composition is composed of three sintering aids (designated SA1, SA2, SA3) and a grain growth modifier (GGM); and it was formed by a cold isostatic pressing process and then densified by a baseline multi-stage gas pressure thermal process. In this reporting period, the baseline sintering aids contents were kept unchanged while the thermal processing parameters and the GGM content were varied. The effects of the variations in thermal process and GGM content were monitored by mechanical properties. All samples were formed by a baseline slip casting process using a baseline Si_3N_4 (BSN). In parallel with the thermal processing and GGM variation experiments, a parallel green forming processing refinement effort was also conducted.

(A) Composition and Thermal Processing Refinement

- Effects of Thermal Processing on Properties

The properties of the material (AS800-1), which has baseline composition and was sintered under the baseline thermal schedule, are shown in the first row of Table 1. The strength of this material at room temperature (R.T.) is 804 MPa (116.6 ksi) with a Weibull modulus (m) of 19. The Weibull modulus was calculated using test bars which failed at a large silicon nitride grain (1 out of 21 test bars failed at machining-type flaws and have been excluded from the Weibull correlation). Although large silicon nitride grains were the predominant fracture origins, it should be noted that the large grains are beneficial to the long-crack toughness of the material. In order to obtain a balance between enhancing the strength without degrading the toughness, the size and population of these strength limiting large grains should be reduced and the population of the medium size grains should be increased. In order to achieve a good understanding of the microstructure/property relationship, the fracture origins will be closely monitored and the failures due to green processing and machining flaws will be excluded from the analysis.

The effects of changes in the thermal processing schedule was investigated. The baseline schedule has two holding stages, designated intermediate and high temperature hold stages. The initial investigation

was focussed on the effect of introducing an initial stage hold, at a lower temperature, prior to the intermediate temperature hold. The effects of this change on material properties, comparing with AS800-1, are illustrated in Table 1. All three materials listed in Table 1 have the same composition and were processed identically, except for the initial hold step. The data show that the differences on fast-fracture strength among the three samples are small, but there is a definite improvement in strength from AS800-1 to AS800-3. AS800-3 shows a tighter strength distribution and better elevated temperature strength compared to AS800-1. For all three materials the predominant fast-fracture origins at all temperatures are a large silicon nitride grain.

TABLE 1
Effect of Change in Thermal Cycle

Material	Initial Hold	Strength, MPa				
		R.T.	1100°C	1200°C	1300°C	1400°C
AS800-1	None	804±51 m=19 (n=20)		573±63 (3)	525±30 (3)	447±18 (3)
AS800-2	$T1^{o}C/t_1h$	791±3 m=24.5 (n=15)	644±47		521±17 (3)	471±5 (3)
AS800-3	$(T1+100)^{o}C/t_1h$	821±41 m=23.4 (n=15)		604±36 (2)	536±8 (2)	473±15 (2)

m: Weibull modulus. n: No. of test bars used to calculate m.

Additionally, the inclusion of the initial hold has an impact on the short crack toughness, as indicated by indentation strength data, Fig. 1. The indentation load used ranged from 2 to 10 N (the as-indented crack size for a 2 N load was about 15 μm, and for a 10 N load it was about 40 μm). The data show that the short-crack-growth resistance of the AS800-1 is the lowest and AS800-3 the highest. The higher short-crack toughness of AS800-2 and AS800-3 suggests that, as a result of the initial hold, these two materials contain a larger population of smaller β-Si_3N_4 grains than that of AS800-1, which results in improved short-crack toughness.

o Effects of Grain Growth Modifier on Strength and Toughness

The effects of reducing the GGM loading on strength and toughness were examined. Material AS800-4 was prepared with 47 wt% less GGM than the baseline, and was sintered using the same thermal schedule as the one used for AS800-3. Its average room-temperature strength (ten bars with large grains as fracture origins) is 752±48 MPa, 9% lower than that of

AS800-3. Compared to AS800-3, the average size of the large-grain fracture origins for AS800-4 is noticeably larger. The larger grain size is attributed to the lower amount of GGM in AS800-4 than in AS800-3. The coarser microstructure of AS800-4 would result in improved long-crack toughness. Indeed, the measured indentation strength at 98 N (about 120 μm crack size) is 397 MPa, compared to 368 MPa for AS800-3 for AS800-4.

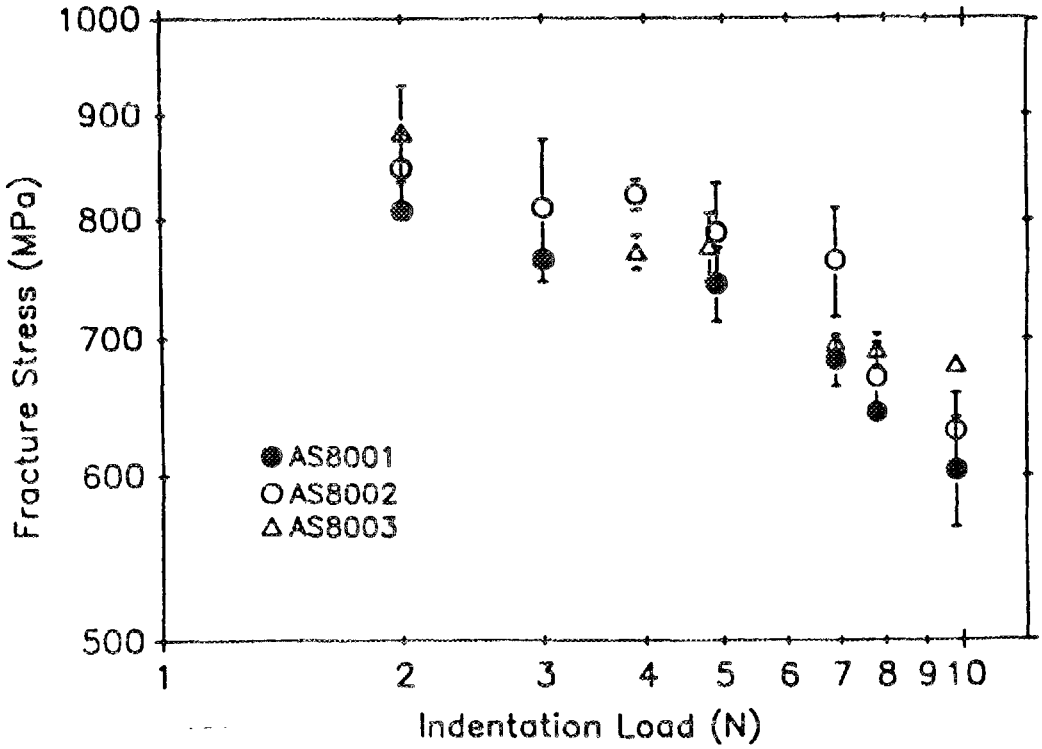

Figure 1. Room Temperature Short-crack Toughness of ISR Si_3N_4 as Indicated by the Retained Strength After Indentation.

o Long-Term Properties

The oxidation resistance of the AS800 materials were evaluated at 1300 and 1000°C using machined MOR bars. The weight gain and post-oxidation room-temperature 4-pt bend strength results after oxidation at 1300°C/100 h/air are shown in Table 2. The data for AS800-1, 2, and 3, show that the samples (AS800-2, AS800-3 vs. AS800-1) which were sintered with an initial hold had less weight gain. The data also suggest that the lower level of GGM (sample AS800-4) leads to better oxidation resistance at 1300°C. An old slip-cast sample (SN312) of the AS800 general composition sintered with the schedule similar to the one used

for AS800-2 had the lowest weight gain but it had the highest strength drop, Table 2. The drop in strength after the oxidation may be due to both the oxidation and the crystallization of the grain boundary phase at 1300°C.

TABLE 2
1300°C Oxidation Results

Material	1300°C/100 hour/Air			
	Weight Gain (mg/cm^2)	Strength (MPa)	Average Strength Loss (%)	Fracture Origin*
AS800-1	0.44 0.43	665 756	12	SLG SOP
AS800-2	0.33 0.37	716 577	18	SOP VP
AS800-3	0.38 0.25	721 705	13	SLG VI
AS800-4	0.15 0.12	701 606	13	SLG SOP
SN312	0.19 0.11	579 595	24	SLG SLG

* SLG: surface large grain. SOP: surface oxidation product.
VP: volume pore. VI: volume inclusion.

The 1000°C/100 h/air oxidation results are shown in Table 3. The data show that SN312 has the most severe oxidation and strength loss, compared to the other three materials. The difference in oxidation resistance between these materials is believed due to different levels of one of the sintering aid additives, with the baseline composition having a higher amount of this component. In addition, higher temperature for the initial hold, i.e., materials AS800-3 and AS800-4 versus AS800-2, appears to improve the material's oxidation resistance at 1000°C.

Only a limited number of stress rupture (4-pt) tests were performed in this reporting period, and they were all for AS800-2 at 1000°C. Under 490 MPa (70 ksi) one bar failed in 0.25 hour. A second bar was tested at 448 MPa (65 ksi) and it survived more than 100 hours. This second bar was then tested at 490 MPa (70 ksi) and it survived more than 100 hours. Neither bar tested at 1000°C showed any creep deformation. Another AS800-2 bar was tested at 1200°C under a 490 MPa load, and it was intact after more than 150 hours with a steady state

creep rate of 1.0×10^{-9}. Previously, two test bars with composition identical to that of SN312 were tested under the same 1200°C/490 MPa condition; both bars survived 100 hours with an average steady state creep rate about 5×10^{-10}. Their lower creep rates presumably are due to their lower concentration of the sintering aid component discussed above.

TABLE 3
1000°C Oxidation Results

Material	1000°C/100 hour/Air				
	Weight Gain (mg/cm^2)	Oxidation Thickness(μm)	Strength (MPa)	Average Strength Loss(%)	Fracture Origin
AS800-2	0.15 0.12	10-20	793 768	1	SLG SLG
AS800-3	0.03 0.04	5	838 731	4	SLG SLG
AS800-4	0.09	8	721	4	SLG
SN312	0.18 0.20	50-70	449 574	34	SLG SOP

(B) Green Forming Refinement

The objective of this effort is to explore potential AS800 material property improvements through refinement of the green forming process, which includes slip preparation, pressure slip casting, drying, and presintering. The potential for improving green microstructures to reduce the amount of sintering aids required for densification and grain growth and thus improve high temperature properties shall also be investigated. The slip casting process developed should have the potential of casting large complex shaped components.

Based on the past experience at Allied-Signal, the green forming behavior and the properties of the densified ISR Si_3N_4 materials are very sensitive to the properties of the raw materials. Thus, in order to maintain consistency and reproducibility, a sufficient quantity of raw materials, including Si_3N_4 (baseline) and GGM powders, of the same grades as those used in the other efforts (presented in (A) were acquired. Characterization of the powders by zeta potential vs. pH and zeta potential vs. dispersant concentration curves were performed. The results indicated that the GGM powder is compatible with the pH and dispersant used in the AS800 slip casting process. Two batches of

baseline AS800 composition slip were prepared using the baseline slip preparation procedure. Green plates approximately 2" by 3" by 0.6" with no visually detectable cracks or distortion were successfully cast from both batches. The plates were calcined using the baseline calcination cycle for ISR Si_3N_4, and the calcined plates did not show any visible cracks or distortion. The average density of the calcined plates is 1.93 g/cc (58% theoretical). These plates are to be sintered using the baseline cycle for property and microstructure evaluation to provide a baseline for the subsequent green process refinement experiments.

Status of milestones

Work is progressing on schedule.

Publications

None.

1.2.3 Oxide Matrix

Dispersion-Toughened Ceramic Composite

T. N. Tiegs, S. D. Nunn, P. A. Menchhofer, C. A. Walls, and K. Ploetz
(Oak Ridge National Laboratory)

Objective/scope

Initially, this work involved development and characterization of SiC whisker-reinforced ceramic composites for improved mechanical performance. To date, most of the efforts involving SiC whisker-reinforced alumina, mullite, silicon nitride, and sialon have been completed. In addition, studies of whisker-growth processes were initiated to improve the mechanical properties of SiC whiskers by reducing their flaw sizes and, thereby, improving the mechanical properties of the composites. Currently, in situ acicular grain growth is being investigated to improve fracture toughness of silicon-nitride materials.

Technical highlights

In Situ Toughening of Silicon Nitride by Microstructure Development

Microstructure Development During Hot Pressing - A series of silicon-nitride materials to assess the role of additive chemistry on elongated-grain growth, fracture toughness, and high-temperature properties has been fabricated and machined into test specimens. The compositions, hot-pressing conditions, mechanical properties and phase compositions have been previously reported. The mechanical properties are reported under WBS 3.2.1.3 of the present progress report. Oxidation tests of the materials are currently being performed at 1000°C, and those results are summarized in Figs. 1 and 2. Previous results had shown severe oxidation problems with silicon nitrides having high rare-earth additive contents at temperatures of 800°C. Further testing of these materials at temperatures of 700°C indicate that the materials also exhibit oxidation problems even at these relatively low temperatures as shown in Fig. 3.

Mechanical property reductions associated with the crystallization of the glass phase in silicon-nitride systems have long been observed in numerous silicon-nitride systems.[1-3] Samples have been fabricated in the hot press where crystallization with and without applied pressure has been done to determine if the volume decreases associated with the crystallization processes affect the property changes. The effect on the strength and toughness is summarized in Table 1. As shown, no real differences could be seen between crystallization done with or without applied pressure.

Numerous studies have shown that the silicon-nitride powder used in fabrication is an extremely important variable in the microstructural development and final properties of the materials.[4-16] To examine these effects, two series of hot-pressed samples were fabricated with various silicon-nitride powders (Table 2). The samples contained either 6% Y_2O_3-2% Al_2O_3 or 4% Y_2O_3 as sintering additives. Flexural-strength measurements for the specimens with 6% Y_2O_3-2% Al_2O_3 additives show a large variation, both at room temperature and at elevated

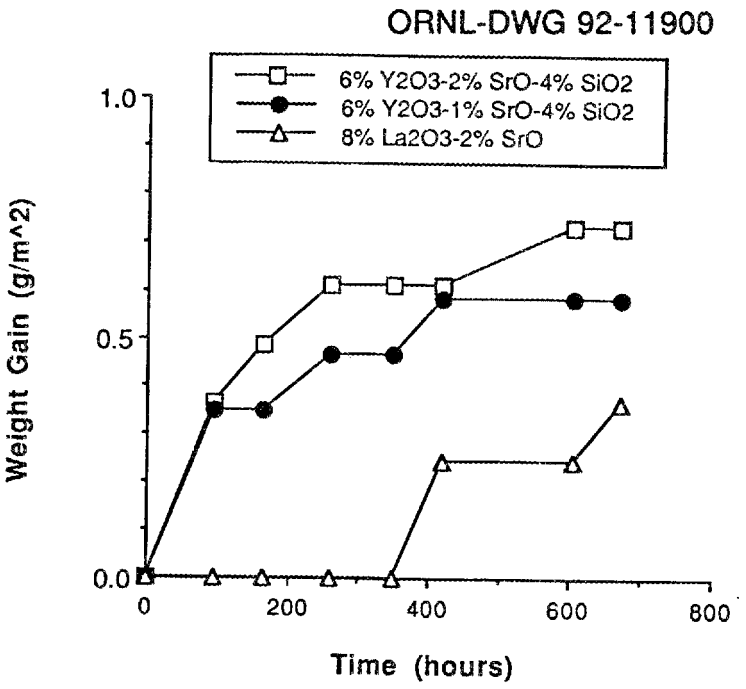

Fig. 1. Summary of weight changes during oxidation of silicon-nitride compositions at 1000°C.

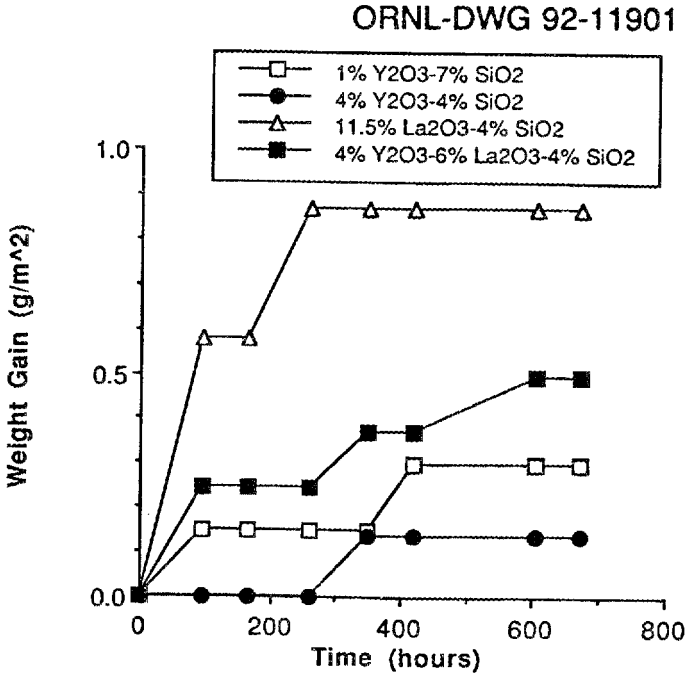

Fig. 2. Summary of weight changes during oxidation of silicon-nitride compositions at 1000°C.

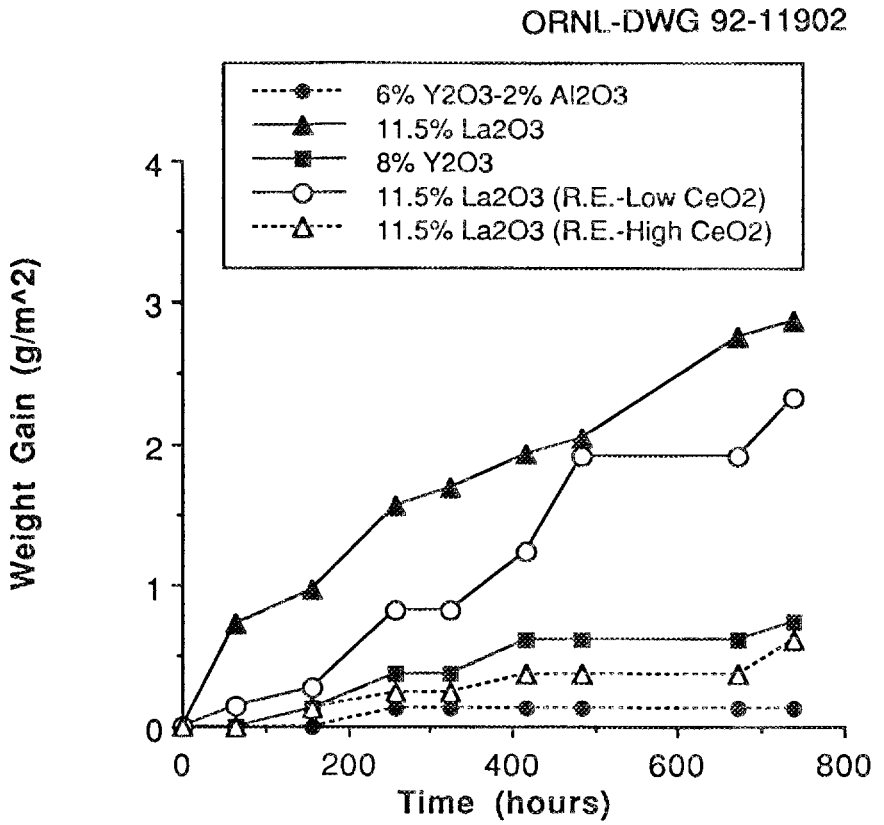

Fig. 3. Summary of weight changes during oxidation of silicon-nitride compositions at 700°C.

Table 1. Summary of results on mechanical property changes during crystallization of grain-boundary phases. Composition of materials was Si_3N_4-6% Y_2)3-2% Al_2O_3. Hot pressed at 1800°C for 90 min. and 24 MPa pressure.

Crystallization Process Parameters	Flexural Strength (MPa)	Fracture Toughness, K_{Ic} (MPa$\sqrt{m}$)
As-fabricated.	770 ± 83	5.83 ± 0.15
1200°C/4 h without applied pressure.	681 ± 110	5.74 ± 0.11
1200°C/4 h with 24 MPa applied pressure.	677 ± 94	5.73 ± 0.25

Table 2. Characteristics of silicon-nitride powders used in fabrication of hot-pressed samples. Manufacturer's reported values.

Manu-facturer	Grade	Mean particle size (μm)	Surface area (m^2/g)	α-Phase content (%)	Oxygen content (wt %)	Total impurity content (ppm)
Ube	E-10	---	11.7	>95%	1.40	<300
Starck	LC-12SX	0.41	19.1	97.5	2.06	<200
Denka	9FW	0.80	10.9	92.1	0.98	<0.5[a]
Denka	P21C3	0.80	11	94.4	1.3	<300
Tosoh	TS-8	---	15	93	1.5	<0.11[a]
Tosoh	TS-10	---	14.6	97	1.3	<400
Tosoh	TS-10Y	---	9.6	99	0.8	<0.06[a]

[a]Values in wt %.

temperature (Table 3). Fracture surfaces are currently being examined to determine the types of flaws to explain the large variations in strength. Additional silicon-nitride powders are also being tested and will be reported in later progress reports.

Microstructure Development During Hot Pressing Of Refractory Grain-Boundary Phase Compositions - As reported previously, samples have been fabricated by hot pressing with 1 to 12% rare-earth oxide (Y_2O_3, La_2O_3, or Yb_2O_3) and 1 to 8% SiO_2 additives to take advantage of some of the good, high-temperature properties exhibited by these materials. The phase relationships for the samples fabricated to date are shown in Fig. 4. Testing of the mechanical properties revealed that the SiO_2 additions were not well dispersed and resulted in low strength as shown in Table 4. Microstructures of these materials have been reported previously.

Microstructure Development During Gas-Pressure Sintering - Gas-pressure sintering (GPS) is one technique used to grow elongated grain structures and obtain high-toughness silicon nitrides with refractory grain-boundary phases. Initial samples have been fabricated at ORNL and the results reported previously. The GPS furnace, which had not been operational since August 1991, was finally put back into service during the present reporting period. Several furnace runs were made, and the results are reported below.

Microstructure Development During Gas-Pressure Sintering Of Refractory Grain-Boundary Phase Compositions - As reported above, materials with rare-earth silicates as the grain-boundary phase can exhibit good, high-temperature properties. In addition to those fabricated by hot pressing, samples were formed by

Table 3. Summary of results on flexural strength testing of silicon-nitride materials fabricated with different starting powders. Samples contained 6% Y_2O_3-2% Al_2O_3 and were hot pressed at 1800°C for 90 min

	Flexural strength - four-point bend		
Powder source	Room temperature	1000°C	1200°C
Ube E-10	1142 ± 125	–	938 ± 28
Starck LC-12SX	1048 ± 137	–	337 ± 36
Denka 9FW	960 ± 50	–	310 ± 18
Denka P21C3	1014 ± 40	473 ± 42	442 ± 8
Tosoh TS-8	598 ± 27	517 ± 161	--
Tosoh TS-10	798 ± 26	701 ± 18	–
Tosoh TS-10Y	834 ± 54	472 ± 34	–

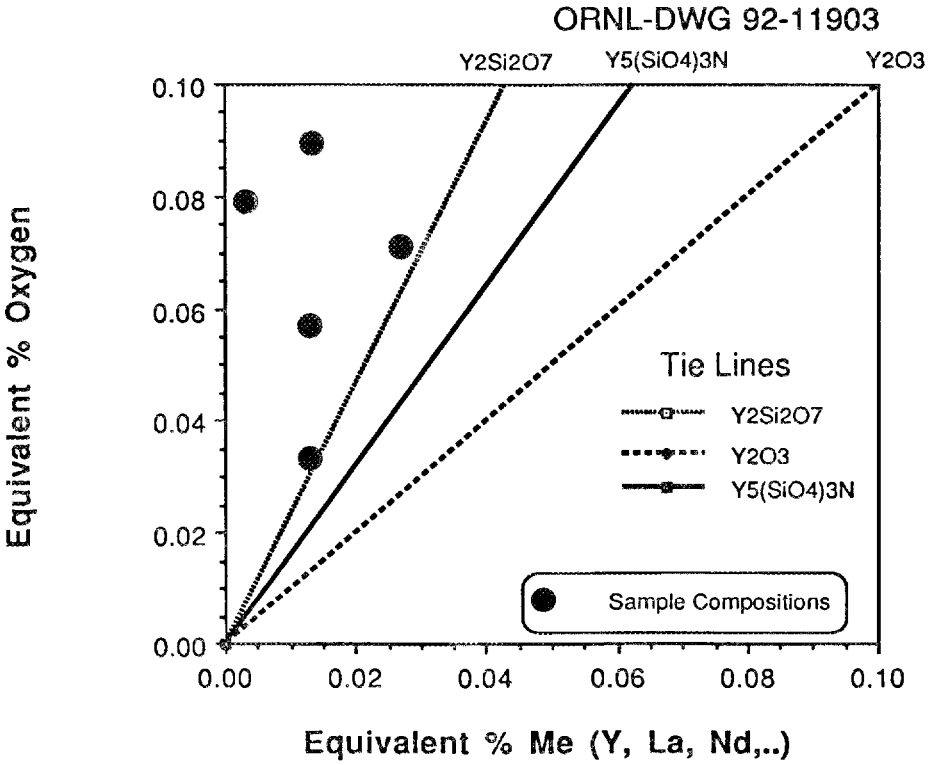

Fig. 4. Corner of Si_3N_4-SiO_2-YN-Y_2O_3 phase diagram showing relative composition of samples in current study. Silica associated with silicon nitride taken into account in calculating total equivalent oxygen.

Table 4. Flexural strength of silicon-nitride compositions with refractory grain-boundary phases. Poor dispersion of the SiO_2 addition resulted in the low strengths.

Additive Composition	25°C	1200°C	1400°C
	Flexural Strength (MPa)		
4% Y_2O_3-8% SiO_2	848 ± 80	627 ± 97	472 ± 70
8% Y_2O_3-4% SiO_2	635 ± 157	---	---
8% La_2O_3-7% Yb_2O_3-4% SiO_2	872 ± 22	749 ± 29	614 ± 71

either slip casting or cold isostatic pressing and fired in the gas-pressure-sintering furnace. The results on densification behavior are summarized in Table 5. All of the samples contained from 2.5 to 2.8 equivalent % rare-earth sintering aid, while the initial oxygen content varied between 4.3 to 7.7 equivalent %. The effect of the oxygen content on the densification behavior is shown in Fig. 5.

Because of the good densification exhibited by the materials with the high-oxygen contents, sintering was also examined at 1 atm nitrogen pressure at temperatures from 1750 to 1850°C. As shown in Table 6, high densities were achieved in all these samples.

The specimens that had densities > 95 % T.D. are currently being machined into, modulus of rupture (MOR) bars for mechanical property testing. Initial examination of fracture surfaces revealed significant grain growth in the gas-pressure-sintered materials.

Microstructure Development During Gas-Pressure Sintering Of Alternate Grain-Boundary Phase Compositions - A series of samples with alternate grain-boundary phases have been fabricated by turbomilling and slurry casting. The grain-boundary phases include the rare-earth oxide and nitride apatites. The grain-boundary phases anticipated in the current samples include a wide range of stable apatites of composition $Sr_2Y_8(SiO_4)_6O_2$, $Ba_2Y_8(SiO_4)_6O_2$, and $Sr_2La_8(SiO_4)_6O_2$. Sintering in the gas-pressure-sintering furnace was performed, and the results on densification are summarized in Table 7. The samples contained from 2.3 to 2.7 equivalent % metal-oxide sintering aid, while the initial oxygen content varied between 4.1 to 7.7 equivalent %. As with the samples with the grain-boundary phases based on rare-earth silicates, there is a correlation between the oxygen content and the densification behavior as shown in Fig. 6.

Because of the good densification exhibited by the materials with the high-oxygen contents, sintering was also examined at 1 atm nitrogen pressure at

Table 5. Summary of results on densification of gas-pressure-sintered silicon-nitride compositions with rare-earth silicates as the grain-boundary phases

Sample No.	Nominal additive composition	1850/1900[a] Bulk density (g/cc)	Density (% T. D.)	1850/1950[b] Bulk density (g/cc)	Density (% T.D.)
SC-205	8% Y_2O_3	2.37	71.8	2.28	69.2
SC-220	4% Y_2O_3-6% La_2O_3	2.43	73.7	---	---
SC-209	2%Y_2O_3-8% La2O3	2.86	87.8	3.00	92.0
SC-276	4% Y_2O_3-6% La_2O_3-2% SiO_2	3.13	93.9	3.22	96.6
SC-277	4% Y_2O_3-6% La_2O_3-2% SiO_2-0.2% SrO	3.28	98.5	3.22	96.7
SC281	8% Y_2O_3-4% SiO_2	3.24	99.7	3.27	100
SC-282	3% Y_2O_3-5% La_2O_3-4% SiO_2	3.27	99.1	3.28	99.5
SC-283	11% La_2O_3-4% SiO_2	3.32	99.5	3.33	99.8

[a]Sintered at 1850°C for 2 h under 50 psi nitrogen pressure and then 1900°C for 2 h under 300 psi nitrogen pressure.

[b]Sintered at 1850°C for 2 h under 50 psi nitrogen pressure and then 1950°C for 2 h under 300 psi nitrogen pressure.

temperatures from 1750 to 1850°C. As shown in Table 8, high densities were achieved in these samples with the exception of the BaO-containing materials.

These specimens are currently being machined into MOR bars for mechanical property testing. Initial examination of fracture surfaces revealed significant grain growth in the gas-pressure-sintered materials.

References

1. D. A. Bonnell, T. Y. Tien, and M. Ruhle, "Controlled Crystallization of the Amorphous Phase in Silicon Nitride Ceramics," *J. Am. Ceram. Soc.* **70**(7), 460-65 (1987).

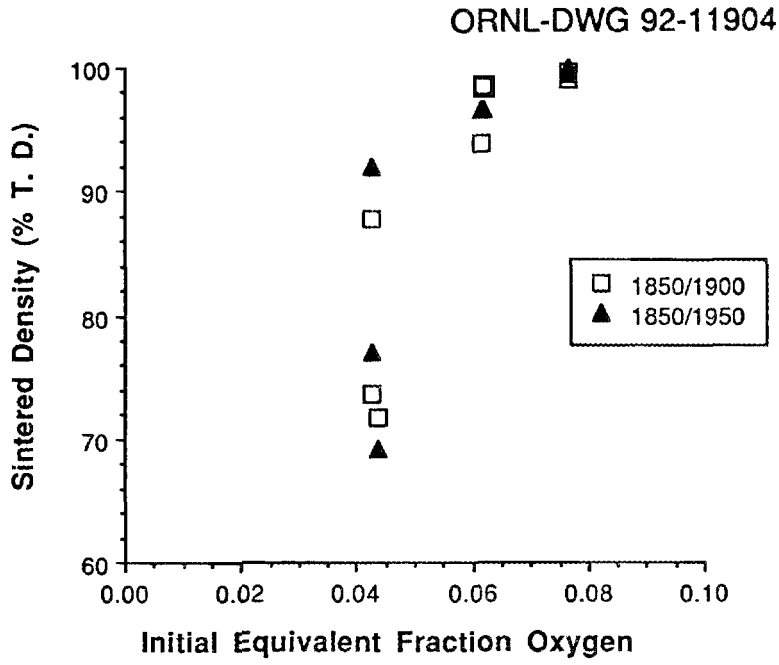

Fig. 5. Correlation between densification behavior of gas-pressure-sintered silicon-nitride compositions with rare-earth silicates as the grain-boundary phases and equivalent oxygen content.

Table 6. Summary of results on densification of silicon-nitride compositions with rare-earth silicates as the grain-boundary phases sintered at 1 atm nitrogen

Sample No.	Nominal additive composition	1750[a] Bulk density (g/cc)	Density (% T.D.)	1800[b] Bulk density (g/cc)	Density (% T.D.)	1850[c] Bulk density (g/cc)	Density (% T.D.)
SC-281	8% Y_2O_3-4% SiO_2	3.10	95.4	3.19	98.1	3.21	98.9
SC-282	3% Y_2O_3-5% La_2O_3-4% SiO_2	3.21	97.2	3.22	97.7	3.28	99.4
SC-283	11% La_2O_3-4% SiO_2	3.30	98.8	3.31	99.0	3.32	99.5

[a]Sintered at 1750°C for 4 h under 15 psi nitrogen pressure.
[b]Sintered at 1800°C for 4 h under 15 psi nitrogen pressure.
[c]Sintered at 1850°C for 4 h under 15 psi nitrogen pressure.

Table 7. Summary of results on densification of gas-pressure-sintered silicon-nitride compositions with rare-earth apatites as the grain-boundary phases

Sample No.	Nominal additive composition	1850/1900[a] Bulk density (g/cc)	Density (% T. D.)	1850/1950[b] Bulk density (g/cc)	Density (% T. D.)
SC-253	8% Y_2O_3 2% SrO	2.38	72.6	--	--
SC-261	4% Y_2O_3-2% SrO-4% SiO_2	3.06	91.3	3.00	89.6
SC-262	6%Y_2O_3-1% SrO-4% SiO_2	3.20	95.5	3.12	93.2
SC-263	8% La_2O_3-2% SrO	2.32	69.3	2.41	72.0
SC-264	8% La_2O_3-2% SrO 4% SiO_2	2.76	82.3	--	--
SC-290	11% La_2O_3 2% SrO 3% SiO_2	3.34	99.1	3.34	99.1
SC-291	8% Y_2O_3-3% BaO-3% SiO_2	3.02	91.9	3.06	93.1
SC-293	8% Y_2O_3-2% SrO-3% SiO_2	3.26	99.6	3.29	100

[a]Sintered at 1850°C for 2 h under 50 psi nitrogen pressure and then 1900°C for 2 h under 300 psi nitrogen pressure.

[b]Sintered at 1850°C for 2 h under 50 psi nitrogen pressure and then 1950°C for 2 h under 300 psi nitrogen pressure.

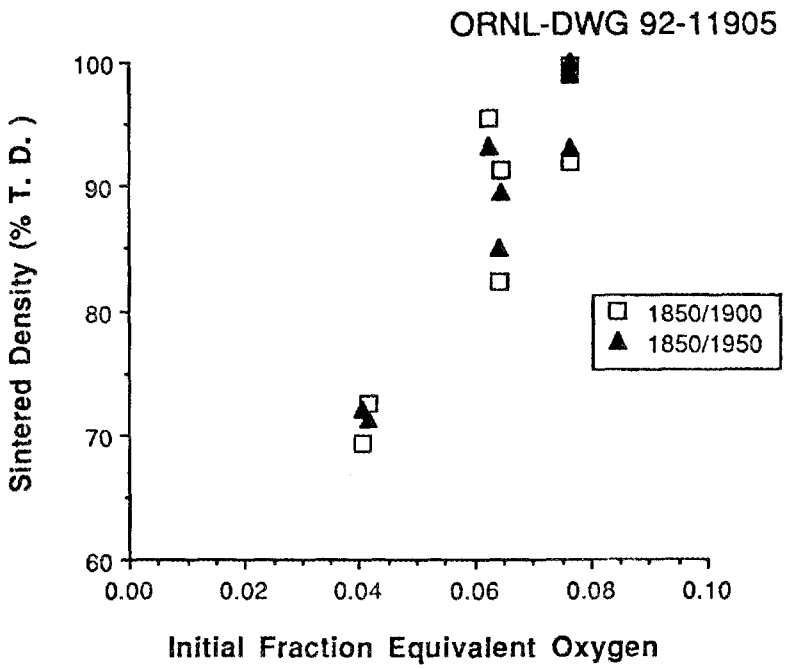

Fig. 6. Correlation between densification behavior of gas-pressure-sintered silicon-nitride compositions with rare-earth apatites as the grain-boundary phases and equivalent oxygen content.

Table 8. Summary of results on densification of silicon-nitride compositions with rare-earth apatites as the grain-boundary phases sintered at 1 atm nitrogen

Sample No.	Nominal additive composition	1750[a] Bulk density (g/cc)	Density (% T.D.)	1800[b] Bulk density (g/cc)	Density (% T.D.)	1850[c] Bulk density (g/cc)	Density (% T.D.)
SC-290	11% La_2O_3 2% SrO 3% SiO_2	3.31	98.2	3.34	99.2	3.35	99.4
SC-291	8% Y_2O_3- 3% BaO- 3% SiO_2	2.55	77.6	2.81	85.4	2.67	81.3
SC-293	8% Y_2O_3- 2% SrO- 3% SiO_2	3.20	97.9	3.23	98.9	3.21	98.2

[a]Sintered at 1750°C for 4 h under 15 psi nitrogen pressure.
[b]Sintered at 1800°C for 4 h under 15 psi nitrogen pressure.
[c]Sintered at 1850°C for 4 h under 15 psi nitrogen pressure.

2. Buljan et al., "Ceramic Matrix Composites," pp. 55-67 in *Ceramic Technology for Advanced Heat Engines Project Semiannual Progress Report for October 1988 Through March 1989*, ORNL/TM-11239, Martin Marietta Energy Systems, Inc., Oak Ridge Natl. Lab., 1989.

3. Buljan et al., "Ceramic Matrix Composites," pp. 93-108 in Ceramic Technology for Advanced Heat Engines Project Semiannual Progress Report for April 1989 Through September 1989, ORNL/TM-11489, Martin Marietta Energy Systems, Inc., Oak Ridge Natl. Lab., 1990.

4. F. F. Lange, "Fracture Toughness of Si_3N_4 as a Function of the Initial a-Phase Content,"*J. Am. Ceram. Soc.*, **62**(7-8), 428-30 (1979).

5. G. Wötting and G. Ziegler, "Powder Characteristics and Sintering Behavior of Si_3N_4-Powders," *Powder Met. Internat.* **18**(1), 25-32 (1986).

6. T. Ekstrom, N. Ingelstrom, R. Brage, M. Hatcher, and T. Johansson, "a-ß Sialon Ceramics Made from Different Silicon Nitride Powders," *J. Am. Ceram. Soc.* **71**(12), 1164-1170 (1988).

7. T. Shimamori, H. Matsuzaki, T. Kato, Y. Tajima, and Y. Matsuo, "High Temperature Properties of Post Sintered Silicon Nitride," pp. 737-44 in *Proceedings of the 2nd International Symposium on Ceramic Materials and Components for Engines*, ed. W. Bunk and H. Hausner, Verlag Deutsche Keramische Gesellschaft, Bad Honnef, Germany, 1986.

8. D. D. Lee, S. L. Kang, G. Petzow, and D. N. Yoon, "Effect of a to ß(ß') Phase Transition on the Sintering of Silicon Nitride Ceramics," *J. Am. Ceram. Soc.* **73**(3),767-769 (1990).

9. W. Braue, G. Wötting, and G. Ziegler, "Influence of Impurities in Different Si_3N_4-Powders on High-Temperature Properties of Sintered Materials," pp. 71-80 in *British Ceramics Proceedings, Special Ceramics 8*, Institute of Ceramics, Shelton, U. K., 1986.

10. G Wötting, E. Gugel, G. Schwier, and H. Lange, "Processing for Improved Fracture Toughness of Dense Silicon Nitride," pp. 647-61 in *Ceramic Transactions, Ceramic Powder Science. IV*, Vol. 22, Am. Ceram. Soc., Westerville, Ohio, 1990.

11. K. Ichikawa, "The Influence of Si_3N_4 Powder Characteristics on Sintering Behavior," pp. 107-116 in *Silicon Nitride-1*, Elsevier Applied Science, New York, 1989.

12. G. Franz, B. Laubach, U. Wickel, G. Wötting, and E. Gugel, "Optimization of a High Purity Silicon Nitride Powder Concerning Sintering and Mechanical Properties," pp. 1-12 in *Proceedings of the 3rd International Symposium on Ceramic Materials and Components for Engines*, ed. V. J. Tennery, Amer. Ceram. Soc., Westerville, Ohio, 1989.

13. V. Vandeneede, A. Leriche, F. Cambier, H. Pickup, and R. J. Brook, "Sinterability of Silicon Nitride Powders and Characterization of Sintered Materials," pp. 53-68 in *Non-Oxide Technical and Engineering Ceramics*, ed. S. Hampshire, Elsevier Applied Science, New York, 1986.

14. N. Itoh, T. Sasamoto, T. Sata, K. Komeya, and A. Tsuge, "Impurities in Silicon Nitride Raw Materials and Correlation with Mechanical Strength of the Hot-Pressed Body," *Yogyo-Kyokai-Shi*, **90**, 209-13 (1979).

15. W. Braue, G. Wötting ,and G. Ziegler, "Impact of Compositional Variations and Processing Conditions on Secondary Phase Characteristics in Sintered Silicon Nitride Materials," pp. 883-96 in *Ceramic Microstructures '86: Role of Interfaces*, ed. J. A. Pask and A. G. Evans , Materials Science Research, Vol. 21, Plenum Press, New York, 1987.

16. G. Wötting and G. Ziegler, "Influence of Powder Properties and Processing Conditions on Microstructure of Sintered Si_3N_4," pp. 951-62 in *Ceramic Powders*, ed. P. Vincenzini, Elsevier, Amsterdam, 1983.

Status of milestones

Milestone 123111, "Fabricate high-toughness silicon nitride materials with elongated grain microstructures," was not completed due to delays in operation of gas-pressure-sintering furnace.

Publications

None.

1.3 THERMAL AND WEAR COATINGS

Fabrication and Testing of Corrosion-Resistant Coatings

D. P. Stinton, J. C. McLaughlin, and D. W. Graham (Oak Ridge National Laboratory)

Objective/scope

Sodium corrosion of SiC and Si_3N_4 components in gas turbine engines is a potentially serious problem. The outer surfaces of SiC and Si_3N_4 parts oxidize at high temperatures to form an SiO_2 layer that inhibits further oxidation. However, sodium that is present in high-temperature combustion atmospheres reacts with the SiO_2 layer, such that it is no longer protective. The objective of this program is to develop a coating that will protect the underlying SiC or Si_3N_4 from sodium corrosion and provide simultaneous oxidation protection. To evaluate the behavior of potential materials such as stabilized ZrO_2 or HfO_2, TiO_2, $Al_2O_3 \cdot TiO_2$, and Ta_2O_5 in sodium-containing atmospheres, the corrosion resistance of hot-pressed samples of these materials will first be evaluated. A chemical vapor deposition (CVD) process will be developed for the application of the most promising coatings. The effect of the combustion environment upon coating characteristics, such as microstructure, strength, adherence, and other properties, will then be evaluated.

Technical progress

The development of oxide coatings to protect SiC or Si_3N_4 heat engine components from sodium corrosion continued this period. Protective coatings being investigated in this evaluation include Ta_2O_5 and $ZrTiO_4$ because their low coefficients of thermal expansion match that of SiC or Si_3N_4 and because of their likely good corrosion resistance. Coatings of Ta_2O_5 with varying morphologies have been produced by CVD onto Si_3N_4 GN-10 substrates obtained from Garrett. To investigate the effects of process parameters on coating morphology, an initial set of experiments was statistically designed to study deposition temperature, deposition pressure, and reactant flow rates. After completion of the set of 16 experimental runs, the coatings were evaluated for weight gain, coating thickness, grain size, morphology, and microstructure. Many of the deposits were of very low density and consisted of powder deposited on the substrate surface. A statistical evaluation revealed that the densest coatings were deposited at low pressures (2 kPa), high temperatures (1250°C), and low concentrations of $TaCl_5$ ($\approx$ 2%).

A second, statistically designed experiment was planned to better investigate low pressure (2 kPa) deposition at high temperatures (1200 to 1300°C), low $TaCl_5$ concentrations (1 to 3%) and high oxygen concentrations (16 to 20%). The design calls for eight runs plus a centerpoint that is duplicated for a total of 10 runs. The eight points form a 2^3 factorial design. All coatings from the statistically designed experiment were characterized using optical microscopy and scanning electron microscopy. Coatings deposited at 1300°C contained large, columnar grains.

Unfortunately, the large columns did not grow together and left large voids present (Figs. 1 and 2). Coatings deposited at 1200°C also contained

9201641

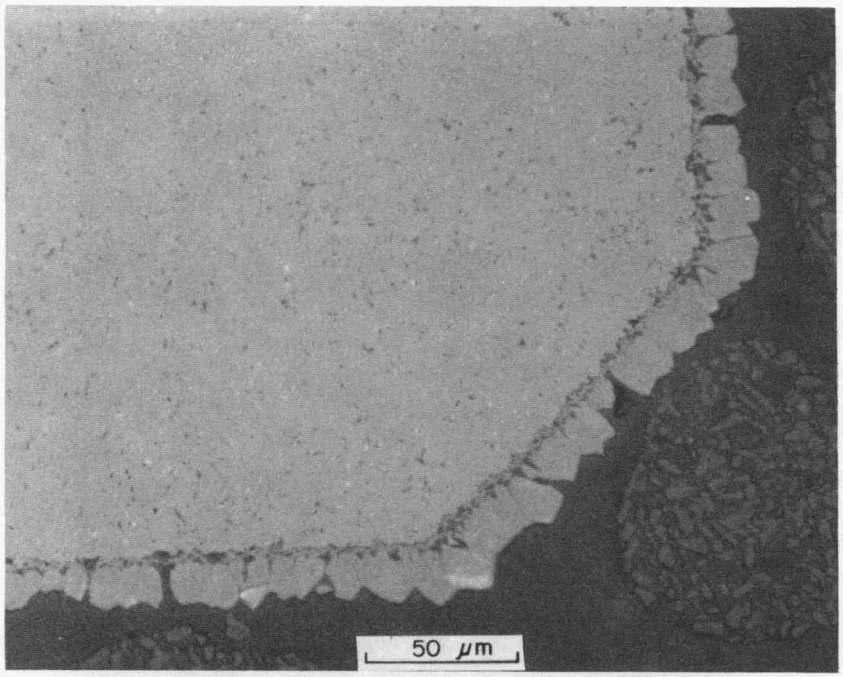

Fig. 1. Optical micrograph illustrating the dense, adherent coatings deposited at 1300°C.

columnar grains; however, the columns were smaller with much smaller voids between columns (Figs. 3 and 4). The effect of reactant ($TaCl_5$) concentration was less evident, however, and higher concentrations (~ 5%) appeared to produce less dense, powdery deposits. Further optimization of the coating morphology will be required to produce continuous coatings that are impermeable to sodium-containing gases.

27032

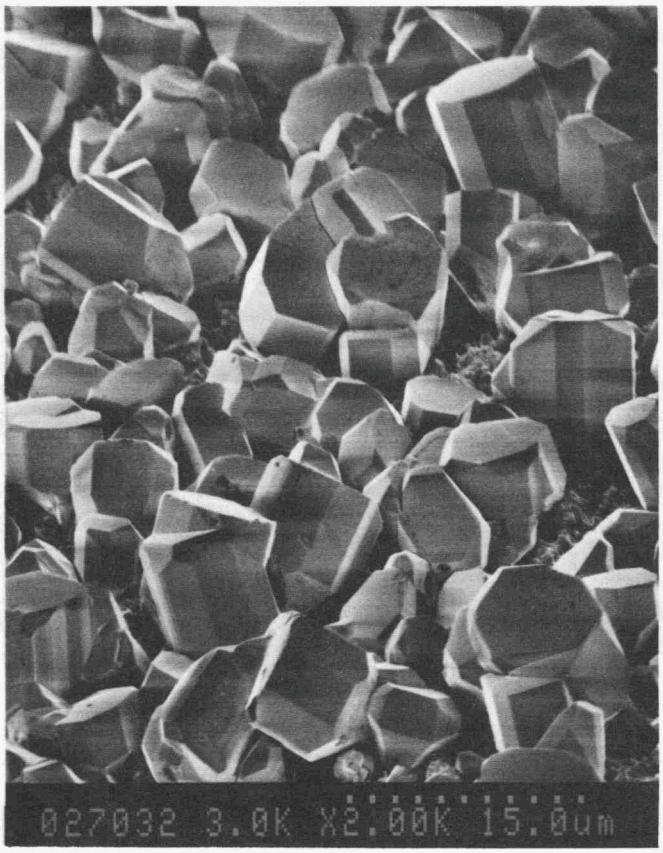

Fig. 2. Scanning electron micrograph illustrating the large, columnar grains produced by the 1300°C deposition temperature.

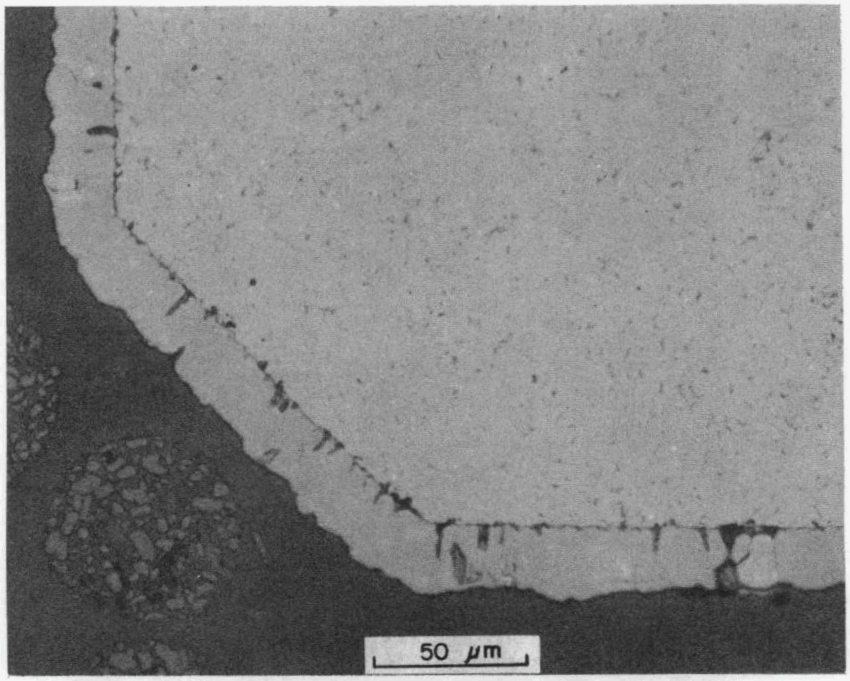

Fig. 3. Optical micrograph illustrating the reduced grain size of deposits produced at lower temperatures.

26845

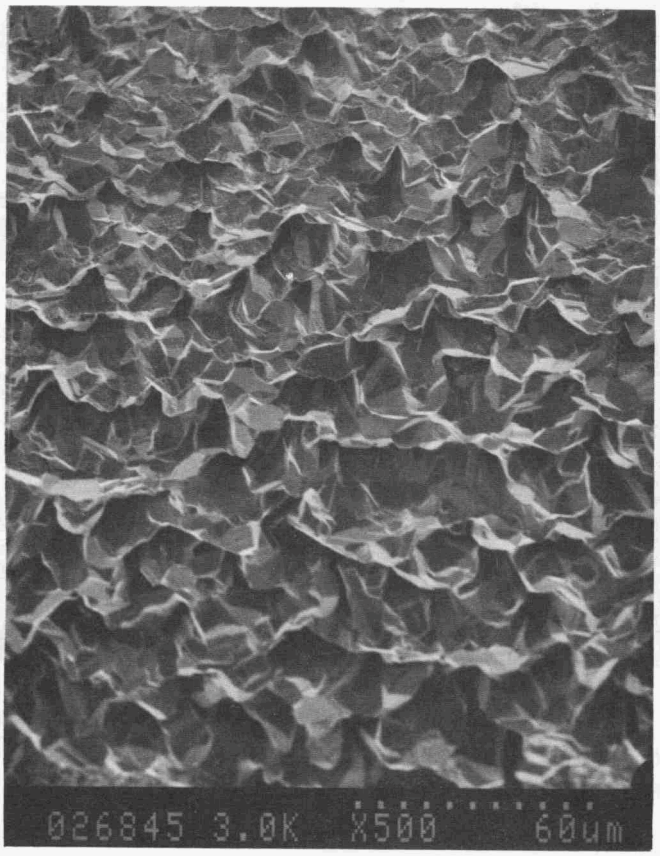

Fig. 4. Scanning electron micrograph illustrating the reduced amount of porosity present in coatings deposited at 1200°C.

Development of Adherent Ceramic Coatings to Reduce Contact Stress Damage of Ceramics
- S. Wayne, D. O'Neil, and J.H. Selverian (GTE Laboratories Incorporated)

Objective/Scope

The objective of this program is to develop oxidation-resistant, high toughness, adherent coatings for silicon-based ceramics for use in an advanced gas turbine engine. These coatings will be deposited by chemical vapor deposition (CVD) onto reaction bonded Si_3N_4 (RBSN), sintered SiC (SSC), and hot pressed Si_3N_4 (HSN). The coating will be designed to provide the best mix of mechanical, thermal and chemical properties for the application.

Technical Highlights

The propagation of a crack through the Al_2O_3+ZrO_2 composite coating on a silicon nitride substrate was modelled. Results suggest that as a vertical crack propagates through the coating it is only partially deflected by the interface. Therefore, improvements in the toughness of the interface are expected to have a small influence on these types of cracks.

Computer Simulation of Crack Propagation

This semiannual describes modeling work performed on sections (ii) and (iii) of the new milestone added to this contract in June,1991. Section (i) of this new milestone has been completed, and was described in the August, 1991 bimonthly for the contract. We describe here the model and results for numerical simulation of a single-pass scratch test, and crack propagation due an initial flaw.

Single Layer with Interface - *Initial Vertical Flaw*

Studies were performed on a single-layer coating of Al_2O_3+ZrO_2 on a substrate of silicon nitride. Subsequent sections will describe results for a multi-layer coated substrate. Loads were imposed on the body in the form of residual thermal stress, and mechanical loads resulting from solid body contact with friction. The finite element model allows automatic changes in mesh topology due to crack growth, and a bimaterial fracture model which takes into account the different fracture toughnesses of the coating, interface, and substrate when the cracks are at or near the interface. Results indicate that, subject to these loads, a vertical flaw in the coating propagates approximately downward until the coating-substrate interface region. Once the crack has entered the interface, it moves away from the contact loads along the interface a distance of approximately half the coating thickness, after which it continues in a direction nearly normal to the net direction of the applied load. Since the crack did not continue along the interface, improvements in the interface bond strength would not have significantly influenced the crack growth direction.

Geometry

A finite element mesh was created to simulate the cross-section of a wide sample (plane-strain) of a single layer coated substrate. Coating thickness was 2 microns, substrate thickness was arbitrary, and assigned a value of 58 microns.

The plane of the mesh is shown in Figure 1. For the single layer analysis the AlN interlayer was not used. The model was simply Al_2O_3+ZrO_2 on a Si_3N_4 substrate. The width of the model was 60 microns. A set of boundary markers exists between the elements which describe the coating and those that define the substrate. These boundary markers locate the bimaterial fracture boundary. During remeshing, this boundary must lie on element boundaries to keep the interface coherent. The model initially was crack-free. A vertical flaw 0.5 microns long was positioned 1 micron from the mechanical load. As the crack propagated, the model was automatically remeshed to take into account the change in surface, the bimaterial interface, and the stress concentration at the crack tip. Eight noded quadratic elements were used for the original mesh. Mesh changes were mapped with 6 noded triangular elements, and the crack tip

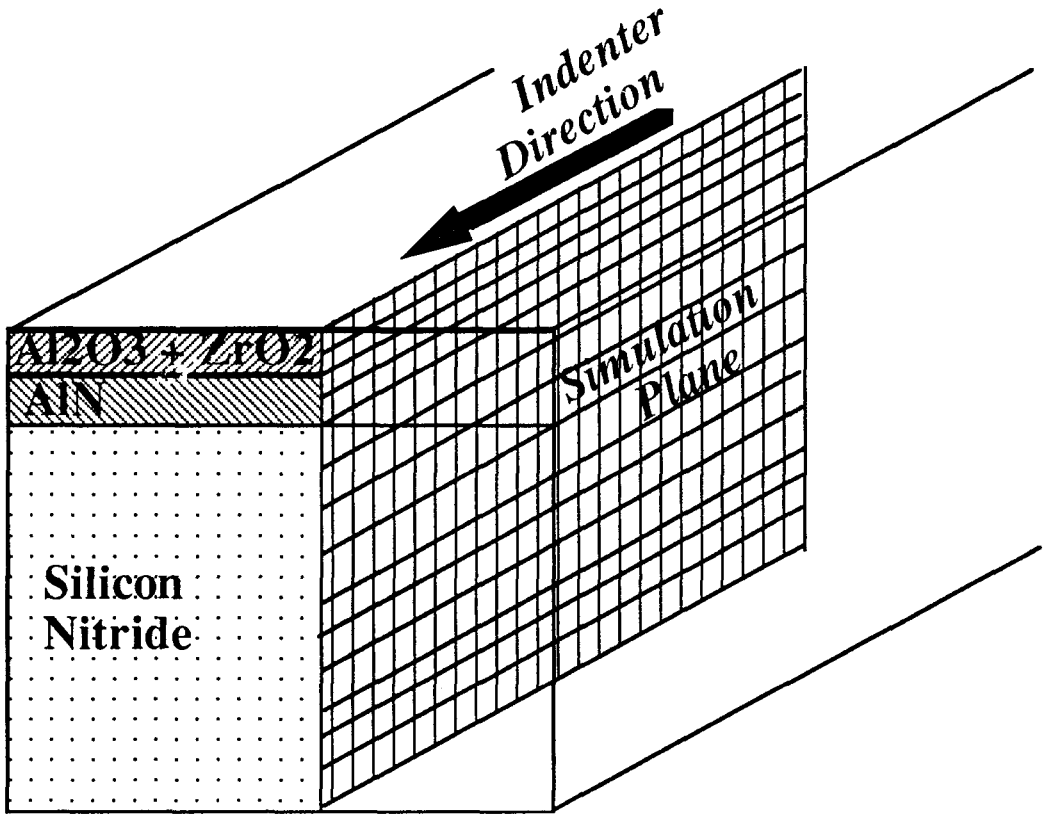

Figure 1. Schematic of the finite element mesh relative to microstructural cross section. Direction and positioning of scratch test indenter is shown.

was modeled with 6 noded singularity elements. When the crack tip was at or near the bimaterial interface, singularity elements were not used. For each crack increment, the next propagation direction was predicted by using a maximum energy release rate criterion, which is also applicable in the region of the interface. The energy release rate was calculated by comparing the energy released by the system for candidate directions in each of the materials in the vicinity of the crack tip. Once a direction was found, the crack length was increased a small amount and the calculation repeated. This procedure was continued until no significant change in the direction of crack propagation was seen.

Boundary Conditions

Thermal loads were applied to the entire body by including a temperature change of -1000°C into the analysis. This temperature is typical of temperatures used in the CVD process for this material system. It was assumed that the coating was applied to the substrate in the CVD chamber in a stress-free state and that stresses were generated upon cooling by thermal expansion mismatch between the coating and the substrate. A mechanical load was also applied to the coating. The mechanical loads represents the load applied by solid body contact. The load was distributed over a 1 micron region; the shape of the distribution was parabolic. The magnitude of the maximum value of the distribution was scaled such that the stress results were normalized from zero to one. The coefficient of friction used was 0.5, resulting in the same form of the distribution of shear stress on the surface of the coating. Figure 2 is a schematic of the boundary conditions. As previously mentioned, the AlN interlayer, while shown in Figure 1, was not used in the single layer analysis. On the lower edge of the model, the central node of the edge was pinned, and all other nodes on the edge were constrained in the vertical direction.

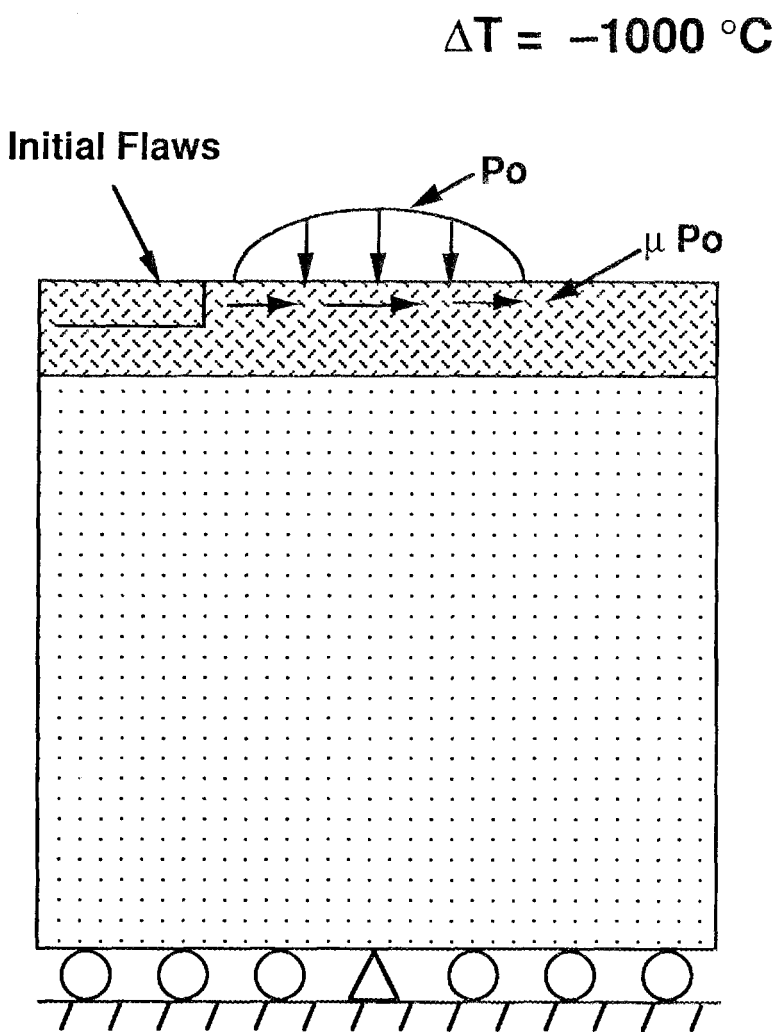

Figure 2. Schematic of the boundary conditions used in the fracture simulation. Coefficient of friction was 0.5. The value of 'p' (the maximum magnitude of the load distribution) was assigned a value such that the stress results are normalized.

Material Properties

The coating material was Al_2O_3+ZrO_2 and the substrate was silicon nitride. Both materials were modeled as elastic in both thermal and mechanical properties. Material properties were assigned to the coating, substrate and interface. Elastic and thermal properties for the coating and substrate are shown in Table 1. The interface energy release rate as a function of mode-mixity is shown in Figure 3.

Crack Propagation Studies

The crack propagation occurred over 14 crack increments, after which the direction of crack growth remained constant. Since the crack crossed the bimaterial interface, the bimaterial interface fracture model was used for several crack growth steps. Other crack growth steps used linear elastic fracture mechanics theory solved using finite element methods. This bimaterial fracture model has been implemented into a finite element framework, and the key concept in the numerical scheme is that the crack is predicted to propagate in the direction of maximum energy release rate. This energy release rate is analogous to that described for homogeneous fracture theory. The difference is that there may be several candidate directions where the energy release

Table 1. Material properties used for substrates and coating layers.

Material	Young's Modulus (GPa)	Poisson's Ratio	Fracture Toughness (MPa$\sqrt{m}$)	Thermal Expansion Coeff. (/°C) x 10^{-6}
Al_2O_3	390	0.22	-	7.8
AlN	340	0.24	1.0	4.9
Interface	320	0.255	-	3.8
SiC	207	0.22	-	4.3
Al_2O_3+ZrO_2	380	0.22	5.0	9.4
Si_3N_4	296	0.27	3.5	2.7

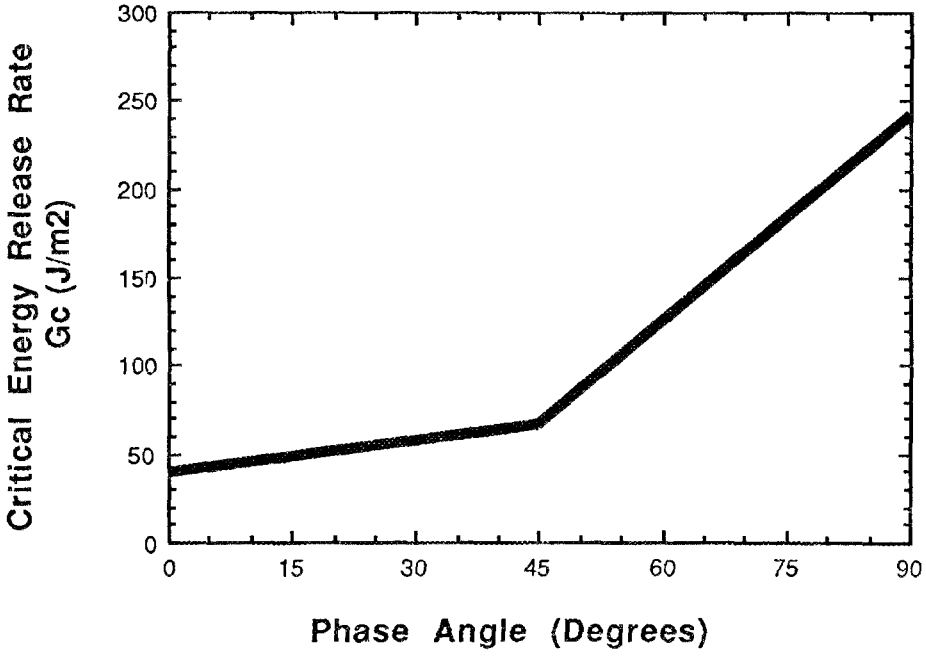

Figure 3. Energy release rate for the interface as a function of mode mixity. A mode-mixity of 0.0 describes pure mode I loading at the crack tip, and a mode-mixity of 90 (degrees) describes pure mode II loading at the crack tip.

rate is a maximum. All candidate directions for all materials must be considered and compared. The method was developed to apply in cases where the crack tip is in or near a bimaterial interface. Figure 4 shows the finite element mesh prior to crack growth. The upper four elements comprise the coating region. Elements below the upper four comprise the substrate. An enlargement of the initial vertical flaw, showing the original and deformed shape of the coated system is shown in Figure 5. Note that the deformed shape was a result of the thermal, normal and shear loads on the structure. Figure 6 illustrates the direction of crack growth prior to crossing the bimaterial

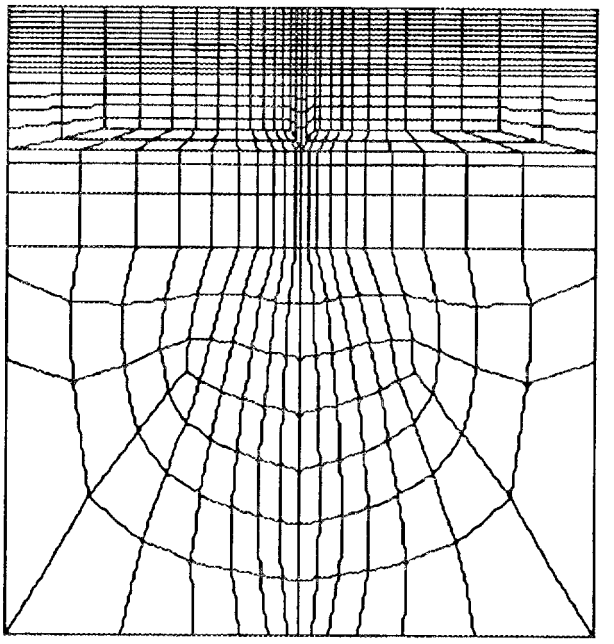

Figure 4. Initial (uncracked) mesh used in the fracture simulation study. The top four elements are the Al_2O_3+ZrO_2 coating material.

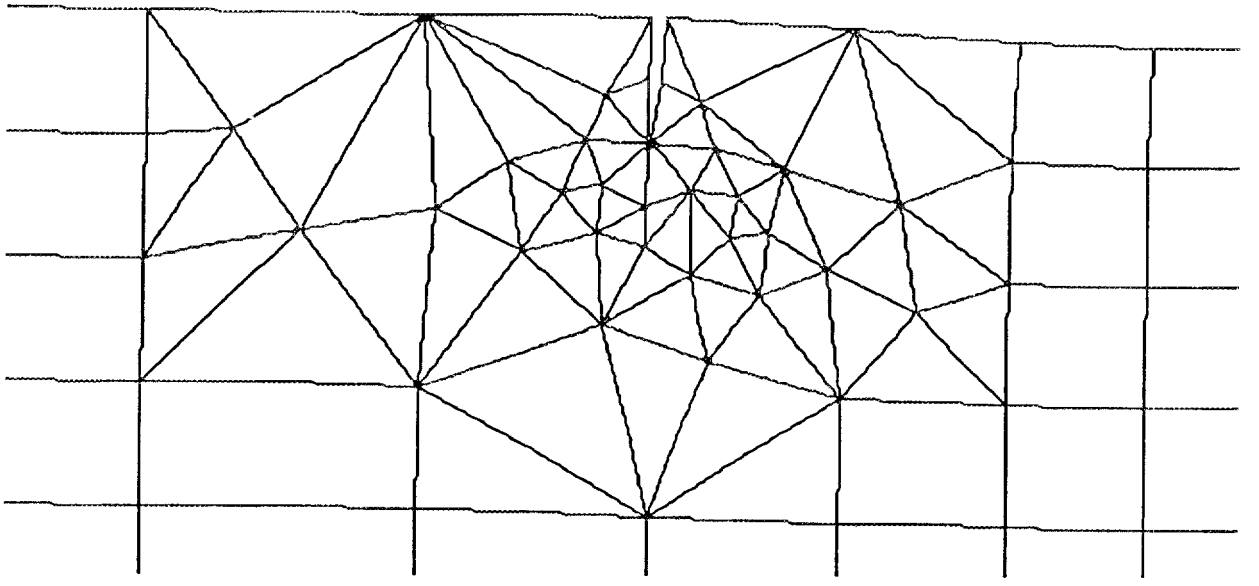

Figure 5. Initial vertical flaw, 0.5 microns long (1/4 coating thickness).

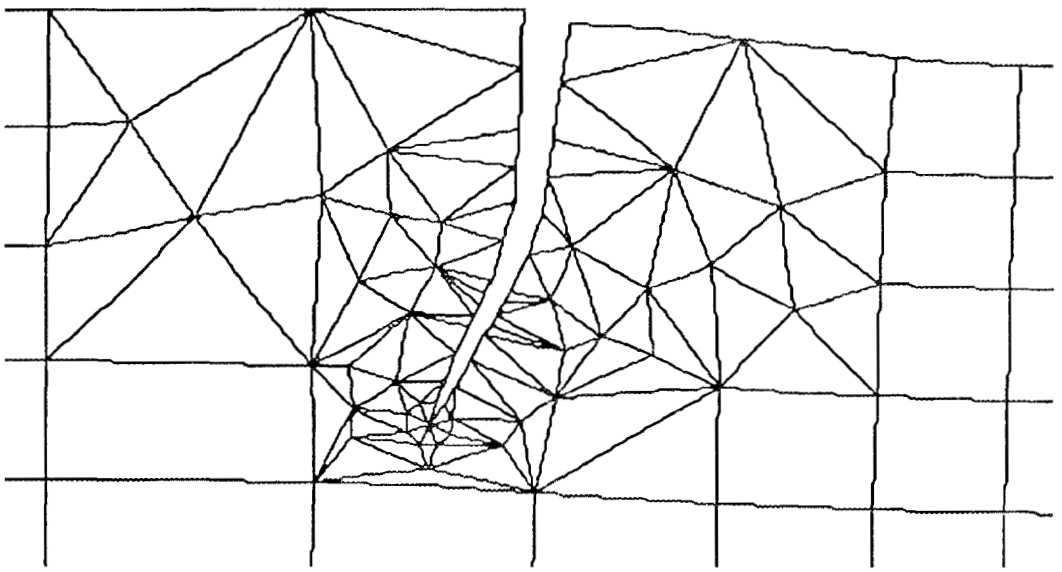

Figure 6. Deformed shape and crack growth direction prior to crossing the bimaterial interface.

interface. The crack has begun a slight turn away from the applied mechanical loading. Figure 7 shows the deformed shape for the final crack increment. Note that the crack did not remain in the interface, as it would for a material with a lower range of interface fracture toughnesses (lower G_{Ic} curve), and also that the final crack direction is approximately normal to the applied mechanical loading direction. The fracture modeling of coated systems continues in the next section with a two-layered coated substrate; under the same thermal and mechanical loads.

Multilayer Analysis - *Initial Vertical Flaw*

Simulations of a single-layer fracture were reported in the previous section. Here we describe the model and results for numerical simulation of a single-pass scratch test of a substrate with two coating layers, and crack propagation due to an initial vertical flaw.

Geometry

The finite element mesh was created to simulate the cross-section of a wide sample (plane-strain) of a double-layer coated substrate. Coating thicknesses were 2 microns, substrate thickness was arbitrary, and assigned a value of 58 microns. The plane of the mesh is shown in Figure 1. The boundary conditions are those shown in Figure 2.

Material Properties

The top-layer coating material was Al_2O_3+ZrO_2, the second (middle) coating layer as AlN, and the substrate was silicon nitride. All materials were modeled as elastic in both thermal and mechanical properties. Material properties were assigned to the coatings, substrate and interface. The interface energy release rate as a function of mode-mixity for both material interfaces is shown in Figure 8.

Crack Propagation Studies

The crack propagation occurred over 27 crack increments, after which the direction of crack growth remained constant; along the AlN-substrate interface. Since the crack crossed both bimaterial interfaces, the bimaterial interface fracture model was used for several crack growth steps. Other crack growth steps used linear elastic fracture mechanics theory which was solved using finite element methods.

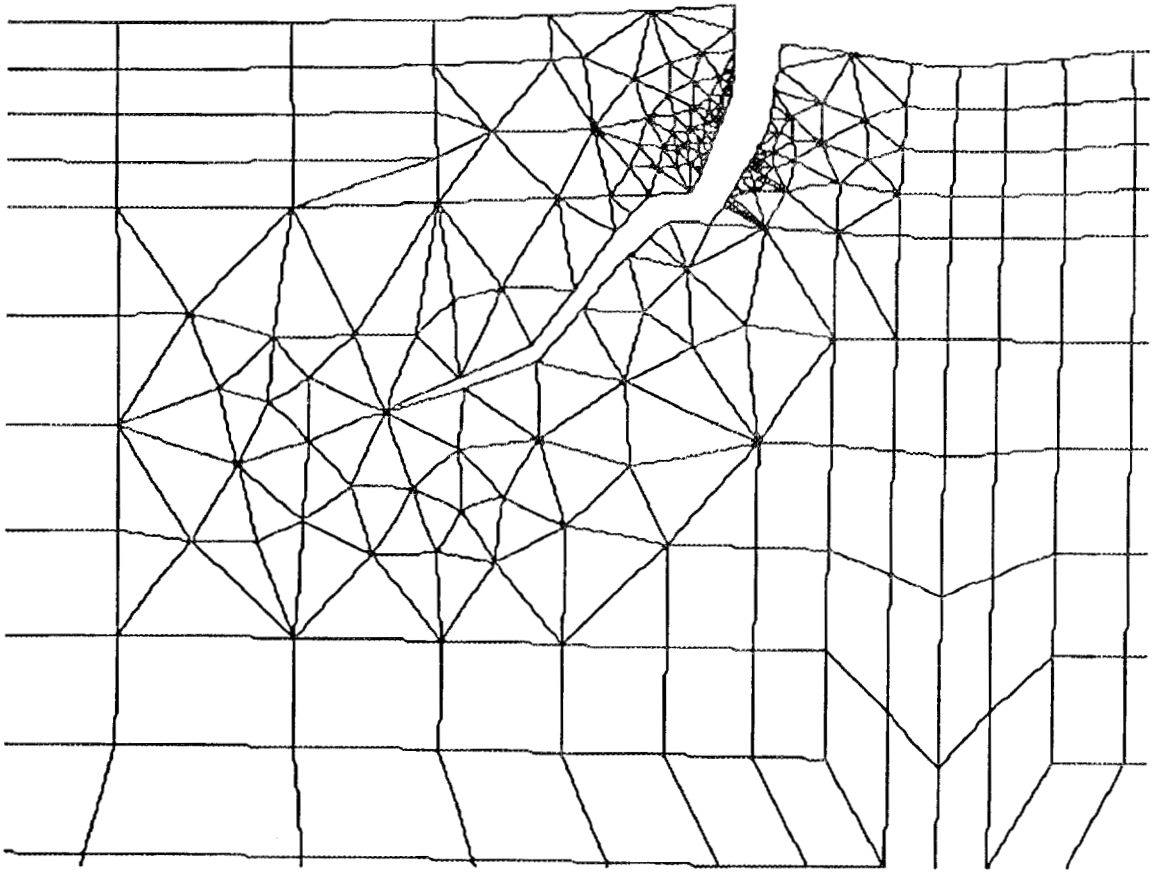

Figure 7. Deformed shape and crack path in final increment.

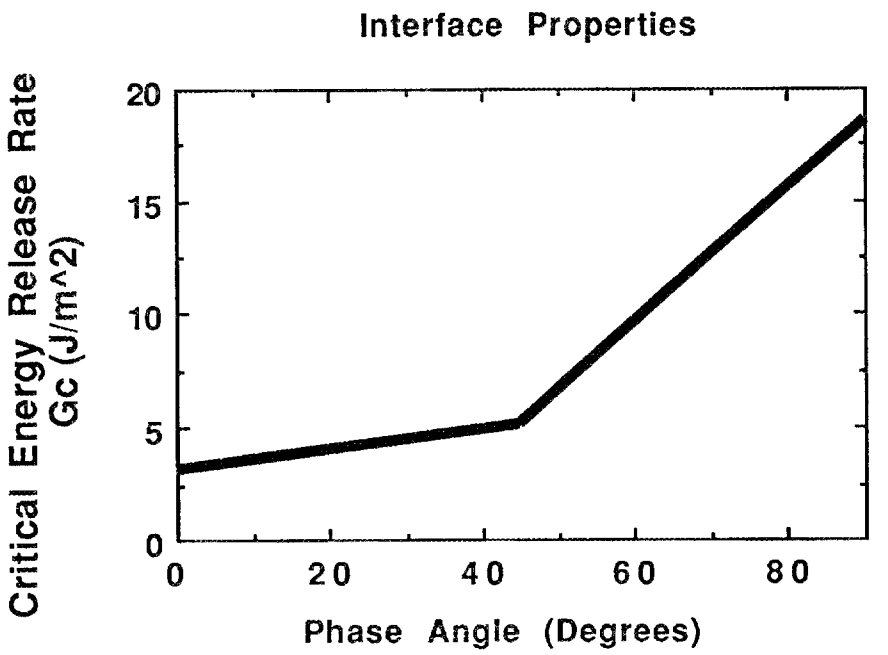

Figure 8. Energy release rate for both interfaces as a function of mode mixity. A mode-mixity of 0.0 describes pure mode I loading at the crack tip, and a mode-mixity of 90 (degrees) describes pure mode II loading at the crack tip.

Figure 9 shows the finite element prior to crack growth. The upper four elements (in the vertical direction) comprised the top-layer (Al_2O_3+ZrO_2). The next four elements in the vertical direction comprised the second layer (AlN). Elements below the upper eight modeled the substrate. A zoom of the initial vertical flaw, showing the original and deformed shape of the coated system is shown in Figure 10. Note that the deformed shape was a result of the thermal, normal and shear loads on the structure.

Figure 11 illustrates the direction of crack growth as the crack entered the first material interface. The Al_2O_3+ZrO_2 layer would no longer provide oxidation resistance. The crack has begun a slight turn away from the applied mechanical loading at this stage in the crack history.

Figure 12 shows the deformed shape for the final crack increment. Note that the crack did not remain in the top interface, but continued through the middle AlN layer to the silicon nitride substrate. These results indicate that both coating layers have been completely fractured. A solution to this type of failure could be to design the first material interface (increased toughness) such that the crack would not penetrate into the second coating layer.

Results indicated that, subject to these loads, a vertical flaw in the coating propagated approximately downward until the first coating-substrate interface region. Once the crack entered this first interface, it traveled for a distance of about 20% of the coating thickness, then changed direction and advanced into the second coating material. While traversing both coating layers, the crack traveled in a direction nearly normal to the net direction of the applied load. Since the crack continued to the substrate surface, it was anticipated that the surface would be exposed to outer gaseous conditions.

The fracture modeling of coated systems continues with a two-layered coated substrate with initial horizontal flaws; under the same thermal and mechanical loads.

Multilayer Analysis - *Initial Horizontal Flaw*

Two analyses have been performed. The first had the initial horizontal flaw positioned at the middle of the second coating layer. In this case, the crack did not cross any of the material interfaces during crack growth. Figures 1 and 2 show the model and boundary conditions prior to crack growth. With regard to the mesh the upper four elements (in the vertical direction) comprised the Al_2O_3+ZrO_2 layer coating. The next four element in the vertical direction comprised the second layer (AlN) coating region. Elements below the upper eight modeled the

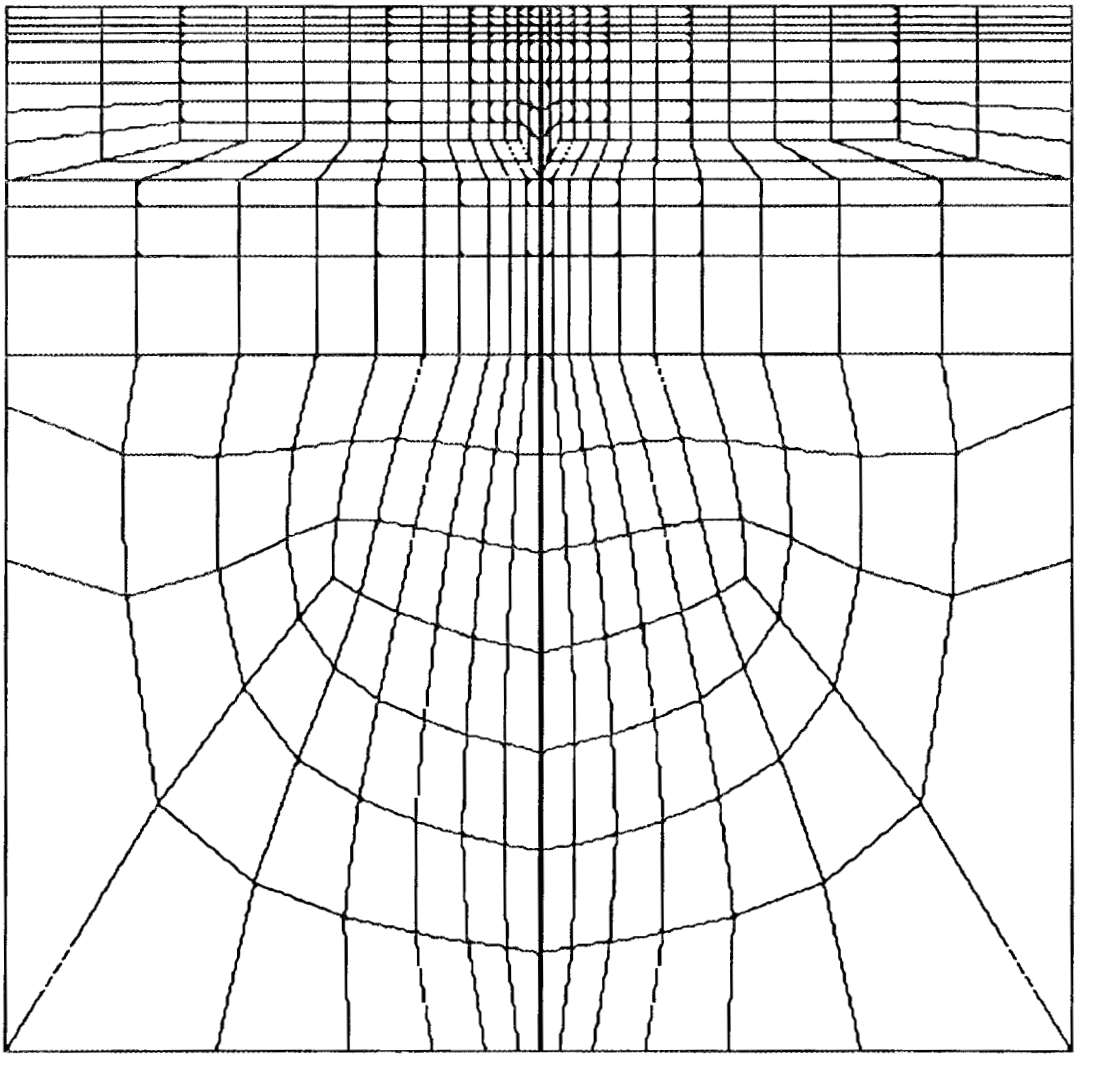

Figure 9. Initial (uncracked) mesh used in the fracture simulation study. The top four elements are the Al_2O_3+ZrO_2 coating material. The next four were the AlN coating material.

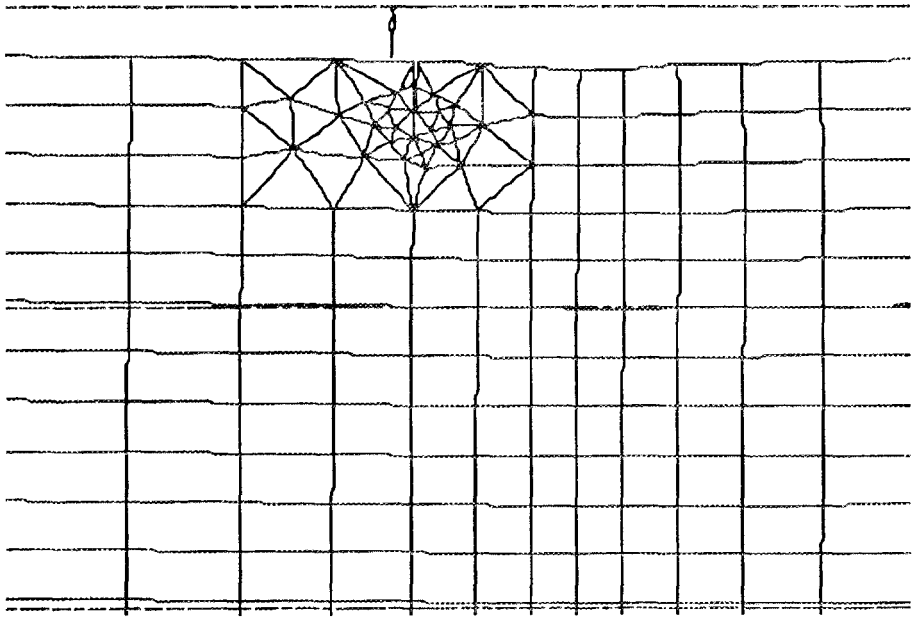

Figure 10. Initial vertical flaw, 0.5 microns long (1/4 coating thickness). Solid lines are deformed geometry (thermal and mechanical loads). Dashed lines are undeformed geometry.

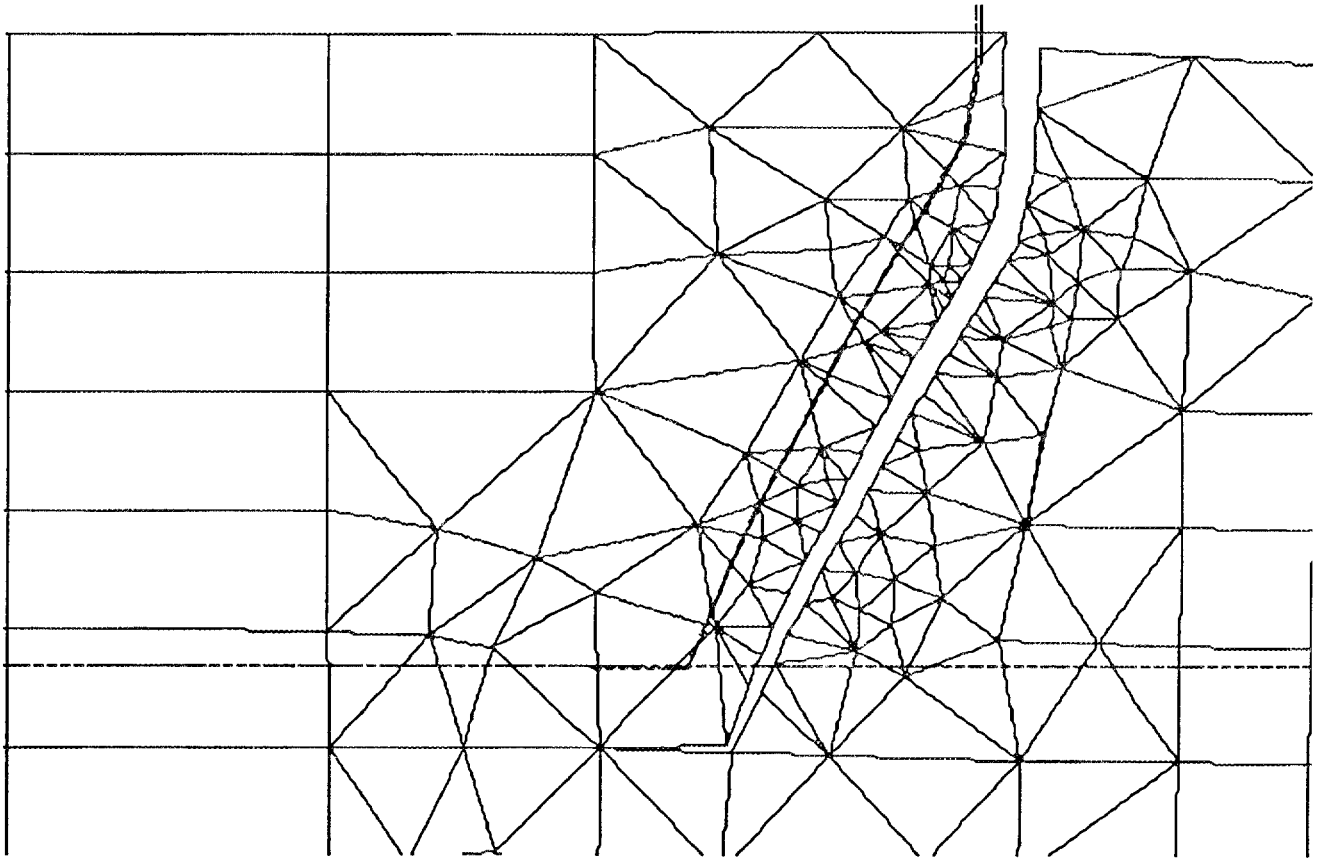

Figure 11. Deformed shape and crack growth direction as the crack encountered the top bimaterial interface.

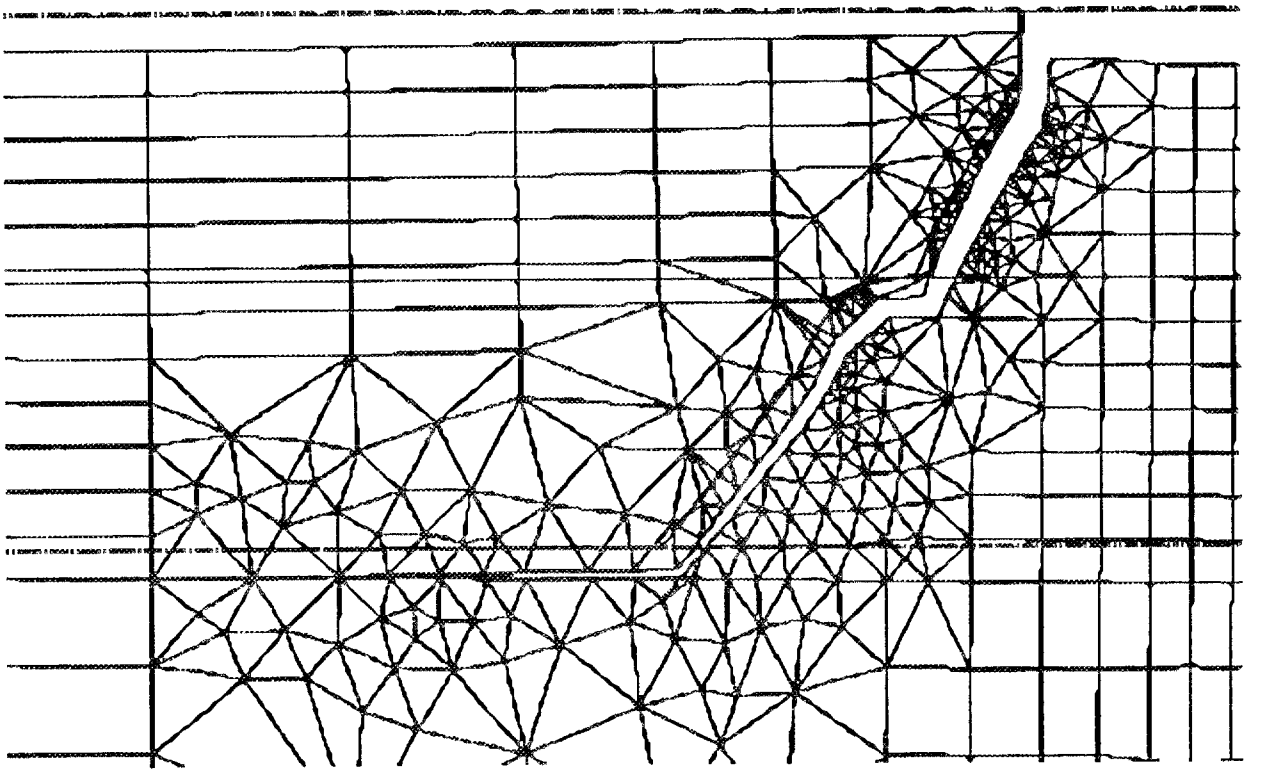

Figure 12. Deformed shape and crack path in final increment. The crack has propagated through both coating layers.

substrate. A zoom of the initial horizontal flaw, showing the original and deformed shape of the coated system is shown in Figure 13. Note that the deformed shape was a result of the thermal, normal and shear loads on the structure. Figure 14 illustrates the direction of crack growth in the final stage of simulation. The crack is directed upwards toward the free surface, then curves away from the applied mechanical load.

The second simulation was performed with an initial horizontal crack in the top coating layer. It was positioned in the middle of this layer. A zoom of the initial horizontal flaw, showing the original and deformed shape of the coated system is shown in Figure 15. Note that the deformed shape was a result of the thermal, normal and shear loads on the structure. Figure 16 illustrates the direction of crack growth in the final stage of simulation. The crack is directed upwards toward the free surface, and the analysis was halted as the crack neared the surface. Since the horizontal cracks were directed away from the substrate, an opportunity exists to design the coating layer such that manufacturing flaws are highly oriented in the horizontal direction, which would promote coating stability and thus oxidation resistance of the substrate.

Since cracks were predicted to move away from the substrate material, the oxidation resistance of the substrate could be preserved during crack growth of this type. It should also be emphasized that this was not the case with initial vertical flaws, which propagated to the substrate.

Status of Milestones

Milestone	Due	Status
Microstructural evaluation of the $Al_2O_3+ZrO_2$ composite layer.	12/89	Completed.
Studies of first generation coating configuration to determine cause of failure during oxidation tests at 1200°C and 1375°C.	03/90	Completed.
Modification of coating configuration to improve oxidation resistance at greater than or equal to 1200°C.	06/91	Cancelled. Replaced by Phase IIA.
Feasibility study of measuring friction coefficient and contact stress damage using conventional pin-on-disk or ball-on-disk wear tests.	12/90	Completed.
Performance tests of modified coating configuration including i) 500 hour oxidation, ii) thermal shock, and iii) flexure strength.	12/91	Cancelled. Replaced by Phase IIA.
Test feasibility of coating a commercial part or equivalent.	03/91	Cancelled. Replaced by Phase IIA.
Computer simulation of i) residual stress in coating due to CVD cycle and thermal expansion mismatch, ii) coating response to load from single pass scratch test, and iii) crack propagation due to initial flaws. Computer calculations will be verified using scratch testing and microscope inspection.	12/91	Completed.
Submit draft of final report covering Phase II results.	4/92	Completed.

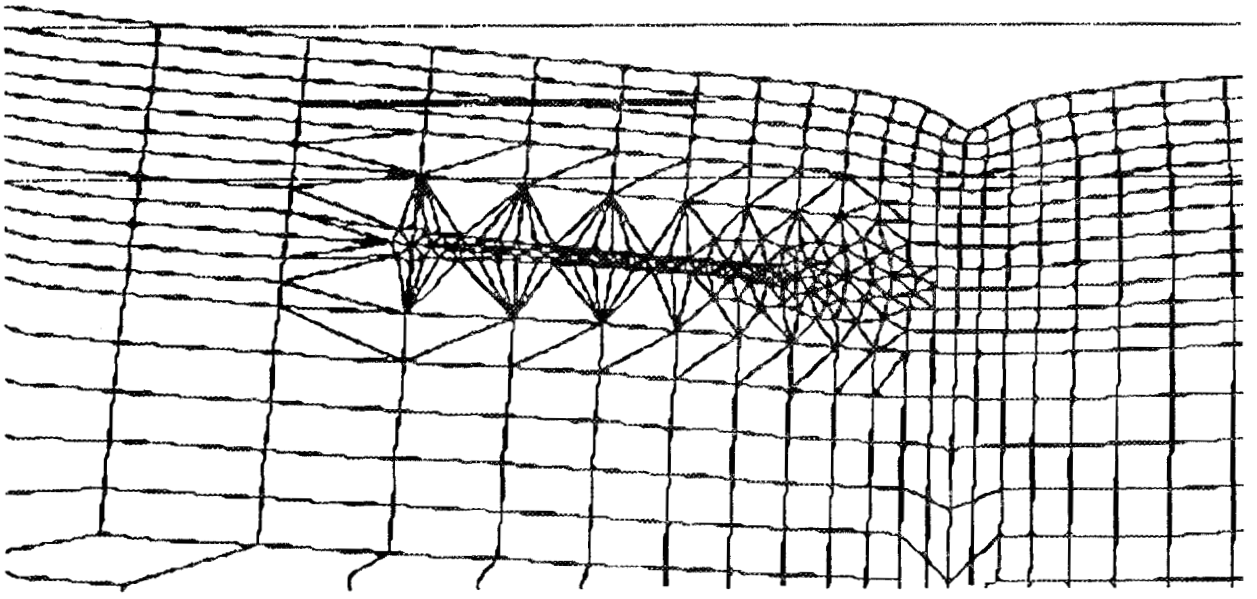

Figure 13. Initial horizontal flaw in the second coating layer. The flaw is positioned at the middle of the layer. Solid lines are deformed geometry (thermal and mechanical loads). Dashed lines are undeformed geometry.

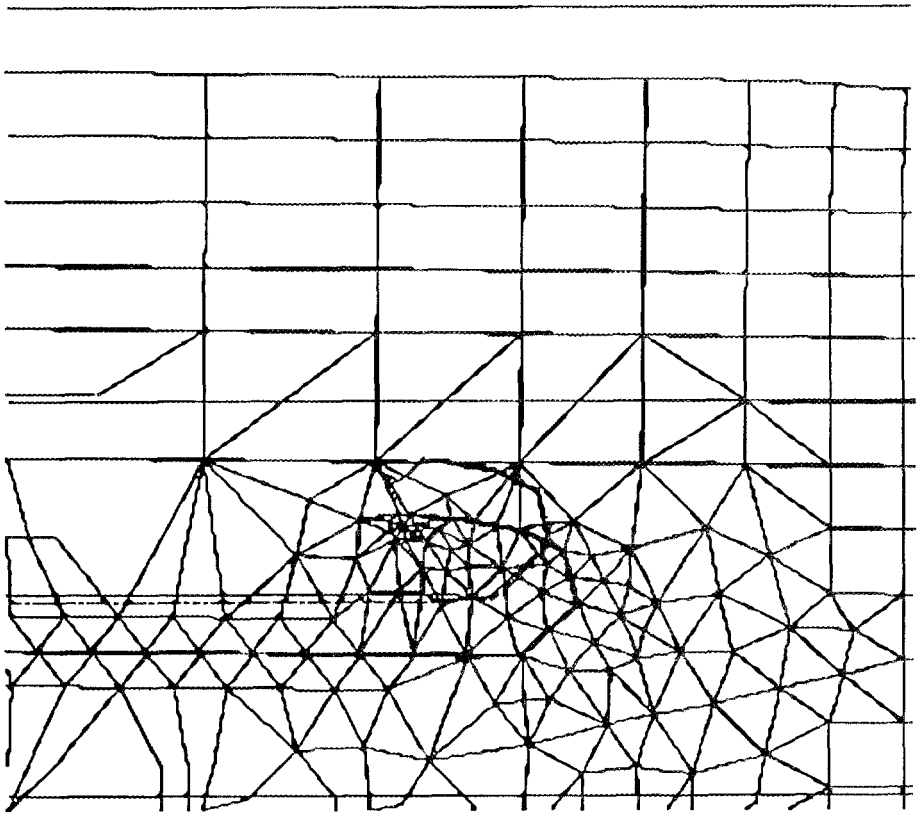

Figure 14. Deformed shape and crack path in final increment for the case where the initial flaw was in the second (middle) coating layer. The crack has been directed away from the substrate.

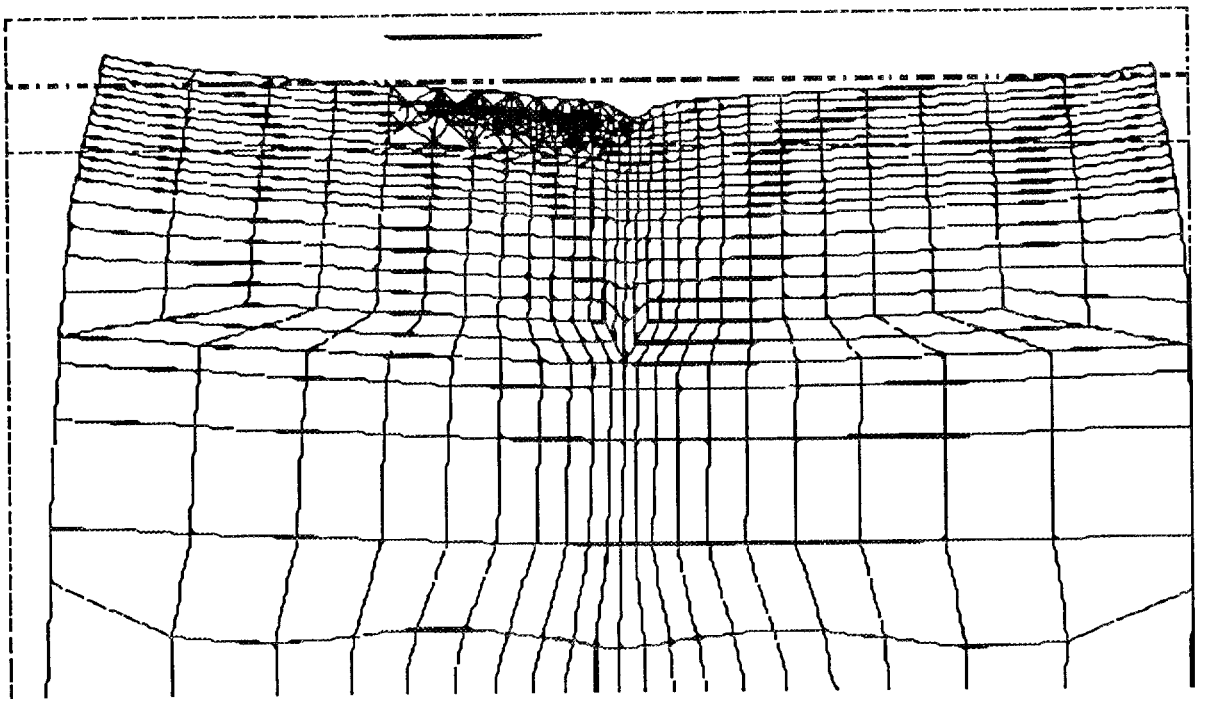

Figure 15. Initial horizontal flaw in the top coating layer. The flaw is positioned at the middle of the top layer. Solid lines are deformed geometry (thermal and mechanical loads). Dashed lines are undeformed geometry.

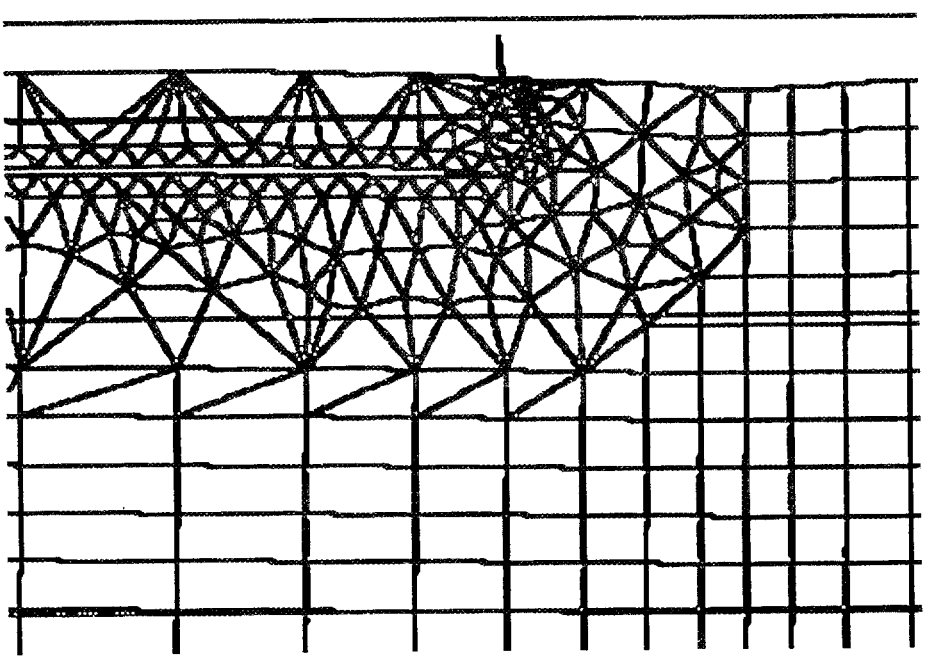

Figure 16. Deformed shape and crack path in final increment for the initial flaw in the top coating layer. The crack has been directed away from the substrate.

Publications

A talk titled "Effect of Al_2O_3 + ZrO_2 CVD Coatings on the MOR Strength of Si_3N_4 and SiC," was presented by J. Selverian at the 1991 American Ceramic Society Conference.

A poster titled "Fracture Strength, Weibull Modulus, and fracture Toughness Measurements of Thin CVD Ceramic Coatings on Substrates," was presented at the Materials Research Society Fall Meeting in Boston MA.

A paper titled "Strength and Toughness Measurement of Thin Brittle Coatings on Substrates" was submitted to Thin Solid Films.

A paper titled "Errors in Curve Fitting of Profilometer Data" was submitted to the Journal of Vacuum Science and Technology B.

References

None.

Development of Adherent Coatings to Reduce Contact Stress Damage of Ceramics - V. K. Sarin (Boston University)

Objective/Scope

The development of oxidation/corrosion resistant, high toughness, adherent coating configurations for silicon based ceramic substrates for use in advanced gas turbine engines.

Technical Progress

Fully dense and adherent SiO_2 coatings have been grown on Si_3N_4 substrates.

Thermodynamic Studies:

The thermodynamic calculations(using the NASA program[1]) were used to determine limiting criteria for the growth of SiO_2 and aid in establishing rate-limiting gaseous species Additionally, they were used to determine the range of input conditions which would produce SiO_2 at equilibrium. Using Tetraethoxysilane($Si[OC_2H_5]_4$) as a source, it was found that the presence of free carbon and CO influence the formation of SiO_2 (Figure 1). Since $Si(OC_2H_5)_4$ is the only reacting species, thermodynamically a change in its mole fraction in the inlet gas composition does not affect the mole fraction of the products of the reaction. However, at 1225°C, SiO_2 siezes to form and is replaced by the formation of SiC. At this very point, an increase in the CO content and a decrease in free carbon. Based on these results, the influence of the presence of CO on the overall reaction is being investigated. It is our intention to investigate the influence of the addition of CO_2 on this reaction.

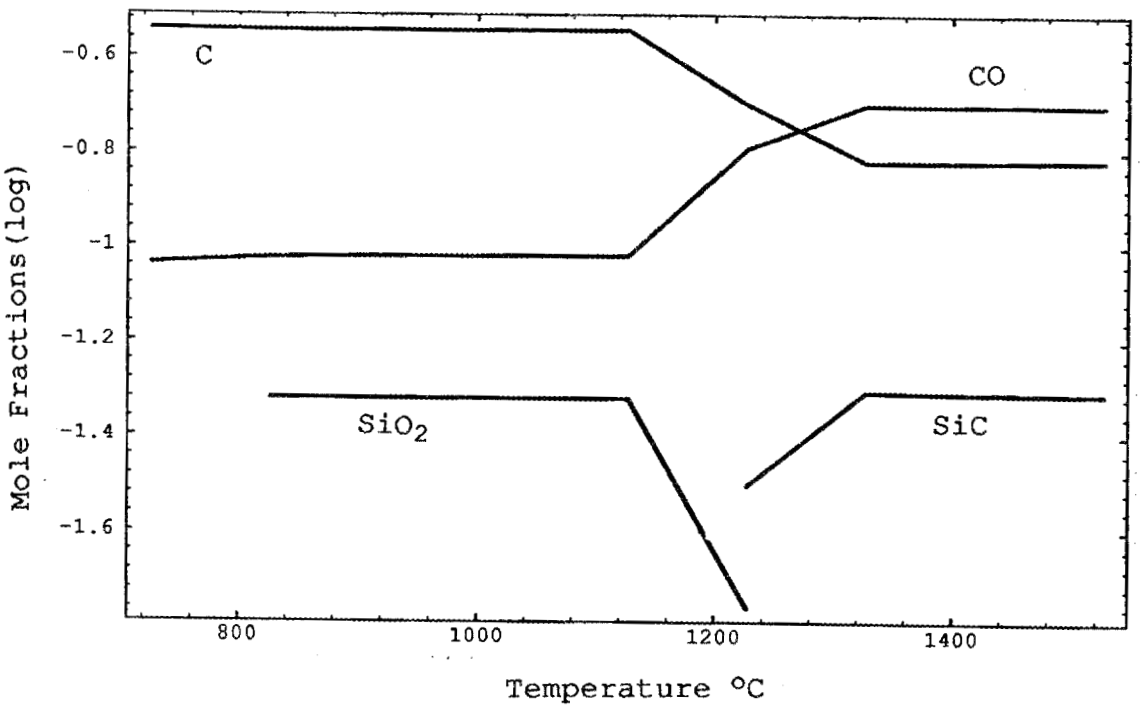

Figure 1: Thermodynamic Plots of the Concentration of the species as a function of temperature.

Process Development:

Fully dense SiO_2 coatings have been successfully deposited by using $Si[OC_2H_5]_4$ as a source, and Ar as a carrier gas between 800-900°C and 50-100 Torr pressures. The CVD reactor has been modified so that these coatings can now be grown in conjunction with other refractory coatings such as Al_2O_3 and AlN. Additionally, a dry pumping system has been incorporated to help in obtaining consistent and repeatable coatings, and eliminate the problems associated with liquid ring seal pumps.

Characterization:

X-Ray analyses have confirmed the presence of SiO_2 (Low-Quartz). Silicon Oxynitride (Si_2ON_2) has also been detected. It is projected that this phase may be formed at the interface and may be useful in enhancing the adherence characteristics of these coatings. Post-annealing treatments and higher process temperatures are currently being investigated to increase the level of Si_2ON_2 and its effect on adherence.

The Microscratch Test[2] was used to measure the adherence of the SiO_2 coatings. This test encompasses scratching a metallographically polished surface of the coated article normal to the coating/substrate interface, exposing a portion of the interface-substrate-coating. A scratch is generated generally perpendicular to the interface via a diamond indenter is applied starting from the substrate towards the coating material. These scratching steps were repeated with increasing normal loads until the onset of crack formation at the coating/substrate interface. This value is used as a measure of the work energy or shear stress required to debond the coating, and therefore an indication of its adherence. Figure 2 shows the crack formation at 30 grams load. It seems that crack initiation occurs in the substrate and then continues leading to debonding of the coating. Thicker coatings will be investigated to see if this effect can be avoided, as has been observed in TiC coated cemented carbide (WC-Co) substrates.

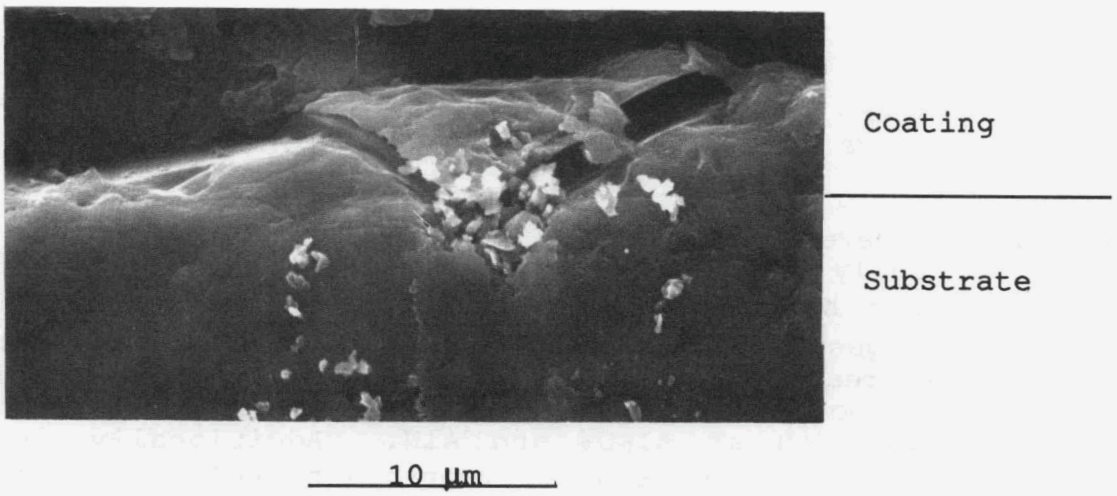

Figure 2: SEM micrograph showing the debonded SiO_2 coating on a Si_3N_4 substrate at 30 gram normal load.

Although 30 grams is a relatively good adherence value for most refractory coating on a Si_3N_4 substrate, it is lower than those observed for AlN on Si_3N_4 which were typically found to be in the 50-60 gram range. Process modification to alter the level of Si_2ON_2 at the interface is being investigated to try and improve the adherence of these coatings.

Post-annealing at 1200^0C and above is being investigated to try and enhance the adherence of these SiO_2 coatings on Si_3N_4 substrates. Preliminary results indicate no effect on the coating for short times (1 hour) at 1200^0C. It should be noted that previous tests have shown that some of the AlN coatings blistered under similar conditions. Equipment has now been setup for thermal cycling and oxidation studies in air up to 1700°C. Ramping rates up to 50°C per minute will be available for these studies .

Status of Milestones

	Schedule	Status
Deposition of chemically graded SiO_2 coatings on Si_3N_4 substrates.	6/92	On Schedule
Composite Al_2O_3/SiO_2 coatings on SiO_2 coated substrates.	12/92	On Schedule
Development of the complete coating configuration for contact stress, oxidation,and corrosion resistance evaluation.	6/93	On Schedule

Publications

None

References

1. Gordon, and McBride, "Computer Program for Calculation of Complex Chemical Equilibrium Compositions, Rocket Performance, Incident and Reflected Shocks, and Chapman-Jouguet Detonations", NASA SP-273, 1989.
2. V.K. Sarin, Unpublished.

Wear-Resistant Coatings

M. H. Haselkorn (Caterpillar Inc.)

Objective/Scope

The goal of this technical program is to develop wear-resistant coatings for piston ring and cylinder liner components for low heat-loss diesel engines.

Friction and wear screening in Phase I identified plasma sprayed high carbon iron-molybdenum and chromia-silica coatings as candidate piston ring wear coatings. Plasma sprayed chromia-silica and high carbon iron-molybdenum coatings, as well as, a low temperature arc vapor deposited (LTAVD) chrome nitride coating were identified as candidate cylinder liner wear coatings. The cast iron porcelain enamel coatings exhibited unsatisfactory wear rates because of porosity in the coating.

The three main technical tasks for Phase II are further optimization of the LTAVD chrome nitride and cast iron porcelain enamel wear coatings and the process scale-up of wear-resistant plasma coatings for cylinder liners.

The optimization of the LTAVD chrome nitride coating involves the development of an adherent 15 micron thick coating which meets the friction and wear goals of this program. The cast iron porcelain enamel process optimization centers on developing a CIPE composition with a minimum of porosity. The process scale-up of the plasma coatings will first develop I.D. plasma spray parameters for coating cylinder liners. Next, simulated cylinder liner specimens will be coated and the friction and wear properties of these coatings be determined using reciprocating friction and wear testing using both new and "used" engine oil.

Technical Progress

In Phase I, a 3-5 micron thick low temperature arc vapor deposited (LTAVD) chrome nitride coating was applied to cast iron substrates which met the friction and wear goals of the contract. However, wear curves generated showed that even with wear coefficients of less than 10-8 mm3/N-m, a 5 micron thick coating will not meet commercial diesel engine durability requirements. The wear curves showed a 15 micron thick LTAVD chrome nitride coating is required to meet these durability requirements. For this reason, the overall goal of this task is the development of a 15 micron thick, adherent chrome nitride coating which can be applied to the inner diameter of cast iron cylinder liners. This task was divided into four subtasks:

1. Optimization of LTAVD chrome nitride coating parameters,

2. Development of a 15 micron thick LTAVD chrome nitride coating containing an intermediate layer,

3. Determination of the effect of single vs. multiple alternative layers on the adherence of 15 micron thick LTAVD chrome nitride coatings, and

4. Friction and wear characterization of selected 15 micron thick LTAVD chrome nitride coating systems.

The optimization of the LTAVD chrome nitride coating parameters studied the effect of bias voltage, substrate temperature, nitrogen partial pressure, current of LTAVD guidance system, and substrate cleaning procedures on coating adherence, composition, roughness, thickness (deposition rate) and microhardness. Only nitrogen partial pressure and substrate cleaning procedures had any significant effect on coating adherence or microhardness.

After optimization of the LTAVD chrome nitride coating parameters, five sets of six cast iron coupons, each containing one of the following intermediate layers: AISI 403 stainless steel, AISI 403 stainless steel plus chromium, titanium, titanium plus titanium nitride and chromium were prepared. A 15-micron thick chrome nitride layer was applied on top of each intermediate layer. In addition, a 15 micron thick coating, consisting of alternating layers of chromium and chromium nitride was prepared. The coating thickness and uniformity were determined on all the LTAVD chrome nitride plus intermediate coating systems after coating. Next, both the coating adherence and microhardness of each coating system were determined both prior to and after the following thermal shock testing:

1. Ten cycles from room temperature to 450 C in 10 minutes followed by an air cool to room temperature, and

2. Ten cycles from room temperature to 650 C in 10 minutes followed by a quench into boiling water.

All the LTAVD chrome nitride coating systems were uniformly applied and exhibited an excellent physical appearance both prior to and after the thermal shock testing. No coating spallation was observed on any of the coating systems either during or after the thermal shock testing. Finally, all the coating systems had excellent adherence to the cast iron substrates both prior to and after the thermal shock testing.

Using these test results as a guide, the following coating systems were selected to be characterized for friction and wear on a Hohman A-6 friction and wear machine: chromium/ chromium nitride, chromium/chromium nitride layers, and titanium/titanium nitride intermediate layer in combination with a chromium/ chromium nitride layered top coat.

The process scale-up of the wear-resistant coatings for cylinder liners began by designing and running statistical experiments to determine the effect of primary gas flow, current, voltage, spray distance and carrier flow on coating microstructure and hardness, as well as, deposition efficiency.

The results of these experiments were then used to build a predictive equation used for selecting three sets of coating parameters for both the chromia-silica and high carbon iron-molybdenum plasma spray powders. The coating parameters selected produced the optimum plasma spray coating microstructure and hardness. In addition, the predictive equation showed that there is a trade-off between high coating deposition efficiency and the optimum microstructure.

Next, both chromia-silica and high carbon iron-molybdenum powders will be plasma sprayed next using the three sets of plasma selected for verification of the predictive model. Once the verification is completed, each of the powders will be plasma sprayed on Hohman rub shoes, using the three sets of parameters selected. The friction and wear properties of each coating will then be determined.

Norton's Ceramic Machining Technology Center was selected to do the initial machining studies of the Cost Effective Machining task. A fully programmable Huffman HS-75R 5 axis CNC grinder was used by Norton for the machining. Norton rotated the machine head 90 degrees and built a special chuck to enable the Huffman to do surface grinding. Initially, a machining program which produced a surface finish and grind line pattern on Falex specimens similar to that obtained with I.D. grinding of a cylinder liner was used. However, because of nonuniform grinding wheel wear, which resulted in wavy surfaces, the machining program had to be modified. The new program produced similar surface finishes to what would be obtained with I.D. grinding, except the grind lines will be oriented differently. Norton has completed grinding approximately 80 percent of the specimens.

The cast iron porcelain enamel compositions (CIPE) evaluated in Phase I all exhibited very poor wear coefficients. An optical microscopy analysis of the coatings showed that all the coatings contained bubbles in the microstructure. The bubbles lowered the compressive strength of the CIPE and as a result, the CIPE crushed under the loading of the ceramic counterface during the pin-on-disk testing.

In Phase II this CIPE development is continuing. The program will investigate different CIPE compositions, and the effect of changing both application and firing processing parameters for each CIPE composition. The overall goal is the determination of a CIPE composition and processing method which will result in the least amount of bubbles in the microstructure.

Four CIPE compositions, two application methods, addition of fining agents to the CIPE compositions (fining agents are used in glass melting to reduce bubble formation), and decarburization of the cast iron substrate before applying the CIPE were evaluated. An alkali borosilicate frit consisting of silica, nickel, cobalt, and lithium oxides produced a CIPE with the least porosity. Additions of fining agents to this composition had very little, if any, effect on reducing porosity. Increasing the firing times for this composition increased the amount of porosity. Finally, decarburizing the substrate prior to applying and firing the CIPE did not reduce the porosity of the CIPE.

Material Development of Thick Thermal Barrier Coating (TTBC) Systems

M. B. Beardsley (Caterpillar Inc.)

Objective/scope

The objective of this program is to advance the fundamental understanding of thick thermal barrier coating systems for application to low heat rejection diesel engine combustion chambers. Areas of TTBC technology that will be examined include powder characteristics and chemistry; bond coat composition; coating design, microstructure, and thickness as they affect properties, durability, and reliability; and TTBC "aging" effects (microstructural and property changes) under diesel engine operating conditions.

Technical progress

TTBC Powders

The 15 TTBC ceramic powders to be evaluated have been selected. The following chemistries will be evaluated:

- 8 wt% yttria stabilized zirconia
- 20 wt% yttria stabilized zirconia
- 24 wt% ceria, 2-3 wt % yttria stabilized zirconia
- Calcium titanate
- Mullite

In addition, 8 wt% yttria stabilized zirconia ceramic powder will be used to evaluate different manufacturing methods which are:

- Fused and crushed
- Spray dried
- Spray dried and sintered
- HOSP (METCO proprietary process)
- Sol gel

The effects of impurities will be evaluated using the 8 wt% yttria zirconia spray dried and sintered material. The spray dried and sintering manufacturing method will be used for this evaluation to allow greater control over the purity levels. Silica and alumina impurity levels will be controlled to provide powders with a high, mid-range and low concentrations, but other impurity oxides will also be monitored.

To determine the process variations between manufacturing lots and their affect on coating properties, material will be tested from three separate manufactured lots. For the evaluation, 8 wt% yttria zirconia manufactured by the HOSP method will be used.

The evaluation of two additional suppliers of material will also use 8 wt% yttria zirconia as a baseline material. The current 8 wt% yttria zirconia made by Zircoa Inc. and used by Caterpillar in ongoing engine test work will be one material. The other material will be from Met Tech.

Powder characteristics of chemistry, crystallographic phase analysis, apparent density, Hall flow, and particle size are being determined. The surface area of the powder is being determined by BET analysis. Powder morphology characterization by optical and SEM microscopy coupled with image analysis completes the characterization of the powders prior to spraying.

Ten of the 15 powders have been procured and shipped to Caterpillar. Spraying of these powders to determine the parameters to be used is currently underway. Each set of powders will be evaluated for the effect of the following spray parameters:

- Primary gas type (argon, nitrogen)
- Primary gas flow rate
- Secondary gas flow rate (hydrogen)
- Amperage
- Carrier gas flow
- Powder feed rate

The settings used to evaluate these parameters were selected using a statistically designed experiment. The experimental design is a response surface methodology analysis which allows optimization of the spray parameters. Thirty-six sets of parameters are being used in the experiment. Responses being measured are:

- Deposition efficiency
- Thermal diffusivity and conductivity
- Density and porosity
- Microstructure

Parameters which give the optimum deposition efficiency (high), thermal conductivity (low), and microstructure will be select for each coating and used in preparation of coating samples for further characterization. Each material sprayed at the selected parameters will be characterized for the following:

- Phase analysis
- Gas permeability
- Surface finish
- Thermal conductivity
- Thermal expansion
- Elastic modulus
- Bond and through thickness strength
- Tensile strength
- Compressive strength
- Cyclic fatigue strength in bending
- Residual stress

Bond Coats

Work at State University of New York to date has been concentrated on the characterization of available bond coat powders to be used in their evaluation. Particle size analysis, chemistry, phase analysis, and SEM particle morphology have been done. Selection of the coatings for spraying will concentrate on determining the role of chrome and yttrium in the bonding and oxidation process.

Oxidation studies of four bond coat materials has been completed by State University of New York. The nickel-based bond coat alloys studied were Ni-20Cr, Ni-5Al, Ni-20Cr-6Al and Ni-17-Cr-6Al-0.5Y. The test coupons were obtained from free-standing deposits fabricated by air plasma spraying.

Oxidation tests were conducted for 100 hours at 400 C, 600 C, and 800C in flowing air with 29% humidity. The specimens were not given any post-spray surface treatment. The specific weight gains were measured following the oxidation tests. Metallographic examination, using optical microscopy, and x-ray diffraction studies of the oxidized coupons were conducted.

The specific weight gain results indicate that the NiCrAl and NiCrAlY exhibit the best oxidation resistance of the alloys tested but the test temperature is also a major factor, Figure 1. For bond coat temperatures below 500 C, the NiCr bond coat would have similar oxidation resistance as the NiCrAl and NiCrAlY bond coats. The next set of tests will evaluate the oxidation protection the bond coats provide low alloy steel substrates. The performance of the nickel based alloys will also be compared to that of iron-based bond coat materials.

Status of milestones

All milestones are on schedule.

Publications

None.

1.4 JOINING

1.4.1 Ceramic-Metal Joints

Joining of Ceramics for Heat Engine Applications
M. L. Santella (Oak Ridge National Laboratory)

Objective/scope

The objective of this task is to develop strong, reliable joints containing ceramic components for applications in advanced heat engines. The overall emphasis of this task is on studying the brazing characteristics of silicon nitride and silicon carbide. The techniques of direct brazing, as well as vapor coating ceramics, to circumvent wetting problems will be applied to these materials. The specific areas of emphasis for this activity during FY 1992 will be on: (1) continuing the study of high-temperature brazing of silicon nitride and the effects of thermal aging on joint strength, and (2) initiating a study of the brazing characteristics of sintered α-SiC.

Technical highlights

Annealing of Si_3N_4 braze joints: Flexure bars of Ti-vapor-coated Si_3N_4 brazed with Au-25Ni-25Pd wt % filler metal were annealed in vacuum for 100 h at temperatures of 600, 700, and 800°C and then tested at room temperature. The results from these tests are presented in Table 1. Initial indications are that annealing at 600 and 700°C does not adversely affect room-temperature strength, while annealing at 800°C produces a significant decrease in room-temperature strength compared to the test results for specimens that were not annealed. The retained strength for

Table 1. Results for room-temperature flexure testing of annealed Si_3N_4 braze joint specimens.

Specimen ID	Bar width (mm)	Bar thickness (mm)	Fracture load (kg)	Fracture strength (MPa)	Annealing temp. (°C)
819-1	3.0861	2.5654	40.02	368.1	600
819-2	3.0810	2.5654	44.07	406.0	600
819-3	3.0610	2.5654	48.48	449.6	600
818-4	3.0759	2.5527	55.85	520.6	700
818-5	3.0861	2.5400	--	No test	700
818-6	3.0734	2.5425	48.53	456.3	700
818-1	3.0734	2.5400	37.81	356.2	800
818-2	3.0480	2.5425	36.84	349.3	800
818-3	3.0937	2.5527	32.08	297.3	800

the 800°C specimens was still reasonably high, however. Metallographic examination of these specimens and more extensive testing are planned.

Metallography of Si_3N_4 braze joint test bars: Previous testing of unaged joint specimens showed that high strength was maintained up to 700°C but that it dropped precipitously at 800°C. The microstructures of these Si_3N_4 braze joints were examined in detail by scanning electron microscope (SEM) and electron microprobe (EPMA). Microchemical analysis of a braze joint specimen in the EPMA confirmed that the bulk of the filler metal layer was composed of an Au-rich matrix with a composition near that of the unreacted filler metal: 49.2Au-24.5Ni-23.8Pd-0.4Si-2.1Ti wt %. The Si content resulted from reaction between the Ti vapor coating and the Si_3N_4; the Ti resulted from dissolution of part of the vapor coating in the filler metal during brazing. An Ni-rich second phase (approximately 43.0Ni-34.8Au-19.2Pd-1.7Si-1.3Ti wt %) was also found throughout the filler metal layer, but its composition could not be accurately determined because of its small size. Line scanning showed that there were only slight fluctuations of Au, Ni, and Pd through the bulk of the reacted filler metal layer and that Ti was localized near its original position on the Si_3N_4 surfaces. Also, no unusual enrichment of Si was found in the reaction layers near the brazed Si_3N_4 surfaces.

SEM examination of the tensile face of a specimen tested at 800°C showed that the microstructure at the brazed Si_3N_4 surfaces was much more complicated than previous observations indicated. A thin, multi-phase layer was found at the Si_3N_4 surface, as shown in Fig. 1. This thin layer

Y32978

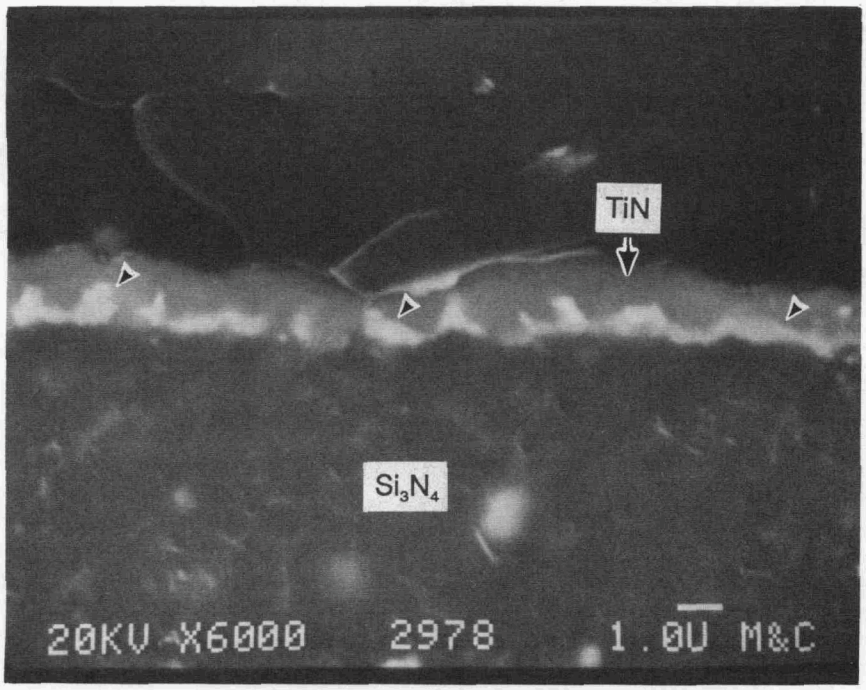

Fig. 1. SEM micrograph at Si_3N_4 surface of braze joint specimen tested at 800°C. A TiN reaction layer formed on the Si_3N_4 during brazing. The arrowed feature is a metallic phase at the Si_3N_4/TiN interface.

appeared to be composed of a metallic phase rich in Au and Pd, and TiN. Figure 1 shows the somewhat surprizing feature that the metallic phase was actually situated between the Si_3N_4 and a continuous layer of TiN.

The mating half of the test bar shown in Fig. 1 is shown in Fig. 2. The nearly continuous reaction layer at the bottom of this micrograph had a composition of 75.9Ni-11.3Pd-7.5Au-5.0Si-0.3Ti wt %. The Si content of this layer is relatively high but not so much so that melting in the range of 800°C would be expected.

Y32979

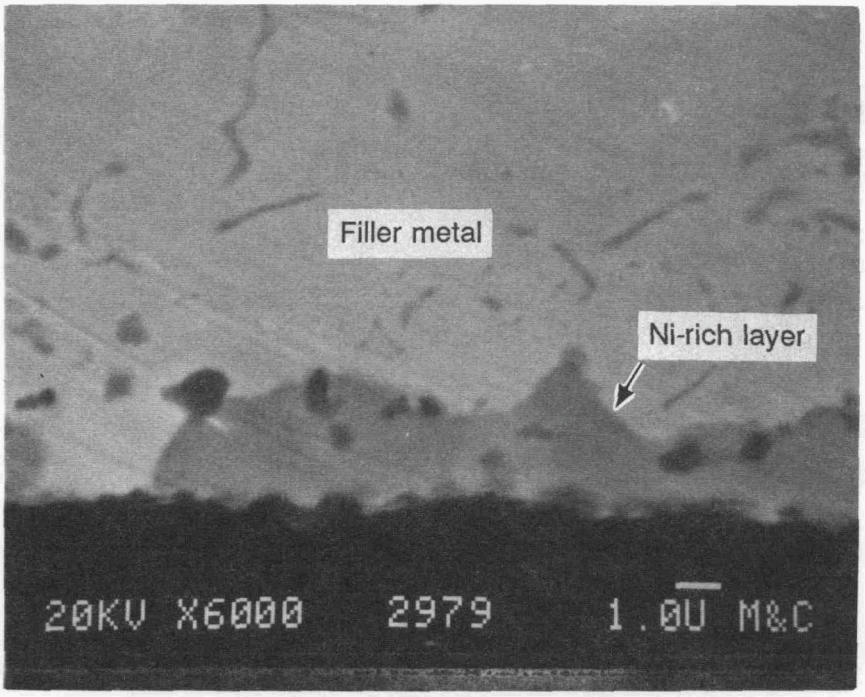

Fig. 2. Mating half of specimen shown in Fig. 1. The preferred failure path in this specimen was along the interface between the TiN reaction layer and the metallic filler metal phases.

Comparison of Figs. 1 and 2 indicates that the preferred fracture path in this specimen was near the interface between the TiN reaction layer and the metallic phases of the braze layer. Based on the observations made to date, liquation of an Si-rich phase near the brazed Si_3N_4 surfaces cannot be ruled out as the dominant failure mode for these brazing materials. However, other mechanisms may have operated as well. Further analysis of these joints will be required to better understand their fracture behavior and limitation to temperatures below 800°C.

SiC brazing: Initial wetting experiments on SiC were begun. The alloys presently being evaluated are: a Cu-Ag eutectic alloy, a Cu-Ag-Ti active braze filler metal, an Au-18Ni alloy, an Ni-20Cr alloy, and pure Cu, Ag, Ni, and Au.

Status of milestones

141110 Complete analysis of joint strength data from Ti-vapor-coated silicon nitride braze joints - December 31, 1991. A draft report is available.

Publications

None

Unpublished work

None

Analytical and Experimental Evaluation of Joining Silicon Nitride to Metal and Silicon Carbide to Metal for Advanced Heat Engine Applications -S. Kang (GTE Laboratories Incorporated)

Objective/Scope

The goal of Phase II is to optimize materials systems and joint designs building on the results of Phase I. The work shall also include demonstration of the potential for scale-up of the joint size to interfacial areas of commercial significance, applicability of the analytical joint modeling tools and the ability to use these tools to design and predict the mechanical and thermal stability of the larger joints. These joints, referred to as "scale-up" joints, shall have the ceramic shaft at least 0.8 inches in diameter. The goal is to develop a system which can perform in an engine such as the ATTAP engine. The anticipated environment will be oxidizing and will have joint temperatures of 650°C or higher. Improved joint materials systems shall be developed to optimize the combination of competing properties, which include ductility, yield strength, and creep resistance. The effect of each of these properties on joint performance shall be examined using the FEM model. Finally, a program of mechanical testing shall be carried out to confirm the effectiveness of the modeling program. This shall include torsion tests, thermal and mechanical fatigue, and creep testing. In addition, an analytical and experimental program in service life prediction will be undertaken.

Technical Progress

Design/Failure Analysis

The October 1991 bimonthly described in detail the new probabilistic failure model for ceramic components which are affected by plastic deformation of adjoining materials. The model has been interfaced with the CARES probabilistic failure code. A finite element analysis was performed on the total ceramic-to-metal joint, taking into account the plastic deformation in the braze and interlayer materials. Prior finite element analyses which were performed with a crack in the ceramic material for varying distances and angles with respect to the braze-ceramic interface provided energy release data. A best fit curve was then made for the energy release rate data to result in stress coefficients which modify the stress state before using the CARES code.

The best fit curve described in the previous bimonthly has been modified and the stress correction factor (fc) used in this study is described as below:

$$f_c = \exp\left\{ a\frac{K_{IC}}{\sigma_o\sqrt{h}} + b\frac{K_{IC}\sqrt{t}}{\sigma_o h} + c\frac{K_{IC}^2}{\sigma_o^2\sqrt{th}} \right\}$$

where,

a=0.0837
b=0.0447
c=0.0711

Figure 1 defines the variables near the interface.

The new failure criterion was tested on ceramic-to-metal joints containing nickel and moly interlayers with Incoloy 909 and Inconel 718 structural components, respectively. Figure 2 shows the probability of failure versus applied torque on the two joint systems with experimental results. Both penny shaped crack and Griffith crack were assumed to find the failure envelop. The new model shifted the failure curves, resulting in a less conservative failure prediction for both joint systems, and for both penny shaped and Griffith cracks. The reason for the shift in new model (or "modified" as indicated on Figure 2) was that previous models did not account for the fracture energy absorbed by plastic work of an adjoining material (the braze layer). Therefore, it predicted

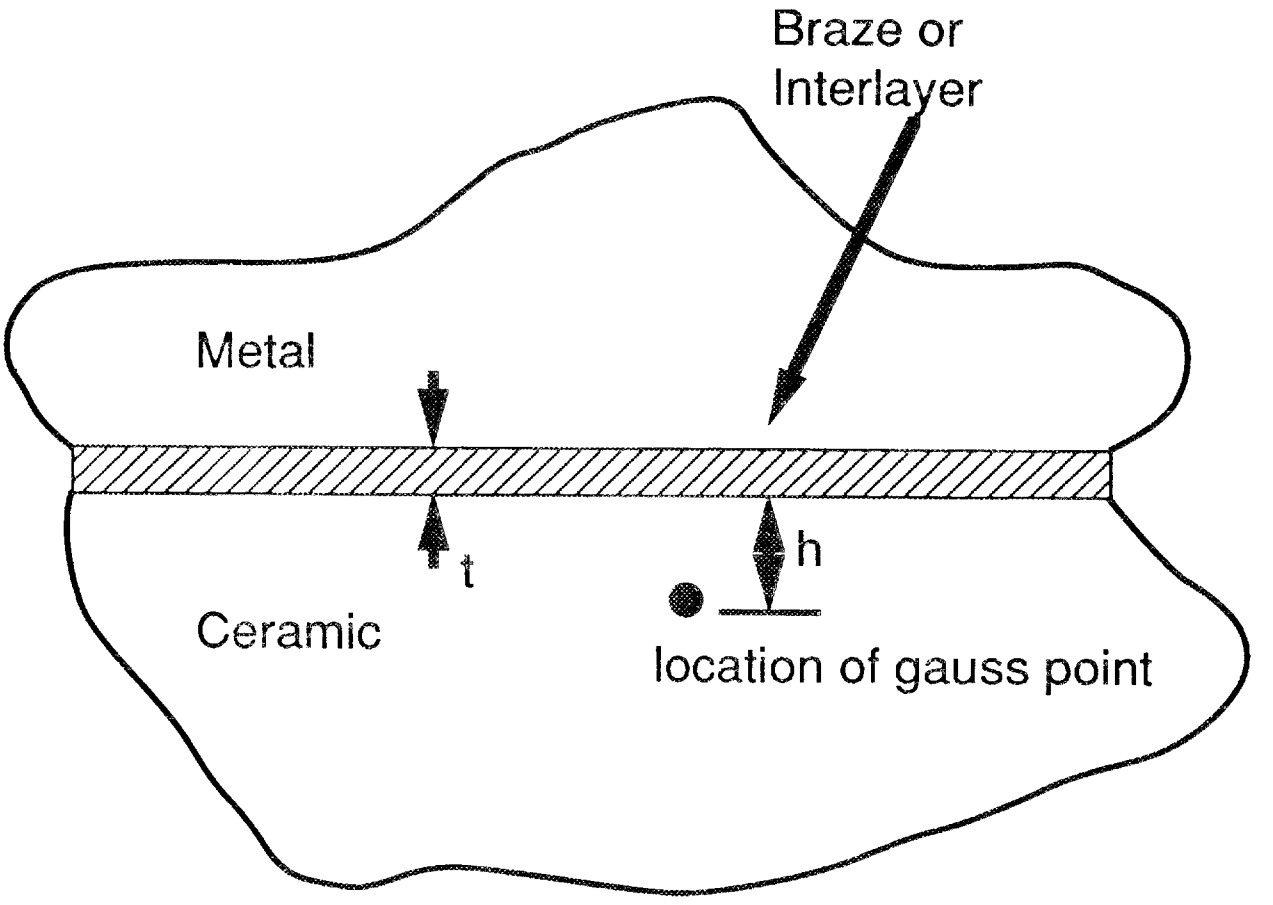

Figure 1. Definition of terms used in the stress correction factor (fc)

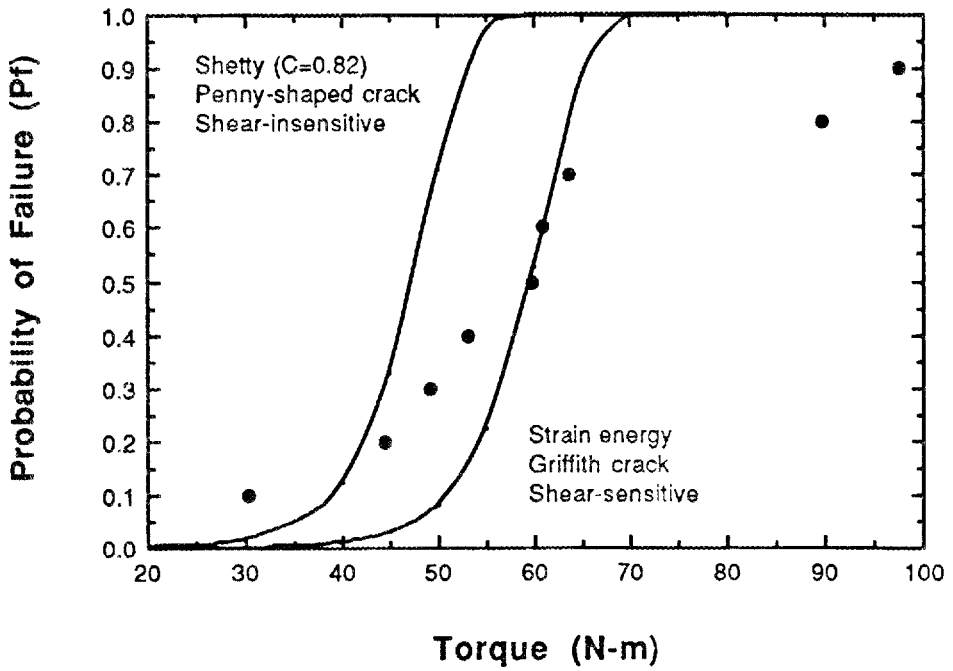

Figure 2a. Predicted and experimental values of the brazed joint strength measured in torsion (Si_3N_4/Ni/Incoloy 909). Two failure theories were used: 1) Shetty criterion with $\bar{C}$ = 0.82, penny-shaped crack, and a shear-insensitive Batdorf crack density and 2) coplanar strain energy release rate, Griffith crack, and a shear-sensitive Batdorf crack density.

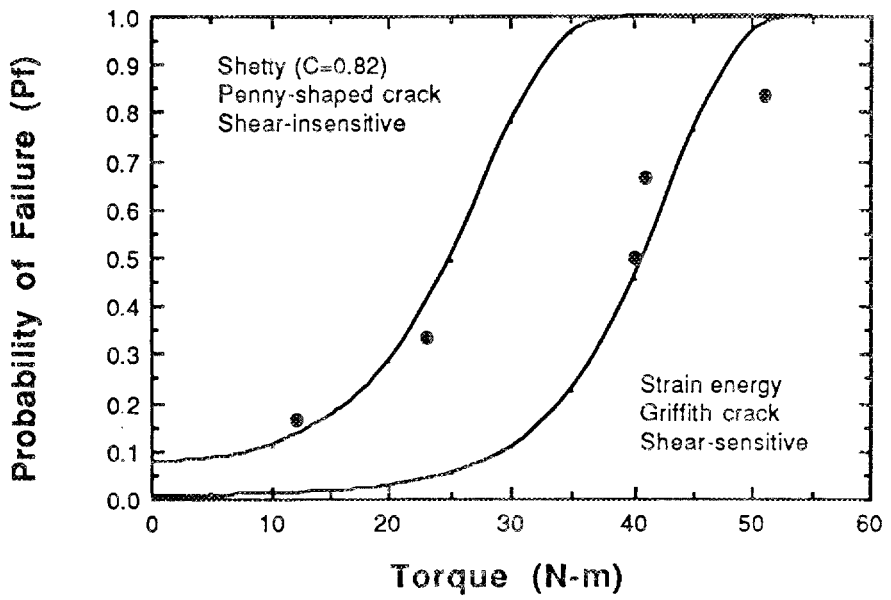

Figure 2b. Predicted and experimental values of the brazed joint strength measured in torsion (Si_3N_4/Mo/Inconel 718). Two failure theories were used: 1) Shetty criterion with $\bar{C}$ = 0.82, penny-shaped crack, and a shear-insensitive Batdorf crack density and 2) coplanar strain energy release rate, Griffith crack, and a shear-sensitive Batdorf crack density.

that a larger applied torque could be tolerated for a specified probability of failure. It is to be noted that, especially for the Incoloy 909 material system, the new failure model predicts much closer to the experimental results. It is believed that the new failure model will provide more accurate prediction for ceramic failure where some plastic work is encountered in manufacturing or service.

Brazing Alloy Development

Evaluation of Raw Material : PY6

Room temperature torsion tests were performed with cylindrical PY6 samples of 0.5" dia.x 4.0" long for base line data. PY6 silicon nitride was prepared for Phase II in the same way as was done for Phase I. It was sintered first and further densified by HIPing at 1825 °C using a glass encapsulation technique. The final products were in the form of rectangular bars or cylindrical rods. All sample surfaces were polished down to 0.03μm with alumina powder for experiments. Torsional strength of those rods are shown in Table 1. Average torsion strength of PY6 for Phase II was about 85% of previous results in Phase I. The weibull plot (Figure 3) showed the similar reduction in strength. The batch process for powder preparation and densification might have resulted in the difference.

Torsion Testing of the Ceramic-Metal Joints

A total of 29 ceramic-metal joints were produced using SK-1 and 2 alloys which, in previous reports, were designated as B and C alloys, respectively. Alloy SK-1 has Mo in addition to Ni, Cr and Fe while Alloy SK-2 has Ni, Cr and Fe as secondary elements. It was found that new high temperature brazing alloys, especially SK-1, resulted in significant gain in the torsional strength of the joints at 650°C with a moderate loss at room temperature. As shown in Table 2, the average joint strength made of SK-1 was 309 in-lb at 650 °C whereas the strength at room temperature was 380 in-lb. The high temperature torsional strength is far better than what we observed from the Au-Pd-Ni system of Phase I (10-60 in-lb). It is to be noted that the new alloy maintained the room temperature strength up to 650°C with little scatter in the failure strength values. Alloy SK-2 did not provide any gain in strength at low and high temperatures compared to those of Phase I. Lower strength values with new brazing alloys at room temperature than that of the Au-Pd-Ni system (avg. 540 in-lb) were attributed to high residual stress resulted from the low ductility of these new alloys.

For the production of PY6/Ni/Incoloy 909 joints, an optimum processing temperature was selected from the range of 1100°C and 1150°C on the basis of joint strength. As illustrated in Tables 2 through 4, high temperature performance (at 650°C) was improved with Alloy SK-1 as the processing temperature decreased from 1150°C to 1100°C. Room temperature strength of the joints made of Alloy SK-1 seemed to be less sensitive to the change in the processing temperatures. In contrast, the joints from Alloy SK-2 showed improved room temperature torsional strength from 340 in-lb to 590 in-lb as the processing temperature increased. However, Alloy SK-2 did not provide any noticeable improvement in high temperature performance regardless of the processing conditions. Of these three processing conditions, joints held at 1100°C for 30 minutes have resulted in the optimum performance.

Inferior performance of the joints at higher brazing temperature, i.e., 1150°C, was presumed to be related to the excessive phase separation and to the extent of interaction between Ti-coating and PY6 substrate. It was observed from the microstructural study that Alloys SK-1 and SK-2 consisted of Au- and Ni-rich solid solution phases. The Au-based solid solution phase tends to segregate on the ceramic side from Ni phase due to its low melting point, enabling the ceramic-metal to bond at relatively low temperature (<1150°C). Thus, high temperature properties of the joints can be degraded due to the increased amount of Au phase in the vicinity of ceramic/braze interface as the brazing temperature increases. Excellent high temperature performance of Alloy SK-1 could be attributed to the presence of a high temperature strengthener such as Mo in the system. It is expected that other solid solution strengtheners like Nb and V might provide the same effect as shown with Mo in the system. No significant difference in joint strength was observed at room temperature from the joints made with Alloys SK-1 and 2. This indicates that both alloys have similar tensile properties which control the level of residual stress at the joints.

Table 1. Torsional strength of the PY6 material.

Material	Test Temperature (°C)	Torque (in-lbs)	Shear Strength (psi)	Rotation	Diameter of gauge section (")
Si_3N_4 of Phase I	RT	2,110	85,970	0.40°	0.50
	650°C	525	171,123	1.84°	0.25
Si_3N_4 of Phase II	RT	2,000		3.25	0.50
		1850		2.92	0.50
		1700		2.8	0.50

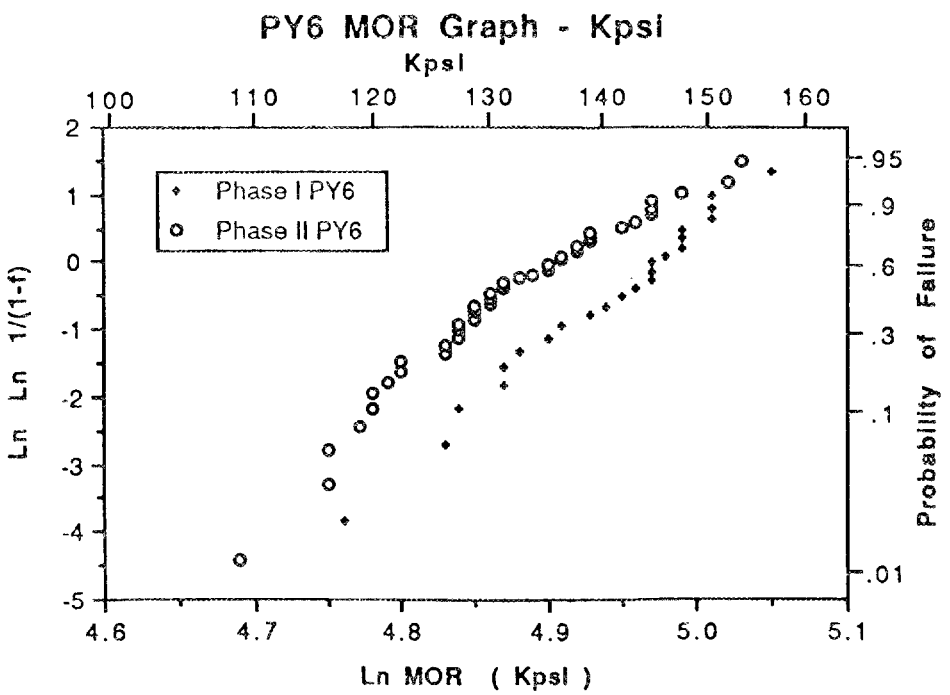

Figure 3. Weibull Plot of PY6 Silicon Nitride

Table 2. Torsional strength of the PY6 /Ni/Incoloy 909 system brazed at 1100°C for 30 minutes

Braze Alloys	Test Temperature (°C)	Torque (in-lbs)	Alignment (")	Rotation (°)	Failure Mode
Au-Pd-Ni* (ref.)	RT	Avg. 540			Ceramic
	650	Avg. 40			Slipped
SK-1	RT	405	0.003	1.23	Failure in Ceramic
		420	0.008	1.30	"
		305	0.005	0.88	"
	650	307	0.015	1.23	Failure in Ceramic
		290	0.019	0.95	"
		330	0.019	1.20	"
SK-2	RT	400	0.020	1.25	Failure in Ceramic
		400		-	"
		315	0.005	0.92	"
		350	0.004	0.96	"
		240	0.002	-	"
	650	325	0.009	-	Failure in Ceramic
		15	0.005	-	50% unbonded
		90			Slipped

* Joints were brazed at 1180°C for 3-4 minutes.

Table 3. Torsional strength of the PY6 /Ni/Incoloy 909 system brazed at 1125°C for 20 minutes

Braze Alloys	Test Temperature (°C)	Torque (in-lbs)	Alignment (")	Rotation (°)	Failure Mode
SK-1	650	220	0.014	2.5	Ceramic
SK-2	650	68	0.026	0.25	Slipped

Table 4. Torsional strength of the PY6 /Ni/Incoloy 909 system brazed at 1150°C for 30 minutes

Braze Alloys	Test Temperature (°C)	Torque (in-lbs)	Alignment (")	Rotation (°)	Failure Mode
SK-1	RT	400	0.014	1.15	Failure in Ceramic
		440	0.010	1.25	"
	650	340	0.010	1.20	Slipped
		72	0.015	0.37	Slipped
	750	40	0.017	1.15	Slipped
SK-2	RT	475			
		650	0.014	2.25	
		640	0.015	1.87	
	650	10	0.018		
		75	0.028	0.27	
		50		0.15	

Creep Test and Torsional Fatigue of Ceramic-Metal Joints

The main goal of this alloy development is to produce ceramic-metal joints which can survive at high temperature without a significant loss of room temperature performance. From Phase I of the program, it was found that the joints made of Au-Pd-Ni were not able to sustain any significant load (> 20 in-lb) at 650°C even if those performed successfully at room temperature. Therefore, the primary goal was to design braze alloys with high temperature creep properties.

Creep strengths of the joints made between PY6 silicon nitride and Ni was evaluated with shear samples at 525°C. Intended bond area was 1 cm^2 and testing was done by compression shear in argon atmosphere. Preliminary results showed that the joints with B alloy survived more than 80-100 hours at 1000 lbs, constant dead load (6.7 ksi initial shear stress). These are better than those of Au-Pd-Ni and Au-Ni which survived at this load for 10-15 hours. Creep tests done at higher load (1500lbs) or at higher temperature (650°C) showed inconsistent results; some of the samples failed during loading at a lower load than expected from hot tensile tests. This presumed to be related to the strong sensitivity in the joint formation to joint geometry and processing conditions. Effect of the joint geometry on the creep performance was investigated with those of cylindrical samples describe below.

Table 5 summarizes the creep test result of SK-1 cylindrical joints at 650°C. At 185 in-lb torque level, the rupture lives of four joints were 3.5 hours, 10.5 hours, >100 hours, and >160 hours, respectively. Testing of the first two samples were completed by rupture failure at the interface between braze and PY6. These samples showed a high portion of unbonded area (>30%) in the joints. Testing of the other two joints were stopped after 100- and 160-hour creep without failure. The performance of these joints at 650°C was outstanding compared to other ceramic-metal joints produced with any existing braze alloys. Excellent performances were expected as long as the bonded area exceeds more than 80% of the intended area.

The first sample showed the creep rate of 4.5×10^{-2}°/hr, and the failure came when it rotated about 0.22° more from the end point of the first stage creep (0.50°). The steady state creep of the third sample started from 0.552° and stopped at 0.640° in 100 hours, resulting in the

Table 5. Torsional rupture of the PY6 /Ni/Incoloy 909 system at 650°C

Braze Alloys	Constant Torque (in-lbs)	Alignment (")	Rotation (°)	Time to Rupture (hrs)	Creep Rate (°/hr)
SK-1	185	0.034	0.58°	3.5	4.5×10^{-2}
	185	0.022	1.265	10.5	6.7×10^{-2}
	185	0.025	0.640	>100*	8.8×10^{-4}
	185	0.008	1.317	>160 (1 week)	4.6×10^{-3}

*Experiment was stopped after 100 hours creep at 650°C due to a planned electrical shut-down at the Labs..

creep rate of 8.8×10^{-4} °/hr. The significant difference in creep rate must be related to the quality of the joined area, i.e., the percentage of unbonded area and its distribution.

Figure 4 is a plot of creep behavior of the fourth sample which survived more than 160 hours (1 week) at 650°C. The average creep rate of the second stage was 4.6×10^{-3}°/hr, which is five times higher than that of the third sample. If this creep rate can be used for the third sample, the useful life of this sample would be more than 800 hours. This result in creep life was quite significant for future application of this type of joints since the expected life of an automotive engine is no more than 3000 hours.

A significant difference in the creep rates were recorded during the second stage of the creep. The change in the creep rate was always found to be associated to temperature fluctuation from 620°C to 670°C. This implies that small change in use-temperature could cause a significant effect on the rupture lives of the joints in this temperature range. The heating was done by an induction heating unit. As shown in the table, the creep rate was not related directly to the rupture life of the joint. The rates seemed to be strongly controlled by the distribution of unbonded area.

Excellent high-temperature creep performance was due to the dual phase structure of SK-1 alloy. Most deformations were expected to occur in the Au-Ni-Cr phase at high temperature, while the Ni-Cr-Fe phase gave rise to obstruction to the flow of the Au-rich phase. However, the existence of two different phases of different melting points entailed inconsistency in bonded area after brazing process. There is a need to develop a better processing technique or modified alloy to ensure the consistent bonded area to improve the reliability of the joints.

Four joints were brazed at 1100°C for 30 minutes and tested for torsional fatigue strength at room temperature and 650°C. The amplitude of torque was 35-185 in-lb, which represented actual conditions in an automotive engine during idling and accelerating stages. As shown in Table 6, the room temperature fatigue properties of SK-1 joints are excellent, far exceeding the specified number of cycles (1000 cycles) at this torque amplitude. A joint made of SK-2 did not survive a single cycle, but failed during loading. Also, a SK-1 joint tested at 650°C failed during spanning the torque amplitude from 110 in-lb torque. The frequencies of fatigue tests were 1.5 and and 0.04 Hz for room temperature and 650°C, respectively. The low frequency used for the fatigue test at 650°C was to simulate the acceleration rate of an engine, roughly 12.5 seconds for 0 to full speed. It is possible for SK-1 joints that the repeated cycling might accelerate the second stage creep rate at high temperature, causing premature failure. More tests will be done to verify if this is a general trend of these joints at 650°C.

Thermal Fatigue of Brazed Joints

The idle temperature used for thermal fatigue tests was 335°C for the Si_3N_4 as used in the final report of Phase I. The Si_3N_4 required approximately 130 seconds to reach 650°C from 335°C and return again. Ten cermic-metal joints were produced using Alloys SK-1 and SK-2 and

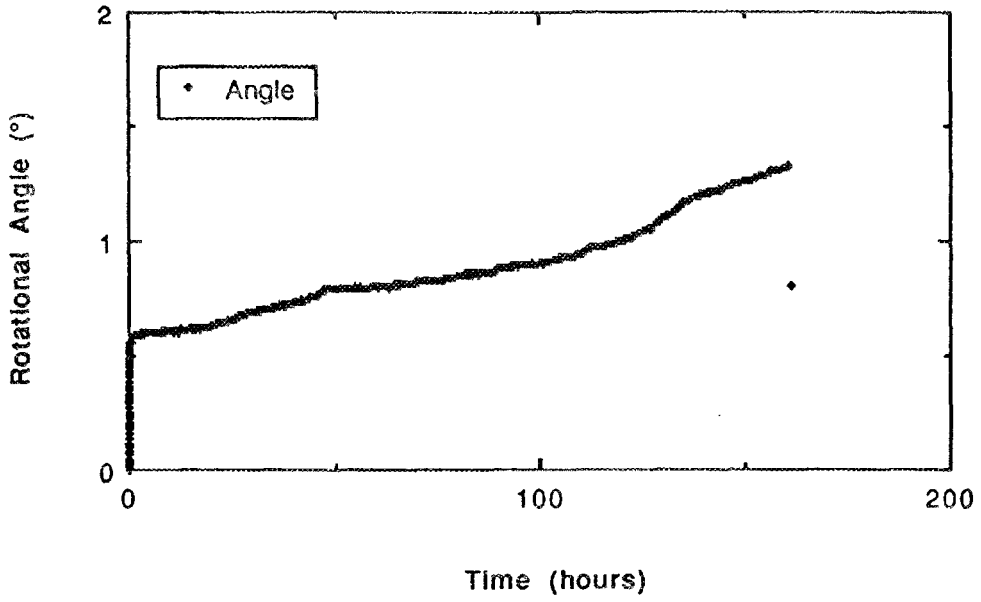

Figure 4 650°C Creep Behavior of Ceramic-Metal Joints (SK-1)

Table 6. Torsional fatigue of the PY6 /Ni/Incoloy 909 system

Braze Alloys	Test Temperature (°C)	Torque Amplitude (in-lbs)	Alignment (")	Rotation (°)	Number of Cycles for Failure
Au-Pd-Ni (ref.)	RT	35-185			>1,000,000
		70-370			>1,000,000
SK-1	RT	35-185	0.016	0.59	427,440
		35-185	0.020	0.51	>1,000,000
	650	35-185	0.025		Failure during loading
SK-2	RT	35-185	0.026		Failure during loading

subjected to 1000 thermal cycles as described above. The dimension of the joints is the same as in Phase I. These joints were examined for the cracks in the ceramic part nondestructively prior to the thermal fatigue tests and reexamined after thermal tests by a microfocus X-ray to see if there are any cracks developed during thermal cycling. It was found that none of the joints showed any evidence of cracking. It implies either that the thermal fatigue did not cause any cracking or the sizes of cracks were under the limit of x-ray detectability which is about 1μm.

Status of Milestones

4/27/92 Final report (draft) of Phase II was submitted to ORNL for review.

Publications

J. Selverian and S. Kang published a paper entitled "Ceramic-Metal Joints Brazed with Palladium Alloys," in the J. of Am. Welding Soc., (1992).71[1] p25s-35s .

1.4.2 Ceramic-Ceramic Joints

Analytical and Experimental Evaluation of Joining Silicon Carbide to Silicon Carbide and Silicon Nitride to Silicon Nitride for Advanced Heat Engine Applications - G. J. Sundberg, J. A. Wade, and F. J. Wu (Norton Company)

Objective/scope

Joins of hot isostatically pressed (HIP'ed) Si_3N_4-4wt% Y_2O_3 (NCX-5100 family) and sintered Beta-SiC (NCX-4500) were developed during Phase I of the contract and were demonstrated to have mechanical properties attractive for advanced heat engine applications.[1] An experimental database was developed for both materials based upon limited MOR and buttonhead tensile tests. Within the limitations of this database, analytical/numerical models were developed for prediction of join reliability. The purpose of this program is to develop joining technologies for HIP'ed Si_3N_4 with 4wt% Y_2O_3 and for a siliconized SiC (NT-230) for various geometries including: butt joins, curved joins and shaft to disk joins. In addition, more extensive mechanical characterization of silicon nitride joins to enhance the predictive capabilities of the analytical/numerical models for structural components in advanced heat engines will be provided. Mechanical evaluation will be performed by: MOR at 22°C and 1370°C, stress rupture at 1370°C, high temperature creep, 22°C tensile testing and spin tests.

Technical progress

This semi-annual report covers the startup of the ceramic Joining Program, Phase II at Norton Company. The experimental approach for join development and mechanical evaluation have been defined after review of Phase I progress and discussions with production personnel involved with the manufacture of silicon nitride and siliconized silicon carbide. A program schedule with major milestones has been developed and submitted to ORNL.

Certain issues worthy of concern will be addressed during development of silicon nitride joining capability for new join configurations (Tasks 1.2 and 1.4). Phase I joins were of high quality across $20cm^2$ cross sections with the exception of the incomplete densification of the join interface within 1.5mm of the external surface of joined bodies. Elimination of the near surface void will minimize finish grinding of joined components. Improved of the join green strength of joins is desirable to reduce undesirable handling rejections encountered in Phase I.

Methods of joining NT-230 silicon carbide using a slip interlayer will be developed in Tasks 2.1, 2.2 and 2.4 for dense, post-siliconized bodies and unsiliconized bodies with subsequent siliconization. The effect of slip interlayer modification upon the mechanical properties prior and subsequent to siliconization will be studied. Particle size distribution of the slip, method of slip application and the use of additives will be evaluated to obtain a uniform, join interlayer with properties similar to the parent material.

1.1 Si3N4 Butt Joints - Creep Resistance

1.1.1 Creep Resistance Evaluation Procedure

Sample Preparation and Evaluation Conditions

Tensile specimens (Figure 1) ground from the NCX-5101 silicon nitride joins made with a slip interlayer for Phase I model development[1] are undergoing creep evaluation. The NCX-5101 designation refers to a Si_3N_4-4wt% Y_2O_3 of a specific raw material and process used in this program.

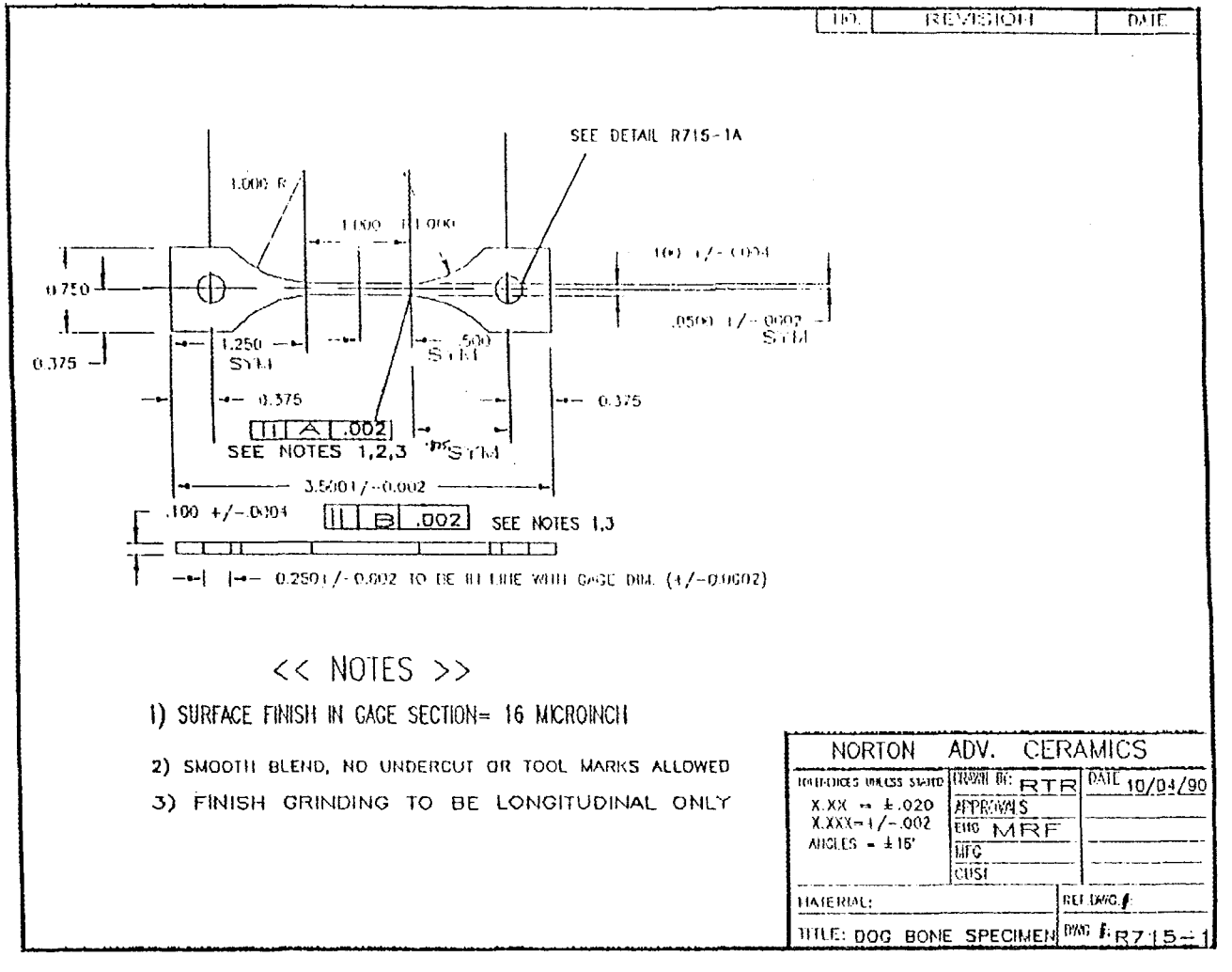

Figure 1: Tensile Creep Specimen

The average gage section and thickness of the tensile specimens are measured prior to testing with a dial caliper to a precision of 0.001 inches. Tensile tests are performed under the following conditions. Completed data with interpretation will be presented in future reports as it is available.

Table 1: Tensile Creep Evaluation Matrix

Temperature (°C)	Stress (MPa)
1250	250
1250	225
1300	225
1300	200
1370	150
1370	140
1370	120
1400	120
1400	100

The desired stress is used to calculate the applied load and the load is then programmed into the ramp profile of the creep testing load controller.

Load Profile - The typical profile includes a pre-load of 20 lbs. The pre-load was maintained throughout the temperature ramp and pre-soak. After 24 hours, the load was ramped at a rate of 50 pounds per minute to 85% of the final load. The rate was then reduced to 25 pounds per minute to the final load and maintained +/- 1 pound for the duration of the test.

Temperature Profile - The furnaces were ramped from 22°C to the temperature of creep evaluation. The furnace was heated to 1200°C at 25°C per minute, then to soak temperature at 10°C per minute, and maintained +/- 1°C to the conclusion of the test.

Laser Extensometer Targets - Multiple laser extensometer targets are positioned about the join to determine the variation of strain rate within the region containing the join as compared with the two regions not containing the join (Figure 2). Two targets positioned at the extremities of the gage section and two targets positioned adjacent to the join provide the comparative strain data.

A modified target[2] (Figure 3) with a 45° bevel slot and the thickness decreased to 1.27mm minimized the tendency for slipping as the gage section elongates. Additionally, a longer moment arm increased the normal force along the line contact and improved the resistance to slipping.

Extensometry - The actual strain is measured with laser dimensional sensors manufactured by Zygo Corporation.[3] Zygo model 1101 sensors were modified for hot object measurement and an increased passline extension for ten to twelve inch transmitter to object separation to accommodate the furnace. The system measurement resolution is 10^{-7}m, and the measurement precision is +/- 1 μm at 1400°C. Both the laser transmitter and receiver are mounted on precision linear translation tables with one inch manual barrel micrometer drives.

The measurement data was conditioned and formatted in the Zygo-1100 processor. The system can be programmed to measure several dimensions simultaneously. Measurements were always taken between the same side of laser target pairs to allow for any uniform dimensional changes of the targets due to oxidation or other reactions at high temperature. This change proved to be more effective than the original unslotted targets.

Data Acquisition - The testing supervisory computer is linked to the Zygo-1100 processor via synchronous RS-232 communication line. The test system control program prompts the 1100 processor for the average of the 100 most recent measurements in a moving queue. The data was

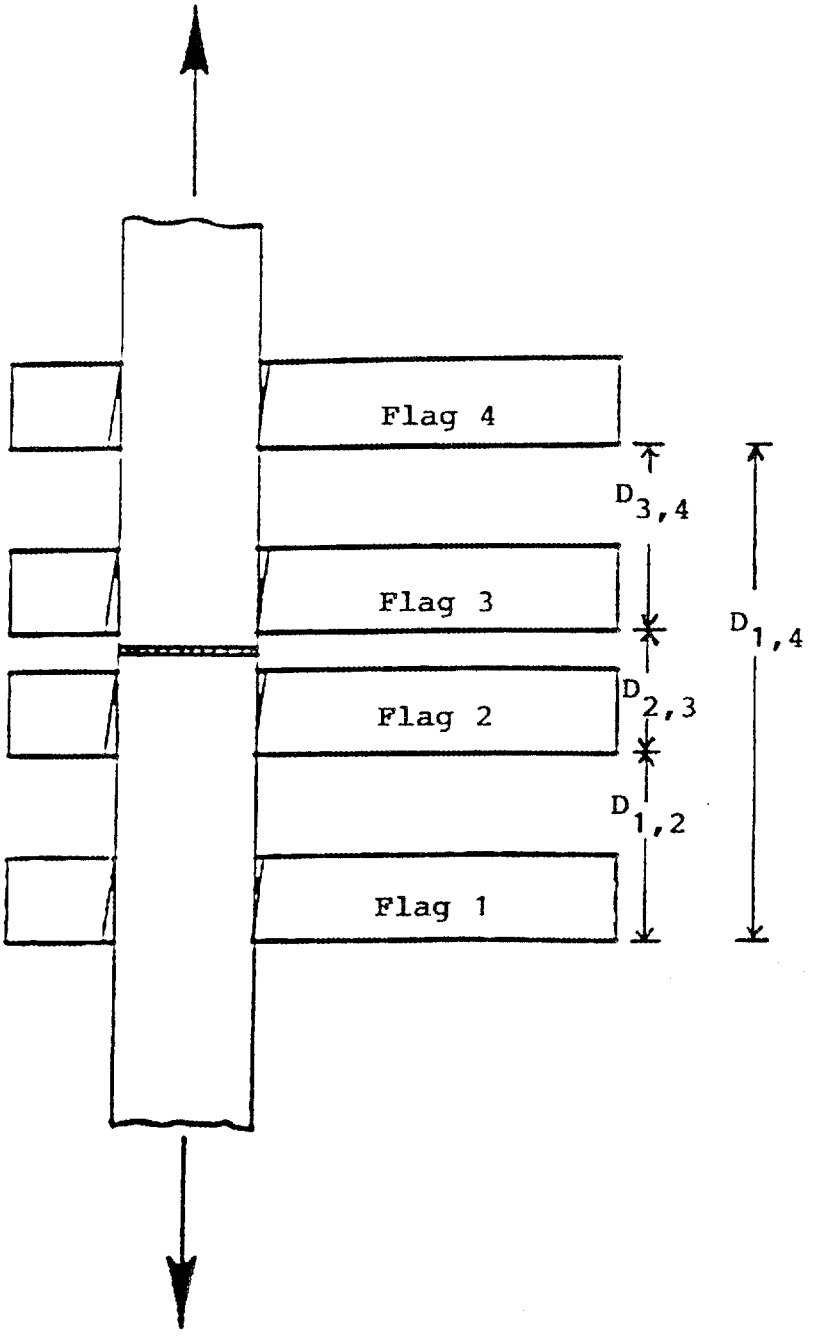

Figure 2: Extensometer Flag Arrangement

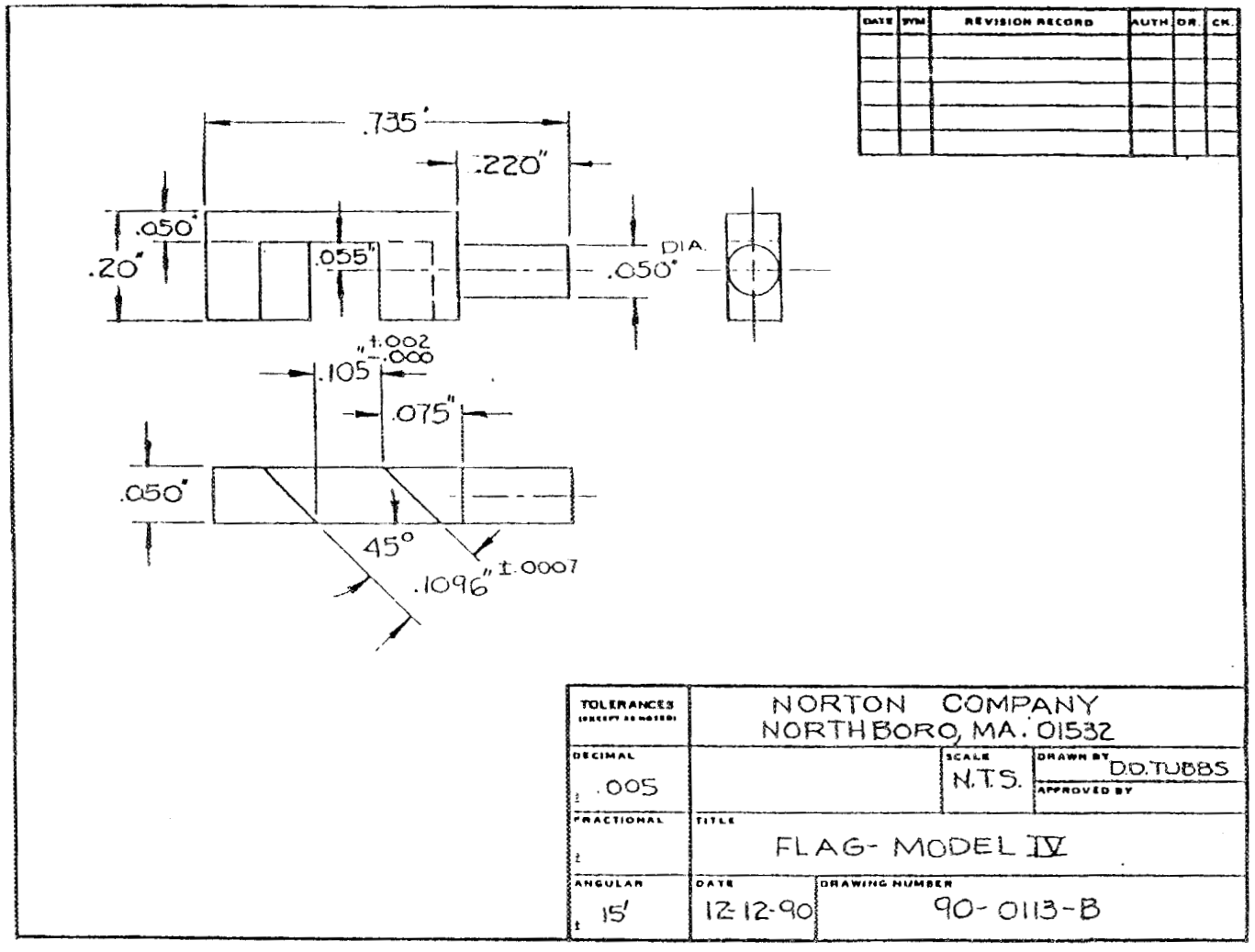

Figure 3: Laser Extensometry Target

parsed and logged into fields with a time stamp. The load was also logged with a time stamp in a separate file or recorded on a stripchart. At the end of a test, the data is run through an RPL procedure in RS/1[4] to check for proper column entry and deletion of errors and empty fields. A preliminary creep strain versus time plot is generated at this time to evaluate the test run. A sample curve of the raw data (Figure 4) displays creep strain for the entire gauge section (*Strain 1-4*) and the region about the join (*Strain 3-4*). The curve labeled *Strain 2-3* is a strain independent target which is sometimes used to record the linearity of the laser system over time. This is useful in distinguishing actual strain related phenomena from logging errors.

1.2 Si_3N_4 Curved Joint - Development

NCX-5101 Si_3N_4 was formed by cold isostatic pressing, green machined into curved shapes and joined in the green state. Three types of join interlayers were used: no slip and two different aqueous slips made with dispersed NCX-5101 powder. The two aqueous slips (A and B) although applied similarly, differ in method of preparation and pre-conditioning of the silicon nitride green joins. The A slip and method of application was formerly used for Joining, Phase I mechanical characterization and analytical modeling[1]; and Task 1.1 of Joining, Phase II. The dense curved silicon nitride joins were fabricated from two sub-components: a disk of 82mm outside diameter and 41mm inside diameter into which a solid cylindrical disk was bonded. The join plane, within the resultant aggregate body, is formed at the contact of the two disks at a diameter of 41mm (Figure 5). Hot isostatic pressing of all joins resulted in bodies of theoretical bulk density.

Microfocus x-radiography of each join indicated complete densification of the join interlayer with the exception of two areas of 1mm x 0.5mm dimension on the type A join at the external surface of the join interlayer.

Mechanical Characterization

Green Shear Strength Testing - Improved green strength is desirable to decrease handling rejections caused by poor green join strength prior to hot isostatic pressing. Join shear strength was measured after a pre-sintering step, prior to hot isostatic pressing using a shear fixture manufactured of alpha silicon carbide (Figure 6). A hollow load ring of larger inner diameter than the join interlayer was used to support the joined disk while a load was applied to the center of the join with a solid cylindrical disk. The top face of the upper load disk was curved to minimize bending moments. The entire assembly was placed upon a platen and a Instron Model 4206 test frame was used at a cross-head speed of 0.50mm/min to apply the load until failure. Failure was defined by a sudden decrease of applied load plotted as a function of cross-head displacement. The failure load divided by the area of the join interlayer yielded shear strength (Table 2).

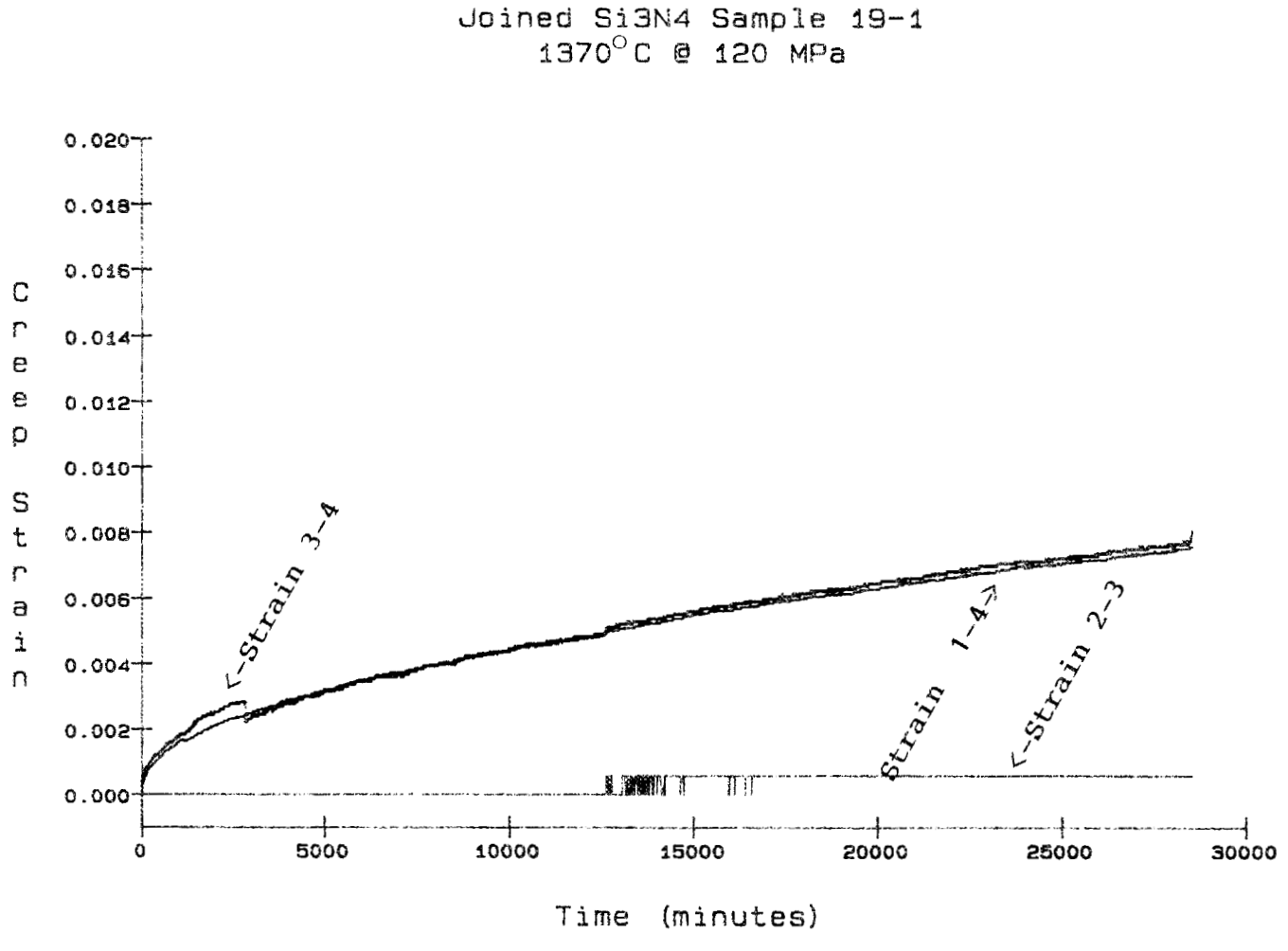

Figure 4: Creep Strain as a Function of Time

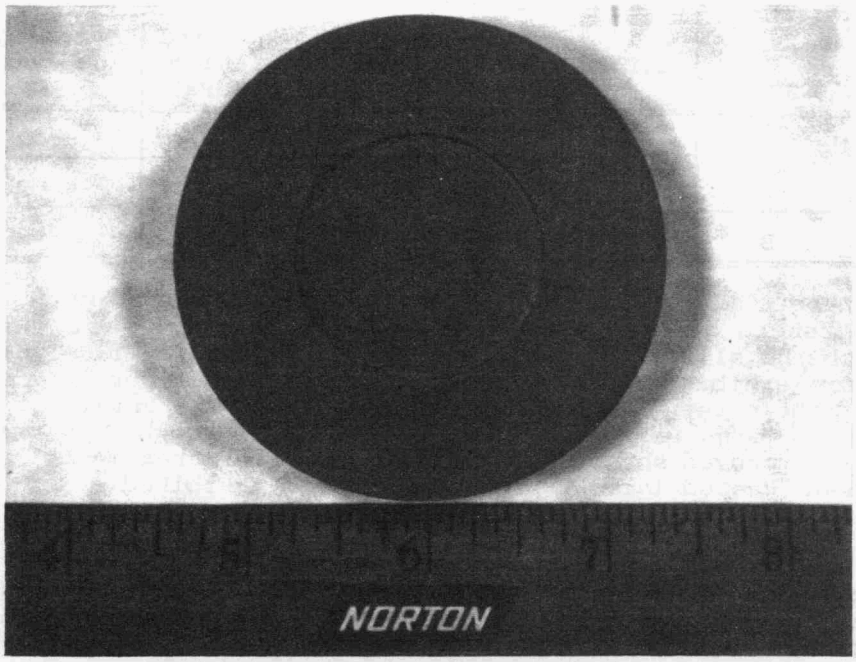

Figure 5: NCX-5101 Silicon Nitride Curved Join

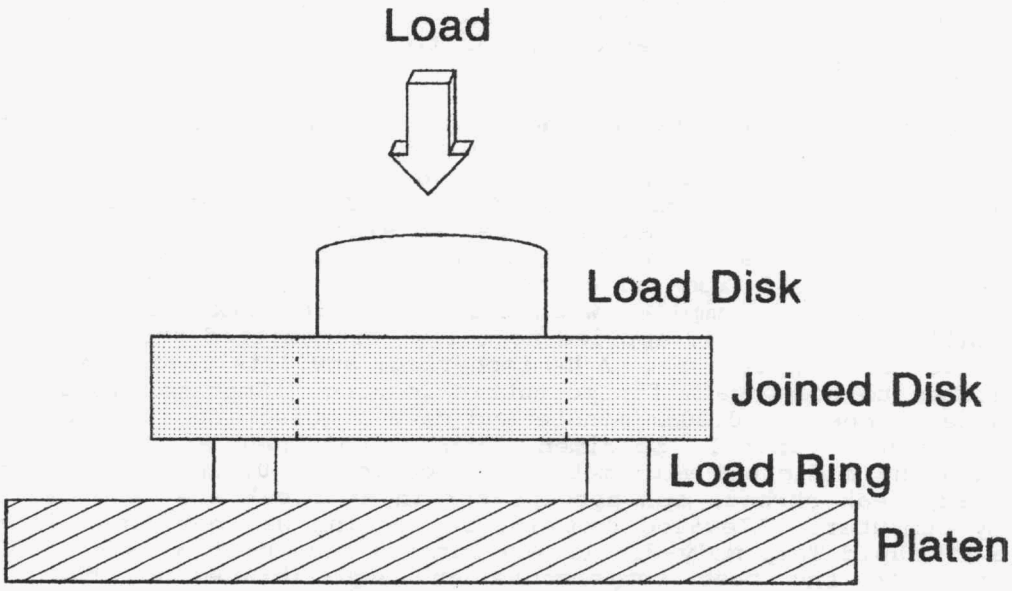

Figure 6: Shear Test Configuration

Table 2: Green Silicon Nitride Curved Join Shear Strength

Slip Type	Join I.D.	Mean Green Shear Strength (kPa)	Standard Deviation (MPa)	Quantity Tested
No Slip	8,9	589.8	121.8	2
A	5,6	330.9	81.3	2
B	2,3	1831.3	515.9	2

The type B slip join interlayer provided a significant improvement in green strength over no slip and type A join interlayer. The type A joins and the no slip joins failed at the join interlayer. Type B joins after failure exhibited separation at the join interlayer in addition to fracture of the external and internal join disk. The origin of fracture for the type B joins is uncertain. However, it is known that the B joins had markedly improved shear strength over the other treatments. Analysis of post shear tested type A join interlayers exhibited a powdery slip residue that was easily removed. Slip residue of type B join interlayers was firmly bonded to the parent materials.

Flexure Specimen Preparation - All joins were diamond sectioned after x-ray microfocus radiography for optical inspection to determine join integrity (Figure 7 and 8). The slip A join and no slip join both exhibit incomplete densification of the join interlayer at the external surface of the joins (Figure 9 and 10). Sectioned surfaces of the slip B join were apparently completely dense. The slip B join could be observed as a dark line (Figure 11), while the dense regions of the slip A and no slip joins were not optically detected.

Additional diamond grinding yielded 12 flexure specimens per each curved join. All flexure specimens were made and tested according to the MIL-STD-1942 (MR) A geometry specifications. The join plane was located at the center of the bar, perpendicular to the longitudinal (tensile) axis of the specimen.

Fast Fracture Flexural Testing - All flexural tests utilized the MIL-STD-1942 (MR) Specimen Size A. Room temperature testing utilized a Sintech Model 1 test frame. An Instron 4206 test frame was used for high temperature tests. All flexure tests for join development used an outer span of 20mm and an inner span of decreased size, 5mm, on a rolling pin fixture to increase the probability of failure within the join. Flexure fixtures manufactured from silicon carbide (NC-203) were modeled after the Quinn design and complied with 1942(MR). The fixture is mounted horizontally with the load applied normally, transmitted through a ball bearing, at room temperature. A hemispherical anvil is used at elevated temperatures to compensate for eccentric loading. Specimen loading at a cross-head speed of 0.20mm/minute and data acquisition is handled by automated machine control. Specimen width and thickness are measured and recorded using a digital micrometer to accuracy of 0.01mm. Peak load, break load, peak stress, and percent strain at break are recorded and saved by computer. Elevated temperature testing was performed in air using a CM Rapid Temp moly-disilicide furnace heated at a rate of 50°C per minute to the test temperature and equilibrated at the test temperature for 10 minutes prior to testing. The test apparatus has been evaluated and approved by representatives of ORNL/HTML.

The results of 22°C and 1370°C flexure strength tests of the curved silicon nitride joins are summarized in Tables 3 and 4. The small quantity tested of each join type was low and analysis is preliminary.

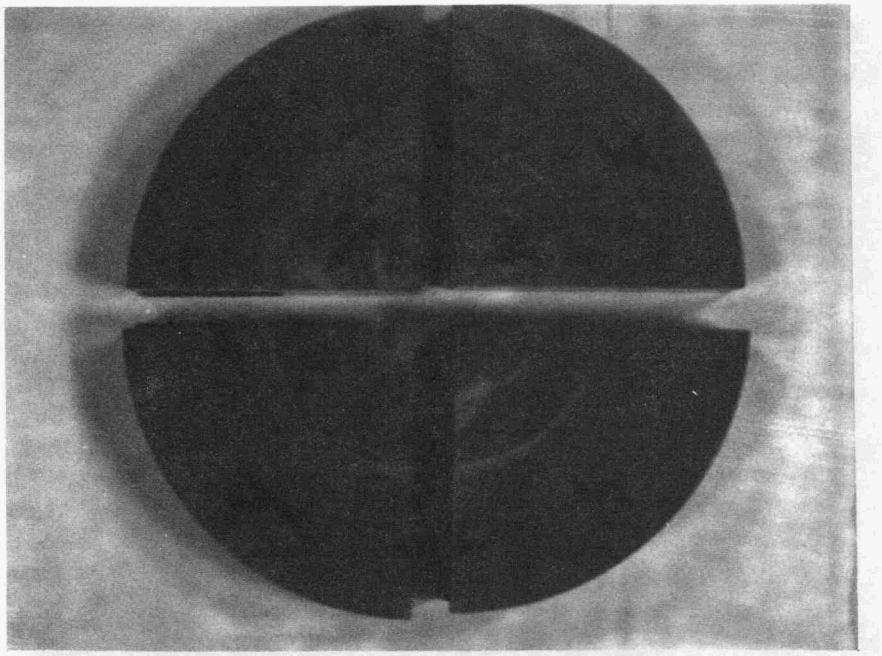

Figure 7: Sectioned NCX-5101 Silicon Nitride Curved Join

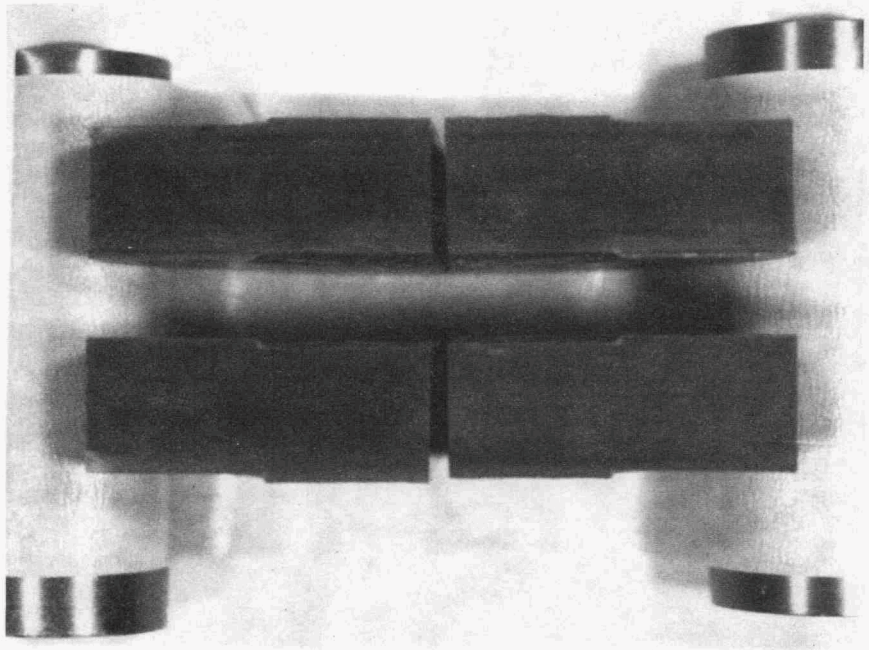

Figure 8: Cross Section of NCX-5101 Silicon Nitride Curved Join

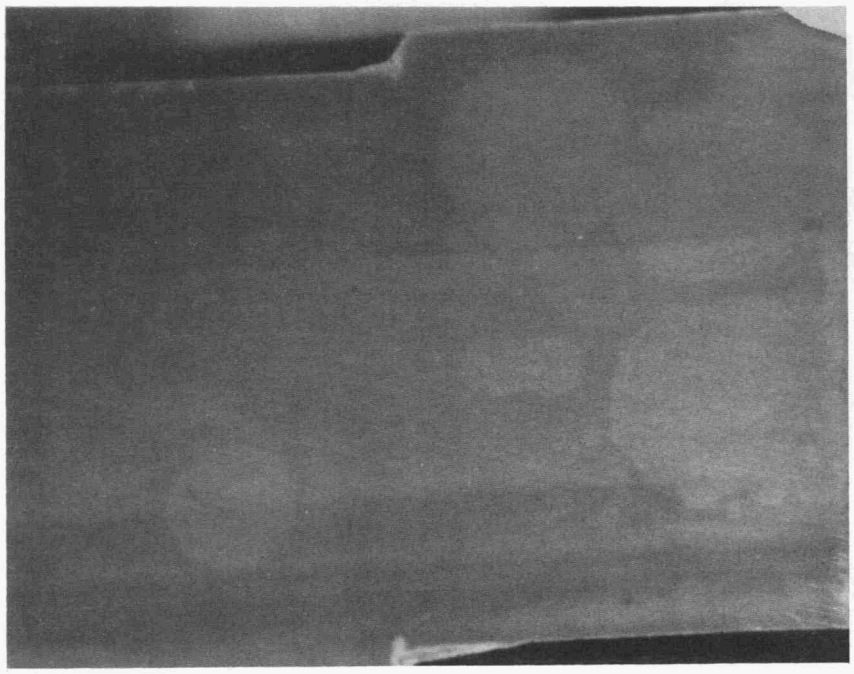

Figure 9: NCX-5101 Silicon Nitride Curved Join Section With Type "A" Slip Interlayer

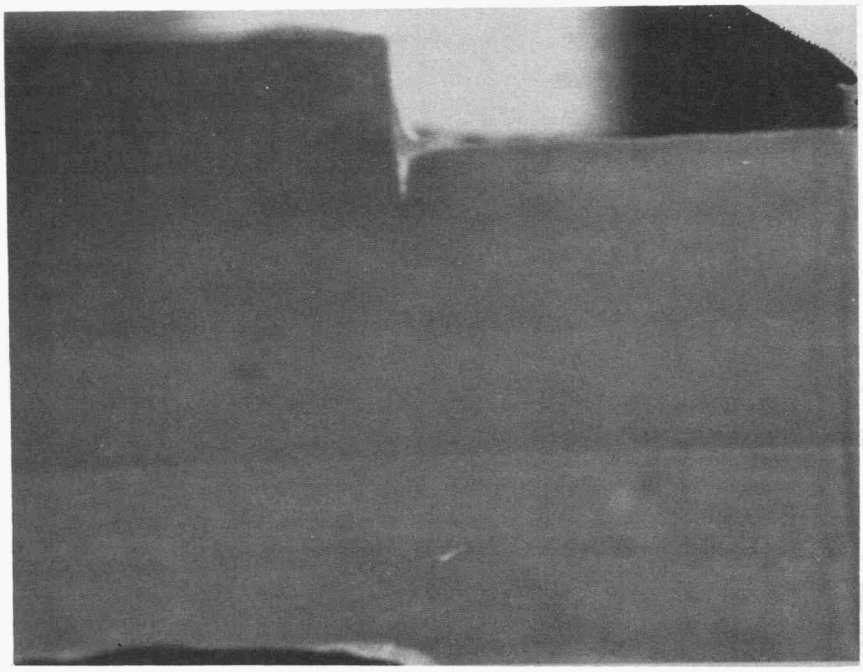

Figure 10: NCX-5101 Silicon Nitride Curved Join Section With No Slip Interlayer

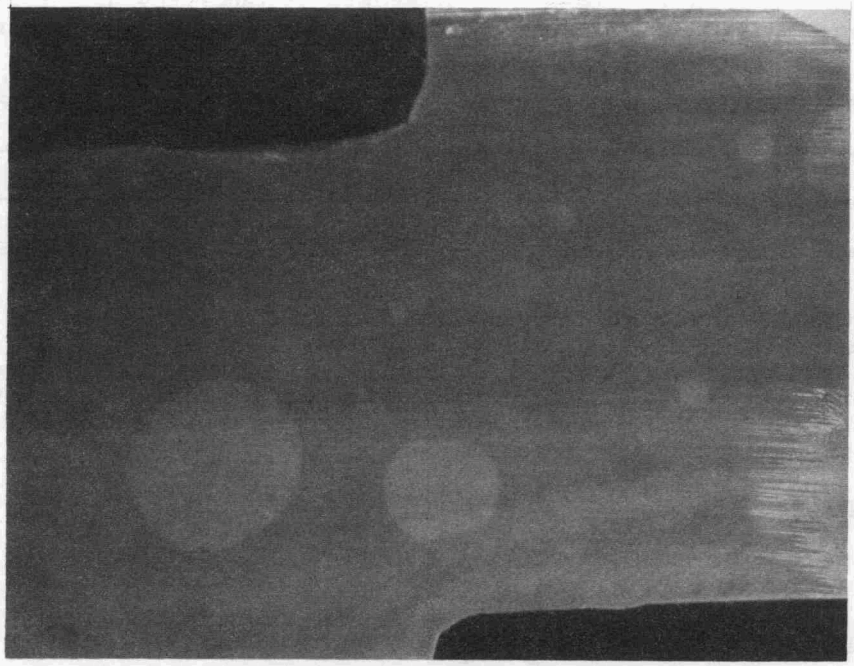

Figure 11: NCX-5101 Silicon Nitride Curved Join Section With Type "B" Slip Interlayer

Table 3: Silicon Nitride Curved Join Flexure Strength at 22°C

Slip Type	Join I.D.	Mean Flexure Strength (MPa)	Standard Deviation (MPa)	Quantity Tested	Join Failures
B	1	771	108	6	0
A	4	832	130	5	1
No Slip	7	722	132	7	3

Table 4: Silicon Nitride Curved Join Flexure Strength at 1370°C

Slip Type	Join I.D.	Mean Flexure Strength (MPa)	Standard Deviation (MPa)	Quantity Tested	Join Failures
B	1	626	28	5	1
A	4	623	28	6	0
No Slip	7	582	30	4	1

Tentatively, there was an insignificant statistical difference between the 22°C and 1370°C flexure strengths of each type of joining method. However, the joins manufactured without slip exhibited the lowest mean flexure strength and the highest frequency of failures within the join interlayer at 22°C and 1370°C. Additional join manufacture and testing are in progress to provide more conclusive analysis.

Status of milestones

Tasks 2.1a,b were delayed due to billet manufacture. The overall work package remains unaffected.

Publications

None

References

1. M.R. Foley, G.A. Rossi, G.J. Sundberg, J.A. Wade, F.J. Wu, *Analytical and Experimental Evaluation of Joining Silicon Carbide to Silicon Carbide and Silicon Nitride For Advanced Heat Engine Applications, Final Report, Subcontract 86X-SB045C*, Norton Company, September 30, 1991, 56-86.

2. M.R. Foley et al, *Analytical and Experimental Evaluation of Joining*, 44.

3. Zygo Corporation, Laurel Brook Road, P.O. Box 488, Middlefield, CT, 06455-0448.

4. RS/1 is a trademark of BBN Software Products, 10 Fawcett St., Cambridge, MA 02138.

2.0 MATERIALS DESIGN METHODOLOGY

INTRODUCTION

This portion of the project is identified as project element 2 within the work breakdown structure (WBS). It contains three subelements: (1) Modeling, (2) Contact Interfaces, and (3) New Concepts. The subelements include macromodeling and micromodeling of ceramic microstructures, properties of static and dynamic interfaces between ceramics and between ceramics and alloys, and advanced statistical and design approaches for describing mechanical behavior and for employing ceramics in structural design.

The major objectives of research in Materials Design Methodology elements include determining analytical techniques for predicting structural ceramic mechanical behavior from mechanical properties and microstructure, tribological behavior at high temperatures, and improved methods for describing the fracture statistics of structural ceramics. Success in meeting these objectives will provide U.S. companies with methods for optimizing mechanical properties through microstructural control, for predicting and controlling interfacial bonding and minimizing interfacial friction, and for developing a properly descriptive statistical data base for their structural ceramics.

2.1 MODELING

2.1.1 Modeling

Microstructural Modeling of Cracks - J.A.M. Boulet (University of Tennessee, Knoxville)

Objective/scope

The goal of the study is to develop mathematical procedures by which existing design methodology for brittle fracture could accurately account for the influence of protrusion interference on fracture of cracks with realistic geometry under arbitrary stress states. To predict likelihood of fracture in the presence of protrusion interference, a simulation will be developed. The simulation will be based on a three-dimensional model of cracks with realistic geometry under arbitrary stresses.

Technical progress

During the past six months, effort has been focused on two computer codes, BRIDGE and DDID, discussed in previous reports[1]. The progress made on each code is discussed below.

As reported previously,[2] the DDID code has not yet performed correctly for nonplanar cracks. Many possible sources of this discrepancy have been eliminated, and the likely source of the problem has been isolated. A suitable repair is under development.

All of the various matrices that must be calculated by the BRIDGE code,[3] have been programmed and are being tested. (Details of the calculations for one of the matrices have been reported.[2]) The test problem is a solid cube with an embedded rectangular crack. The centroids of the crack and the cube coincide, and the crack plane is parallel to two opposing faces of the cube. The loading is uniform tension on these two opposing cube faces. When the crack is absent, the problem is solved by the code BINTEQ.[4] When the cubical boundary is absent (the crack domain is infinite), the problem is solved by DDID.[5] When both the crack and the cubical boundary are present, the problem is solved by the BRIDGE code. Results of this code are being analyzed to verify that certain expected behavior is observed. For instance, if the crack is much smaller than the cube, the displacements of the crack should approach those of the DDID solution and displacements of the cubical boundary should approach those of the BINTEQ solution. Also, if the tension and the size of the cube are held fixed as the crack increases in size, displacement of the loaded faces of the cube should increase. Once it is verified that these and other expected results have been obtained, the BRIDGE code will be tested on some embedded crack problem for which quantitative results have already been obtained analytically or by the finite element method.

References

1. J. A. M. Boulet, " Microstructural Modeling of Cracks," in *CTAHE Project Bimonthly Technical Progress Report to DOE Office of Transportation Systems, February-March, 1992*, Oak Ridge National Laboratory, Oak Ridge, Tennessee, 1992.

2. J. A. M. Boulet, " Microstructural Modeling of Cracks," pp. 211-213 in *CTAHE Project Bimonthly Technical Progress Report to DOE Office of Transportation Systems,*

October-November, 1991, ORNL/CF-91/375, Oak Ridge National Laboratory, Oak Ridge, Tennessee, 1991.

3. J. A. M. Boulet, " Microstructural Modeling of Cracks," pp. 217-219 in *CTAHE Project Semiannual Progress Report for April 1991 through September 1991*, ORNL/TM-11984, Oak Ridge National Laboratory, Oak Ridge, Tennessee, 1992.

4. T. A. Cruse, "Numerical solutions in three dimensional elastostatics," *Int. J. Solids Struct.* 5(12), 1259-1274 (1969).

5. T. A. Cruse and G. Novati, "Traction-BIE Solutions for non-planar and surface cracks," presented at 22nd National Symposium on Fracture Mechanics, June 26-28, Atlanta, Georgia, 1990.

Status of milestones

Work is behind schedule.

2.2 CONTACT INTERFACES

2.2.1 Static Interfaces

Elastic Properties and Adherence of Thin Films and Coatings

Debra Joslin (Department of Materials Science and Engineering,
The University of Tennessee)

Objective/Scope

The objective of this research is the examination of the effects of ion bombardment on the structure of thin ceramic films on ceramic substrates. The material combinations will include oxide films that have (a) no solid solubility, (b) limited solid solubility, and (c) complete solid solubility with the substrate material (also an oxide). Techniques for determination of elastic and plastic properties of thin films or coatings on ceramic substrates and for the determination of the strength of the bond between the film and substrate, which are currently being developed, will be used to determine the hardness, elastic modulus, and adherence of each material combination. The main testing techniques will be the ultra-low load microindentation tester (Nanoindenter), and thermal cycling tests.

Technical Highlights

Metal films (Cr or Zr) were grown on sapphire (Al_2O_3) to thicknesses of approximately 50 nm by electron beam evaporation. These samples were implanted at room temperature with 320 keV Kr ions to fluences of 1×10^{16} and 1×10^{17} ions-cm^{-2}. The energy was chosen such that the maximum energy deposition occurs at the film/substrate interface. To retain a portion of unimplanted film, an area of each sample was masked during the implantation. Rutherford backscattering spectrometry (RBS) was performed on each of the samples to look for mixing of the metal film and the Al_2O_3.

After bombardment, no mixing of the Cr and Al_2O_3 was observed by RBS analysis at either fluence. However, some mixing of the Zr and Al_2O_3 was observed after bombardment to both fluences. From the spectra shown in fig 1 , it is evident that some sputtering of the Cr film has occurred during bombardment--the peak width of the Cr signal has narrowed, and the Al edge has moved to higher energy. The results are similar for implantation to 1×10^{16} Kr-cm^{-2} (not shown). From the spectra in fig. 2, chemical mixing has occurred in the Zr/Al_2O_3 system. The leading edge of the Al signal has moved toward higher energy, while the trailing edge of the Zr signal has moved toward lower energy. The height of the Zr signal has decreased, indicating that either some Zr was lost, or that another species (eg., O or Al) has been incorporated into the film. This is also evident from the spectra for implantation to 1×10^{16} Kr-cm^{-2} (not shown) Examination of the sample implanted to 1×10^{17} Kr-cm^{-2}.by scanning electron microscopy shows that the surface of the film is considerably roughened; however, preliminary data obtained from x-ray photoelectron spectroscopy (XPS) shows that the substrate is not exposed through pinholes, tears, etcetera.

The sample which had been implanted to a fluence of 1×10^{17} Kr-cm^{-2} was depth profiled using x-ray photoelectron spectroscopy (XPS). The spectra obtained reveal the presence of metallic Zr and Al, as well as their oxides ZrO_2 and Al_2O_3 near the film/substrate interface (fig. 3). Aluminum oxide is also found near the surface of the sample. Subsequent scanning electron microscopy on the sample revealed many pinholes in the film through which the Al_2O_3

substrate may be detected by XPS. The unimplanted area of the film will be depth profiled at a later date. If deoxidized Al is present near the interface in the unimplanted region, then the deoxidation is not the result of ion mixing.

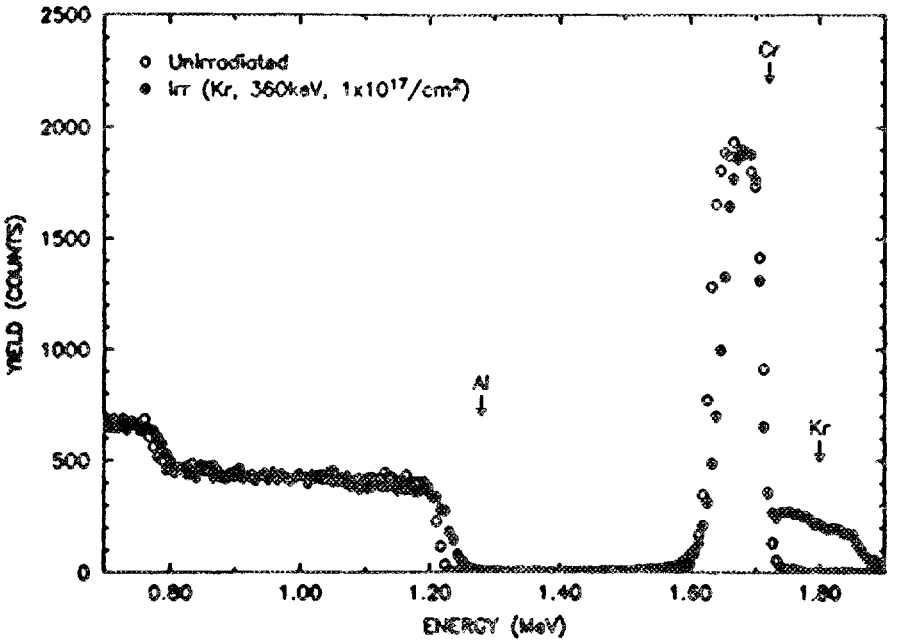

Figure 1. Rutherford backscattering spectra for a Cr film on Al_2O_3 showing spectra for an unimplanted region and a region implanted with 320 keV Kr to a fluence of 1 x 10^{17} ions-cm^{-2}.

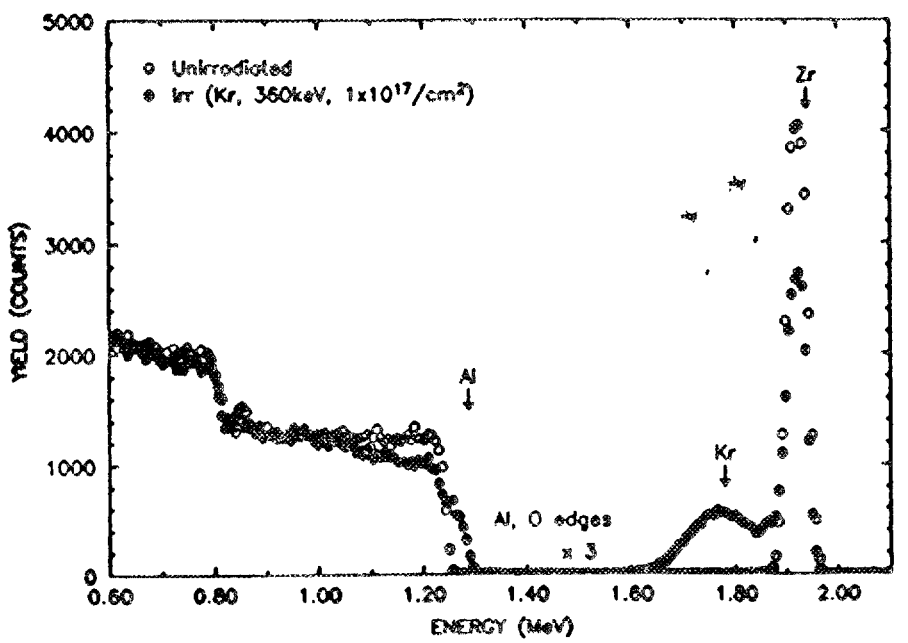

Figure 2. Rutherford backscattering spectra for a Zr film on Al_2O_3 showing spectra for an unimplanted region and a region implanted with 320 keV Kr to a fluence of 1 x 10^{17} ions-cm^{-2}.

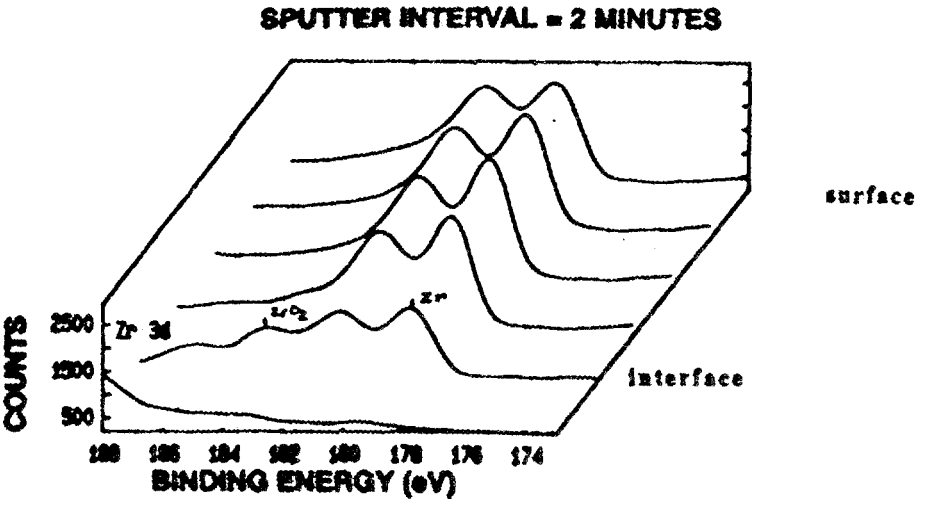

Figure 3. X-ray photoelectron spectra for a Zr film on Al_2O_3. Note the presence of metallic Zr and Al, as well as their oxides ZrO_2 and Al_2O_3 near the film/substrate interface.

Also during this report period, oxide films (Cr_2O_3 or ZrO_2) were grown on sapphire (Al_2O_3) to thicknesses of approximately 80 nm by rf sputter deposition. These samples were implanted at 825 C with 475 keV Kr ions to fluences of 5×10^{16} and 8×10^{16} ions-cm^{-2}. The energy was chosen such that the maximum energy deposition occurs at the film/substrate interface. To retain a portion of unimplanted film, an area of each sample was masked during the implantation. Rutherford backscattering spectroscopy (RBS) was performed on each of the samples to look for mixing of the film and the Al_2O_3.

After bombardment, approximately 40% of the films had been sputtered away during the implantation. Thus, no mixing could be distinguish in the RBS spectra. Depth profiling using x-ray photoelectron spectroscopy (XPS) will be perfomed during the next report period to determine whether any mixing took place.

Sample preparation for transmission electron microscopy of specimens previously irradiated and reported on in earlier progress reports is ongoing.

Status of Milestones

N/A

Publications

None

2.2.2 Dynamic Interfaces

Studies of Dynamic Contact of Ceramics and Alloys for Advanced Heat Engines - P. A. Gaydos and K. F. Dufrane (Battelle)

Objective/Scope

The objective of the program is to develop an understanding of the friction and wear processes of ceramic interfaces based on experimental data. The supporting experiments are to be conducted at temperatures to 650 C under reciprocating sliding conditions reproducing the loads, speeds, and environment of the ring/cylinder interface of advanced engines. The test specimens are to be carefully characterized before and after testing to provide detailed input to the model. The results are intended to provide the basis for identifying solutions to the tribology problems limiting the development of these engines.

Technical Highlights

Apparatus

The apparatus developed for this program primarily uses specimens of a flat-on-flat geometry, which facilitates specimen procurement, finishing, and testing. The apparatus reproduces the important operating conditions of the piston/ring interface of advanced engines. The specimen configuration and loading is shown in Figure 1. A crown with a 32 mm radius is ground on the ring specimen to ensure uniform contact. The ring specimen holders are pivoted at their centers to provide self-alignment. A chamber surrounding the specimens is used to control the atmosphere and contains heating elements to control the temperature. The exhaust from a 4500 watt diesel engine is heated to the specimen temperature and passed through the chamber to provide an atmosphere similar to that of actual diesel engine service. A summary of the testing conditions is presented in Table 1.

Wear Testing

The current direction of this program is to conduct wear tests with a variety of advanced coatings on actual engine components instead of using specially prepared specimens. Caterpillar, Inc. has been supplying the components under a related subcontract. Cutting specimens from components removes the manufacturing variability that might be encountered when preparing the specimens. In order to run wear tests using sections of actual piston rings and cylinder liners, a means of holding the narrow, curved ring sections was needed. It was decided to use the ring groove in a piston to hold the ring sections. A piston was obtained and a slice containing the top ring groove was removed. Small plates were tacked on the ends of each holder to

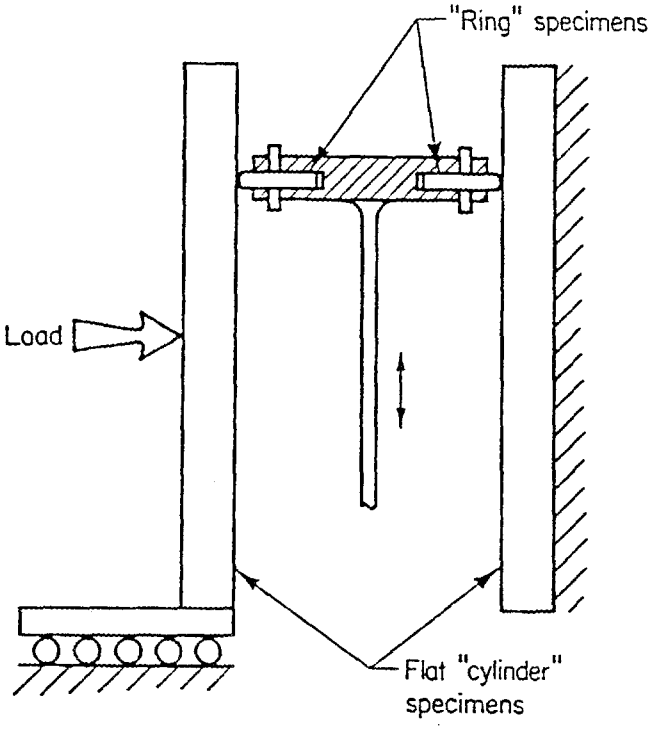

FIGURE 1. TEST SPECIMEN CONFIGURATION AND LOADING

TABLE 1. SUMMARY OF TESTING CONDITIONS

Sliding Contact:	Dual flat-on-flat
"Cylinder" Specimens:	12.7 x 32 x 127 mm
"Ring" Specimens:	3.2 x 19 x 19 mm
"Ring" crown radius:	32 mm
Motion:	Reciprocating, 108 mm stroke
Reciprocating Speed:	500 to 1500 rpm
Average Specimen Speed:	1.8 x 5.4 m/s
Load:	to 950 N
Ring Loading:	to 50 N/mm
Atmosphere:	Diesel exhaust or other gases
Measurements:	Dynamic friction (during test) Specimen wear (after test)

capture the ring section as shown in Figure 2. The outer radius of the piston segment was reduced so that the ring section protruded from the holder when it was seated in the bottom of the groove.

Baseline wear tests with ring and cylinder liner specimens supplied by Caterpillar were obtained during this reporting period. Tables 2 and 3 summarize the wear results for the two coatings. The wear rates of both the cermet and the aluminum titanate ring coatings averaged 1×10^{-7} $mm^3/N\text{-}m$ for the 260 C temperature tests. The lower temperature tests resulted in wear rates which were three times lower on average. Higher oil viscosity at lower temperatures is presumably the reason for the difference.

Tests were to be conducted with additional ring materials for a comparison with the baseline obtained above. One such ring material was recently supplied for testing. Unfortunately, it was provided in the form of a second compression ring and would not fit the set of curved ring specimen holders made from the top ring groove. New ring specimen holders were made from sections containing the second ring groove, but several attempts to align them properly in the rig have been unsuccessful. No meaningful wear results have been obtained thus far; additional work will be conducted later if possible.

Three ring coatings that showed promise in work by Cummins Engine have been ordered for additional wear testing. The coatings purchased are listed below.

Coating	Supplier
• "100 % dense" Cr_2O_3	BIRL
• 88/12 WC-Co	Turbine Metal Technology
• 80/20 Cr_3C_2-NiCr	Turbine Metal Technology

The surfaces of these coatings will all be lapped before testing.

Status of Milestones

The study is progressing in accordance with the overall milestone schedule.

Publications

None.

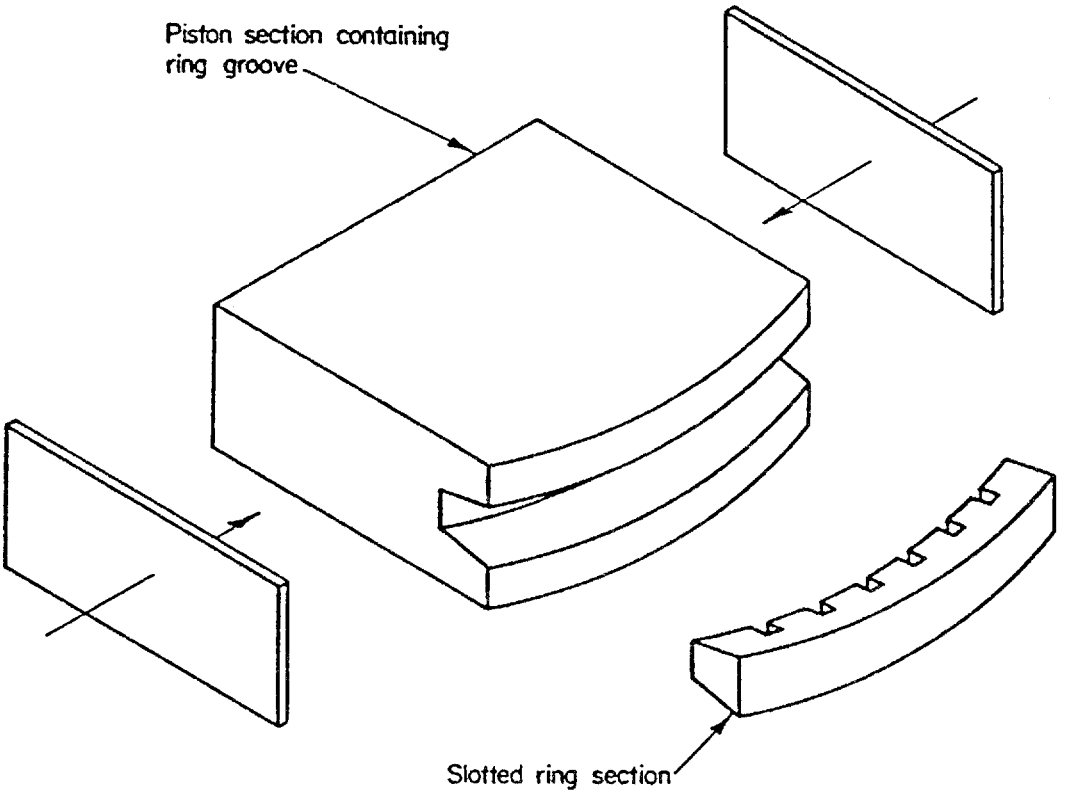

FIGURE 2. CURVED RING SPECIMEN HOLDER

TABLE 2. WEAR RATES OF CERMET (KP107E) RING COATINGS ON SCA COATED CYLINDER LINERS

Test Number & Portion	Test Temperature (°C)	Run Duration (Min.)	Wear Rate of Specimen in Left Position (mm^3/N-m)	Wear Rate of Specimen in Right Position (mm^3/N-m)	Average Wear of Both Specimens (mm^3/N-m)
95a	25	60	4×10^{-8}	4×10^{-8}	4×10^{-8}
96a	25	60	4×10^{-8}	*	4×10^{-8}
b	260	240	1×10^{-7}	*	1×10^{-7}
97a	25	60	4×10^{-8}	1×10^{-8}	3×10^{-8}
b	260	240	2×10^{-7}	9×10^{-8}	1×10^{-7}
98a	25	60	2×10^{-8}	1×10^{-8}	2×10^{-8}
b	25	240	2×10^{-8}	1×10^{-8}	2×10^{-8}
c	260	120	6×10^{-8}	1×10^{-7}	8×10^{-8}

Test conditions: SDL-1 lubricant, 500 rpm, 10.3 N/mm ring loading

*Right specimen became misaligned during run and wore unevenly

TABLE 3. WEAR RATES OF ALUMINUM TITANATE (KP123) RING COATINGS ON SCA COATED CYLINDER LINERS

Test Number & Portion	Test Temperature (°C)	Run Duration (Min.)	Wear Rate of Specimen in Left Position (mm^3/N-m)	Wear Rate of Specimen in Right Position (mm^3/N-m)	Average Wear of Both Specimens (mm^3/N-m)
99a	25	60	5×10^{-9}	7×10^{-8}	4×10^{-8}
b	260	240	1×10^{-7}	1×10^{-7}	1×10^{-7}
100a	25	60	2×10^{-7}	1×10^{-8}	1×10^{-7}
b	260	240	8×10^{-8}	9×10^{-8}	8×10^{-8}

Test conditions: SDL-1 lubricant, 500 rpm, 10.3 N/mm ring loading

Development of Standard Test Methods for Evaluating the Wear Performance of Ceramics

P. J. Blau (Oak Ridge National Laboratory)

Objective/scope

The goal of this effort is to improve consistency in reporting ceramic wear data by helping to develop one or more standard test methods for quantitatively determining the wear resistance of structural ceramics, in reciprocating sliding, a type of motion which is experienced by several types of engine wear parts. Initial contact with American Society for Testing and Materials (ASTM) Committee C-28 on Advanced Ceramics indicated that there was interest in this activity, but wear-test development normally falls within the scope of ASTM's G-2 committee on "Wear and Erosion." P. J. Blau chairs Task Group G02.40.07, "Reciprocating Sliding Wear Testing," within the G-2 committee, and is tailoring that standard test method specifically for ceramics.

Technical highlights

During this period, we: (a) obtained specimen materials, (b) assembled test kits, (c) confirmed the list of round-robin testing participants and mailed test kits to them, and (d) conducted tests on the effect of specimen-handling procedures (i.e., cleaning and weighing) on friction behavior and wear measurement accuracy. In addition, a series of special, ORNL-designed specimen ball clamps were machined to be sent with the test kits to allow the owners of commercial, Cameron-Plint wear machines to use the size ball we supplied.

Specimen Materials. Two types of materials were selected for the round-robin testing program: tool steel and silicon-nitride ceramics. The tool steel specimens are of two types: M-50 tool steel for the slider ball specimen, and 0-1 tool steel for the flat specimens. Bearing-grade, Norton Noralide NBD 200 balls were purchased from Norton Company to be used with flat specimens of sintered, reaction-bonded silicon nitride (SRBSN) contributed by Eaton Corporation.

Test Kit Assembly. Each test kit used for the round-robin testing program contains the following:

- 1 tool steel ball and 2 tool steel flats,
- 1 silicon nitride ball and 2 silicon nitride flats,
- 1 set of instructions (testing protocol),
- 2 forms to use for reporting raw data, and
- 1 special ball clamp and machining drawings for same.

Tool steel flats were packed in a protective oil to reduce corrosion problems during shipping. Each ball and flat specimen was numbered. A computer spreadsheet was set up to track the location of specific specimens, dates, and the status of testing.

Participants. The following have agreed to participate in the round-robin testing program and have been sent kits:

Dr. Howard Hawthorne, National Research Council of Canada
Mr. Glenn Elliott, Caterpillar Tech Center

Mr. Peter Vernia, General Motors Research and Environmental Staff
Dr. Malcolm Naylor, Cummins Engine Company
Mr. Ken Budinsky, Eastman Kodak Company
Mr. Alex Alliston-Greiner, Cameron-Plint, United Kingdom (U.K.)
Mr. Carlton Rowe, Mobil Research

ORNL will also participate using a standard test kit packed like the others. Additional participation by the National Institute for Standards Testing (NIST) and the National Physical Laboratory (U.K.) is being considered. Kits were mailed in early May 1992, one week later than the expected April 30, 1992, date of milestone #222203. It is anticipated that test results will begin coming in during July and August 1992. It is hoped that the statistical analysis of test data will be complete by the subsequent ASTM G-2 committee meeting in December 1992.

Specimen Cleaning and Handling. When developing a new wear-test standard, attention to specimen cleaning and handling procedures is important. Experiments were conducted to determine whether it was necessary to take special precautions (i.e., wear clean gloves and use tongs) when handling the test specimens. A series of reciprocating friction experiments with tool steel pairs and silicon-nitride sliding pairs was conducted. Dry sliding with clean specimens was compared with tests in which the ball specimen or the flat specimen was rubbed on an individual's thumb prior to testing. Figure 1 shows that the effect of skin oil and perspiration had a much larger and more prolonged effect when the flat specimen was contaminated than when the ball specimen was contaminated. The greasy, flat friction coefficients of about 0.1 agree well with published values for the friction of greasy materials in general. It was determined, however, that as long as clean hands were used, there was no effect on wear measurements in which weighing with an analytical balance was involved. In general, as long as proper care is taken, extraordinary specimen-handling procedures seem not to be required for the subject test method.

Future Plans

During the next period, we will conduct tests using a standard test kit. In addition, we have acquired special ASTM software for evaluating round-robin test data, and we will compare the results of this software with other software we obtained from NIST to do the same sort of evaluation.

References

None.

Status of milestones

Completed milestone 222203, Distribute first specimen set to round-robin participants (5/8/92).

ORNL-DWG 92-11821

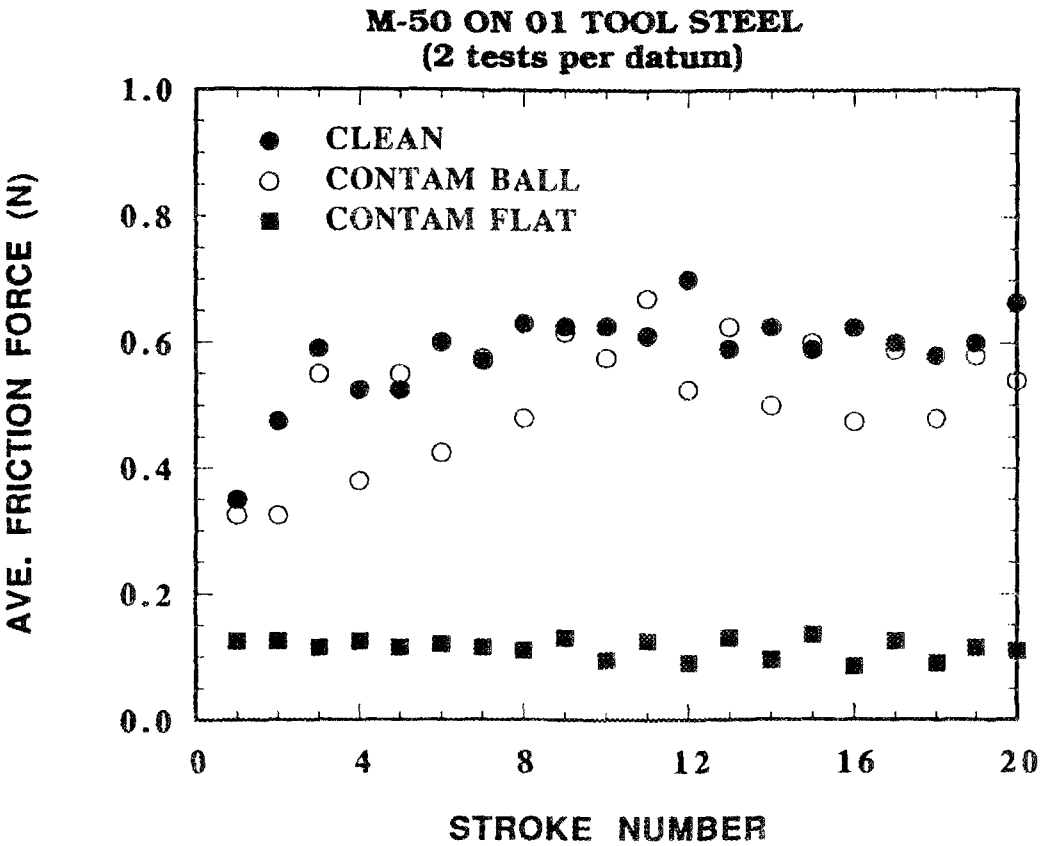

Fig. 1. The effect of various types of specimen contamination on the friction force of M-50 tool steel sliding on 01 tool steel. "Clean" means both ball and flat specimen were tested after solvent cleaning. "Contam Ball" means the slider specimen was rubbed on the investigator's thumb before testing. "Contam Flat" means the 01 tool steel flat specimen was rubbed with a thumb prior to testing. Clearly, the handling of the slider specimen was less noticeable than finger oil on the flat specimen.

Publications/presentations

Presentation: P. J. Blau, R. L. Jackson, and C. S. Yust, "Specimen Cleaning Effects on the Friction Break-in Behavior in Sliding Wear Tests," ASTM G-2 Committee's Workshop on Selection and Use of Specimen Cleaning Methods for Wear Testing, Louisville, Ky, June 17, 1992.

2.3 NEW CONCEPTS

Advanced Statistical Concepts of Fracture in Brittle Materials
C. A. Johnson and W. T. Tucker (General Electric Corporate Research and Development)

Objective/Scope

The design and application of reliable load-bearing structural components from ceramic materials require a detailed understanding of the statistical nature of fracture in brittle materials. The overall objective of this program is to advance the current understanding of fracture statistics, especially in the following four areas:

- Optimum testing plans and data analysis techniques.
- Consequences of time-dependent crack growth on the evolution of initial flaw distributions.
- Confidence and tolerance bounds on predictions that use the Weibull distribution function.
- Strength distributions in multiaxial stress fields.

The studies are being carried out largely by analytical and computer simulation techniques. Actual fracture data are then used as appropriate to confirm and demonstrate the resulting data analysis techniques.

Technical Highlights

Work during the previous reporting period emphasized effort on generalized tests of goodness-of-fit for the size-scaled Weibull distribution. Quantitative tests of goodness-of-fit are helpful in judging applicability of a chosen distribution function and validity of resulting estimates of strength and probability of failure. Many factors may contribute to a lack of agreement between an assumed distribution and the experimental fracture data. It is useful to categorize these factors into three types: statistical sampling errors, testing errors and model inadequacies.

- Statistical sampling error is the disagreement between a distribution and data sampled from the distribution that occurs in all non-infinite data sets. This disagreement occurs to some degree, even when the data is truly from the assumed distribution. In occasional data sets, a large degree of statistical sampling error may be present, thus suggesting that some other factor may be the source of the disagreement.
- Testing errors or measurement errors, as the term implies, are caused by problems in measurement of the data (strengths in our case). Testing errors can add either a constant, a proportional, or a random component of error to the true fracture strengths. An example of a testing error is the error incurred during bend testing due to axial frictional forces caused by "fixed-pin" bend fixtures. These frictional errors are primarily of a proportional nature because the magnitude of the error in stress is proportional to the fracture load and therefore the fracture stress. In

addition to the proportional error, there can be a component of random testing error present from the same bend fixtures. The coefficient of friction may vary from specimen to specimen (due to differences in surface roughness, etc.). Therefore, the magnitude of the error in stress may not be in the same proportion to the fracture load in all specimens tested.

- Model inadequacies are the third possible source of lack of agreement between fracture data and the assumed distribution. The model in the case of probabilistic strength analysis is the Weibull distribution function with all associated assumptions and complications (such as multiple flaw populations, time-dependent changes in strengths, etc.). If the assumed strength distribution is different from the true underlying distribution, then the experimental data may have a poor fit when forced to the assumed distribution function.

It is intuitive to tolerate some level of disagreement between measured strengths and the best fit of the data to the assumed distribution function. This intuition is justified because the first of the above sources of disagreement, statistical sampling error, is universally present to some degree and is not necessarily a sign of either measurement error or model inadequacy. If statistical sampling error is the only source of disagreement between data and distribution, then there is no reason to reject the assumption that the model is correct nor is there reason to suspect measurement errors.

Unfortunately, one seldom has independent information stating that neither measurement error nor model inadequacy are present in a given data set. Therefore judgement must be made on whether the magnitude of disagreement is sufficient to consider a source of error other than statistical sampling error. In the absence of suitable quantitative methods, many investigators resort to "eye-ball" tests on a graphical representation of the data. If the assumed strength behavior is two-parameter Weibull, then a plot of the data on a Weibull probability plot is expected to yield a well-behaved linear relationship. If the data points are markedly non-linear on such a plot, it is tempting to conclude that the assumed distribution is invalid. In extreme cases, this eye-ball test may be justified. In most cases, however, an eye-ball test is undesirable because judgments are defined by arbitrary, subjective criteria that are certainly different from investigator to investigator and, moreover, can lead to unwarranted conclusions.

Quantitative goodness-of-fit tests are much more desirable because they remove the subjectiveness, they yield identical results when used by different investigators, and the statements that result from the tests are statistically valid. Effort on goodness-of-fit tests within this contract has concentrated on variations of the Kolmogorov-Smirnov (K-S) test.

Statistical procedures such as the K-S test define a quantitative measure of the degree of "lack-of-fit" of the observed data set to the hypothesized (assumed) distribution. This quantity is then compared to tables that list the frequency of observing any given value for that measure of lack-of-fit. The tables were generated with only random statistical sampling error (no testing error or model inaccuracies). Therefore, if the frequency (significance level) obtained from the table is sufficiently small, it provides a "signal" that the fit of the data to the assumed distribution is unusually poor. The issue of what action to take when a data set fails a goodness-of-fit test is a complex one. When tests fail at small significance levels, statistical procedures suggest considering factors other than statistical sampling error as the source of the disagreement. This does not imply that the hypothesized distribution will be abandoned for another, or that the hypothesized

distribution is in some way incorrect. It just means that the probability of occurrence of the observed disagreement is so small that it is reasonable to consider other sources of the disagreement as being likely. The level of significance at which an action is taken is a complex function of "risk tradeoffs" which are unique to each individual problem. More discussion of this topic will be covered in future reports.

The remainder of this report will describe the K-S test for goodness-of fit as it applies to problems of probabilistic strength analysis. The first of three sections reviews the common usage of K-S tests, points out that tables of the critical K-S statistic are inappropriate for most strength analysis problems, and demonstrates how Monte Carlo simulations can be used to generate appropriate tables. The second section demonstrates the technique on fracture strengths of sintered silicon carbide and introduces the concept of simultaneous inference. The third section then describes remaining challenges in the development of rigorous goodness-of-fit tests for problems that involve pooled strength data from multiple specimen sizes and geometries.

I. Kolmogorov-Smirnov Tests for Goodness-of-Fit

The K-S test compares a set of observations (fracture strengths in our case) with a distribution function that is expected to describe the cumulative probability of observation (the Weibull two-parameter distribution in our case) and makes statistical statements concerning the likelihood that the observed data were sampled from the stated distribution. The test defines a statistic, D, also referred to as the K-S statistic, that is simply the maximum difference in cumulative probability between the observed data and the distribution. Judgments on the goodness-of-fit are made by comparing D with tables of critical values of the K-S statistic that are available in statistics textbooks and handbooks.

Proper use of these K-S tables requires that the Weibull parameters of the tested distribution be chosen independent of the observed strength data. If the adjustable parameters of the Weibull distribution are estimated through use of the observed strength data, then clearly the requirement of independence, as defined above, has not been satisfied. Unfortunately, in ceramic strength analyses, there is typically no other (independent) means of choosing the Weibull strength parameters. Therefore, a new test or a modification of the K-S test is required to handle this common situation. The discussion to follow in this section will first demonstrate the K-S test assuming independence. Then a modified K-S test will be described and demonstrated that can handle the situation where the Weibull parameters are derived from the same data being tested for goodness-of-fit. Comparison of results from the two analyses will be used to demonstrate the magnitude of error that can occur from use of conventional K-S analysis when the Weibull parameters were estimated from the strength data.

For discussion in this section, consider a hypothetical material from which 20 tensile specimens were fabricated and tested. The 20 strengths were analyzed and fit to the Weibull two-parameter distribution using a maximum likelihood estimator to estimate the Weibull parameters. The resulting strengths are plotted on Weibull probability axes on Figure 1. The straight line is the Weibull cumulative behavior as defined by the maximum likelihood estimates of the parameters. The data have some scatter about the straight line which then raises the question of whether or not this degree of scatter is indicative of non-Weibull behavior.

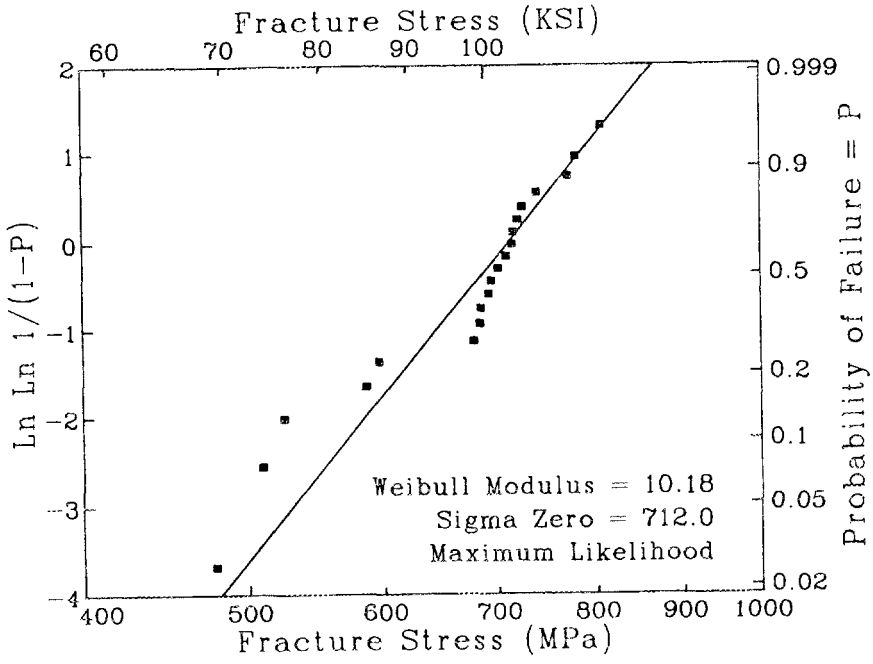

Figure 1

Figure 2 displays the same data in a K-S plot where cumulative probability of failure is plotted versus fracture strength. (Note that both axes on Figure 2 are linear, unlike the axes of Weibull probability plots.) Included on Figure 2 are two curves. The smooth continuous curve is the cumulative distribution function corresponding to a Weibull distribution with maximum likelihood estimated parameters. The smooth curve is labeled as $P(\sigma)$. The "stepped" curve is an empirical distribution function that is generated from the fracture strengths by ordering all N strength values from weakest to strongest and assigning a ranking number i to each strength where i varies from 1 to N. A vertical step is placed in the stepped curve at each observed strength. The value of the ordinate to the left of each step is (i-1)/N and to the right is i/N. The stepped empirical distribution curve is defined as $P_n(\sigma)$.

The K-S test goes on to define the statistic, D, which is the maximum vertical deviation between the two curves. In equation form:

$$D = \max |P_n(\sigma)-P(\sigma)|$$

The D for this example is 0.208. The position and magnitude of D is illustrated on Figure 2. Judgments on the goodness-of-fit from the K-S test are then made based only on the number of strength observations and the value of D. For the case of 20 strength observations, the critical D value at a 0.05 significance level is 0.294 (from handbook tables of critical D values such as Reference 1). Since the observed D value is less than 0.294, one would conclude that there is no reason to reject the fit of this assumed distribution at the 5 percent level of significance. In other words, if this problem were repeated many times and if statistical sampling error were the only source of error in each analysis, then 95 percent of the time, D would be less than 0.294.

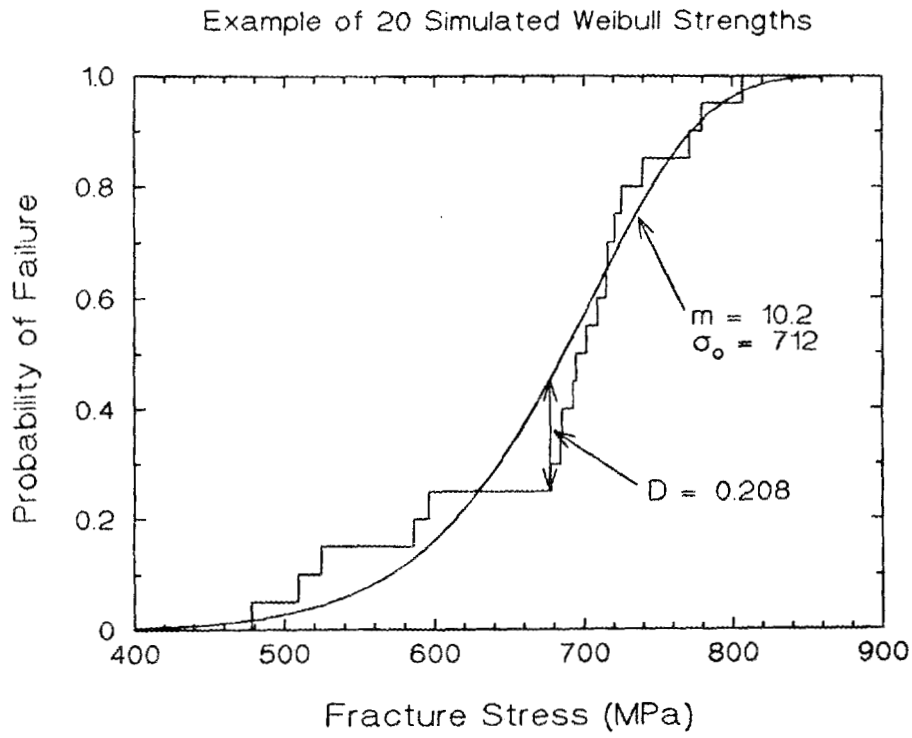

Figure 2

But remember that the tabled values assume a type of independence between $P(\sigma)$ and $P_n(\sigma)$ that is not justified here. In this analysis, $P(\sigma)$ was derived in part from $P_n(\sigma)$.

Monte Carlo simulation has been used to generate critical values of D for both independence and dependence of $P(\sigma)$ and $P_n(\sigma)$. Of course, in the case of independence, the D values should be in agreement with handbook values. This requirement of agreement with handbook values has been used as a check of validity for the simulation techniques employed herein. The entire simulation must be repeated for each sample size of interest.

The simulation randomly chooses specimens from an infinite population of possible specimens that are consistent with Weibull strength behavior. The "true" values of the Weibull parameters for the population are chosen in advance and are, therefore, known. In the simulation, we randomly pick 20 specimens at a time, determine their strengths, estimate the Weibull parameters using maximum likelihood, prepare a plot similar to Figure 2, and determine D in two ways. The first D (referred to here as D_1) is measured relative to the true underlying distribution, and the second (referred to as D_2) is measured relative to the maximum likelihood estimate of the underlying distribution. The D included in Figure 2 is therefore an example of a value of D_2. This process of simulation and analysis is repeated many times (typically 1000) to accumulate a large number of D values for this same type of problem. If we count how many D_1 values are greater than 0.294 in this exercise, we should find approximately 5 percent. (In fact, this is precisely how the handbook tables were defined.) The 1000 values of D_1 from this simulation then allow us to estimate any conventional tabled value of the critical D values for a sample size of 20

measurements. In a parallel fashion, the 1000 values of D_2 will allow us to generate new critical D values that are applicable in the common situation where the tested Weibull distribution is not independent of the fracture data.

Results of a simulation for a sample size of 20 is included on Figure 3 where the critical value of the K-S statistic is plotted versus significance level of the test. There are five relationships included on Figure 3. The following describes each, one at a time:

- The open squares were taken directly from the table of critical D values for a sample size of 20 published in Reference 1. As discussed earlier and as indicated by the key, these table values apply to tests of goodness-of-fit where the two Weibull parameters are "known" or defined from information that is independent of the 20 strength measurements being considered.

- The solid line was generated using a Fortran subroutine included in Reference 2. The subroutine can generate a conventional D value for any arbitrary significance level and sample size, therefore allowing the generation of a smooth, continuous curve. Again, these D values are for cases where the Weibull parameters are "known" or defined from independent information. The solid line is slightly higher than the square data points. This difference is believed to be caused by the asymptotic approximation used in the routines of Reference 2. As the sample size increases, this difference should decrease.

- The upper dashed line is one of the relationships generated during the simulation described above. The D_1 values were ranked from largest to smallest; a significance level was assigned to each D_1 according to (i-0.5)/1000, where i is the ranking number; and the resulting 1000 points were connected with a line. The D_1 values were generated in comparisons with the "true" Weibull distribution. Therefore the resulting dashed line should again be used when the Weibull parameters are "known" or independently defined. The dashed line clearly is in excellent agreement with the tabled values (square data points). The small irregularities in the dashed curve are caused by statistical sampling error during the simulation. A simulation with 10,000 groups of 20 strengths would reduce this variation. For most applications, however, the uncertainty in critical D value reflected by the irregularities in the D_1 curve of Figure 3 is acceptable.

- The lower dashed or broken line was also generated during the simulation. In this case the D_2 values were used to create the line. The D_2 values were generated in comparisons of the observed strengths with the maximum likelihood estimate of the distribution for <u>each</u> respective data set. Therefore, this relationship is the proper one to use when testing the goodness-of-fit of a set of fracture strengths with the Weibull distribution defined by maximum likelihood estimation of the Weibull parameters from the same data. It is clear from Figure 3 that the critical values of D_2's are substantially smaller (indicating better expected fit) than conventional D_1's. The sign of this difference should not be surprising. If the distribution parameters are chosen to provide the best fit to a given data set complete with its unique statistical sampling error, then of course, the fit will be quite good (better even than that given by the true values of the Weibull parameters), and the resulting D_2's should be smaller than the corresponding D_1's.

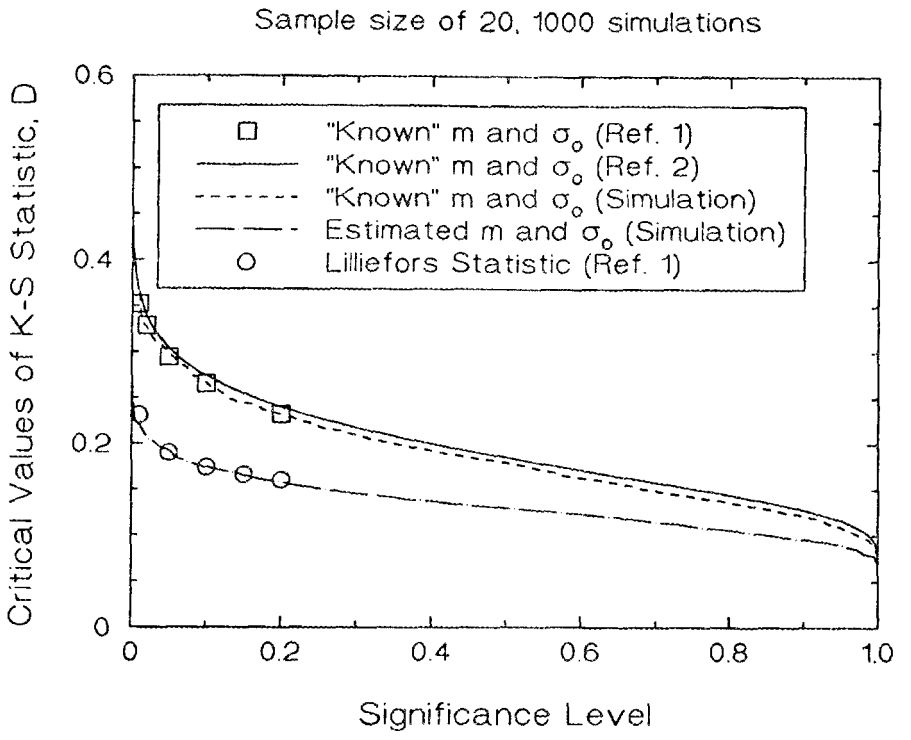

Figure 3

- The open circle data points on Figure 3 are tabled values of the Lilliefors statistic as included in Reference 1. In 1967, Lilliefors (Reference 3) recognized the problem of using the K-S statistic in evaluating goodness-of-fit when the tested distribution was derived from the sampled data. At that time, he performed simulations similar to those done herein, but he carried out the analysis for the normal (Gaussian) distribution. The critical values from that simulation are known as the critical values of the Lilliefors statistic and are used in a similar way as the critical D values of the K-S test. The almost perfect agreement of the Lilliefors statistic (for the normal distribution) with the broken line of Figure 3 (for the Weibull distribution) suggests that the tabled values of Lilliefors may be much more general than expected. Even if they are not in perfect agreement, from a practical standpoint, Lilliefors' tables of critical values are clearly a reasonable and preferred alternative to conventional K-S tables when testing the goodness-of-fit of strength data to a Weibull distribution with parameters defined from the same data. Reference 4 provides other approaches to K-S tests on data sets where the adjustable parameters are derived from analysis of the same data set.

Figures 4 and 5 are similar to Figure 3 but cover sample sizes of 5 and 50 respectively. Each figure includes the five relationships discussed above for Figure 3. Several points of comparison and contrast in Figures 3, 4 and 5 are worth noting:

- The squares (tabled values of K-S) are always in good agreement with the upper dashed line (simulated values of K-S).

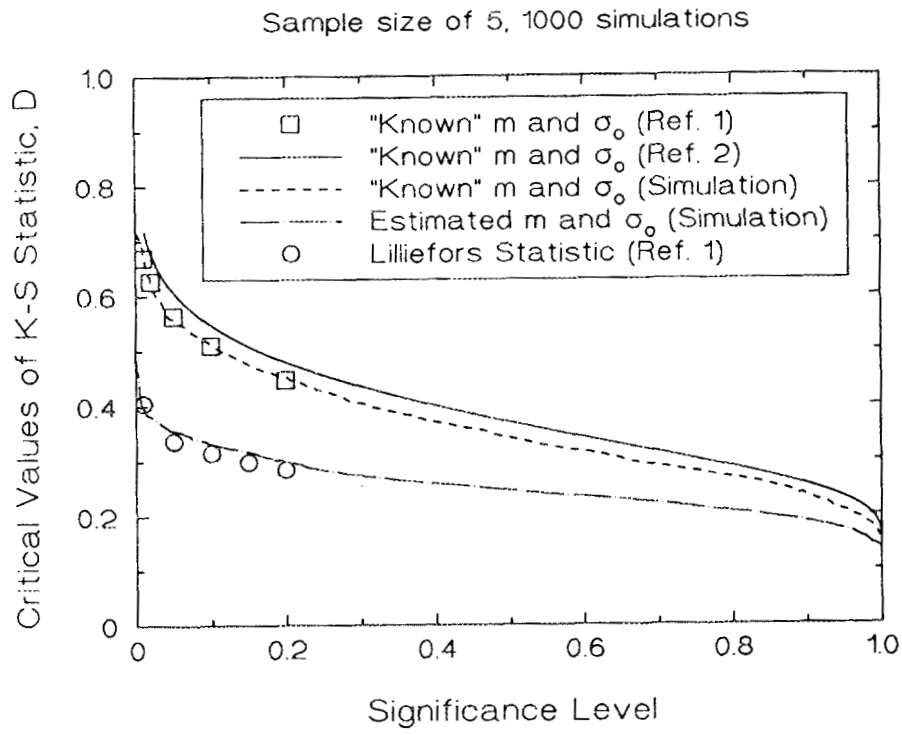

Figure 4

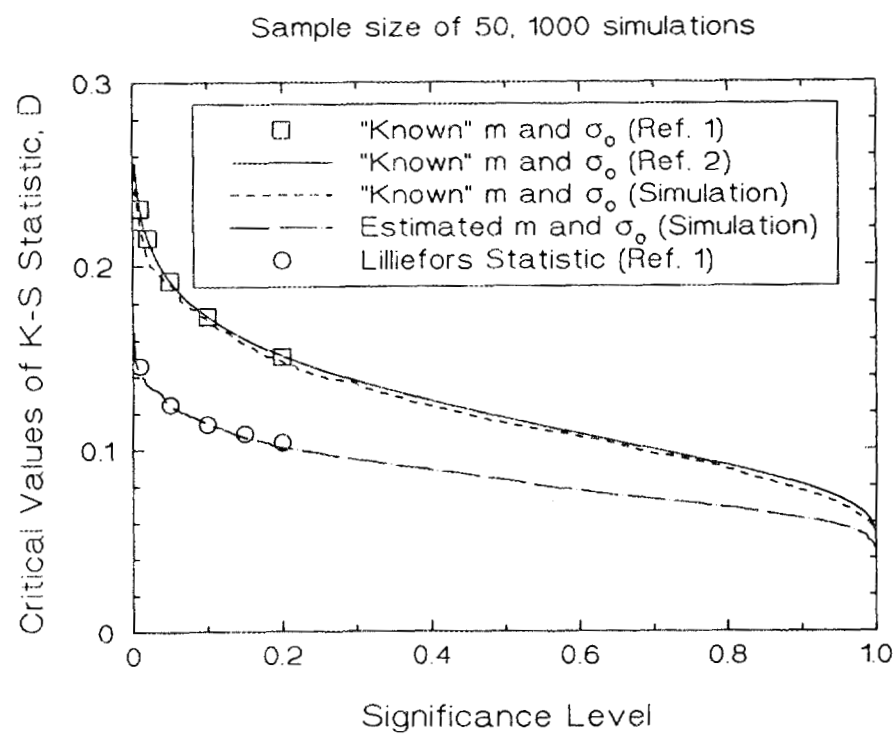

Figure 5

- As the number of samples decreases, the solid line (asymptotic approximation of K-S) shifts progressively farther above the squares and dashed line. This is consistent with the asymptotic nature of the solution used for the solid line. For small sample sizes, the tabled and simulated results are more accurate and preferred.

- As the samples size decreases, the circles (Lilliefors statistic) appear to consistently fall below the broken dashed line (simulation of D_2). Therefore, the unexpected applicability of the Lilliefors statistic to the Weibull distribution may break down at small sample sizes.

The simulations that resulted in Figures 3, 4 and 5 have been carried out for many other sample sizes. Figure 6 summarizes the critical D_2 values for eight different sample sizes from five to 50.

Now reconsider the 20 strength measurements of Figures 1 and 2. The D value of 0.208 is reanalyzed in Figure 7. The curves in Figure 7 are the two simulation-generated curves for "known" and estimated Weibull parameters from Figure 3. If the distribution being tested is independently defined, then using the upper curve, one can state that this magnitude of disagreement should occur slightly more than 30 percent of the time--not particularly disturbing and no reason to reject the assumption that this two-parameter Weibull distribution is applicable. But the adjustable parameters of the tested distribution were determined from the 20 strengths, therefore the lower curve should be used. Using the lower curve, one then concludes that the observed D value will occur less than two percent of the time. Therefore, the test of goodness-of-fit would indicate a rather poor fit to the Weibull distribution, even at the 0.02 significance level. The most important conclusion from this hypothetical example is that unwarranted inferences will often result when

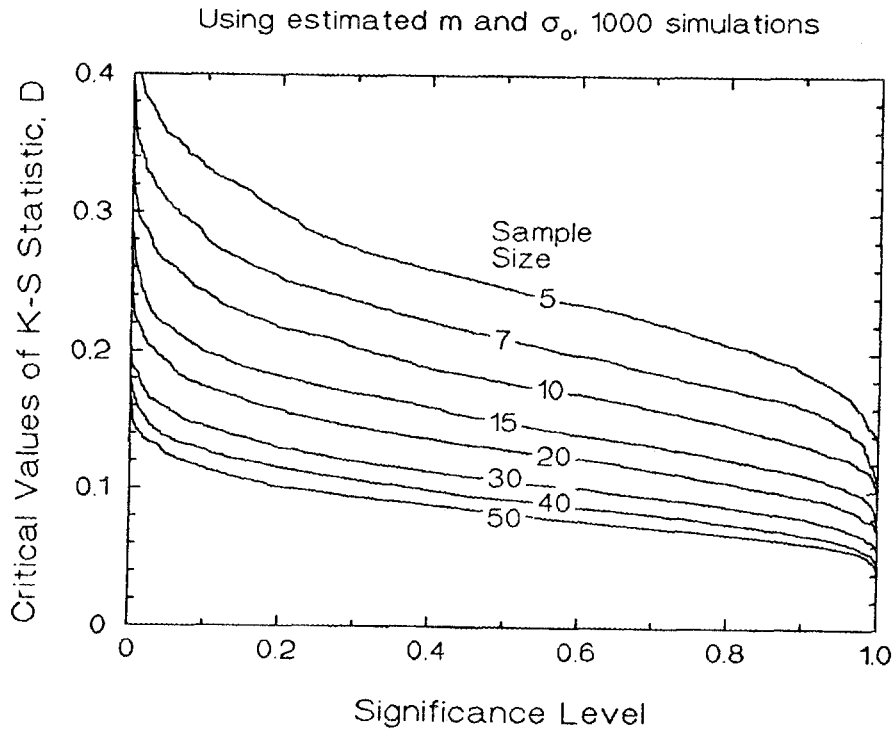

Figure 6

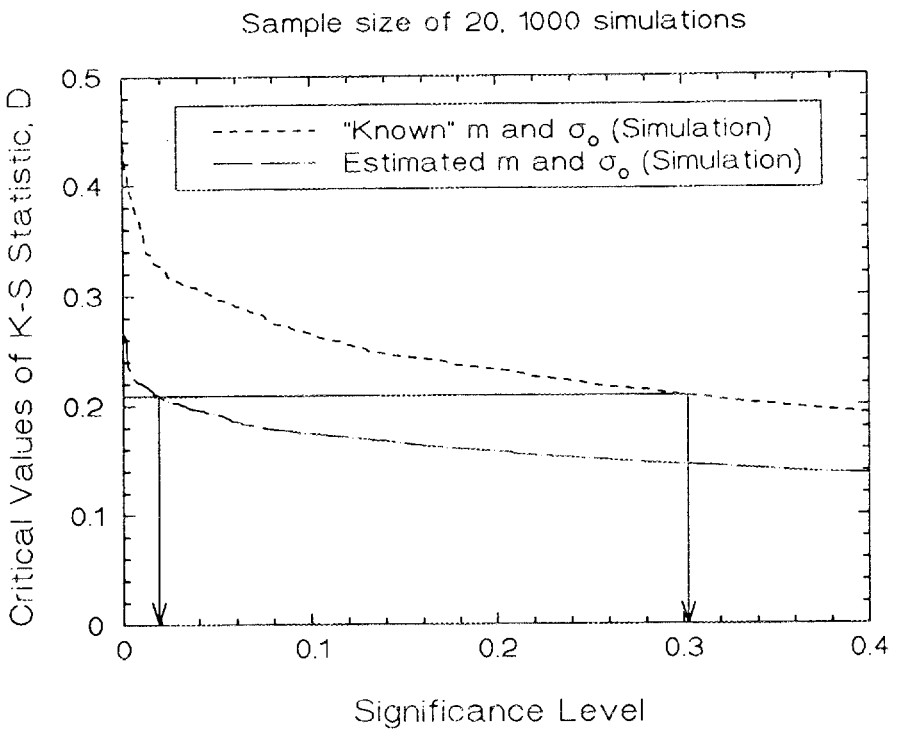

Figure 7

conventional tables of critical K-S values are used in this common type of ceramic strength analysis.

The simulation studies considered two other aspects of K-S tests:

- In the earlier discussion of simulations, no mention was made about the "true" values of the Weibull parameters used. The reason for this apparent oversight is that the results (as displayed in Figures 3-6) are independent of the parameters chosen. This has not been analytically proven, but has been demonstrated by repeating the simulation for different true values of parameters. (These repeat simulations use the same seed for the random number generator to insure the same sequence of normalized fracture strengths in each.) Repeat simulations with markedly different true values of Weibull parameters yielded virtually identical sequences of D_1 and D_2 values. Accordingly, the simulation curves in Figures 3-6 are independent of the Weibull parameters. This is convenient because it allows graphical and/or tabular summaries of critical values that are applicable for any true Weibull parameters. The independence also has implications about the general applicability of the Lilliefors statistic. Within the family of all Weibull moduli are distributions that run the gamut from extreme skewness of one sign, through near-symmetry (for m = 3.6), to extreme skewness of the opposite sign. This family serves as reasonable approximations of many different types of continuous, unimodal distribution functions--all of which seem to be adequately used with the Lilliefors statistic. Finally, an earlier statement claimed that these simulations yielded "virtually" identical sequences. The statement was softened with the word virtually to allow for inconsequential differences due to single-precision round-off errors, etc. Each number in the sequence of D_1 values was typically found to be

independent of true Weibull parameters to 6 or 7 significant digits (consistent with single precision calculations). Derivation of D_2 values, however, requires an iterative maximum likelihood estimate of Weibull parameters that typically estimates the parameters to 4 or 5 significant digits. Therefore it is not surprising that the sequence of D_2 values was typically found to be independent of true Weibull parameters to only 4 or 5 significant digits.

- Maximum likelihood was chosen herein for estimation of Weibull parameters due to the optimum statistical efficiency of maximum likelihood (discussed and demonstrated in earlier reports of this contract). A practical question, however, is whether the critical D_2 values of Figures 3-6 can validly be used to evaluate goodness-of-fit when the Weibull parameters are estimated using linear regression. To answer this question, two additional simulations were performed and are summarized in Figure 8. The simulations were both for a sample size of 20, similar to Figure 3. One simulation used maximum likelihood to derive D_2's while the other used linear regression. The sequence of D_1's is independent of estimator and is therefore common to both simulations. As seen in Figure 8, the D_2 curves for the two estimators are close to each other, but the maximum likelihood behavior is lower by an amount that is judged to be larger than the uncertainty associated with the 1000 simulations used herein. Tabled values of the Lilliefors statistic are also included on Figure 8 and are in much better agreement with the maximum likelihood curve. The fact that the linear regression estimator yields larger D_2 values is consistent with the lower statistical efficiency of this estimator. The lower efficiency results in poorer fits with the data (poorer on average) which, in turn, results in larger D_2 values. Finally, the seed for the random number generator was

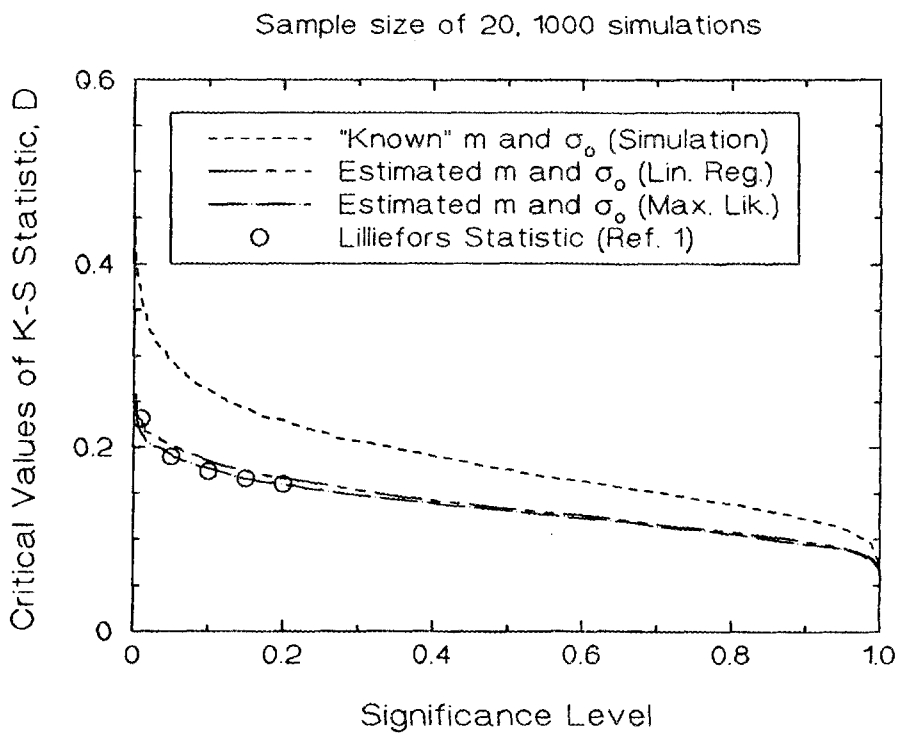

Figure 8

again common for the two simulations. The seed used in Figure 8, however, was different than that for Figure 3, thus accounting for minor differences in the "bumps" of the D_2 maximum likelihood curves.

II. Demonstration of K-S Tests on Silicon Carbide Strength Data

This section will demonstrate K-S tests on actual Class I strength data (single specimen size and geometry). The Class I strength data used herein are from the bend strength studies of GE sintered beta silicon carbide that have been used for many previous demonstrations of statistical analyses in this contract. The study included both three-point and four-point bend tests of three different specimen sizes, MIL STD 1942MR sizes A, B and C. This data has typically been used as an example of a Class IV data set where specimen size and stress distribution were both varied within the pooled data set. For use in this demonstration of K-S methods for Class I problems, however, the data will be treated as six independent strength analysis problems. For each subgroup, a K-S test was used to determine the goodness-of-fit of the observed data when compared with the Weibull strength distribution defined by maximum likelihood analysis of that subgroup alone. In this Class I reanalysis of the data, no effort was made to force a common set of Weibull parameters for all subgroups.

Results of these six analyses are summarized in Figures 9-20 with two figures for each analysis. Figures 9 and 10 are for analysis of the three-point A specimens and will be described in detail. The remaining 10 figures of this series are similar paired figures for the other five analyses.

Figure 9 includes the 18 strength measurements of the 3-point A data set plotted on Weibull probability axes. The straight line is the strength distribution defined by the maximum likelihood Weibull parameters. The strengths appear to be in reasonable agreement with the straight line, but as discussed above, it is well known that different individuals have different thresholds for what is "reasonable agreement."

The K-S statistical procedure for the three-point A data set is included on Figure 10. The stepped curve is the observed strength distribution (empirical distribution) and the smooth curve is the maximum likelihood estimate of the distribution. The maximum vertical offset, D, between the two curves is 0.1475 and is located at the position indicated on the figure. As described in the previous section, proper interpretation of this D value requires a simulation to derive a "table" of critical D_2 values for problems with 18 strength observations where the Weibull parameters were estimated from the 18 strength observations themselves. The table of D_2 values from that simulation resulted in a significance level, P_2, of 0.352 for the observed D. The significance can be interpreted as follows: if the underlying strength distribution is properly described by the two-parameter Weibull distribution with unknown parameters, then disagreements (between the observed and estimated distributions) of this magnitude or larger will be observed 35.2 percent of the time. Usually people are not "disturbed" by such "high" significance levels. One would therefore conclude that the scatter of observed strengths about the estimated curve on Figures 9 and 10 is consistent with the assumed Weibull model of strength behavior.

K-S analyses were also carried out for the other five silicon carbide subgroups with graphical display of the results included in Figures 11-20. The results of all six subgroups are summarized in Table I. (For comparison, the Weibull parameters from Class IV maximum likelihood analysis of the pooled data set are also included in Table I.) None of

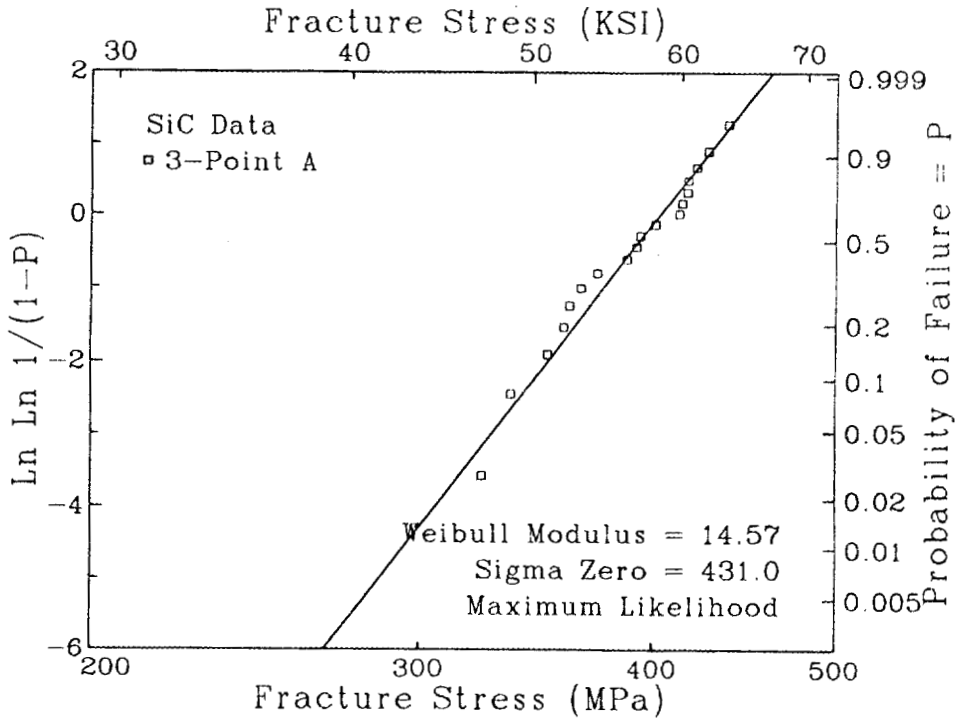

Figure 9

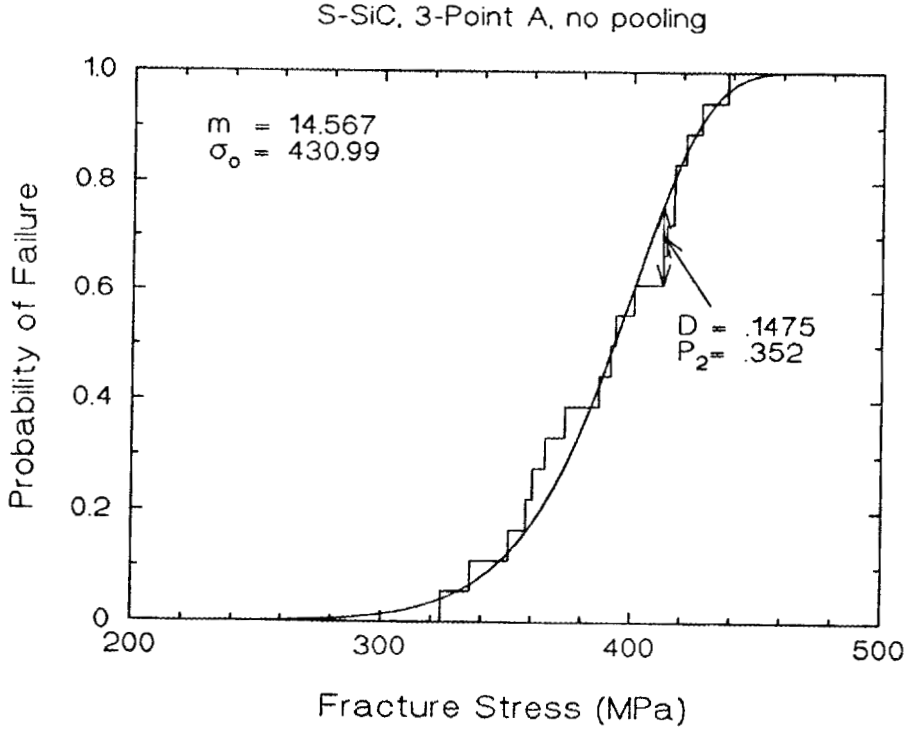

Figure 10

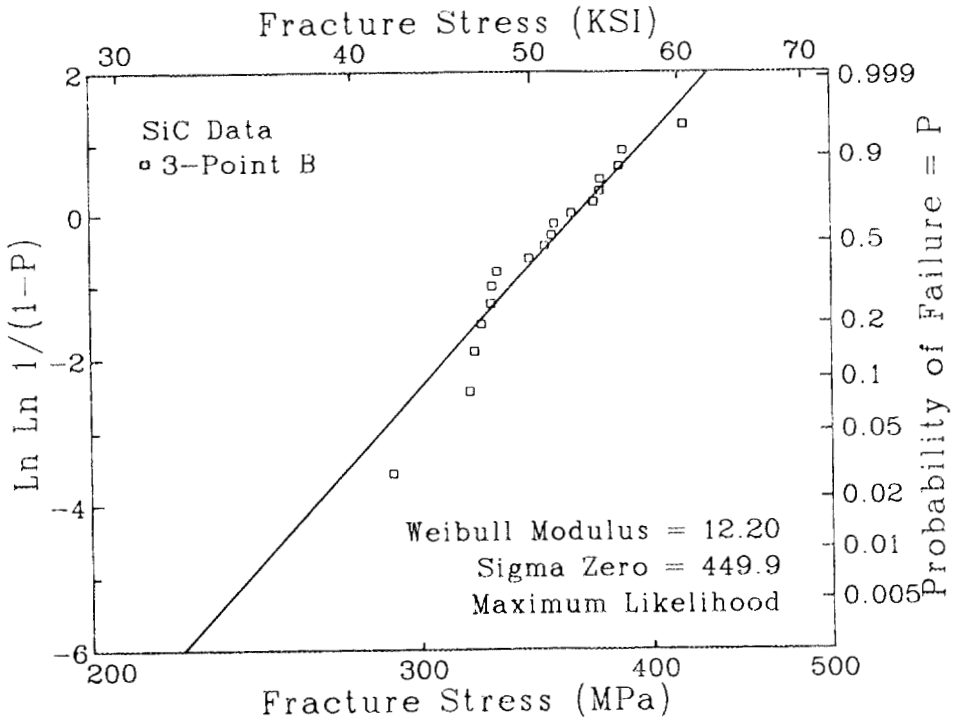

Figure 11

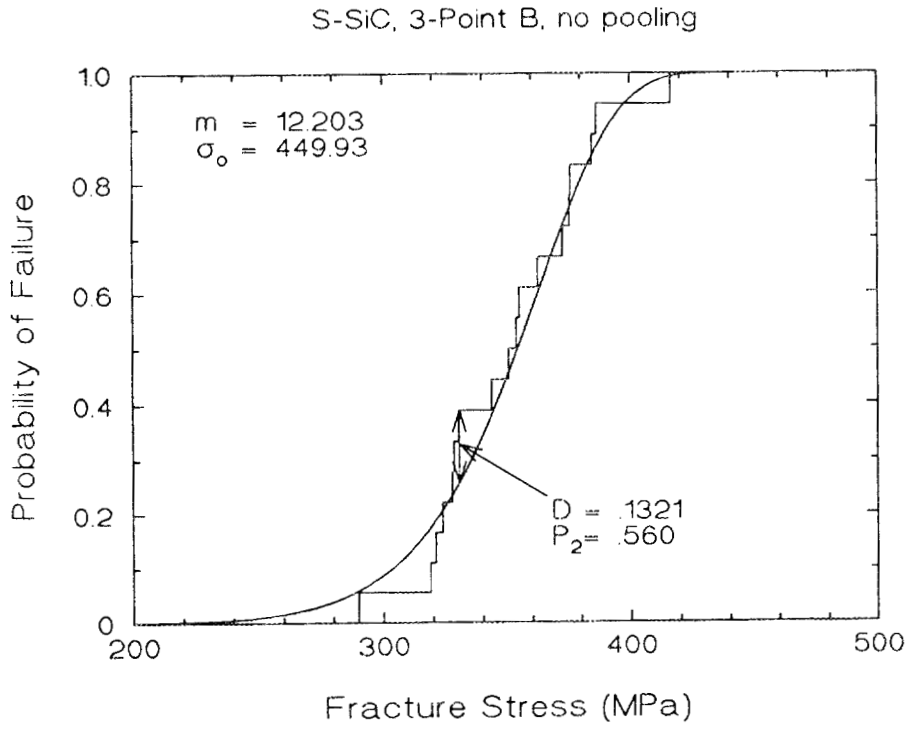

Figure 12

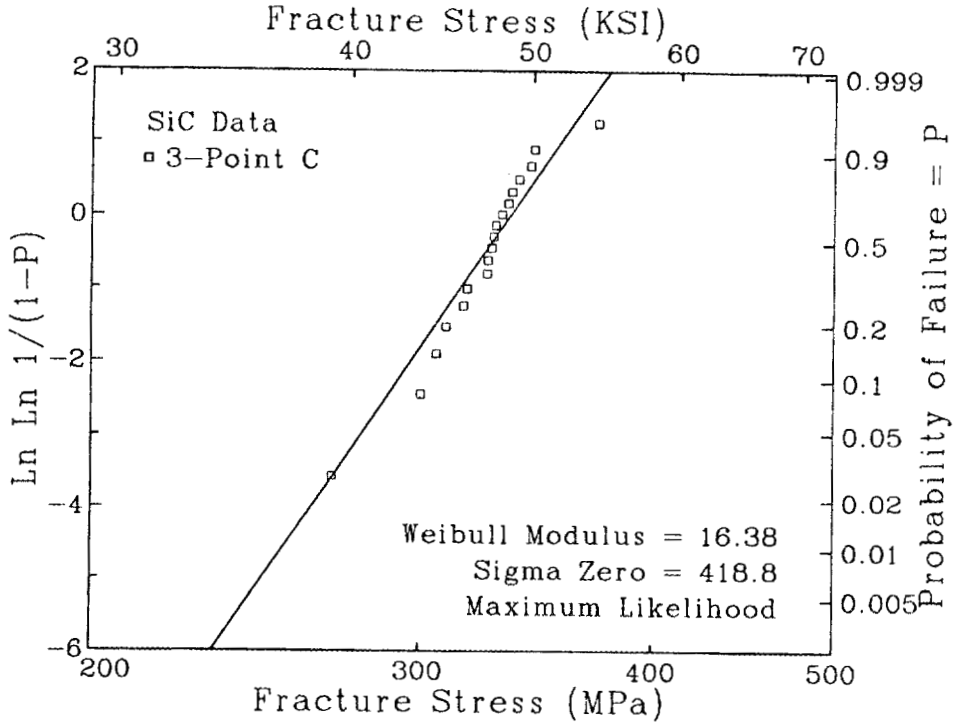

Figure 13

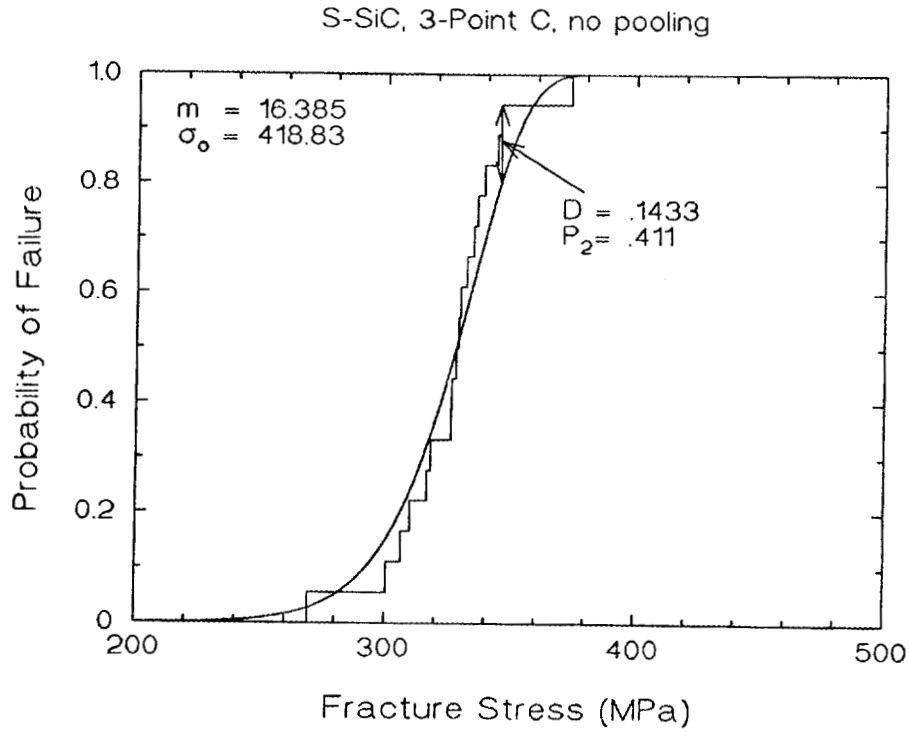

Figure 14

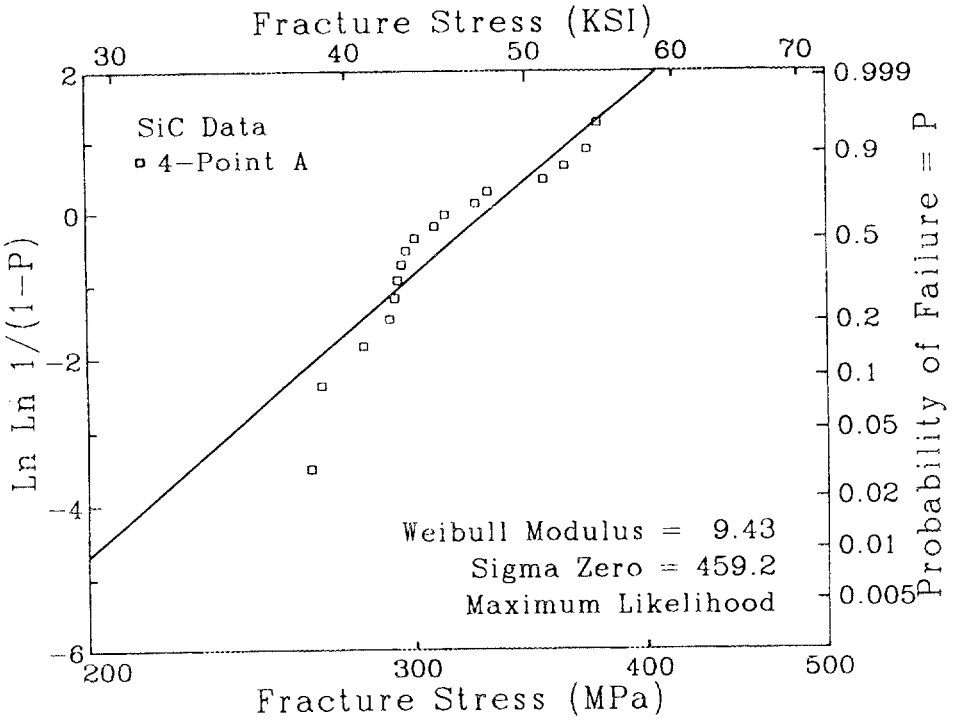

Figure 15

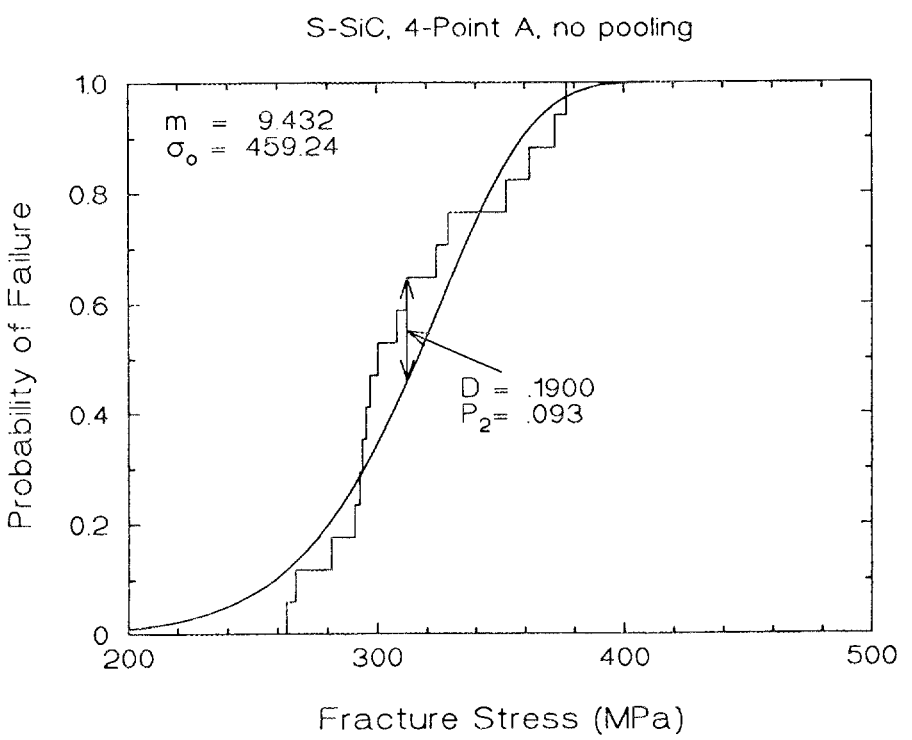

Figure 16

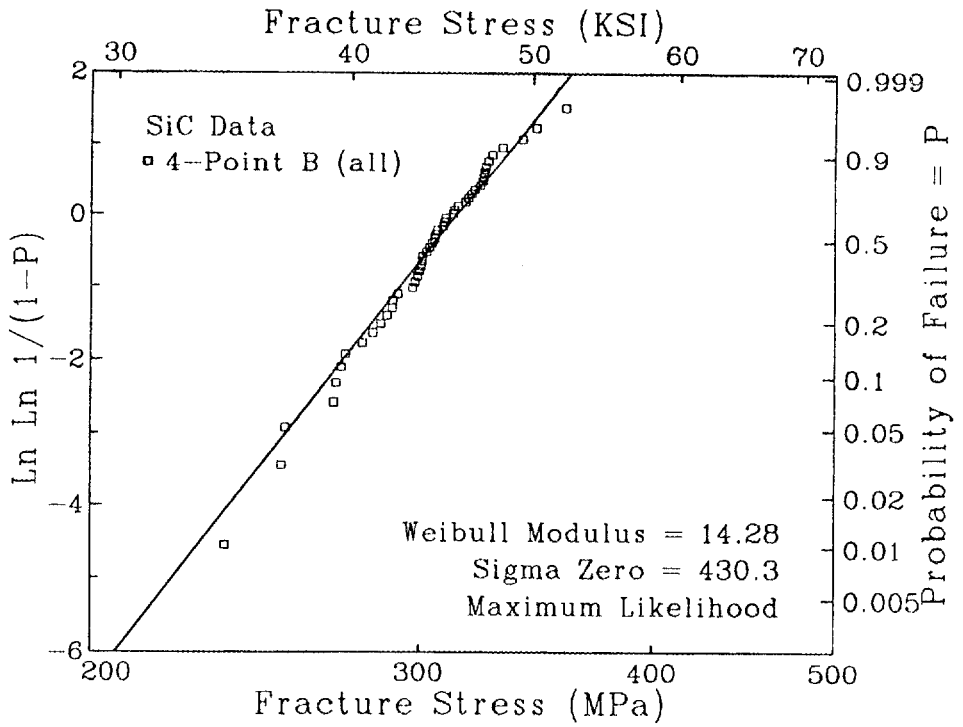

Figure 17

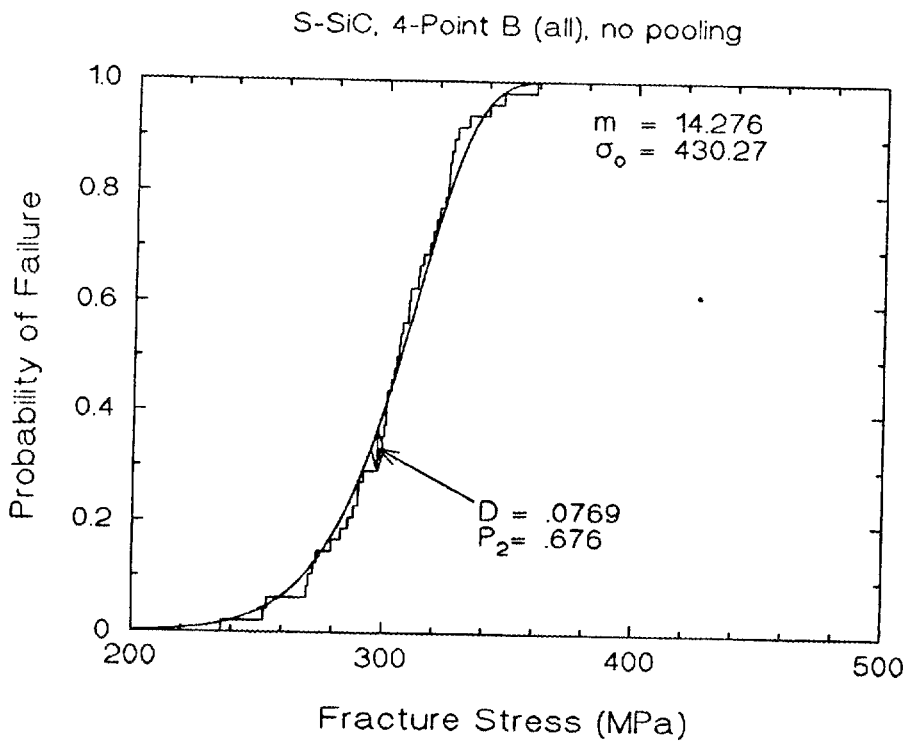

Figure 18

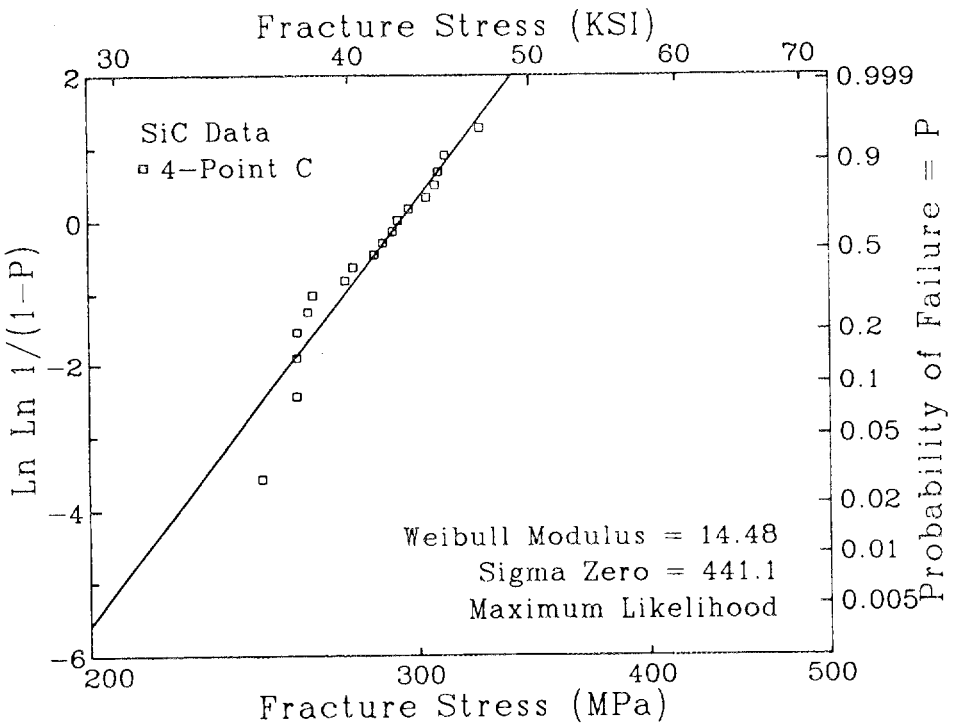

Figure 19

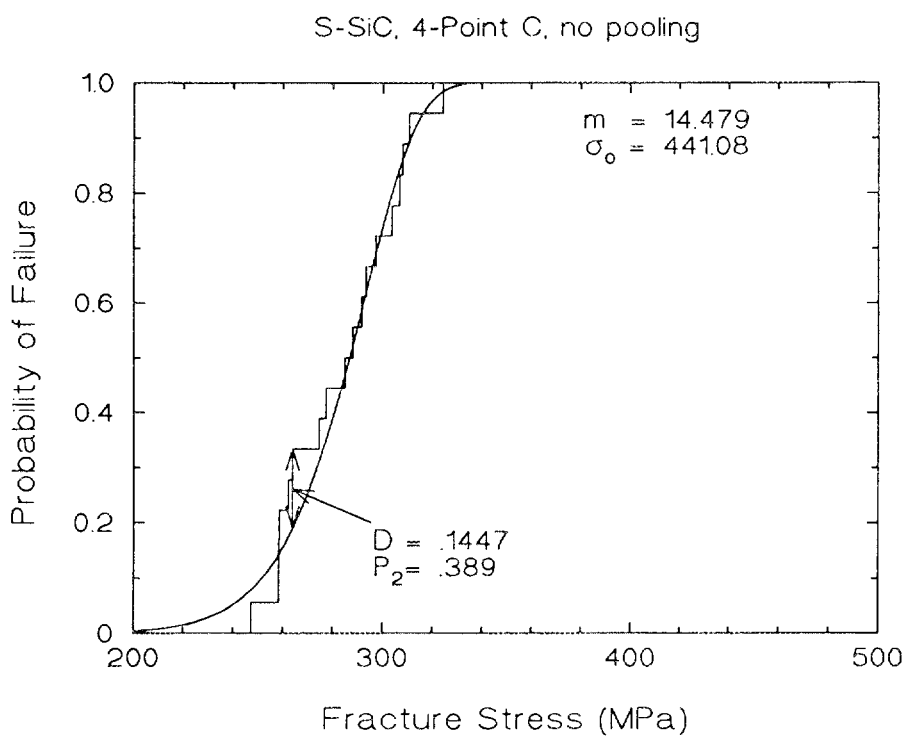

Figure 20

TABLE I

Specimen Geometry	Number of Specimen	Weibull Modulus	σ_0	D_{max}	P_2 Significance
3-pt A	18	14.57	431.0	0.1475	0.352
3-pt B	18	12.20	449.9	0.1321	0.560
3-pt C	18	16.38	418.8	0.1433	0.411
4-pt A	17	9.43	459.2	0.1900	0.093
4-pt B	48	14.28	430.3	0.0769	0.676
4-pt C	18	14.48	441.1	0.1447	0.389
All	137	14.22	433.1	---	---

the six significance levels is particularly disturbing. The smallest is that for the four-point A specimens of Figures 15 and 16 with a P_2 significance of 0.093. This subgroup would fail a 0.10 test of significance, but failure at this modest level would not generally be considered reason to question the tested distribution function. Furthermore, one can argue that even this apparent doubt of the assumed distribution function may not be justified.

The basis for the previous statement lies in the fact that the analysis of the six silicon carbide subgroups is really a problem involving "simultaneous inference." Since the issue of simultaneous inference is one of the most difficult problems of goodness-of-fit analyses in Class IV problems, this will be a good opportunity to introduce the topic. Probabilistic statements such as the one made earlier about the three-point A specimens ("...then disagreements of this magnitude or larger will be observed 35.2 percent of the time") are statistical inferences. Table I summarizes six such inferences. While it is tempting to look for the smallest significance in such a list, doing so complicates interpretation of that number. The smallest number is not the significance of a random observation but, rather, is the significance of the worst fit of six such observations. Stated another way, if six independent measurements of significance are made in a material where the null hypothesis is justified, then they should be uniformly spread from zero to one. Therefore, the smallest of those six numbers will typically be much less than 0.5. In such problems of simultaneous inference, one cannot pick the smallest observed significance and interpret it as would be done for a single test of significance.

A useful approach for dealing with such problems of simultaneous inference builds on the statement of the previous paragraph that six independent measurements of significance should be uniformly spread from zero to one. Another level of K-S testing is ideally suited to test the validity of such behavior. Figure 21 is a K-S test of the six P_2 significance values where they are compared to the assumed (hypothesized) uniform distribution which is simply a diagonal straight line from (0,0) to (1,1). Since the adjustable parameters of the expected distribution have not been derived from the data, the maximum D value of 0.324 can and should be compared with conventional tabled values of critical D's (D_1's) instead of critical D_2's as used on the direct tests of the strength distribution. This results in a P_1 significance of 0.417.

In other words, if this whole exercise of testing the fit of six independent subgroups of specimens is repeated many times and if the Weibull two-parameter distribution is indeed the underlying strength distribution for each subgroup, then 41.7 percent of the time, the distribution of the six P_2's will be less uniform than that of Figure 21. Therefore, the six observations of significance are not unusual, and the relatively poor fit of the four-point A specimens to Weibull seems to be a common (even expected) event for one of the six independent subgroups to experience.

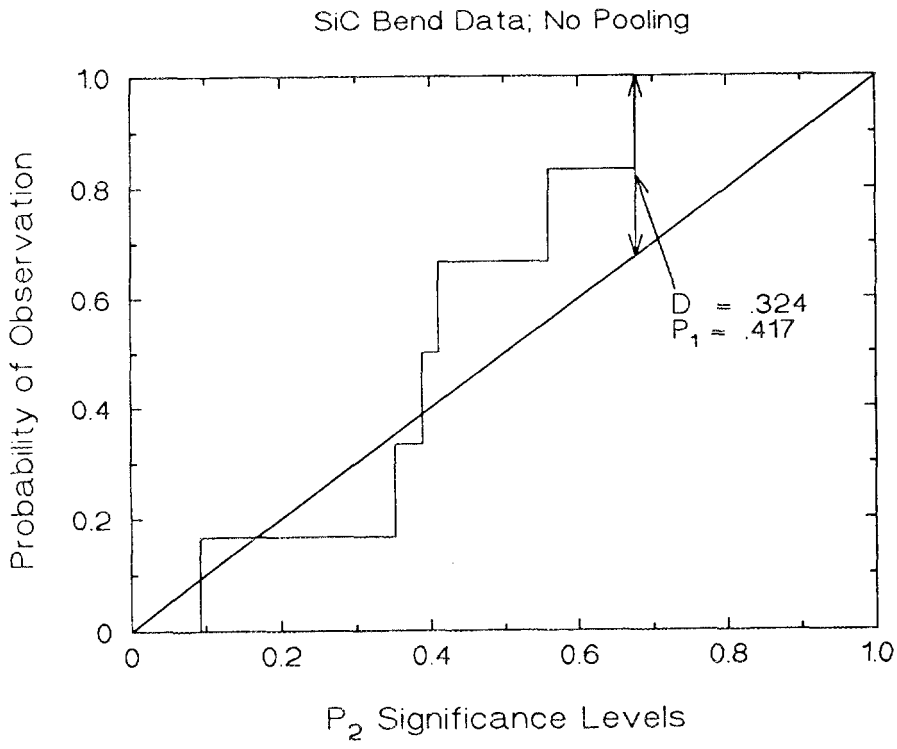

Figure 21

III. K-S Tests on Class IV Problems of Pooled Data

The comments in the previous section were relative to a Class I analysis of strengths (no pooling of data). The following discussion will consider how the approach to goodness-of-fit testing changes when applied to Class IV problems, where fracture data from multiple specimen sizes and geometries may be pooled together to better characterize the underlying strength distribution.

As an example, the silicon carbide data of Table I can be pooled to yield a single maximum likelihood estimate of the Weibull parameters using algorithms described in previous reports. The strength distribution from those parameters can be compared with the actual data in several ways. One convenient way is shown on Figure 22 where all strengths have been transformed to probabilities of failure of three-point B specimens and plotted on Weibull probability axes. (The choice of a size and geometry to transform all data is arbitrary: the relative positions of points are independent of that choice.)

From Figure 22, it is easy to recognize that the four-point A strengths (diamond shaped symbols) seem to "disagree" with the trend of the total data set. Therefore, a desirable feature of a Class IV goodness-of-fit test would be the ability to test individual subgroups that may have apparent disagreements with the pooled behavior. Such a test would allow judgments to be made on the important underlying assumption of material homogeneity that may not be justified in this data set.

Although the homogeneity test appears particularly important in this data set, there are at least five aspects of goodness-of-fit of the data that can be tested.

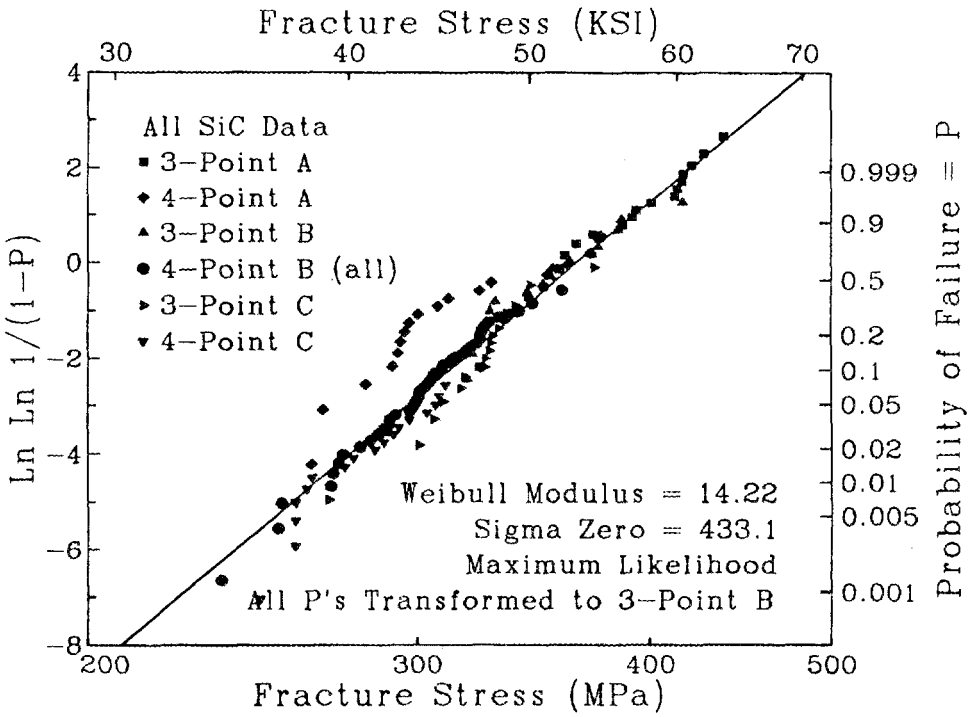

Figure 22

- Material homogeneity between subgroups—compare to assumed uniformity
- Variability in strengths within subgroups—compare to Weibull model
- Specimen size effects between subgroups—compare to Weibull model
- Stress distribution effects between subgroups—compare to Weibull mode
- Overall behavior—compare to Weibull model

Work is continuing on development and validation of K-S and other approaches to evaluate each of these aspects of goodness-of-fit in Class IV problems and to handle the associated inference problems that arise from use of simultaneous statistical tests.

References

1. W.J. Conover, "Practical Nonparametric Statistics", John Wiley & Sons Inc., New York.

2. W.H. Press, et.al., "Numerical Recipes--The Art of Scientific Computing", Cambridge University Press, 1989.

3. H.W. Lilliefors, "On the Kolmogorov-Smirnov Test of Normality with Mean and Variance Unknown", J. of Am. Stat. Assoc., 62, 399-402.

4. R.B. D'Agostino and M.A. Stephens, Goodness-of-Fit Techniques, Marcel Dekker, Inc., 1986.

Status of Milestones

On schedule.

Publications

C.A. Johnson and W.T. Tucker, "Advanced Statistical Concepts of Fracture in Brittle Materials," In Engineered Materials Handbook, Volume 4: Ceramics and Glasses, ASM International, 1992.

C.A. Johnson and W.T. Tucker, "Statistical Procedures for Estimating Component Strengths and Associated Confidence Bounds," Submitted for Proceedings of 1991 ATD/CCM Meeting held October 28-31, 1991.

3.0 DATA BASE AND LIFE PREDICTION

INTRODUCTION

This portion of the project is identified as project element 3 within the work breakdown structure (WBS). It contains five subelements, including (1) Structural Qualification, (2) Time-Dependent Behavior, (3) Environmental Effects, (4) Fracture Mechanics, and (5) Nondestructive Evaluation (NDE) Development. Work in the Structural Qualification subelement includes proof testing, correlations with NDE results and microstructure, and application to components. Work in the Time-Dependent Behavior subelement includes studies of fatigue and creep in structural ceramics at high temperatures. Research in the Environmental Effects subelement includes study of the long-term effects of oxidation, corrosion, and erosion on the mechanical properties and microstructures of structural ceramics. Work in the Fracture Mechanics subelement includes development of techniques for measuring the tensile strength and creep resistance of ceramic materials at high temperatures, and testing ceramic materials at high temperatures under uniaxial tension. Work in the NDE Development subelement is directed at identifying approaches for quantitative determination of conditions in ceramics that affect their structural performance.

Major objectives of research in the Data Base and Life Prediction project element are understanding and application of predictive models for structural ceramic mechanical reliability, measurement techniques for long-term mechanical property behavior in structural ceramics, and physical understanding of time-dependent mechanical failure. Success in meeting these objectives will provide U.S. companies with the tools needed for accurately predicting the mechanical reliability of ceramic heat engine components, including the effects of applied stress, time, temperature, and atmosphere on the critical ceramic properties.

3.1 STRUCTURAL QUALIFICATION

Microstructural Analysis of Structural Ceramics

B. J. Hockey and S. M. Wiederhorn
(National Institute of Standards and Technology)

Objective/Scope

The objective of this part of the program is to identify mechanisms of failure in structural ceramics subjected to mechanical loads at elevated test temperatures. Of particular interest is the damage that accumulates in structural ceramics as a consequence of high temperature exposure to stresses normally present in heat engines.

Design criteria for the use of ceramics at low temperature differ from those at high temperature. At low temperature ceramics are elastic and brittle; failure is controlled by a distribution of flaws arising from processing or machining operations, and the largest flaw determines the strength or lifetime of a component. By contrast, at high temperature where ceramics are viscoelastic, failure occurs as a consequence of accumulated, or distributed damage in the form of small cavities or cracks that are generated by the creep process. This damage effectively reduces the cross-section of the component and increases the stress that must be supported. Such increases in stress are autocatalytic, since they increase the rate of damage and eventually lead to failure as a consequence of loss in cross section. When this happens, the individual flaw loses its importance as a determinant of component lifetime. Lifetime now depends on the total amount of damage that has occurred as a consequence of the creep process. The total damage is now the important factor controlling lifetime.

Recent studies of high temperature failure of the non-oxide ceramics intended for use for heat engines indicates that for long term usage, damage accumulation will be the primary cause of specimen failure. Mechanical defects, if present in these materials, are healed or removed by high temperature exposure so that they have little influence on long term lifetime at elevated temperature. In this situation, lifetime can be determined by characterizing the damage and the rate of damage accumulation in the material at elevated temperatures. In ceramic materials such as silicon nitride and SiAlON, such characterization required high resolution analyses because of the fine grain size of these materials: hence the need for transmission electron microscopy as an adjunct to the mechanical testing of ceramics for high temperature applications is apparent.

In this project, the creep and creep-rupture behavior of several ceramic materials will be correlated with microstructural damage that occurs as a function of creep strain and rupture time. Materials to be studied include: SiAlON; hot-pressed silicon nitride; sintered silicon carbide. This project will be coordinated with WBS 3.4.1.3, Tensile Creep Testing, with the ultimate goal of developing a test methodology for assuring the reliability of structural ceramics for high temperature applications.

Technical Highlights

During the past six months analytical TEM has been used to examine the effect of microstructure on the tensile creep behavior of Garrett GN-10 silicon nitride. The results of this study, which is nearing completion, provide a general description of the microstructure of this material and of the cavity growth process which ultimately determines creep lifetime. As with most other grades of silicon nitride, creep deformation and rupture are primarily governed by the properties of the intergranular glassy phase that remains after liquid-phase sintering.

Experimental Technique

The results described in this report were obtained by analytical transmission electron microscopy (TEM/EDS). Observations were made on samples of Garrett GN-10 silicon nitride which were subjected to tensile creep to rupture at various stresses at temperatures from 1250 - 1375 C. In each case, multiple slices were made parallel to the tensile stress axis to obtain sections from the interior and from the near (external) surface of the test samples. TEM sample preparation followed conventional, ceramic techniques.

Results and Discussion

Examination of GN-10 revealed a silicon nitride matrix of variable grain size and morphology, Fig. 1. Grain shapes tended to be either equi-axed or acicular (typically, with aspect ratios of three or more); grain dimensions ranged from roughly 0.2 to 3 microns, although grain dimensions of up to 5 microns were not uncommon. The microstructure of both crept and uncrept (as-received) also contained a relatively high volume fraction of crystalline second phase grains of sub-micron size, Fig. 2, which result from partial devitrification of the intergranular glass present during sintering. Based on electron diffraction, devitrification in GN-10 is found to result in two different crystalline second phases: one, a hexagonal phase isomorphic with $Y_5(SiO_4)_3N$ (i.e. N-Apatite or "H-phase"); the other, a monoclinic phase isomorphic with $Y_4Si_2O_7N_2$ ("J-phase"). Preliminary compositional analyses by EDS, moreover, indicates that both crystalline phases contain ~2 w/o Ca and that the hexagonal phase contains ~ 6 w/o Sr while the monoclinic phase contains ~ 4 w/o Sr. In both phases, Sr and possibly Ca appear to substitute for yttrium relative to the "pure" isomorphic forms.

Examination of GN-10 also revealed the presence of a residual glassy interphase separating most, if not all, crystalline grains. Here, the presence of glass was indicated by imaging under diffuse dark-field conditions and by the detection of Y, Sr, and O at these interfaces by EDS. Under conditions where the interfaces could be directly imaged, the thickness of the glassy layer separating adjacent silicon nitride grains was typically 1 nm. or less, Fig. 3a, while for interfaces separating the matrix grains and the secondary crystalline phases, glassy layers in excess of 1 nm. in thickness were generally

Figure 1. Representative view of microstructure of GN-10 silicon nitride illustrating varied β-Si_3N_4 grain size and morphology.

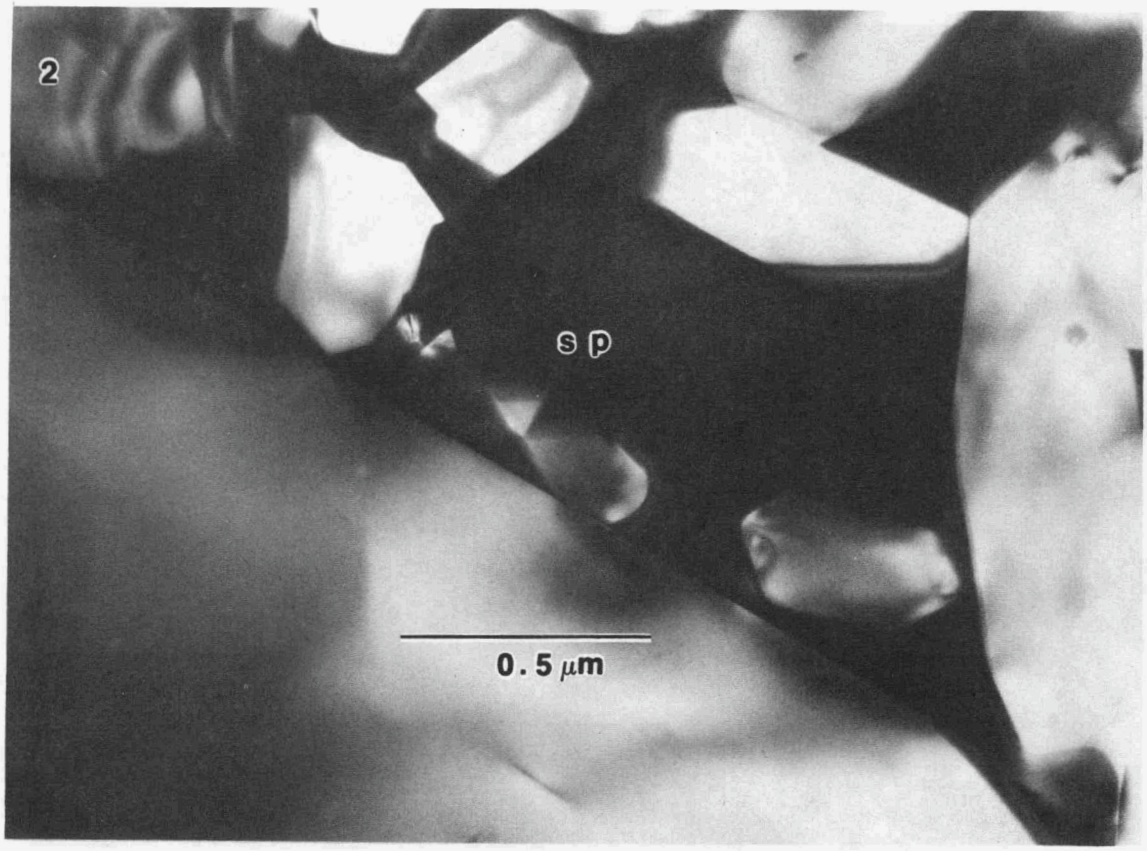

Figure 2. Crystalline second phase (dark contrast) produced in GN-10 by partial devitrification of intergranular glass originally present during processing.

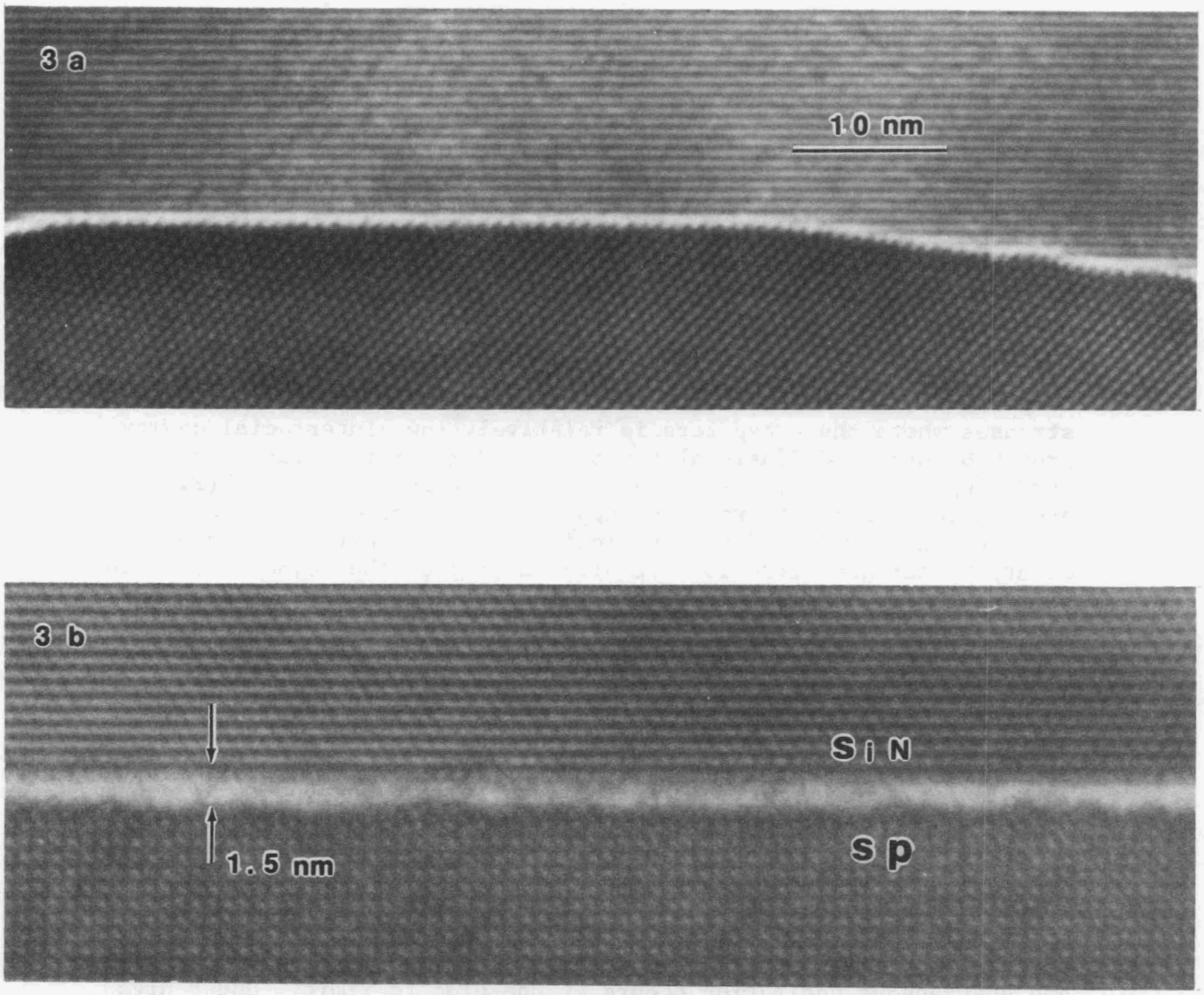

Figure 3. a) High resolution image of interface between adjacent silicon nitride grains indicating the presence of a glassy interphase, typically, 1 nm. or less in thickness. b) High resolution image of interface between silicon nitride grain (top) and crystalline second phase (bottom). Typically, glassy interphases greater than 1 nm. in thickness were indicated.

found, Fig. 3b. Although quantitative analysis of the glass composition was not possible, detectable Ca was not found in the glass, and comparative EDS results indicate a significant increase in the strontium to yttrium ratio for the glass compared to the secondary crystalline phases. These results suggest that devitrification, which occurs after processing (either during cool-down or during a post-processing anneal), significantly alters the "equilibrium" concentration of glass, specifically resulting in a relative enrichment of Sr and depletion of Y and Ca.

Although the residual glass composition and, hence, its properties cannot be quantified, the important role of the glass phase in determining creep behavior can be seen in results describing the cavitation process. Based on examination of GN-10 samples crept under different conditions, normal grain displacements result in cavity nucleation within the glassy interphase and cavity growth occurs rapidly along the interface to form creep cracks. The process of rapid, crack-like cavity growth appears to depend on stress and temperature, which determines the creep rate. At temperatures and stresses where the creep rate is relatively low, interfacial cavity growth occurs by diffusional transport. Despite the crack-like morphology (Fig. 4a), the advancing cavity tips are blunted (Fig.4b) and, in most cases, there is no apparent widening of the interface ahead of the cavity. This description suggests that cavity growth occurs by surface diffusion (or dissolution) of the adjacent silicon nitride grains coupled with rapid interfacial transport through the glassy interphase; otherwise, cavity growth by dissolution would be restricted and lead to the formation of discrete cavities of limited size. Apparently, even at moderate temperatures (e.g. 1250 C), the bulk diffusivity of the glassy interphase is sufficiently high to allow rapid interfacial cavity growth and crack formation. Alternatively, at temperatures and stresses for which the creep rate is relatively high, rapid interfacial cavity growth appears to occur by a viscous hole growth mechanism. Under these conditions, the advancing cavity tips are relatively sharp, glass ligaments often remain within the cavity, and the interface ahead of the cavity tip appears wider and often contains discrete cavity nuclei, Fig. 5. Apparently, the normal displacement rates are too rapid to allow relaxation by either diffusive transport or viscous flow of the glass and spontaneous cavitation occurs at the elastic limit. Under high stain rate conditions, the creep behavior of GN-10 appears ultimately limited by the viscous properties of the retained glass phase.

Currently, results obtained on GN-10 are being compared with those obtained previously on GTE AY6 and Norton NT154, and will be described in two related papers: one, comparing the microstructural characteristics of these materials; the other, discussing cavitation behavior. Future plans include analysis of GTE PY6 after tensile creep and the correlation of TEM results on cavity size and density in NT154 samples with results obtained by density measurement and by low angle neutron and X-ray scattering.

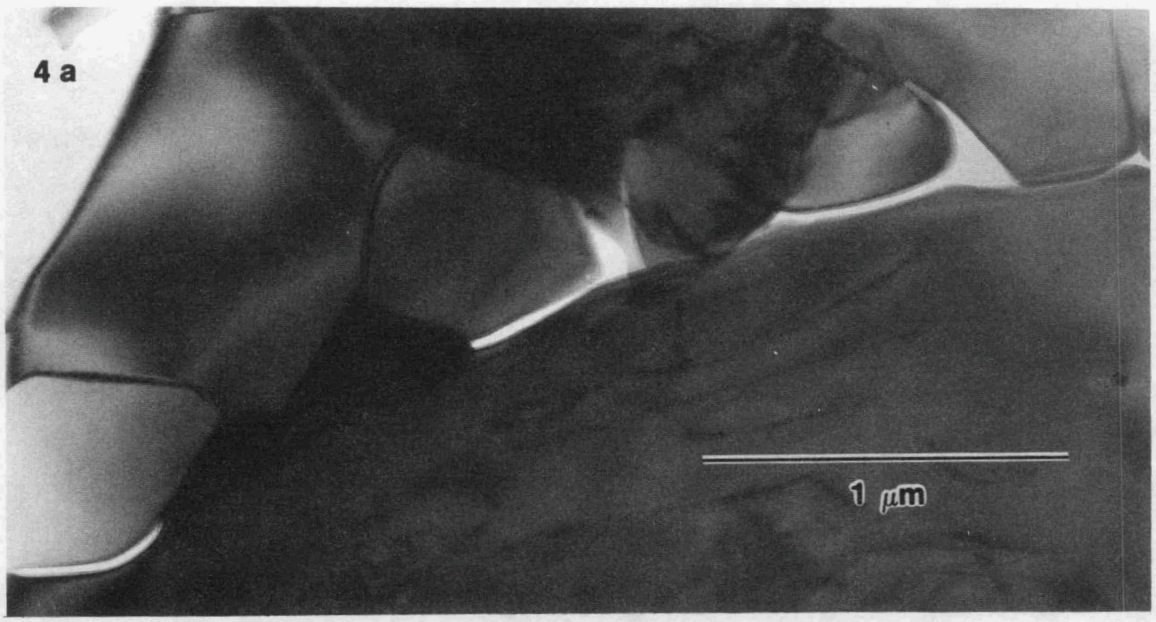

Figure 4. a) Segmented creep crack produced in GN-10 by rapid cavity growth along individual two-grain interfaces.

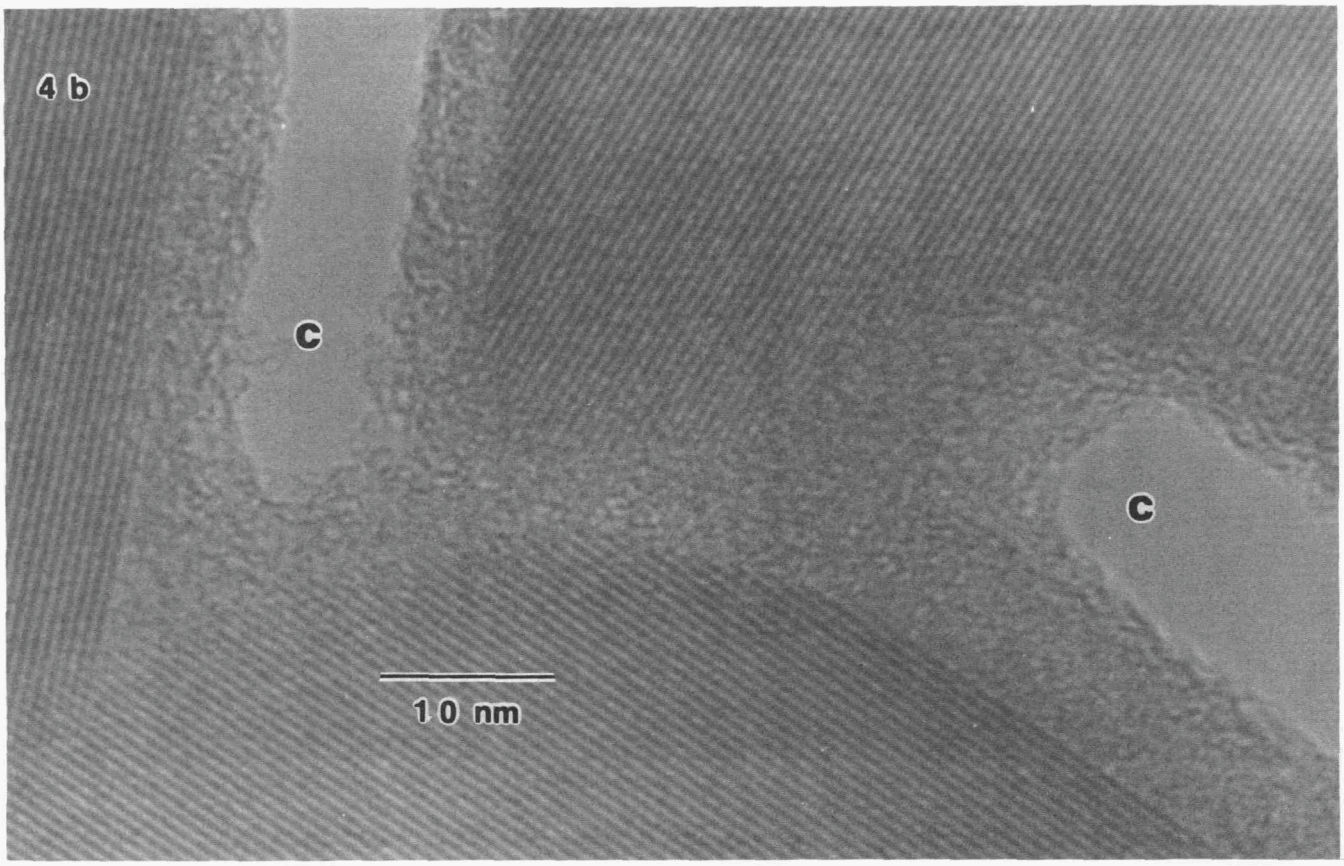

Figure 4. b) High resolution image of crack-like cavities arrested at triple grain junction. Cavity morphology is characteristic of growth under low strain rate conditions and suggests growth by matrix dissolution and rapid interphase transport.

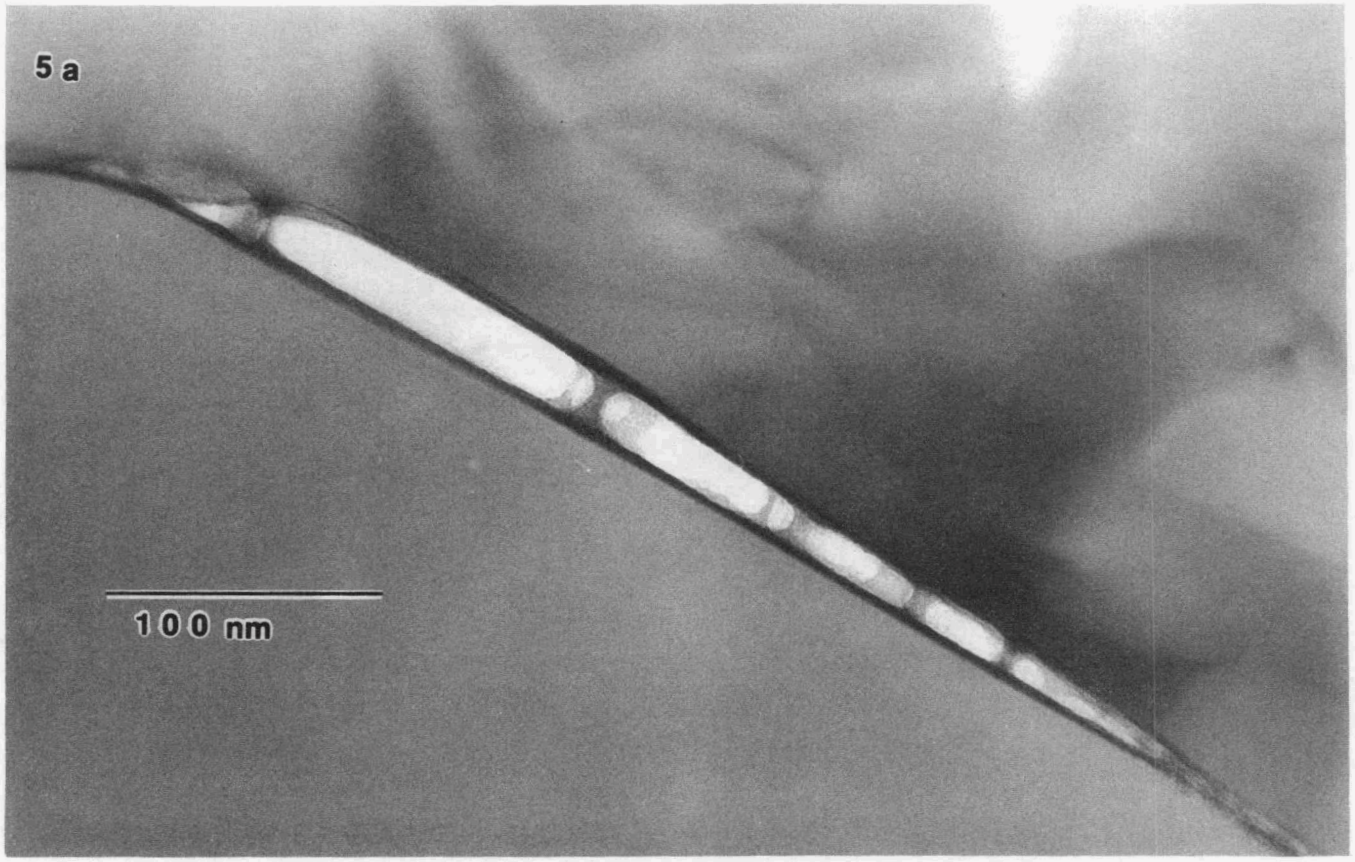

Figure 5. a) Crack-like interfacial cavity produced in GN-10 under high strain rate conditions. Note glassy ligaments still connecting displaced surfaces.

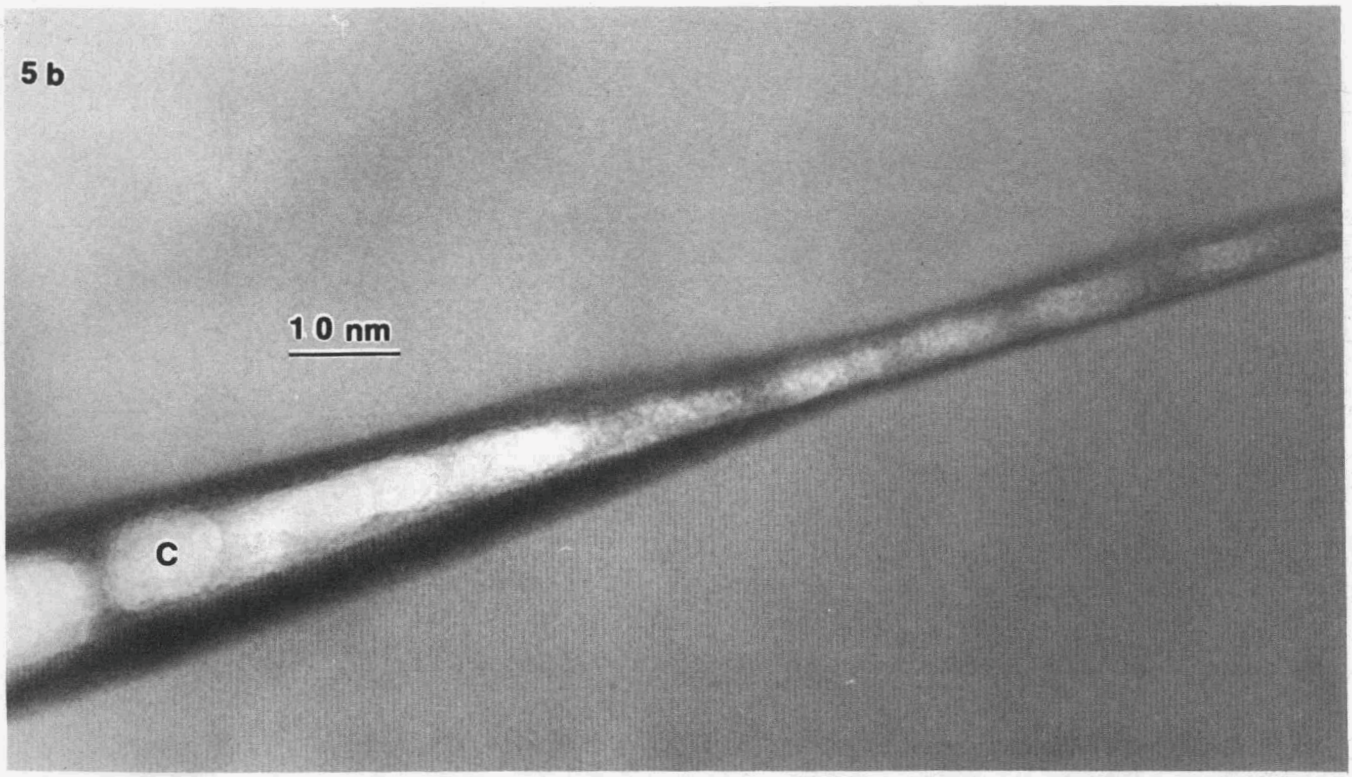

Figure 5. b) Detail of cavity tip region (lower right, Fig. 5a). In comparison with Fig. 4a, note atypical interface width ahead of cavity, tapered cavity tip morphology, and discrete cavities within glassy interphase.

Status of Milestones

All milestones are on schedule.

References

None

Mechanical Properties and Microstructural Characterization of Si_3N_4 Ceramics

K. L. More, T. A. Nolan, and L. F. Allard
(Oak Ridge National Laboratory)

Objective/scope

The objective of the research is to use analytical and high-resolution electron microscopy to characterize the microstructure of Norton Si_3N_4 ceramic materials following mechanical strength (tensile) testing at elevated temperatures in air. This work represents a collaboration with several institutions including Norton/TRW (R. L. Yeckley), the University of Dayton (N. L. Hecht), and Allied-Signal Aerospace Co. (M. N. Menon). Another commercial-grade Si3N4 material, Kyocera's SN-260, was also characterized before and after four-point-bend creep experiments.

Technical highlights

The material under investigation is a hot-pressed Si_3N_4 supplied by Norton containing 4.0 wt % Y_2O_3 intentionally added as a sintering aid. The material was annealed to crystallize the grain-boundary phase as part of the Norton processing procedure. During the past year, Norton has altered its manufacturing parameters to produce an "improved" version of their NT-154 material. Two batches of this improved material have been characterized to date. The first was an experimental batch designated LM74 that was subjected to high-temperature mechanical testing in the Mechanical Properties User Center of the HTML. The second was a production batch that has the new major product designation NT-164. No mechanical tests of NT-164 at high temperature have been completed as of this report. High-temperature testing of LM74 revealed considerable performance improvement when compared to standard NT-154. For example, at 150 MPa and 1370°C, a typical specimen of NT-154 had a steady-state creep rate of 1.4×10^{-8} s^{-1} and failed after 232 h. An LM74 specimen tested under the same conditions had a creep rate of 4.9×10^{-9} s^{-1} and failed after 956 h. Similar results were obtained at other stress levels.

Microstructural differences between the improved material and NT-154 (and most other sintering aid-containing silicon nitride ceramics) were identified that explain the improved properties. The microstructure and failure mechanisms of NT-154 have been studied extensively, and detailed results have been reported in previous CTAHE bimonthly and semiannual reports. A brief summary of these results is reported herein to give perspective to the observations made on the microstructure of the improved material. The microstructure of NT-154 is composed of a "bimodal" distribution of Si_3N_4 grains which consisted of clusters of extremely small Si_3N_4 grains, usually < 0.2 μm, surrounded by larger, usually acicular, Si3N4 grains, > 0.5 μm in size, with many $>> 1$ μm. X-ray diffraction (XRD) revealed that the Si_3N_4 is typically β-phase, but some specimens have contained as much as 10% residual α-phase. Transmission electron microscopy (TEM) revealed that most of the compounds associated with the sintering aid are crystalline and localized in pockets. X-ray and electron diffraction and energy dispersive x-ray elemental analysis (EDS) show the primary grain-boundary phases to be α-$Y_2Si_2O_7$ (JCPDF 38-223) and $Y_5(SiO_4)_3N$ (JCPDF 33-1459). Finally, and most importantly, high-resolution TEM

revealed that Si_3N_4 grains were separated by a yttrium-containing amorphous film of from 0.5 to 1.5 nm thickness.

The LM74 and the NT-164 materials appear to be very similar in structure and composition and will thus be described jointly. Like the NT-154, they have a bimodal distribution of grain sizes and shapes. This is quite obvious in Fig. 1, a lower magnification TEM showing the general microstructure. XRD reveals that the phases present are also similar to NT-154 with one major exception: both LM74 and NT-164 contained an additional secondary phase, Si_2ON_2 (JCPDF 33-1162). The location and distribution of this phase, in relation to other phases in the microstructure, have yet to be determined by TEM and electron diffraction. All of the yttrium-containing phases appear to be completely crystallized. The most remarkable difference between NT-154 and the new material is the lack of an observable amorphous film separating the Si_3N_4 grains. A high-resolution TEM of a typical grain boundary between two grains in the NT-164 is shown in Fig. 2. Similar observations were made on LM74 untested and after creep testing. Inset in Fig. 2 is a typical grain boundary from NT-154 showing an amorphous film, about 1.5 nm thick, separating two Si_3N_4 grains. The absence of an observable amorphous film utilizing high-resolution TEM in the new material does not mean that there are no impurities remaining at these boundaries. Preliminary results on the new Hitachi field emission gun (FEG)-TEM (one of which has been purchased for the HTML) indicate that very small quantities of yttrium-containing material remain at these boundaries.

In summary, the new Si_3N_4 material has grain boundaries that have very small amounts of amorphous materials associated with sintering additives remaining when compared to earlier formulations as well as Si_3N_4 materials from other manufacturers. This lack of amorphous materials appears to result in a major improvement in the high-temperature creep properties. Microstructural changes associated with creep deformation and failure mechanisms of both NT-154 and NT-164 will be discussed in future progress reports.

Kyocera SN-260 silicon nitride has also been characterized by XRD and electron microscopy in both the as-received condition and after flexure creep tests at 1370°C. The results of these studies are reported here.

XRD from the surface of an as-received flexure bar showed only β-Si_3N_4 and an unidentified crystalline phase that had a high intensity relative to the β-phase. No evidence of a glassy component was seen in the X-ray patterns. TEM of the as-received material showed a microstructure of β-grains in a crystalline matrix. The matrix (or grain-boundary) phase was determined to comprise 15 to 20% of the specimen by volume. No voids were seen in the as-received material (Fig. 3). Energy dispersive spectra (EDS) acquired from the grain-boundary material showed Yb, Si, and O to be present. Quantitative analysis of the grain-boundary phase in comparison to a standard of Yb_2-Si_2O_7 indicated that the grain-boundary phase was consistent with a composition of Yb_2SiO_5. This would be an analogue to the Y_2SiO_5 phase commonly found in silicon nitrides that use Y_2O_3 as a sintering aid. However, the X-ray powder diffraction file lists no such compound, so the precise identification of the matrix structure is still not complete.

The grain-boundary phase was further characterized by high-resolution TEM and EDS analysis using an FEG-TEM to get elemental information from the two-grain junctions. Figure 4 shows a high-resolution image that confirms the grain-boundary pocket to be essentially totally crystalline but with some residual amorphous material in the corners of a triple point. The two-grain junctions typically contained amorphous material in a layer 0.5 to 1 nm thick. Spectra acquired from the FEG-TEM showed that significant YB was

YP15524

Fig. 1. TEM of Norton Si_3N_4 (batch LM74) showing the typical bimodal distribution of large acicular grains (see area A) and smaller equiaxed grains. (Magnification 100,000X)

YP15522

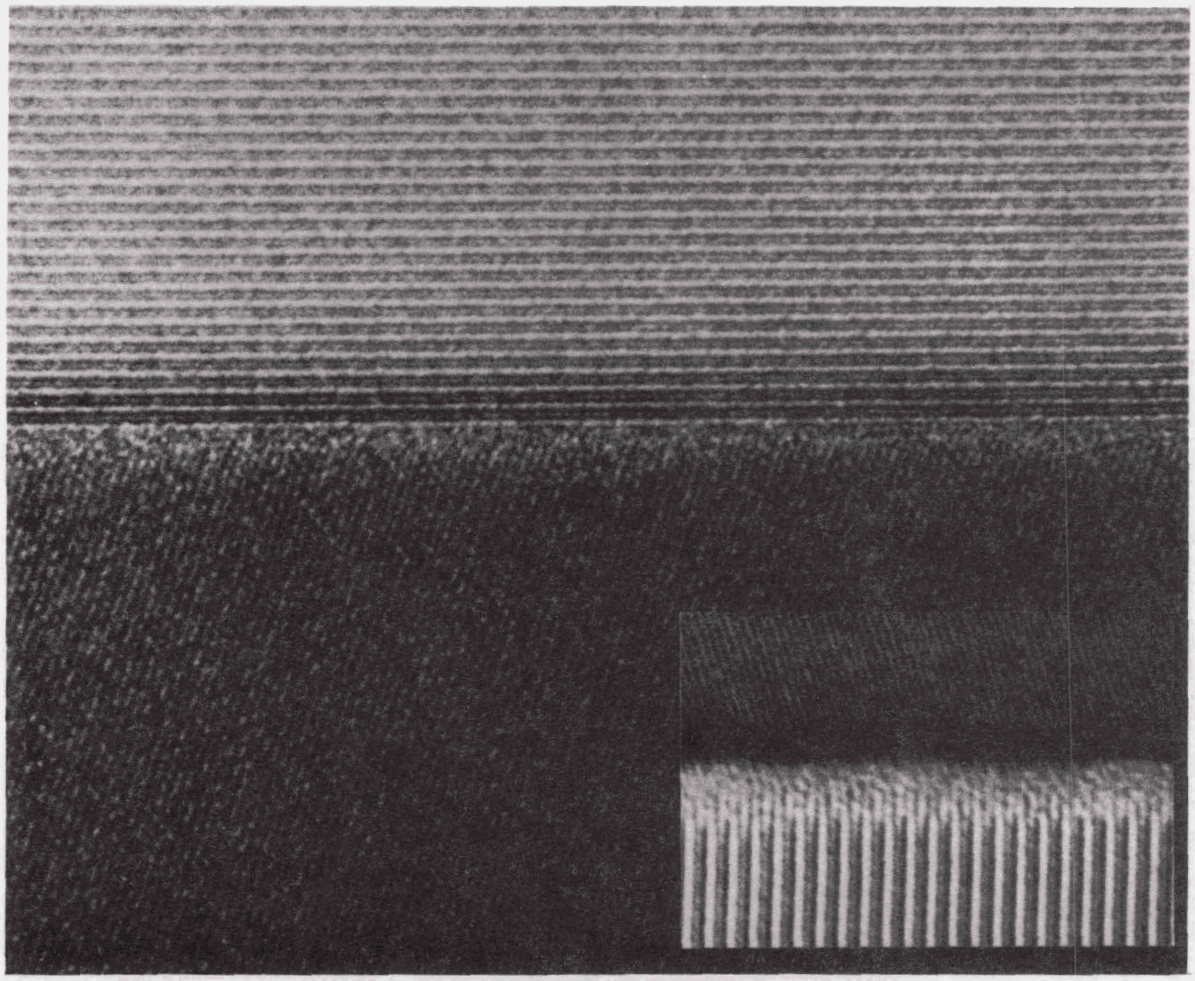

Fig. 2. High-resolution TEM of Norton NT-164 Si_3N_4 showing little or no observable amorphous material separating grains. Inset is a similar micrograph of NT-154 showing an approximately 1.5 nm amorphous layer separating grains. (Magnification 5,000,000X)

YP15523

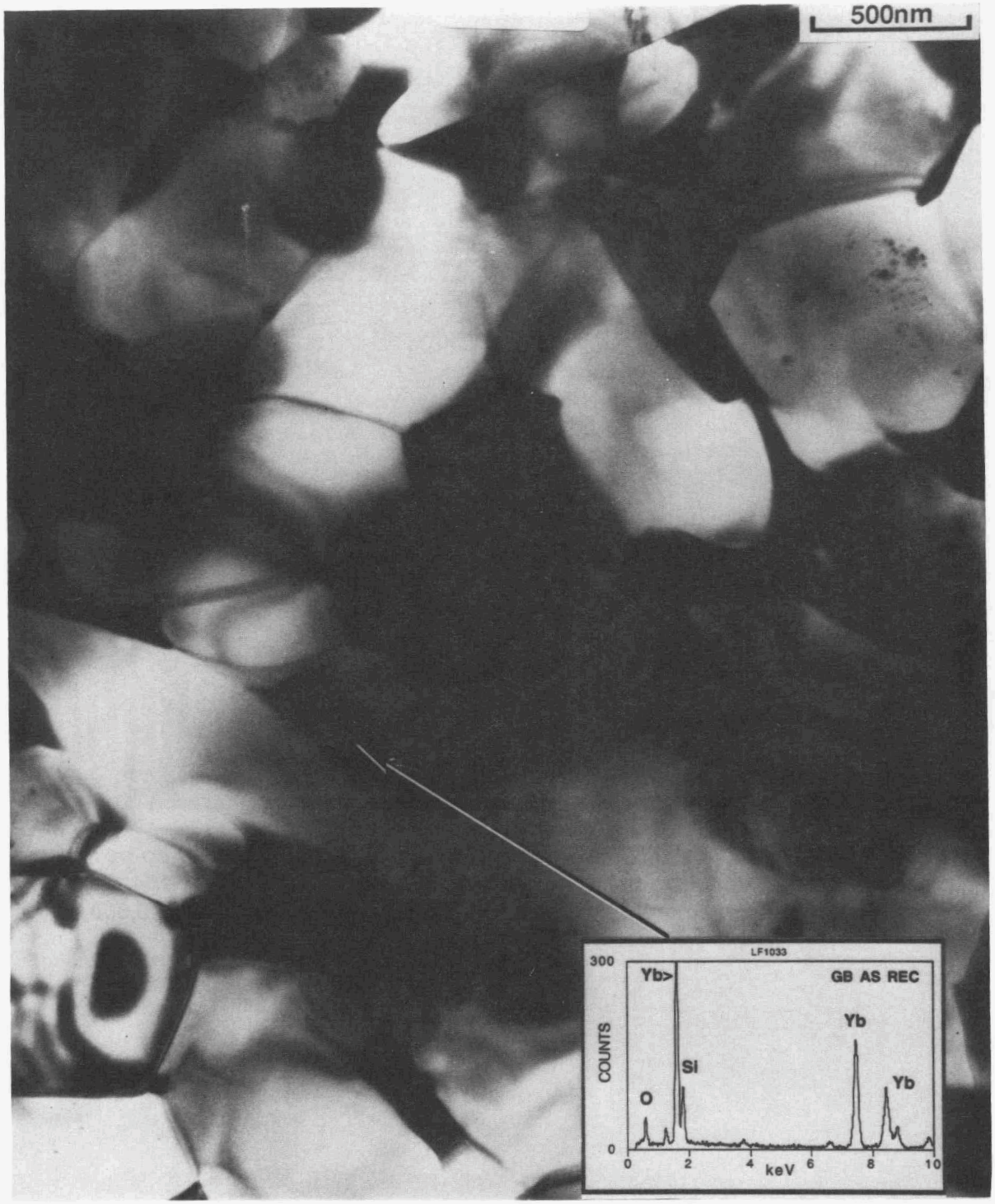

Fig. 3. As-received Kyocera SN-260. Light grains are β-Si_3N_4. Dark pockets are grain-boundary phase containing Yb and Si.

YP15524

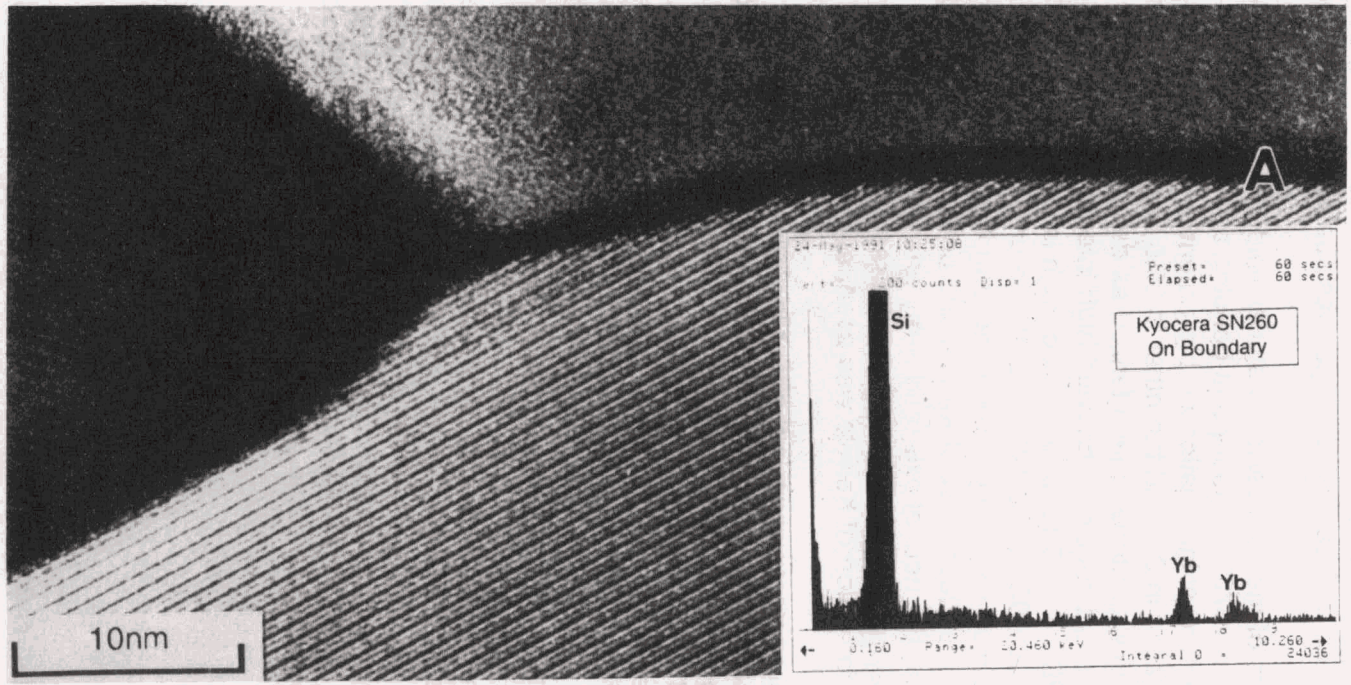

Fig. 4. High-resolution TEM image of grain-boundary pocket showing amorphous layer between silicon nitride grains. EDS spectrum from area A shows presence of Yb in the boundary.

present in the two-grain junctions (inset in Fig. 4). The pockets were typically single crystals, but in some instances, large pockets showed a boundary between crystalline regions indicating that the crystallization process proceeded from two different points within the pocket and was completed to create a boundary in the interior of a pocket. No evidence of crystal defects, such as dislocations or twins, was seen in the grain-boundary pockets.

Fast fracture of flexure bars of the as-received material yielded a flexure strength of 560 MPa. Creep tests were run at 1370°C in four-point bending at 70% of the fast-fracture strength (350 MPa) to get initial information on the potential mechanisms of creep in this material. One specimen failed in 9 h and the other in 35.5 h under these test conditions. The 35.5-hr specimen was further characterized as described hereafter. X-ray analysis of the surface of the as-crept specimen showed high intensity from a $Yb_2Si_2O_7$ phase identified as Keiviite (JCPDS no. 25-1345) and, also, high intensity from an SiO_2 phase identified as crystobalite (JCPDS no. 39-1425). Both the unidentified phase and the β-Si_3N_4 seen in the original specimen were very weak, indicating that oxidation processes during creep testing has formed a surface layer of Keiviite and crystobalite. Accordingly, the tested bar was sectioned near the neutral axis, and X-ray analyses were re-run. In the interior of the specimen, the X-ray results were identical to the results from the as-received specimen. No indication of the formation of Keiviite was seen, and the unidentified phase again showed strong intensity.

Figure 5 shows the typical microstructure in the tensile region of the SN-260 subjected to the above creep test conditions. No apparent changes were observed in the nature of the grain-boundary pockets. These areas exhibited no tendency to develop twins under creep stresses, and no changes in composition were noted. However, a significant number of voids were observed at triple points in the microstructure as a result of the creep tests. There was no evidence for the formation of cavities at two-grain junctions in the microstructure, as are often seen in creep specimens in Y_2O_3-fluxed silicon nitrides. Also, no cavities at two-grain junctions or voids at triple points were seen in a specimen taken from the region of the neutral axis. This indicates that the voids in the tensile region were a result of the stresses at temperature and not simply a heat-treating effect. The short duration of the test, or differences in the chemistry of the amorphous grain-boundary material as compared to Y_2O_3 fluxed ceramics, could account for the lack of cavity formation at two-grain junctions in the tensile region. These observations suggest that the mechanism of creep in this material is primarily grain sliding with possibly long-range solution-reprecipitation playing some role.

Status of milestones

Program on schedule.

Publications

1. K. L. More, D. A. Koester, and R. F. Davis, "Microstructural Characterization of a Creep-Deformed SiC Whisker-Reinforced Si_3N_4 Composite," *Ultramicroscopy* **37**, 263 (1991).

2. K. L. More, D. A. Koester, and R. F. Davis, "The Role of Interfaces in the Creep-Deformation of a SiC Whisker-Reinforced Si_3N_4 Composite," p. 382 in *Electron Microscopy*

YP15521

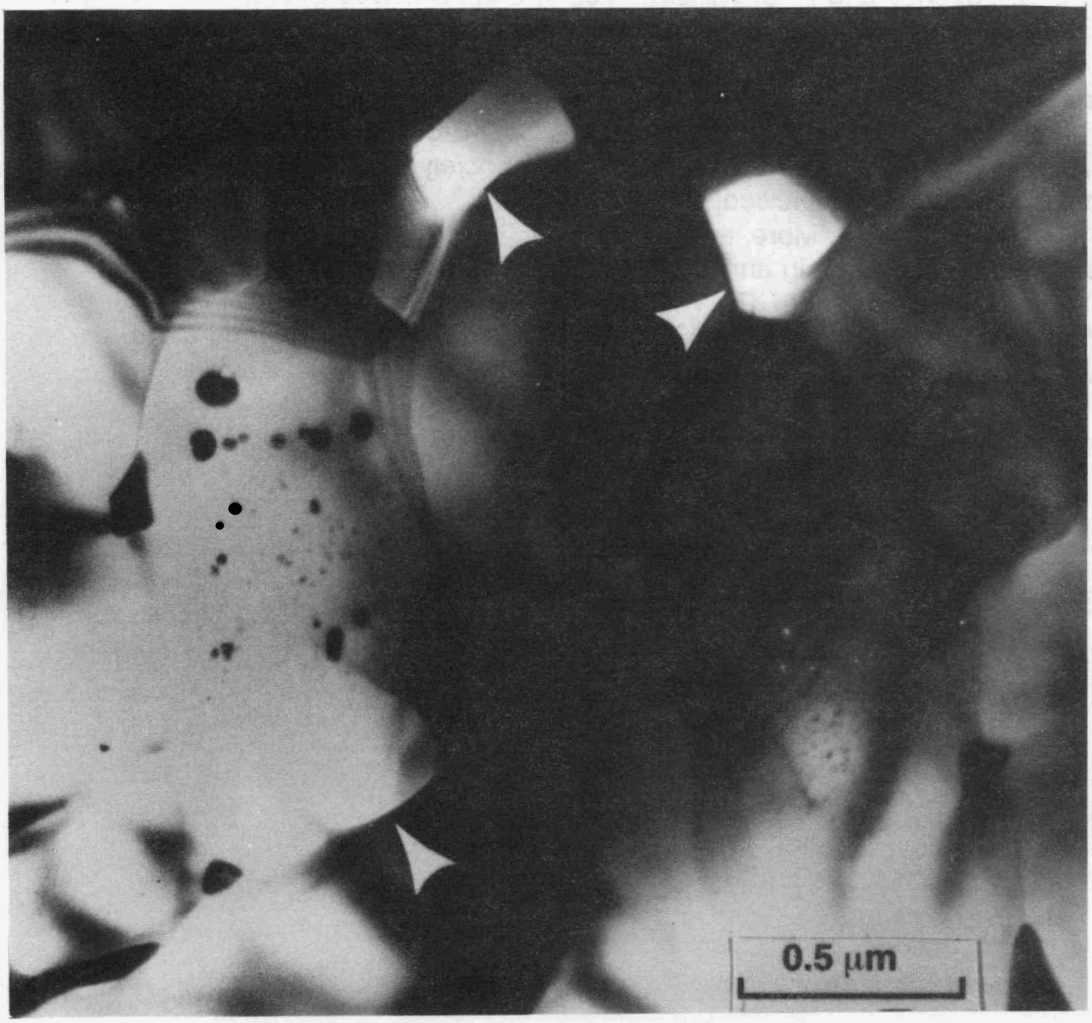

Fig. 5. The SN-260 material shows voids at triple points after creep tests.

1990, ed. L. D. Peachey and D. B. Williams, Vol. 4, San Francisco Press, San Francisco, 1990.

3. D. A. Koester, K. L. More, and R. F. Davis, "Deformation and Microstructural Changes in SiC Whisker-Reinforced Si_3N_4 Composites," J. Mater. Res. **6**[12], 2735 (1991).

4. K. L. More, "Defect Characterization in a CVD α-Si_3N_4" p. 936 in *Proceedings of the 49th Annual Meeting of the Electron Microscopy Society of America*, ed. G. W. Bailey, San Francisco Press, San Francisco, 1991.

5. D. A. Koester, K. L. More, and R. F. Davis, "The High Temperature Creep of a SiC Whisker-Reinforced Si_3N_4 in an Air Ambient," submitted to *J. Mater.Res.*

6. T. A. Nolan, L. F. Allard, D. W. Coffey, C. R. Hubbard, and R. A. Padgett, "Microstructure and Crystallography of Titanium Nitride Whiskers Grown by a VLS Process," *J. Am. Ceram. Soc.* 74[11], 2769 (1991).

Project Data Base

B. L. Keyes (Oak Ridge National Laboratory)

Objective/scope

The objective of this task is to develop a comprehensive computer data base containing the experimental data on properties of ceramic materials generated in the total effort. This computer system should provide a convenient and efficient mechanism for the compilation and distribution of the large amounts of data involved. The data base will be available in electronic form to all project participants. In addition, periodic hard-copy summaries of the data, including graphical representation and tabulation of raw data, will be issued to provide convenient information sources for project participants.

Technical highlights

The Ceramic Technology Project (CTP) Data Base presently contains 6788 test results on 27 different types of tests, 345 material characterizations, 13 lubricant characterizations, 101 coating characterizations, and 2087 associated records containing various metadata. A more detailed description is shown in Table 1.

Work on the computerized interface for the data base will begin in June 1992, instead of in March 1992, as originally planned, so that new data could be added with enough lead time to obtain the necessary background information before the next data base summary report is prepared. During the updating effort, data base personnel found the biggest problem was missing test background information. Few ceramics mechanical properties tests are standardized [i.e., American Society for Testing and Materials (ASTM) standards], and testing facilities and method vary somewhat among laboratories. A little research usually revealed the test methods but not always. Work will continue on finding missing information during the data input period.

The updating effort concentrated on establishing a consistency in nomenclature of materials, batch codes, and other search fields, as well as locating missing information. Since no widely accepted, standardized naming convention exists for ceramics at this time, data base personnel decided to stay with the manufacturer's name, such as NT-154 for Norton/TRW's silicon-nitride ceramic, for the material name. A cross-reference file, created to locate various aliases given to a particular ceramic, will be incorporated into the search menus in the user interface to be written later this year.

Data from all types of mechanical properties tests are now being collected for input to the data base. Most of the information collected during this period has been four-point bend test results on silicon nitrides because this seems to be a popular combination at the moment. Other test types on other materials will also be added as the data become available. All contributions are welcome.

Table I. CTAHE Data Base Summary as of September 30, 1991

Material class	Brazed specimens					Creep	Cyclic fatigue	Density	Dynamic fatigue	Elasticity
	MOR 4	Shear str.	Toughness	Torsion	Tor fatigue					
Alumina							15		9	28
Alumina + reinforcing fibers								7		
Alumina + zirconia										
Mullite										2
Mullite + reinforcing fibers										11
Silicon carbide		12						10	13	15
Silicon nitride	69	48		15	7	88	19	28	21	24
Silicon nitride + reinforcing fibers							15	2		16
Zirconia	160	58	2				51	158		119
Zirconia + reinforcing fibers										
Other				6				4		
Totals	229	118	2	21	7	88	100	209	43	215

Material class	Fracture toughness	Hardness	Interrupted fatigue	MOR 3-Pt. bend	MOR 4-Pt. bend	Oxidation rate	Poisson's ratio	Shear modulus	Tensile	Thermal conductivity
Alumina	39	4			411				28	3
Alumina + reinforcing fibers	39				144				11	34
Alumina + zirconia					7					
Mullite	1			1	4					
Mullite + reinforcing fibers	12			9	22					
Silicon carbide	29	27			236					
Silicon nitride	94	112		10	954	1	2	1	149	23
Silicon nitride + reinforcing fibers	53				144	3	17	16	86	9
Zirconia	347	24	239		1554				50	
Zirconia + reinforcing fibers					2				36	
Other	3	39			59					
Totals	617	206	239	20	3537	4	19	17	360	69

Table 1. CTAHE Data Base Summary as of September 30, 1991 (continued)

Material class	Thermal contraction	Thermal diffusivity	Thermal expansion	Thermal shock	Torsion	X-Ray diffraction	Material char.	Chemistry
Alumina			1	2			13	14
Alumina + reinforcing fibers		18	4	6			94	
Alumina + zirconia	23		21				8	
Mullite							2	
Mullite + reinforcing fibers							24	
Silicon carbide			23			17	9	57
Silicon nitride		23	59		3	49	60	7
Silicon nitride + reinforcing fibers		17	14				56	
Zirconia						72	38	44
Zirconia + reinforcing fibers							5	
Other			35		4		36	17
Totals	23	58	157	8	7	138	345	139

Material class	Wear resistance	Coatings	Lubricants	
Alumina based	9	3		
Alumina + reinforcing fibers	1			
Silicon carbide	3			
Silicon nitride	22			
Chromia based	98	20		
Zirconia based	13	15		
Enamels	5	10		
Other	126	53	13	
Totals	277	101	13	
Grand total (characterization data)				459
Grand total (test data only)				6788

B. L. Keyes attended a joint meeting of ASTM C28 and E49 at the National Institute for Standards Testing (NIST) in Gaithersburg, Maryland, on December 18, 1991, to discuss material designation fields required to completely define a specific ceramic and to discuss future joint ventures in standard development. Results of the meeting were a revised guideline docu-ment on material designations of ceramic materials and the initial exchange of ideas on property fields for flexure tests at room and elevated temperatures. More work will be done on the properties of ceramics in the near future.

Status of milestones

All data base summary reports are now in publication. Work is continuing on updating and adding new data to the data base in preparation for the next data base summary report, to be completed in draft form through September 1992, and for the computerized user interface to be started in June 1992.

Publications

The Ceramic Technology for Advanced Heat Engines Project Data Base: September 1990 Summary Report is in publication.

The Ceramic Technology for Advanced Heat Engines Project Data Base: March 1990 Summary Report is in publication.

The Ceramic Technology for Advanced Heat Engines Project Data Base: September 1991 Summary Report is in publication.

3.2 TIME-DEPENDENT BEHAVIOR

Fracture Behavior of Toughened Ceramics

H. T. Lin, P. F. Becher, and W. H. Warwick (Oak Ridge National Laboratory)

Objective/scope

Ceramic composites, such as fiber- and whisker-reinforced ceramics, particulate phase composites, and ceramics with similar grain structures, offer important advantages for heat engine applications. Chief among these is the improved fracture toughness that can be achieved by appropriate design of microstructural and material parameters. Previous studies show that these materials often exhibit substantial improvements in damage, thermal shock, and slow crack-growth resistances. However, design of such systems must also consider those factors influencing their performance at elevated temperatures.

In response to these needs, studies are conducted to determine the mechanical properties, (e.g., creep, delayed failure, strength, and toughness) at elevated temperatures for these toughened ceramics. Particular emphasis is placed on understanding how microstructure and composition influence the mechanical performance at elevated temperatures and the stability of these properties for extended periods at these temperatures. The knowledge gained from these studies provides input on how to modify materials to optimize their mechanical properties for the temperature ranges of interest.

Technical highlights

The research efforts during this past six months were devoted to the evaluation of the toughness and creep behavior of *in-situ* reinforced silicon-nitride ceramics with highly developed acicular (whisker-like) grain microstructure. These Si_3N_4 materials were fabricated with sintering systems of 2Al3Y4La (SC138), 2Al6La (SC216 and SC127), 2Al6Y (SC252), 11La (SC162), 4Y6La (SC218), and 2Sr6Y (SC253) and under W.B.S. Element 1.2.3.1 (Dispersion-Toughened Ceramic Composite).

Toughness Behavior of In-Situ Reinforced Si_3N_4 Ceramics

The objective of this task is to provide an understanding of the effects of the oxide-sintering additives and microstructure characteristics on the toughness behavior of *in-situ* reinforced Si_3N_4 ceramics. The influence of test temperature on the fracture resistance in air is also evaluated. The fracture toughness at both room and elevated temperatures was characterized via a multiple indentation and fracture method.[1] The bend bars were prepared such that the tensile axis and surface were perpendicular to hot-pressing direction. Indentation loads ranging from 9.8 to 490 N were employed in order to study the R-curve behavior at room temperature. The indentation load used for toughness measurement at temperatures up to 1300°C in air was 294 N. The bend bars were fractured in four-point loading with inner and outer span lengths of 6.35 and

19.05 mm, respectively, at a crosshead speed of 0.51 mm/min for room-temperature test and at a loading rate of approximately 50 MPa/s for high-temperature test. Three specimens were tested at each indentation load and/or test temperature. Scanning electron microscopy (SEM) was used to evaluate the operative toughening mechanisms contributing to the increased fracture resistance.

Room Temperature: Figures 1 and 2 show the fracture toughness versus crack length data as a function of sintering additives for Si_3N_4 ceramics with elongated grain structures at room temperature. In general, the *in-situ* reinforced Si_3N_4 ceramics exhibit increasing crack-growth resistance with crack length (i.e., R-curve behavior). The toughness results indicate that the degree of R-curve response (the rate of rise of fracture resistance with crack length) and toughness value are, in part, dependent upon the oxide additives used in this study. For alumina-containing materials (Fig. 1), the materials with 2Al3Y4La, or 2Al8La, exhibit relatively slowly rising R-curve with initial extension of crack length as compared to 2Al6Y material. However, the fracture toughness value at the plateau of R-curve is quite similar for all of the Si_3N_4 materials with Al_2O_3. The R-curve behavior for materials free of Al_2O_3 (11La, 4Y6La, and 2Sr6Y) is illustrated in Fig. 2. The toughness results indicate that the

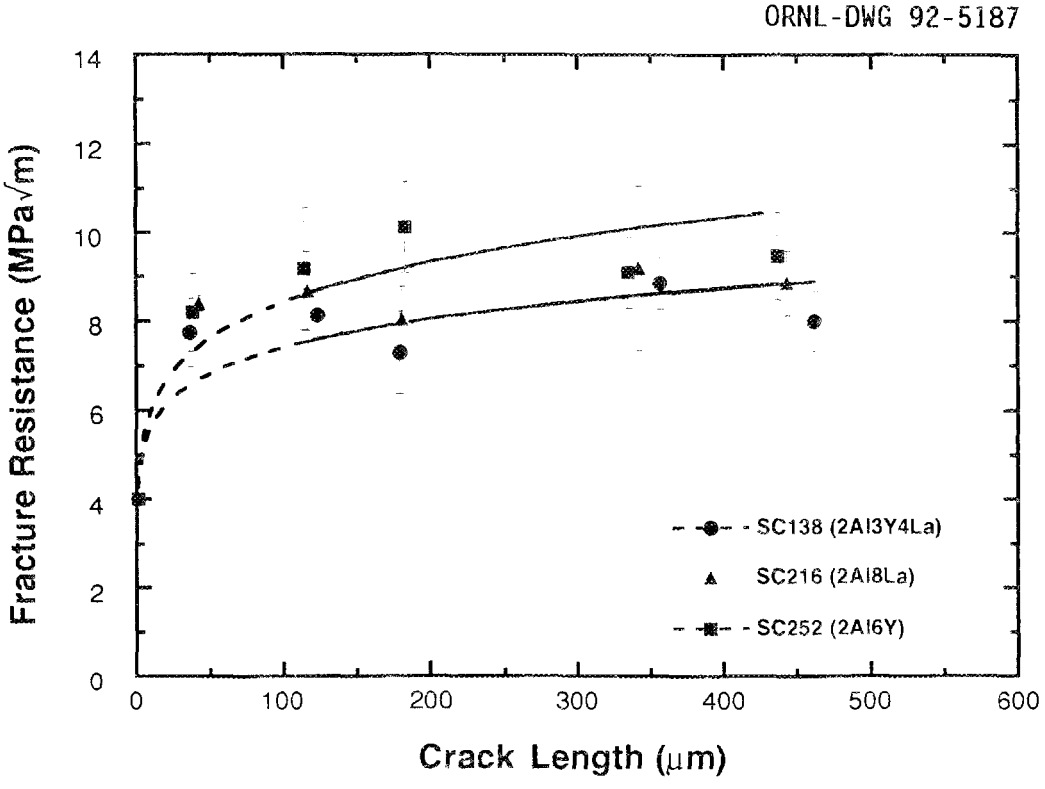

Fig. 1. Fracture resistance versus crack length curves for alumina-containing silicon-nitride ceramics.

ORNL-DWG 92-5188

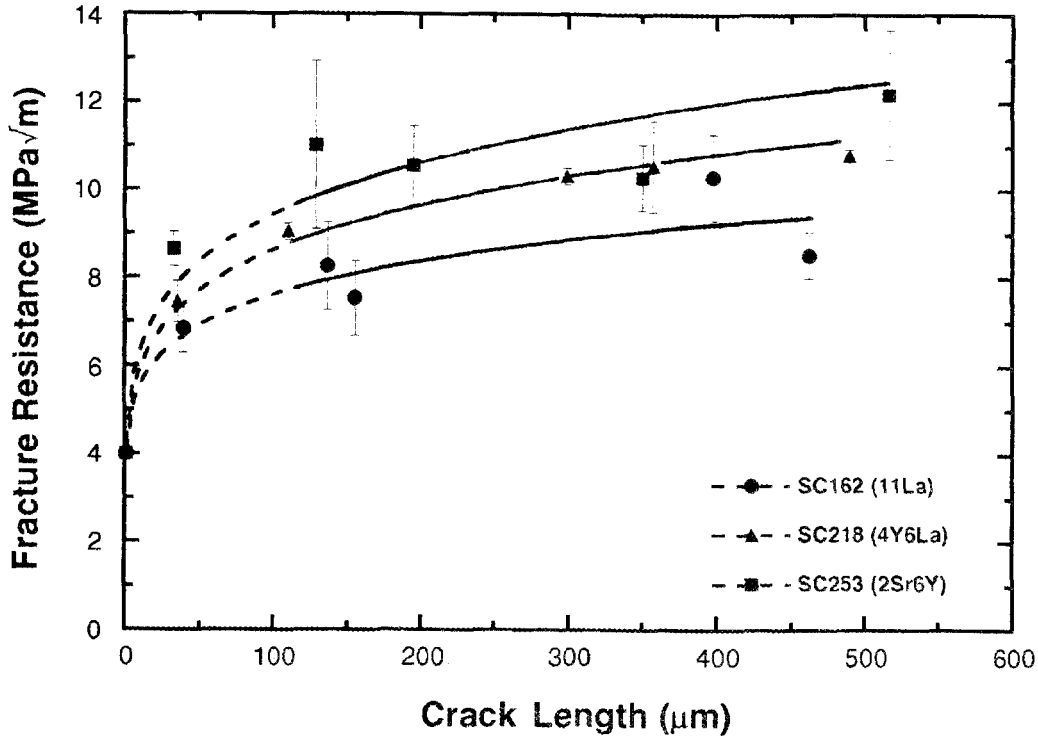

Fig. 2. Fracture resistance versus crack length curves for silicon-nitride ceramics with 11La, 4Y6La, and 2Sr6Y sintering additives.

2Sr6Y material exhibits the strongest R-curve response and highest toughness value among these alumina-free Si_3N_4 materials, while the 11La materials reveals a marked contrast behavior to the material with 2Sr6Y (the least response of R-curve and lowest toughness).

The difference in the R-curve responses and toughness values among the Si_3N_4 materials investigated could arise from the explicit differences in the elongated grain structures such as distribution of grain size and aspect ratio. However, the preliminary SEM examinations on the fracture surfaces of all of the as-fabricated materials reveal that the elongated microstructure is quite similar. Therefore, differences in chemistry, which lead to different thermomechanical properties, bonding, and volume content of grain-boundary phase(s), may contribute to the differences in the observed R-curve response and fracture resistance. The SEM observations of the crack paths indicate that the enhancement in fracture resistance of the *in-situ* reinforced Si_3N_4 ceramics is due to a combination of toughening mechanisms of crack bridging and pullout of elongated grains. The elongated grains behind the crack tip impose a crack-closure stress to counteract the externally applied stress, thus increasing the fracture resistance.

Elevated Temperature: Figures 3 and 4 show the fracture toughness data of *in-situ* reinforced Si_3N_4 as functions of test temperature and

ORNL-DWG 92-5189

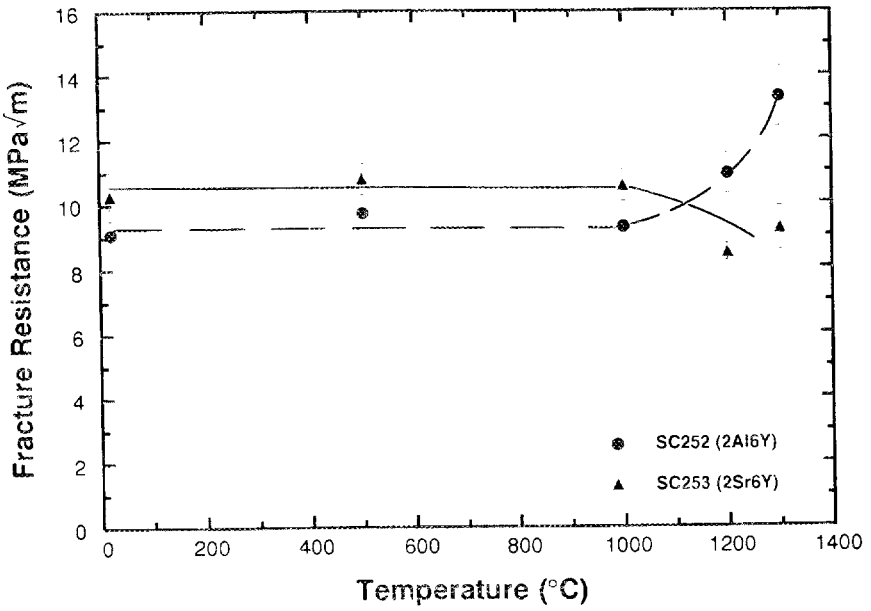

Fig. 3. Fracture resustance versus temperature curves for silicon-nitride ceramics with 2Al6Y and 2Sr6Y.

ORNL-DWG 92-5190

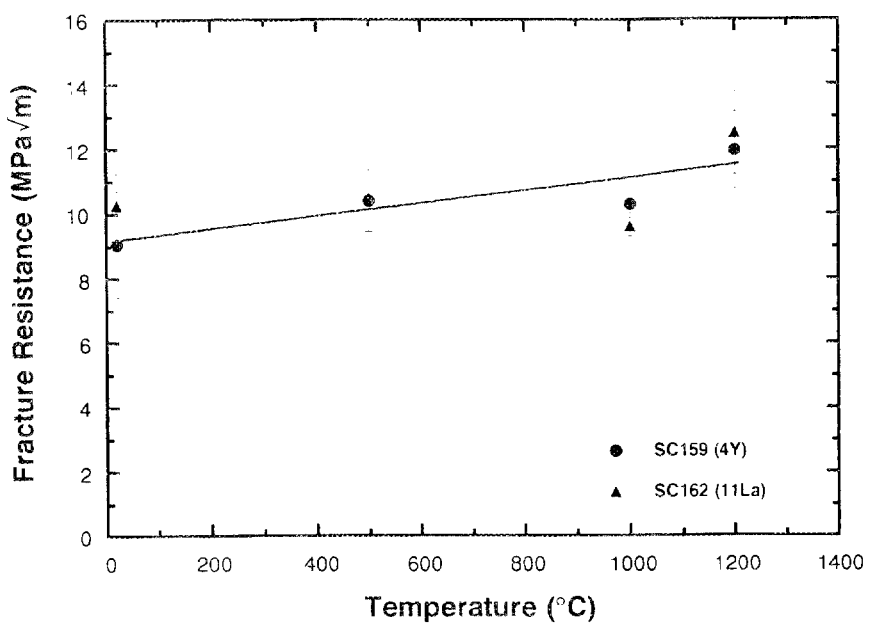

Fig. 4. Fracture resistance versus temperature curves for silicon-nitride ceramics with 4Y and 11La.

sintering additives. The results indicate that the toughness of Si_3N_4 materials with the 2Al6Y and 2Sr6Y sintering additives is insensitive to increases in test temperature up to 1000°C in air (Fig. 3). In contrast to the 2Sr6Y material exhibiting a 16% decrease in toughness, the 2Al6Y material shows a substantial increase (43%) in apparent toughness when the temperature exceeds 1000°C. This substantial increase in apparent fracture resistance of 2Al6Y material likely is associated with the softening of intergranular glassy phases. Viscous flow processes would also contribute to the observed significant strength degradation at elevated temperatures.[2,3] On the other hand, a change in interfacial bonding and effectiveness of crack bridging and pullout mechanisms due to the crystallization process of intergranular glassy phases at elevated temperatures may result in a decrease in fracture toughness.

The toughness results for materials with 4Y and 11La are shown in Fig. 4. The toughness versus temperature data shows that the fracture resistance of both Si_3N_4 materials increases with test temperature up to 1200°C under the test conditions employed in the present study. The contribution to the positive temperature dependence of fracture toughness is still uncertain at present and needs to be explored.

Creep Behavior of In-Situ Reinforced Si_3N_4 Ceramics

The studies of the strength and toughness behavior of Si_3N_4 ceramics containing elongated grain structure indicate that the mechanical responses of Si_3N_4 materials at elevated temperatures in air are governed by the residue intergranular phases introduced by the oxide-sintering additives.[2-4] The marked reduction in fracture strength that occurs at temperatures ≥ 1200°C in air is attributed to the onset of the softening of intergranular phases and/or oxidation reaction. The principal source of the degradation in mechanical properties arises from the creep-type processes. Therefore, a study of flexural creep has been initiated in this reporting period to understand the relationship between the temperature at which a significant decrease in strength occurs and the creep rates. The flexural creep study in air was conducted at temperatures from 1200 to 1370°C using selected applied stresses.

Figure 5 shows the flexural creep data for silicon-nitride ceramics with sintering additives of 2Al6Y and 2Sr6Y at 1200°C at stresses ranging from 100 to 408 MPa. The creep data of Norton NC132 hot pressed with 1 wt % MgO is also included for comparison.[5] The results indicate that in spite of the difference in sintering additives, the 2Al6Y material (SC252) and NC132 exhibit identical creep properties at 1200°C under the stress range employed. The results also show that the 2Sr6Y-containing material exhibits creep rates that are three to four times lower than those of NC132 and 2Al6Y materials (SC252). Furthermore, the 2Sr6Y material exhibits a creep strain after 100 h at 1200°C/100 MPa, which is an order of magnitude less than those for NC132 and SC252. Regression analysis of the creep rate versus stress data reveals a creep-stress exponent of one for each material. For ceramic materials with intergranular liquid phases, a stress exponent of one is generally attributed to viscous creep mechanism.

The fracture strength results reported previously have shown that the materials containing 2Sr6Y exhibited much better retention of strength at 1200°C in air than 2Al6Y materials.[2,3] This is, in part, due to the fact

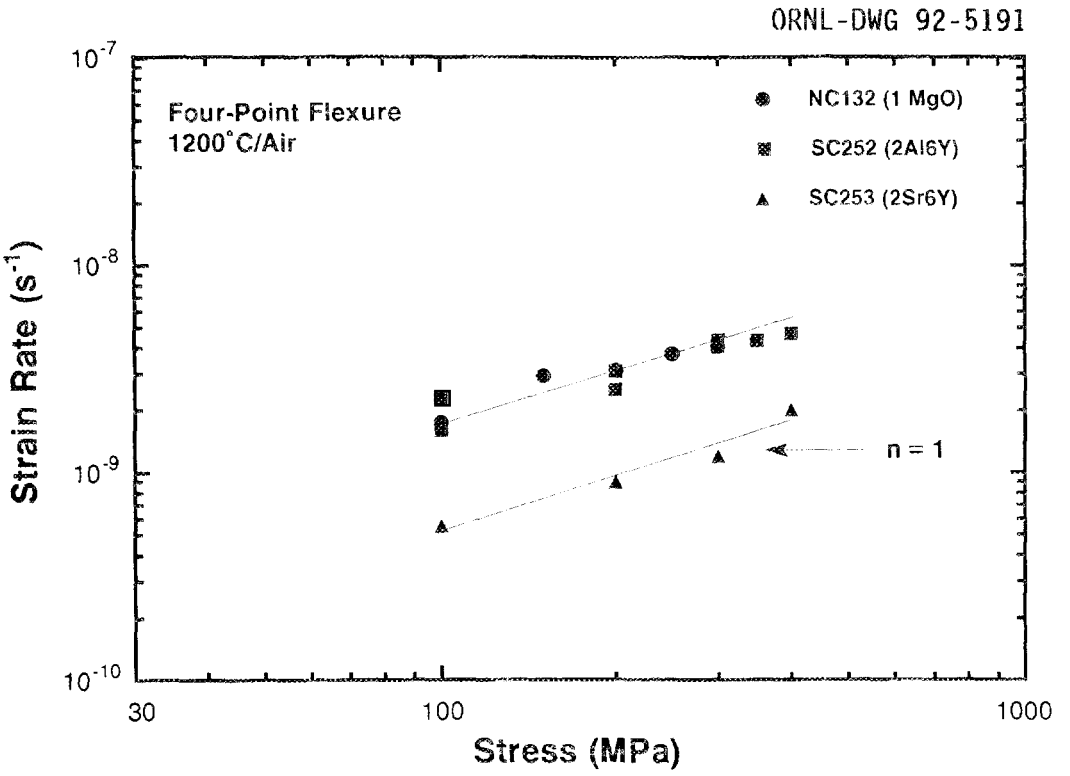

Fig. 5. Creep rate versus applied stress curves for silicon-nitride ceramics with elongated grain structure.

that the intergranular glassy phase in 2Sr6Y material is more refractory (thus, higher viscosity) than that in 2Al6Y material, which is indicated by the much better creep resistance of the 2Sr6Y material.

Status of milestones

On schedule.

Publications

None.

References

1. R. F. Cook and B. R. Lawn, "A Modified Indentation Toughness Technique," *J. Am. Ceram. Soc.* 66(11), C-200-C201 (1983).

2. H. T. Lin, P. F. Becher, and W. H. Warwick, "Fracture Behavior of Toughened Ceramics," pp. 32-36 in *Ceramics Technology Project Bimonthly Technical Progress Report ORNL/CF-91/281*, June 28, 1991.

3. H. T. Lin, P. F. Becher, and W. H. Warwick, "Fracture Behavior of Toughened Ceramics," pp. 31-33 in *Ceramics Technology Project Bimonthly Technical Progress Report ORNL/CF-91/316*, August 30, 1991.

4. H. T. Lin, P. F. Becher, and W. H. Warwick, "Fracture Behavior of Toughened Ceramics," pp. 31-34 in *Ceramics Technology Project Bimonthly Technical Progress Report ORNL/CF-91/375*, December 31, 1991.

5. H. T. Lin, unpublished results.

Cyclic Fatigue of Toughened Ceramics

K. C. Liu, H. Pih, C. O. Stevens, and C. R. Brinkman
(Oak Ridge National Laboratory)

Objective/scope

The objective of this task is to develop, design, fabricate, and demonstrate the capability to perform tension-tension dynamic fatigue testing on a uniaxially loaded ceramic specimen at elevated temperatures. Three areas of research have been identified as the main thrust of this task: (1) design, fabrication, and demonstration of a load train column that truly aligns with the line of specimen loading; (2) development of a simple specimen grip that can effectively link the load train and test the specimen without complicating the specimen geometry and, hence, minimize the cost of the test specimen; and (3) design and analysis of a specimen for tensile cyclic fatigue testing.

Technical progress

Cyclic fatigue testing of GN-10 Si_3N_4

Cyclic fatigue tests were continued on GN-10 Si_3N_4 at 1150°C. Test parameters and results obtained to date are summarized in Table 1, and data are plotted in Fig. 1. Filled symbols indicate the specimens were fractured at the test condition; open symbols indicate the test conditions were changed at the number of cycles to the next higher cyclic stress amplitude until failure occurred as indicated. Since the high-cycle (> 5×10^5 cycles) fatigue strength of GN-10 at 1150°C was not known, a cyclic stress amplitude of 380 MPa was selected as a starting point. After the first specimen was cycled for about 1×10^6 cycles with no indication of imminent failure, the cyclic stress amplitude was increased in steps of about 14 MPa on average after completing a block of about 50,000 cycles until failure occurred at 460 MPa.

Once the high-cycle end of the fatigue strength was determined, the low-cycle fatigue life can be deduced approximately. Therefore, the second specimen was cycled to 440 MPa at the onset. The cyclic stress amplitude was increased to 460 MPa at the end of 451,560 cycles. The specimen failed after completing a total of 717,160 cycles. Results of this test are consistent with that of the first specimen, showing the fatigue strength of this material at 1150°C may be at the level of about 460 MPa in the high-cycle range.

On the basis of the above finding, the third specimen was cycled to 480 MPa at the onset. The specimen failed after completing a total of 5359 cycles, which fell within the target range. Due to the limited number of test results, the fatigue curve of GN-10 Si_3N_4 at 1150°C was determined visually. A comparison indicates that the fatigue strength of GN-10 at 1150°C may be comparable to or only marginally lower than that of NT-154. Examination of Fig. 1 further indicates that the difference between the fatigue strength at the high-cycle end and the corresponding tensile strength was about 43% of the latter at 1250°C. The difference narrowed to 36 and 25%, as temperature decreased to 1200 and 1150°C, respectively. If this trend continues as temperature further decreases, the fatigue curve will become flat indicating that there may be little or no fatigue damage occurring due to cyclic loading at low temperatures.

Table 1. Results of tensile and cyclic fatigue tests of GN-10 Si_3N_4 at elevated temperatures

Specimen	Temp. (°C)	Tensile/cyclic stress to fracture [MPa (ksi)]	Intermediate cyclic stress [MPa (ksi)]	Number of cycles at intermediate loading	Number of cycles to failure
357-2	1150	585.6, (84.9)			1
357-3	1150		380, (55.1)	1,005,272	(1,005,272)*
			397, (57.6)	44,813	(1,050,085)
			408, (59.2)	50,925	(1,101,010)
			420, (61.0)	148,636	(1,249,646)
			436, (63.2)	51,887	(1,301,533)
			447, (64.9)	69,351	(1,370,884)
		460, (66.7)		10,442	1,381,326
357-4	1150		440, (63.8)	451,560	451,560
		460, (66.7)		265,600	717,160
357-5	1150	480, (69.6)			5,359
350-1-2	1200	514.2, (74.6)			1
340-2-5	1200	350, (50.8)			41,845
350-2-4	1200		300, (43.5)	1,139,464	(1,139,464)
			313, (45.4)	59,332	(1,198,796)
			326, (47.3)	87,222	(1,286,018)
		337, (48.9)		43,446	1,329,464
338-1-2	1250	472.5, (68.5)			1
331-1-1	1250	285, (41.3)			59,308
350-2-5	1250	250, (36.3)			221,774

*Numbers in parenthesis indicate number of cycles accumulated at the end of intermediate loading.

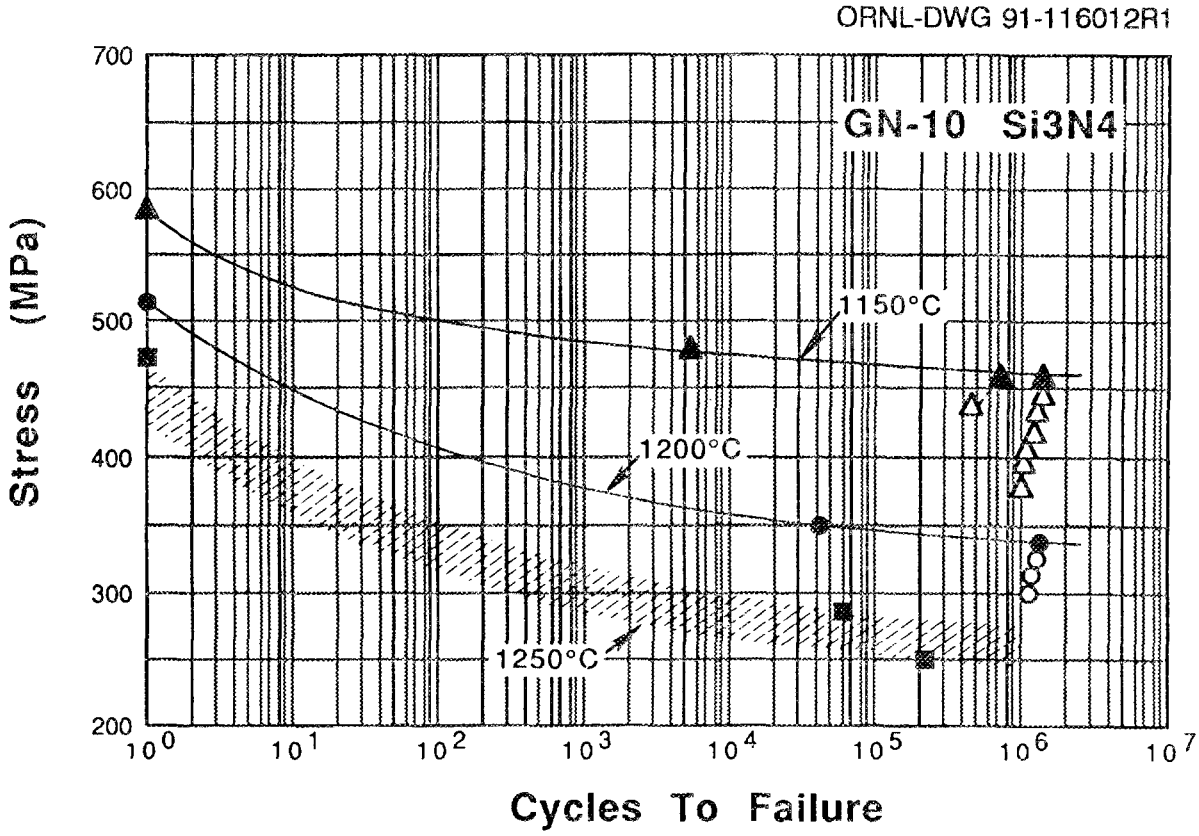

Fig. 1. Tensile fracture and cyclic fatigue behavior of GN-10 Si_3N_4 tested at elevated temperatures.

Acoustic emission (AE) studies of ceramic fatigue

Acoustic emission studies were conducted on SiC_w/Al_2O_3 composite specimens under cyclic fatigue loading. Results indicated that the AE detecting system was capable of predicting the imminence of failure of the composite material under cyclic loading by showing an accelerated increase in energy/count rate prior to fracture, as was the case in an earlier AE study on sintered Si_3N_4. However, early detection of the potential failure sites, far in advance to actual failure, remains difficult at this time because the potential fracture initiation defects do not prevail at the early stage of fatigue life on many competing AE sources that are distributed rather randomly along the length of the tensile specimen. Therefore, the technique relying on identification of change in energy/count rate needs further refinement to accomplish accurate estimation of residual life and to predict exact location of failure site.

Both composite specimens tested failed outside the sensor section between the two AE sensors. Figure 2 shows a plot of energy versus location for composite specimen No. 1. Although actual failure occurred beyond sensor 2 (outside the monitoring section between two sensors), a high-energy peak located at the proximity of sensor 2 indicated otherwise. The false indication of the fracture site was a result of the deficiency in the location algorithm, which calculated the location of an AE event based on the differential

ORNL-DWG 92-11853

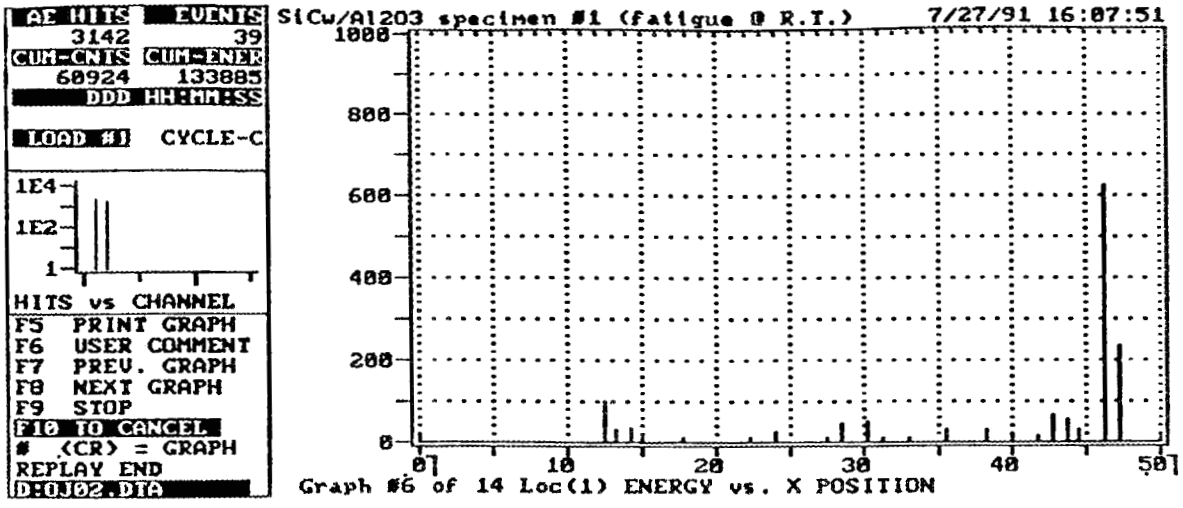

Fig. 2. AE energy versus location plot for an SiC_w/Al_2O_3 specimen tested under cyclic fatigue loading.

between AE wave arrival times monitored at the sensors. Any AE event occurring outside the sensor zone yielded the maximum time differential, hence indicating the location of failure at the nearest sensor point. Furthermore, in many cases, the energy peak would not indicate exactly on the sensor location since the paths and speed of AE waves to the sensors could not be estimated accurately *a priori*.

A draft report has been prepared covering results of the AE study on cyclic fatigue behavior of ceramic and ceramic composite materials.

Creep testing of NT-154 Si_3N_4

Experimental efforts were continued on creep testing of NT-154 Si_3N_4. All specimens tested were annealed at 1370°C for 150 h. Activities that occurred during this reporting period are as follows.

Creep behavior at 1200°C

Specimen 13-10: Test was initiated at 1200°C under an initial stress of 250 MPa, which was increased to 275 MPa at t ~ 1000 h and to 300 MPa at t ~ 2000 h. The specimen failed after 135 h of testing at 300 MPa, as shown in Fig. 3. The purpose of this test was to investigate the effects of strain histories on creep deformation.

Specimen 13-14: Test has been completed. The test was initiated at 1200°C under 175 MPa. Subsequently, the test temperature was increased in steps of 50°C at a time interval of about 1000 h, as shown in Fig. 4. The specimen fractured in about 10 min after the test temperature increased to 1350°C. A comparison shows that the creep-strain rate at t = 2000 h for this specimen was about the same (~2.0×10^{-10} s^{-1}) as that at t = 2000 h for specimen 20-56 tested under the same condition (175 MPa/1250°C) as seen in Fig. 7. The creep rate accelerated significantly when temperature was increased to 1300°C. However, the creep rate slowed down to ~1.3×10^{-9} s^{-1} during the last 500 h of testing. Interestingly, the creep rate was almost the same as that of specimen 20-47

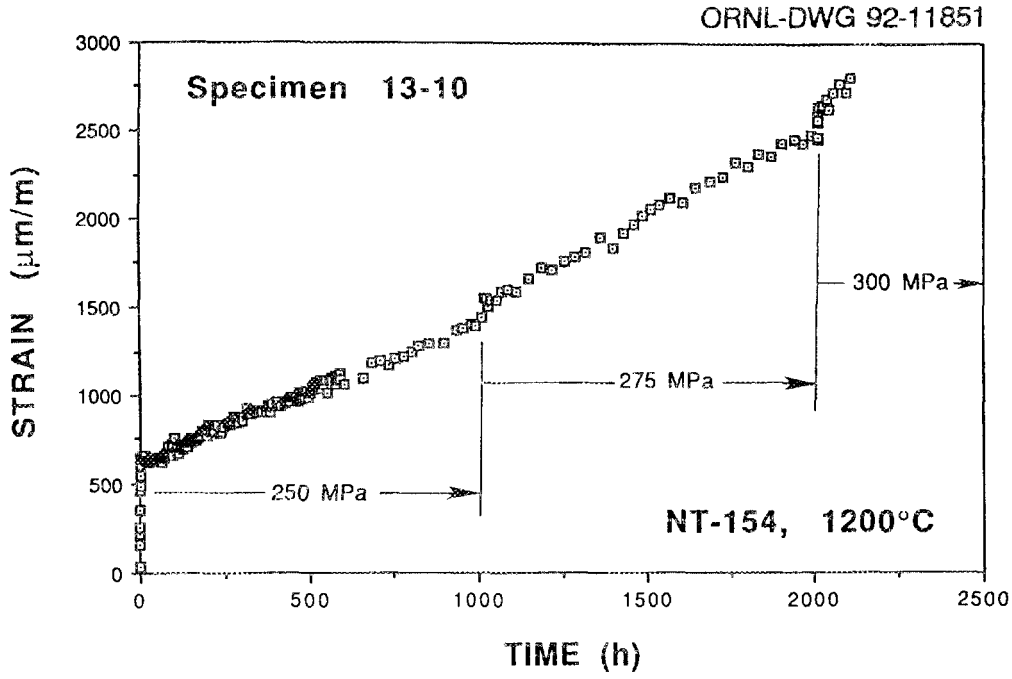

Fig. 3. Creep curve of NT-154 Si_3N_4 (specimen 13-10) tested at 1200°C with an initial stress of 250 MPa, which was increased in steps of 25 MPa at the end of each time interval of 1000 h until failure.

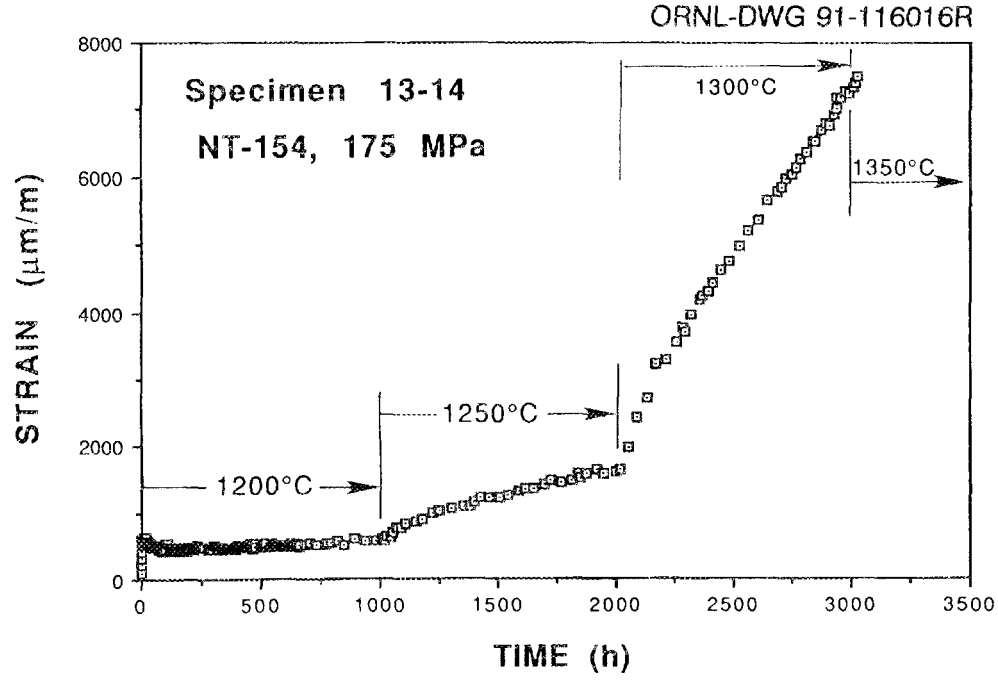

Fig. 4. Creep curve of NT-154 Si_3N_4 (specimen 13-14) tested initially under an applied stress of 175 MPa at 1200°C. Subsequently, the test temperature was increased in steps of 50°C at the end of each time interval of 1000 h until failure.

tested under the same condition (175 MPa/1300°). The creep curve of specimen 13-14 was replotted in Fig. 5 such that both curves started at zero time to facilitate comparison. The creep rates at the end of both curves are about the same also, suggesting that this material may have a relatively weak memory of time and strain histories.

Creep behavior at 1250° C

Specimen 13-04: The test has been completed. The specimen was loaded initially to 150 MPa, then subsequently raised in steps of 25 MPa at a time interval of about 1000 h. Increases in creep-strain rate were observed, as the applied stress was increased in steps, as shown in Fig. 6. The specimen fractured after about 500 h of testing under 225 MPa. The creep rate determined from the last 200 h of testing was higher than that of specimen 20-59 by a factor of about two. Specimen 20-59 was crept under the same test conditions but loaded to 225 MPa at the onset.

Specimen 20-56: The test is continuing at 1250° C under a constant stress of 175 MPa. A total of about 0.62% strain has been accumulated after 7300 h of testing to date, as shown in Fig. 7. Creep rate was reasonably steady at a rate of about 2×10^{-10} s^{-1} until the test was interrupted by a power failure that occurred at t = 5211 h. The creep rate increased by about 50% after the test was restarted. However, it decelerated gradually to the steady-state creep rate after an additional 1000 h of testing.

Specimen 20-00: The specimen has been tested at 1250° C under an applied stress of 150 MPa. A total of about 0.25% strain was accumulated after about 3750 h of testing, as shown in Fig. 8. Restarting of the test at t = 1745 h due to a power failure did not appear to have changed the subsequent creep behavior. The creep rate was determined from the last 1500 h of the creep curve to be 8.7×10^{-11} s^{-1}. The test is continuing.

Specimen 20-32: This is a new test and the last one for this series of specimens made from lot-"20". The specimen is being tested at 1250° C under an applied stress of 225 MPa. The stress will be stepped down at the end of each 1000 h of testing in creep by a step of 25 MPa. This test is intended to study the effect of strain history in the reverse process contrasting to that used in testing of specimen 13-04, in which the stress was stepped up in an increment of 25 MPa at the end of each 1000 h of testing.

Creep behavior at 1370° C

Specimen 19-44: This specimen has been tested at 1370° C under an applied stress of 75 MPa. Test results obtained to date are shown in Fig. 9. This specimen exhibited a short transient creep range followed by a fairly long range of steady-state creep. Therefore, the creep behavior was thought to be more consistent with that of specimens made from lot-"CP" until the creep rate decelerated rapidly after t > 2000 h, showing a creep rate of about 7×10^{-10} s^{-1} during the last 500 h of testing. If the trend continues, the creep behavior beyond t > 2000 h will be consistent with that of specimens used in this series of experiments. The test is continuing.

In summary, observations based on data obtained to date indicate that the creep behavior of NT-154 at elevated temperatures was consistent and reasonably predictable provided that the material was annealed and obtained from the same lot.

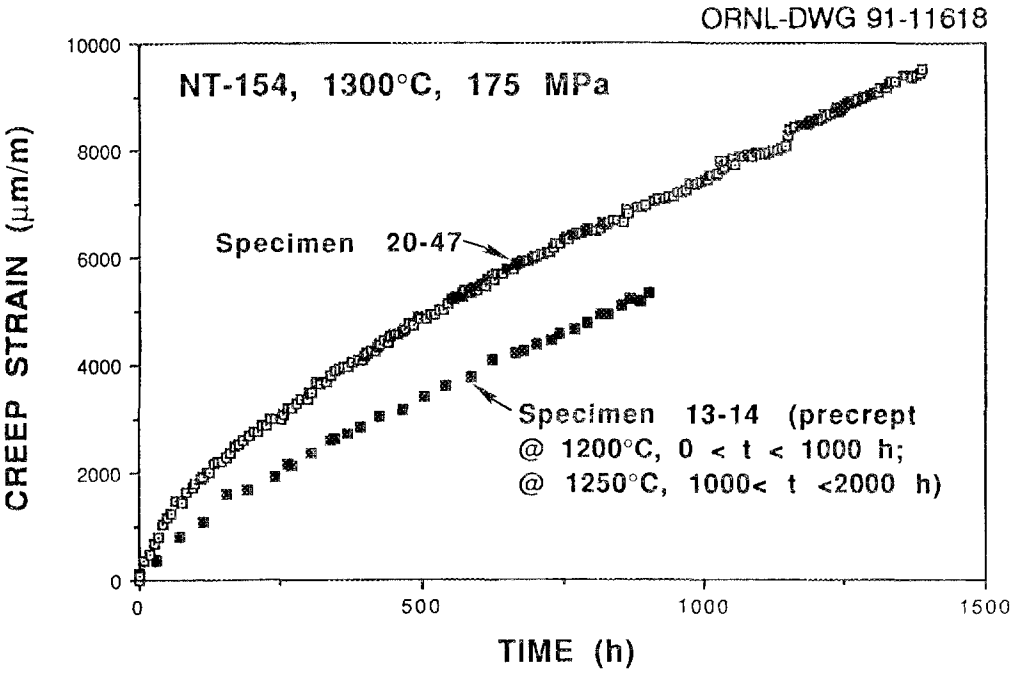

Fig. 5. Comparison of creep curves for an annealed specimen (20-47) and a precrept specimen (13-14) tested at 1300°C under 175 MPa.

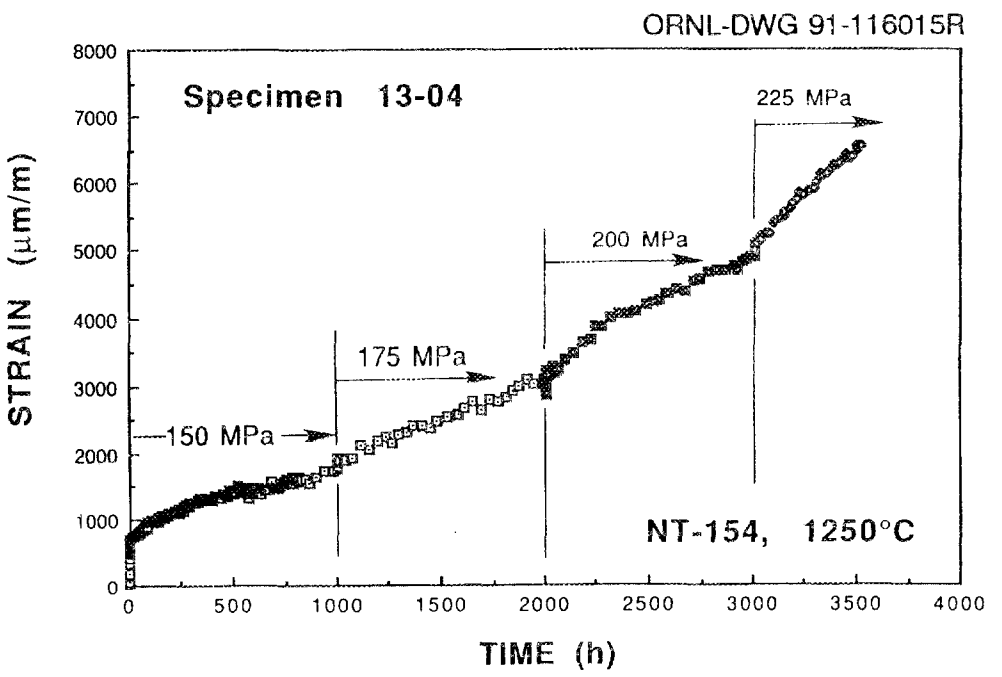

Fig. 6. Creep curve of NT-154 Si_3N_4 (specimen 13-04) tested at 1250°C with an initial stress of 150 MPa. The stress was increased in steps of 25 MPa at the end of each time interval of 1000 h. The specimen fractured after about 500 h of testing under the maximum stress of 225 MPa.

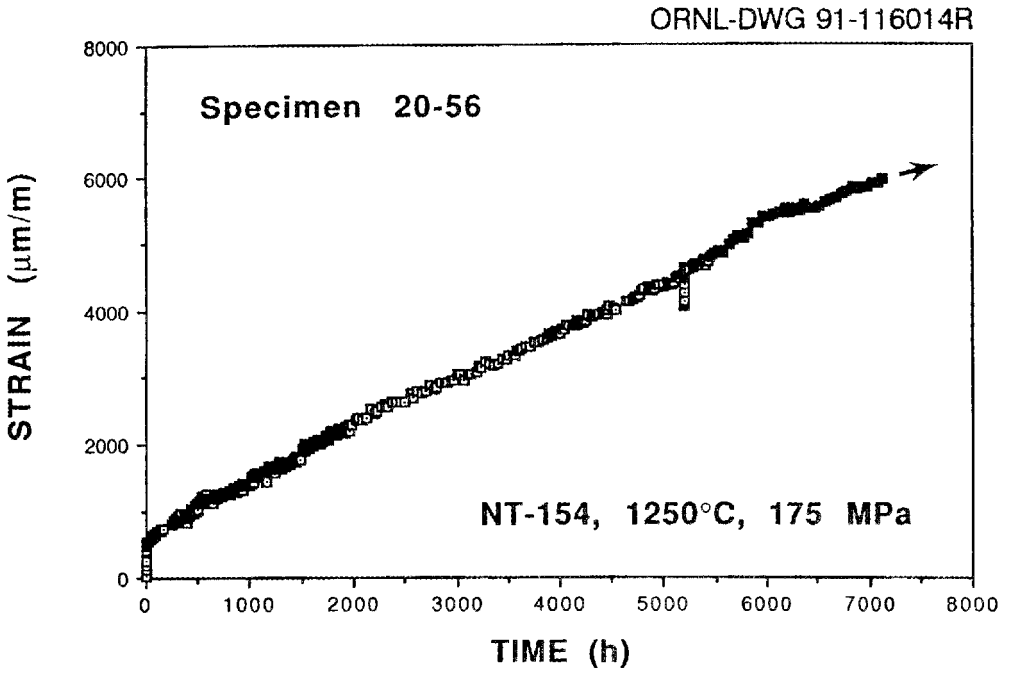

Fig. 7. Creep curve of NT-154 Si_3N_4 (specimen 20-56) tested at 1250°C under an applied stress of 175 MPa. The arrow indicates the test is continuing.

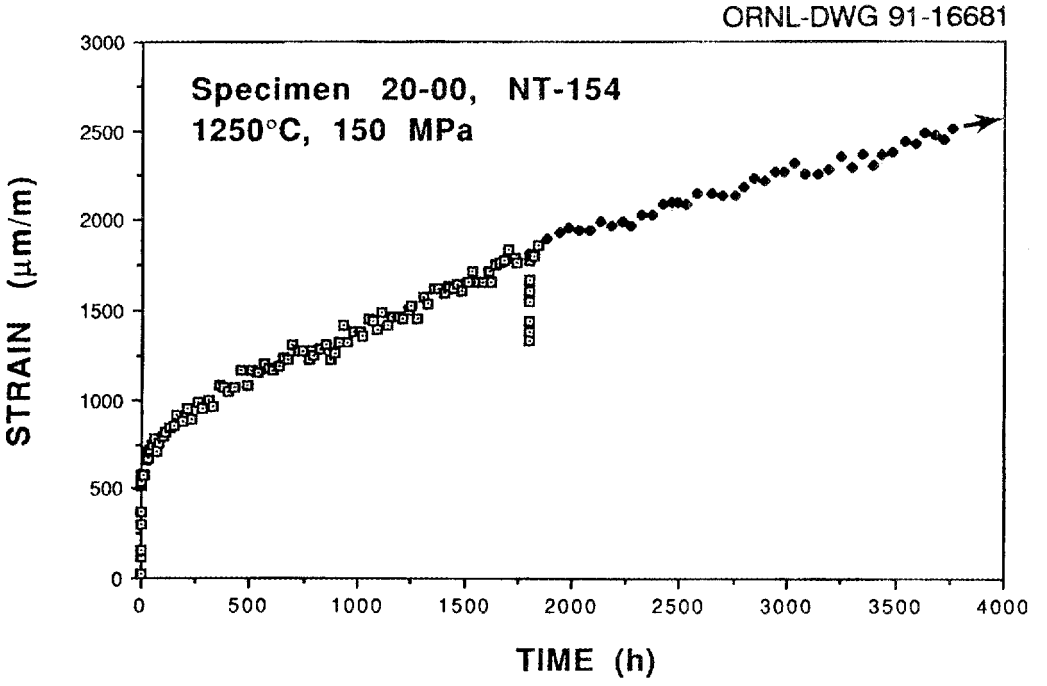

Fig. 8. Creep curve of NT-154 Si_3N_4 (specimen 20-00) tested at 1250°C under an applied stress of 150 MPa. The arrow indicates the test is continuing.

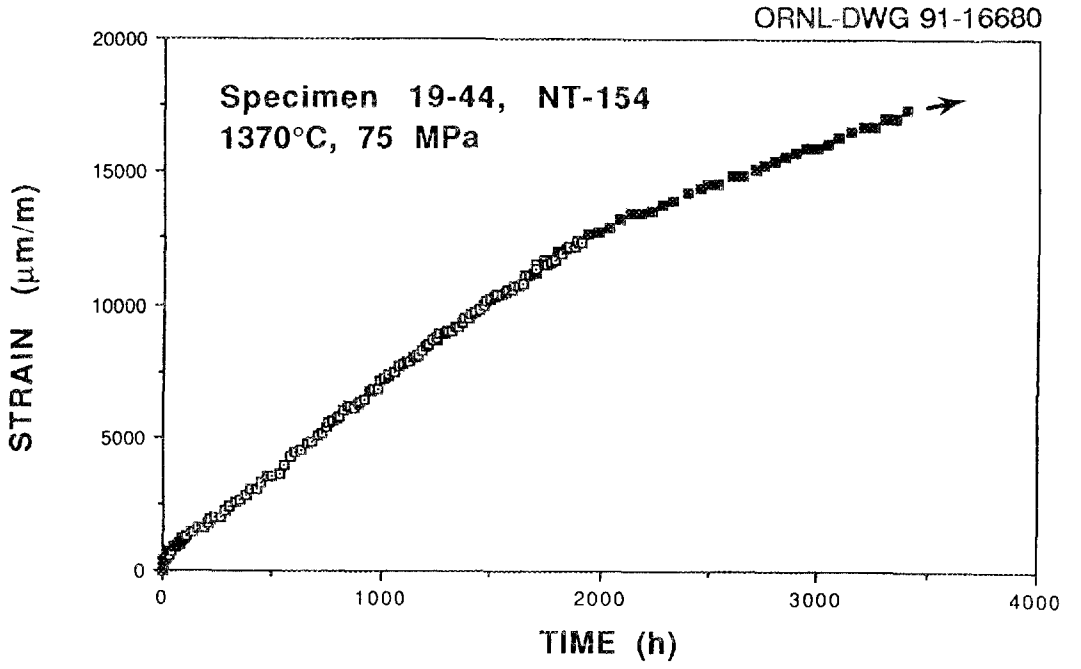

Fig. 9. Creep curve of NT-154 Si_3N_4 (specimen 19-44) tested at 1370°C under an applied stress of 75 MPa. The arrow indicates the test is continuing.

ATTAP tensile rupture/creep testing

Screening tests (task 1) were performed on Garrett Auxiliary Power Division (GAPD) tensile rupture specimens of GN-10 and NT-154 in support of the ATTAP program. The purpose of the screening tests is to identify stress levels required to yield the appropriate times-to-failure for tensile rupture characterization tests (Task 2), which are to follow upon completion of the screen tests. The stepped stress-rupture mode was used to test three specimens for each material, one for each test temperature at 1204, 1260, and 1315°C. All screening tests were to begin with an initial stress of 207 MPa (30 ksi). The stress level was then stepped up 70 MPa (10 ksi) every 24 h until specimen failure occurred. Test results were summarized in Table 2, and data were plotted in Figs. 10 through 15. The information was also transmitted to GAPD for a review to configure a test matrix for Task 2 tensile rupture characterization tests.

Status of milestones

1. Completed a draft report covering results of tensile creep rupture tests of GN-10 Si_3N_4 by November 30, 1991 (Milestone 321507).

2. Completed preliminary study of cyclic fatigue behavior of ceramic and ceramic composite materials using AE techniques by March 31, 1992 (Milestone 321414).

Table 2. Summary of tensile-rupture screening tests on GN-10 and NT-154 specimens

Specimens	Temperature °C(°F)	Initial stress, MPa (ksi)	Failure stress, MPa (ksi)	Total creep strain %	Time to failure (h)
GN-10	1204 (2200)	207 (30)	276 (40)	0.2	28.3
	1260 (2300)	103 (15)	207 (30)	0.8	79.3
	1315 (2400)	69 (10)	138 (20)	1.22	52.7
NT-154	1204 (2200)	207 (30)	345 (50)	0.105	68.8
	1260 (2300)	207 (30)	345 (50)	0.126	50.2
	1315 (2400)	207 (30)	276 (40)	0.23	27.8

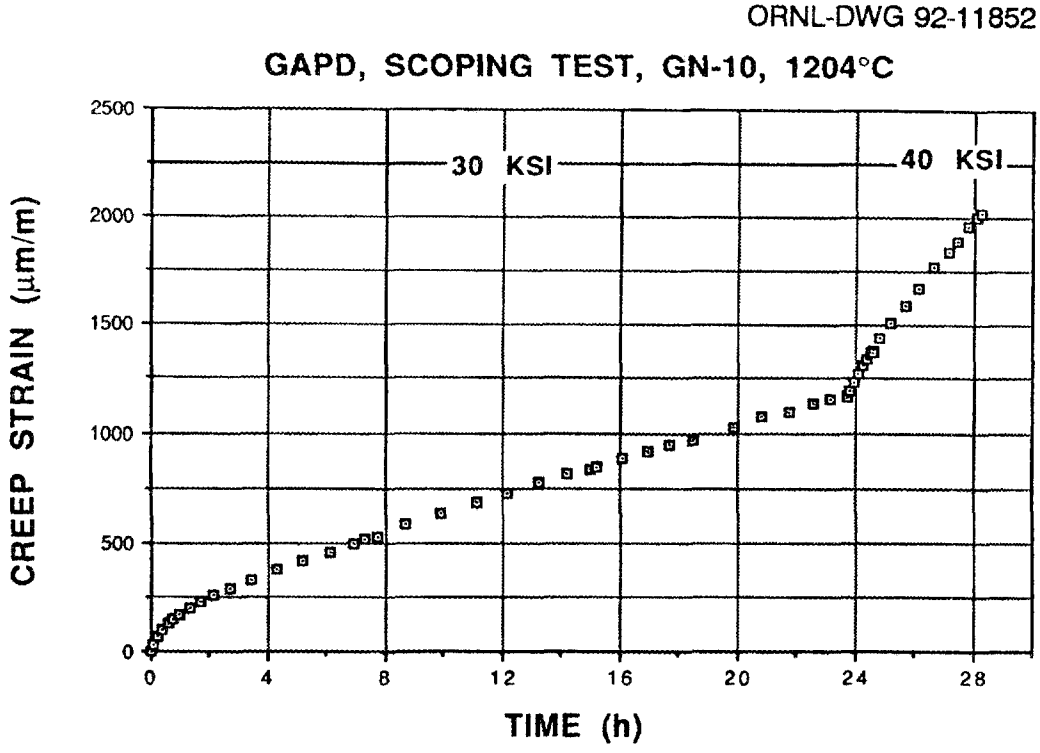

Fig. 10. Results of stepped creep tests on GN-10 Si_3N_4 at 1204°C with an initial stress of 207 MPa (30 ksi). The specimen failed at t = 28.3 h after the applied stress was increased to 276 MPa (40 ksi) at t ≈ 24 h.

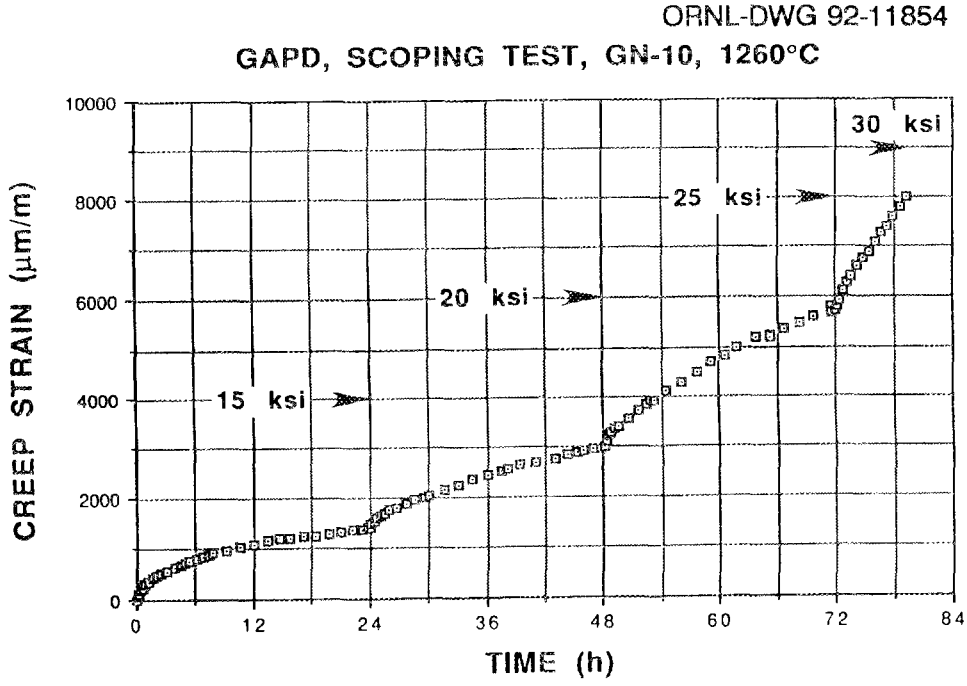

Fig. 11. Results of stepped creep tests on GN-10 Si_3N_4 at 1260°C with an initial stress of 103 MPa (15 ksi) and subsequent stresses in increments of 69 MPa (10 ksi) at the end of each time period of 24 h until specimen failure occurred at t = 79.3 h.

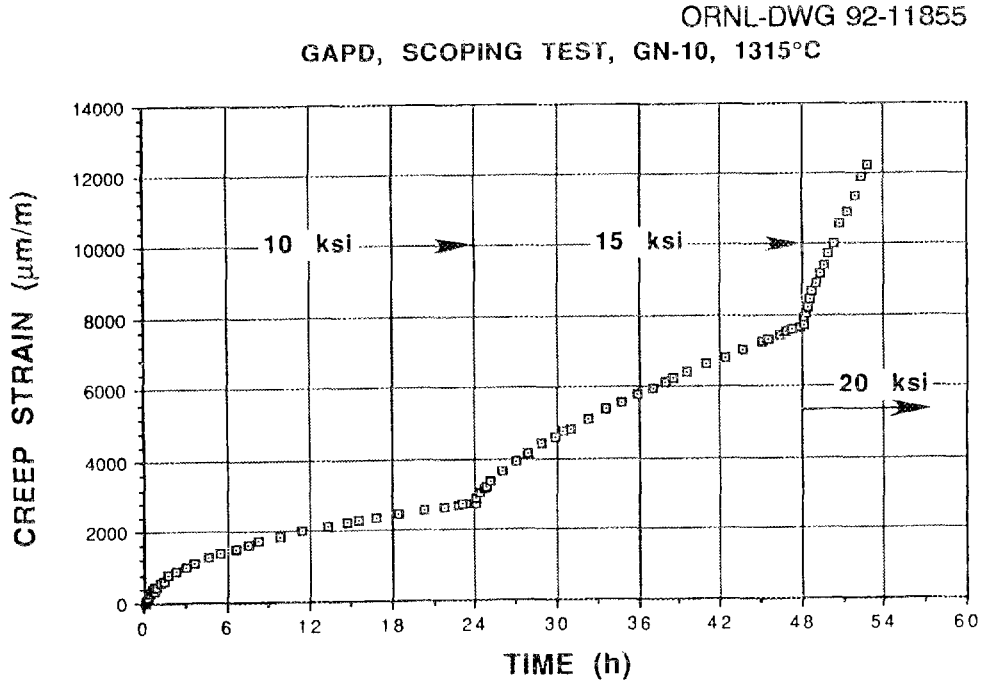

Fig. 12. Results of stepped creep tests on GN-10 Si_3N_4 at 1315°C with an initial stress of 69 MPa (10 ksi) and subsequent stresses in increments of 69 MPa (10 ksi) at the end of each time period of 24 h until specimen failure occurred at t = 52.7 h.

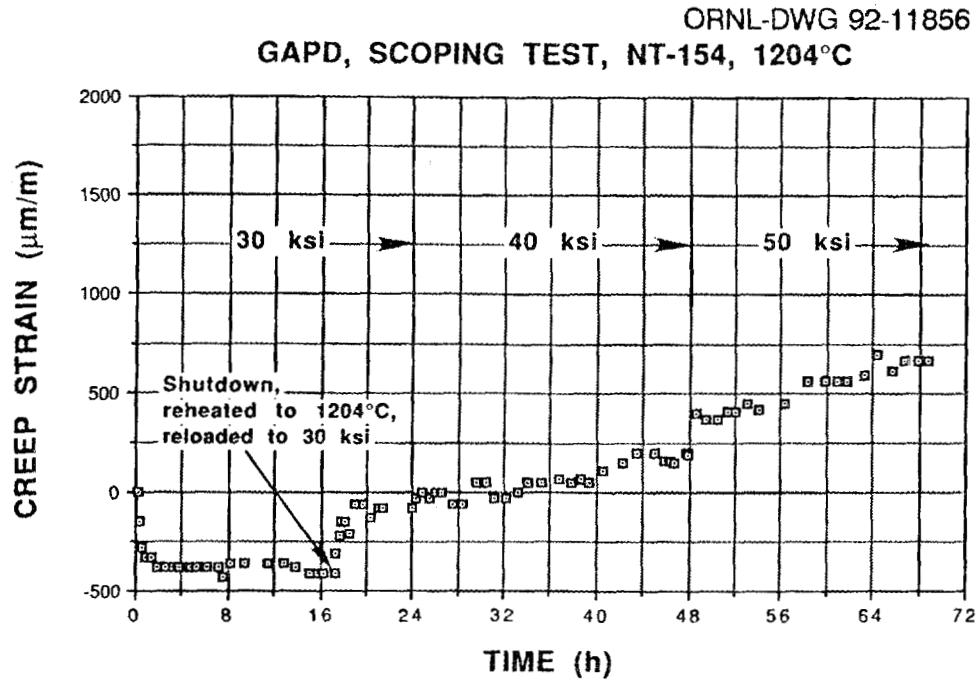

Fig. 13. Results of stepped creep tests on NT-154 Si_3N_4 at 1204°C under various levels of stresses as indicated. The negative creep strain indicated at the onset of creep test was a result of extensometer drift and not the true creep behavior. The test was interrupted at t = 16.3 h due to a heater problem.

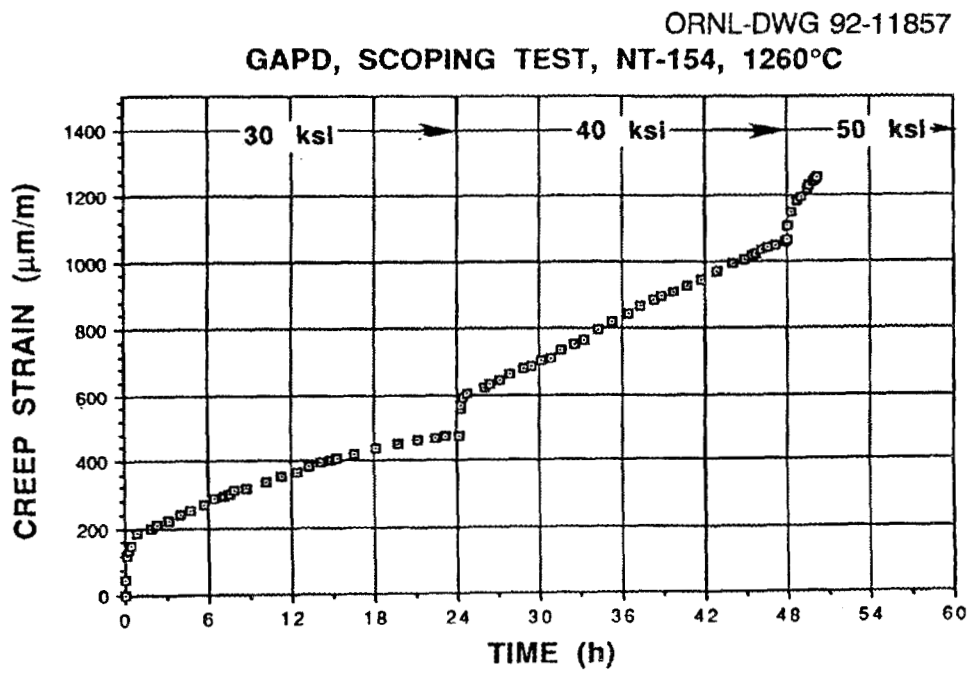

Fig. 14. Results of stepped creep tests on NT-154 Si_3N_4 at 1260°C under various stress levels as indicated. The specimen failed at t = 50.2 h.

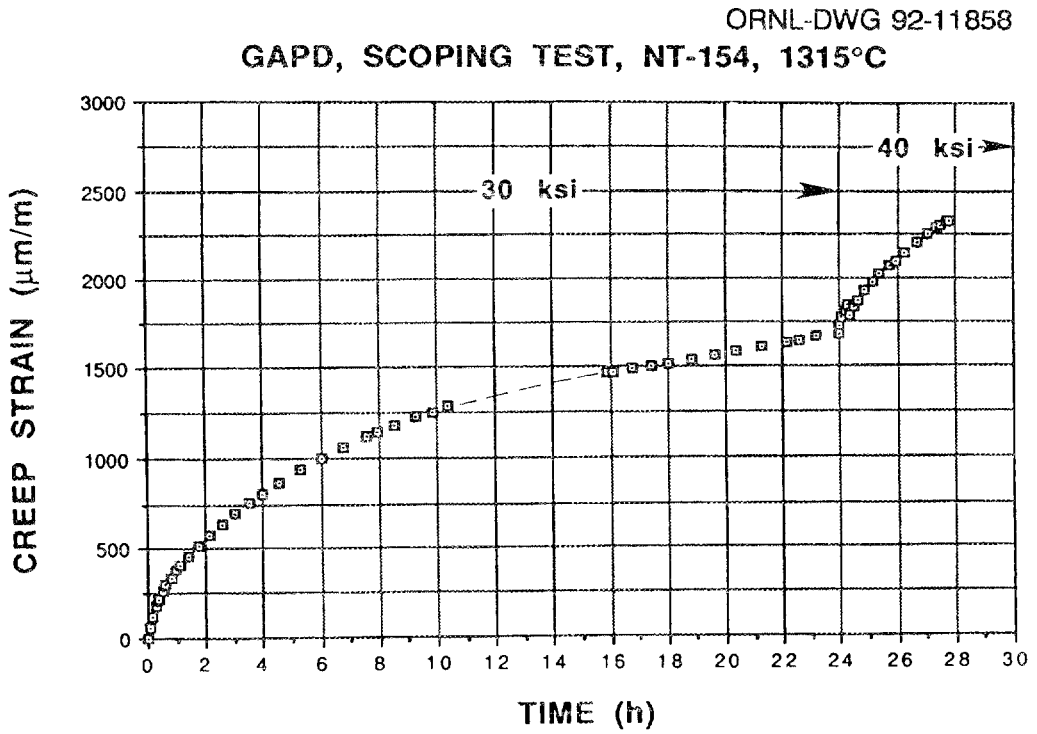

Fig. 15. Results of stepped creep tests on NT-154 Si_3N_4 at 1315°C with an initial stress of 207 MPa (30 ksi). The specimen failed at t = 27.8 h after the applied stress was increased to 276 MPa (40 ksi) at t = 24 h. The recording pen pegged out during the period of the data gap (~10.5 < t < ~16 h) indicated by a dashed line.

Publications

1. J. L. Ding, K. C. Liu, C. R. Brinkman, and D. R. Johnson, "Development of a high-temperature deformation and life-prediction model for advanced silicon-nitride ceramics," reviewed for publication.

2. K. C. Liu and J. L. Ding, "A mechanical extensometer for high-temperature tensile testing of ceramics," reviewed for publication.

Rotor Data Base Generation

M. K. Ferber and M. G. Jenkins
(Oak Ridge National Laboratory)

Objective/scope

The goal of the proposed research program is to systematically study the tensile strength of a silicon-nitride ceramic as a function of temperature and time in an air environment. Initial tests will be aimed at measuring the statistical parameters characterizing the strength distribution of three sample types (two tensile specimens and one flexure specimen). The resulting data will be used to examine the applicability of current statistical models, as well as sample geometries, for determining the strength distribution.

In the second phase of testing, stress-rupture data will be generated by measuring fatigue life at a constant stress. The time-dependent deformation will also be monitored during testing so that the extent of high-temperature creep may be ascertained. Tested samples will be thoroughly characterized using established ceramographic, SEM, and transmission electron microscopy (TEM) techniques. A major goal of this effort will be to better understand the microstructural aspects of high-temperature failure including:

(1) extent of slow crack growth,
(2) evolution of cavitation-induced damage and fracture,
(3) transition between brittle crack extension and cavitation-induced growth, and
(4) crack blunting.

The resulting stress-rupture data will be used to examine the applicability of a generalized fatigue-life (slow-crack-growth) model. If necessary, model refinements will be implemented to account for both crack blunting and creep damage effects. Insights obtained from the characterization studies will be crucial for this modification process. Once a satisfactory model is developed, separate stress-rupture (confirmatory) experiments will be performed to examine the model's predictive capability. Consequently, the data generated in this program will not only provide a critically needed base for component utilization in automotive gas turbines but also facilitate the development of a design methodology for high-temperature structural ceramics.

Technical progress

Studies of the elevated-temperature mechanical properties of a high-performance silicon nitride (PY6)* were continued this reporting period. PY6 is fabricated by hot isostatic pressing (HIP) using 6 wt % yttria as the densification aid. The microstructure typically consists of 1- to 6-μm-long acicular grains surrounded

*PY6 silicon nitride, GTE Laboratories, Inc., Waltham, Massachusetts.

by nominally equiaxed grains 0.1 to 1.0 μm in diameter. This morphology leads to a relatively dense microstructure. The silicon-nitride grains, which are generally in the form of β-Si_3N_4, are separated by relatively thin layers of an amorphous yttrium silicate. The intergranular phase is also present in the triple points as a crystalline yttrium silicate. The exact phase composition of these intergranular compounds depends upon the HIP conditions.

During this reporting period, the evolution of creep damage (primarily in the form of grain-boundary cavities) in PY6 silicon nitride was studied by periodically measuring the elastic modulus, E, during creep testing at 1370°C. Data were generated using button-head tensile specimens (6.35-mm gage diameter and 35-mm gage length), which were machined from isopressed and HIPed rods 160 mm long and 22 mm in diameter. Based upon the studies of Suresh and Brockenbrough,[1] E should be sensitive to this level of creep damage. The value of E was calculated from the stress-strain curves generated by first unloading the specimen to 10 to 25% of the creep stress, σ_a, and then reloading back to σ_a. The measurement of E involved the periodic application of an unload/load cycle to the statically loaded button-head tensile specimen (Fig. 1). E was calculated from the slope of the stress-strain curves generated during each cycle at 24-h intervals until the specimen failed.

Figure 2 shows the total strain and E as functions of time for an applied stress of 62 MPa. For times less than 250 h, E decreased slightly, which is consistent with the expected evolution of creep damage. However, E appeared to reach a minimum value for times in the range 250 to 300 h. A second finding of interest is that the strain versus time curve in Fig. 1 exhibited no evidence of tertiary creep. Previous data generated at 60 MPa (dashed line in Fig. 1) revealed a significant tertiary strain component preceding failure. The failure time of the specimen tested at the 62 MPa stress was also substantially greater than that of the specimen tested at 60 MPa.

In order to verify these findings, additional PY6 specimens were tested at 70 and 85 MPa. As shown in Fig. 3, the elastic modulus calculated from the 70 MPa static stress test decreased slightly during the early portion of the test (< 400 h). For exposure times exceeding 400 h, E approached a constant value. The strain-time curve for the specimen tested at 70 MPa revealed both a longer fatigue life and lower creep rate compared with the specimen tested previously at 68 MPa (dashed line). The tertiary regime for the 70 MPa curve was not as pronounced as in the 68 MPa test. Similar results were obtained from the static stress test at 85 MPa.

As shown in Fig. 4, a major effect of this cycling was to increase the fatigue life over that measured under "no cycle" conditions (baseline data in Fig. 4). The relative increase in fatigue life, t_f (cycled)/t_f (not cycled), was dependent upon the number of cycles applied prior to failure (Fig. 5).

The differences in the strain-time behavior observed for the specimens used for the E measurements and that for the specimens tested previously were apparently a result of the unload/load cycles applied during the creep test. Based upon previous studies,[2] it is likely that viscoelastic strain recovery occurring during the

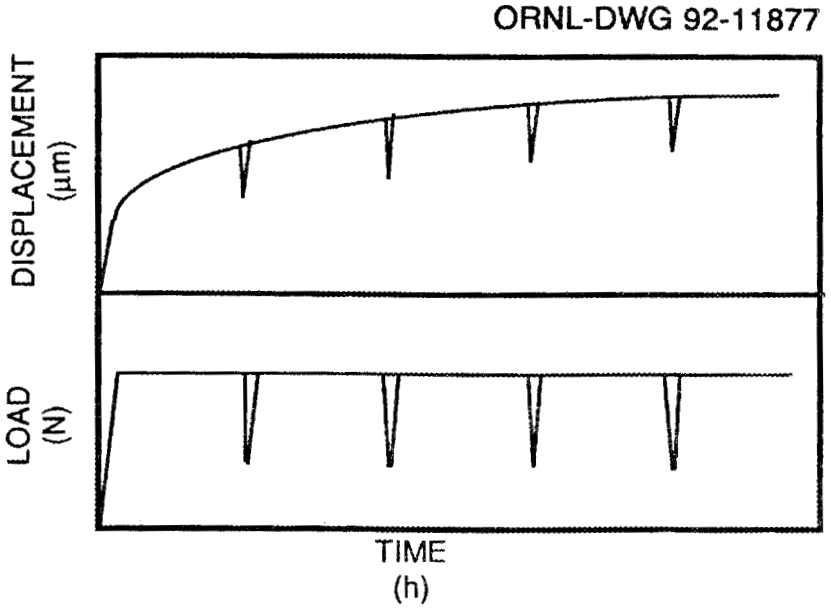

Fig. 1. Schematic representation of load and displacement-time profiles associated with the elastic modulus measurements. Each unload/load cycle generally required less than 60 s for completion.

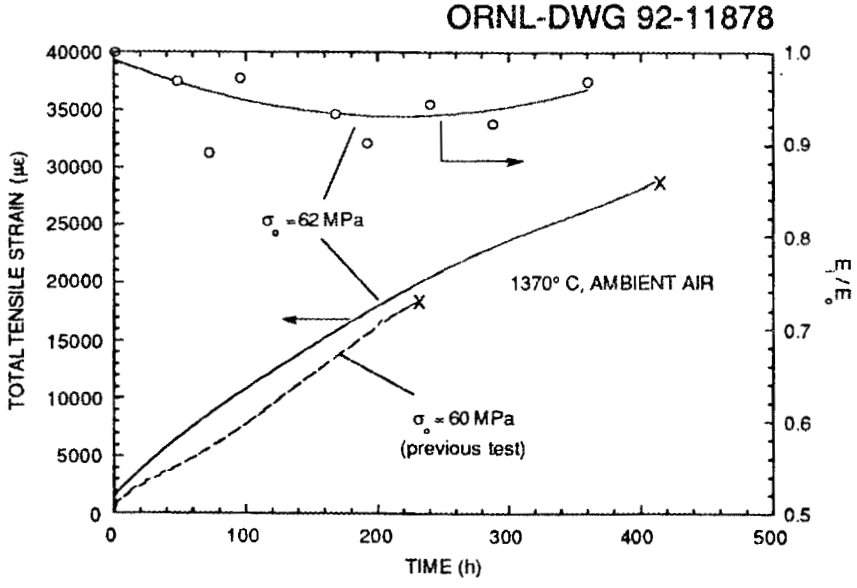

Fig. 2. Time dependence of total strain and elastic modulus for specimen tested under a 62 MPa applied stress at 1370°C.

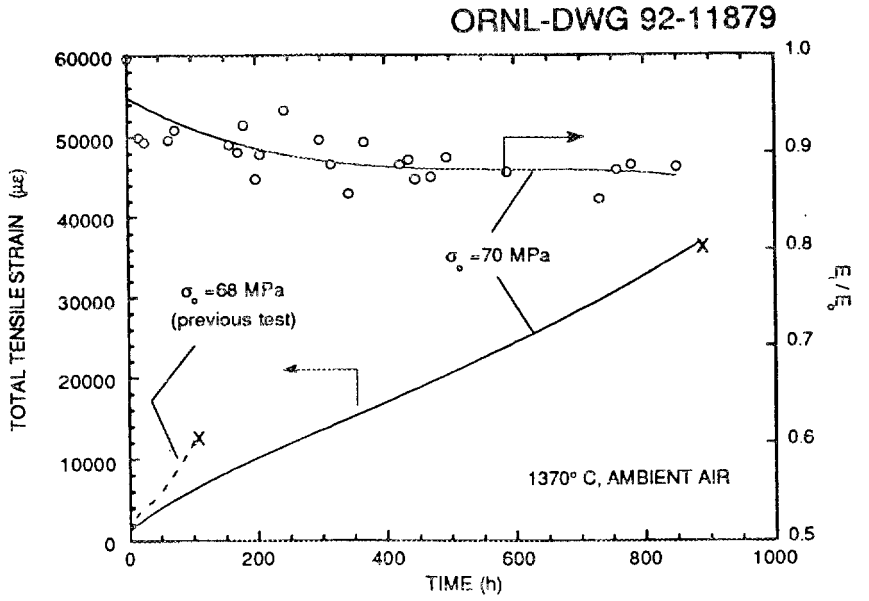

Fig. 3. Time dependence of total strain and elastic modulus for specimen tested under a 70 MPa applied stress at 1370°C.

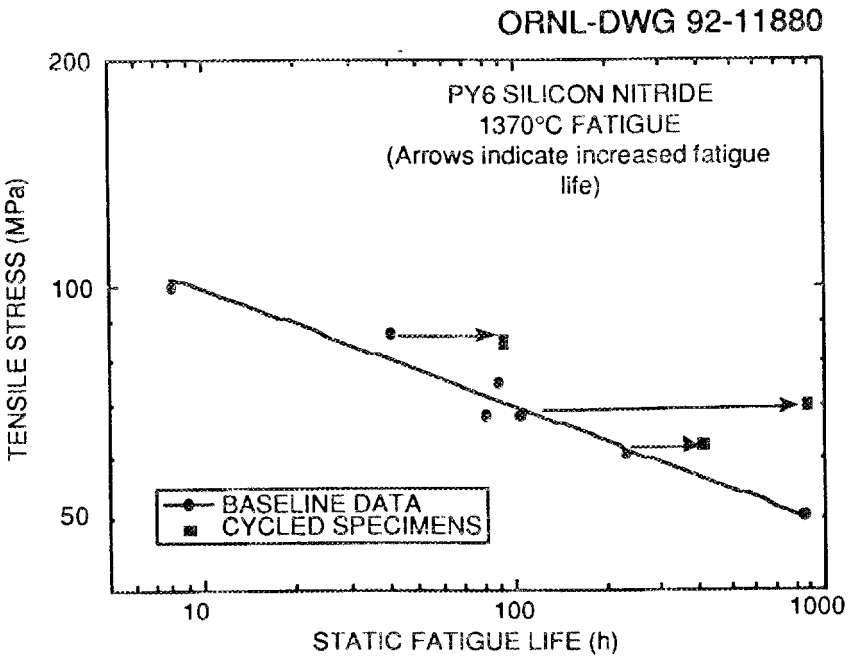

Fig. 4. For creep tests conducted at 1370°C, the fatigue life of specimens subjected to periodic cycling was significantly greater than that for specimens subjected to a static load only.

ORNL-DWG 92-11881

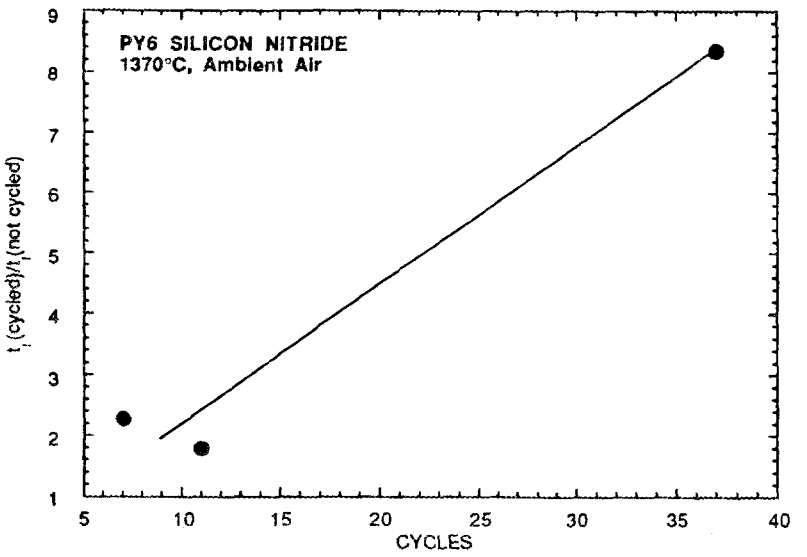

Fig. 5. Relative increase in static fatigue life for the cycled specimens was proportional to the number of unload/load cycles.

initial unloading effectively reduced the driving force for subsequent cavitation. This conclusion is consistent with SEM observations, which showed much lower cavity densities in the specimens tested at 62 and 70 MPa. It also explains the tendency for E to approach a constant value with time as well as the absence of a significant tertiary component in the strain-time curves. Finally, because of the perturbation of unload/load cycling upon the cavitation behavior, the periodic measurement of E during static-load testing does not appear to be a useful method for estimating the time dependency of creep-damage evolution.

In order to better characterize the effect of cyclic loading upon the fatigue characteristics of the PY6 material, a series of low-frequency (0.1 to 10 Hz) cyclic-fatigue tests at 1150, 1260, and 1370°C will be examined during the next six months. The baseline static fatigue characteristics at each temperature have recently been verified from dynamic fatigue tensile tests in which the fracture strength, σ_f, was measured as a function of stressing rate, $d\sigma/dt$. Results from these tests are shown in Figs. 6*(a)*-6*(c)*. The parameter, N, in these figures represents the fatigue exponent in the expression;

$$\sigma_f = A\,(d\sigma/dt)^{1/(N+1)}, \qquad (1)$$

where A is a constant. When failure is controlled by slow crack growth, N should be equal to the value determined from static fatigue tests. In this case, N is calculated from the expression,

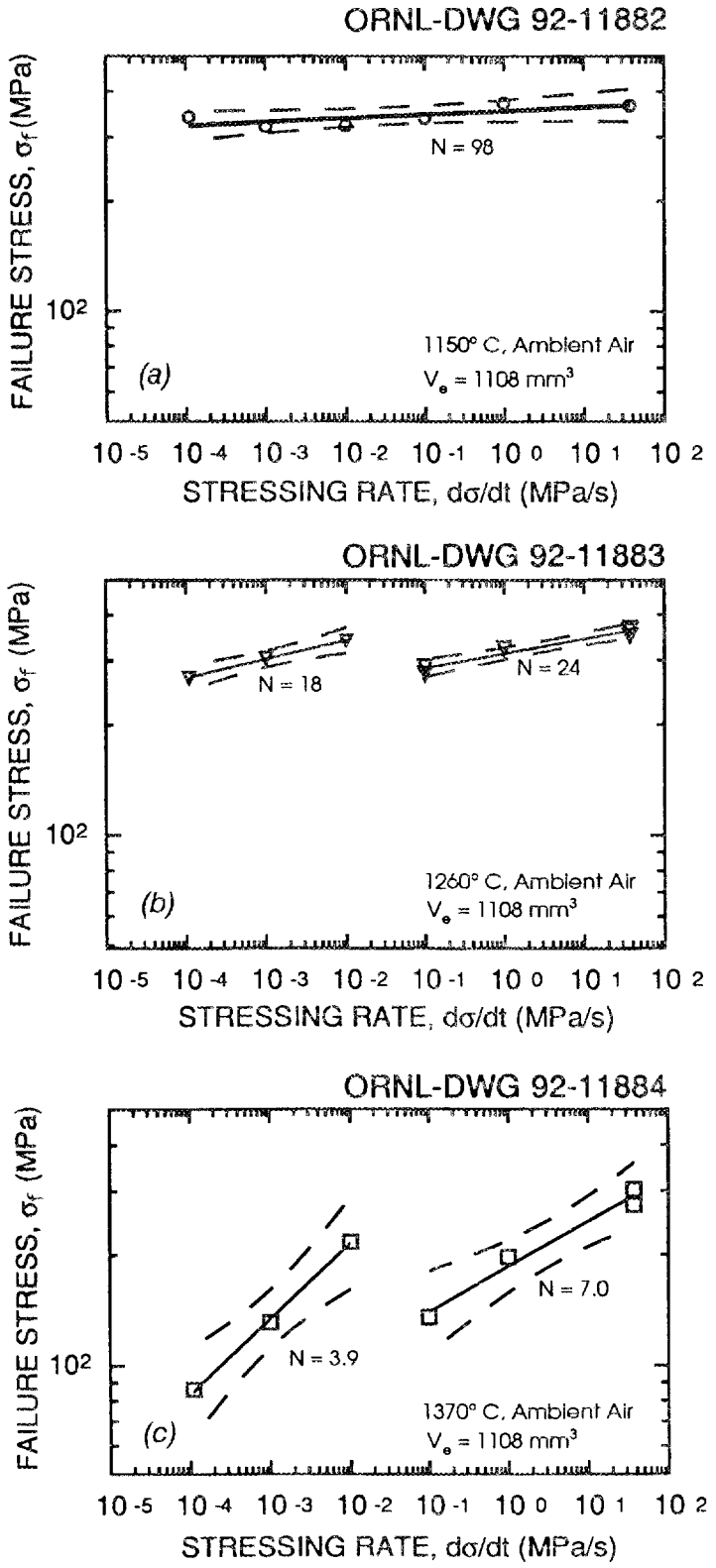

Fig. 6. Dynamic fatigue data for PY6 silicon nitride generated at 1260 and 1370°C revealed two distinct failure regimes. No change in failure mode was indicated for the 1150°C data: *(a)* 1150°C, *(b)* 1260°C, and *(c)* 1370°c.

$$t_f = B\,(\sigma_a/\sigma'_o)^N, \qquad (2)$$

where σ_a is the applied stress, σ'_o is a normalizing parameter (=1 MPa), and B is a constant.

In Figs. 6*(b)* and 6*(c)*, the dynamic fatigue data measured at 1260 and 1370°C reveal a transition in fatigue behavior at stressing rates < 10^{-1} MPa/s. As shown in Figs. 7*(a)*-7*(c)*, this transition corresponds to generation of large, nonlinear strains preceding failure. In the low-stressing-rate regime at 1370°C, the static and dynamic fatigue exponents are comparable (N = 4 to 6). Based upon static stress, this value of N is consistent with creep-controlled fatigue. This has been confirmed by SEM studies, which show that grain-boundary cavitation occurs at stressing rates of $\leq 10^{-2}$ MPa/s. In the higher stressing rate regime, the N values are much greater, indicating a change in failure mechanism related to slow crack growth of a single flaw, again in agreement with static fatigue data.[5]

The dynamic fatigue data can be used to estimate the effective fatigue failure times, t_{feff}, using the expression;

$$t_{feff} = t_{fd}/(N+1), \qquad (3)$$

where t_{fd} is the failure time for the dynamic fatigue test. For this calculation, the fracture stress in dynamic loading is assumed to be equal to the effective applied stress in the static fatigue test. Figures 8*(a)*-8*(c)* compare the fatigue life characteristics determined from Eq. (3)with those measured in Ref. 5. The values of t_{feff} calculated from the low-stressing-rate regimes ($\leq 10^{-2}$ MPa/s) at 1260 and 1370°C represent a reasonable extension of the static fatigue data. In the case of the high-stressing-rate regions, the corresponding σ_a versus t_{feff} curves are shifted to much lower fatigue lives consistent with the change in failure mechanism. Although the calculation of t_{feff} is based on a somewhat simplified analysis (i.e., equivalent slow-crack-growth failure mode), the comparisons shown in Figs. 8*(a)*-8*(c)* illustrate the utility of the dynamic fatigue technique for the study of high-temperature failure modes.

Status of milestones

All milestones are on schedule.

Publications

M. G. Jenkins, M. K. Ferber, R. L. Martin, V. T. Jenkins, and V. J. Tennery, "Study and Analysis of the Stress State in a Ceramic, Button-Head, Tensile Specimen," ORNL/TM 11767, Martin Marietta Energy Systems, Inc., Oak Ridge National Laboratory, September 1991 (Distributed January 1992).

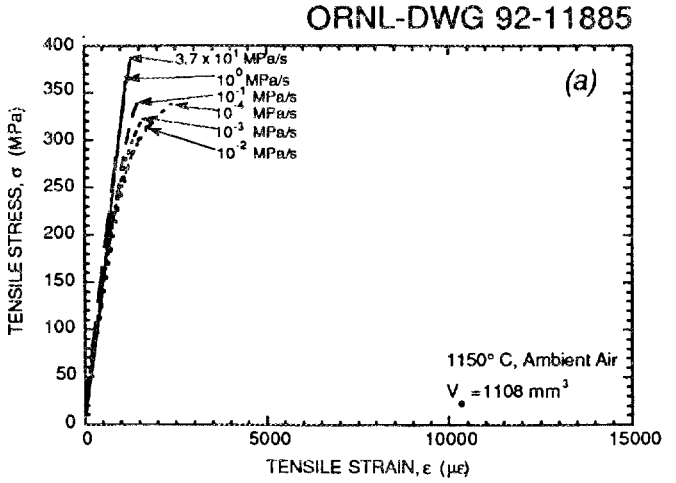

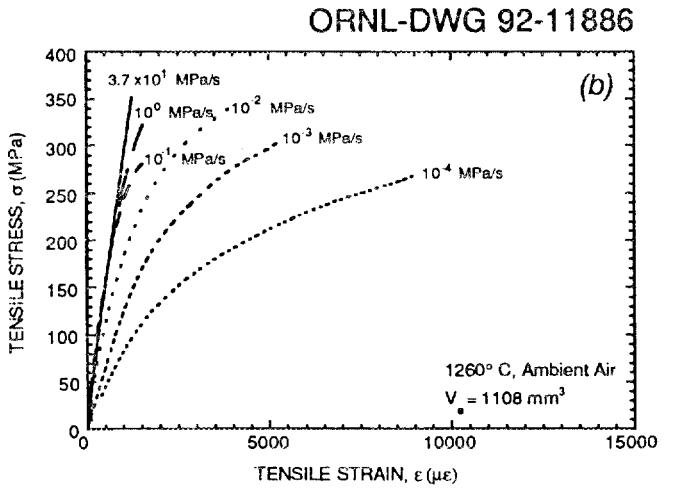

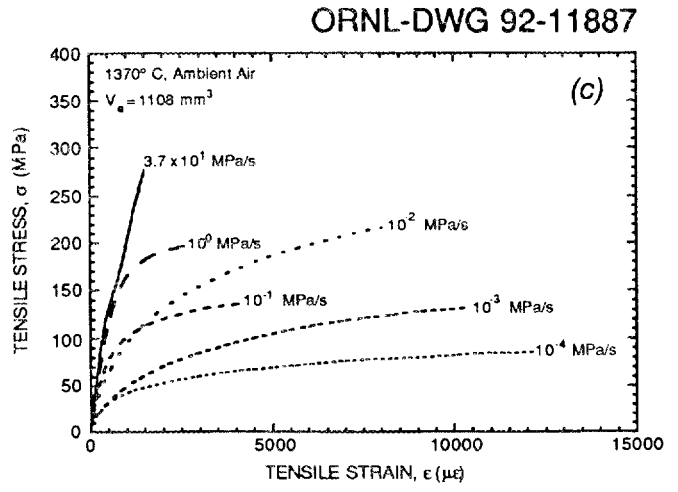

Fig 7. Dynamic fatigue stress-strain curves indicate the change in failure mechanism was accompanied by nonlinear strains prior to failure: *(a)* 1150° C, *(b)* 1260° C, *(c)* 1370° C.

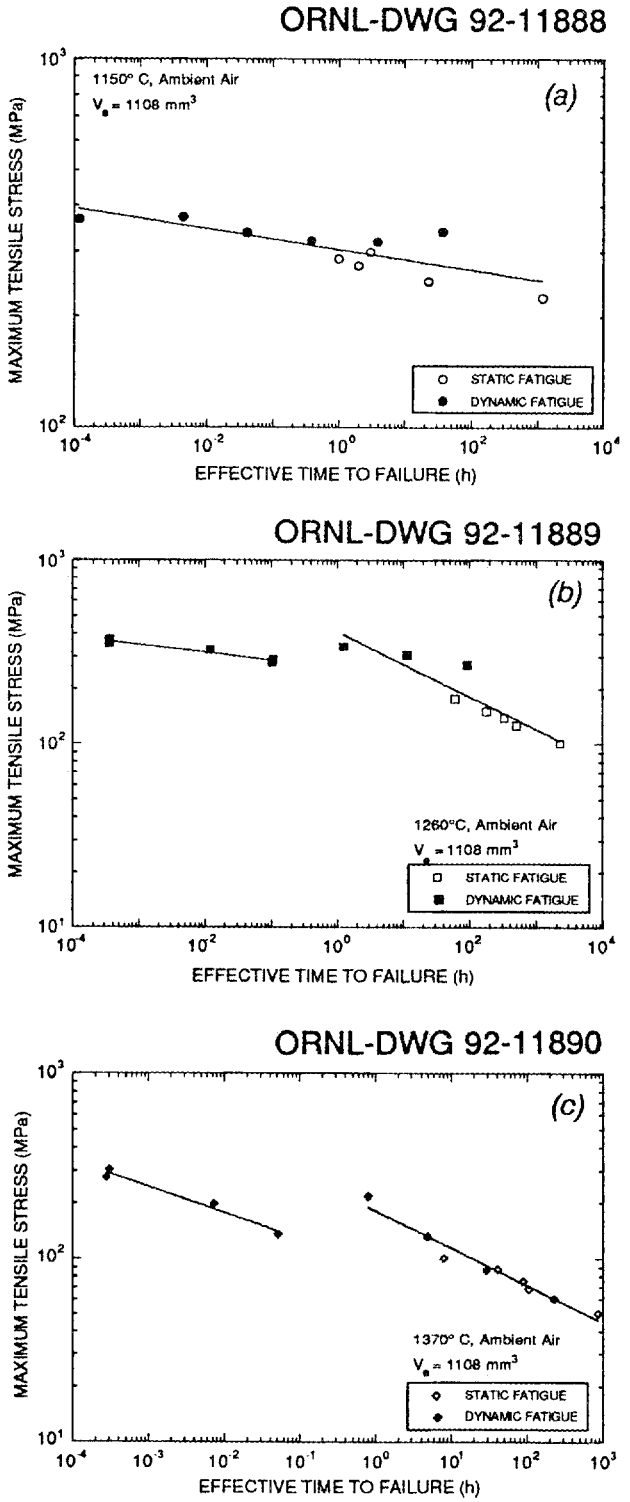

Fig. 8. Static fatigue data generated at 1260 and 1370°C (ref. 5) were in good agreement with effective fatigue lives predicted from the low-stressing-rate dynamic fatigue data: *(a)* 1150° C, *(b)* 1260° C, *(c)* 1370° C.

M. K. Ferber and M. G. Jenkins, "Evaluation of the Strength and Creep-Fatigue Behavior of a HIPed Silicon Nitride," accepted for publication in *J. Amer. Ceram. Soc.* (March 1992).

M. K. Ferber and M. G. Jenkins, "Evaluation of the High-Temperature Mechanical Reliability of a HIPed Silicon Nitride," to be published in *Proceedings of the Automotive Technology Development Contractors' Meeting*, held in Dearborn, Michigan, October 1992.

M. K. Ferber and M. G. Jenkins, "Empirical Evaluation of Tensile Creep and Creep Rupture in a HIPed Silicon Nitride," *Proceedings of the Fifth International Conference on Creep*, Orlando, Florida, May 17-21, 1992, ASM International, Materials Park, Ohio, 1992.

M. G. Jenkins, M. K. Ferber, and J. A. Salem, "Creep and Slow Crack Growth Mechanisms Related to Macroscopic Creep Behavior of a Silicon Nitride Ceramic at Elevated Temperatures," to be published in *Proceedings of the 1992 SEM Spring Conference on Experimental Mechanics*, held in Las Vegas, Nevada, June 8-11, 1992, Society of Experimental Mechanics, Bethel, Conn., 1992.

M. G. Jenkins, "Effect of Bending on the Room-Temperature Tensile Strengths of Structural Ceramics," to be published in *Proceedings of the 1992 SEM Spring Conference on Experimental Mechanics*, held in Las Vegas, Nevada, June 8-11, 1992, Society for Experimental Mechanics, Bethel, Conn., 1992.

References

1. S. S. Suresh and J. R. Brockenbrough, "A Theory for Creep by Interfacial Flaw Growth in Ceramics and Ceramic Composites,"*Acta Metall. Mater.* **38** [1], 55-68, (1990).

2. F. F. Lange, D. R. Clark, and B. I. Davis, "Compressive Creep of Si_3N_4/MgO Alloys. Part 2: Source of Viscoelastic Effect," *J. Mater. Sci.* **15**, 611-15 (1980).

3. M. K. Ferber and M. G. Jenkins, "Rotor Data Base Generation," pp. 340-61 in *Ceramic Technology for Advanced Heat Engines Project Semiannual Progress Report for October 1990 Through March 1991*, ORNL/TM-11859, Martin Marietta Energy Systems, Inc., Oak Ridge National Laboratory, July (1991).

4. M. K. Ferber and M. G. Jenkins, "Evaluation of the High-Temperature Mechanical Reliability of a HIPed Silicon Nitride," accepted for publication in *J. Amer. Ceram. Soc.* (March 1992).

Toughened Ceramics Life Prediction

Jonathan A. Salem and Sung R. Choi (NASA Lewis Research Center)

Objective/Scope

The purpose of this research is to understand the room temperature and high temperature [≤1370°C (2500°F)] behavior of toughened ceramics as the basis for developing a life prediction methodology. A major objective is to understand the relationship between microstructure and the mechanical behavior within the bounds of a limited number of materials. A second major objective is to determine the behavior as a function of time and temperature. Specifically, the room temperature and elevated temperature strength and reliability, the fracture toughness, slow crack growth and the creep behavior will be determined for the as-manufactured material. The same properties will also be evaluated after long-time exposure to various high temperature isothermal and cyclic environments. These results will provide input for parallel materials development and design methodology programs. Resultant design codes will be verified.

Technical Highlights

The creep behavior of a SiC whisker-reinforced silicon nitride and a similar monolithic silicon nitride was determined in flexure in air at 1250°C. Steady-state creep data were obtained for the two materials as a function of applied stress, and the appropriateness of bend test data as input to life prediction models was evaluated from the conventional elastic solution and from the results of specimen curvature measurement. The mechanisms of creep deformation of the composite and monolithic materials were determined from SEM and TEM analyses.

Experimental Procedures

The materials used in this study were based on Garrett GN-10 composite and monolithic Si_3N_4's. The material fabrication has been described in detail elsewhere [1,2]. Briefly, a silicon nitride powder composition was slip cast into 50 mm diameter by 75 mm height billets, glass encapsulated by the ASEA method and hot-isostatically pressed to produce monolithic silicon nitride material. Part of the same power batch was blended with 30 vol % SiC whisker by ACMC and processed with the same procedures and additives as the monolithic. Etched microstructures of the two materials are depicted in Figure 1. High temperature strength, fracture toughness, crack growth resistance, fatigue susceptibility and oxidation behavior of the two materials was previously reported [1-5].

Billets of both composite and monolithic materials were cut so that the longitudinal axes of the specimens were parallel to the billet height.

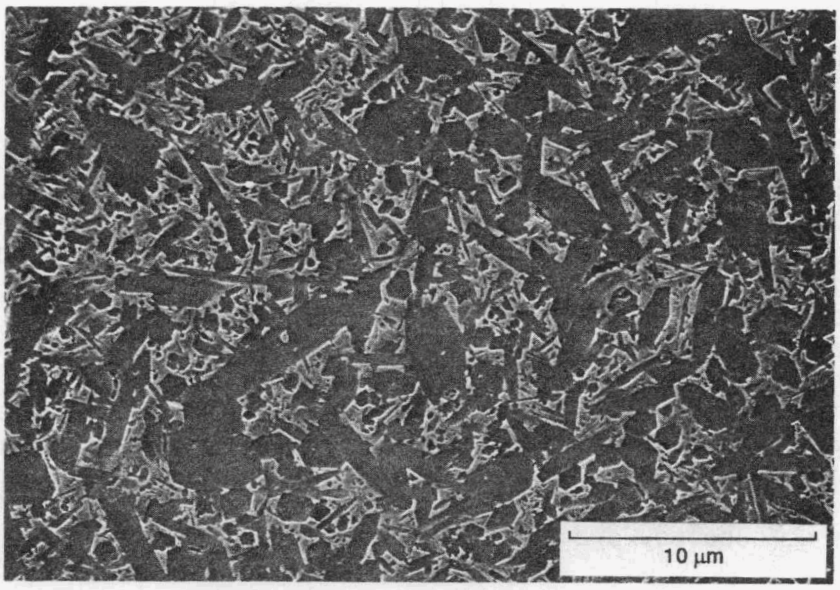

(a) Si_3N_4.

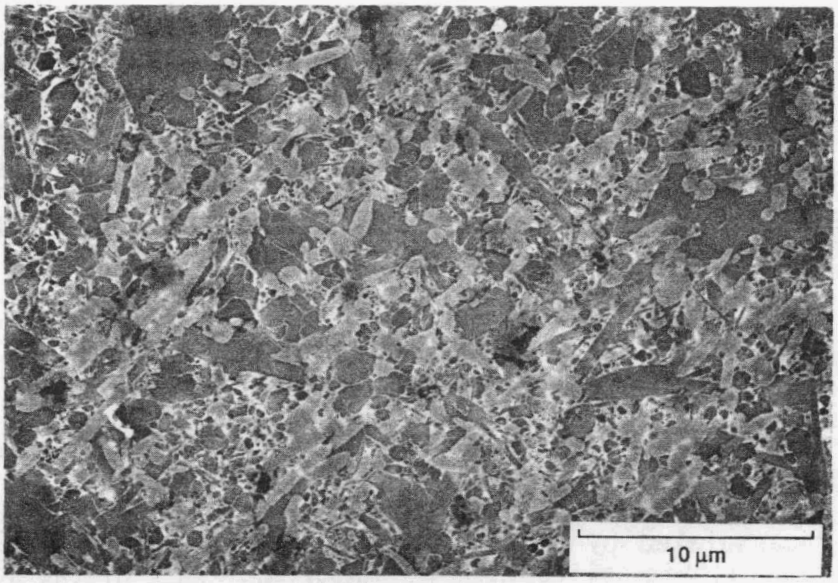

(b) SiC_w/Si_3N_4.

Figure 1. Etched microstructures of monolithic (a) and SiC whisker-reinforced (b) silicon nitride materials.

All faces and bevels of the test specimens were ground with # 320 diamond wheels and the edges were hand-polished lengthwise with # 600 grit SiC paper to eliminate spurious failures from the edges. The final specimen dimensions were 3 by 4 by 50 mm in height, width and length, respectively.

Creep tests were conducted with a lever arm compression creep test machine (Applies Test Systems, Butler, PA) using a SiC four-point bend fixture with inner and outer spans of 20 and 40 mm, respectively. Stress levels from 200 to 370 MPa were applied at 1250°C in air. The displacement measurement system included an LVDT with a three-point extensometer made of Al_2O_3 gage rod with SiC tips. The SiC tips were in contact with the specimen tensile surface at the center and beneath the inner load points. Relative deflection was measured and strain was calculated by a data acquisition system. Strain calculations were made assuming a constant radius of curvature between the inner load points. The following relation based on the elastic solution was used [4]

$$\epsilon_{max} = 4hd/L_i^2 \qquad (1)$$

where ϵ_{max} is the maximum strain in the outer fiber, d is the relative deflection of the bar center with respect to the inner load points, and L_i is the inner span. Additional creep testing was performed using short specimens measuring 3 by 6 by 25 mm in height, width and length, respectively. Testing was done in air at 1250 °C with an electromechanical testing machine (Instron 8562) by using a four-point SiC bend fixture with 10 and 22 mm spans. It was found that the creep behavior remained the same regardless of the specimen dimensions (either 3x4x50 mm or 3x6x25 mm).

To check the validity of the creep equations based on the elastic solution, permanent deflections of the crept specimens were determined lengthwise by using a machinist optical microscope with a traveling stage. The deflection curve thus obtained was fitted to the following polynomial equation

$$y(x) = \alpha x^n + \beta x^{n-1} + \ldots\ldots + ax^5 + bx^4 + cx^3 + dx^2 + ex + f \qquad (2)$$

where x is the distance along the beam specimen (see Figure 5), and α to f are coefficients to be evaluated with a functional fit analysis. The deflection curve was used to calculate radius of curvature of the crept specimen, which in turn was used to check the validity of creep equations based on the elastic solution by Hollenberg [6]. A fifth order polynomial was sufficient to fit the deformation curves with a correlation coefficient $r^2_{coef} \geq 0.99$. A similar method to this was used by Jakus and Wiederhorn to calculate creep parameter N [7]. Details of these results will be discussed in the next section.

The residual strengths of the specimens that survived creep testing were determined at room temperature using a four-point bend fixture with 20/40 mm spans and an actuator speed of 0.2 mm/min. The fast fracture residual strength indicates the degree of strength degradation due to creep-associated damage.

Also, to check if neutral axis shifted during creeping, deformation measurements across the specimen height were made on the short specimens at applied stresses of 224 to 370 MPa. This was done by putting three scratch lines (≈ 2 mm between adjacent lines) within the inner span on a polished side surface of the specimen [8]. The scratch marks were made with a Vicker's microhardness indenter. A similar method using two straight rows of "Vicker's impression marks" 2 mm apart was used by Chen and Chuang [9] to measure neutral axis shift. The post-creep visibility of the scratch mark was far better than the indentation impression marks, as shown previously [8].

SEM and TEM analyses were used to reveal morphology of crept surfaces and to understand creep mechanisms of the two materials.

Results and Discussion

For many advanced ceramics, creep deformation in the steady state region is usually expressed by Norton's law

$$\dot{\epsilon} = A\,\sigma^N \tag{3}$$

where A is a constant associated with creep compliance, σ is the nominal maximum applied stress, and N is the stress exponent during steady state. This relation for bend beam specimens is based on the conventional assumption that creep in tension is identical to creep in compression [6].

A typical example of creep strain as a function of time at an applied stress of σ = 350 MPa is shown in Figure 2. This figure shows that the apparent creep strain and the creep strain rate of the composite material are substantially greater than those of the monolithic material, thereby resulting in a shorter lifetime for the composite than the monolithic. Most of the test specimens exhibited a steady-state creep regime for the applied stresses of 200 to 370 MPa.

The results of the creep strain-rate measurements (elastic solution) as a function of applied stress are summarized in Figure 3. Note that creep strain rate for the composite material is greater than that for the monolithic for all the applied stresses except σ = 200 MPa. Also note that a transition in the $\dot{\epsilon}$-σ curve occurred for the composite material at a stress of σ = 320 MPa, resulting in a significantly enhanced creep strain rate above 320 MPa. The stress exponent (N) was obtained by linear regression of the Log $\dot{\epsilon}$ vs. Log σ curve, based on Eq. (3), and the assumption of no neutral axis shift. The stress exponent for the monolithic material was N = 1.2. The composite material, however, exhibited much higher stress exponents; N = 3 for σ < 320 MPa and N = 19 for σ > 320 MPa, respectively. These results indicate that the composite material exhibited higher creep susceptibility as compared to the monolithic material. A similar result of relatively poor composite behavior was also found for high temperature (≥ 1200 °C) slow crack growth (fatigue) [5].

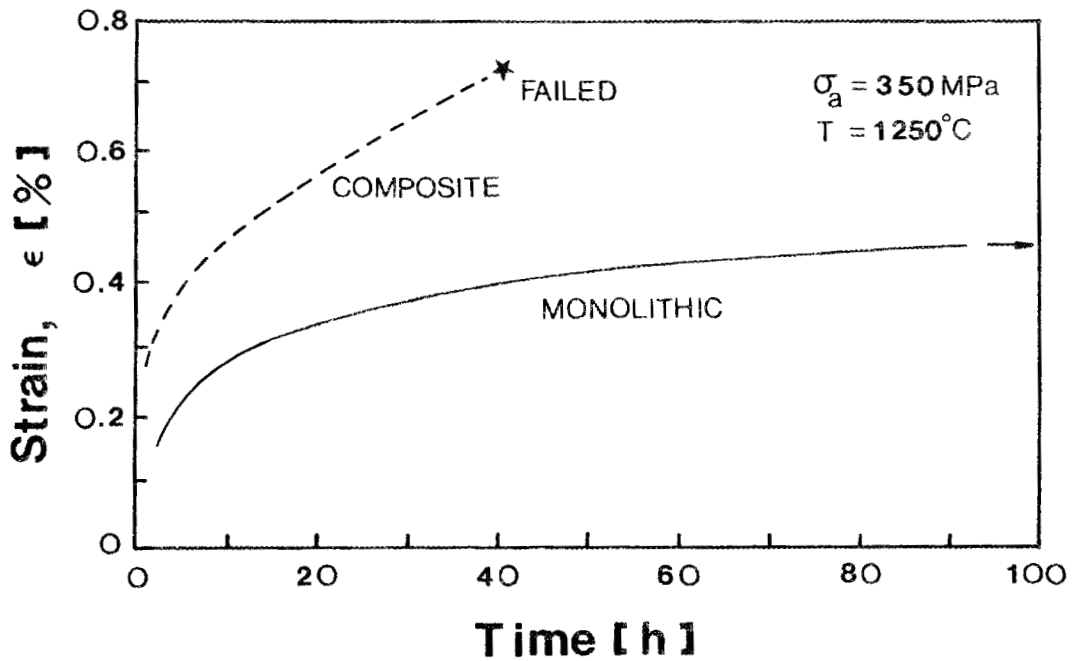

Figure 2. Creep strain as a function of time for 30 vol % SiC_w/Si_3N_4 composite and monolithic silicon nitrides at an applied stress of 350 MPa at 1250°C in air.

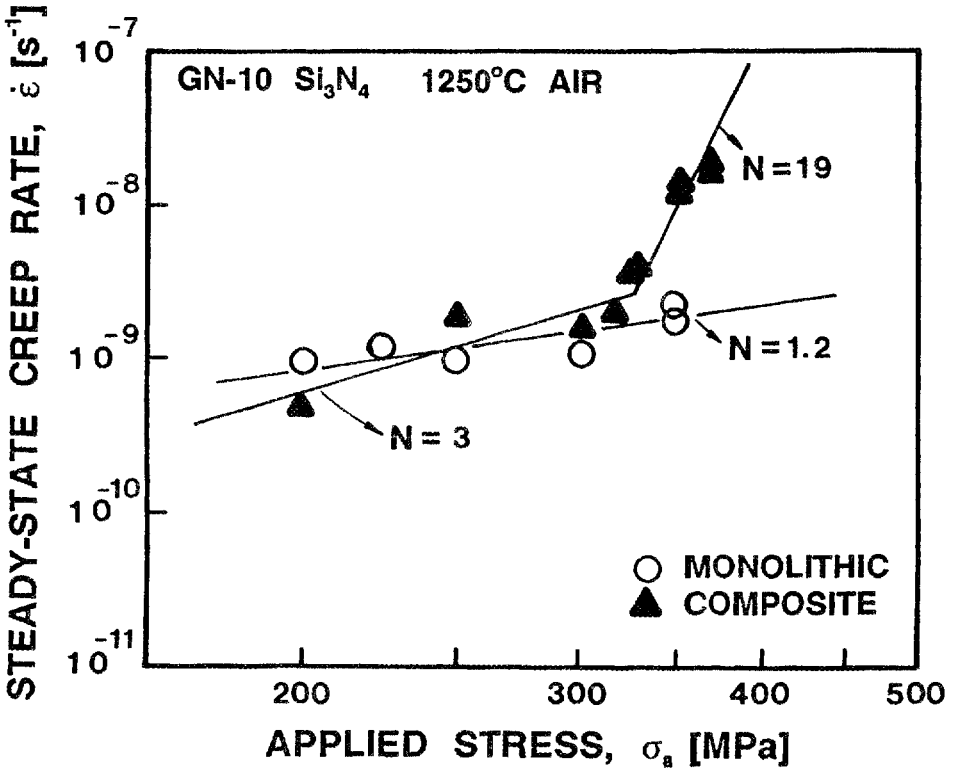

Figure 3. Steady-state creep rate as a function of applied stress for composite and monolithic silicon nitrides. N is the stress exponent defined in Eq. (3).

The results of the room temperature residual strength measurements of the specimens that did not fail during the creep testing are presented in Figure 4, where residual strength is plotted as functions of the applied stress and elapsed time. The residual strength for the zero elapsed creep time (t = 0) was obtained from post oxidation strength measurements [2]. It is evident from Figure 3 that the residual strength of the monolithic material was always higher than that of the composite. Also, the degree of strength degradation as a function of applied stress and elapsed time was substantially higher for the composite than the monolithic. This indicates that the larger creep deformation of the composite resulted in more strength limiting damage.

Some typical specimen deformation curves obtained at applied stresses of σ = 200 and 300 MPa are shown in Figure 5, where x is the distance along the beam length and y is the permanent deflection due to creep. This figure indicates that for a given applied stress and elapsed time, more creep deformation occurred for the composite than the monolithic, as indicated by the results in Figure 3. The polynomial fits of the data shown in Figure 5 are summarized in Table 1. The table includes applied stress, material, fitting coefficients (α to f) and the coefficient of correlation (= r^2_{coef}). The deflection curves, like those in Figure 5, can be used to obtain the curvature as a function of specimens position (x). The specimen curvature can be calculated using the following equation once deflection curve (y(x)) is known

$$1/\rho = (d^2y/dx^2)/[1 + (dy/dx)^2]^{3/2} \tag{4}$$

where $1/\rho$ is the curvature.

The resulting curvature, corresponding to Figure 5, obtained from Eq. (4) and the data in Table 1 is presented in Figure 6, where Log $(1/\rho)$ is plotted as a function of Log (x) for applied stresses of 200 and 300 MPa. By combining Eq. (3) with the resultant bending force across the specimen and the strain-curvature relation, which is based on the elastic solution, the curvature can be readily derived in terms of applied bending moment as follows [6]

$$1/\rho = A\ [M/\Phi]^N \tag{5}$$

where M is the applied bending moment (expressed as M = Px with P being a reaction force at the outer loading point of the specimen) and Φ is the constant associated with A and N and the specimen geometry. Substituting M = Px into Eq. (5) and taking logarithm both sides yield

$$\text{Log}\ (1/\rho) = N\ \text{Log}\ x + B \tag{6}$$

where B = Log $[A(P/\Phi)^N]$. Equations (5) and (6) indicate that on a logarithmic plot the curvature is a linear function of x with a slope of N in the outer span; however, the curvature in the inner span is constant because of the constant moment therein. Equation (6) also indicates that the stress exponent N can be obtained from the slope when Log $(1/\rho)$ is

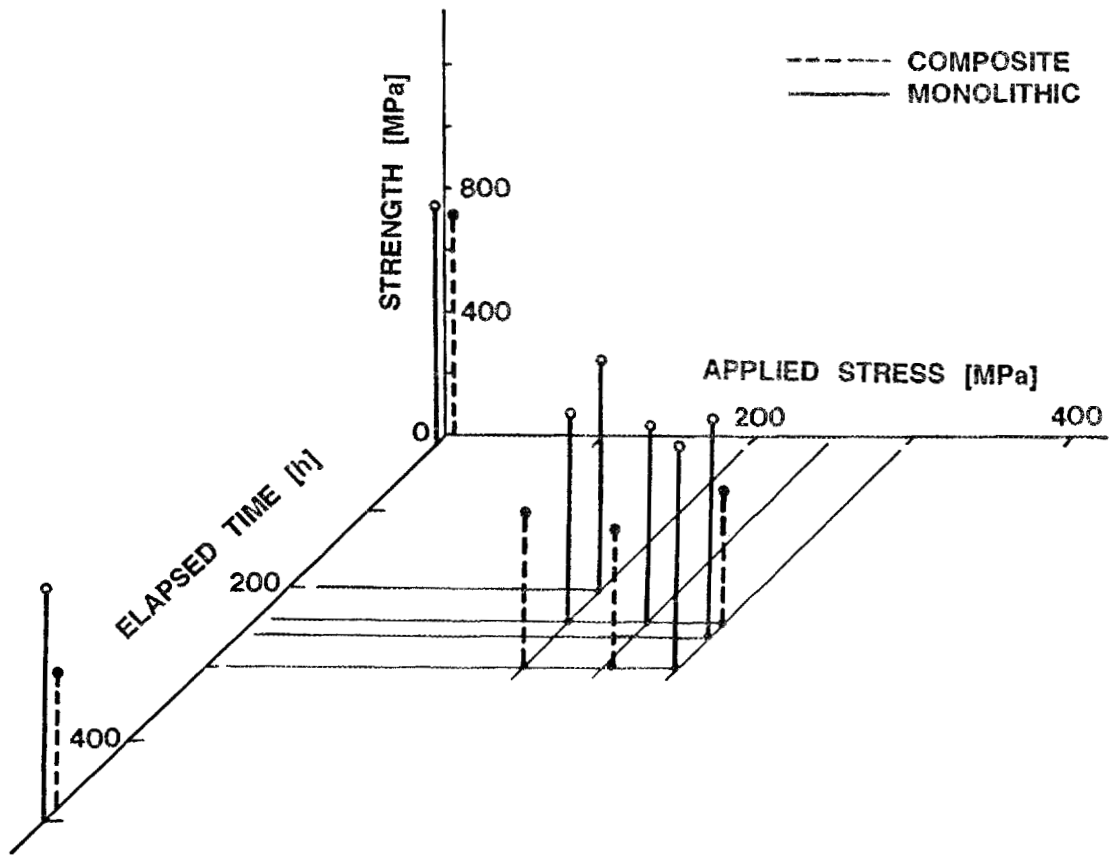

Figure 4. Room-temperature residual strength of crept monolithic and composite specimens as a function of applied stress and elapsed time.

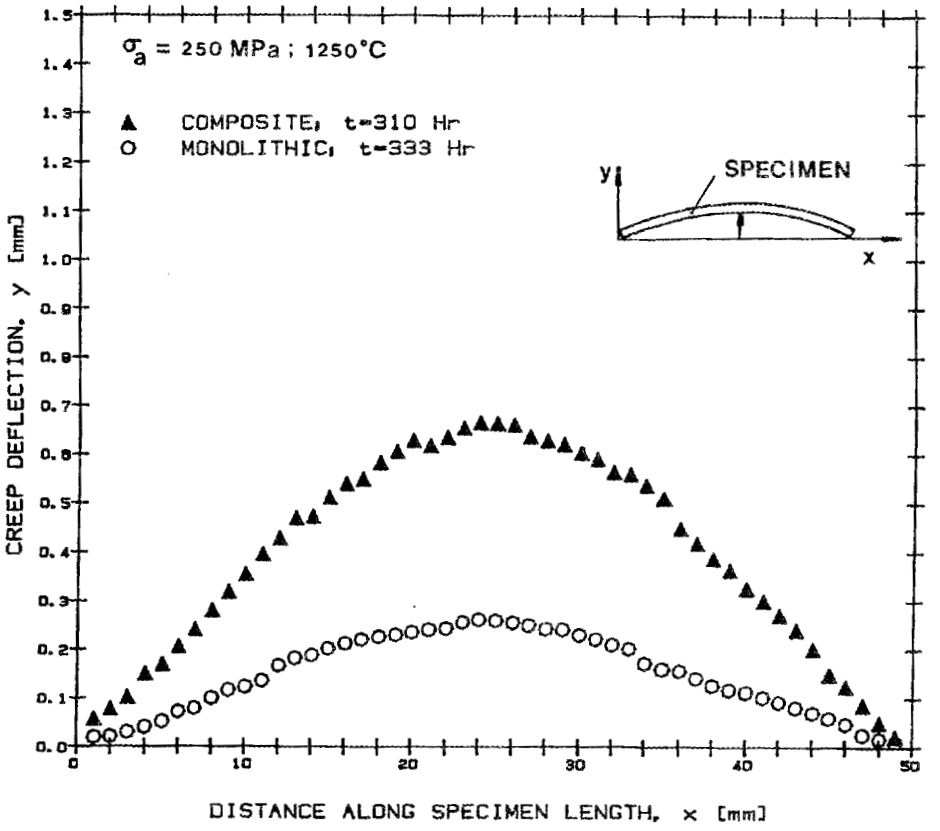

(a)

Figure 5. Creep deflection as function of distance along specimen length (x) for composite and monolithic materials at stresses of σ = 250 MPa (a) and σ = 300 MPa (b).

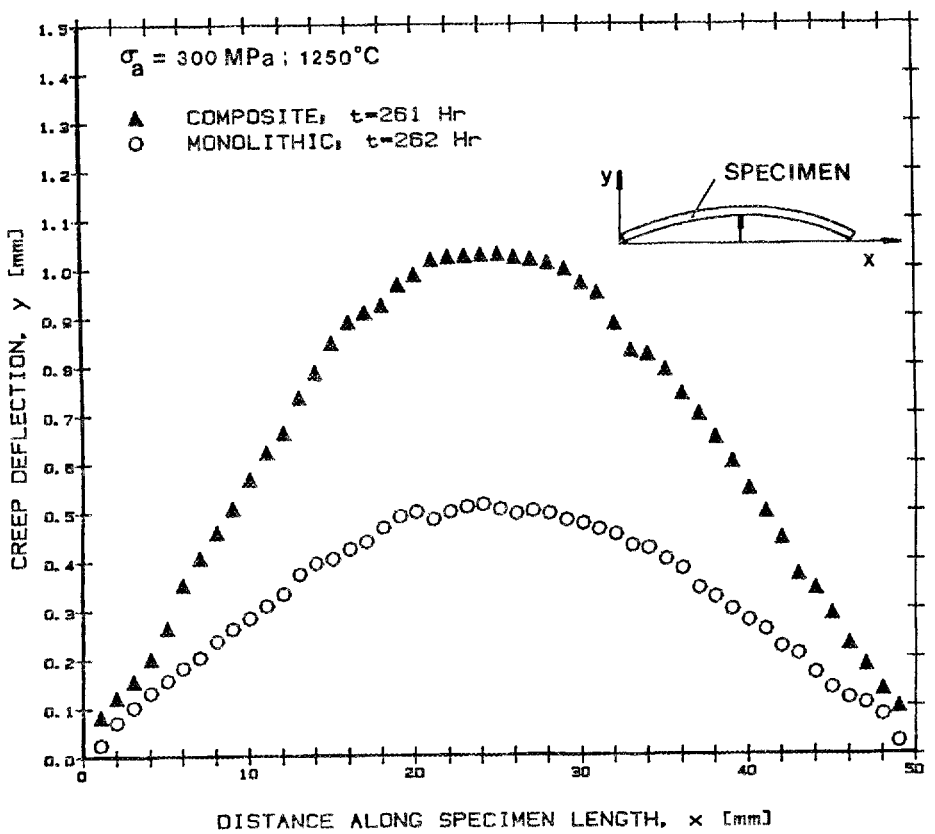

(b)

Figure 5 (continued). Creep deflection as function of distance along specimen length (x) for composite and monolithic materials at stresses of σ = 250 MPa (a) and σ = 300 MPa (b).

Table 1. Coefficients for polynomial expressions representing creep specimen deformation as a function of position

	Applied Stress (MPa)			
	Composite		Monolithic	
Constant*	200	300	200	300
a	-9.8662×10^{-9}	-1.6352×10^{-8}	1.6549×10^{-9}	-1.6376×10^{-9}
b	1.6110×10^{-6}	3.3642×10^{-6}	9.3028×10^{-8}	7.2578×10^{-7}
c	-9.4506×10^{-5}	-2.1764×10^{-4}	-1.9840×10^{-5}	-5.9651×10^{-5}
d	1.7078×10^{-3}	3.8488×10^{-3}	2.8031×10^{-4}	8.9510×10^{-4}
e	0.0104	0.0335	0.0136	0.0240
f	0.0330	0.0364	4.0534×10^{-3}	0.0143
r^2_{coef}	0.9961	0.9988	0.9948	0.9974

Notes:

1. A 5th order polynomial equation was used:

$$y = ax^5+bx^4+cx^3+dx^2+ex+f$$

2. r^2_{coef} is the square of the correlation coefficient.

plotted as a function of Log (x). The curves in Figure 6 shows that Log ($1/\rho$) is not a linear function of Log (x) in the outer span, and that Log ($1/\rho$) is not constant in the inner span, inconsistent with Eqs. (5) and (6). However, assuming that Eqs. (5) and (6) are applicable in an approximate sense, the creep stress exponent N was evaluated from Eq. (6) and the result is presented in Table 2. The average N parameter is N = 2.89 and N = 1.57 for the composite and monolithic, respectively. These values of N parameters are very comparable to those (N = 3 and N = 1.2 for the composite and monolithic materials, respectively) obtained from Eq. 3 and the results in Figure 3. The general consistency between the two methods suggests that tensile creep is nearly equal to compressive creep for these materials with applied stresses $\sigma < 320$ MPa. This implies that the variation in curvature and associated neutral axis shift in the inner span did not drastically effect the average, computed value of N. Note that the creep parameter N for the monolithic material is close to unity (N = 1.2). It can be shown that for N = 1.0, creep deformation is symmetric between the tension and compression sides and neutral axis shift does not occur.

The results of the neutral-axis-position determinations, based on the scratch mark technique described in the Experimental Procedure section, are presented in Figure 7. The strains as a function of location

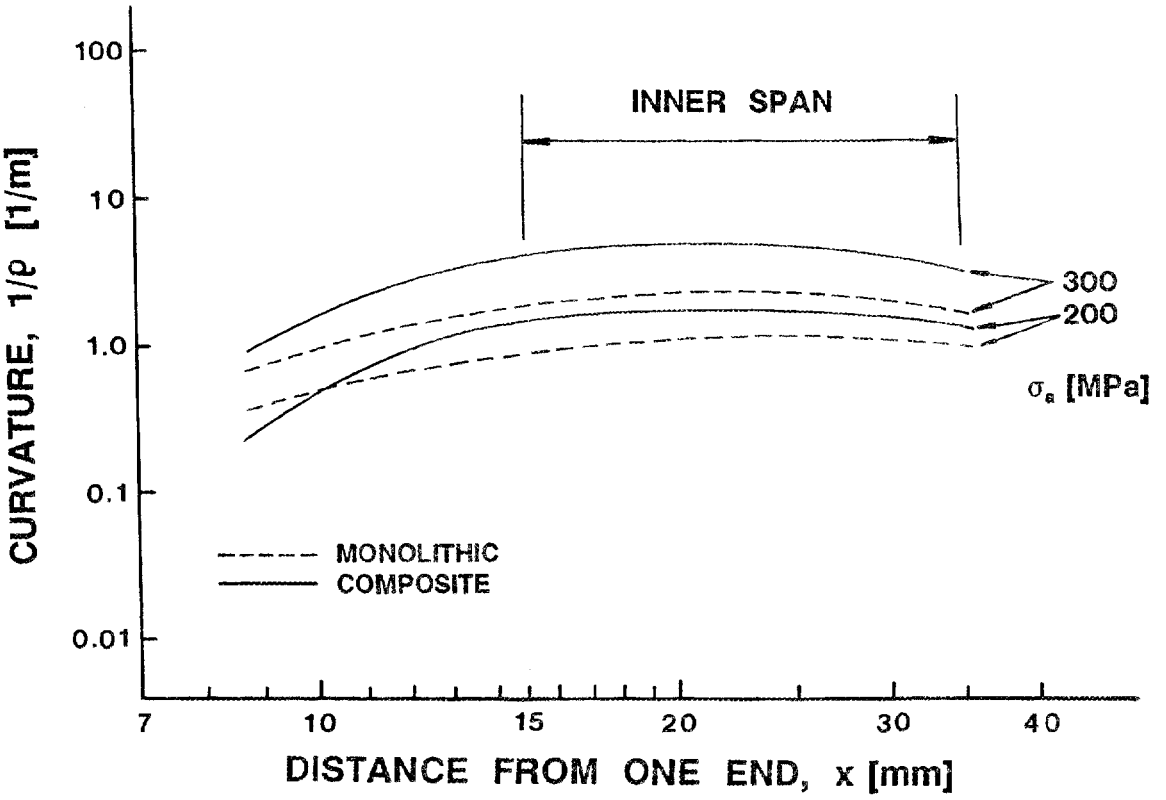

Figure 6. Curvature as a function of distance from one end of specimens crept at σ = 200 and 300 MPa.

Table 2. Stress exponent (N) determined with Eq. (6)

Material	Applied Stress (MPa)	N	r_{coef}
Composite	200	3.098	0.9644
	300	2.541	0.9768
	Average:	2.89	
Monolithic	200	1.513	0.9961
	300	1.620	0.9923
	Average:	1.57	

along the y axis are presented for the different applied stresses and sustained times at 1250°C. For comparison, the results obtained previously for Ceralloy Si_3N_4 and stainless steel [8] are also included in the figure. The results in Figure 7 show that the neutral axis is not clearly defined by a systematic trend in strain along the y axis. Instead, a wide scatter in strains along the y axis is exhibited. In fact, difficulty was encountered in measuring accurate distances between the two adjacent scratch lines because the visibility was obscured by severe oxidation. This poor visibility, as well as low the small creep strain, resulted in a wide scatter in measured strain. In contrast, the data obtained from Ceralloy Si_3N_4 showed a systematic trend of neutral axis shift to the compression side for all test condition, as seen in the figure. Also note that the neutral axis of a stainless test bar that was subjected to creep at σ = 250 MPa at a temperature of 700°C remained almost unchanged, indicating that tensile and compressive creep are identical to each other, as expected for a ductile metal [8]. The success of the scratch mark technique to measure creep strain across the specimen height depends on the relative creep and oxidation rates of a given material. Notwithstanding the difficulty in obtaining accurate strain due to oxidation, the results in Figure 7 in general show that the amount of neutral axis shift may be insignificant within the applied stress range of 224 to 320 MPa, consistent with the results obtained from the evaluation of N parameter. However, for the monolithic specimen that was crept at σ = 370 MPa for t = 19 h, the neutral axis shift is evident as seen in Figure 7(C). Note that the N parameter at stresses σ> 320 MPa is N = 19 (see Figure 3) so that neutral axis shift is expected to be inevitable. Therefore, creep testing in pure tension and pure compression is needed to completely characterize creep behavior of the composite material when the applied stress is above 320 MPa because of neutral axis shift.

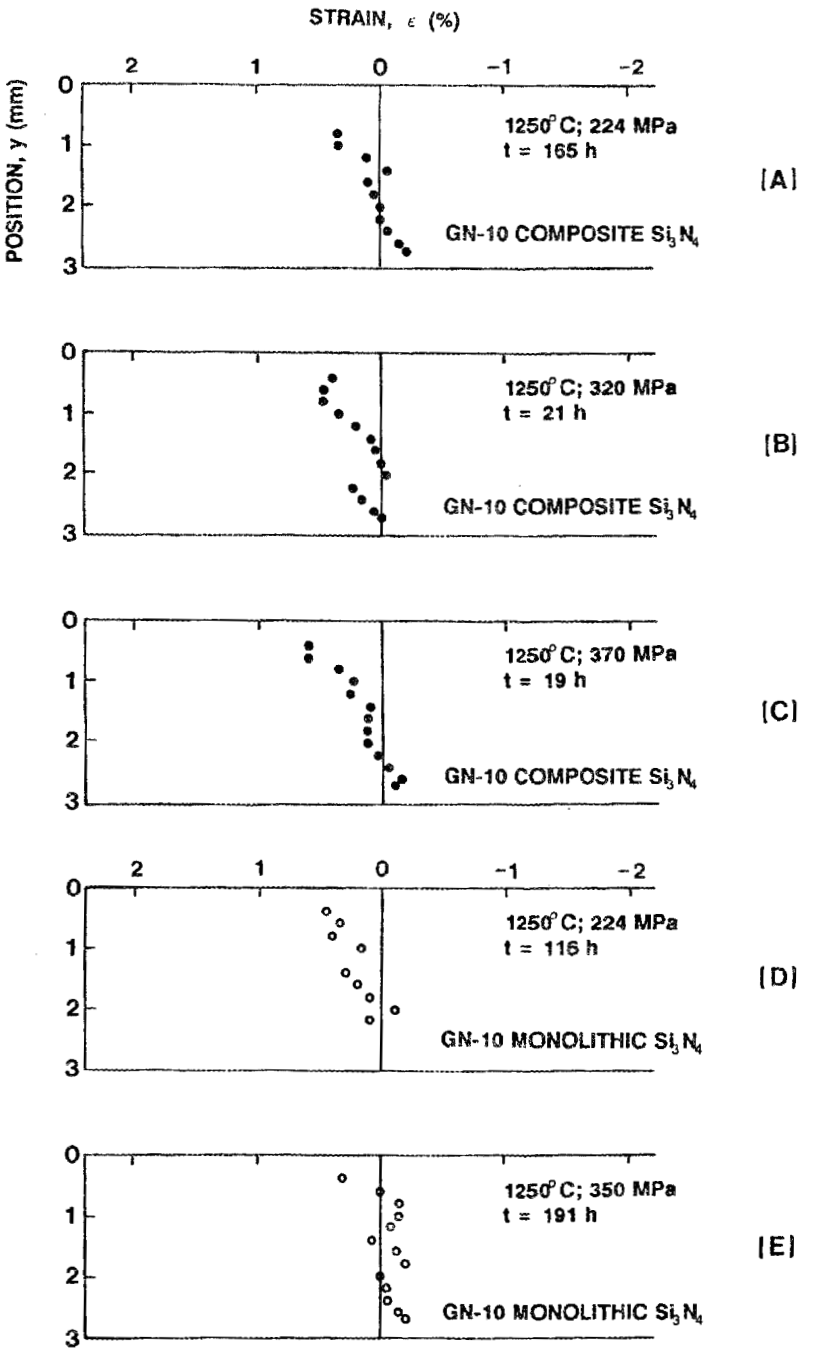

(a)

Figure 7. Flexure creep strain as a function of specimen height (y) for composite and monolithic silicon nitride (a). For comparison the data for Ceralloy silicon nitride and stainless steel are included (b) [8].

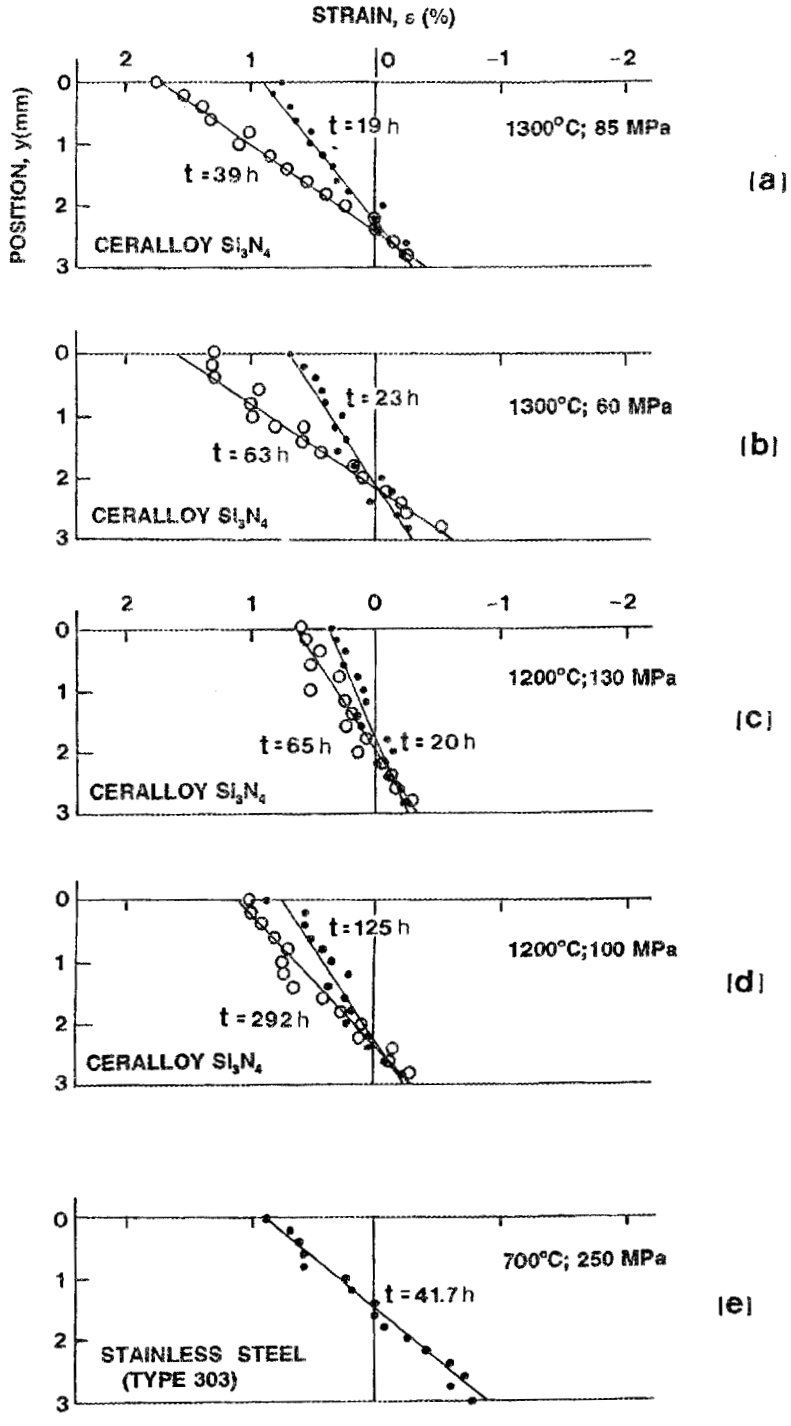

(b)

Figure 7 (continued). Flexure creep strain as a function of specimen height (y) for composite and monolithic silicon nitride (a). For comparison the data for Ceralloy silicon nitride and stainless steel are included (b) [8].

The tensile surfaces of the crept specimens are shown in Figure 8. At a small applied stress of σ = 224 MPa, there was no difference in surface morphology between the two materials and no crack generation was apparent, as seen in Fig. 8(a) and 8(b). At a higher applied stress of σ = 320 MPa, the tensile surface of the composite specimens exhibited many cracks that were perpendicular to the applied stress, Fig. 8(d) and 8(e). In contrast, the surface of the monolithic specimens revealed no appreciable crack formation, as with a low stress of σ = 240 MPa, Fig. 8(c). This result is consistent with the results shown in Figure 2, which indicate that creep rate is insensitive to applied stress up to 320 MPa.

Transmission electron micrographs of the as-received materials are shown in Figure 9. Both materials exhibited hexagonal beta Si_3N_4 grains with dislocations. Spherical pores were contained within glassy regions, and grain junction porosity existed at regions with less glassy phase. The whiskers, shown in Figure 9(a), were heavily faulted and were occasionally stuck together. The cross-section was core-like and contained impurities at the center. An unexpected feature of the whiskers was regions that were decomposed to carbon, evidently from the processing of the silicon nitride, Fig. 10(a). Image analysis of polished section of the composite indicated 1.7% of the material (5.1% of the whiskers) to be decomposed to carbon, as shown in Figure 10(b).

Creeping of the monolithic at 250 MPa resulted in cavity formation at glassy regions between the grains, as shown in Figure 11. Creeping of the composite at 250 MPa resulted cavity formation between grains, along whisker/grain interfaces, and at decomposed regions, as shown in Figure 12. The decomposed regions frequently appeared to have degenerated into very porous regions, as shown in Figure 13. In addition to the cavitation, the composite exhibited formation of large cracks, as shown in Figure 14. The cracks may form because the decomposed whiskers are porous and thus act as stress concentrations. Further, the decomposition adds free silicon to the grain boundaries and thus may result in enhanced grain boundary sliding. Similar cavity and crack formation resulted when 350 MPa was applied, and microstructural differences to account for the change in creep parameter could not be distinguished via TEM. However, the difference in creep parameters for the small and large stress ranges may be attributed to the neutral axis shift, formation of macro scale cracks, and a possible contaminant drop in materials stiffness. The macro scale cracks observed via SEM appear to result from linking of the cracks observed via TEM (Figure 14).

Conclusions

The monolithic silicon nitride exhibited far better creep resistance than the 30 vol % SiC whisker-reinforced composite silicon nitride in flexure at 1250°C in air. The stress exponents in bending were found to be N = 1.2 and N = 3 for the monolithic and composite materials. At stresses above 320 MPa, however, the composite material exhibited a sharp transition in the creep rate vs. applied stress plot, resulting in a significantly larger stress exponent of N = 19. TEM analysis of the indicated cavitation of the glassy grain boundary phase in both materials, and the formation of macro scale cracks in the composite material tested at larger

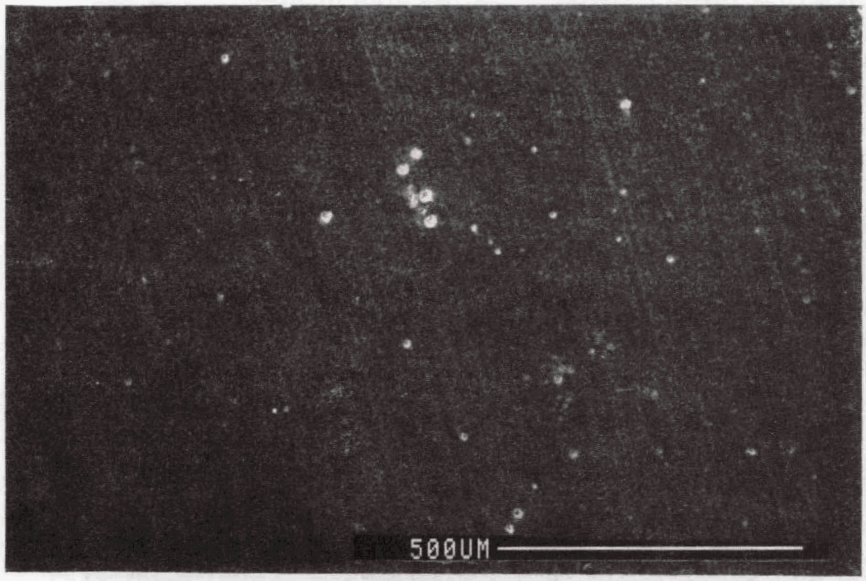

(a)

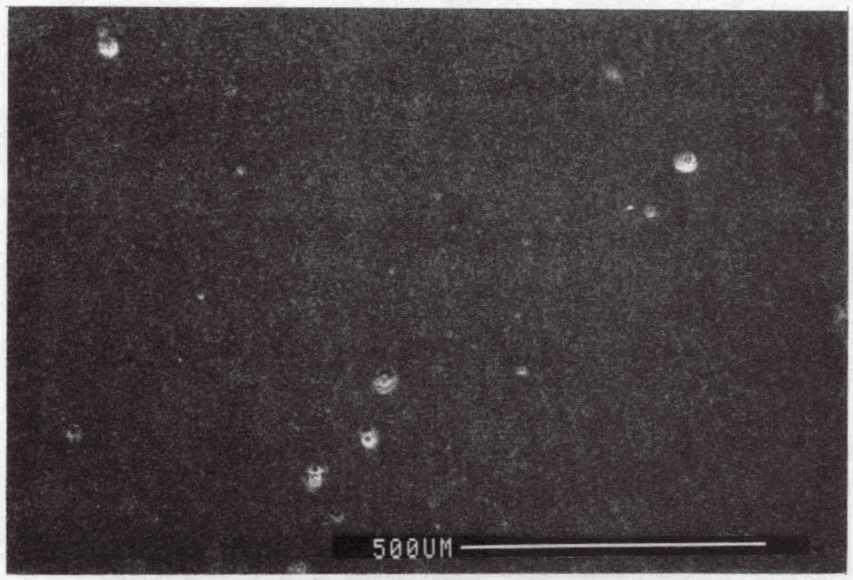

(b)

Figure 8. Surfaces of monolithic (a) and composite specimens (b) subjected to a stress of σ = 224 MPa. Also, surfaces of monolithic (c) and composite (d and e) materials crept at σ = 320 MPa are included.

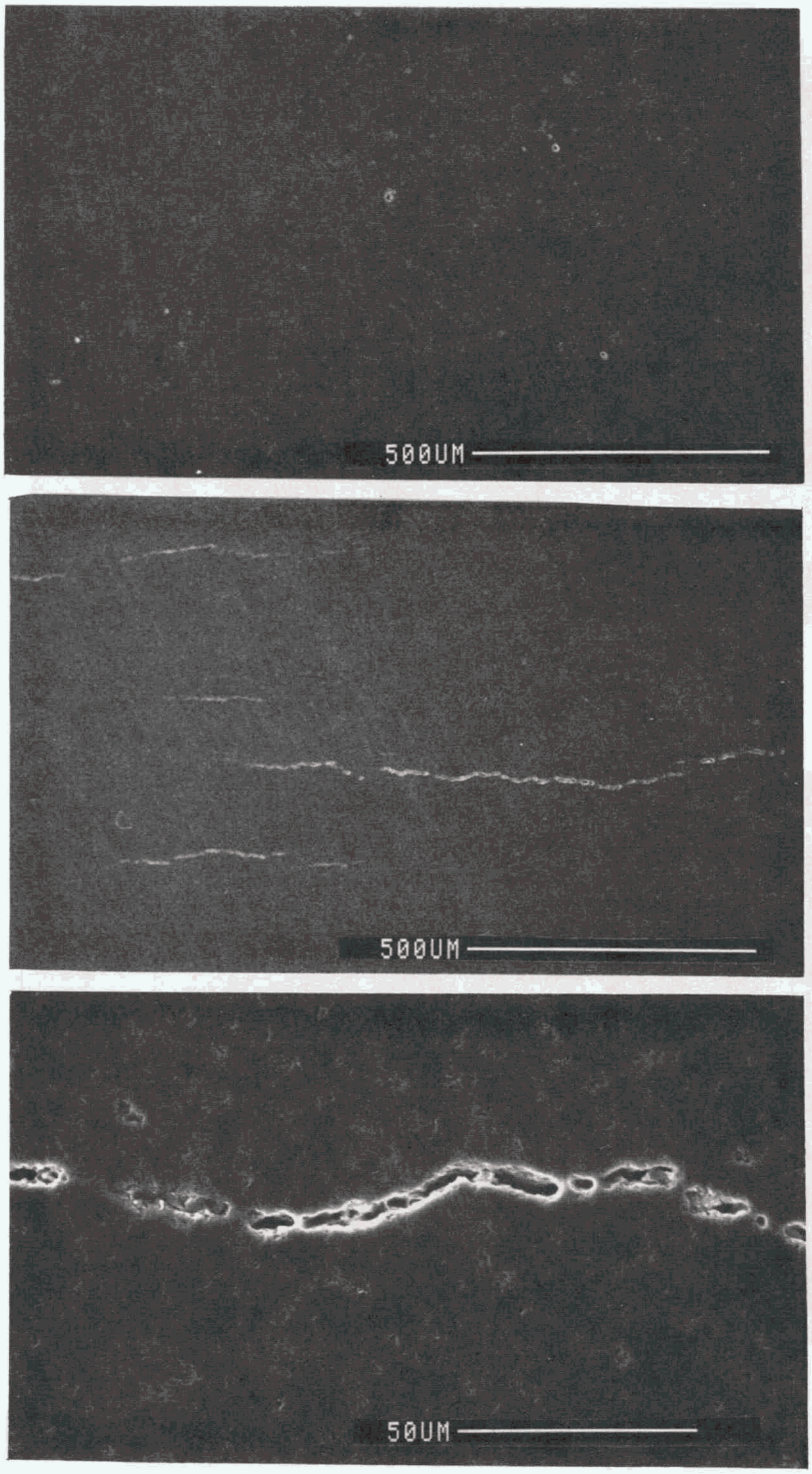

(c)

(d)

(e)

Figure 8 (continued). Surfaces of monolithic (a) and composite specimens (b) subjected to a stress of σ = 224 MPa. Also, surfaces of monolithic (c) and composite (d and e) materials crept at σ = 320 MPa are included.

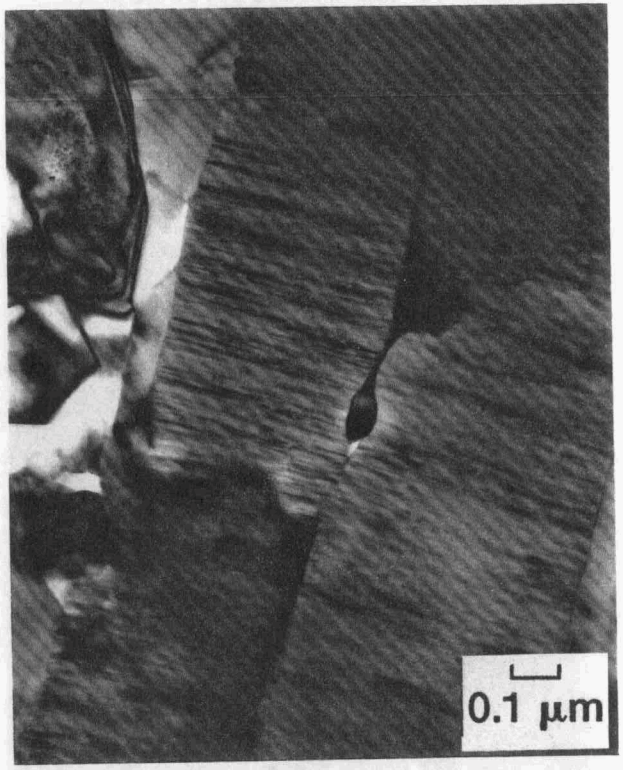

(a)

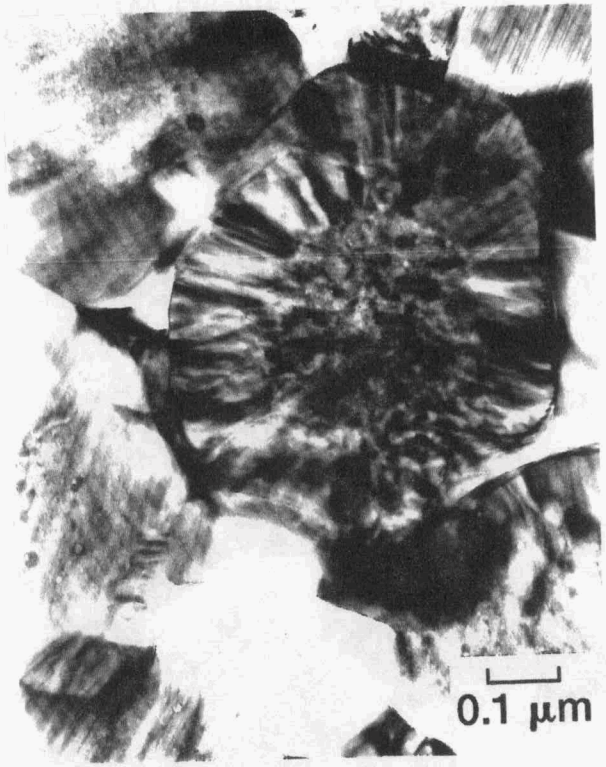

(b)

Figure 9. TEM micrographs of as-received composite (a and b) and monolithic (c and d) materials. Note the heavy faulting and core-like structure of the whiskers.

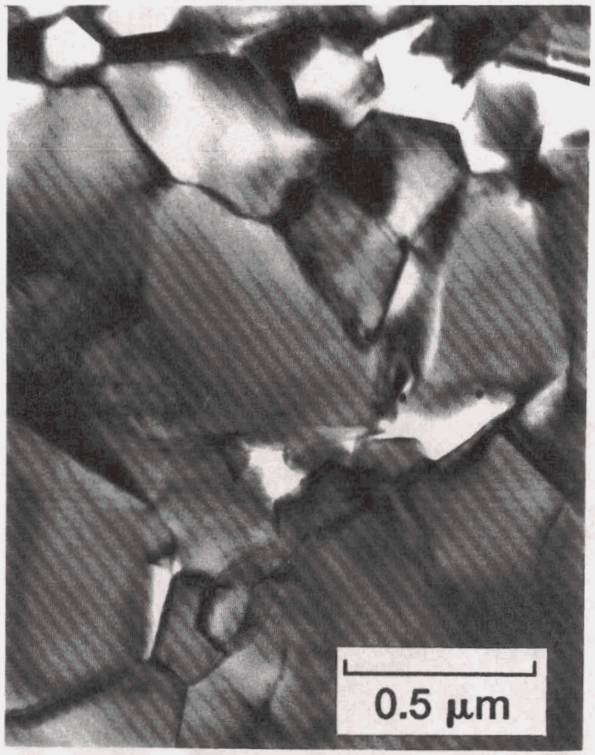

(c)

(d)

Figure 9 (continued). TEM micrographs of as-received composite (a and b) and monolithic (c and d) materials. Note the heavy faulting and core-like structure of the whiskers.

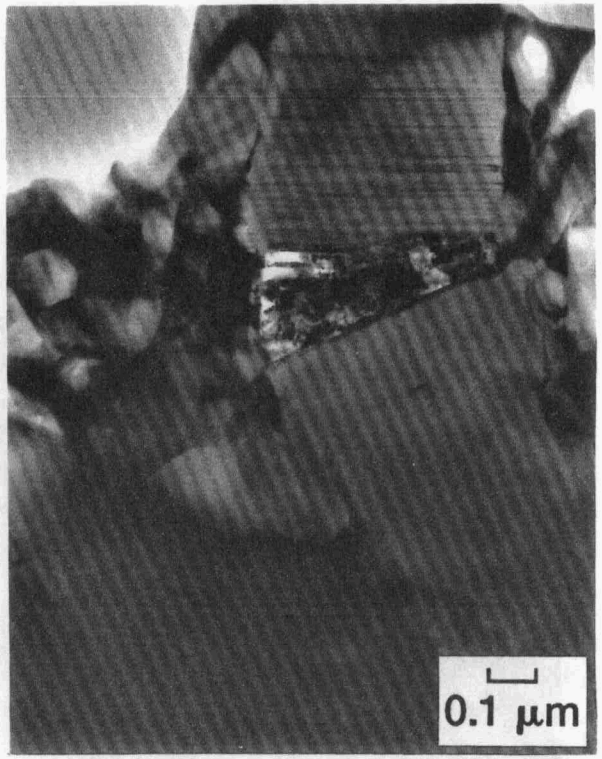

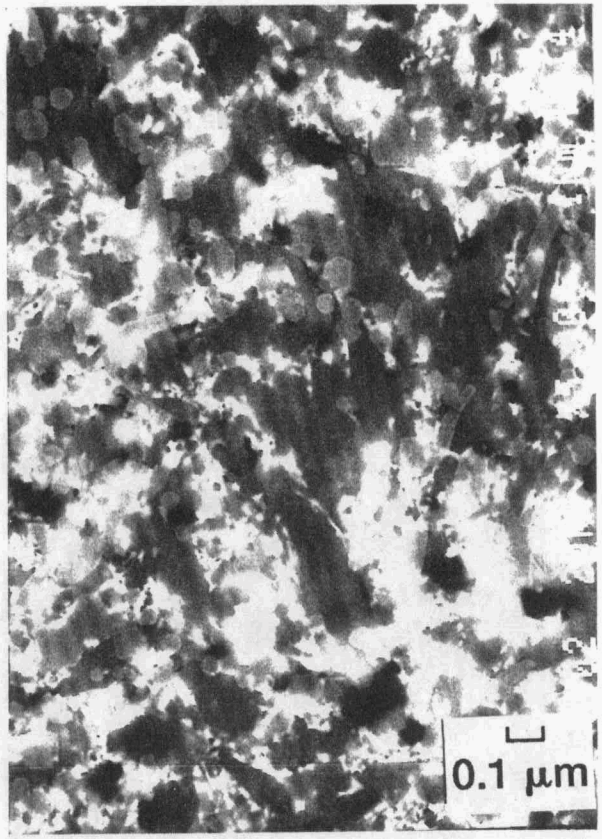

Figure 10. TEM view of SiC whisker partially decomposed to Carbon (a) and backscattered electron image showing decomposed regions (black), glassy regions (white), and Si_3N_4 and SiC regions (grayish).

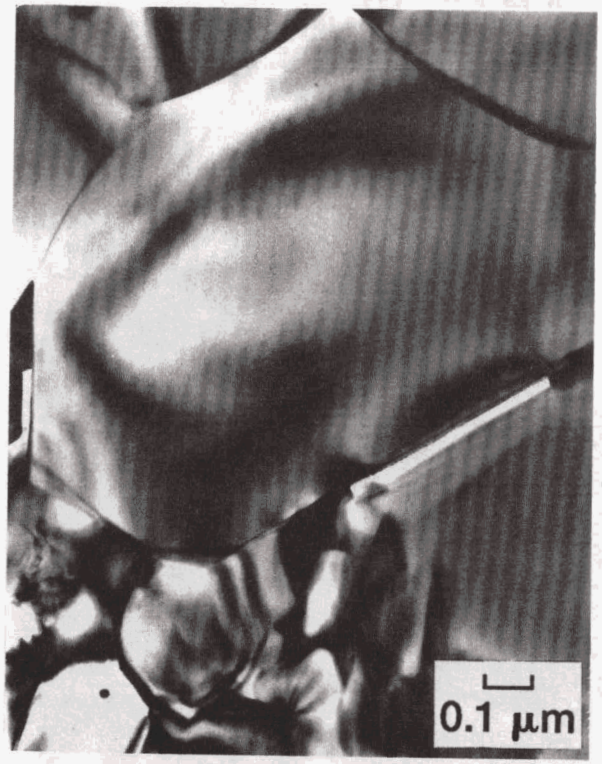

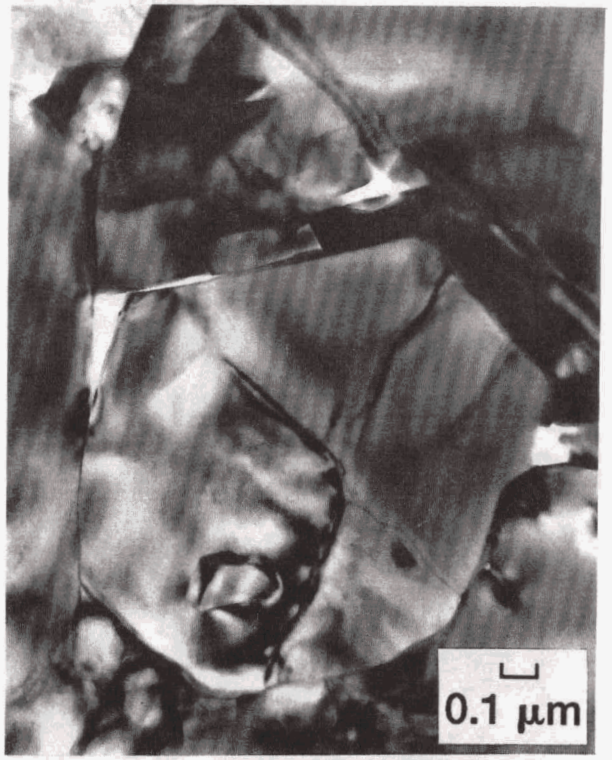

Figure 11. Cavity formation in monolithic material crept at 250 MPa in 1250 °C air.

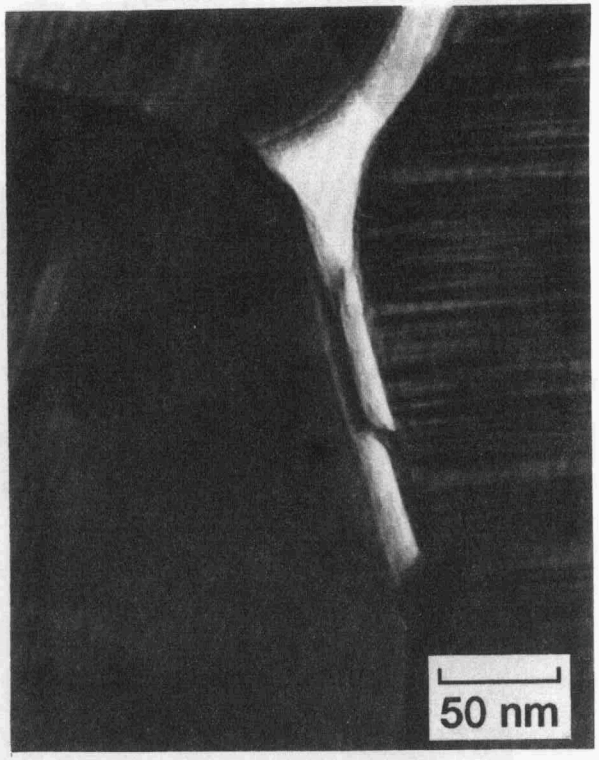

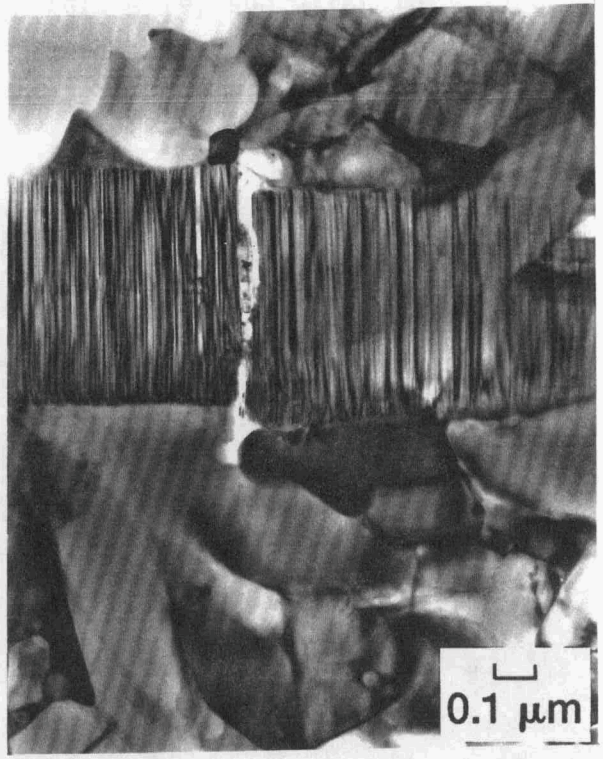

Figure 12. Cavity formation in composite material crept at 250 MPa in 1250 °C air.

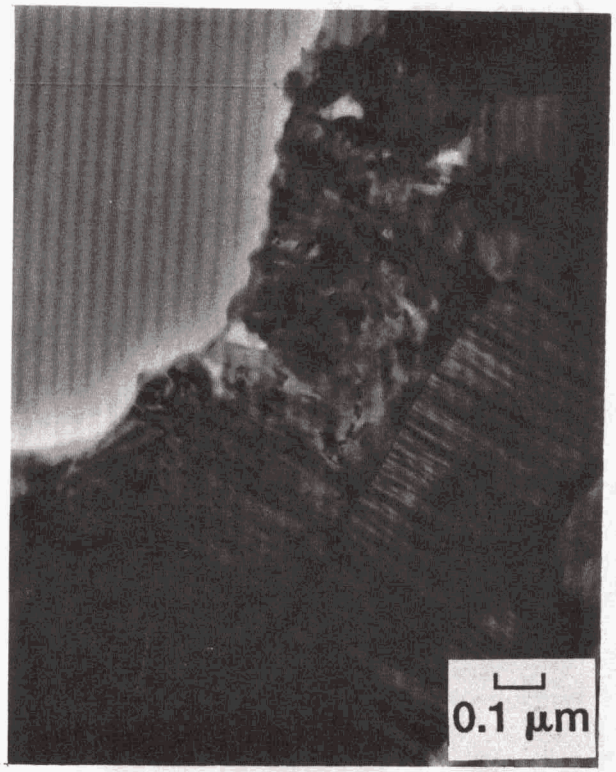

(a)

(b)

Figure 13. Typical regions of decomposed SiC before (a) and after (b) creeping at 250 MPa in 1250 °C air.

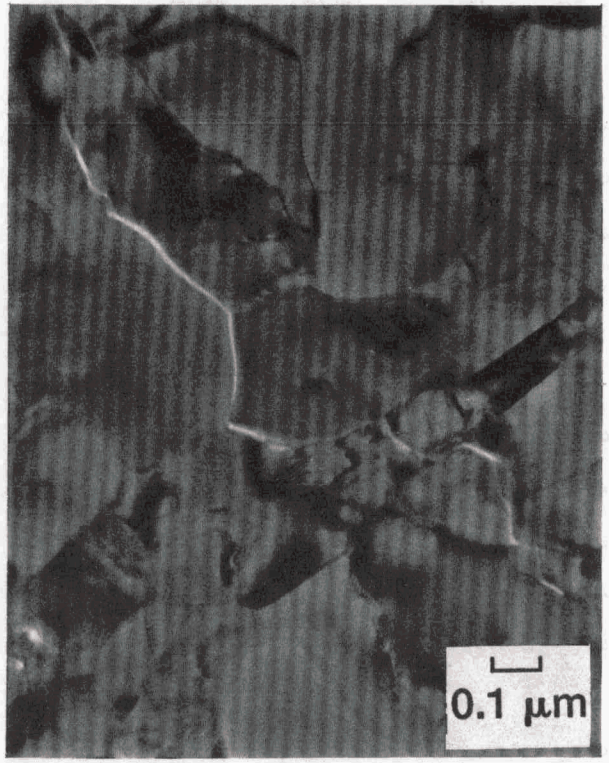

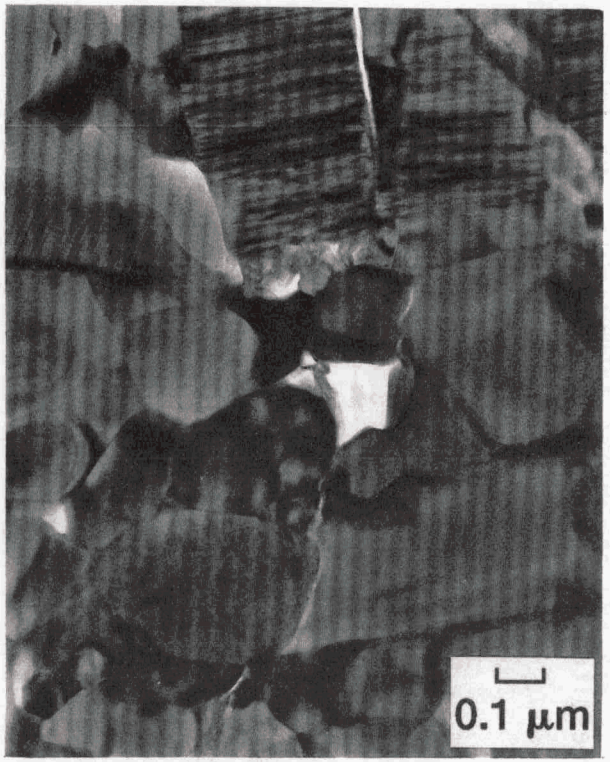

Figure 14. Cracks formed in the composite material after creeping at 250 MPa in 1250 °C air.

stresses. Analysis of the composite materials indicated that about 2% of the SiC whiskers were decomposed to carbon. The decomposed regions may have been sites of preferential cavity formation. The larger stress exponent may have resulted from the formation of voids and macro scale cracks.

Status of Milestone

Milestones are on time.

Publications

None

References

1. J. A. Salem, "Strength and Toughness of Monolithic and Composite Silicon Nitride," NASA TM 102423 (1990).

2. J. A. Salem, S. R. Choi, S. A. Sander, and D. F. Fox, "Elevated Temperature Mechanical Behavior of Monolithic and SiC Whisker-Reinforced Silicon Nitrides," NASA TM 105245 (1991).

3. S. R. Choi, J. A. Salem, and G.J. Gyekenyesi, "Dynamic Fatigue Properties of Silicon Carbide Whisker-Reinforced Silicon Nitride," Ceram. Eng. & Sci. Procd., 12[7-8] 1527-46(1991)

4. S. R. Choi and J. A. Salem, "Comparison of Dynamic Fatigue Behavior Between SiC Whisker-Reinforced Composite and Monolithic Silicon Nitrides," NASA TM 103707 (1991).

5. S. R. Choi and J. A. Salem, "Strength, Toughness and R-Curve Behavior of SiC Whisker-Reinforced Composite Si_3N_4 with reference to Monolithic Si_3N_4, J. Mater. Sci. 27 1491-98 (1992).

6. G. W. Hollenberg, G. R. Terwilliger, and R. S. Gordon, "Calculation of Stress and Strain in Four-Point Bending Creep Tests," J. Am. Ceram. Soc., 54[4] 196-99 (1971).

7. K. Jakus and S. M. Wiederhorn, "Creep Deformation of Ceramics in Four-point Bending," J. Am. Ceram. Soc., 71[10] 832-36 (1988).

8. J. A. Salem and S. R. Choi, Semiannual Progress Report, Ceramic technology for Advanced heat engine Projects, W.B.S. Element 3.2.1.7, (11/1991).

9. C. F. Chen and T. J. Chuang, "Improved Analysis for Flexural Creep with Application to Sialon Ceramics," J. Am. Ceram. Soc., 73[8] 2366-73 (1990).

Life Prediction Methodology

P. K. Khandelwal (Allison Gas Turbine Division General Motors Corporation)

Objective/Scope

The objective of this project is to develop and demonstrate the necessary nondestructive examination (NDE) technology, materials data base, and design methodology for predicting useful life of structural ceramic components of advanced heat engines. The analytical methodology will be demonstrated through confirmatory testing of ceramic components subject to thermal-mechanical loading conditions similar to those anticipated to occur in actual vehicular service. The project addresses fast fracture, slow crack growth, creep, and oxidation failure modes.

Technical Highlights

Flexural Testing

Fast fracture characterization of PY6 MOR bars continued during this reporting period from room temperature to 1400°C. The specimens were nominally 3 X 4 X 50 mm with an inner load span of 20 mm and an outer span of 40 mm. Results are shown in Table I. This testing used the standard loading rate which has a cross-head speed of 0.508 mm/minute (0.020 inch/minute). Fractographic analysis revealed that failure at room temperature was predominantly controlled by surface flaws whereas at elevated temperatures it was both from surface and volume flaws.

Oxidation studies were conducted in static air environment during this reporting period between 1000°C to 1400°C. A total of 130 specimens were exposed at various temperatures from 1 to 500 hours. The weight change per unit surface area and the thickness of the oxide layer was measured as a function of time and temperature. Substantial scatter was observed in the weight change both as a function of temperature and time with no apparent trend. This may be due to variations in the material microstructure or impurities which affect the oxidation kinetics. The thickness of the oxide layer increased linearly with increasing temperature (Figure 1) for specimens exposed for 100 hours. Preliminary results of the X-ray diffraction studies revealed the presence of crystallite, -Si_3N_4, and yttrium-oxynitride phases in the oxide layer. All the specimens were examined before and after oxidation by microfocus X-ray. The results indicated that surface forming small pits within the oxide layer are very difficult to discern from the background fuzzy X-ray image of the oxidized specimen. All the oxidized MOR bars were subsequently tested at room temperature in four point bending. Figure 2 shows the retained strength at ambient temperature after 100 hours of thermal exposure in air.

Table I. Flexural strength of PY6 HIP'ed material (cross head speed = 0.5 mm/min)

Specimen number	Test temp - -°C	Strength -- MPa	Strength -- ksi
34.1716	20	871.57	26.41
34.1717	20	653.49	
34.1718	20	617.56	89.57
34.1719	20	852.28	123.61

Table I. (cont.)

Specimen number	Test temp --°C	Strength -- MPa.	Strength -- ksi
34.1722	20	574.48	83.36
34.1723	20	553.61	80.29
34.1724	20	655.01	95.00
34.1991	20	833.94	120.95
34.1992	20	858.42	124.50
34.1993	20	856.46	125.52
34.1994	20	709.07	102.84
34.1995	20	917.63	133.09
34.1996	20	898.74	130.35
34.1997	20	932.43	135.23
34.1998	20	881.18	127.80
34.1999	20	947.93	137.48
34.2000	20	858.79	124.55
34.2001	20	973.74	141.22
34.2002	20	1033.87	149.95
34.2003	20	947.73	137.45
34.2004	20	949.21	137.67
34.2005	20	1036.41	150.31
34.2006	20	890.91	129.21
34.2007	20	885.99	128.50
34.1725	1000	821.70	119.17
34.1726	1000	848.88	123.11
34.1727	1000	676.34	98.11
34.1728	1000	628.34	90.84
34.1729	1000	853.43	123.78
34.2021	1000	818.17	118.66
34.2022	1000	817.63	118.53
34.2023	1000	768.94	111.52
34.2024	1000	745.13	108.92
34.2025	1000	764.78	110.92
34.1630	1100	620.06	89.93
34.1631	1100	613.75	89.01
34.1632	1100	627.39	90.99
34.1633	1100	481.75	69.87
34.1634	1100	575.06	83.40
34.2008	1100	619.53	139.50
34.2009	1100	642.34	141.94
34.2010	1100	603.76	106.11
34.2011	1100	641.25	77.77
34.2012	1100	667.76	118.94
34.1766	1200	645.73	93.65
34.1767	1200	680.77	98.73
34.1769	1200	629.42	91.32
34.1771	1200	693.42	100.57

Table I (cont.)

Specimen number	Test temp -- °C	Strength -- MPa.	Strength -- ksi
34.1775	1200	453.67	65.80
34.1776	1200	706.92	102.53
34.1777	1200	608.41	88.24
34.2031	1200	666.72	95.83
34.2032	1200	654.94	94.99
34.2033	1200	713.69	103.51
34.2034	1200	675.57	97.98
34.2035	1200	972.92	97.57
34.2036	1200	480.21	69.65
34.2037	1200	618.87	89.76
34.2038	1200	630.59	91.46
34.2039	1200	587.60	85.22
34.2040	1200	661.82	95.99
34.1635	1300	527.11	76.45
34.1636	1300	597.14	86.60
34.1637	1300	634.40	92.01
34.1638	1300	613.11	88.92
34.1639	1300	538.09	78.04
34.1640	1300	676.33	98.09
34.1641	1300	556.88	80.77
34.1642	1300	506.09	73.46
34.1643	1300	582.40	84.47
34.1644	1300	386.79	56.10
34.1760	1300	608.58	88.26
34.1761	1300	620.30	89.96
34.1762	1300	541.85	78.59
34.1763	1300	603.49	83.53
34.1764	1300	592.83	85.89
34.2026	1300	533.81	77.42
34.2027	1300	522.11	75.72
34.2028	1300	545.78	79.16
34.2029	1300	528.09	76.59
34.2030	1300	579.95	84.11
34.1620	1400	505.36	73.29
34.1621	1400	511.17	74.14
34.1622	1400	473.30	68.64
34.1623	1400	433.94	62.94
34.1624	1400	426.59	61.87
34.1625	1400	415.56	60.27
34.1626	1400	463.85	67.27
34.1627	1400	476.97	69.18
34.1628	1400	535.38	77.65
34.1629	1400	421.93	61.19
34.1778	1400	447.14	64.85

Table I (cont.)

Specimen number	Test temp -- °C	Strength -- MPa.	Strength -- ksi
34.1782	1400	443.48	64.32
34.1783	1400	448.00	64.97
34.1784	1400	430.54	62.44
34.1785	1400	430.54	62.44
34.1786	1400	437.16	63.40
34.1787	1400	413.20	59.93
34.1788	1400	448.65	65.07
34.1790	1400	448.65	65.07
34.1791	1400	429.54	62.30
34.1792	1400	421.76	61.17
34.1793	1400	382.46	55.47
34.1794	1400	405.47	55.81
34.1795	1400	431.27	62.55
34.1797	1400	501.30	72.71
34.1798	1400	395.49	57.36
34.1799	1400	425.06	61.65
34.1801	1400	472.61	68.54

Uniaxial Tensile Testing (Buttonhead Specimen)

Fast fracture uniaxial tensile testing continued at Southern Research Institute (SoRI) between 1000°C and 1300°C. The measured strength of each specimen is shown in Table II. Monotonic testing is continuing at SoRI to generate the data base required to support the life prediction code development.

Table II. Uniaxial tensile strength of PY6M HIP'ed material (stress rate= 600 ksi/min)

Specimen number	Test temp -- °C	Strength -- MPa	Strength -- ksi
105A	1000	461.97	67.00
95B	1000	469.83	68.14
121B	1000	451.97	65.55
651B	1000	243.26	35.28
122A	1000	521.54	75.64
125A	1000	423.91	61.48
125B	1000	264.91	38.42
652A	1000	299.87	43.49
124B	1000	482.44	69.97
123A	1000	498.03	72.23
115A	1000	240.08	34.82
118B	1000	451.97	65.55
653B	1100	298.92	43.35
659A	1100	352.21	51.08

Table II (cont.)

Specimen number	Test temp -- °C	Strength -- MPa.	Strength -- ksi
654B	1100	339.37	49.22
658A	1100	395.35	57.34
653A	1100	312.90	45.38
654A	1100	391.11	56.72
655A	1100	263.98	38.29
658B	1100	365.23	52.97
655B	1100	311.38	45.16
657B	1100	356.06	51.64
657A	1100	349.84	50.74
656B	1100	201.33	29.20
338A	1100	420.80	61.03
656B	1100	256.49	37.19
97A	1200	377.21	54.71
243A	1200	522.22	75.74
118A	1200	278.96	40.46
115B	1200	376.01	54.53
110B	1200	457.14	66.30
112A	1200	441.42	64.02
104B	1200	442.80	64.22
107A	1200	403.44	58.51
116B	1200	416.80	60.45
113B	1200	403.44	58.51
109A	1200	370.95	53.80
114A	1200	366.24	53.11
108B	1200	382.52	55.48
94B	1300	309.61	44.90
112B	1300	412.25	59.79
111A	1300	287.59	41.71
108A	1300	350.53	50.84
110A	1300	363.28	52.69
107B	1300	306.10	44.40

Three tensile creep frames have been developed and are being continuously used at SoRI to measure the creep and stress rupture behavior of the button-head specimens between 1200° and 1400°C. Preliminary measurement on limited number of specimens was conducted. Table- II shows the time-to-failure and total strain to failure as a function of applied stress. The minimum creep rate of the present vintage of PY6 material appears to be at least one order of magnitude lower than reported by Ferber and co-workers at Oak Ridge National Laboratories (ORNL). Allison is currently working with ORNL under an user agreement to conduct failure analysis of uniaxial tensile specimens. Fractographic analysis revealed the presence of extensive cavitation at 1400°C under an applied stress of 100 MPa (Figure 3) in 12.97 hours. Both creep testing and failure analysis are continuing.

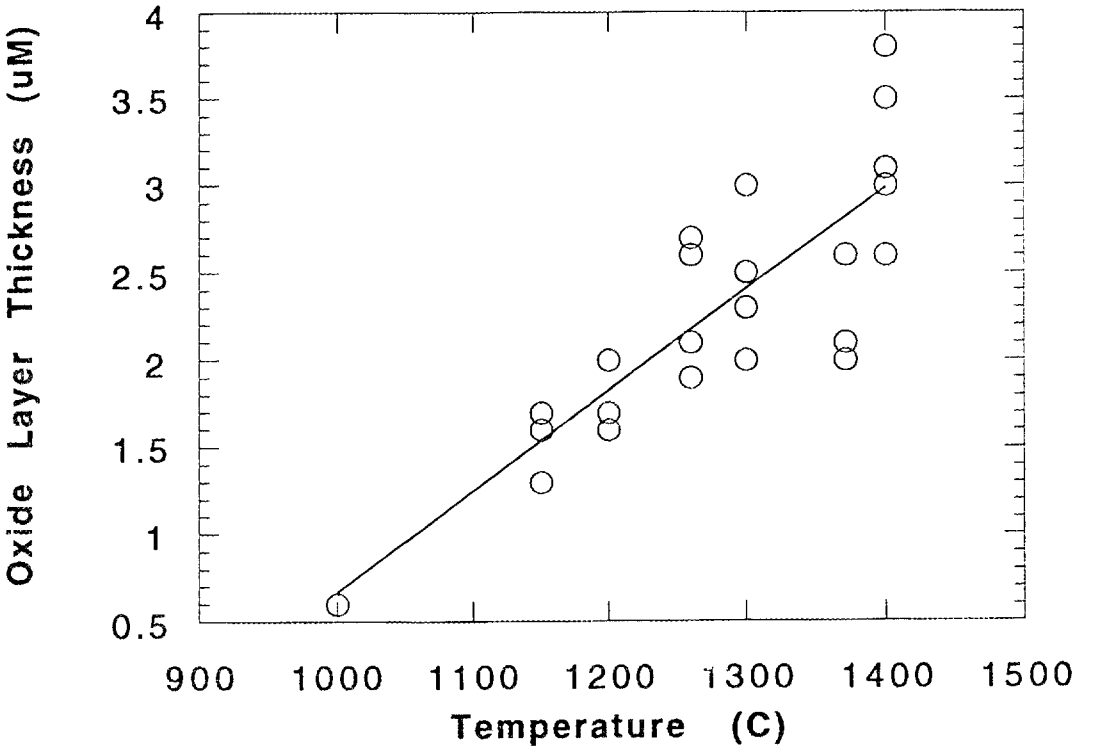

Figure 1. Effect of temperature on the thickness of the oxide layer in air. Exposure time = 100 hr.

Table III. Preliminary creep behavior of HIP'ed PY6 material

Specimen number	Test temp --°C	Applied stress -- MPa	Time to failure t_f (hr)	Total strain to failure -- ( )
90B	1200	290	>266	1570
77A	1300	200	0.73	1570
626B	1300	150	In progress	
90A	1370	87	>101	----
55A	1370	87	.004	1470
80A	1370	75	>387	----
84B	1370	75	287	6770
60A	1400	150	.025	1830
171A	1400	125	2.0	2960
195B	1400	100	12.97	3400
192B	1400	75	844	10190

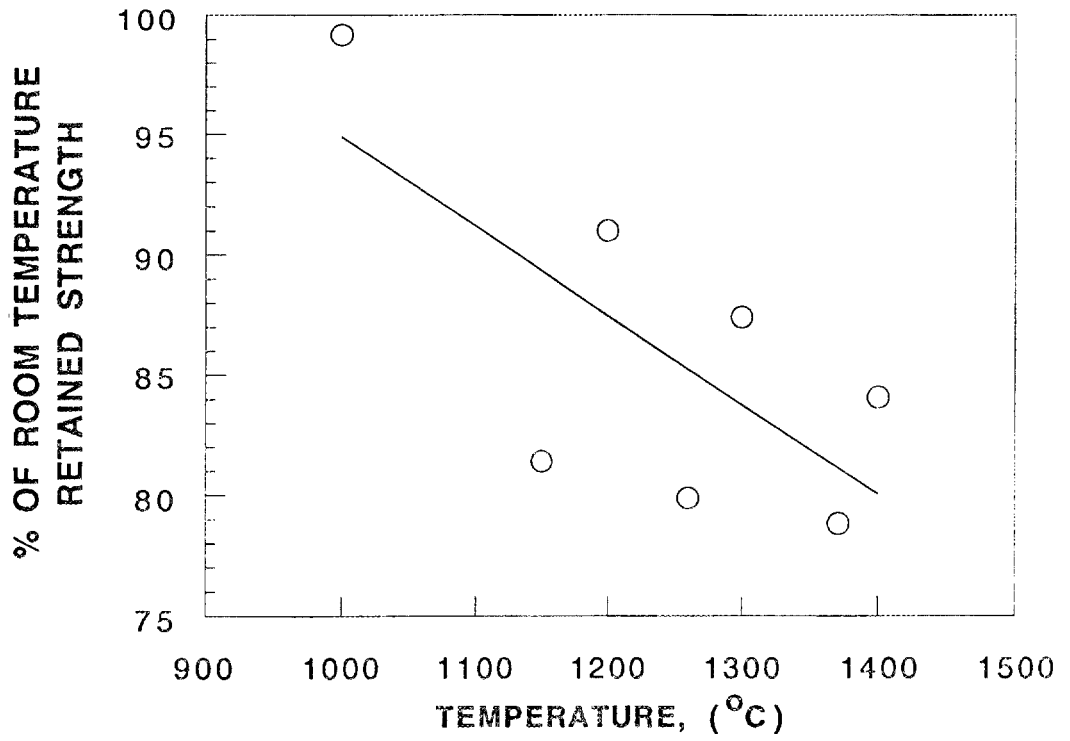

Figure 2. Effect of temperature on the room temperature retained strength of the PY6 material. Exposure time = 100 hr.

Multiaxial Testing

Biaxial creep and stress rupture behavior of circular disks of 31.75 mm (1.25 in) diameter and 2 mm (.080 in) thickness was studied at Battelle Laboratories, Columbus, Ohio, using a ball-on-ring arrangement. The specimen was supported by a ring of 15.625 mm (0.625 in) diameter at the bottom and centrally loaded with a 4.75 mm (0.190 in) diameter silicon nitride ball at the top. The displacement was measured by a LVDT at the bottom center of the disk. Table IV shows the data of the all the specimens to date. The biaxial fast fracture strength at room temperature was measured to be 701 MPa and at 1200°C is about 436 MPa. No failure occurred at or below 355 MPa applied stress both at 1200°C and 1300°C for 200 hours or more indicating a potential lower fatigue limit of the material. When the applied stress was increased, the specimen failed in less than 10 minutes. Further biaxial characterization and fractographic analysis of the material is in progress.

Table IV. Biaxial creep behavior of PY6 HIP'ed material.

Specimen number	Test temp -- °C	Applied. stress -- MPa	Test time -- hr	Comments
34.2560	1200	436	------	Failed
34.2577	1200	350	200	No failure
34.2562	1200	349	200	No failure

Table IV (cont.)

Specimen number	Test temp - °C	Applied stress -- MPa.	Test time -- hr	Comments
34.2242	1300	429	0.0417	Failed
34.2244	1300	391	0.11	Failed
34.2247	1300	355	360	No failure
34.2241	1300	327	200	No failure
34.2243	1300	318	200	No failure

Flexural specimens with Vicker's indentor induced surface cracks at varying orientations from 0 to 45 deg were fabricated to determine the shear sensitive parameter (C). The value of 'C' varied between 1.25 to 1.5 depending on the curve fit method used (Figure 4). It appears, however, that more data will be required at higher angles between 30 to 45 deg to get a better assessment of the 'C' parameter. The value of 'C' for through-cracks has been measured to be 1.5 using the diametrical compression chevron notched specimens which is in good agreement with the above surface crack data.

Figure 3. Creep cavitation of PY6 silicon nitride at 1400°C under 100 MPa uniaxial tensile stress after 12.97 hr.

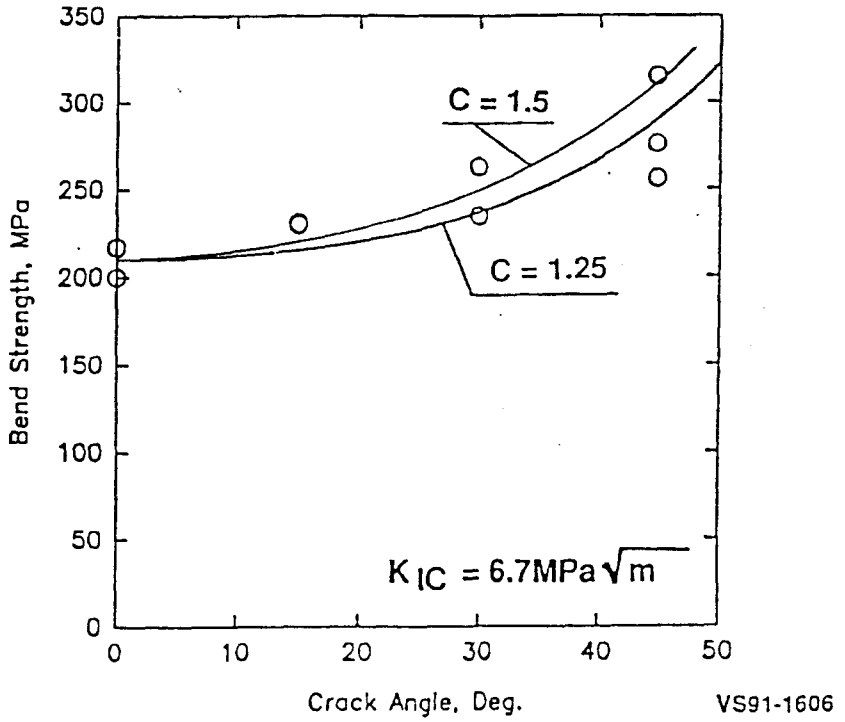

Figure 4. Measurement of shear sensitive parameter 'C' using the controlled flaw method.

Confirmatory Spin Disk

Ninety (90) unmachined confirmatory spin disks were received from GTE Laboratories. The average diameter of the disks was about 114.3 mm (4.5 in) and thickness 12.7 mm (0.5 in). The shaft diameter was about 14.7 mm (0.58 in). The visual examination of the disks reveal surface crack like fold lines at the bottom of disks some of which go through the shaft diametrically. Axial microfocus radiography detected a number of such cracks in all the disks which suggests that the fold lines have finite depth. Radial X-ray inspection of the 20 disks indicated the presence of crack type defects in the shaft and density variation in the disk below the shaft region in the disk center. Fluorescent penetrant inspection (FPI) showed extensive porosity over the entire surface of all the disks, which may be due to the rough surface.

It was decided, based on the dimensions of the as-received disks, to machine the disks to 111.76 mm (4.45 in) diameter and 10.16 mm (0.4 in) thickness to provide 2.5 mm (0.100 in) extra machining stock to eliminate the observed flaws. Finite element stress analysis was conducted using the measured surface and volume Weibull properties of the PY6 material received under this program, Figure 5. The maximum stress of 299.77 MPa (43.5 ksi) occurs in the surface of the disk. However, the probability of failure (POF) is driven by volume flaws. The POF due to surface flaws was determined to be 0.026 compared to 0.486 from volume flaws. This calculation was conducted for 71.1K rpm. failure speed.

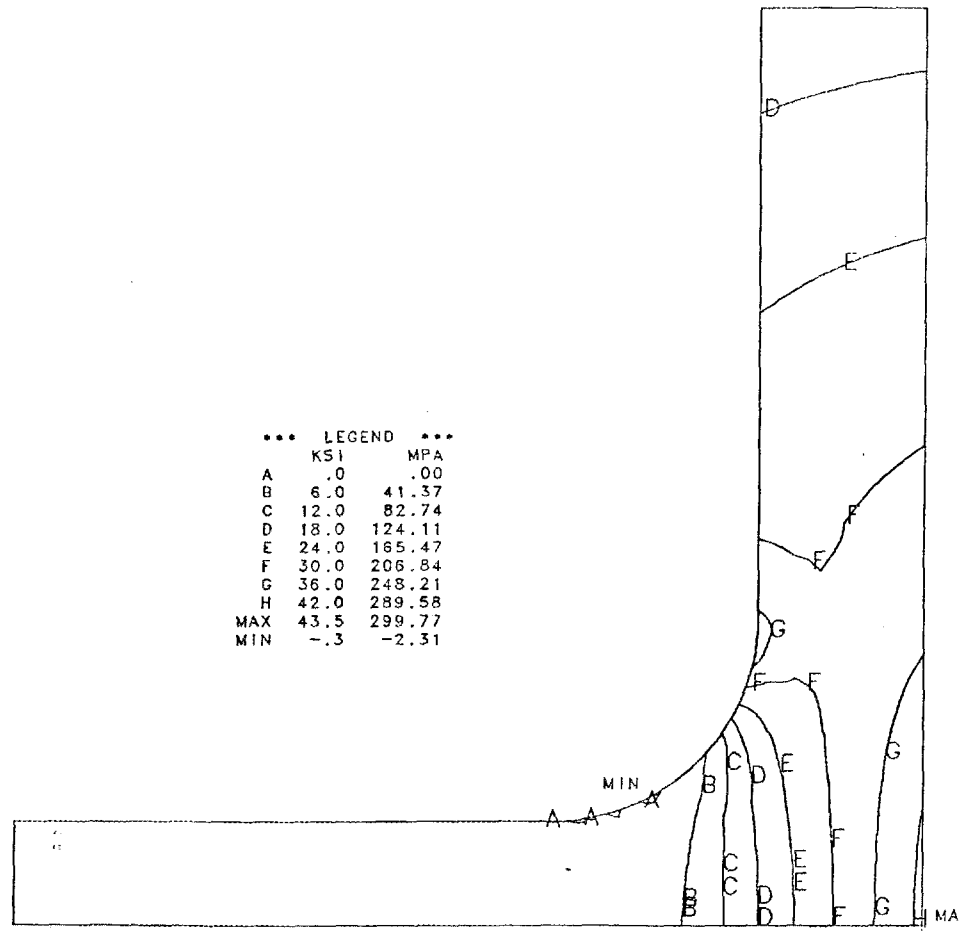

Figure 5. Stress analysis of PY6 HIP'ed silicon nitride disk.

One disk (No. 88) was sectioned to fabricate Type-B MOR bars. The disk was machined such that the thickness of the disk represented the tensile 4 mm surface of the flexural specimen. Microfocus X-ray inspection of the specimens revealed uniformly distributed low density structure. FPI indicated porous material and acoustic microscopy detected discrete flaws. The average room temperature strength of 30 specimens was measured to be 554.76 MPa (80.46 ksi) with a standard deviation of 115.47 MPa (16.75 ksi). The Weibull modulus (m) was determined to be 5.97 using the maximum-likelihood method. Fractographic analysis indicated that the failures occurred from dark inclusions, surface flaws and fold lines. The fold lines are believed to be caused by the injection molding process. The individually injection molded MOR bars generally failed from surface machining defects at room temperature. Majority of the button-head tensile specimens failed from the iron based dark inclusions.

A second disk (No. 91) was machined and was intermittently examined by optical macrography, microfocus X-ray and acoustic microscopy to further confirm the internal quality of the disks. Both the NDE techniques detected cracks and/or flaws in the disk. Acoustic microscopy C-scan images and optical photographs taken intermittently after incremental grinding continued to show the replica of the surface flaws, present in the as -received disk, even after removing about 3 mm material from both the surfaces of the disk. A typical example is shown in Figure 6 which indicates that the cracks were present even after removing 2 mm of the material from the shaft side of the surface. Visual

ULTRASONIC IMAGING - SHAFT SIDE - AFTER REMOVING 2MM MATERIAL

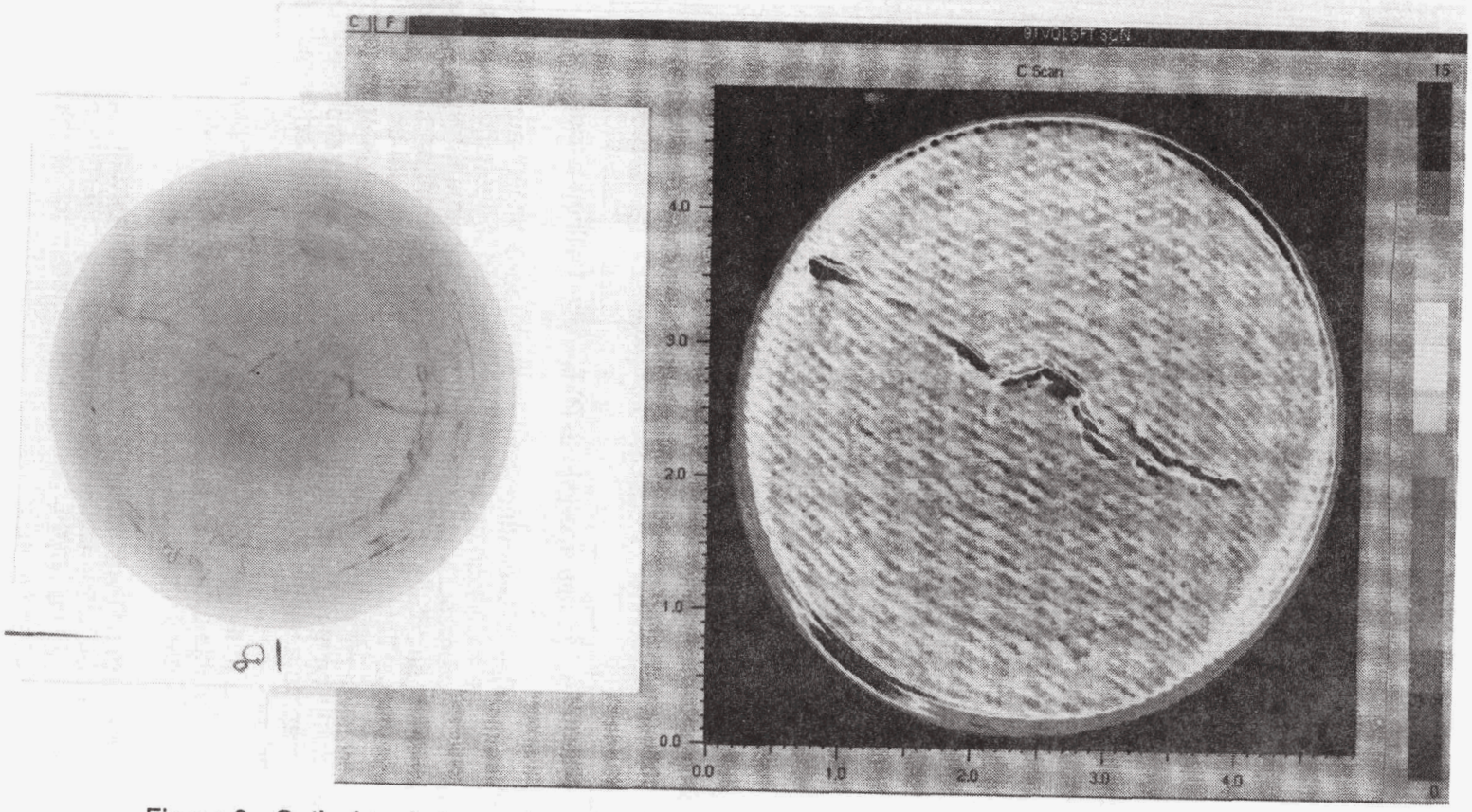

Figure 6. Optical and ultrasonic evaluation of spin disk No. 91 of PY6 injection molded and HIP'ed silicon nitride.

examination after incremental grinding indicated the replica of the surface flaws. The internal area below the shaft also showed the presence of defects at the machined thickness of the disk. These flaws in reality are volume flaws in the disk and are present in the high stress region which strongly suggested that the disk would fail prematurely.

Based on the aforementioned results of disks No. 88 and No. 91 it was decided with the concurrence of Oak Ridge National Laboratories program management that spin disks were unworthy of further testing.

Status of milestones

322201: Computer Implementation of Initial Failure Models--complete
322202: Initiation of MOR Testing--complete
322203: Initiation of Tensile Testing--complete
322204: Initiation of Biaxial Testing--complete
322205: Confirmatory Testing discontinued because of the poor quality spin disks received from GTE
322206: Completion of All Specimen Testing--on schedule
322207: Finalization/Verification of Computer Code--on schedule
322208: Draft Final Report--on schedule
322209: Final Report--on schedule

Publications

P.K.Khandelwal and D.L.Vaccari "Ceramic Life Prediction Methodology of Ceramic Engine Components" submitted for publication in the SAE proceedings of ATD/CCM conference held 28-31 October , 1991, Dearborn, Michigan.

Life Prediction Methodology — J. Cuccio (Garrett Auxiliary Power Division, Allied-Signal Aerospace Company)

Objective/Scope

Garrett Auxiliary Power Division (GAPD) has defined a program to develop the methodology required to adequately predict the useful life of ceramic components used in advanced heat engines. GAPD's approach to ceramic life prediction consists of comprehensive testing of various specimen geometries under both uniaxial and multiaxial loads at different environmental conditions to determine the strength-controlling flaw distributions and to identify various failure mechanisms. This information will be used to develop the flaw distribution statistical models and material behavior models for fast fracture, slow crack growth, creep deformation, and oxidation. As sub-routines, these models will be integrated with stress and thermal analyses into a failure risk integration analytical tool to predict the life of ceramic components. The methodology developed will be verified (for completeness and accuracy) by analytically predicting the life of several ceramic components and testing these components under stress and temperature conditions encountered in ceramic turbine engines.

Technical Highlights

Material Testing and Analysis
H. Fang, N. Menon, and T. Strangman

Material Testing

All required test and confirmatory specimens have been obtained from Norton/TRW Ceramics (NTC). Table 1 summarizes the specimens and their current status. All specimens are NT154 silicon nitride, processed under identical conditions and finish machined and heat treated by NTC. Selected specimens will be notched and precracked for testing. All specimens will be subjected to visual inspection, laser marking, and NDE (which may include fluorescent penetrant, radiography, and ultrasonic inspection) before testing.

GAPD is continuing tensile creep and tensile slow crack growth testing as a User at the ORNL High Temperature Materials Laboratory (ORNL-HTML) under the direction of Drs. M.G. Jenkins and M.K. Ferber of the Mechanical Properties User Center. The specimens are of the ORNL cylindrical buttonhead geometry with a 6.35 mm diameter by 35 mm length gage section. The specimens are loaded in uniaxial tension in Instron screw-driven machines using the ORNL/Instron Supergrips. Instron extensometers with SiC probes are being used to monitor the strain deformation of the gage sections during testing. A schematic of the test setup is shown in Figure 1.

TABLE 1. ORNL LIFE PREDICTION CERAMIC TEST SPECIMEN STATUS

Type of Test	Specimen Size	Surface Machining Direction	Specimen Status
4-Point Bend	MIL-STD-A	Longitudinal	Testing Completed
4-Point Bend	MIL-STD-B	Longitudinal	In Testing
4-Point Bend	MIL-STD-B	Transverse	Testing Completed
4-Point Bend	MIL-STD-B	45 degrees	Testing Completed
4-Point Bend	0.35 x 0.72 x 6 in	Longitudinal	NDE
Chevron Notch	--	--	In Testing
Diametral Compression	--	--	Ready for Testing
Plate Bending	--	--	NDE
Tensile (Fast Fracture and S/R)	--	--	NDE, and In Testing
Pre-cracked Tension/Torsion	--	--	Ready for Testing
Unnotched Tension/Torsion	--	--	NDE
Notched Tensile (Fast Fracture and Stress Rupture)	--	--	Visual Inspection
Rectangular Flaw Growth	--	--	NDE, Ready for Testing
Square Flaw Growth	--	--	Visual Inspection
Spin Disk	--	--	NDE

8491(06)-1

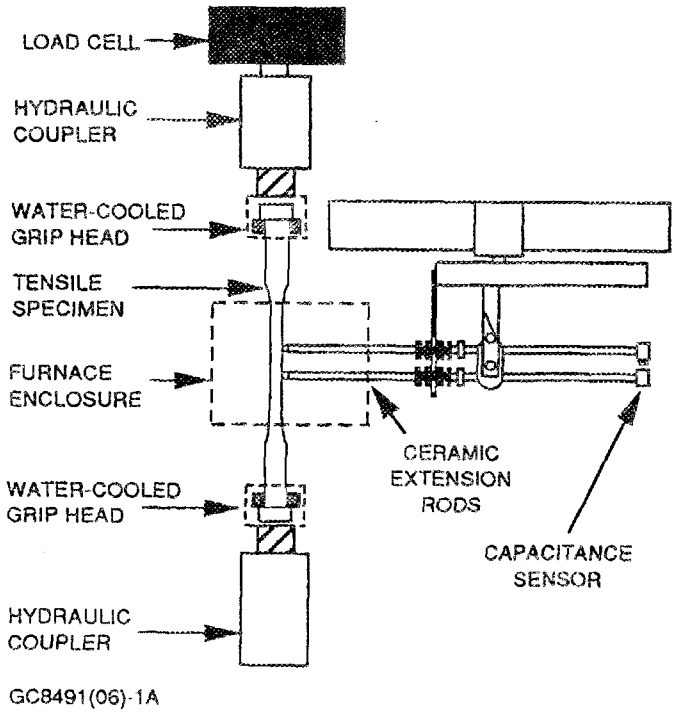

Figure 1. Schematic of ORNL-HTML Test Setup.

Sixty-three specimens have been tested at temperatures between 982C to 1400C. Table 2 summarizes the test temperature, load, time to failure, and strain to failure data for these specimens.

Models have been developed by Dr. N. Menon of GAPD to predict both primary and secondary creep rates and stress rupture life of NT154 silicon nitride in the temperature range of 1149C to 1400C.

Figure 2 shows a comparison of predicted NT154 primary and secondary creep rates (solid lines), calculated using the initial models, versus actual test data (symbols). The agreement between the model predictions and test data is excellent. Similar comparisons are shown in Figure 3 for the stress rupture model, plotting predicted NT154 rupture lifetime (solid lines) and test data (symbols). In Figure 3(a), the dashed line represents the minus three sigma (-3σ) standard deviation calculated from the model; this line is included to illustrate how well the model prediction fits the experimental data. Details of these models have been submitted for publication in the Journal of the American Ceramic Society.

Specimens are being examined with the scanning electron microscope (SEM), using a special sample preparation technique developed by M. Ferber and M. Jenkins of ORNL-HTML to facilitate observation of cavities. The gage sections of the specimens are partially notched in the transverse plane, i.e. parallel to the fracture surface, and then broken in a low-energy mode to create a clean fracture surface. The quantity and size of the cavities appear to increase as a function of test time and temperature. Characterization of the fracture origins is in progress.

TABLE 2. SUMMARY OF PRELIMINARY TENSILE CREEP TEST RESULTS

Specimen ID	Test Temp., C	Applied Stress σ_0, MPa	Time to Failure t_f, hrs	Total Strain to Failure ε_f, $\mu\varepsilon$
3-29	1400	150	80	16,350
1-21	1400	140	96	18,270
1-10	1400	130	192	21,930
2-125	1400	130	139	16,500
1-4	1400	125	341	22,820
2-114	1400	110	411	24,570
2-68	1400	100	462	25,800
2-123	1400	90	478*	15,110
2-35	1400	85	597*	14,970
2-55	1371	210	1.4	3,510
1-9	1371	190	68	10,920
1-6	1371	180	62	13,450
1-20	1371	160	209	14,410
2-126	1371	155	24	7,790
2-134	1371	150	171	15,420
3-33	1371	150	75	11,060
2-136	1371	145	122	15,020
2-117	1371	135	587	18,780
2-130	1371	135	280	18,450
2-119	1371	130	>404	>16,720
2-121	1371	125	728	16,950
1-2	1315	250	24	3,640
1-24	1315	240	2.94	2,360
2-64	1315	235	52	6,960
2-111	1315	232.5	297	10,660
1-37	1315	230	244	10,870
2-112	1315	230	168	9,100
2-128	1315	227.5	20	5,260
1-15	1315	225	675*	10,300
1-11	1295	375	0.35	2,230
1-23	1295	300	0.40	790
2-66	1295	200	530*	--

*Test stopped.
**Failed during loading
> = Ongoing test
Uniaxial tension, gage section 6.35 mm diameter, 35 mm length.

8491(06)-2-1

TABLE 2. SUMMARY OF PRELIMINARY TENSILE CREEP TEST RESULTS (Contd)

Specimen ID	Test Temp., C	Applied Stress σ_0, MPa	Time to Failure t_f, hrs	Total Strain to Failure ε_f, $\mu\varepsilon$
2-102	1260	325	1.2	1,420
1-36	1260	300	0.35	5,150
3-44	1260	295	>48	>1,800
2-145	1260	285	379	6,910
1-46	1260	275	6.1	1,130
3-89	1260	275	31	2,690
3-112	1260	275	474*	6,960
3-120	1260	250	838*	7,430
2-56	1204	415	1.3	1,380
2-71	1204	350	2.3	1,190
3-37	1204	340	177	3,550
3-19	1204	335	>187	>3,290
2-74	1204	325	68	2,900
2-31	1204	315	594*	3,630
2-36	1204	300	593*	3,800
1-3	1204	300	517*	1,580
3-41	1149	450	7.0	--
2-47	1149	450	0.08	1,490
2-75	1149	445	0.02	--
2-32	1149	440	376	--
3-31	1149	435	594*	--
2-62	1149	425	32	1,640
2-61	1149	425	**	--
3-109	1149	425	509*	--
2-70	982	475	21	--
3-18	982	455	>403	--
3-27	982	455	~q	--
3-40	982	450	631*	--

*Test stopped.
**Failed during loading
> = Ongoing test
Uniaxial tension, gage section 6.35 mm diameter, 35 mm length.

8491(06)-2-2

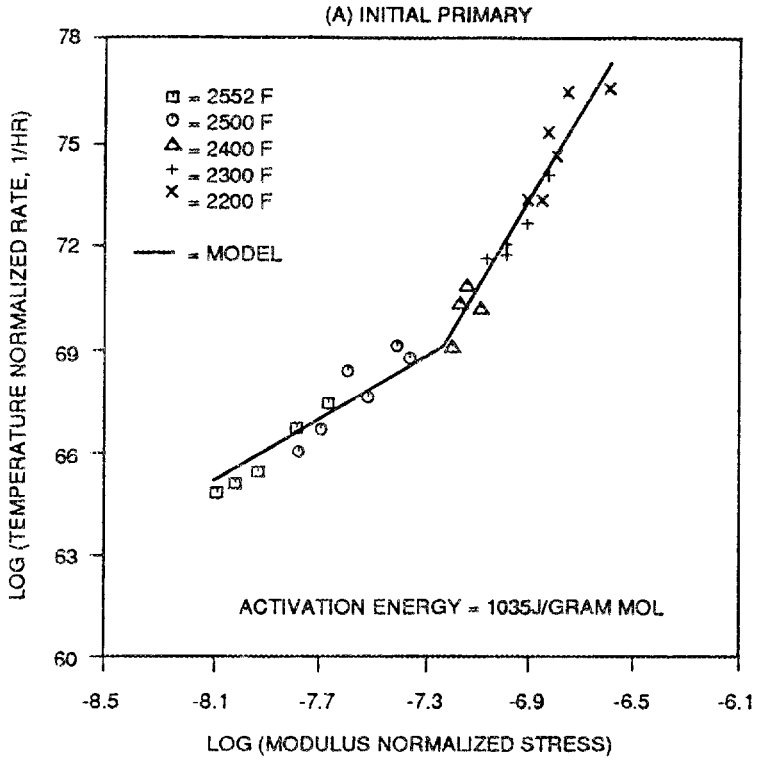

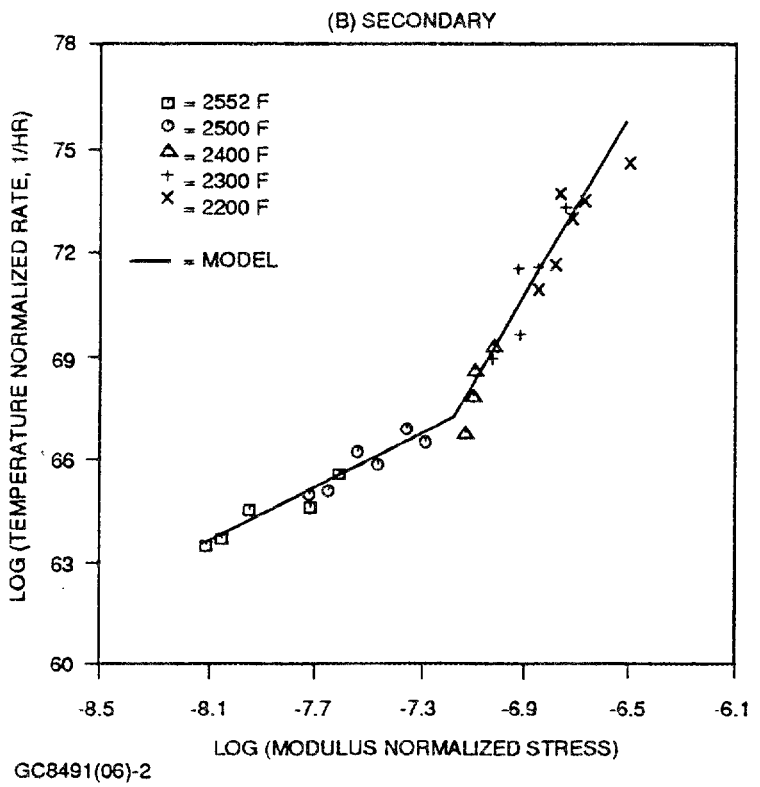

GC8491(06)-2

Figure 2. Predicted NT154 Primary and Secondary Creep Rates Agree With Test Data.

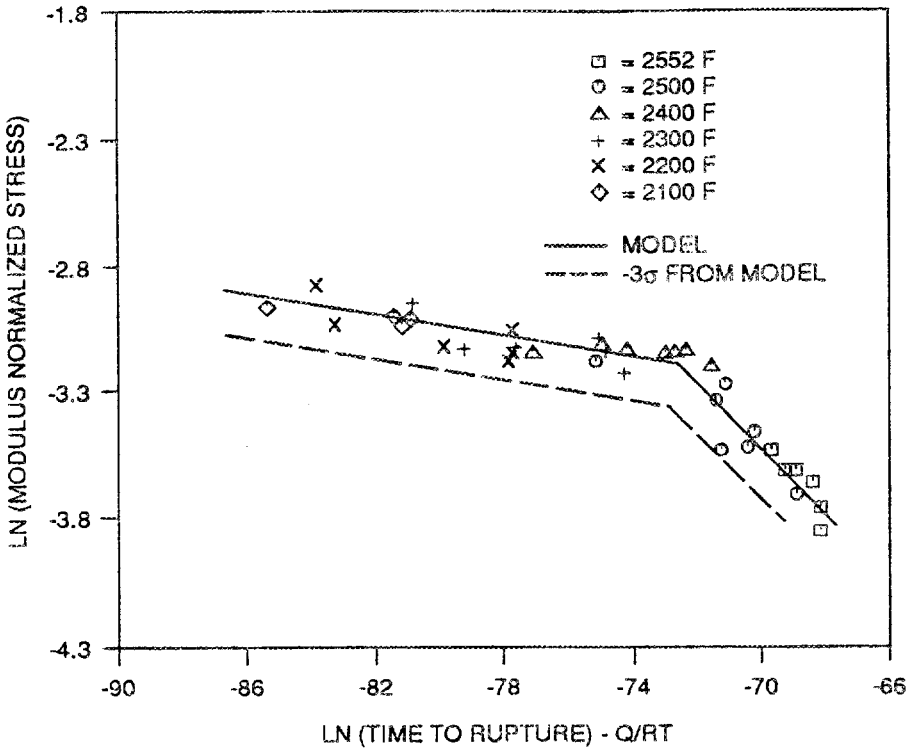

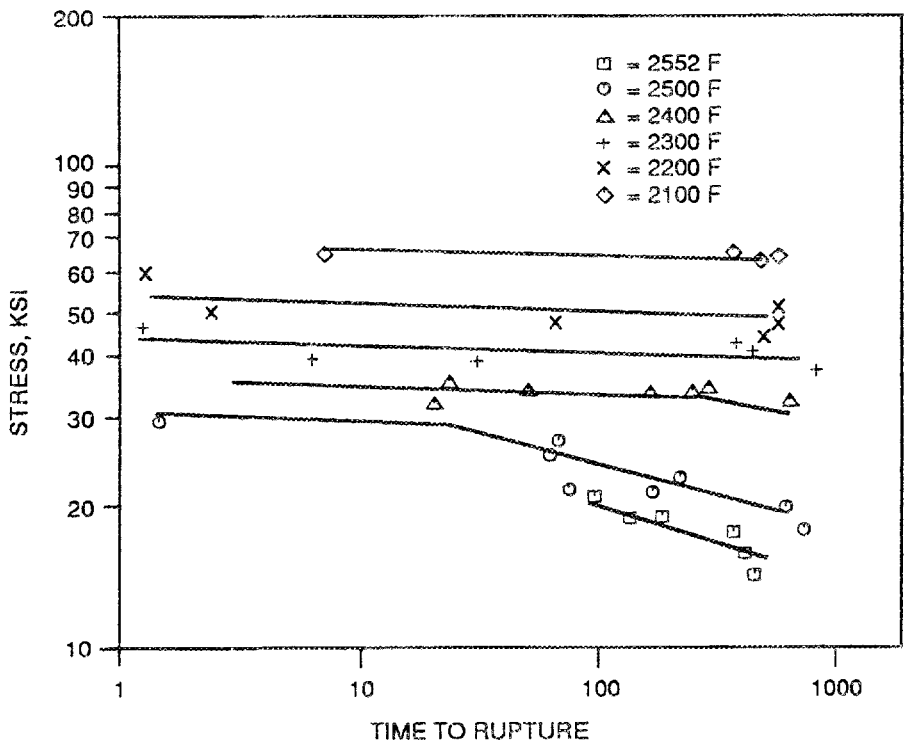

GC8491(06)-3A

Figure 3. Predicted NT154 Stress Rupture Lifetime Agrees With Experimental Data.

The surface strength of silicon nitride components is dependent upon the severity of the gas turbine oxidation environment, which can modify critical surface flaws. Consequently, the overall Ceramic Life Prediction Model must include the effects of oxidation on the strength of NT154.

In this oxidation testing program, 180 MIL-STD-B size transverse machined flexure test bars were exposed to a static air furnace environment at temperatures in the range of 980C to 1400C for times in the range of 1 to 1000 hours. The distribution of test specimens is shown by the symbols in Figure 4. Following exposure, the specimens were tested in four-point bending at room temperature. Test results are shown as lines of realtive strength in Figure 4. Unexpectedly, exposures of 100 hours in the 980C to 1100C range and 10 hours at 1200C resulted in significant improvement in strength, relative to as-received Norton/TRW heat-treated specimens; average specimen strength increased by 38 percent. For exposure times less than or equal to 100 hours in the 1100C to 1400C temperature range, specimen strength decreased, which was expected. The results in Figure 4 also show unusual behavior for exposures longer than 100 hours in the 1100C to 1400C temperature range; the average specimen strength increased with additional exposure time.

Increased specimen strength following exposures greater than 100 hours at temperatures over 1100C has not been previously observed in cyclic oxidation exposures in the Mach 0.3 burner rig ceramic durability tests conducted by GAPD under DOE/NASA Contract No. DEN3-27. The effects of static air furnace and cyclic burner rig exposures at 1260C (2300F) are compared in Figure 5. Up to exposure times of 100 hours, the slopes of the room temperature strength lines (rate of strength decrease) are similar for both types of exposure tests. However, in the cyclic oxidation environment (burner rig tests), the strength continued to decline for exposures longer than 100 hours.

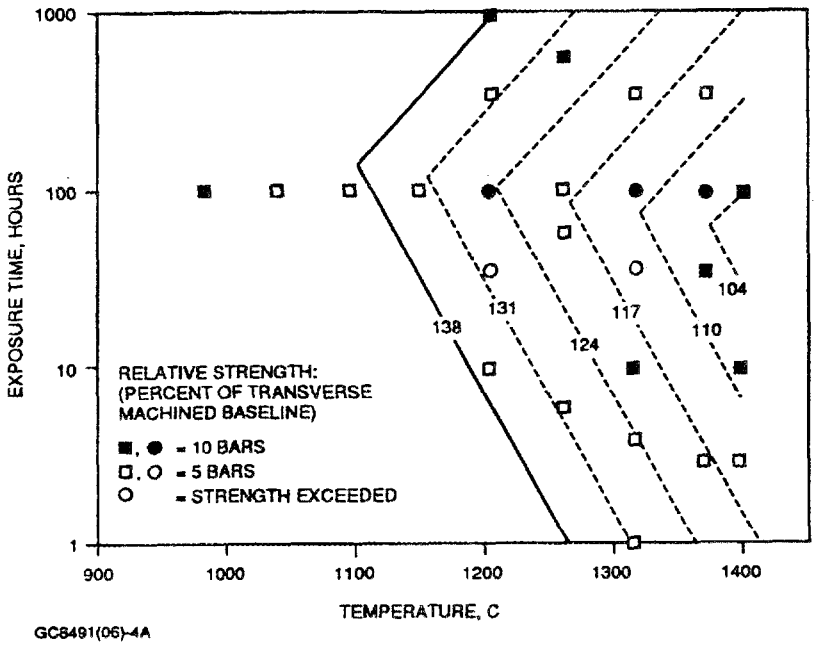

Figure 4. Air Furnace Oxidation Exposure Initially Improves Strength of Transverse Machined Specimens.

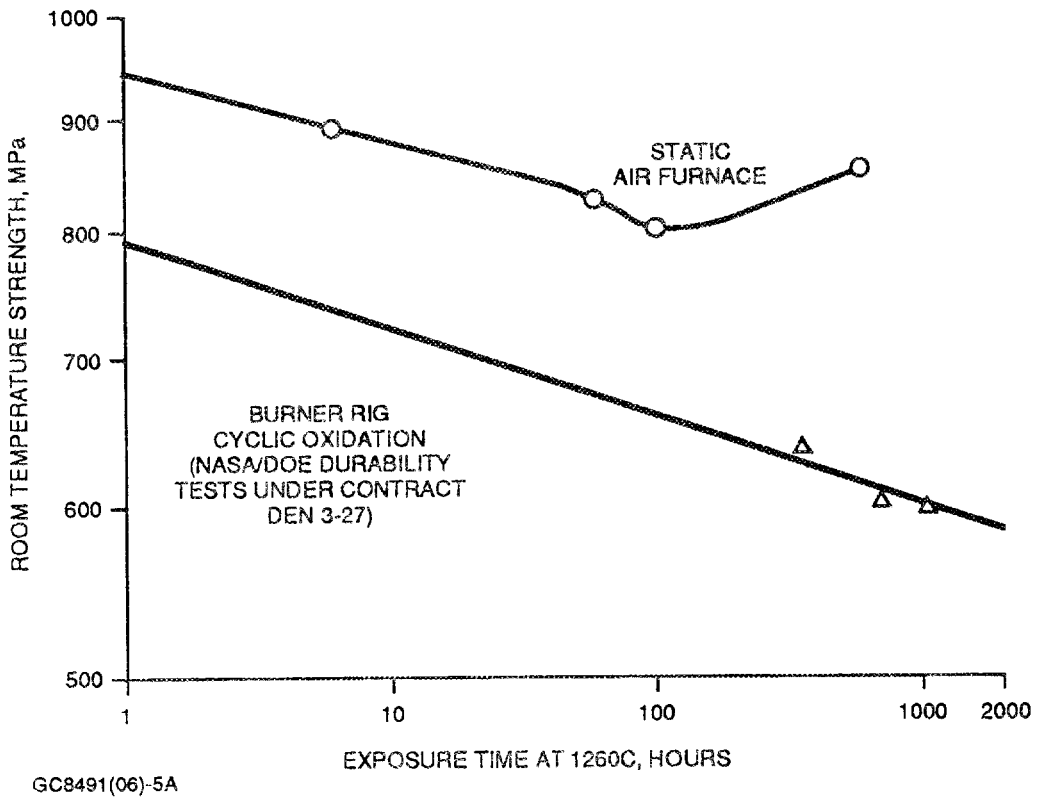

Figure 5. Specimen Strength Declined in Cyclic Oxidation (Burner Rig) Testing.

During the next reporting period, test specimen fracture surfaces will be examined to identify the fracture origins. Models will be developed for both strength retention and oxide layer growth as functions of time and temperature.

Data Analysis and Methodology Development
J. Cuccio, J. Song, D. Wu, and P. Brehm

Significant progress has been made since the last semiannual report in implementing statistical methods to analyze ceramic material test data.

CERAMIC Code Development

New capabilities have been successfully developed for the CERAMIC statistic analysis code, as summarized in Table 3. One objective of the GAPD program is to develop capabilities to determine the confidence interval and to perform bias correction on that confidence interval for a component with multiple failure modes. GAPD has successfully developed and implemented confidence prediction using bootstrap and likelihood ratio methods for both single and multiple failure mode data. Bootstrap methods for confidence interval prediction are also in place for components with combined multiple failure modes and for bias correction on Weibull parameters for single failure mode data.

TABLE 3. NEW CAPABILITIES ARE BEING DEVELOPED FOR CERAMIC CODE

		SINGLE FAILURE MODE		MULTIPLE FAILURE MODES		COMBINED FAILURE MODES	
		BOOT-STRAP	LH RATIO	BOOT-STRAP	LH RATIO	BOOT-STRAP	LH RATIO
CONFIDENCE INTERVAL	$\hat{m}$	✓	✓	✓	✓	✕	✕
	$\hat{\sigma}_o$	✓	✓	✓	✓	✕	✕
	σ_p	✓	✓	✓	✓	✓	→ → →
	R	✓	✓	✓	✓	✓	→ → →
BASIC CORRECTION ON PARAMETERS	$\hat{m}$	✓		→ → →		✕	✕
	$\hat{\sigma}_o$	✓		→ → →		✕	✕
	σ_p	→ → →		→ → →	→ → →		
	R	→ → →		→ → →	→ → →		
BASIC CORRECTION ON CONFIDENCE INTERVAL	$\hat{m}$	✓		→ → →		✕	✕
	$\hat{\sigma}_o$	→ → →		→ → →		✕	✕
	σ_p	→ → →		→ → →	→ → →		
	R	→ → →		→ → →	→ → →		

√ TASK COMPLETED → → → IN PROGRESS ✕ NOT APPLICABLE

$\hat{m}$ WEIBULL MODULUS ESTIMATOR $\hat{\sigma}_o$ CHARACTERISTIC STRENGTH ESTIMATOR

σ_p DESIGN STRESS R RELIABILITY

Theoretical work for confidence interval prediction using likelihood ratio methods has been completed by Dr. Tucker at the General Electric Corporate Research and Development Center (GE-CRDC). This complex solution can be simplistically summarized by the mathematical model described below.

The survival probability of failure mode j to exceed a strength x_i is defined as:

$$S_j(x) = P_{sj}(x) = 1 - P_{fj}(x)$$
$$F_j(x) = P_{fj}(x) \qquad [1]$$
$$f_j(x) = \frac{dF_j(x)}{dx}$$

Where:

$$F_{ji}(x_i) = 1 - e^{-I_{ji}V_{ji}\left(\frac{x_i}{\sigma_o}\right)^{m_j}} \qquad [2]$$

Assuming that there are three active failure modes in a data set, the probability density of a specimen failing by the first mode is:

$$f(x) = f_1(x)S_2(x)S_3(x) \qquad [3]$$

Let:

$$\delta_{ji} = \begin{cases} 1, & \text{for } j = i \\ 0, & \text{for } j \neq i \end{cases} \qquad [4]$$

Then:

$$\delta_{1i} + \delta_{2i} + \delta_{3i} = 1 \qquad [5]$$

Define:

$$\begin{aligned} Li &= \left[f_1(x_i)S_2(x_i)S_3(x_i)\right]^{\delta_{1i}}\left[S_1(x_i)f_2(x_i)S_3(x_i)\right]^{\delta_{2i}}\left[S_1(x_i)S_2(x_i)f_3(x_i)\right]^{\delta_{3i}} \\ &= \left[f_1(x_i)^{\delta_{1i}}S_1(x_i)^{\delta_{2i}}S_1(x_i)^{\delta_{3i}}\right]\left[S_2(x_i)^{\delta_{1i}}f_2(x_i)^{\delta_{2i}}S_2(x_i)^{\delta_{3i}}\right]\left[S_3(x_i)^{\delta_{1i}}S_3(x_i)^{\delta_{2i}}f_3(x_i)^{\delta_{3i}}\right] \end{aligned} \qquad [6]$$

and:

$$L = \sum_{i=1}^{n} \ln L_i \qquad [7]$$

Which is the log-likelihood for the data set to occur for the material in question. Introducing another new parameter:

$$\gamma_{jp} = -I_{ji}V_{ji}\left(\frac{\sigma_p}{\sigma_{oj}}\right)^{m_j} \qquad [8]$$

The problem can be stated as:

$$\begin{cases} \textit{Maximize } L \textit{ with fixed } \sigma_p \\ st.\ \gamma_{1p} + \gamma_{2p} + \gamma_{3p} = \ln\dfrac{1}{1-p} \end{cases} \qquad [9]$$

A solution scheme has been developed and implementation in the CERAMIC computer code has been initiated.

Another area of active development work underway is the use of bootstrap methods to accomplish bias correction for parameter estimates for censored data. When bias correction was performed for Weibull modulus and characteristic strength of a data set with 23 surface failures, 10 edge failures, and 3 volume failures, the unbiased modulus seemed to be worse, especially for volume failure (Figures 6 through 8).

At first, the small number of observations for volume failure was suspected as the main cause, so local constraints were imposed on the simulated data sets, to include only those simulated data sets with numbers of observations within ±20 percent of the observations in the real data set. The results did not show noticeable improvement. Further tests have been devised and work is underway to identify the cause of the problem.

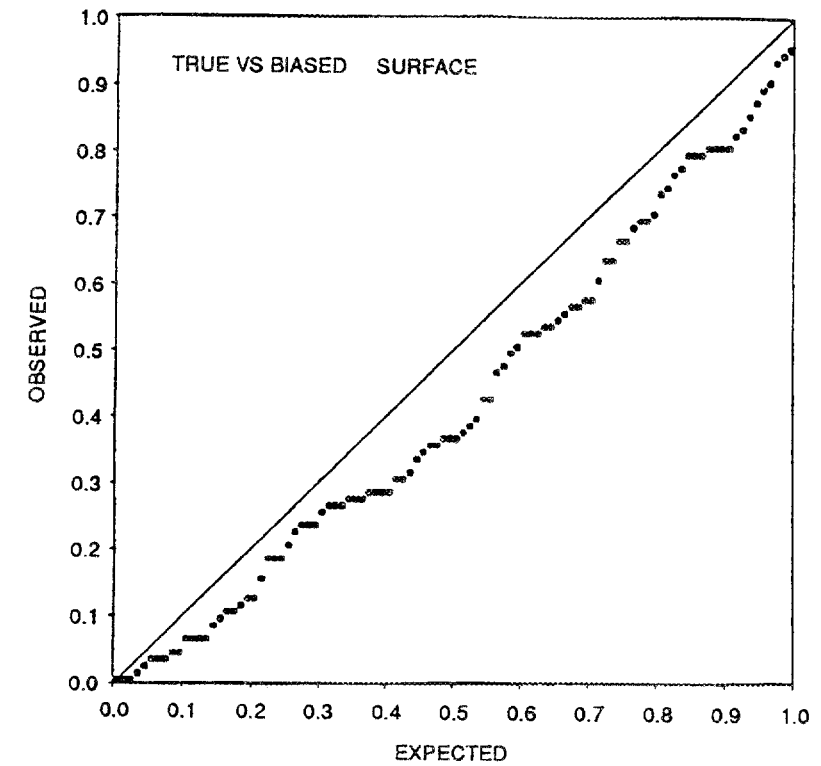

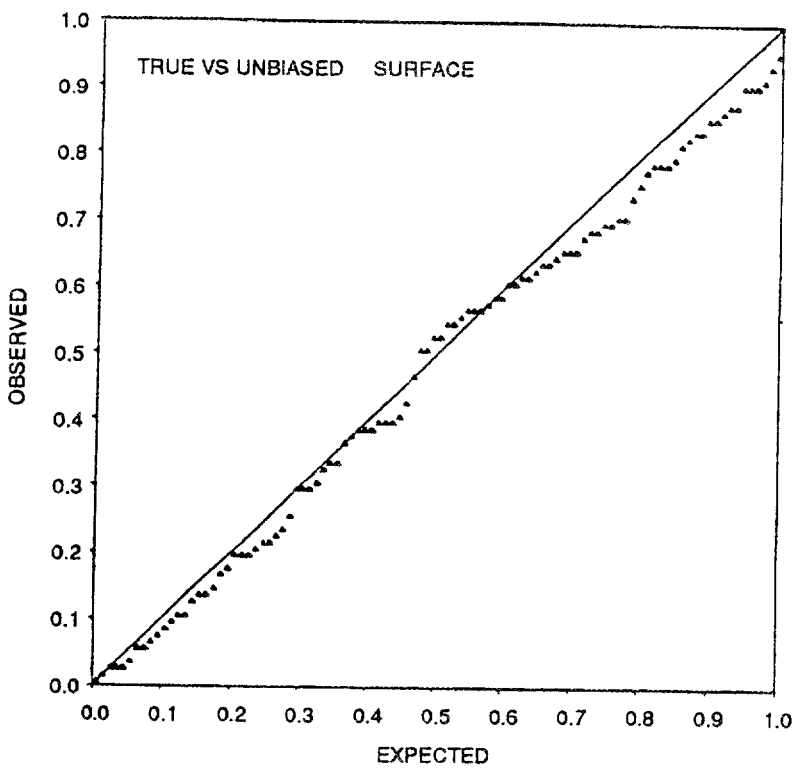

GC8491(06)-7

Figure 6. Comparison of Biased and Unbiased Weibull Modulus for Surface Failure.

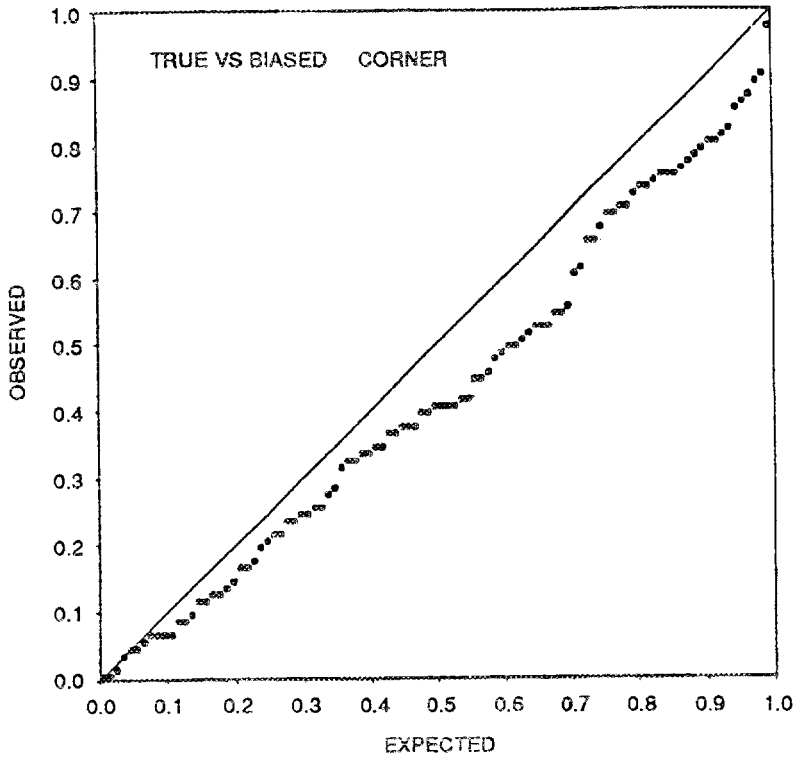

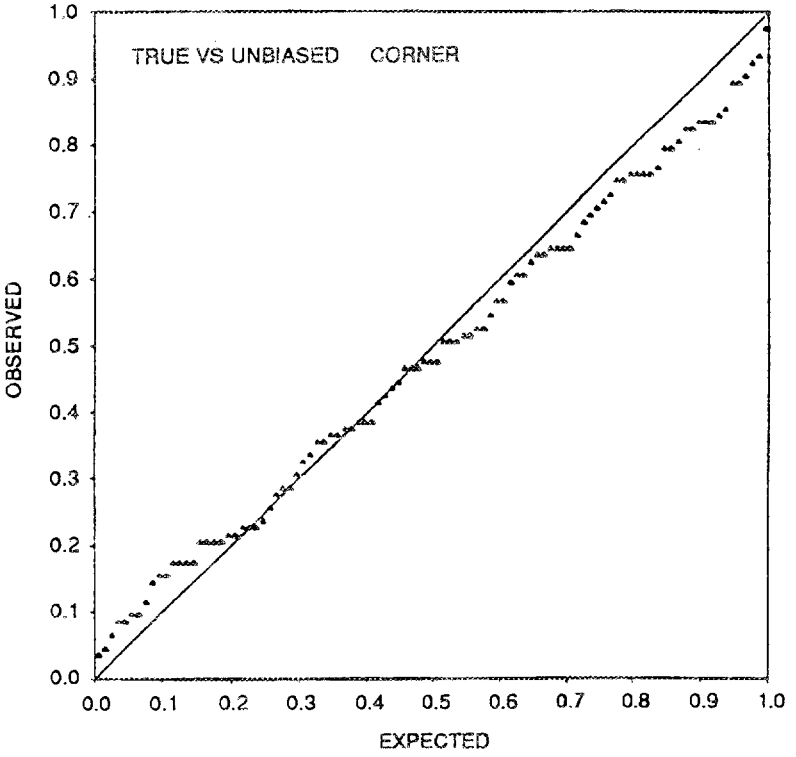

GC8491(06)-8

Figure 7. Comparison of Biased and Unbiased Weibull Modulus for Corner Failure.

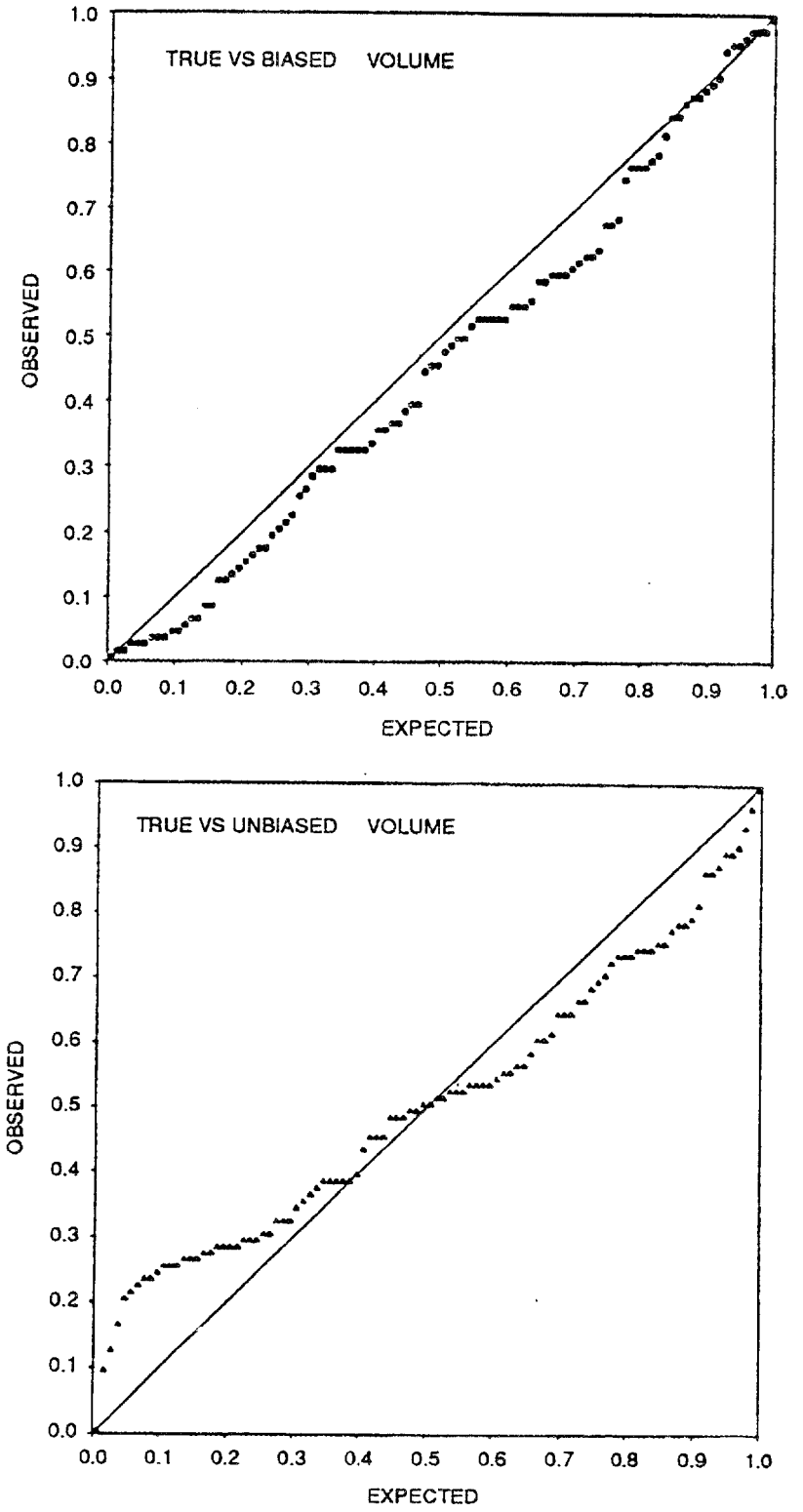

Figure 8. Comparison of Biased and Unbiased Weibull Modulus for Volume Failure.

Multiple Temperature Capability

Since ceramic materials used in gas turbine engines experience a wide range of temperatures, fast fracture strength tests are often conducted at both room and elevated temperature. Treating strength data for different temperatures in Weibull analysis has become important for successful application of ceramics in gas turbine engines. A new method has been developed at GAPD to conduct maximum likelihood analysis with test data at different temperatures, allowing more data to be used for estimating the Weibull modulus and also permitting calculation of failure probability with confidence intervals for a component with non-uniform temperature distribution. This method has been implemented in the CERAMIC Weibull analysis code.

The multiple temperature method developed at GAPD is based on assumptions that the Weibull modulus of structural ceramic materials is temperature independent and the characteristic strength is a function of temperature. These assumptions are supported by earlier Weibull analysis results based on fast fracture data of NT154 specimens at varying temperatures. The data were from tests conducted by the University of Dayton Research Institute (UDRI) and GAPD in the DOE-NASA funded Advanced Turbine Technology Application Program (ATTAP), under Contract No. DEN3-335. When Weibull moduli for each failure mode at different temperatures are plotted (Figures 9 through 11) the variation of Weibull modulus with respect to temperature lies well within the confidence bands and no obvious trend of increasing or decreasing "m" is observed.

Since the Weibull modulus is considered to be temperature independent, a more accurate parameter estimate may be obtained if the analysis is based on all of the fast fracture strength data at various temperatures. In order to perform the Weibull analysis with all the strength data lumped together, an additional variable C_i on the equivalent size and stress state factor I_i is introduced to account for the characteristic strength at different temperatures. Thus, I_i becomes a function of temperature. The theoretical derivation is given as follows:

Assuming that there are a total of n specimens tested at k different temperatures in a fast fracture test data set, and n_j is the number of data points at temperature T_j; I_{ij} is the equivalent stress state factor for the ith specimen at temperature T_j. I_{ij}^* is the temperature-scaled equivalent stress state factor for the ith specimen at temperture T_j. I_{ij}^* is defined as follows:

$$I_{i1}^* = I_{i1}(m)C_1^m \quad \text{for } i = 1, n_1 \quad C_1 = 1 \text{ (reference temperature)}$$

$$I_{i2}^* = I_{i2}(m)C_2^m \quad \text{for } i = 1, n_2 \text{ and } C_2 = \frac{\hat{\sigma}_{o1}}{\hat{\sigma}_{o2}}$$

$$I_{i3}^* = I_{i3}(m)C_3^m \quad \text{for } i = 1, n_3 \text{ and } C_3 = \frac{\hat{\sigma}_{o1}}{\hat{\sigma}_{o3}}$$

$$\ldots$$

$$I_{ij}^* = I_{ij}(m)C_j^m \quad \text{for } i = 1, n_j \text{ and } C_j = \frac{\hat{\sigma}_{o1}}{\hat{\sigma}_{oj}} \qquad [10]$$

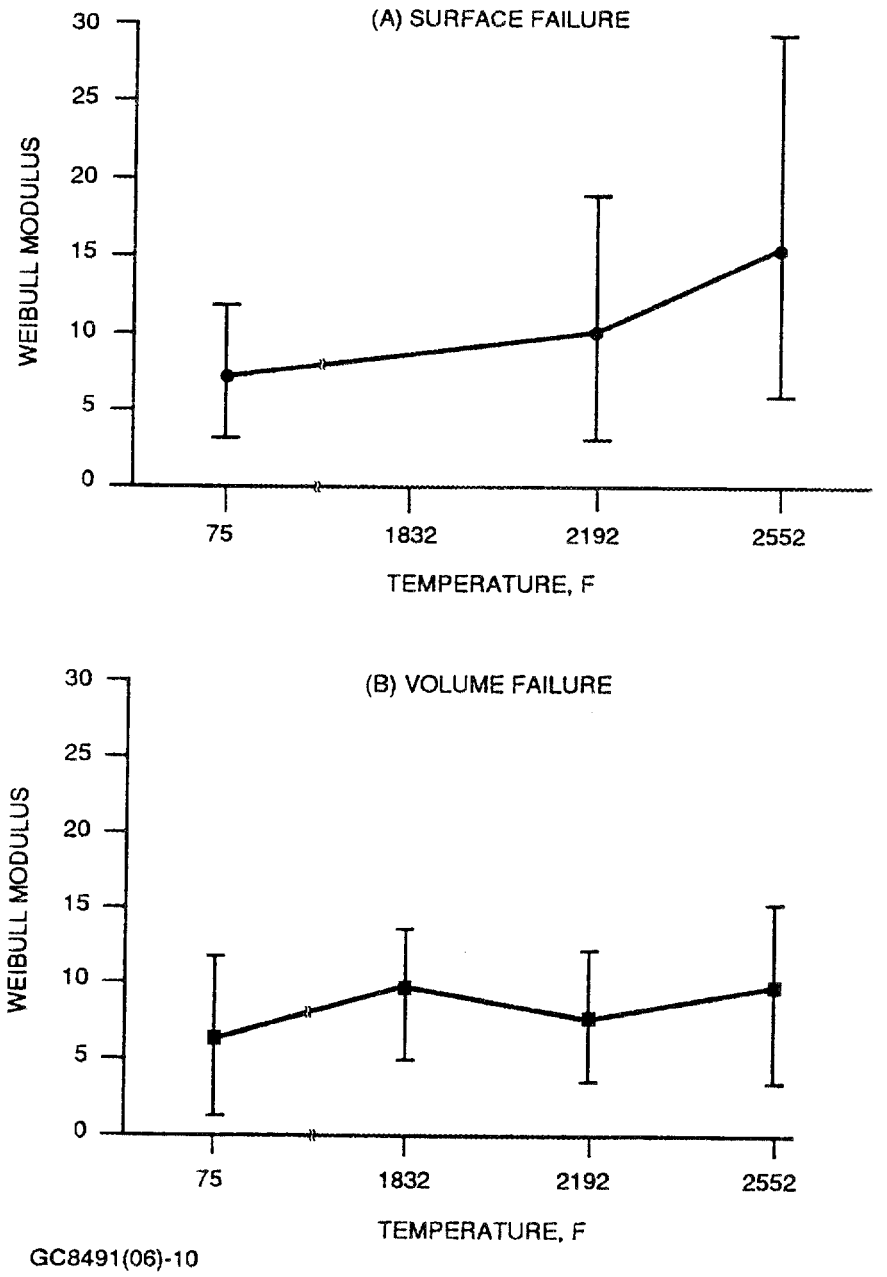

Figure 9. Weibull Modulus Variations Over Temperature for NT154 Tensile Specimens (UDRI Data).

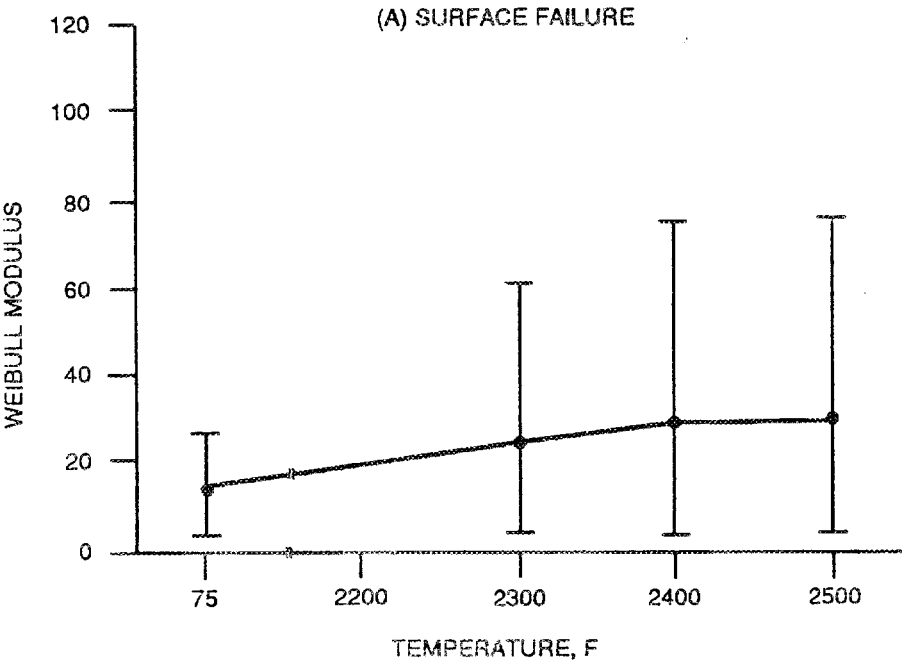

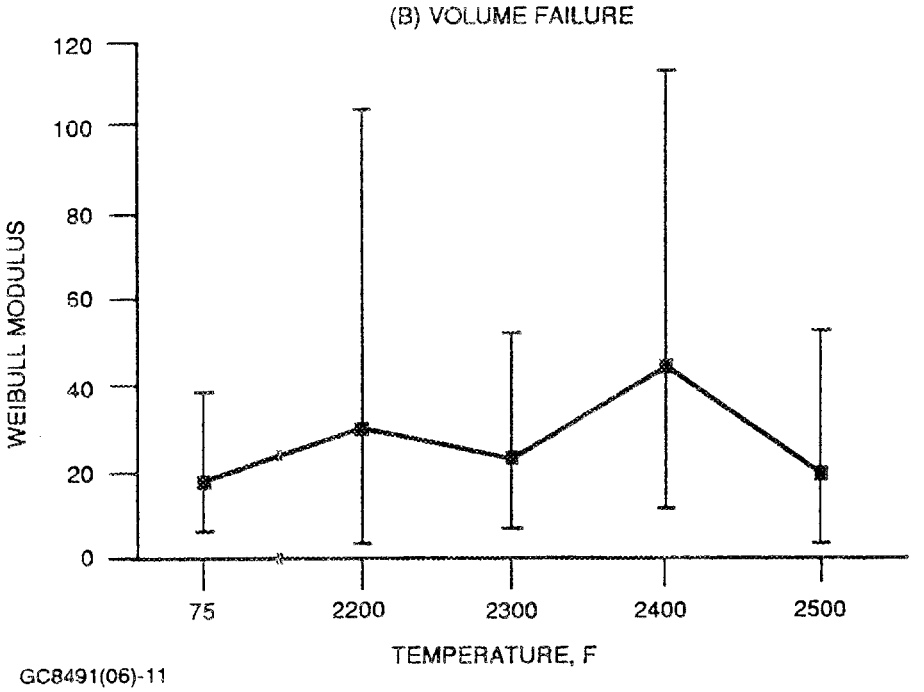

GC8491(06)-11

Figure 10. Weibull Modulus Variations Over Temperature for NT154 Machined Flexure Bars (GAPD ATTAP Data).

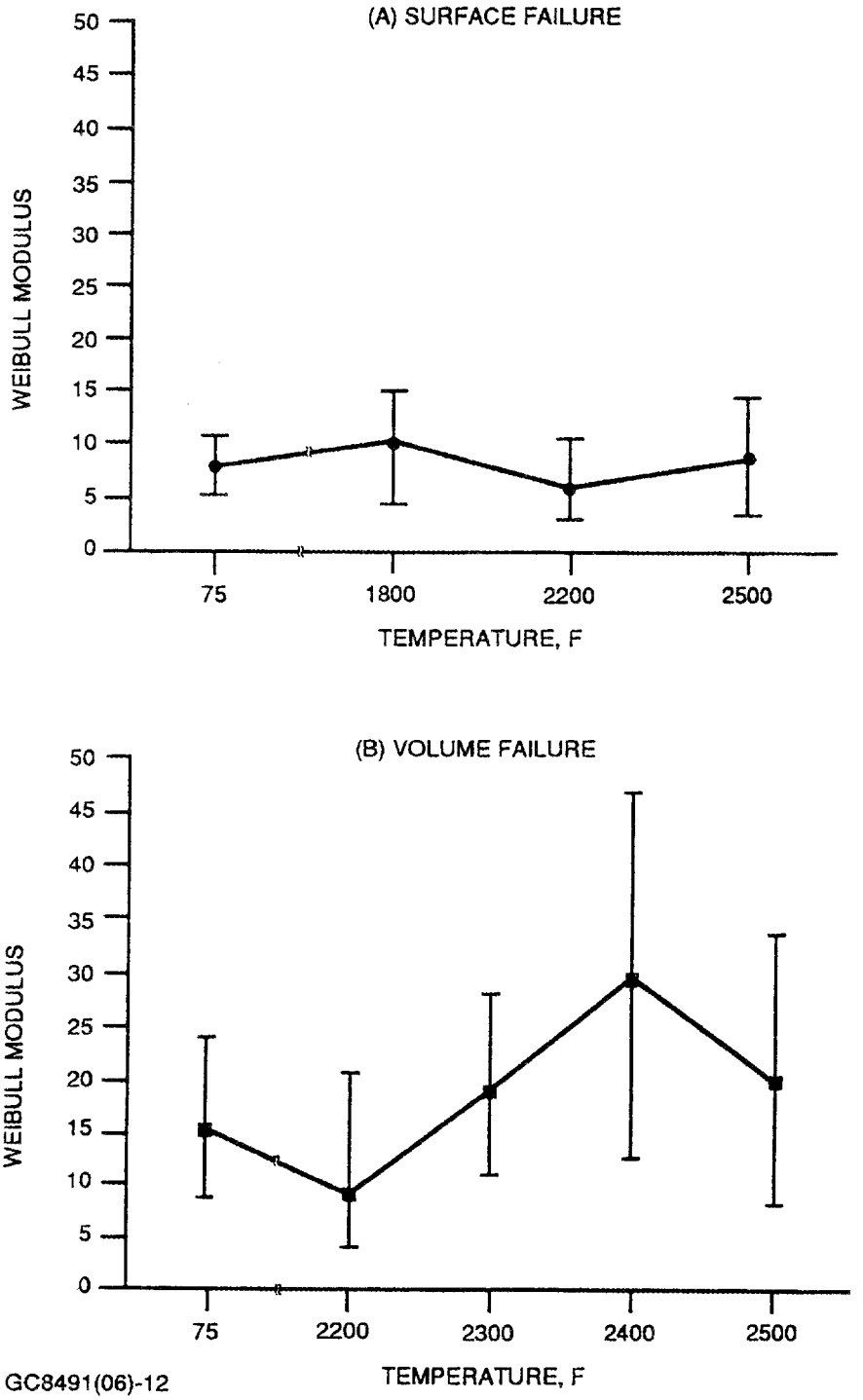

Figure 11. Weibull Modulus Variations Over Temperature for NT154 As-Processed Flexure Bars (GAPD ATTAP Data).

Where: $\hat{\sigma}_{01}$, $\hat{\sigma}_{02}$, $\hat{\sigma}_{03}$, . . . $\hat{\sigma}_{oj}$, are the characteristic strengths for temperatures T_1, T_2, T_3, . . . T_j, respectively.

The estimate of Weibull parameters can be determined as follows:

$$\hat{\sigma}_{oj} = \left[\frac{1}{n_j} \sum_{i=1}^{n_j} I_{ij} \; V_{ij} \sigma_{ij}^{\hat{m}} \right]^{\hat{m}} \qquad [11]$$

$$\frac{1}{\hat{m}} = \frac{1}{n} \sum_{j=1}^{k} \sum_{i=1}^{n_j} \left(\frac{I_{ij}^{*}}{I_{ij}^{*}} + \ln(\sigma_{ij}) \right) \left(\frac{n I_{ij}^{*} V_{ij} \sigma_{ij}^{m}}{\sum_{j=1}^{k} \sum_{i=1}^{n} I_{ij}^{*} V_{ij} \sigma_{ij}^{m}} - 1 \right) \qquad [12]$$

Equations [11] and [12] are used to solve for the estimate of Weibull modulus $\hat{m}$ and the characteristic strength $\hat{\sigma}_{oj}$. The common Weibull modulus is solved with equation [12] over all the strength data points at different temperatures. This $\hat{m}$ is used to calculate the characteristic strength in equation [11] for each temperature over the strength data points of that temperature alone. The new $\hat{m}$ and $\hat{\sigma}$ are then used in equation [10] to calculate the new I_{ij}^{*}. With the updated I_{ij}^{*}, equation [12] is repeated to calcualte a new $\hat{m}$. The iteration begins with an initial $\hat{m}$ which is usually the modulus from only the data points at the reference temperature. Convergence is reached when the difference between the new and old $\hat{m}$ is less than a prescribed small number. Fast convergence has been obtained in all the cases tried.

Equation [12] can be used for all the data points for different temperatures, since all the data points are effectively scaled to the reference temperature, as demonstrated in the following:

$$\dot{\sigma}_{oj} = \left[\frac{1}{n_j} \sum_{i=1}^{n_j} I_{ij}^{*} V_{ij} \sigma_{ij}^{\hat{m}} \right]^{1/\hat{m}} \qquad [13]$$

$$\dot{\sigma}_{oj} = \left[\frac{1}{n_j} \sum_{i=1}^{n_j} I_{ij} C_j^{\hat{m}} V_{ij} \sigma_{ij}^{\hat{m}} \right]^{1/\hat{m}} \qquad [14]$$

$$\dot{\sigma}_{oj} = C_j \left[\frac{1}{n_j} \sum_{i=1}^{n_j} I_{ij} V_{ij} \sigma_{ij}^{\hat{m}} \right]^{1/\hat{m}} \qquad [15]$$

$$\dot{\sigma}_{oj} = C_j \, \hat{\sigma}_{oj} = \hat{\sigma}_{o1} \qquad [16]$$

Where: $\overset{*}{\sigma}$ is the equivalent characteristic strength for temperature j after being scaled to a reference temperature, which should be equal in value to the characteristic strength at the reference temperature.

Although the equations shown above are given for single failure mode data sets, the method has also been successfully applied to data sets with competing failure modes.

A typical example of temperature scaling is shown in Figure 12, using NT154 test data generated by UDRI and GAPD. The strength parameters obtained from the multiple-temperature analysis has enabled calculation of failure probability for the ATTAP impact-resistant ceramic turbine wheel with confidence intervals for various engine conditions.

Risk Integration Code

The risk integration code being developed by GAPD calculates the multiaxial stress state and stress gradient factor I as a function of m for a component under a given loading condition (a given stress distribution) instead of calculating the probability of failure directly. The main benefit of this change is to enable a user to combine the I function with the specimen strength data to determine failure probability distribution with confidence intervals.

Failure probability will not be directly calculated with the risk integration methods being developed; instead, the calculation proceeds as follows:

$$I(m) = \frac{1}{2\pi v} \int \left(\int_0^{\frac{\pi}{2}} \int_0^{2\pi} w(\phi, \varphi) \left(\frac{\sigma_e}{\sigma_m} \right)^m \cos\phi \, d\phi \, d\varphi \right) dv \qquad [17]$$

Where: $\sigma_e = f(\sigma_1, \sigma_2, \sigma_3, \phi, \varphi)$ $\qquad \sigma_m = \max\limits_{x,y,z,\phi,\varphi} \{\sigma_e\}$

$w(\phi,\psi) = \delta\ [(\phi,\psi) - (\phi_o,\psi_o)]$ and ϕ_o,ψ_o is the orientation of the anisotropic flaw population.

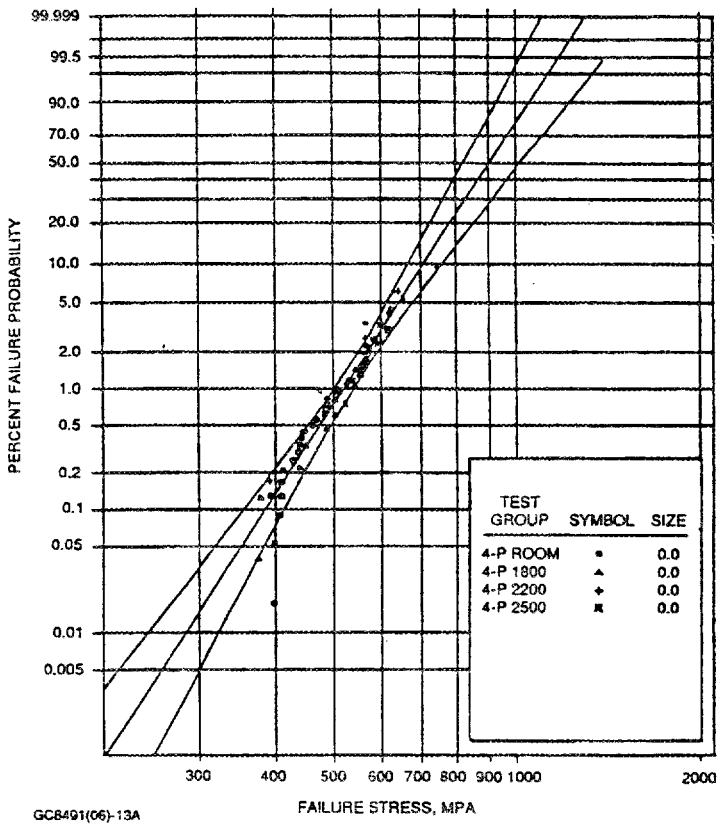

Figure 12. Weibull Analysis of As-Processed Flexure Test Bars With Combined Temperatures (GAPD ATTAP Data).

Numerical schemes have been evaluated to implement this new integration. Gaussian integration will be used for the volume integration. The number of Gaussian points needed in the integration has been determined to be about one half of the value of the Weibull modulus in order to assure good accuracy. Since the spherical integration needs to be carried out at each Gaussian integration point the computation time can be prohibitively expensive. GAPD is studying ways to reduce the amount of computation by using less thorough integration at low stress (risk) elements in a finite element model.

The risk integration code will be used with the CERAMIC statistical analysis code to calculate the strength and life of the ceramic confirmatory specimens (plate bending disks, notched tensile, and spin disks). The confidence intervals from these predictions will be compared with observed strengths and lives to confirm the predictive capabilities of these methods.

NDE Methods Development and Application
J. Wade and B. Meade

Specimen inspections continued during this reporting period; Table 1 lists the inspection status by specimen type. NDE inspection of the MIL-B size flexure specimens and the tensile rod specimens for fast fracture testing was completed.

Precleaning procedures to be applied prior to acoustic microscopy were optimized, including solvent wipes, dry wipes, and brushing to remove air bubbles after the specimen is placed in the water tank. In addition, the transducer was equipped with a water jet to remove air bubbles and dirt during scanning. Proper cleaning is critical to eliminate false indications during surface wave inspection.

Acoustic microscopy has revealed suspect areas in both surface wave and internal inspections. Specimen inspections included several tensile rods previously identified by visual inspection as requiring remachining to eliminate abnormal marks from the gage section. The acoustic microscopy easily detected the marks (Figure 13). Additionally, several other specimens exhibited unusual surface wave indications not identified during visual inspection at 40X magnification. Figure 14 shows a specimen that will be tested as received, with the noted indications. Figure 15 (top) shows a typical suspect indication detected during internal ultrasonic inspection. This indication is larger in amplitude and area than the signal from a 50-micron hole at the same depth (Figure 15, bottom).

Radiographic (RT) and computed tomographic (CT) inspections revealed a number of specimens having apparent density variations. Some specimens exhibited discrete high or low density indications, while others showed more diffuse variations. Figures 16(a) and (b) compare typical discrete and diffuse indications. The indications revealed by the CT inspection were not detected during visual evaluation of the radiographic film of the same specimen. Further digital computer enhancement of the radiographic film is planned.

Status of Milestones

Milestone No. 4, All Specimens Delivered, has been completed.

Publications

A technical paper summarizing GAPD's progress in the ceramic life prediction program during 1991 was submitted for publication by the Society of Automotive Engineers (SAE). A paper describing the creep and stress rupture models for NT154 silicon nitride developed by Dr. N. Menon of GAPD is being prepared for submission to the Journal of the American Ceramic Society.

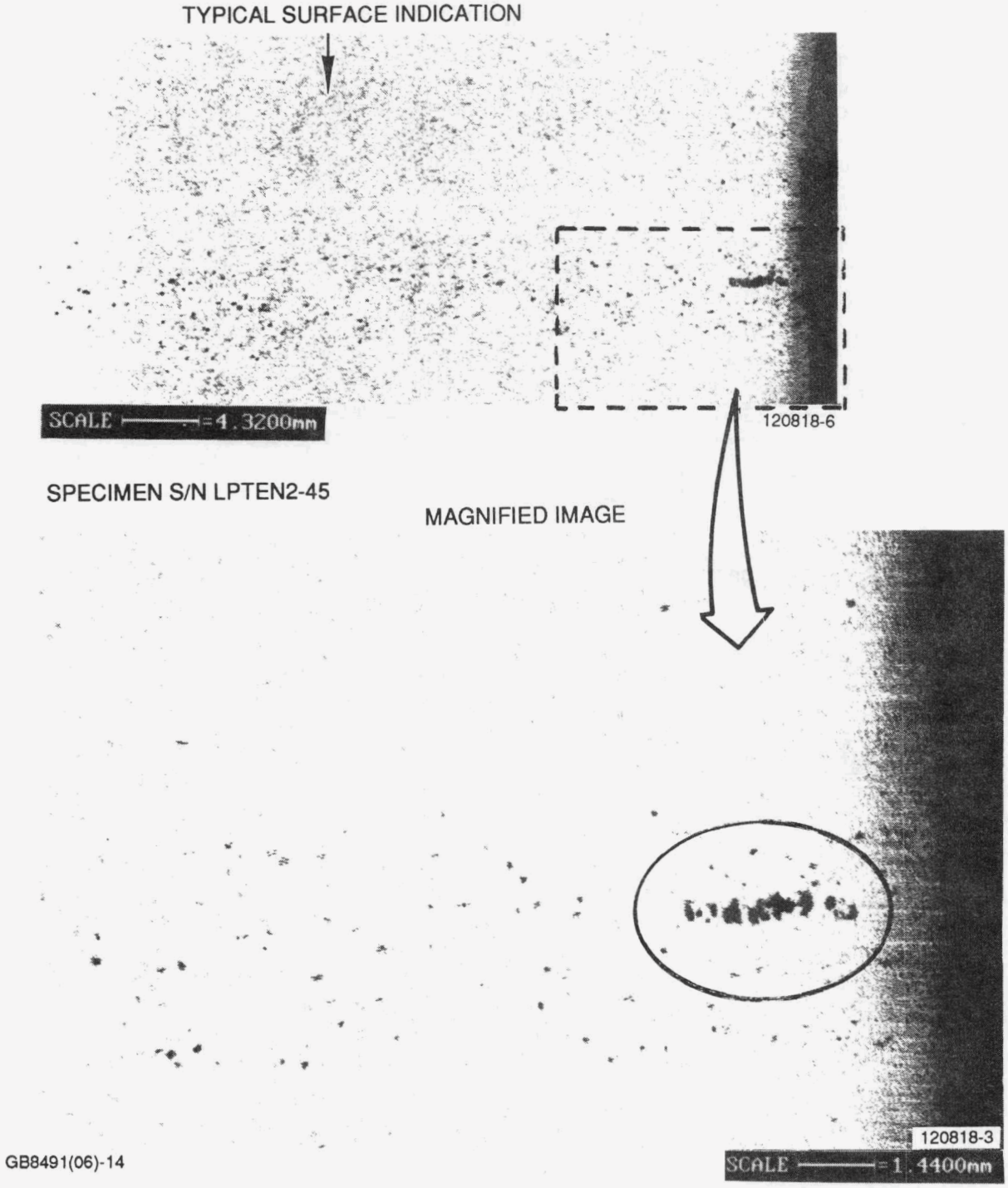

Figure 13. **Acoustic Microscopy Indications on Tensile Rod Specimen. (Machining Marks Are Visible at 40X Magnification, and Will Be Removed Prior to Testing).**

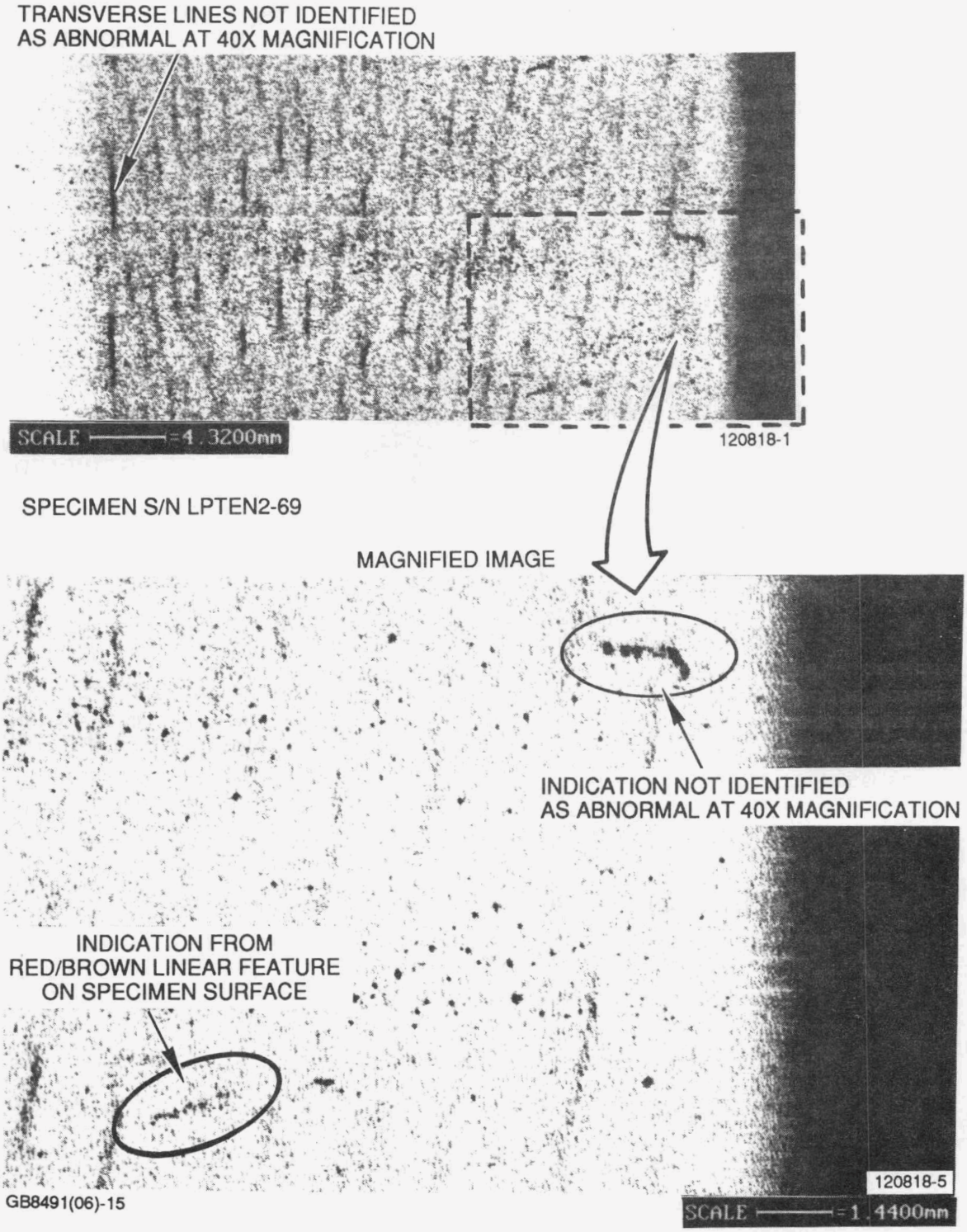

Figure 14. Acoustic Microscopy Indications From Tensile Rod Specimen Without Visual Surface Indications. (Specimen Will Be Tested As Received).

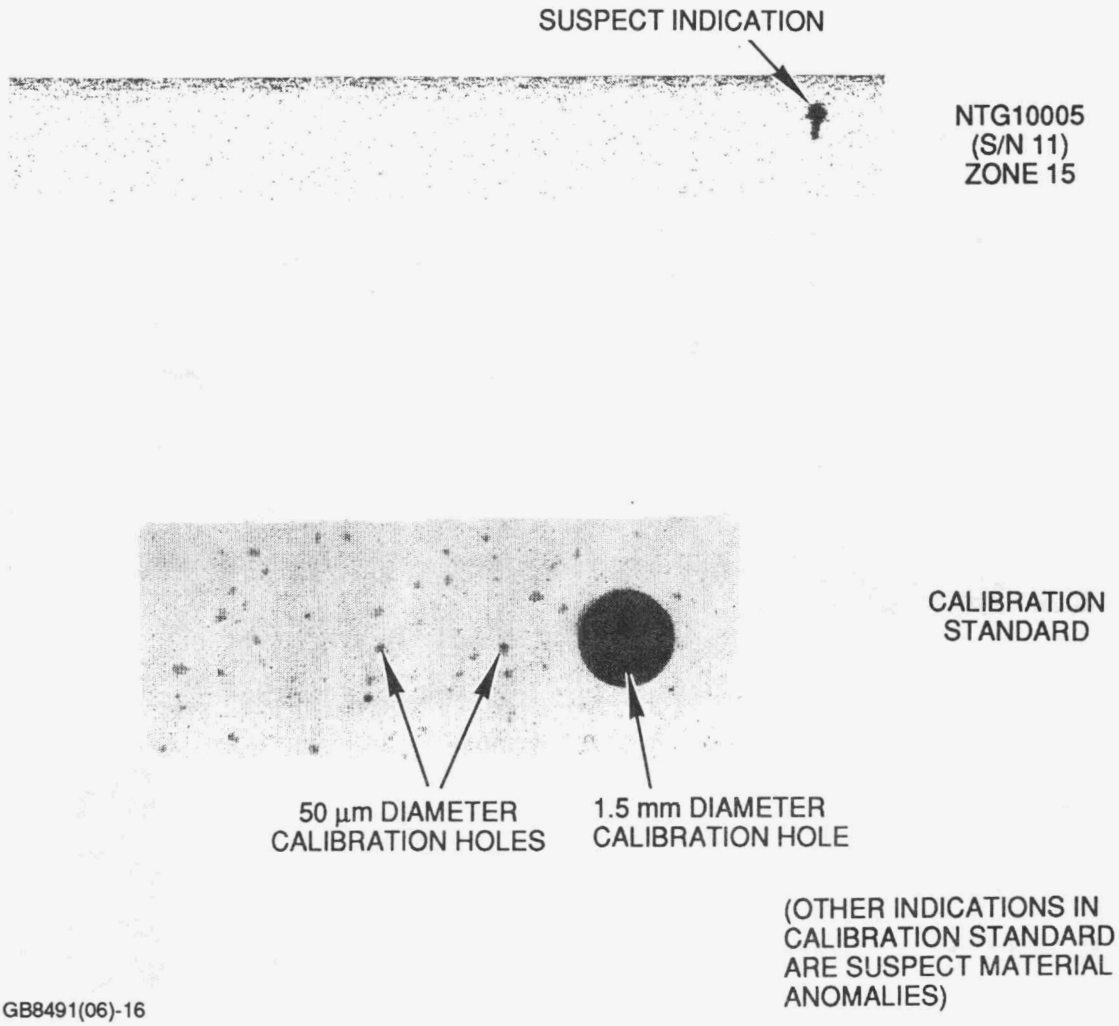

Figure 15. Typical Indication From Internal Acoustic Microscopy.

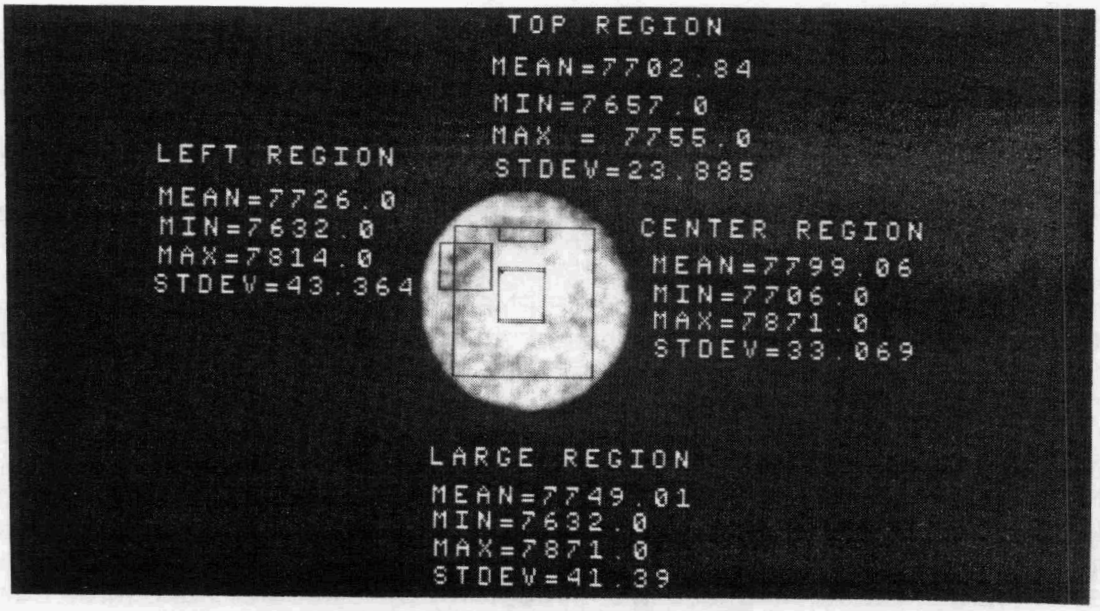

(a) DIFFUSE INDICATION THROUGHOUT

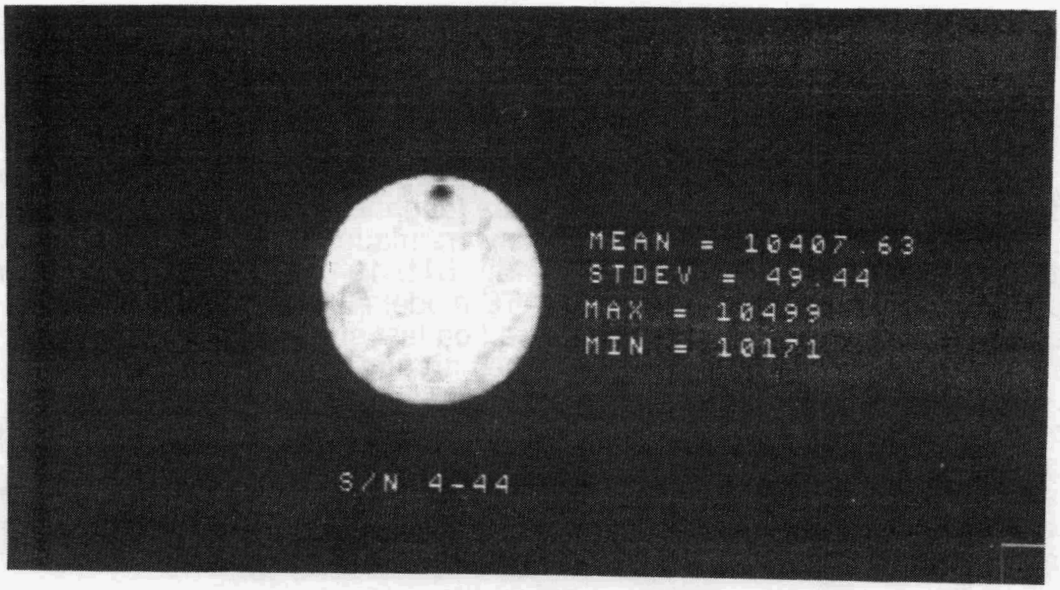

(b) DISCRETE, LESS DENSE INDICATION

GB8491(06)-17

Figure 16. CT Tensile Rod Inspections Showed Density Variation in Cross Sections.

3.3 ENVIRONMENTAL EFFECTS

Environmental Effects in Toughened Ceramics
Norman L. Hecht (University of Dayton)

Objective/scope

Since December 1984, the University of Dayton has been involved in a five-phase project to investigate the effects of environment on the mechanical behavior of commercially available ceramics being considered for heat engine applications. In the first phase of this project, the effects of environment on the mechanical behavior of transformation-toughened ZrO_2 ceramics were investigated. In the second phase, two Si_3N_4 ceramics (GTE PY6 and Norton/TRW XL144) and one SiC ceramic (Hexoloy SA) were evaluated. In the third phase, the tensile, flexural, and fatigue strength of three SiC and six Si_3N_4 ceramics were evaluated at temperatures ranging from 20 to 1400°C. Microstructure, chemistry, and physical properties were also investigated. In the fourth phase, the flexural strength and fatigue behavior of two additional Si_3N_4 ceramics (Kyocera SN-260 and Garrett GN-10) were investigated. In addition, the fatigue behavior of one Si_3N_4 ceramic (Norton/TRW NT-154) was investigated. Efforts to study the tension/compression cyclic fatigue behavior of NT-154 have been delayed because of problems with the Instron test fixture. In phase five, three newly developed SiC and three newly developed Si_3N_4 ceramics are being investigated. In addition, the effects of different machining processes on the mechanical behavior of selected SiC/Si_3N_4 ceramics will be studied.

During the past six months (September 1991 through March 1992), Norton/TRW NT-230, a siliconized SiC, was investigated. In addition, construction of the flexural stress rupture test facility and modification of the tension/compression test system was continued.

Technical progress

Microstructure, chemistry, flexural strength, elastic modulus, hardness, density, coefficient of thermal expansion, and fracture toughness for NT-230 were evaluated.

The flexural strength measurements were made using Instron Universal Testing Machines (Model 1123) following MIL-STD-1942(MR). Elevated temperature measurements were conducted in ATS model #3320 high-temperature furnaces. Flexural strengths were measured on test specimens with nominal dimensions of 3 x 4 x 50 mm with all surfaces ground to a 16-microinch finish [MIL-STD-1942(MR) specimen size B]. The long edges of the tensile surface were beveled to minimize edge failures. Flexural strength was measured using four-point bend test fixtures, and the test specimens were loaded at machine crosshead speeds of 0.004, 0.0004, and 0.00004 cm/sec (0.1, 0.01, 0.001 in/min). The bend fixtures for all measurements were made of SiC. The four-point bend fixtures have an outer span of 40 mm and an inner span of 20 mm.

*Research sponsored by the U.S. Department of Energy, Assistant Secretary for Conservation and Renewable Energy, Office of Transportation Systems, as part of the Ceramic Technology for Advanced Heat Engines Project of the Advanced Materials Development Program under Contract DE-AC05-840R21400 with Martin Marietta Energy Systems, Inc., Work Breakdown Structure Subelement 3.3.1.4.

Fracture origins were determined by optical microscopy (Nikon Epiphot) and SEM (JEOL/SM-80 with EG&G Ortec System 5000 Microanalysis System). The elastic modulus was measured from 20°C to 1350°C using a Grindo-Sonic (Model MR35T) Transient Impulse/Elastic Modulus apparatus. The hardness of the candidate materials measured by a Vickers microindent hardness tester.

The microstructure and chemistry of the candidate materials were also studied. Polished specimens were plasma etched and viewed by optical microscope, and by scanning electron microscope. The microstructure of a polished specimen was also evaluated by image analysis using the Olympus software CUE-2.

Thermal expansion was measured from 25°C to 1400°C using a Theta Industries Dilatronic II (Model 6024). Fracture toughness was measured by the controlled flaw method. An indent load of 500 grams was used.

The results of the flexural strength testing are presented in Table 1. These flexural strength results are also plotted as a function of temperature in Figure 1. As shown in Table I, at 20°C and 1250°C the strength at fast loading is higher than at slow loading, and the strength increased from 20°C to 1250°C. At 1350°C the strength decreased at fast loading and increased on slow loading. The increased strength observed at the 1350°C slow loading conditions are believed due to flaw blunting and possible stress redistribution due to decreasing viscosity of the silicon phase in the grain boundaries. Similar observations have been reported by D. F. Carroll, et al.[1]

Table 1. Flexural Strength Measurements of NT-230 SiC

Temperature (°C)	Loading Rate (cm/s)	Strength (MPa)	Std. Dev. (± MPa)	Failure Initiation Site+
20	0.004	443	38 (8.6%)*	4 vol and 5 surf
20	0.00004	431	32 (7.2%)	4 vol, 1 edge
1250	0.004	504	32(6.3%	7 surf , 2 vol, edge
1250	0.00004	475	67(14%)	4 surf, 1 vol
1350	0.004	466	47(10%)	7 vol, 2 edge, 1 surf
1350	0.0004	521	52(10%)	4 vol, 1 surf
1350	0.00004	518	56(10.8%)	4 vol, 1 surf

*coefficient of variance (std dev/strength x 100)%
+vol - volume, surf - surface

For the 50 specimens tested, 26 specimens failed from volume-initiated flaws, 19 specimens failed from surface-initiated flaws, and four specimens failed from edge-initiated flaws. The fracture initiation site of one specimen was indeterminate due to fragmentation at the site of failure. A large number of the failures observed were initiated at pits. A typical pit flaw and fracture surface is shown in Figure 2.

The pits observed in the siliconized SiC specimens were quite unusual. In almost all cases enlarged grains were observed around the pit. The pits were 40 to 60 μm across. AES scan identified the large grains around the pore as Si. A very unusual pit initiated failure is shown in Figure 3.

---

[1]D. F. Carroll, R. E. Tressler, Y. Tsai, and C. Near, "High Temperature Properties of Siliconized Silicon Carbide Composites," in Tailoring Multiphase and Composite Ceramics, Materials' Science Research, Volume 20, edited by R. E. Tressler, et al., Plenum Press, New York, 1986.

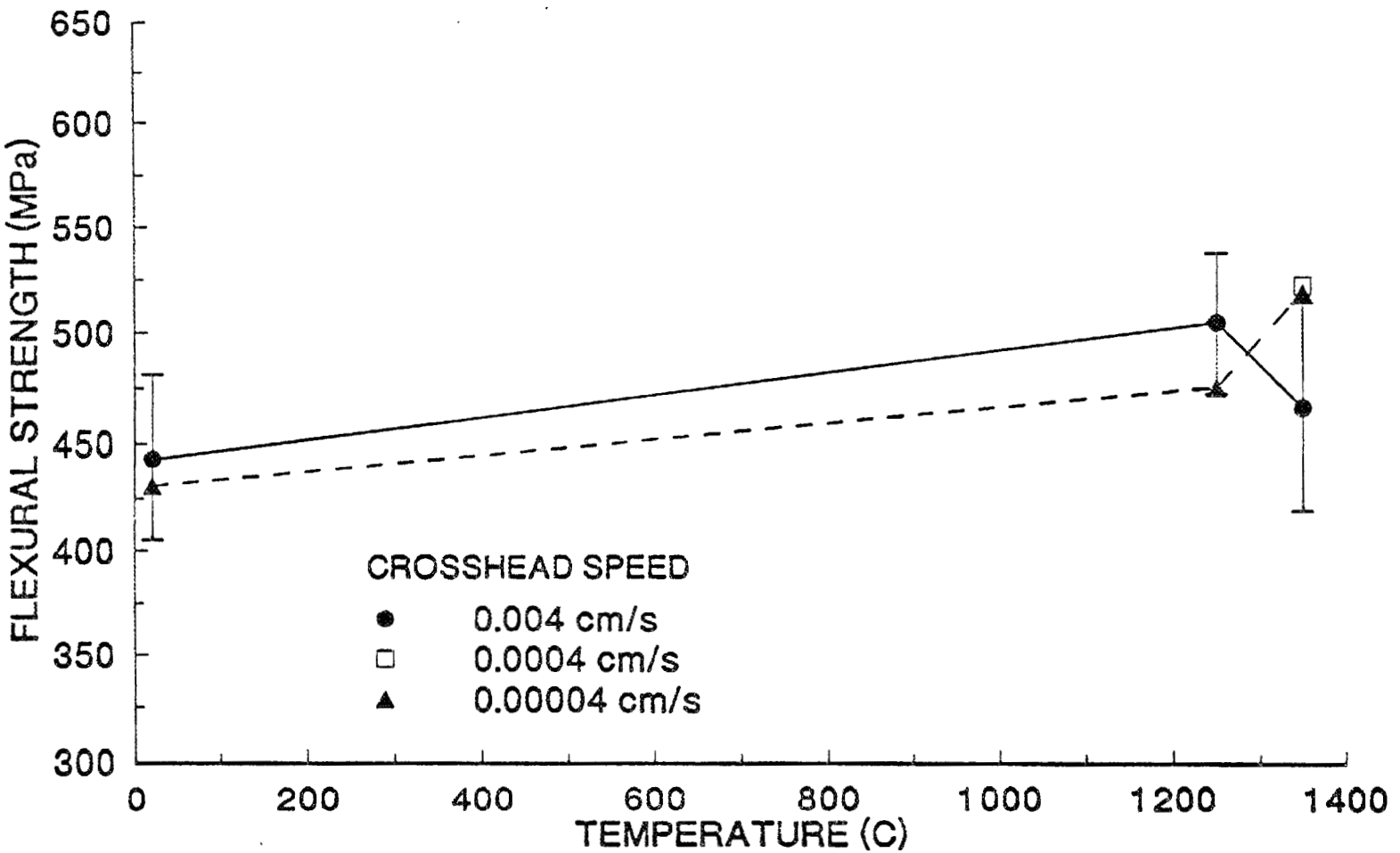

Figure 1. Flexural strength of Norton/TRW NT-230 SiC.

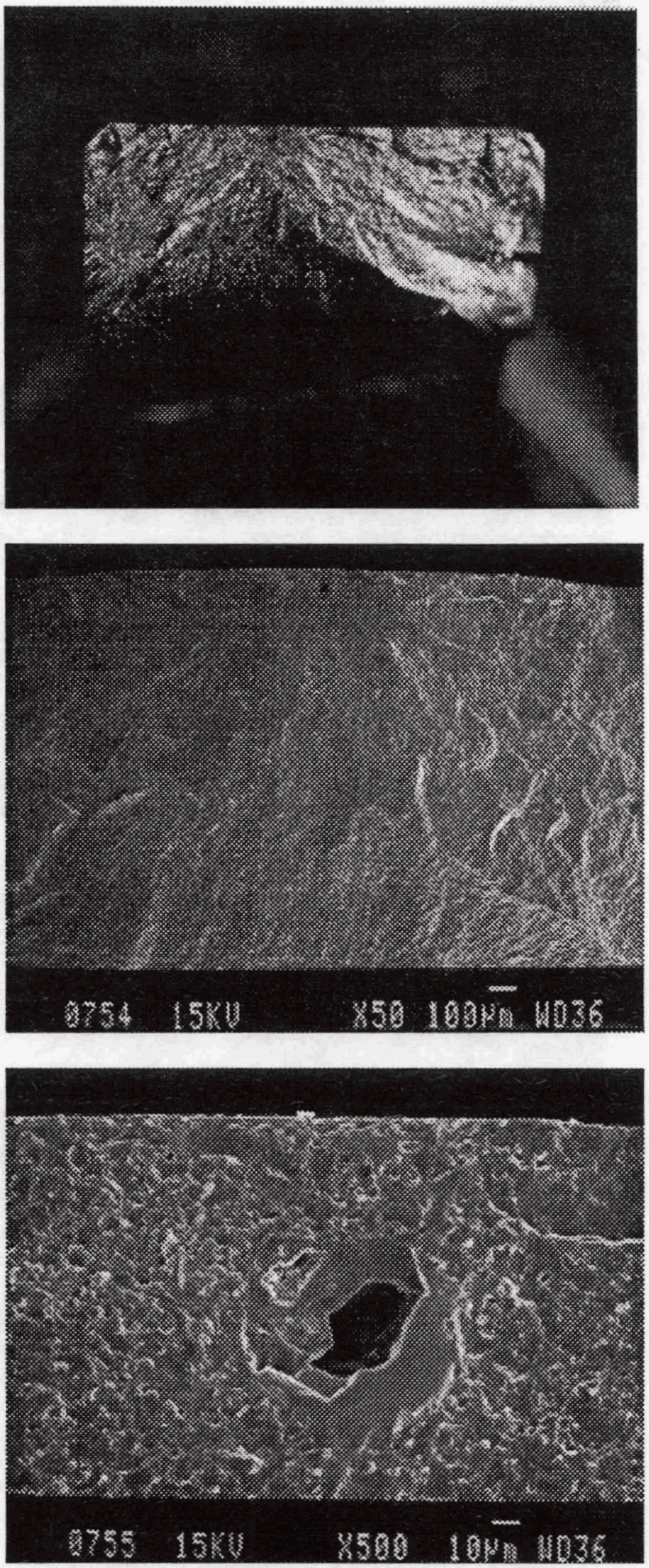

Figure 2. Typical pit initiated failure for NT-230.

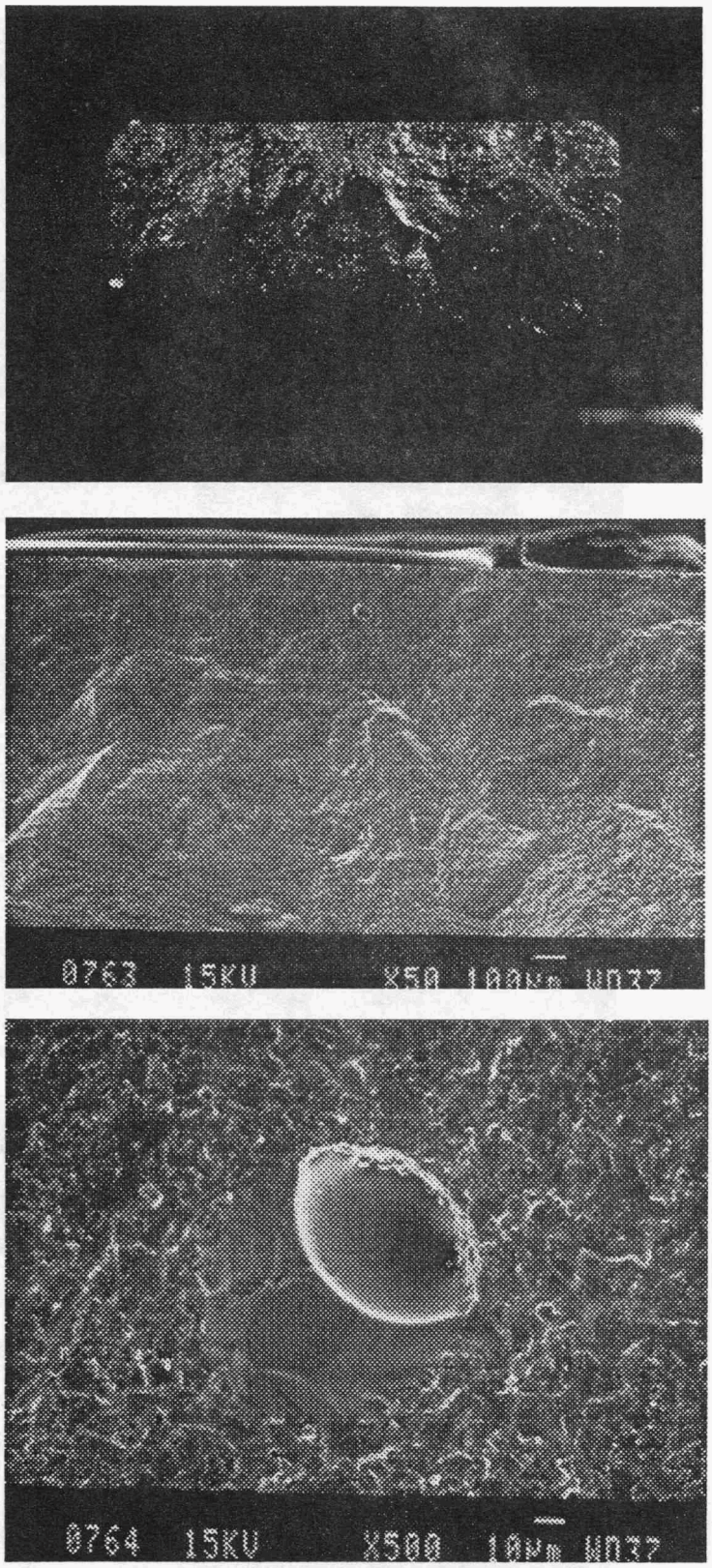

Figure 3. Unusual pit initiated failure for NT-230.

A typical polished section of NT-230 is shown in Figure 4, and a polished and plasma etched specimen is shown in Figure 5. An SEM photomicrograph of this plasma etched specimen is shown in Figure 6. From Figures 5 and 6 it can be seen that the Si has been etched away and the SiC appears to consist of a bi-modal distribution of particulates 1 to 2 μm and 6 to 8 μm. The results of the image analysis of the polished specimen showed that Si has an average volume fraction of 14.4%, the SiC phase has an average volume fraction of 84.4%, and the pore phase has an average volume fraction of 1.2%.

The results of the Property Measurements are summarized in Table 2. Comparing the results in Tables 1 and 2 with the data obtained earlier in this project for Hexoloy SA, it was observed that flexural strengths of NT-230 were higher, Young's modulus lower, density lower, hardness lower, and coefficient of thermal expansion higher than measured for Hexoloy SA.

Table 2. Summary of Property Measurement Results

Average Young's Modulus (GPA)	
20°C	402.3
1000°C	381.6
1250°C	375.4
1350°C	372.1
Density (g/cc)	3.08
Average Hardness (kg/mm^2)	2195*
Coefficient of Thermal Expansion (10^{-6}mm/cm in/°C)	5.87
Fracture Toughness (MPa • $m^{1/2}$)	2.3

*200 g load

During this reporting period the first flexural stress rupture test facility was completed and is in "shake down". The second unit is almost completed. The modifications for the tension/compression test unit is also nearing completion. Modifications of the furnace and the fixture alignment have been completed, and the installation of the hydraulic systems is in progress.

Status of milestones

Milestone 331413 is in progress.

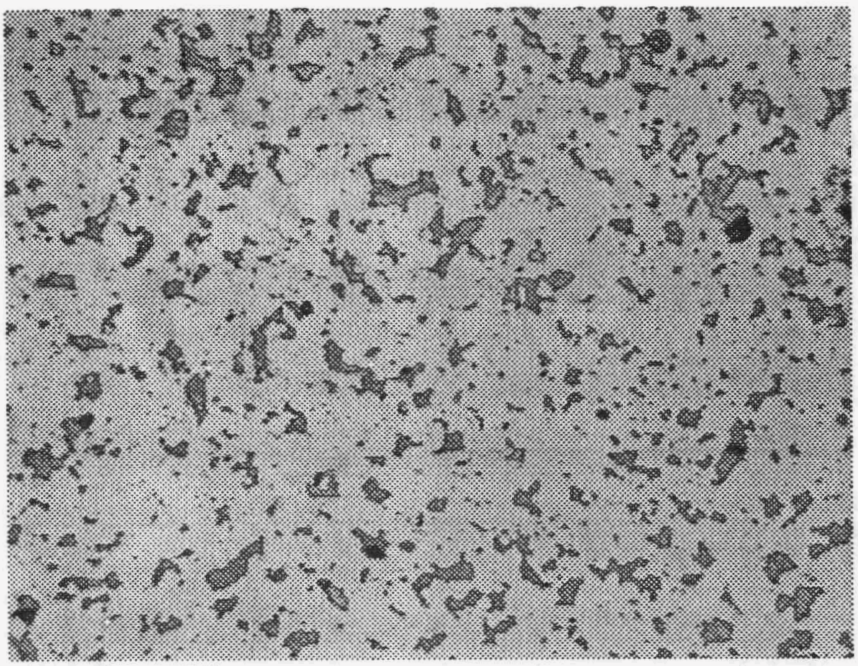

Figure 4. Polished section of NT-230 (500X).

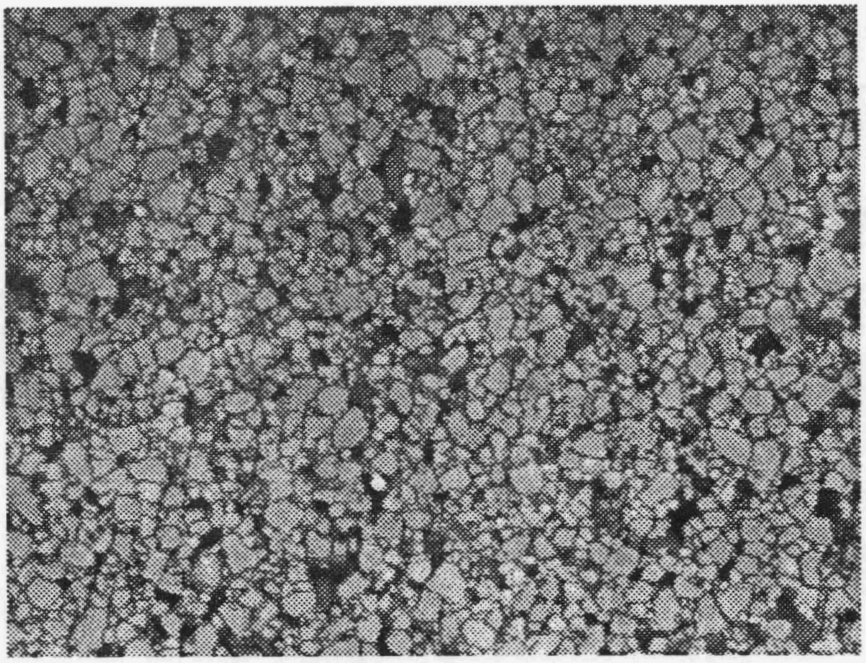

Figure 5. Polished and etched section of NT-230 (500X).

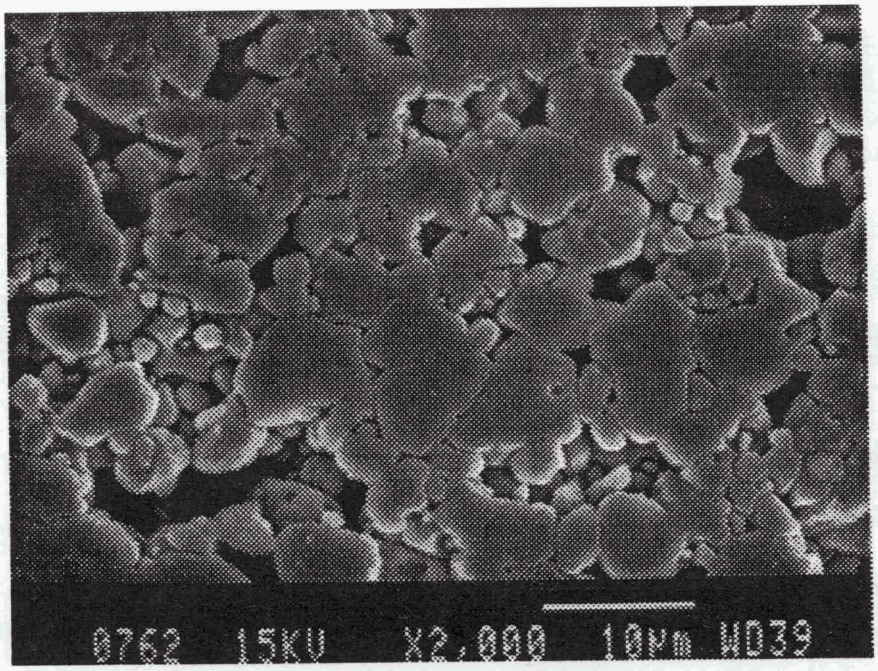

Figure 6. SEM photomicrograph of plasma etched section of NT-230.

3.4 FRACTURE MECHANICS

Testing and Evaluation of Advanced Ceramics at High Temperature in Uniaxial Tension — J. Sankar, A. D. Kelkar, S. Krishnaraj, and B. Wang (Department of Mechanical Engineering, North Carolina A&T State University, Greensboro, NC 27411)

Objective/Scope

The purpose of this effort will be to test and evaluate advanced ceramic materials at temperatures upto 1200° C in uniaxial tension. Testing may include fast fracture strengths, stepped static fatigue strength, and creep strength along with the analysis of fracture surfaces by scanning electron microscope. This effort will comprise of the following tasks:

Task 1. Specifications for testing machine and controls + (procurement) for creep testing.
Task 2. Identification of test material(s) for the present year + (procurement of specimens).
Task 3. Identification of test specimen configuration.
Task 4. Identification and procurement of test grips, high temperature extensometer, and furnace for the creep machine.
Task 5. High temperature fatigue-creep interaction study and tensile testing.
Task 6. Reporting(periodic).
Task 7. Final report.

It is anticipated that this program will help in understanding the behavior of ceramic materials at very high temperatures in uniaxial tension.

Technical Progress

During the semiannual reporting period Oct. '91 to March '92, following were accomplished:

1. Microscopy and microchemical analyses of the GTE SNW 1000 creep samples tested at 1100 ^{o} C, 0.85% σ_f and 1200 ^{o}C, 0.60% σ_f.
2. Installation of a high temperature creep frame with a suitable furnace and a laser extensometer set up.

EDS(Energy Dispersive Spectrum) analysis was performed on creep tested(1100 ^{o} C, 0.85% σ_f and 1200 ^{o}C, 0.60% $\sigma_{f)}$ GTE SNW-1000 samples. The compositions of yttrium, silicon, and aluminum were examined to understand the chemical processes taking place during creep. A schematic of the sections of the creep tested specimens analyzed is illustrated in figure 1A. These were, a) fracture surface, b) a polished section 2mm away from the fracture surface along the transverse(parallel) direction, and c) a polished section 2mm away from the fracture surface along the longitudinal(perpendicular) direction. A silicon wafer for silicon, pure aluminum stub for aluminum, and yttria powder for yttrium were used as the standards for microchemical analysis. A schematic of the pore areas(observed in the polished surface) analyzed using EDS is shown in figure 1B.

Microscopy analysis on a creep sample tested at 1200 ^{o}C(Figs. 2&3) shows the possibility for the linkage of pores during creep testing, and the tests also indicate that the

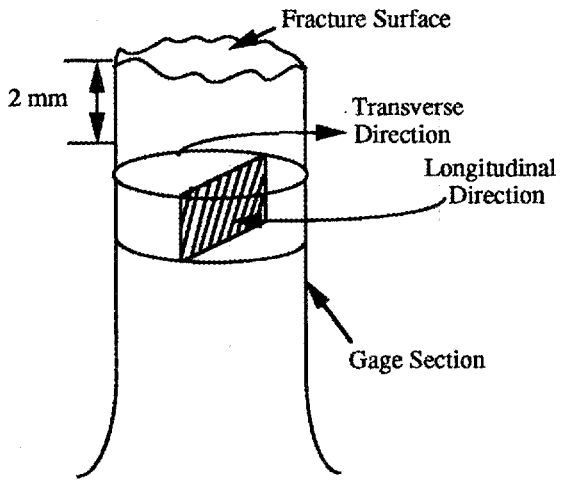

Figure 1A. Sections for Analyses in the Gage Section

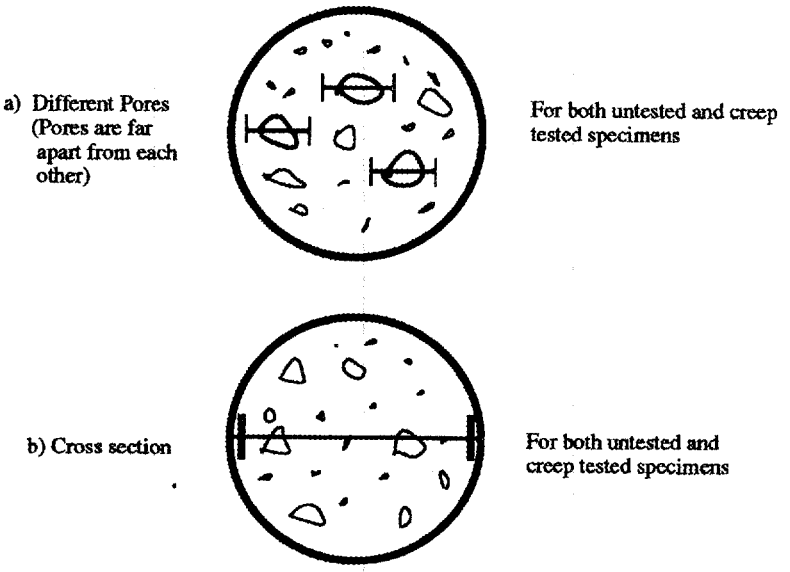

Figure 1B. Pore Areas Tested for EDS Analyses

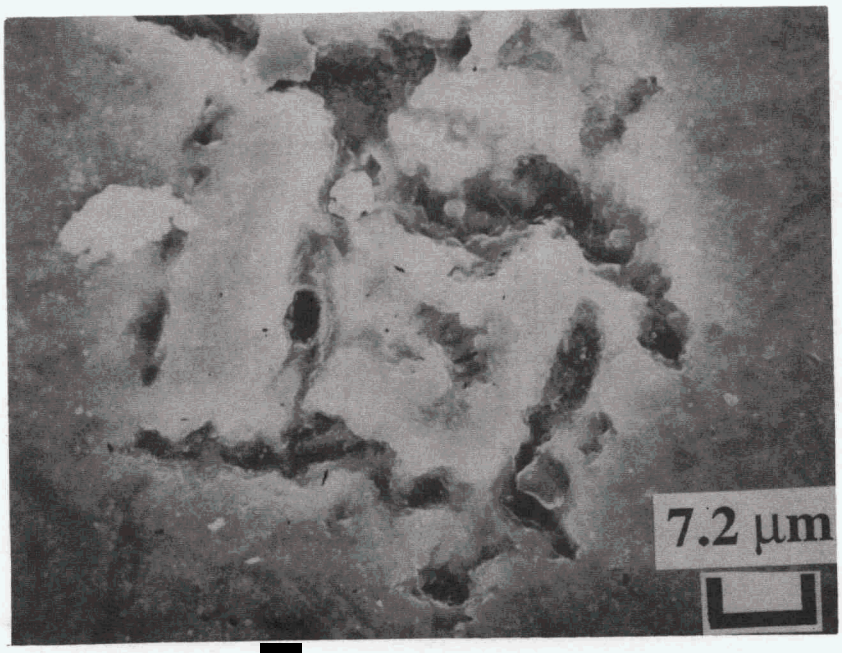

Fig. 2 GTE SNW-1000 Creep Tested Specimen Showing Linking of Small Pores

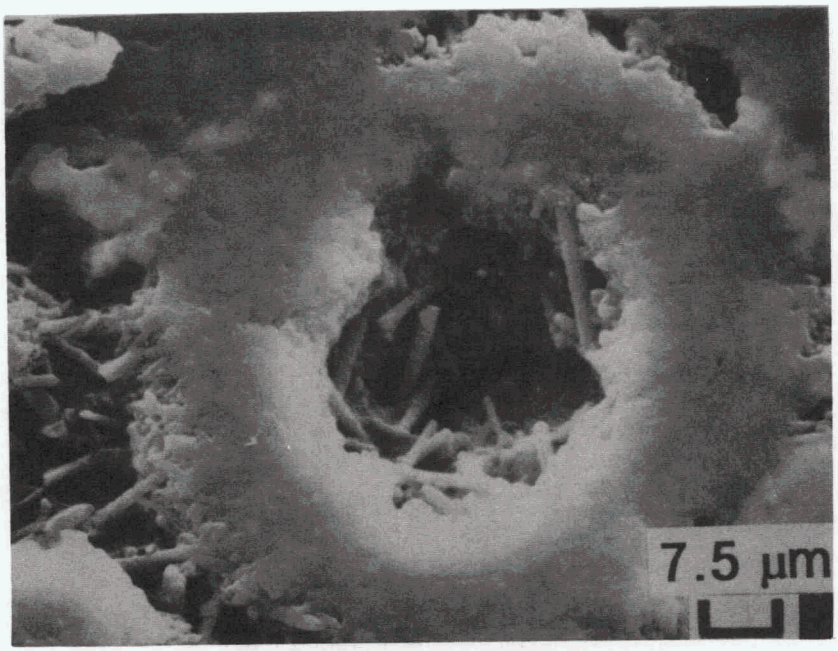

Fig. 3 GTE SNW-1000 Creep Tested Specimen Showing Pore Softening

edges of the pores are softening and the fissures are extending beyond the pores. EDS analyses performed on creep tested(1100 ^{o} C, 0.85% σ_f and 1200 ^{o}C, 0.60% σ_f) GTE SNW-1000 samples samples are shown in figures 4 and 5. From fig. 4 it can be seen that in the transverse direction analysis, diffusion of yttrium into the pores is lesser for samples tested at 1100° C, 0.85 σ_f as compared to that of samples tested at 1200°C, 60% σ_f. When analyzed along the longitudinal(stress) direction(fig. 5), diffusion of yttrium into the pores for samples tested at 1100 ^{o} C, 85% σ_f is more than that of samples analyzed in the transverse direction. This could be an indication that stress, in addition to temperature is a factor in the diffusion process.

The creep frame for the high temperature deformation setup(fig. 6) was transferred from ORNL to A&T. The furnace, furnace controller, laser gaging system, and accessories were received from the Applied Test Systems, Inc., Butler, PA. The setup includes the following:

- Lever arm assembly with a load capacity of 10,000 lbs with precision ratio adjustment(ratio 10:1), and rotatable knife edges.
- High temperature furnace with a maximum temperature rating of 1650 ^{o}C and four(4) Kanthal Super 33 heating elements.
- A two-zone high temperature control system with two(2) separate temperature controller, 3-mode programmable microprocessor, with ramp and soak feature for a maximum of 8 intervals.
- Special collet type buttonhead coupling with water cooling feature(Fig. 7)
- Knife edge alignment couplings.
- Laser gaging system by Laser Mike with measurement range of 0.015 in. - 1.950 in. and a resolution of 2.0 x 10^{-5}in.

As regards to the fatigue-creep interaction study, we have developed a computer program to test the specimens in uniaxial tensile fatigue followed by uniaxial tensile creep. This program can generate a constant or multiple frequency, a constant or multiple number of cycles, and a constant or multiple stress levels.The test matrix for the fatigue-creep interaction study will be as follows:

Test Specifications:

<u>FATIGUE:</u> Tension-Tension constant amplitude triangular waveform
Frequency - 0.5 Hz
Temperature - 1200° C
R-Ratio(min. stress/max. stress) = 0.1
Stressing patterns which are planned to be used:

1. Cycling at 70% of the fatigue strength at 1200° C for 50,000 cycles
2. Cycling at 50% of the fatigue strength at 1200° C for 50,000 cycles
3. Co-axing type - 50% to 70% of the fatigue strength at 1200° C in steps of 10% for a total number of 50,000 cycles

Stressing pattern 3. is called the co-axing type, wherein the specimen is cycled from lower to higher stress levels with a certain number of cycle count in each level.

(Available data from ORNL: Fatigue strength of SNW1000 Si_3N_4 at 1200° C = 140 MPa)

EDS Analysis Results, GTE SNW-1000, Creep Tested Samples
Yttrium Distribution Across Pores in Transverse Direction

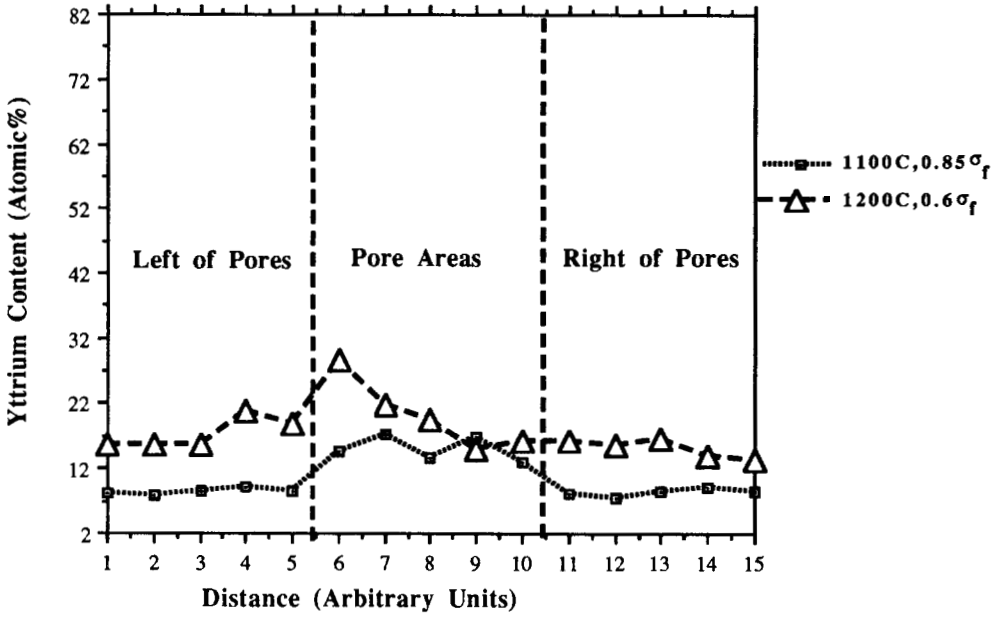

Fig. 4 Average Compositional Variation Across Pores

EDS Analysis Results, GTE SNW-1000, Creep Tested
Yttrium Distribution Across Pores In Longitudinal Direction

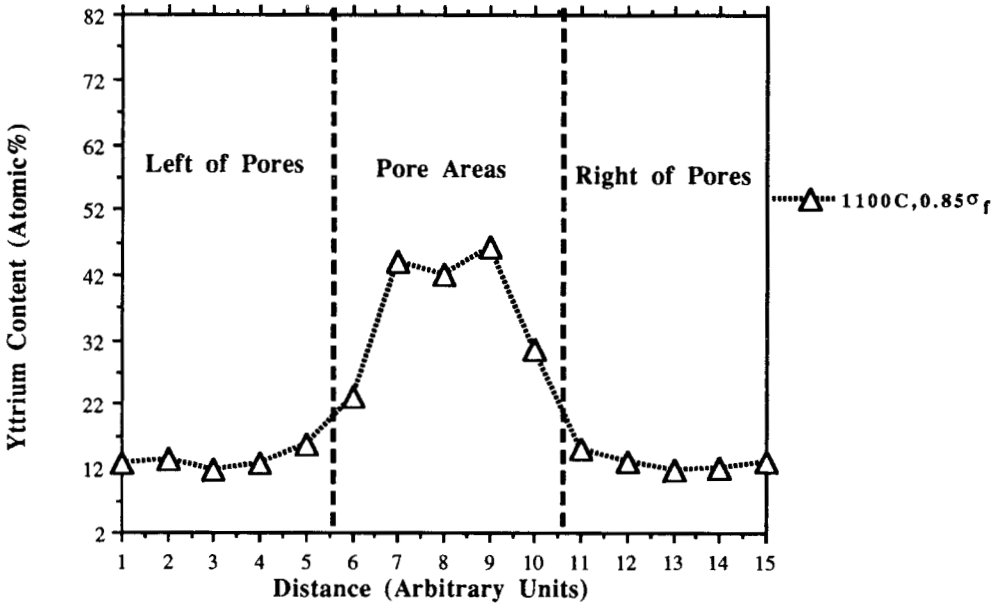

Fig. 5 Average Compositional Variation Across Pores

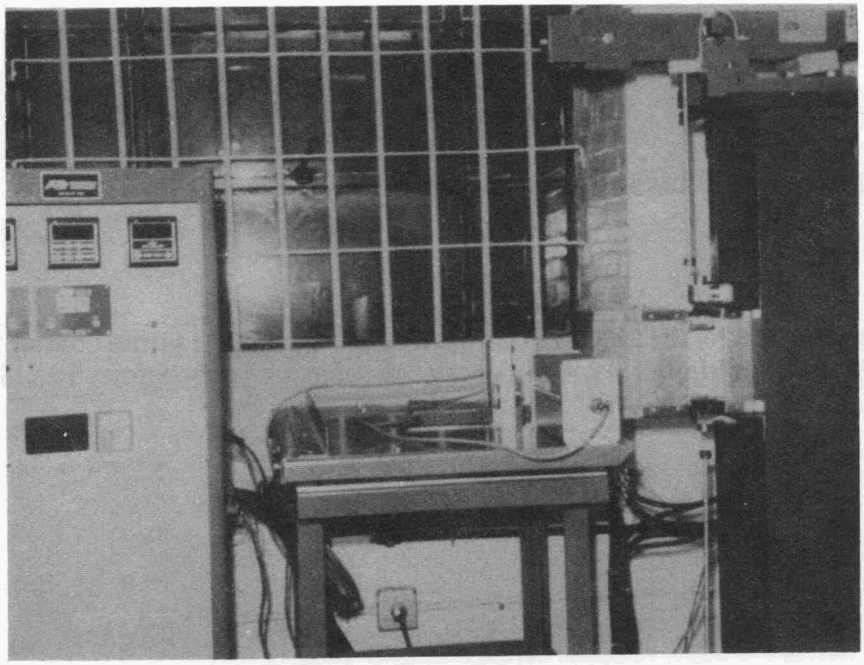

Fig. 6 High Temperature Creep Deformation Setup

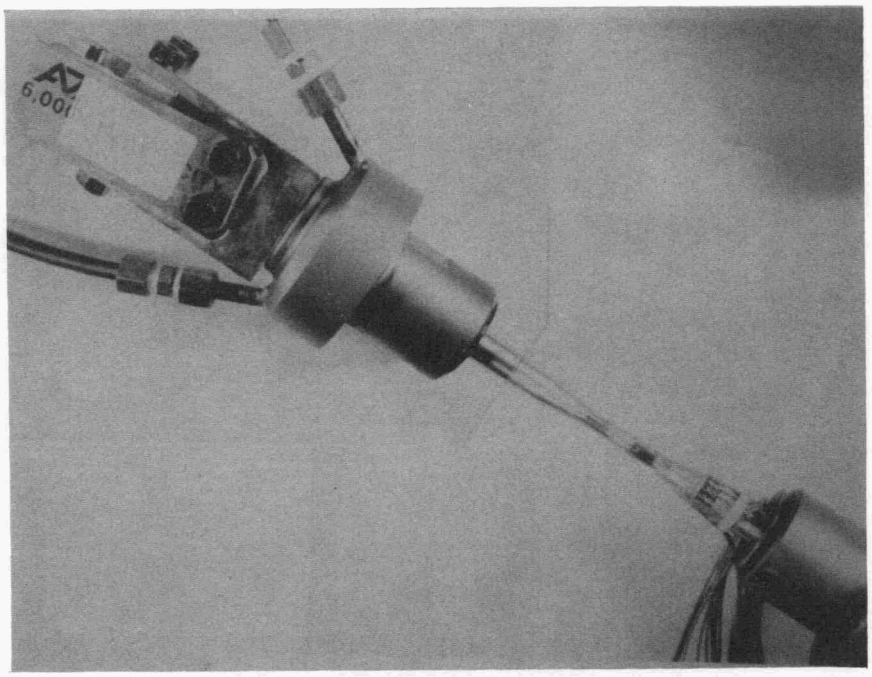

Fig. 7 Special Collet Type Buttonhead Coupling With Water Cooling Feature

CREEP: Uniaxial Tensile Constant Load
Temperature - 1200° C
Load - 40%, 50%, and 60% of the tensile strength at 1200° C
(Available data from A&T: Tensile strength of SNW1000 Si_3N_4 at 1200° C = 230 MPa)

Publications and Presentations
None

Research sponsored by the U. S. Department of Energy under prime contract DE-AC05-840R21400 with the Martin Marietta Energy Systems, Inc., subcontract 19X-89867C

Standard Tensile Test Development

S. M. Wiederhorn, R. F. Krause, Jr., and D. E. Roberts
(National Institute of Standards and Technology)

Objective/Scope:

This project is concerned with the development of test equipment and procedures for measuring the tensile strength and creep resistance of ceramic materials at elevated temperatures. Inexpensive techniques for measuring the creep behavior and strength of structural ceramics have been developed and are being used to characterize the mechanical behavior of these materials. The ultimate goal of the project is to help develop a data base and a test methodology for the structural design of heat engines for vehicular applications.

Technical Highlights:

During the past six months, studies were conducted on the creep and creep rupture of on PY6, a grade of silicon nitride containing ≈6 wght. % Y_2O_3. This work is being performed in collaboration with Pramod Khandelwal of Allison. To date, 23 specimens have been tested in creep. In addition, tensile strengths were measured on 13 specimens in the temperature range 1100 to 1400°C. These data will be part of a data base to compare materials manufactured by different companies.

Experimental Techniques:

Both the specimen design and the test apparatus used in this tensile creep study have been described in reference [1]. This apparatus utilized flat dog-bone shaped samples to which SiC "flags" are attached to define the gauge length. Relative displacements of the flags are continuously monitored during each test either by means of a long range telescope, or by means of a laser extensometer. Gauge lengths measured by the telescope are accurate to ± 2 μm, whereas gauge lengths measured by the laser are accurate to ± 1 μm. To assure thermal stability, specimens were heated at the test temperature for approximately 20 hours before testing. Tests were made over a temperature range of 1200°C to 1400°C and a stress range ≈70 to ≈200 MPa. For most tests, the applied stress was maintained until the specimen failed. In this way, both the creep and creep rupture behavior of the material could be characterized.

Tensile strength data were collected on flat dogbone specimens, which were from the same series of material as those used in the creep studies. Strength data were collected at loading rates of ≈0.06 and ≈6.00 MPa/s. The test temperature ranged from 1000°C to 1400°C. After heating to temperature, specimens were held for a two hour period to assure thermal equilibrium before testing. Specimens loaded at ≈6.00 MPa/s required about 30 seconds for failure, whereas those loaded at ≈0.06 MPa/s required approximately 30 minutes. As was observed earlier by Hecht et al. [2] this difference in rate of loading leads to a significant difference in strength.

Results:

Tensile strength data collected in this study are compared with data collected earlier at Oak Ridge National Laboratories by Ferber and Jenkins [3] and at the University of Dayton Research Institute by Hecht et al. [2], figure 1. Data from NIST were collected on specimens that were about one-tenth the total test volume of the button-head design specimens (ORNL design) used at the other two laboratories. The NIST data collected at the higher loading rate are consistent with the data collected at ORNL, whereas, the data collected at the lower rate are consistent with the data collected at UDRI. The data from ORNL was collected at ≈36 MPa/s, which is about 6 times the rate used at NIST. At temperatures above 1200°C, the difference in loading rate appears to have a significant influence on the strength. Specimens loaded at the faster rate were stronger than those loaded at the slower rate.

Creep tests were collected on two types of equipment at NIST. In one, the displacement was measured by a laser displacement transducer, whereas displacements on the second type of equipment were measured using a long range, high precision telescope [3, 4]. Samples of data obtained by these two techniques are shown in figure 2. As can be seen, resolution is higher on the laser apparatus, as indicated by the smaller degree of scatter of the data points for the laser. Never-the-less, the data taken on the optical telescope are accurate enough to determine the creep rate after extended periods of exposure at elevated temperature. Data taken on the laser apparatus, suggest the occurrence of extended primary creep before failure.

The stress and temperature dependence of the creep behavior was determined by expressing the logarithm of the strain rate, $\dot{\epsilon}$, as the sum of the inverse absolute temperature, 1/T, and the logarithm of the applied stress, σ, for the entire data set.

$$\log(\dot{\epsilon}) = A + n \cdot \log(\sigma) + \Delta H/RT \qquad (1)$$

Where n is the stress exponent, ΔH is the apparent activation energy and R is the universal gas constant. A least squares analysis of the data yielded a stress exponent of ≈7 and an apparent activation energy of ≈1140 kJ/mol for this material. Both of these values are consistent with the those reported earlier by Ferber and Jenkins [3], 5 and 1102 kJ/mol, respectively. Graphical representations of the data for the PY6 are given in figures 3 and 4. In figure 3 the data are temperature compensated to show the stress dependence of the data, whereas in figure 4 the data are stress compensated to illustrate the temperature dependence of the data. For both figures, the data tend to cluster about straight lines, suggesting that the assumed functionality provides a reasonable fit of the minimum creep rate.

Creep rupture data are presented in figure 5 in the form of a Monkman-Grant plot, in which the strain rate is plotted as a function of the time to failure in hours. The data collected in this study, dark squares, approximate a strength line on this type of plot with a slope

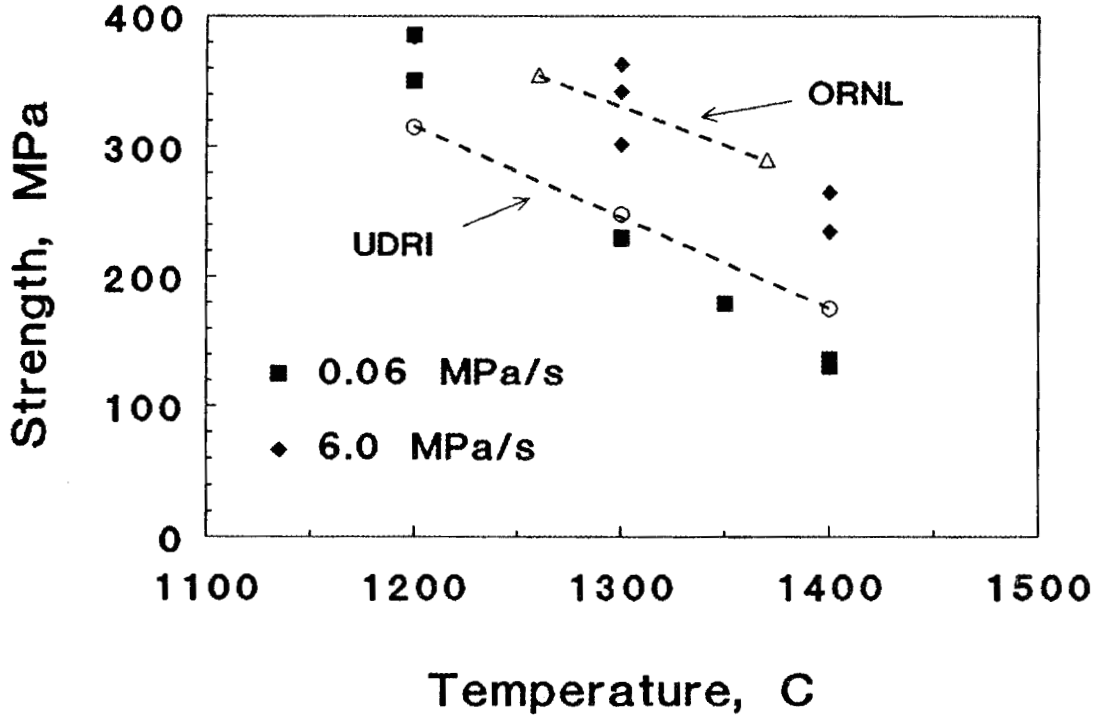

1. A comparison of tensile strength measurements on PY6 made in this study with those made by Ferber and Jenkins [3] and Hecht et al. [2].

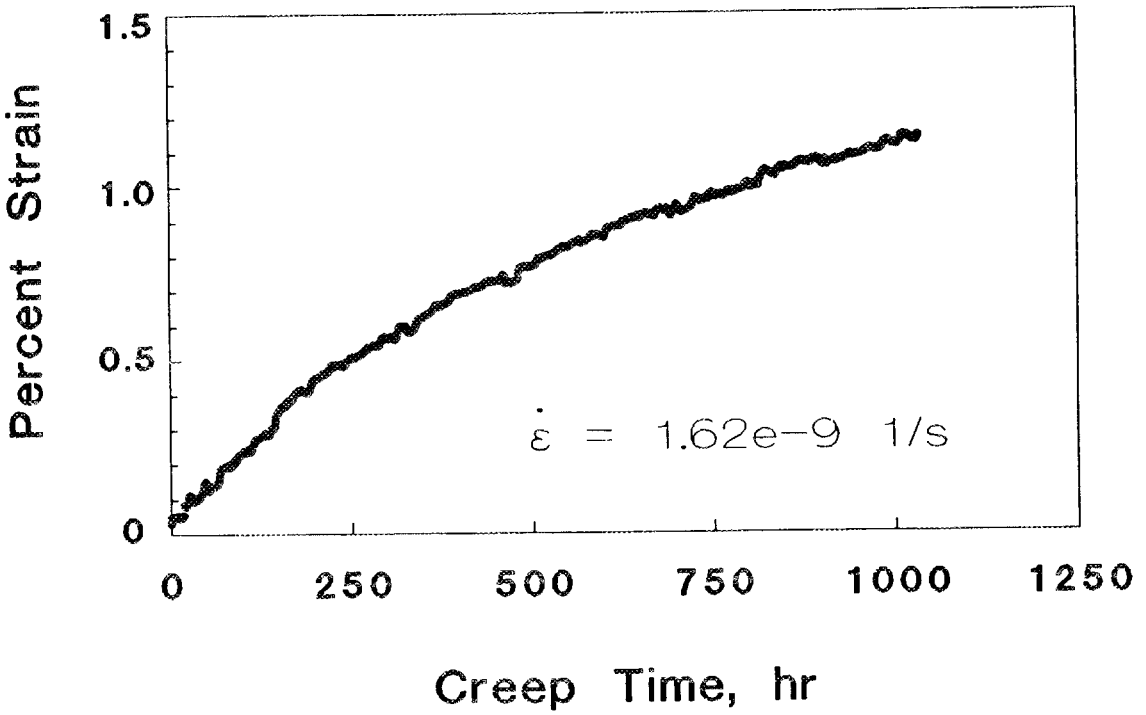

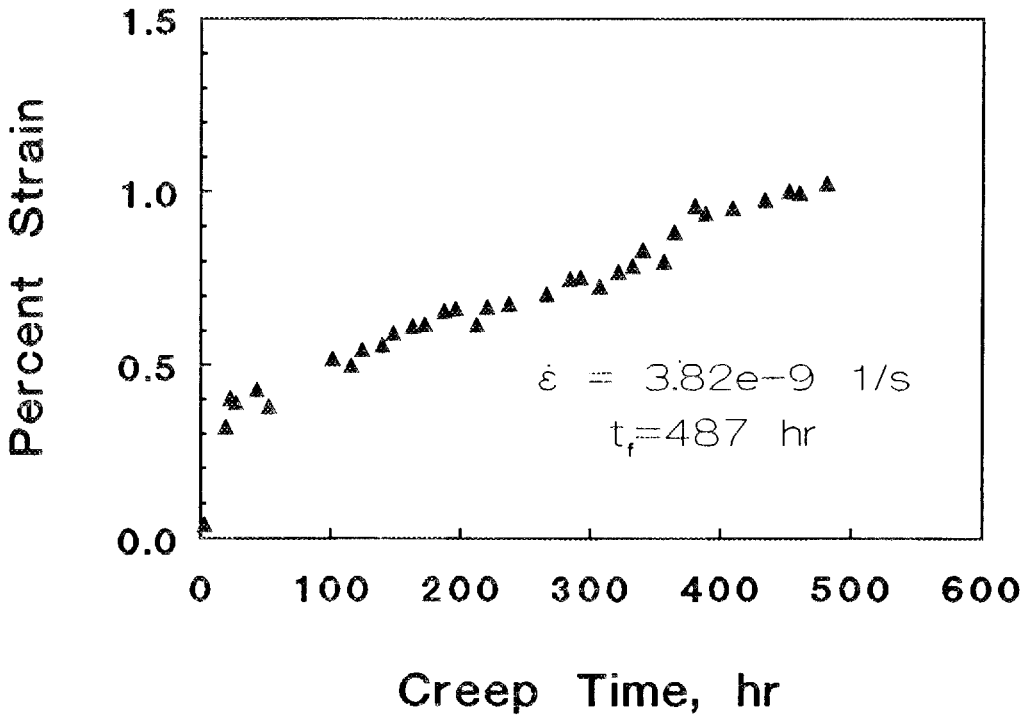

2. Creep measurements made by the (a) laser technique and (b) the technique using a precision telescope.

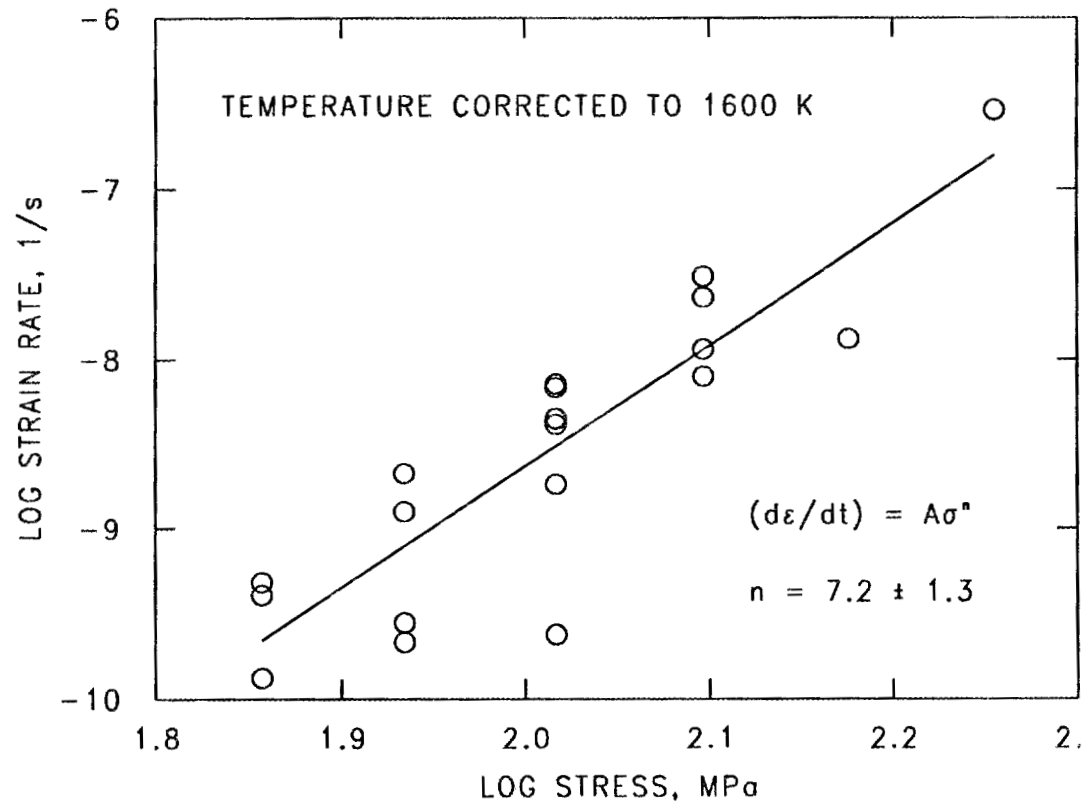

3. Stress dependence of the creep rate. The data have been temperature compensated using equation 1 so that more of the creep data could be used to obtain the stress exponent.

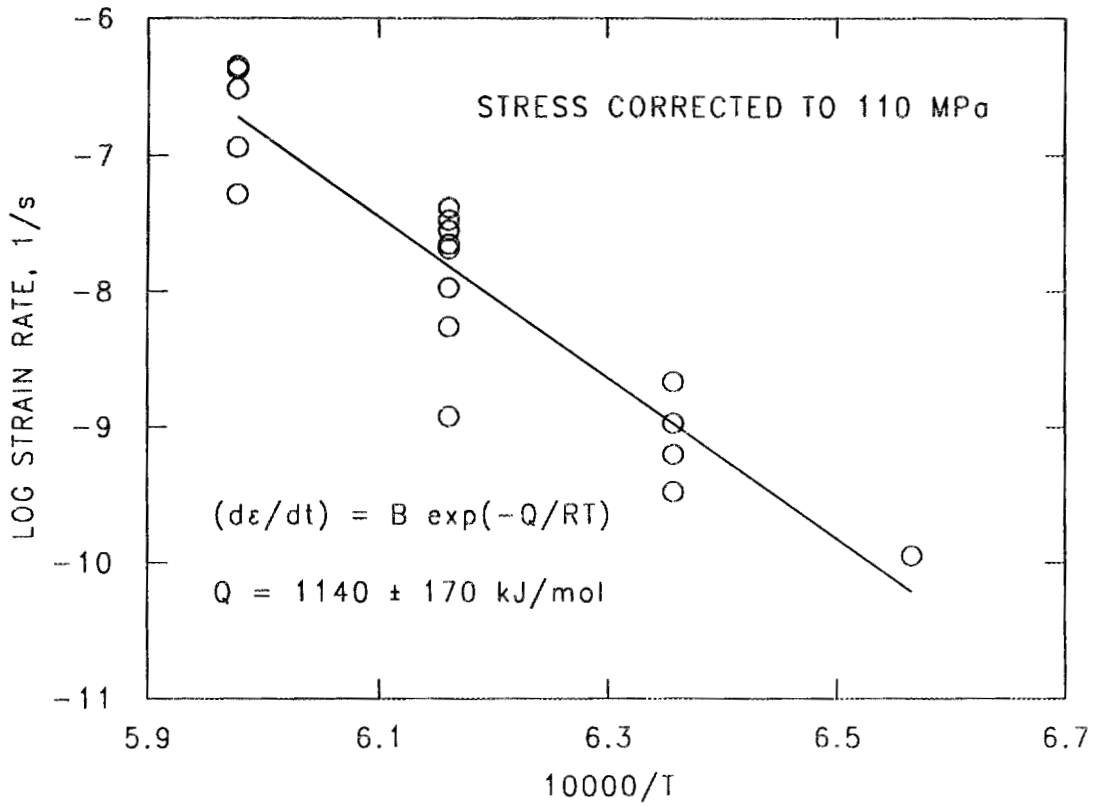

4. Temperature dependence of the creep rate. The data have been stress compensated using equation 1 so that more of the creep data could be used to obtain the apparent activation energy.

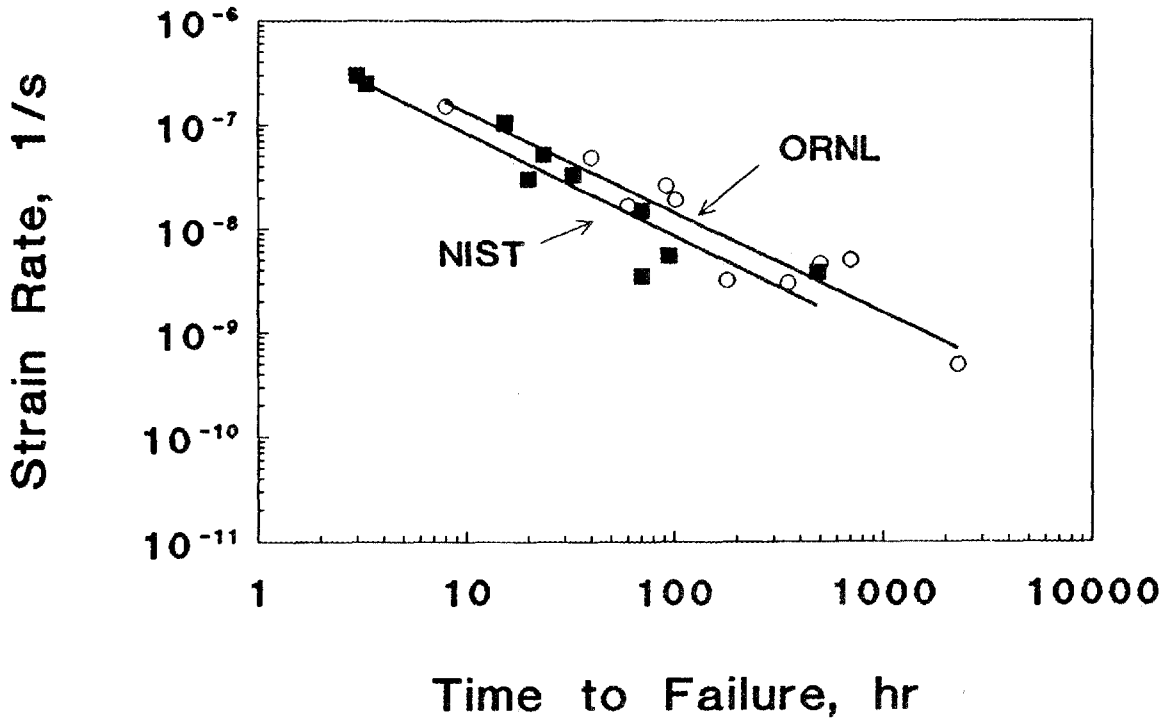

5. Creep rupture data presented in the form of a Monkman-Grant plot. The data collected in this study are compared with those collected by Ferber and Jenkins [3]. Although the two plots are quite close to one-another, the data by Ferber and Jenkins do occur a longer failure time for a given applied stress.

of approximately -1. The date were obtained over a range of temperatures and stresses. The fact that they tend to cluster about a single line indicates that this curve can be used for purposes of lifetime prediction independent of temperature and applied stress.

The creep rupture data collected in this study on PY6 have been compared with data collected at Oak Ridge National Laboratories by Ferber and Jenkins [3], figure 5 . At a given strain rate, specimens tested at ORNL appear to last 50 % longer than specimens tested at NIST. Similar results have been obtained on NT154, a grade of silicon nitride containing only 4% Y_2O_3 [3,5]. This similarity in results suggests a difference between the two types of test specimens or the technique for measurement of creep rate. These differences will be explored further on GN10 specimens made especially for this purpose.

Discussion:

A variety silicon nitrides have now been run in tensile creep [3, 5-7]. For all materials studied, strain to failure ranges from ≈ 0.5 percent to ≈ 2 percent. The observed creep curves are generally observed to fit into two extreme forms of behavior. The creep curve may consist entirely of primary stage creep as has been reported for unannealed grades of NT154 [5] and for other experimental grades of silicon nitride. In this case, a continually decreasing creep rate is observed for the entire lifetime of the test specimen. Failure occurs without the intervention of either secondary or tertiary creep. In other grades of silicon nitride, primary stage creep behavior is followed by steady state creep. This type of behavior has been reported for annealed grades of NT154 [8], for GN10 [8] and for experimental grades of silicon nitride [6]. Tertiary stage creep is not observed prior to failure. This seems to be a general observation of our studies. Tertiary stage creep does not occur in hot-pressed, HIP-ed or sintered silicon nitride. Fracture occurs during primary stage creep, or after the material has entered secondary stage creep. As indicated in figure 2, PY6 seems to have a long primary stage followed by a shorter secondary stage of creep. There appears to be no tertiary creep in this material.

The stress rupture behavior of silicon nitride can be summarized by a procedure proposed by Monkman and Grant [9]. They suggested that the logarithm of the time to failure for an alloy be plotted as a function of the logarithm of the minimum creep rate. On this type of plot, creep rupture data plot as a straight line with a slope of ≈-1, regardless of temperature or applied stress. This relationship was developed originally as an empirical method of correlating creep rupture behavior of high temperature alloys. It has been used for purposes of material development, and as a lifetime prediction method [10]. Data for all of the alloys presented in the original paper clustered in a narrow band on a log-log plot. In this situation, a universal creep rupture curve is obtained, in which case, the temperature and stress dependence of the time-to-failure is determined by the activation energy and the stress exponent of the creep rate. Therefore, it follows that

lifetime of alloys at elevated temperatures can be enhanced by improving creep behavior. The same conclusion is valid for silicon nitride.

In figure 6, silicon nitride creep rupture data from a number of investigations have been plotted on a common diagram. As with high temperature alloys, the creep rupture data tend to cluster around a common curve. The line labeled Kossowsky et al [7] represents the first set of data of this type collected on Norton NC132, a grade of silicon nitride containing magnesia as a sintering aid. At a given creep rate, this material has the longest lifetime, because its strain to failure is greatest, (≈2%). The newer materials contain only yttria, or yttria and other oxides (alumina, strontia) as sintering aids. Although these materials tend to fail in shorter times, for a given creep rate, their resistance to creep as a function of stress and temperature is far better than that of NC132. Consequently, they are much better structural materials at elevated temperatures.

Monkman-Grant curves for the newer grades of silicon nitride cluster within a factor of two of a line predicted from the following equation[1].

$$\log(t_f) = -2.347 - \log(\dot{\epsilon}), \qquad (2)$$

In this equation, the unit of time is hr. Considering how closely the data in figure 6 cluster, the above equation, dashed line in figure 6, can be used as a universal estimate of failure time for silicon nitride. As with structural alloys, it also follows that resistance to creep should be an important guideline for the processing new grades of silicon nitride.

The data in figure 6 imply that for a given creep rate, the further the Monkman-Grant curve is to the right on the diagram, the longer the lifetime. Thus, the curve for NC132 has a lifetime approximately ten times that of NT154, one of the best grades of silicon nitride produced today. While this conclusion is true, it is not of great practical value, because the design of structural components is not based on strain rate, but on applied stress and temperature. To compare these two materials on a more practical basis, the Monkman-Grant equation is expressed in its power law form.

$$t_f = t_o \cdot \dot{\epsilon}^m, \qquad (3)$$

where t_f is the time to failure, and $\dot{\epsilon}$ is the creep rate.

By substituting equation 1 into equation 3, the following equation is obtained [11]:

$$t_f = A \cdot t_o \cdot \dot{\epsilon}_o^{\,m} \cdot \sigma^{n \cdot m} \cdot \exp(-m \cdot \Delta H / R \cdot T) \qquad (4)$$

---

[1] The line was obtained by a visual fit to the data shown in figure 6.

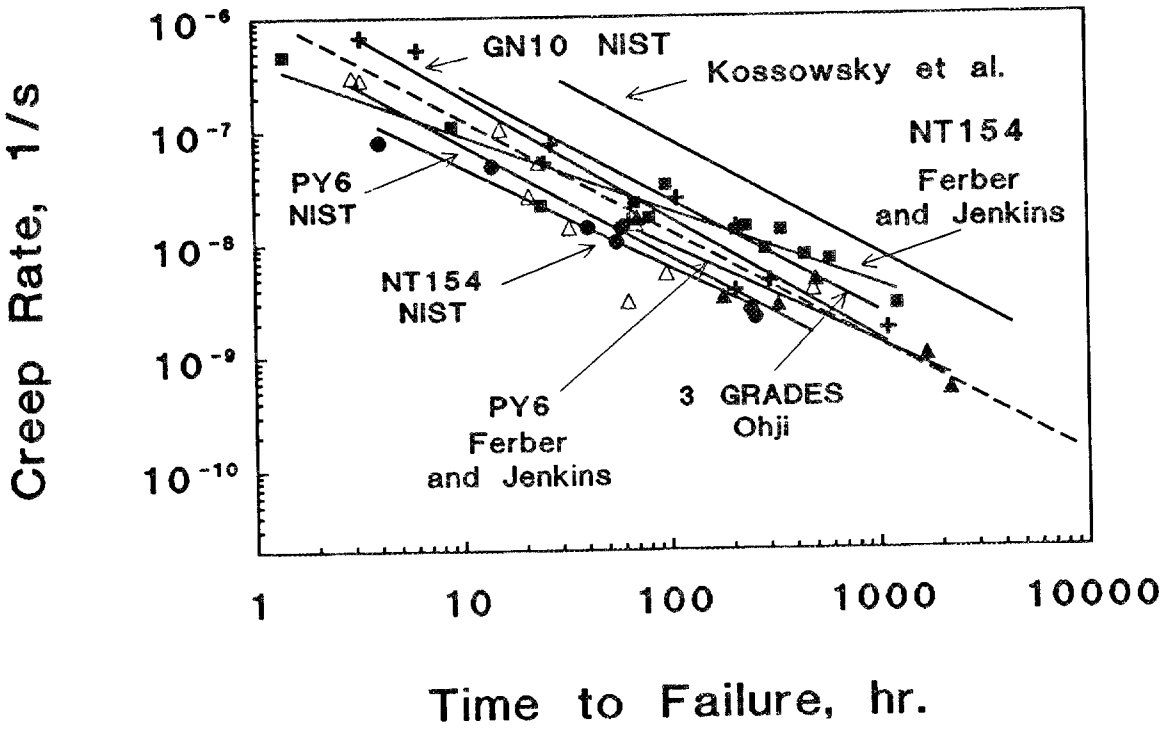

6. A comparison of creep rupture obtained on a variety of commercial and experimental grades of silicon nitride. The dashed line is a visual fit of the data for the newer grades of silicon nitride: $\log(t_f) = -2.347 - \log(\dot{\epsilon})$. The unit of time in this equation is hr.

This equation gives the time to failure as a function of stress and temperature. The equation depends on the operating failure mechanism, as both the activation energy and the stress exponent depend on failure mechanism. Substituting creep data for NC132 and NT154 [5, 7] into equation 4, a comparison between the two materials at 1300°C is obtained, figure 7. For a given temperature and applied stress, lifetime improvements in creep rupture lifetime of approximately five orders of magnitude have been obtained over the past 10 years. This improvement in lifetime has been achieved primarily by enhancing the creep resistance of silicon nitride.

Status of Milestones:

All milestones are on schedule.

Publications:

1. S.M. Wiederhorn, "Creep and Creep Rupture of Ceramic-Matrix Composites," pp 239-264 in Flight-Vehicle Materials, Structures and Dynamics, Assessment and Future Directions, Vol.3, Ceramics and Ceramic-Matrix Composites, Ed. Stanley R. Levine, Series Editors A.K. Noor and S.L. Venerri. American Society of Mechanical

2. S.M. Wiederhorn, R. Krause and D.C. Cranmer, "Tensile Creep Testing of Structural Ceramics," Proceedings of the Annual Automotive Technology Development Contractors' Coordination Meeting, Dearborn, MI, October 28-31, 1991, Society of Automotive Engineers, Inc., 4007 Commonwealth Drive, Warrendale, PA 15096-0001, to be published

References:

1. D.F. Carroll, S.M. Wiederhorn and D.E. Roberts, "Technique for Tensile Creep Testing of Ceramics," J. Am. Ceram. Soc., 72, 1610-14 (1989).

2. N.L. Hecht, S.M. Goodrich, L. Chuck, and D.E. McCullum, "Effects of the Environment on the Mechanical Behavior of Ceramics," Proceedings of the Annual Automotive Technology Development Contractors' Coordination Meeting, P-243, Dearborn, MI, October 22-25, 1990, Society of Automotive Engineers, Inc., 4007 Commonwealth Drive, Warrendale, PA 15096-0001, pp. 199-212.

3. M.K. Ferber and M.G. Jenkins, "Evaluation of the Elevated-Temperature mechanical Reliability of a HIP-ed Silicon Nitride," J. Am. Ceram. Soc., in press.

4. S.M. Wiederhorn, D.E. Roberts, T.-J. Chuang, and L. Chuck, "Damage-Enhanced Creep in Siliconized Silicon Carbide: Phenomenology," J. Am. Ceram. Soc., 71 602-608 (1988).

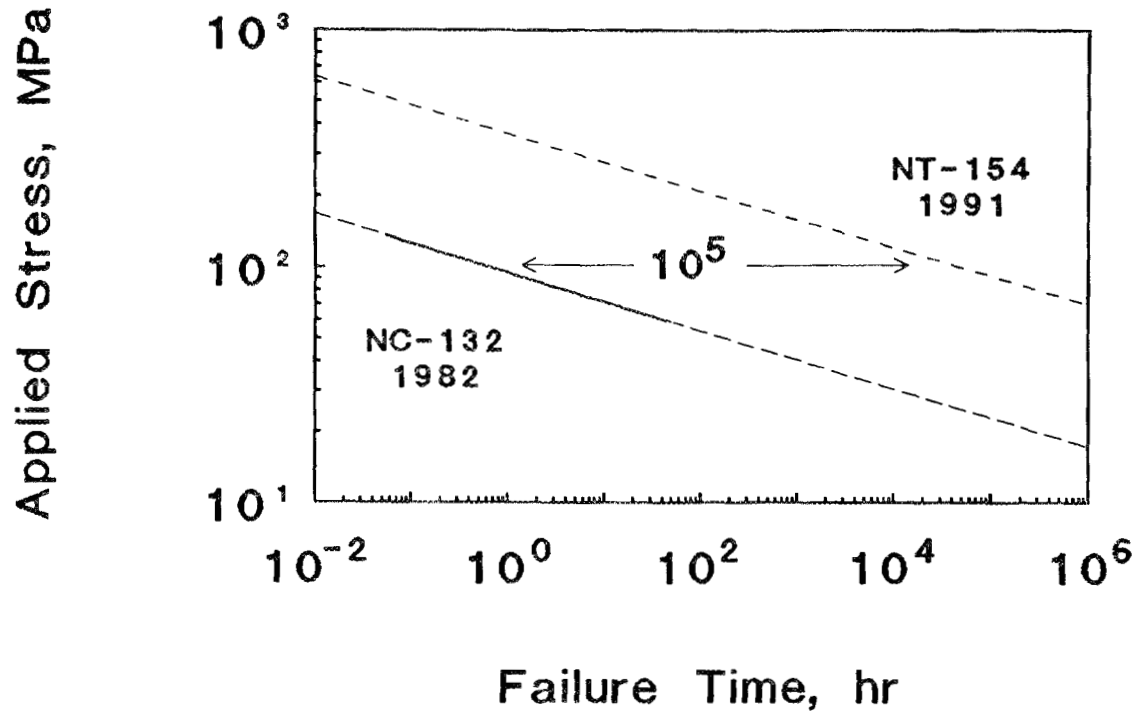

7. A comparison between lifetime of NC132 and a lifetime prediction for NT154. The five orders of magnitude improvement in lifetime is a consequence of materials development programs conducted over the last 10 years. Lifetime improvement is largely a consequence of decreasing the creep rate of silicon nitride as a function of temperature. The newer materials are much more creep resistant than the old ones, and therefore have a greater life expectancy.

5. S.M. Wiederhorn, B.J. Hockey, D.C. Cranmer and R. Yeckley, "Transient Creep Behavior of Hot Isostatically Pressed Silicon Nitride," J. Mat. Sci., in press.

6. Tatstuki Ohji, "Long-Term Creep Testing of Silicon Nitride and Silicon Carbide," paper 6-JX-91, 93rd Annual Meeting of the American Ceramic Society, Cincinnati, OH April 29 to May 2, 1991.

7. R. Kossowsky, D.G. Miller and E.S. Diaz, "Tensile and Creep Strengths of Hot Pressed Si_3N_4." J. Mater. Sci., 10 983-97 (1975).

8. S.M. Wiederhorn, R. Krause and D.C. Cranmer, "Tensile Creep Testing of Structural Ceramics," Proceedings of the Annual Automotive Technology Development Contractors' Coordination Meeting, Dearborn, MI, October 28-31, 1991, Society of Automotive Engineers, Inc., 4007 Commonwealth Drive, Warrendale, PA 15096-0001, to be published

9. F.C. Monkman and N.J. Grant, "An Empirical Relationship between Rupture Life and Minimum Creep Rate in Creep-Rupture Tests," Proc. ASTM 56, 593-620 (1956).

10. Howard R. Voorhees, "Assessment and Use of Creep-Rupture Properties," pp. 329-342 in Metals Handbook Ninth Edition, Vol. 8, Mechanical Testing, American Society for Metals, Metals Park, OH 44073

11. D. C. Cranmer, B. J. Hockey, S. M. Wiederhorn and R. Yeckley, "Creep and Creep-Rupture of HIP-ed Si_3N_4," Ceram. and Eng. Sci. Proc. 12[9-10] 1862-1872 (1991)

3.5 NONDESTRUCTIVE EVALUATION DEVELOPMENT

Nondestructive Characterization
D. J. McGuire (Oak Ridge National Laboratory)

Objective/scope

The purpose of this program is to conduct nondestructive evaluation (NDE) development directed at identifying approaches for quantitative determination of conditions (including both properties and flaws) in ceramics that affect the structural performance. Those materials that have been seriously considered for application in advanced heat engines are all brittle materials whose fracture is affected by structural features whose dimensions are on the order of the dimensions of their microstructure. This work seeks to characterize those features using high-frequency ultrasonics and radiography to detect, size, and locate critical flaws and to measure nondestructively the elastic properties of the host material.

Technical progress

Ultrasonics - W. A. Simpson, Jr., and K. V. Cook

Using a new, 8-bit, commercial, high-speed digitizer that is capable of a 100-MHz real-time sampling rate and equivalent-time sampling rates up to 3200 MHz, we have examined the scattering of ultrasonic surface waves from very small, laser-drilled holes in silicon nitride. The features examined were 20-μm-diam, 20-μm-deep and 10-μm-diam, 10-μm-deep holes. Neither could be detected using our original 4-bit equipment. Both were detected and recorded with the new system. The smaller of these holes is only about 1/12 of a wavelength in both diameter and depth.

We now have two systems capable of performing synthetic aperture processing of ultrasonic ceramic data. The first is an in-house-designed system that uses a commercial, large-volume, ultrasonic tank running under the control of a local 386-based computer. The data are acquired from an equivalent-time sampling digital oscilloscope over an IEEE-488 bus. Although slow, this system can sample at any equivalent-time rate up to 1 GHz. The acquisition of data is completely automated; i.e., after the material parameters are entered from the keyboard, the computer moves the ultrasonic transducer to each sample point of the synthetic aperture, acquires the data from the digital oscilloscope, and stores the data on hard disk. The data are stored as 4-byte, floating-point numbers; thus, each sample point of the aperture results in a 2048-point record on disk (512 points per waveform).

The second system for implementing synthetic aperture processing was a concomitant of the commercial upgrade to our C-scan hardware. In addition to its C-scan and image analysis features, the new system is also capable of generating B-scan records of the scanned sample. In this mode, the full radio frequency (rf) waveform of the ultrasonic signal is digitized and stored for each point of the area scanned. Although the maximum digitizer rate in B-scan mode is 100 MHz, these data are well suited for synthetic aperture processing for frequencies up to 25 MHz or so. A check with the vendor of this software indicated that later releases of the operating system will permit equivalent-time sampling at higher frequencies in the B-scan mode. Since the data are stored as two's complement

8-bit integers, a simple assembly language program was written to allow data generated by our in-house-designed system to be stored as files that can be accessed by the commercial system. In this way, effective sample rates as high as 1 GHz can be realized, while the image analysis capabilities of the commercial package can be used to examine the in-house-generated data.

The impetus driving this work is the physical limitation imposed by the high index of refraction of typical ceramics on the maximum inspection depth achievable by focused transducers. Using synthetic aperture techniques, the depth limitation is removed at the expense of signal-to-noise ratio for a single-point data record. Since records from several adjacent source points are coherently summed for a single field point, however, the flaw signal-to-noise ratio is correspondingly improved. The ultimate detection limit, of course, is set by the requirement that the signal from the target yield at least a single-unit change in the digitizer output at every point of the synthetic aperture.

Although we have previously tested our software for implementing synthetic aperture technology, the union of this programming and the commercial hardware and software allows us to display the results as an image. In Fig. 1, we show the calculated result

YP13634

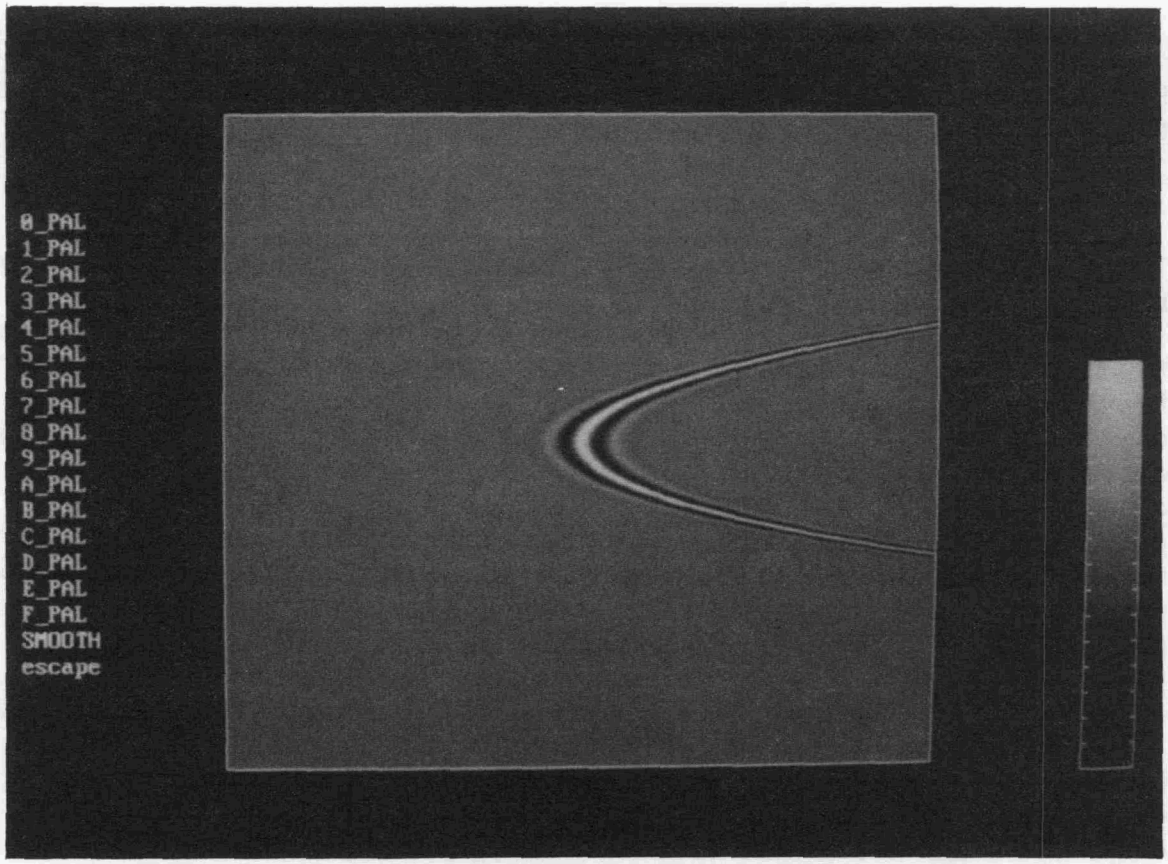

Fig. 1. Computed ultrasonic synthetic aperture response of a single point scatterer.

of the scattering of ultrasonic energy by a spherical radiator in a hypothetical ceramic. The energy is incident from the left, and the abscissa of the figure represents time. The ordinate denotes distance along the synthetic aperture, and the ultrasonic transducer is assumed to be focused at the surface of the sample. The gray scale at the right of the figure defines the intensity of the ultrasonic wave. The most obvious feature of the scattering pattern is the parabolic shape of the signal delay as a function of transducer position. This is easily understood from analysis of the phase of the scattered wave. Let the flaw depth be denoted by d, the wave vector of the ultrasonic energy by k, and the transducer position, referenced to the point on the surface directly above the flaw, by x. The amplitude of the scattered signal in the far field of the scattering center will vary as:

$$\Phi(x) = A(x)e^{ikr}/r \,, \tag{1}$$

where A(x) is a factor that takes into account the directional properties of the incident beam, and r is the transducer focal point-to-flaw distance. But r is given by:

$$r = (d^2 + x^2)^{1/2} \,. \tag{2}$$

Expanding the square root and retaining only the first terms:

$$r \sim d[1 + \tfrac{1}{2}(x/d)^2] \,. \tag{3}$$

Referencing the phase (or signal delay) to that when the transducer is directly over the flaw (x = 0), the phase of the scattered wave is:

$$\phi(x) = \exp(ikx^2/2d) \,. \tag{4}$$

The phase (delay) thus varies quadratically over the synthetic aperture. This characteristic is used to "focus" the synthetic array.

The expression above for the phase variation over the synthetic aperture indicates that the result depends on the flaw depth as well as the transducer position. Since the flaw depth will not, in general, be known *a priori*, the acquired data are processed for each depth, in effect "focusing" the synthetic aperture at that depth. When the actual flaw depth does not correspond to the assumed flaw depth, the flaw signals do not add coherently, and very little or no indication is obtained for the flaw. When the assumed and actual depths correspond, however, the coherent summation yields a strong flaw indication. In this manner, one obtains an image of each depth plane within the sample even though the specimen is scanned only once. With sufficiently fast computer processing available, this advantage should more than compensate for the additional processing required by synthetic aperture techniques over real-time conventional approaches for which the sample must be rescanned for each depth plane to be imaged.

Figure 2 shows the result obtained by processing the data of Fig. 1 using the correct flaw depth. The result is a pronounced sharpening of the transverse (vertical direction in Fig. 2) resolution, locating the flaw very accurately in this direction. The longitudinal (horizontal) resolution is determined by the transducer bandwidth, which is relatively narrow in Fig. 2. It is obvious that the transverse resolution exceeds the longitudinal resolution considerably. For this case, in which true point source excitation

YP13635

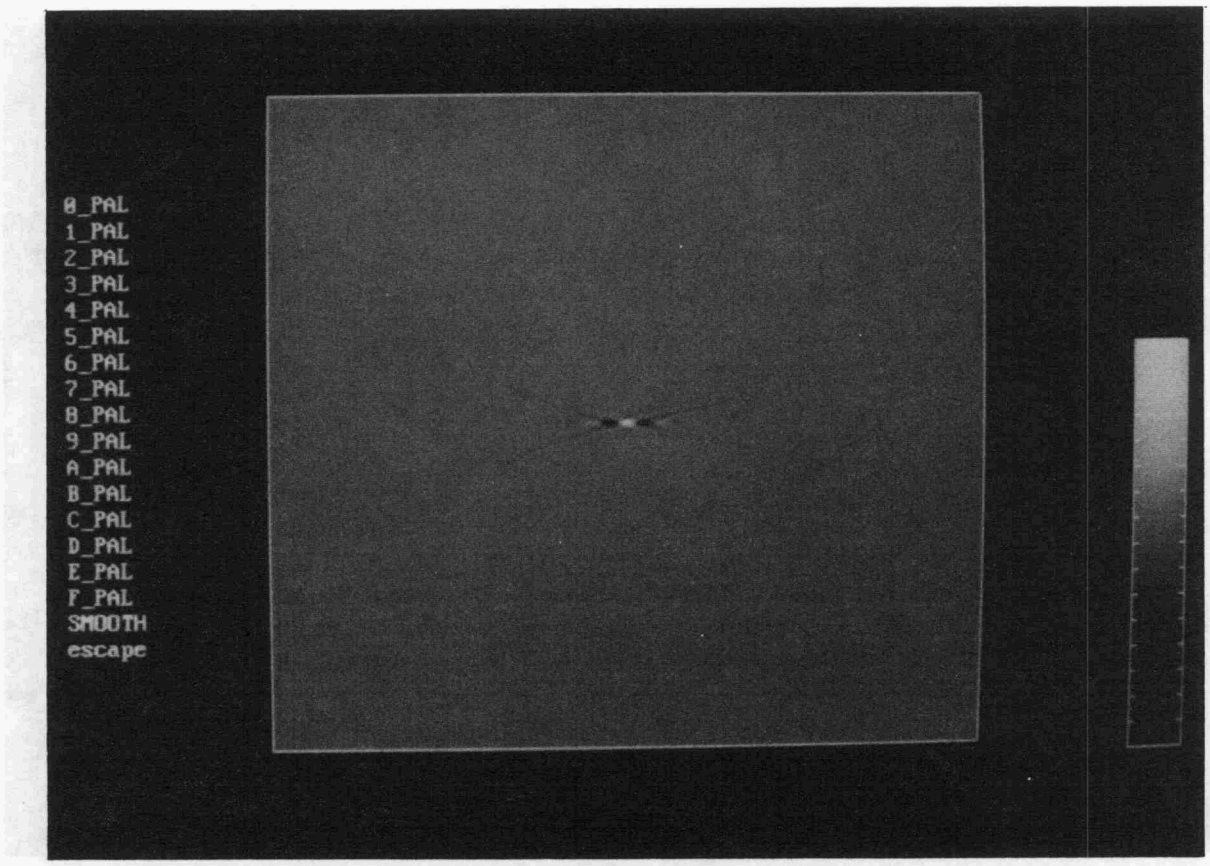

Fig. 2. Processed ultrasonic synthetic aperture data showing detection of a single point defect.

was assumed, the former value agrees extremely well with the calculated result based on the synthetic aperture dimension.

The data of Figs. 1 and 2 were obtained by a linear (i.e., a one-dimensional) synthetic array. In practice, however, we generate a two-dimensional synthetic aperture. The resulting processed image is a three-dimensional view of the flaw distribution throughout the sample volume. This image cannot be displayed with our current in-house or commercial software; accordingly, we are writing software to display the results as a pseudo three-dimensional image on a graphics terminal.

Figure 3 shows the calculated response of two spherical scatterers separated by the Rayleigh criterion. The raw data suggest multiple scatterers, but no information regarding their separation can be determined from the figure. In Fig. 4, however, the raw data have been processed for the appropriate flaw depth and the contrast enhanced until only the peaks of the scattered signals can be seen. The result indicates two closely spaced but clearly resolved point sources. Their separation appears to be greater than the Rayleigh criterion only because of the suppression of the low-amplitude wings of the "spot" size of the synthetic array.

YP13638

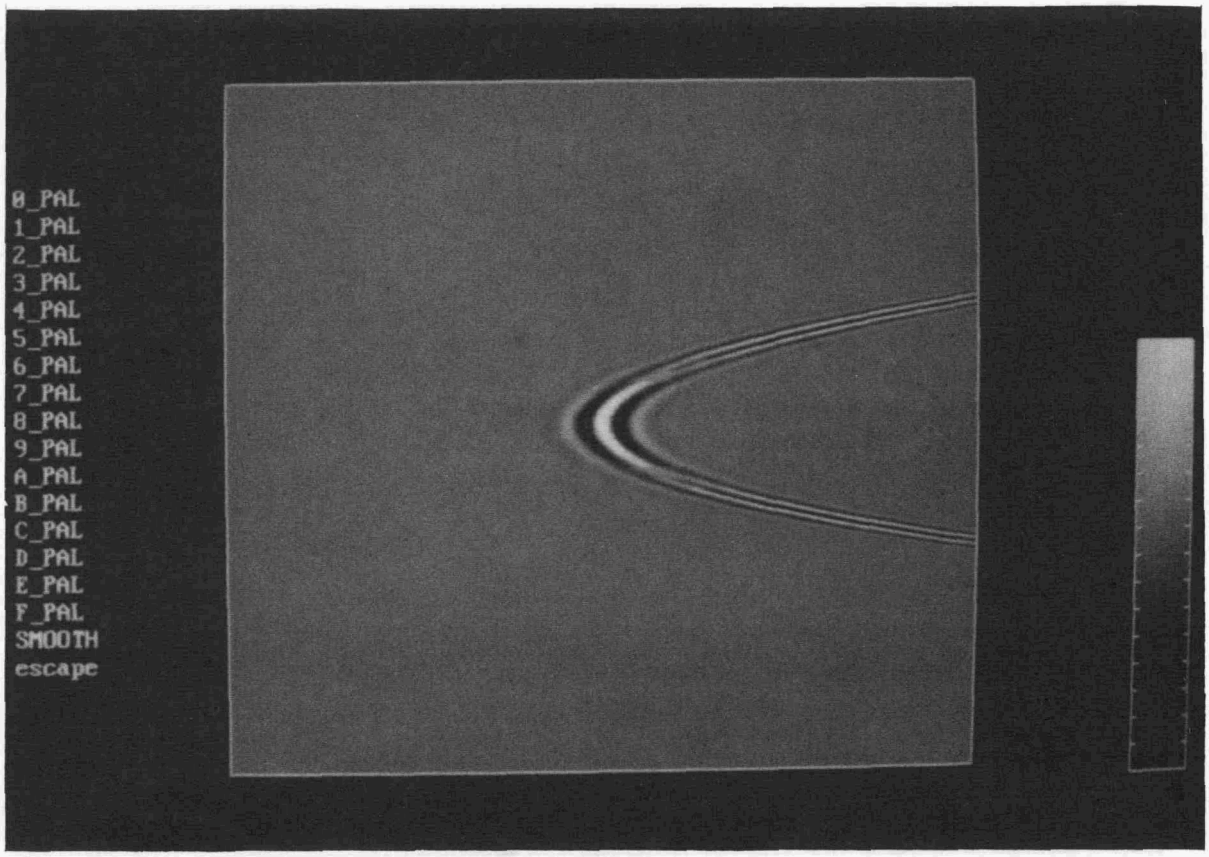

Fig. 3. Computed ultrasonic synthetic aperture response of two point scatterers separated by the Rayleigh criterion.

In the last equation above, we gave the expression for the phase delay produced over a one-dimensional synthetic aperture. For a two-dimensional aperture, the relationship becomes:

$$\phi(x,y) = \exp[ik(x^2 + y^2)/2d] \ , \tag{5}$$

where the position in the aperture is given by the pair x,y, referenced, as usual, to the point in the aperture directly over the flaw. For a two-dimensional scan, the signal-to-noise ratio will generally be larger (relative to a one-dimensional scan) since more points are coherently added for each image point. There is a complicated relationship between the coordinates of a particular point in the synthetic aperture and the data record numbers of the adjacent points to be summed, and this relationship requires very disk-intensive processing of the acquired data. Even using random access data files, most of the processing time is spent simply retrieving data from disks.

In describing synthetic aperture systems, many authors have stated that a desirable goal is to use a transducer capable of producing full 2π solid-angle illumination within the sample so as to maximize the aperture over which a given flaw can be detected. This

YP13640

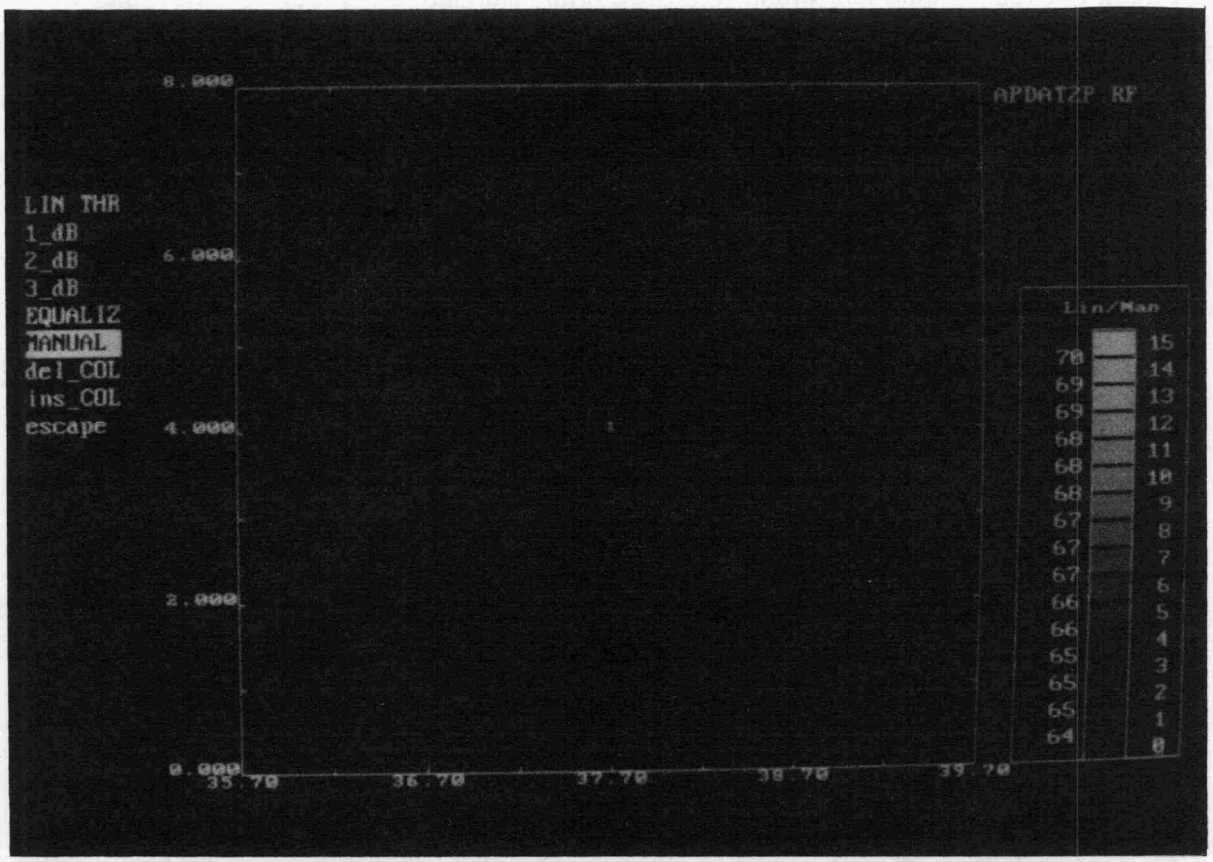

Fig. 4. Contrast-enhanced display of processed synthetic aperture data showing precise location of two point sources.

conclusion is not only wrong; it yields unnecessarily small, single-point, signal-to-noise ratios. Busse[1] et al. have shown that there is an optimum aperture for any given transducer and flaw depth and that the best transducer choice is that which produces a cone of insonification at the flaw as nearly equal in area to this aperture as possible. A larger cone of insonification reduces the signal-to-noise ratio, and a larger aperture extends the processing time with no attendant increase in resolution. The optimum aperture for a given flaw depth is:

$$L = d/(2.44\eta F) , \tag{6}$$

where d is the flaw depth, η is the ratio of the ultrasonic wavelengths in water and the ceramic, and F is the transducer f-ratio. As the latter quantity increases, the optimum synthetic aperture and the maximum aperture available with the given transducer become more nearly equal. Thus, for large flaw depths, a high f-ratio transducer becomes desirable. Unfortunately, for high-frequency ceramics evaluation, this situation is untenable because of higher losses in the water column for long-focus transducers. A

tradeoff between transducer f-ratio and solid-angle illumination is therefore necessary, especially in high-index ceramics such as alumina, silicon nitride, and silicon carbide.

In addition to computed results, we have also acquired and processed experimental synthetic aperture data from flaw standards in aluminum and zirconia. Figure 5 shows the data obtained from a round-bottomed, drilled hole in aluminum. This is a high-frequency scan that was deliberately over-sampled spatially to show the quadratic phase delay predicted by the fourth equation above. The arc in the left-hand third of the figure is the signal scattered from the tip of the hole (the ultrasound is incident from the left). The vertical lines in the right-hand third of the figure are caused by the back-surface reflection. Note the loss of the back-surface signal in the area directly under the flaw. The two arcs to the right of the back-surface indication are signals scattered from the sides of the hole and would not be present for a real flaw.

The data shown in Fig. 5 were acquired at too low a temporal sampling rate (100 MHz) for accurate synthetic aperture processing. (A new version of the software, scheduled for release in the near future, will permit equivalent-time sampling at rates up to 3200 MHz. In the meantime, we have the capability of acquiring the data at rates up to

YP13372

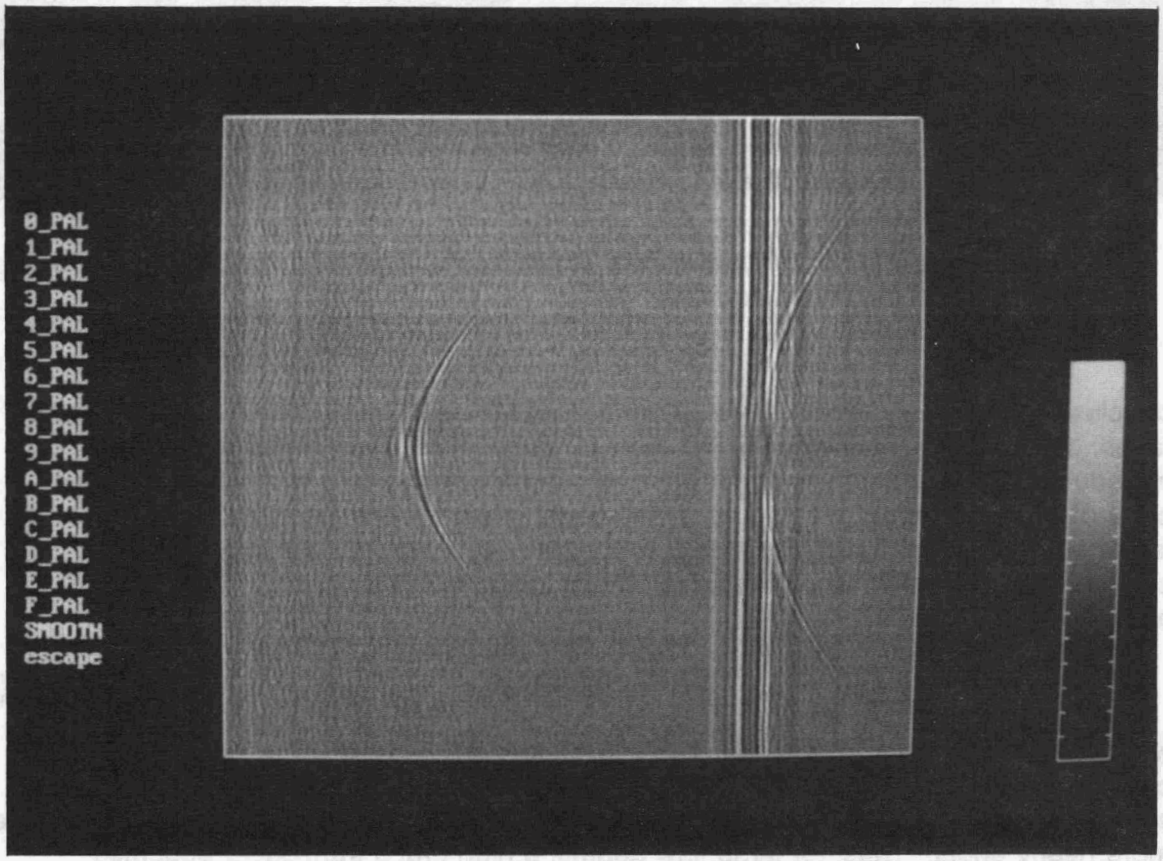

Fig. 5. High-frequency ultrasonic synthetic aperture scan of a flaw standard in aluminum.

1 GHz in our in-house-designed system and importing the files into the commercial system). Accordingly, data were acquired at a lower frequency on the same target and with a spatial sampling interval approximately optimum for the given flaw. The processed results are shown in Fig. 6. The bright spot in the center is the synthetic aperture image of the tip of the drilled hole. The image is approximately two wavelengths in diameter.

In order to minimize the effect of a high index of refraction on synthetic aperture performance, we have been examining flaw standards in zirconia, whose elastic wave refraction index is intermediate between that of metals and alumina. In addition, all of our standards contained numerous natural flaws (voids), as well as the fabricated ones, and provided an excellent opportunity to evaluate the synthetic aperture approach on real flaws. The chosen standard contained a 200-μm drilled hole whose bottom was located about 3 mm from the reverse (beam-entry) surface. A 25-MHz, 25-mm, focused transducer was used to scan the sample, and the transducer, which is an f/4 unit, was focused at the sample surface. The relatively low frequency was necessitated by the maximum 100-MHz sample rate of the on-board digitizer when operating in the synthetic

YP13969

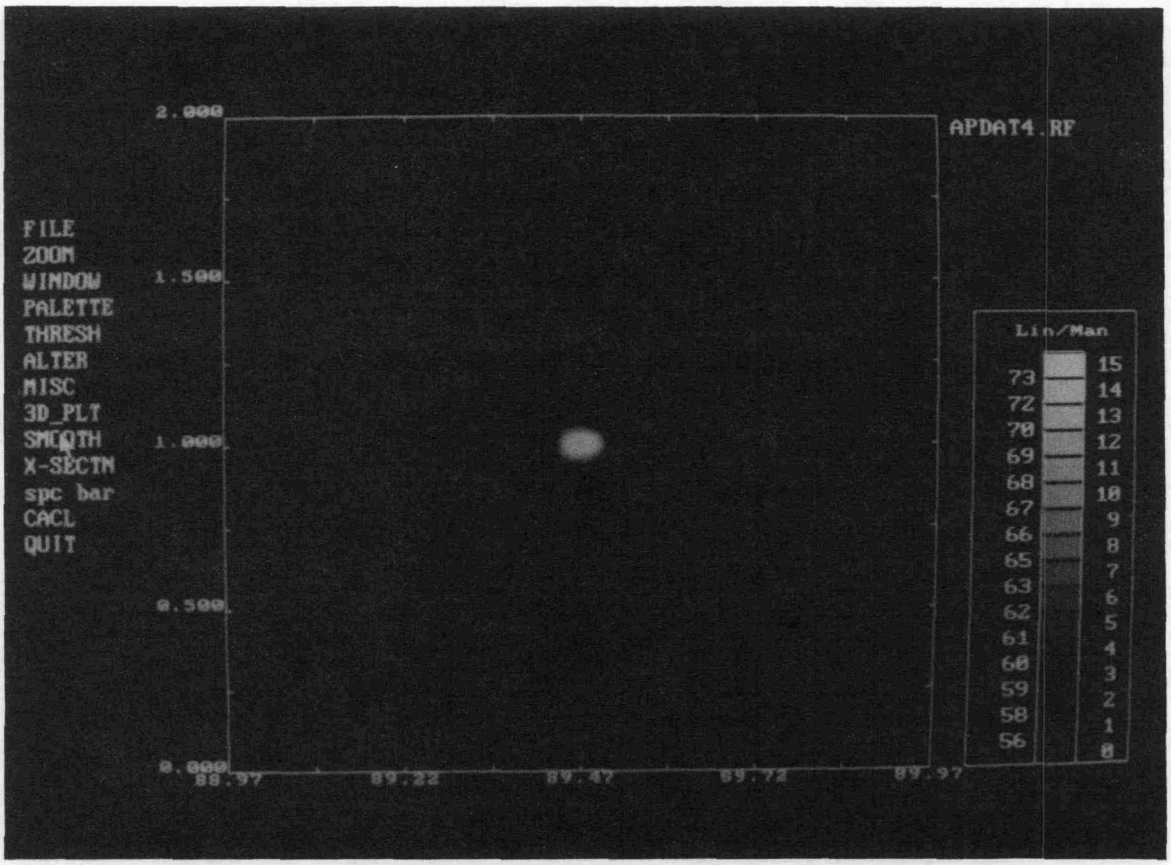

Fig. 6. Ultrasonic synthetic aperture image of a flaw standard in aluminum.

aperture mode. Although it satisfies the Nyquist criterion, this sample rate is a bit low for a purely time-domain technique.

Figure 7 shows the result of an unprocessed synthetic aperture scan of the 200-μm flaw. The vertical bars in the right half of the figure are the oscillations produced by the highly saturated back-surface indication. The characteristic parabolic arc caused by the flaw can be seen just to the left of center. Similar, fainter arcs caused by natural flaws in the 50 to 100-μm range can be seen throughout the left half of the figure. These data were acquired using the optimum spatial and maximum temporal sampling rates.

Figure 8 shows the result obtained after the data of Fig. 7 were processed with our synthetic aperture algorithm and contrast enhanced. The arrow indicates the 200-μm flaw. Several other pointlike indications were noted before the contrast was enhanced to suppress all but the 200-μm flaw response. As expected, only those indications which lay in or near the plane of the standard survived, however.

We continued to extend the synthetic aperture techniques to nonplanar geometries. Only minimal changes to the software will be necessary to implement the approach for

YP14337

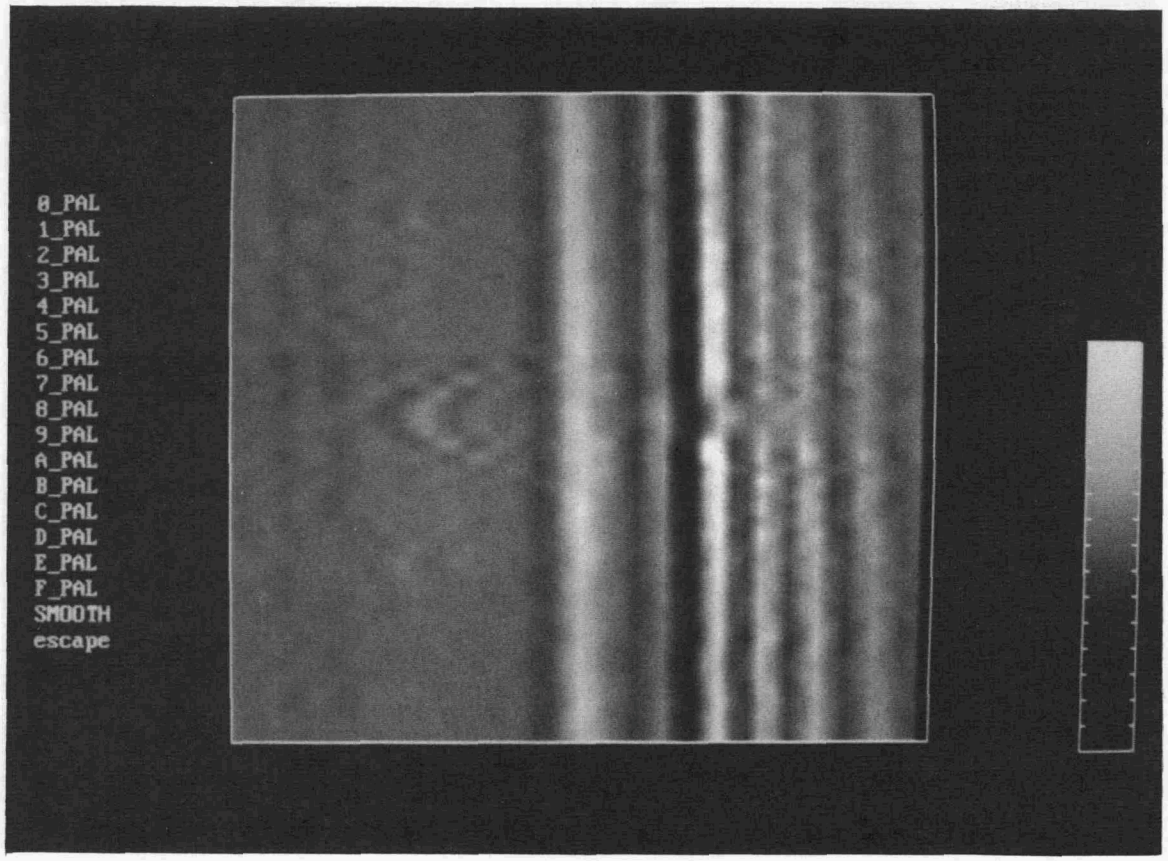

Fig. 7. Synthetic aperture scan showing characteristic parabolic arc response of a 200-μm flaw in zirconia.

YP14338

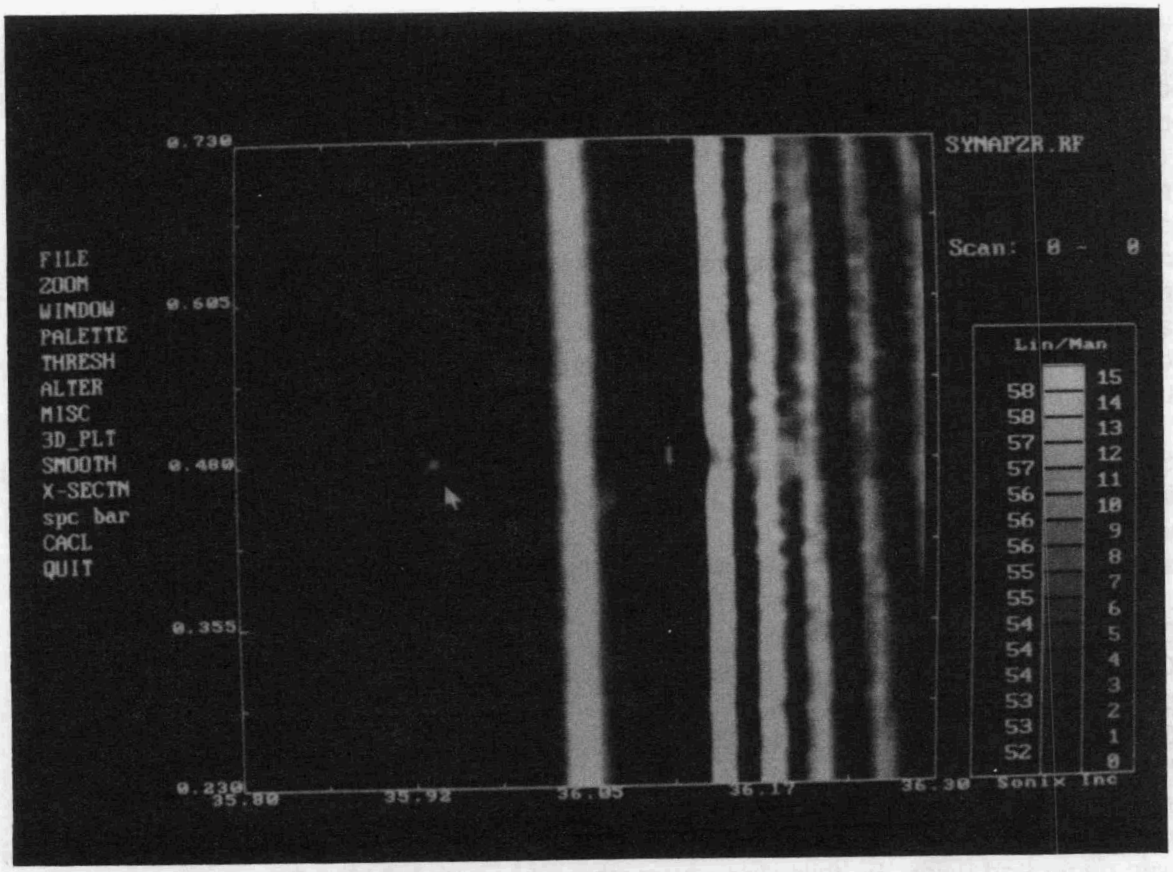

Fig. 8. Processed synthetic aperture scan showing image of 200-μm flaw (arrow) in zirconia.

cylindrical specimens, but considerable hardware development is required since none of our inspection systems possess a turntable. We are examining several designs for adding this capability, or its equivalent, to our existing hardware.

Computed Tomography (CT) - B. E. Foster

The manufacturer, Scientific Measurement Systems (SMS), of our CT system held a Users Conference in Austin, Texas, on October 2-4, 1991. There were approximately 20 attendees from 10 different system owners/users. The morning of the first day was used by SMS personnel for presentations on the current user base and future capability of their CT systems. The afternoon consisted of round-table discussions between SMS and the users on the strengths and weaknesses of the system from a user's perspective. Short presentations by each user on their applications of CT filled the second day. I chaired one session (Future Requirements From Users) on the third day. In addition, we received a status report of new software enhancements, a demonstration of the new Sun-based workstation, and SMS's response to the issues from the round-table discussions.

The Sun-based workstation was shown to increase the display speed by some 5 to 10 times and reconstruction speeds (with four array processors) by about 8 times. Cost estimates for an upgrade to the Sun-based workstation will be on an individual basis. The conference was very beneficial, and the consensus was to schedule a user's conference biannually.

Later in the month, I received about ten days of very intensive training at SMS on novel scanning and reconstruction techniques with particular emphasis on system calibration and image-sharpening routines. We are apparently the only users with the need to scan a wide variety of sample sizes (4-mm to 15-cm diam) in the high-resolution mode, thus requiring very accurate (a few microns) image-sharpening and reconstruction algorithms. Prior to the recent training, it would take several days to accomplish system calibration when changing from a small- to large- diameter sample or vice versa. Now, the time element is considerably reduced.

Following the above training, I calibrated our system for scanning a multiple-hole Si_3N_4 tensile sample with hole diameters and respective depths ranging from 25 to 100 μm in the approximately 5-mm-thick gauge block portion. Four different 100-μm-diam holes were imaged in the high-resolution CT mode. Earlier scans of this sample had merely shown possible indications in the vicinity of the holes.

The system was recalibrated for the seven Si_3N_4 HIP'ed rotors (approximately 50-mm diam) that had been received for evaluation. These rotors were manufactured at ORNL as a part of the Cooperative Research and Development Agreement (CRADA) program with Garrett Ceramics. The identification of the rotors was as follows: 81490, 81490B, 112990, 12391, 20691, 22091, and 22091B. The local interest was primarily in the 15-mm-diam shaft of the rotor. Therefore, several CT slices were taken through the shaft-only region as well as the blades of each of the rotors. A digital radiograph was made of each rotor to accurately determine the location of each CT slice. Each CT image was generated using the following parameters: aperture 0.2 by 0.2 mm with a ray spacing of 0.07 mm, data accumulation time (zap time) at each position 0.01 s, and an energy of 420 kVcp with an intensity of 3 mA. In general, the samples showed surface-type bubbles (2- to 4-mm diam) on the blades and voids (0.2- to 0.5-mm diam) in the internal portion of the shaft.

A digital radiograph of the shaft portion of rotor 112990 (one of the first rotors made) is shown in Fig. 9 (YP13544). The numbers 72.9 and 75.2 to the right side of the shaft image denote the location of the CT slices as referenced from the top of the blades. The darker, linear-type areas that can be seen in the shaft region are better identifiable in the CT slices in Figs. 10 and 11. In Fig. 10 (YP13547), which is the CT slice at the 72.9 location, it clearly shows those linear-type areas to be cracklike indications. In Fig. 11 (YP13548), which is the CT slice at the 75.2 location (only 2.3 mm from the Fig. 10 location), it shows a significant increase in size and quantity of those cracklike indications. The CT slice through the blades shown in Fig. 12 (YP13546) is located 10 mm from Fig. 10, and 62 mm from the top of the blades, it shows a crack in one of the blades at the shaft junction. In addition, the surface bubbles on the blades that were previously mentioned are clearly evident. The doughnut-shaped, dark ring in the center is a reconstruction artifact resulting from the sharp edges and long attenuation paths through the blades.

A CT slice through the blades of one of the last rotors made is shown in Fig. 13 (YP13559). Note the absence of surface bubbles on the blades. Voids in the central portion of the hub are less than 0.5-mm diam. In Fig. 14 (YP13562), the voids detected in

YP13544

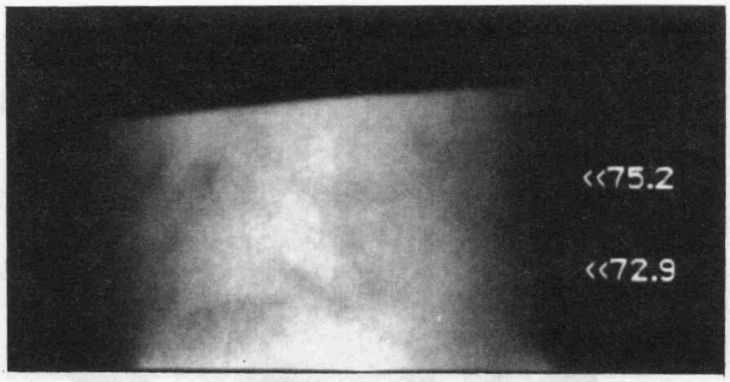

Fig. 9. Digital radiographic image of the shaft region of test 112990.

YP13547

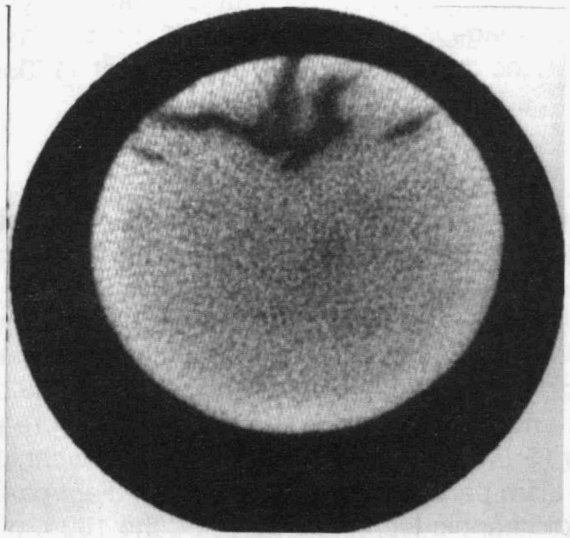

Fig. 10. Computed tomography image in the shaft region 72.9 mm from the top of the blades of test rotor 112990 showing crack-like indications.

YP13548

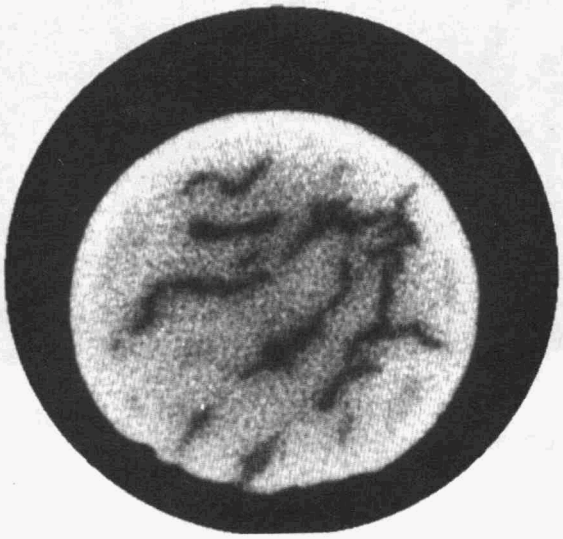

Fig. 11. Computed tomography image in the shaft region 75.2 mm from the top of the blades of test rotor 112990 showing crack-like indications.

the shaft are less than 0.25-mm diam. The darker area in the center is due to inadequate beam-hardening correction. Appropriate beam-hardening correction standards for these samples have been requested.

Three isopressed and HIPed Si_3N_4 MOR bars (3 × 4 × 50 mm), 10 smaller bars (1 × 2.5 × 18 mm), and three disks (2.5 by 33 mm), all impregnated with iron particles of diameters (25, 50, and 100 μm), have been received for evaluation with high-resolution film radiography and tomography. Two of the disks were impregnated with 100-μm particles and one with 25-μm particles. The tomographic technique was successful in detecting the 100-μm-diam particles but not the 25-μm-diam particles in the disks. The high-resolution film radiographic technique detected the 100 μm, and some of the 25-μm-diam particles in the disks. In addition, the 100-, 50-, and some of the 25-μm-diam particles were detected in the bars using the film radiographic technique. The bars are currently being evaluated with tomography.

It was anticipated that these samples might be used as standards; however, the CT slice of the disk containing the 100-μm iron particles showed the particles to be quite numerous and irregular in shape and size. The samples will not be suitable for use as standards; however, the data will be used to determine some benchmarks as to where improvements can be made in the detection sensitivity of discontinuities.

Four silicon-nitride spin disks (115 by 13 mm with a shaft 48 by 13 mm) have been received for inspection with both film radiography and tomography. These disks are part of those fabricated by GTE for Allison that had been rejected because of visible cracking on the surface. Film radiography shows numerous cracks through the 13-mm thickness. Some of the cracking, as detected with tomography, is throughout the 13-mm thickness.

YP13546

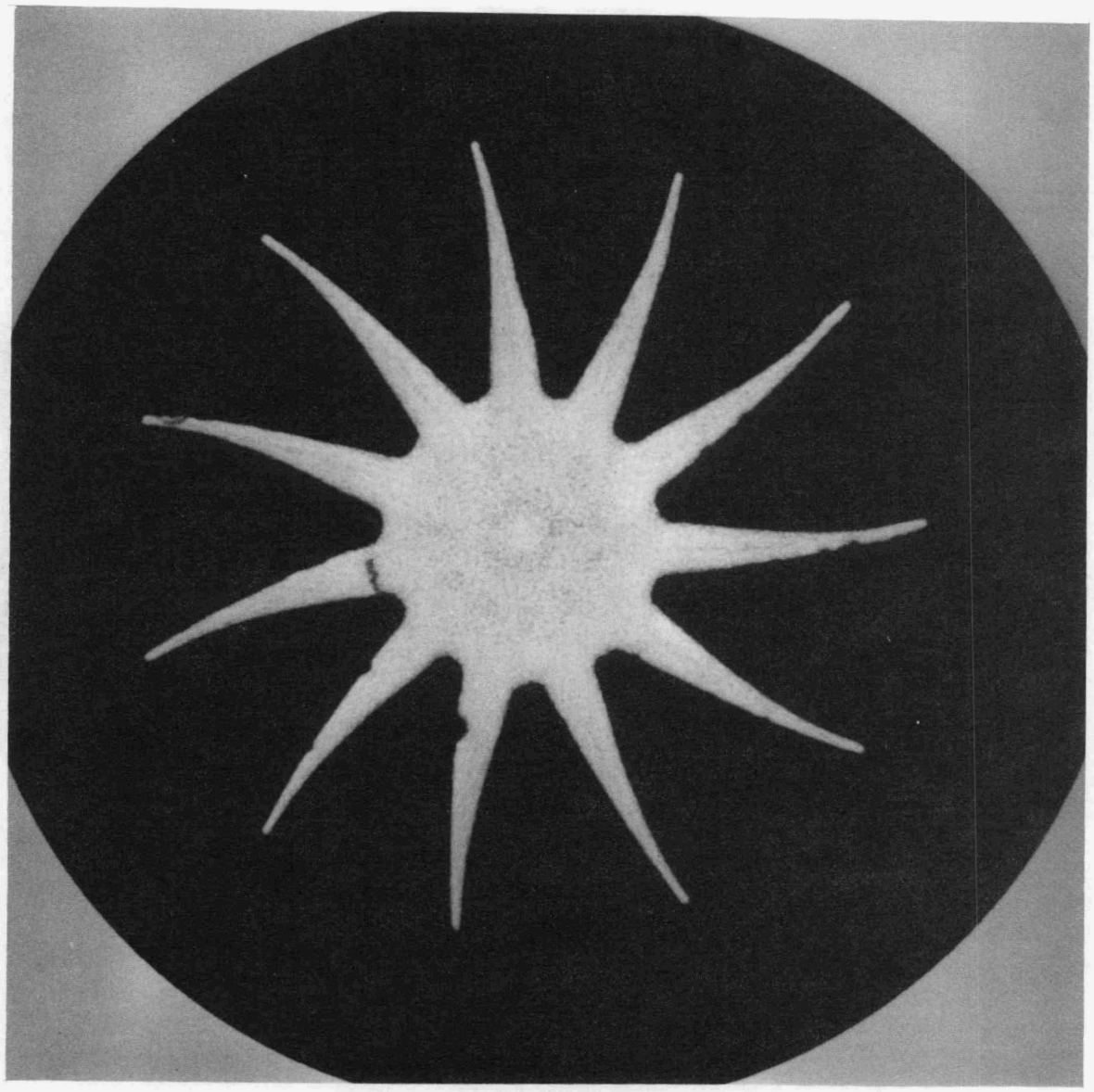

Fig. 12. Computed tomography image in the blade region 62 mm from the top of the blades of test rotor 112990.

YP13559

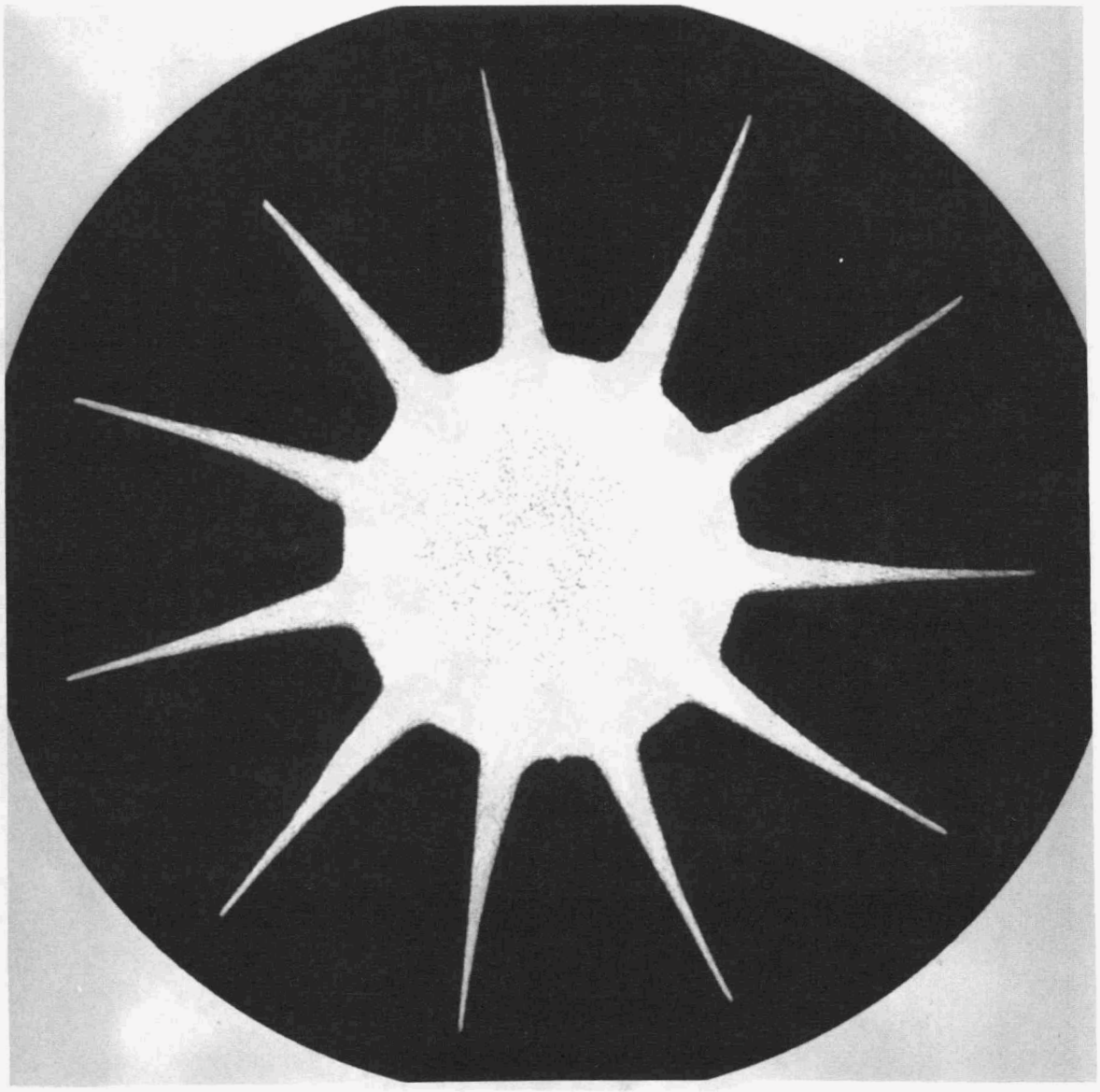

Fig. 13. Computed tomography image in the blade region 54 mm from the top of the blades of test rotor 20691.

YP13562

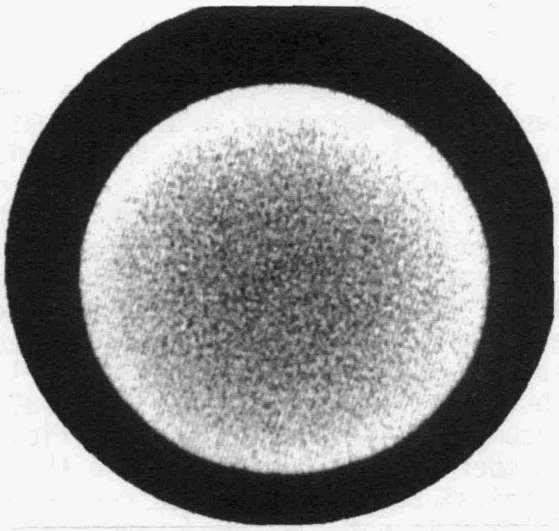

Fig. 14. Computed tomography image in the shaft region 73 mm from the top of the blades of test rotor 20691.

Milestones

On schedule.

Publications

W. A. Simpson, Jr., R. W. McClung, and D. R. Johnson, "Ultrasonic Tests for Advanced Structural Ceramics," pp. 506-13 in *Nondestructive Testing Handbook*, Vol. 7, Sect. 15, Part 1, American Society for Nondestructive Testing, Evanston, Ill., 1991.

References

1. L. J. Busse, H. D. Collins, and S. R. Doctor, *Review and Discussion of the Development of Synthetic Aperture Focusing Technique for Ultrasonic Testing (SAFT-UT)*, NUREG/CR-3625, U.S. Nuclear Regulatory Commission, Washington, D.C., March 1984.

NDE Standards for Advanced Ceramics

R. W. McClung (Oak Ridge National Laboratory)

The development of standards is important for the establishment of reliability and acceptance of advanced structural materials. Committee C-28, on Advanced Ceramics, is organized in the American Society for Testing and Materials (ASTM) to address this issue. One of the activities of the C-28 committee is nondestructive examination (NDE). The Task Group on NDE is reviewing existing standards on NDE (primarily developed for metals) to determine potential applicability for ceramics as well as preparing original standards. Use of existing or modified standards is more efficient than generation of new documents and will ensure the input of a large body of NDE expertise. Close liaison is established with ASTM Committee E-7 on Nondestructive Testing, and documents are in various stages of review, recommendations for change modification, and balloting. R. W. McClung is a member of both committees and the official liaison.

Liaison and technical support have been continued between ASTM Committees C-28 and E-7. To date, 31 NDE standards have been reviewed in detail with recommendations made to E-7 for modifications to identified documents. Successful action is complete on 14 documents, E-7 balloting action is in progress on 6 items, and the others require action by C-28. A table of ultrasonic velocities in typical ceramic materials prepared by C-28 and submitted to E-7 for incorporation in an existing NDE standard had a successful E-7 subcommittee ballot and committee and Society ballot. A document on fabrication of seeded voids in pressureless-sintered ceramics balloted in C-28 at the subcommittee level was revised for a concurrent ballot at both committee and subcommittee levels. The document, now designated C-1212, also passed the Society ballot. At the E-7 meeting in February 1992, appropriate contacts were made to ensure ongoing activity in response to C-28 requests on documents on radiography, ultrasonics, and liquid penetrants. Plans are being made in C-28 for potential procedures for (1) fabricating reference specimens containing seeded inclusions and laser-drilled holes and (2) measurements of porosity in ceramics using ultrasonic velocity. Toward development of "radiographic equivalence factors," a list was made of recommended materials to be sought in various thicknesses for initial studies. Suggestions included Al_2O_3, SiC, and three compositions of Si_3N_4 varying in additives (between 4 and 12%). A new subcommittee (C-28.07) on composites has been formed. The Task Group on NDE has been asked to provide technical support.

X-ray Computed Tomographic Imaging – W. A. Ellingson, D. L. Holloway, J. Ling (Argonne National Laboratory) H. C. Yeh and J. P. Pollinger, (Garrett Ceramic Components of Allied-Signal Aerospace Corporation)

Objective/scope

The objective of this program is to develop X–ray computed tomographic (CT) imaging technology for application to structural ceramic materials. This technique has the potential for mapping short–range (<5 mm) and long–range (>5 mm) density variations (to perhaps 0.5–1%), detecting and sizing high– and low–density inclusions, and detecting and sizing (within limits) cracks in green–state and densified ceramics. Use of 3-D CT (volume CT) imaging allows the capability of interrogating the full volume of a component and is noncontacting. It is also relatively insensitive to part shape and thus can be used to inspect components with complex shapes, such as turbocharger rotors, rotor shrouds, and large individual turbine blades.

Technical progress

The work this reporting period covers application work relative to X-ray computed tomography using Argonne National Laboratories 3-D microfocus system on phase III of this research program relative to detection of whisker distributions (likely to be manifested and detected as density variations) in as-cast pressure slip-cast SiC(w)/Si_3N_4 (Garrett's GN-10 material). This a continuing joint project between Argonne National Laboratory and Garrett Ceramic Components of Allied-Signal Aerospace Corporation of Torrance, California.

We have all of the specimens of SiC(w)/Si_3N_4 billets (length/diameter ratio = 1.5 and 2.5) made by pressure slip-casting.

In all cases the casting pressure was 40 psi and the mold type was plaster of paris. The configuration of the casting is shown in Fig. 1. Note that the dewatering was in 2 directions: radially and axially (bottom only).

The microfocus X-ray CT scanner data were acquired using 339 projections, 259 x 259 reconstruction, with pixel sizes of 141.5 mm in the X and Y direction and a slice thickness of 2 mm. The X-ray data were 125 KVp at .15 ma. We changed the data acquisition methods to better account for CCD camera/image intensifier dark current and to better adjust for center of rotation. In addition, this period we added remotely controlled shutters to restrict image intensifier exposure region.

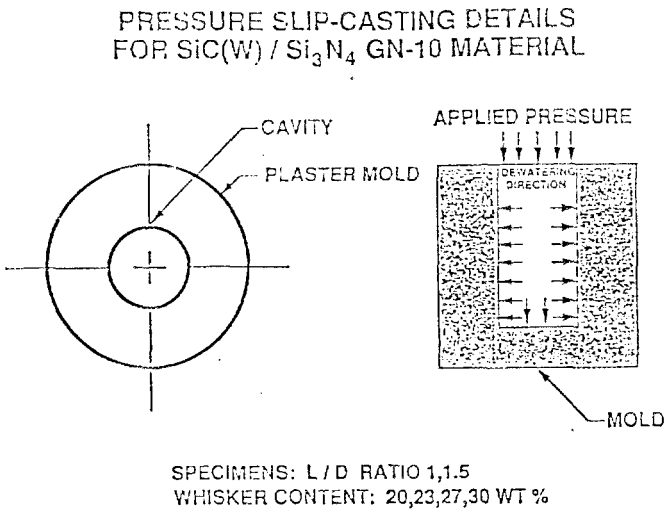

Fig. 1. Schematic diagram of dewatering/mold configuration for pressure-slip-cast SiC(w)/Si_3N_4 GN-10 ceramic materials

The casting data for the two sets of specimens is given below in Table 1.

Table 1. Casting data

	Billett Identification	Whisker Content Wt.%	Slip Solids Content wt.%	Slip viscosity cps	Bulk density at demolding g/cc
	91A-013	20	69.8	135	2.07
SET 1	S-910002	23	68	93	2.47
L/D = 1.5	S-910362	27	65	105	2.15
	S-910373	30	63	362	2.30
	S920030-2	20	69.8	191	1.09
SET 2	S920033-2	23	68	167	1.04
L/D = 2.67	S920042-1	27	65	96	1.79
	S920048-2	30	63	136	1.67

The comparison between destructive analysis and nondestructive analysis was done on specimen L/D = 1.5 of 27 and 30 wt.% whiskers. At each of three axial positions, L/4, L/2 and 3L/4, X-ray computed tomographic image data (in the form of an image gray scale) was obtained at four azimuthal positions, 0, 90°, 180 and 270°. At each azimuthal position, the center and five 2 mm X 2 mm regions, contiguous and radially directed were measured. The 0° degree data are the data which should agree with the destructive data. We noted the angular (azimuthal) orientation by scribing marks on the cylinder walls. These <1 mm deep grooves are easily detected by the X-ray CT scanner images and are readily visible for destructive correlation orientation.

The comparison between the destructive data and the nondestructive X-ray CT data are shown in Fig. 2–4 for the 27 wt.% whiskers and Figs. 5–7 for the 30 wt.% whisker specimens.

Several observations are clear; (1) the higher the maximum gray scale, the higher was the actual measured density. (2) measurable gray scale differences, (≈1%) corresponds in general to ≈0.5% change in measured density, (3) although the absolute point to point comparison has some experimental error, the rate of change in density is mapped almost exactly by the X-ray CT image data, (4) the radial variation in density at any given azimuthal position is very low and (5) the center of the cylinder is about 25% less dense than the outside in both cases.

Because of budget limitations, the 20 and 23 wt.% specimens of L/D = 1.5, and all of the L/D = 2.67 will be delayed. We hope to be able to complete these data analysis by the next semi-annual report.

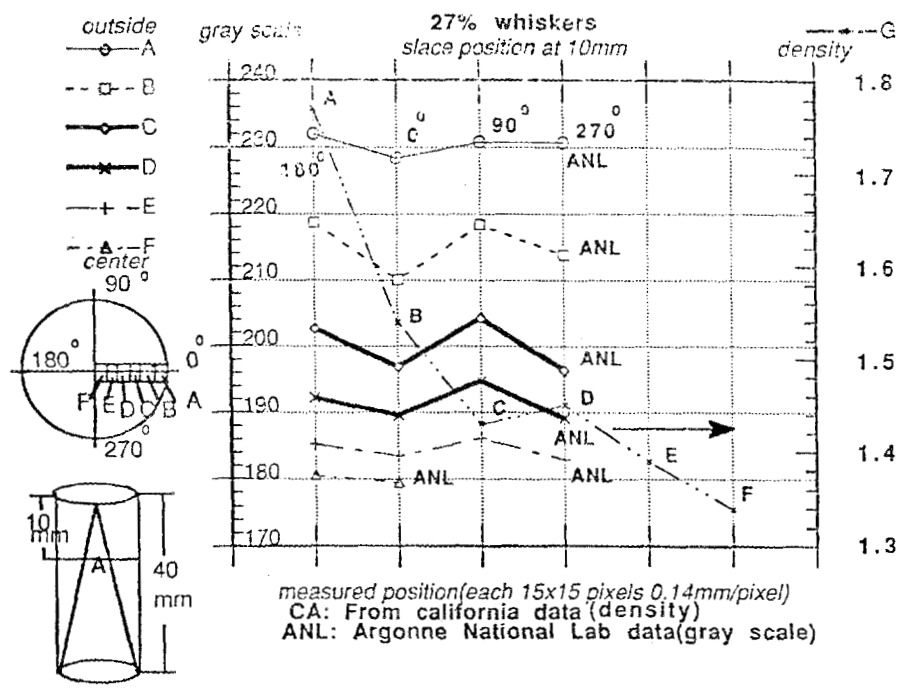

Fig. 2. Comparison between destructive density measurements and nondestructive density measurements on pressure slip-cast SiC(w)/Si_3N_4. State of ceramic was air-dried after slip-casting. Section A at L/4.

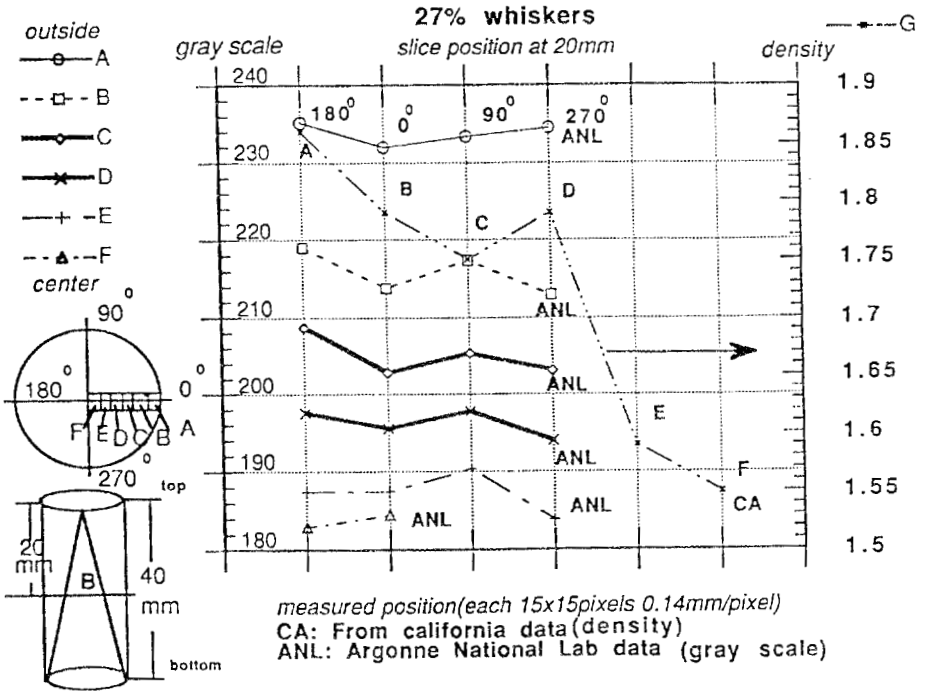

Fig. 3. Comparison between destructive density measurements and nondestructive density measurements on pressure slip-cast $SiC(w)/Si_3N_4$. State of ceramic was air-dried after slip-casting. Section B at L/2.

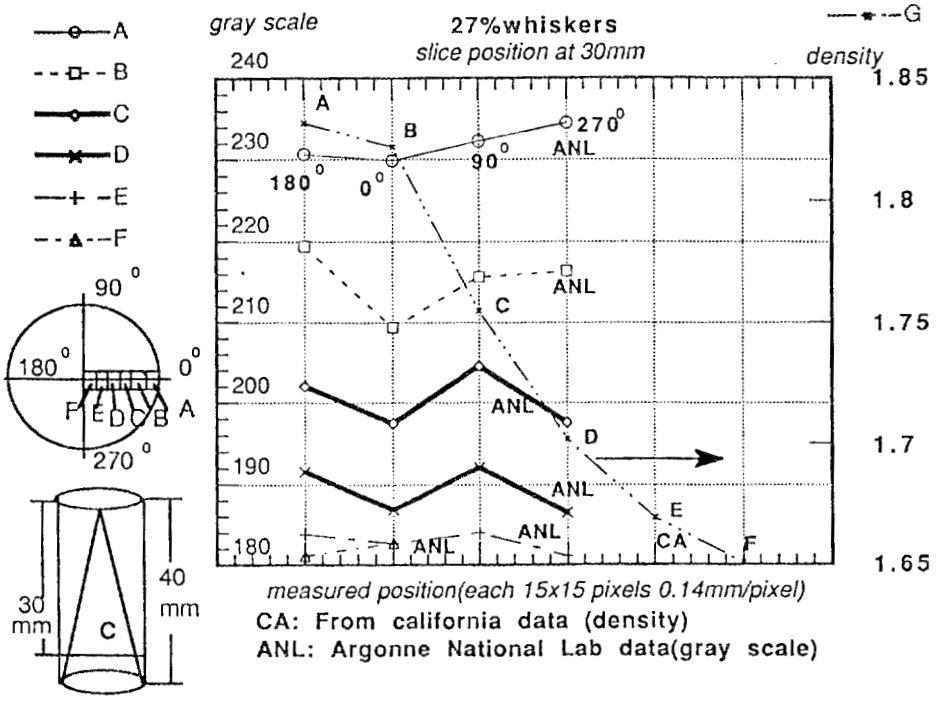

Fig. 4. Comparison between destructive density measurements and nondestructive density measurements on pressure slip-cast $SiC(w)/Si_3N_4$. State of ceramic was air-dried after slip-casting. Section C at 3L/4.

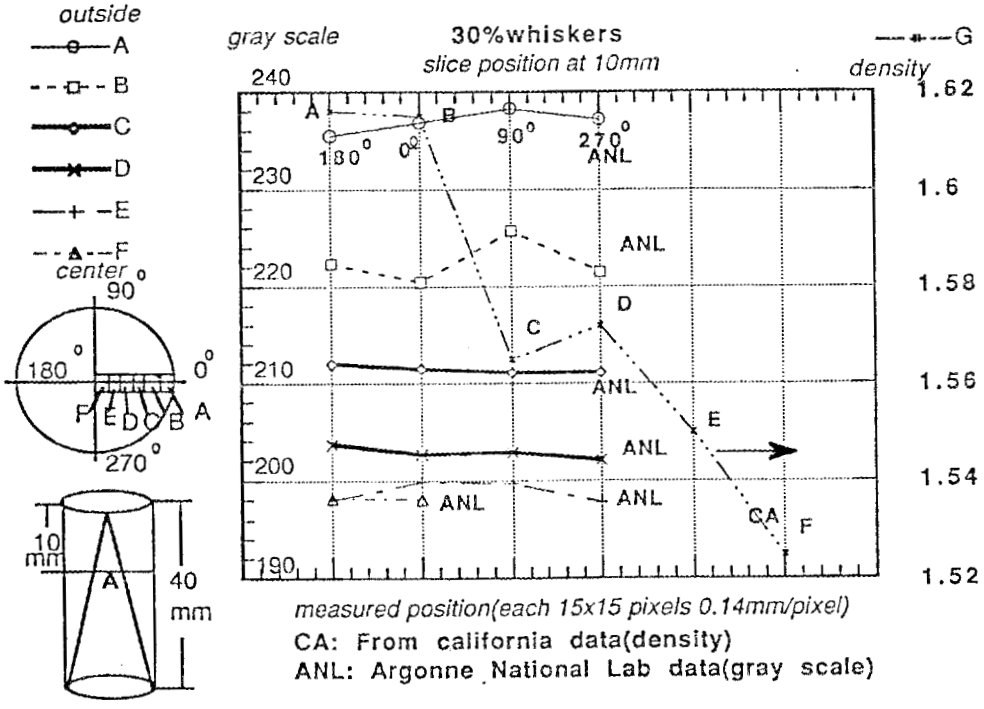

Fig. 5. 30 volume percent whiskers. Comparison between destructive density measurements and nondestructive density measurements on pressure slip-cast SiC(w)/Si_3N_4. State of ceramic was air-dried after slip-casting. Section A at L/4.

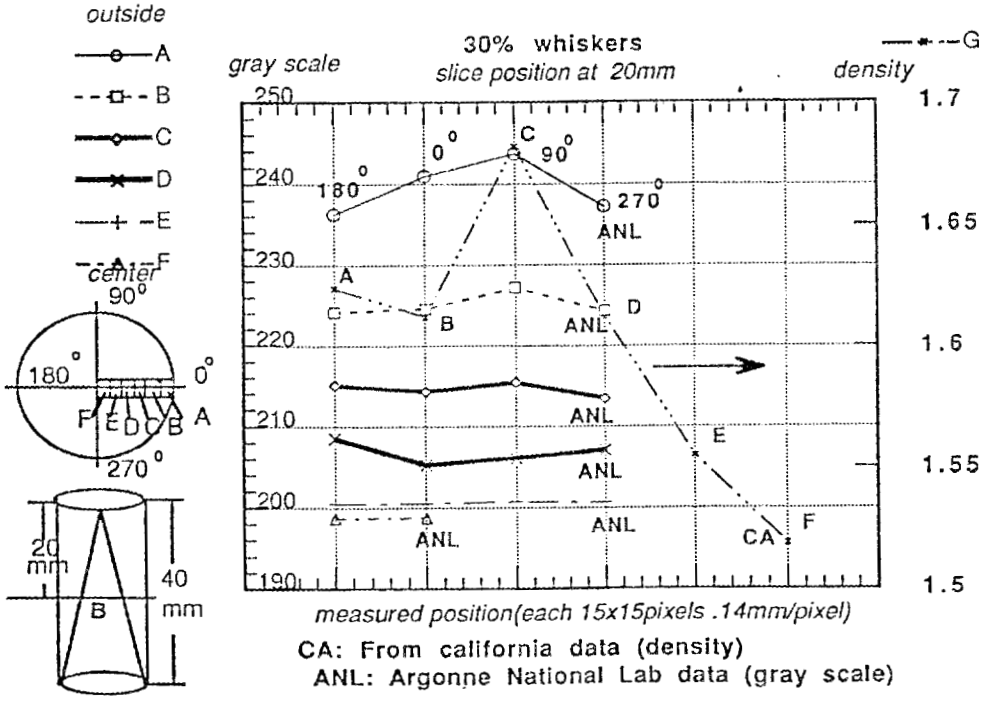

Fig. 6. 30 volume percent whiskers. Comparison between destructive density measurements and nondestructive density measurements on pressure slip-cast SiC(w)/Si_3N_4. State of ceramic was air-dried after slip-casting. Position at L/2.

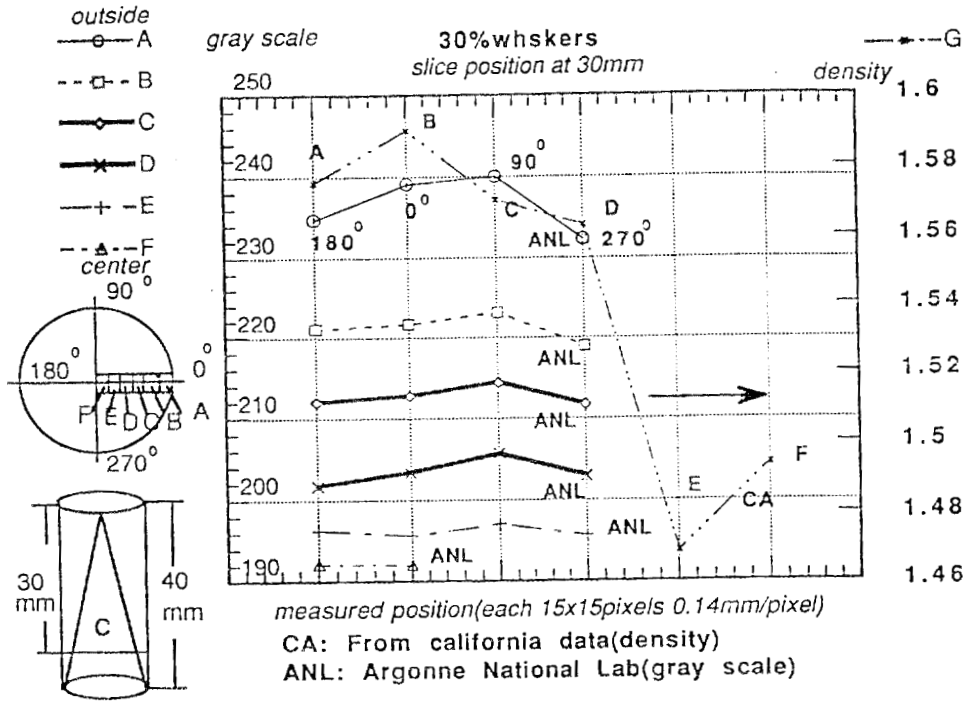

Fig. 7. 30 volume percent whiskers. Comparison between destructive density measurements and nondestructive density measurements on pressure slip-cast $SiC(w)/Si_3N_4$. State of ceramic was air-dried after slip-casting. Position at 3L/4.

Nuclear Magnetic Resonance Imaging – S. L. Dieckman
A. C. Raptis, W. A. Ellingson (Argonne National Laboratory),
and H. Yeh and J. P. Pollinger (Garrett Ceramic Components
of Allied-Signal Aerospace Corporation)

Objective/Scope

The objectives of this task are to: (1) utilize NMR imaging techniques to study the distribution of whiskers and other possible variations in composite pressure slip-cast green-state (as cast) billets; (2) conduct destructive analysis of the same billets (to be performed by Garrett Ceramic Components a Division of Allied Signal Corp.); (3) correlate the results obtained from the NMR imaging techniques with those obtained from both the 3-D X-ray and the optical microscopy.

Technical Highlights

Proton (H^1) NMR spectroscopic studies of the benzene-imbibed as-cast Si_3N_4/Si_3N_4 whisker-reinforced composites produced spectra which exhibited an unexpectedly wide benzene linewidth. This linewidth, which averaged 4 kHz, is roughly three orders of magnitude larger than linewidths acquired on homogeneous solution-state benzene specimens. Additionally, similar spectroscopic results were obtained on water-imbibed and methylene chloride-imbibed composite specimens. It was determined that the experimental linewidths observed in these heterogeneous systems are dominated by localized magnetic field inhomogeneities caused by large differences in the magnetic susceptibility of Si_3N_4 and the solution-state contrast medium. Since susceptibility induced line broadening can not be eliminated for a given substrate and solvent, it is necessary to design an imaging experiment which is capable of imaging under these conditions.

To this end, a three-dimensional (3D) NMR imaging technique based upon two phase encoding and one readout gradient was implemented, see Fig. 1. This method encodes the entire sample space by perturbing the net spin magnetization vector with the initial RF pulse, applying phase encoding magnetic field gradients in two spatial dimensions, then finally frequency encoding in the third dimension. In practice, the phase encoding gradients are varied in a step fashion (the dashes in Fig. 1) to map out the 3-D space with the appropriate sampling in phase space. Reconstructions are then often performed by applicating a complex 3-D FFT.

The 3-D phase encoding imaging methodology implemented here has several distinct advantages over other commonly employed 3-D imaging sequences. The advantages of particular interest for imaging of the benzene imbibed specimens described above are: (1) the ability to sample the 3-D space equally in all dimensions, and (2) the ability to acquire data shortly (< 0.5 ms) after initial excitation by the RF pulse. This is crucial in

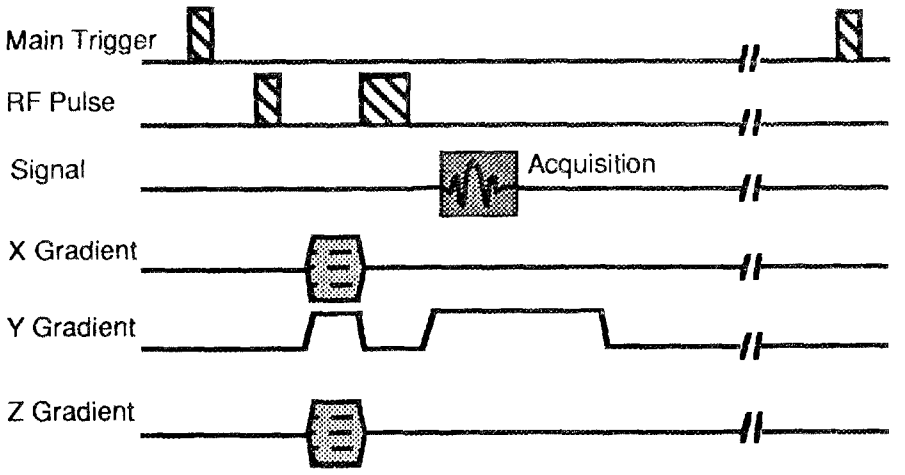

Fig. 1. Schematic drawing of the three-dimensional (dual phase encoding frequency encoding) pulse sequence employed in this study.

these studies given that the signal observed from the benzene in this heterogeneous mixture decays away rather quickly (~1.0 ms).

To facilitate reconstruction of the data sets, image reconstruction computer programs based upon 3-D FFTs were developed specifically for the NMR data sets. These programs incorporate a variety of share-ware and user written algorithms to insure versatility and portability among VMS and Unix platforms. Matrix size limitations (due to computer space limits) encountered in the development of these programs currently limited the reconstructions to 128^3 (16 Mega byte complex data). The image reconstructions require approximately 29 minutes of CPU time and approximately 10^8 page faults on ANL's local Vax 8700. Thus the overall reconstruction time of a 3-D 128^3 image is approximately 4 to 6 hours when the Vax is experiencing a normal work load. Significant time savings can however be realized if one is willing to settle for a 64 x 64 x 128 image. These programs will be ported to an IBM 6000 model 530 in the near future. It is expected that the reconstruction times will be cut by a factor of 12 to 15 on the IBM platform.

Using the above 3-D imaging methodology and reconstruction techniques, imaging studies were performed on benzene imbibed specimens containing 20 and 23 wt.% SiC fiber Si_3N_4 matrix composites. Transverse grey scale images of the 20 and 23 wt.% specimen along with plots of radially grey scale intensity across the image is shown in Fig. 2a - 3f and Fig. 3a - 3f, respectively. Similarly, longitudinal grey scale images of the 20 and 23 wt.% specimen along with plots of radially grey scale intensity across the image is shown in Fig. 4a - 4f and Fig. 5a – 5f, respectively. These image data sets were initially acquired and reconstructed with 1 mm resolution in each dimension. Subsequently, the images were spatially averaged to allow direct comparison to the destructive testing results which have a 2 mm minimal resolution limit.

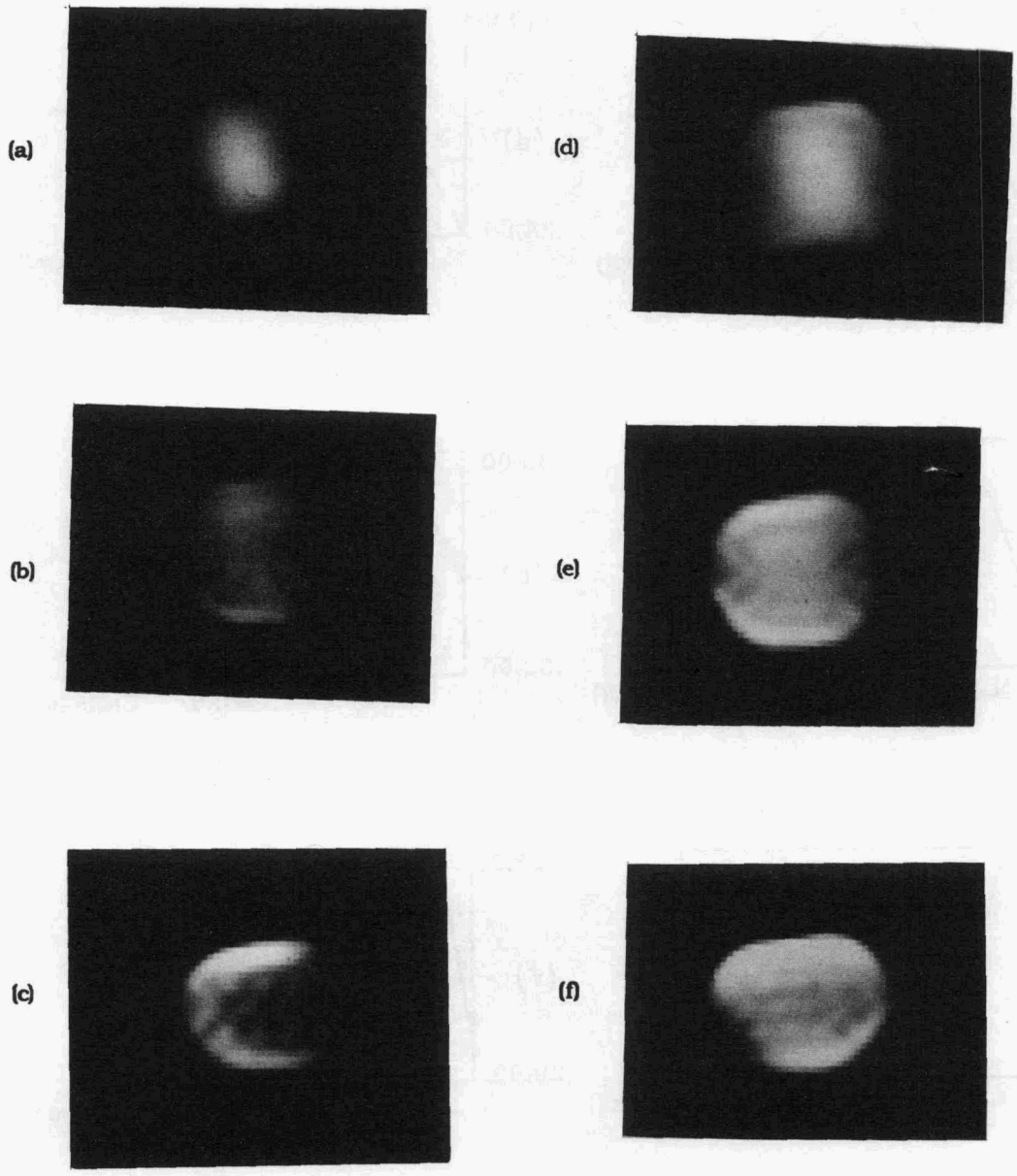

Fig. 2. Representative cross sectional thin views "slices" of three-dimensional NMR imaging data obtained on the 20 (Fig. 1a - 1c) and 23 (Fig.1d - 1f) wt.% whisker-reinforced, as-cast composite imbibed with benzene. Images were acquired, reconstructed and displayed with 1 mm resolution in all three dimensions. The photos displayed are of slices from the top (2 mm inside the specimen) (a&d), the exact specimen center (b&e) and 2 mm from the bottom of the specimen (c&f).

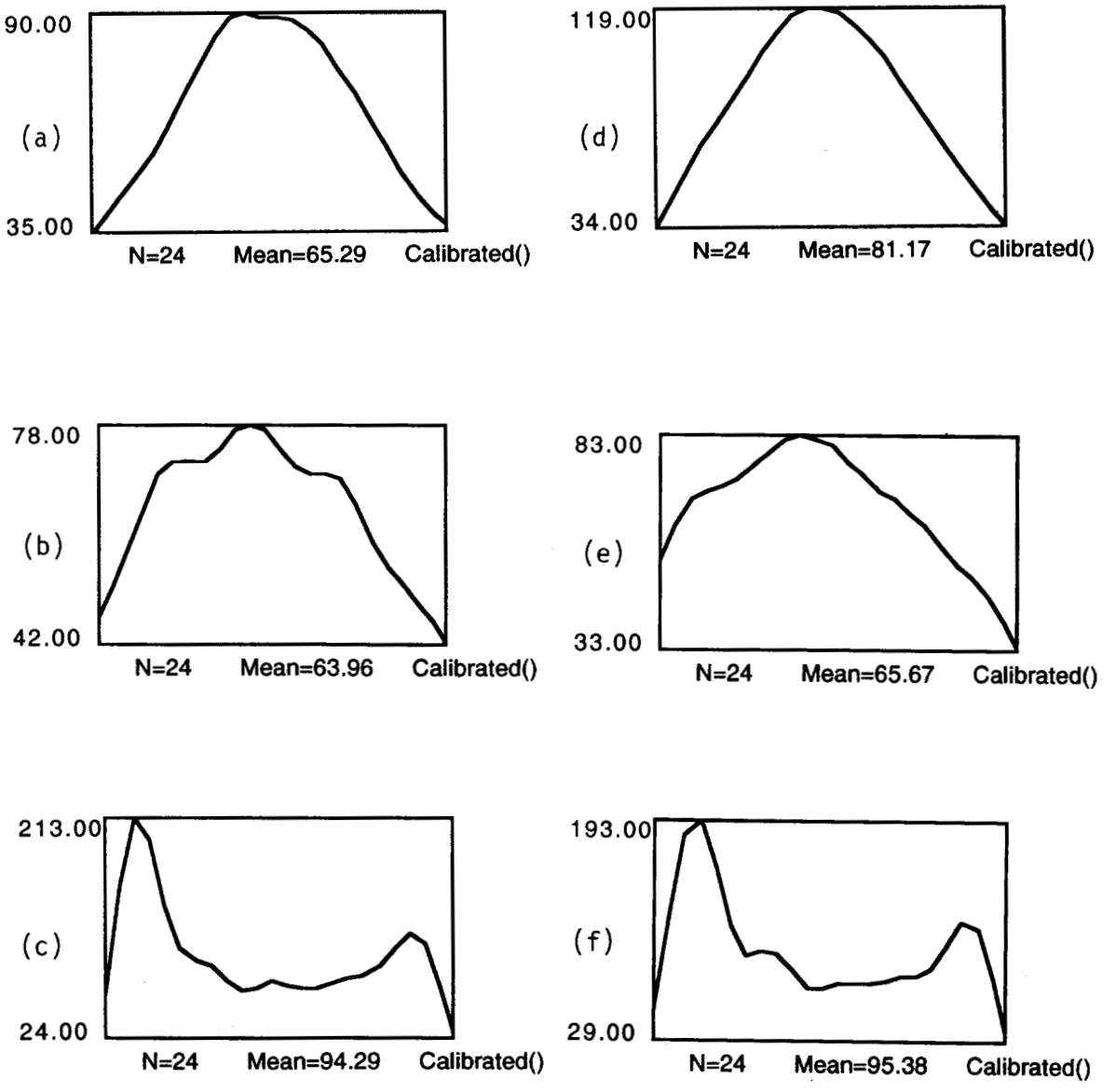

Fig. 3. Plots of radial grey scale intensities taken from the corresponding photos in Fig. 2. Significant differences in distribution of image contrast agent are indicated in the plots.

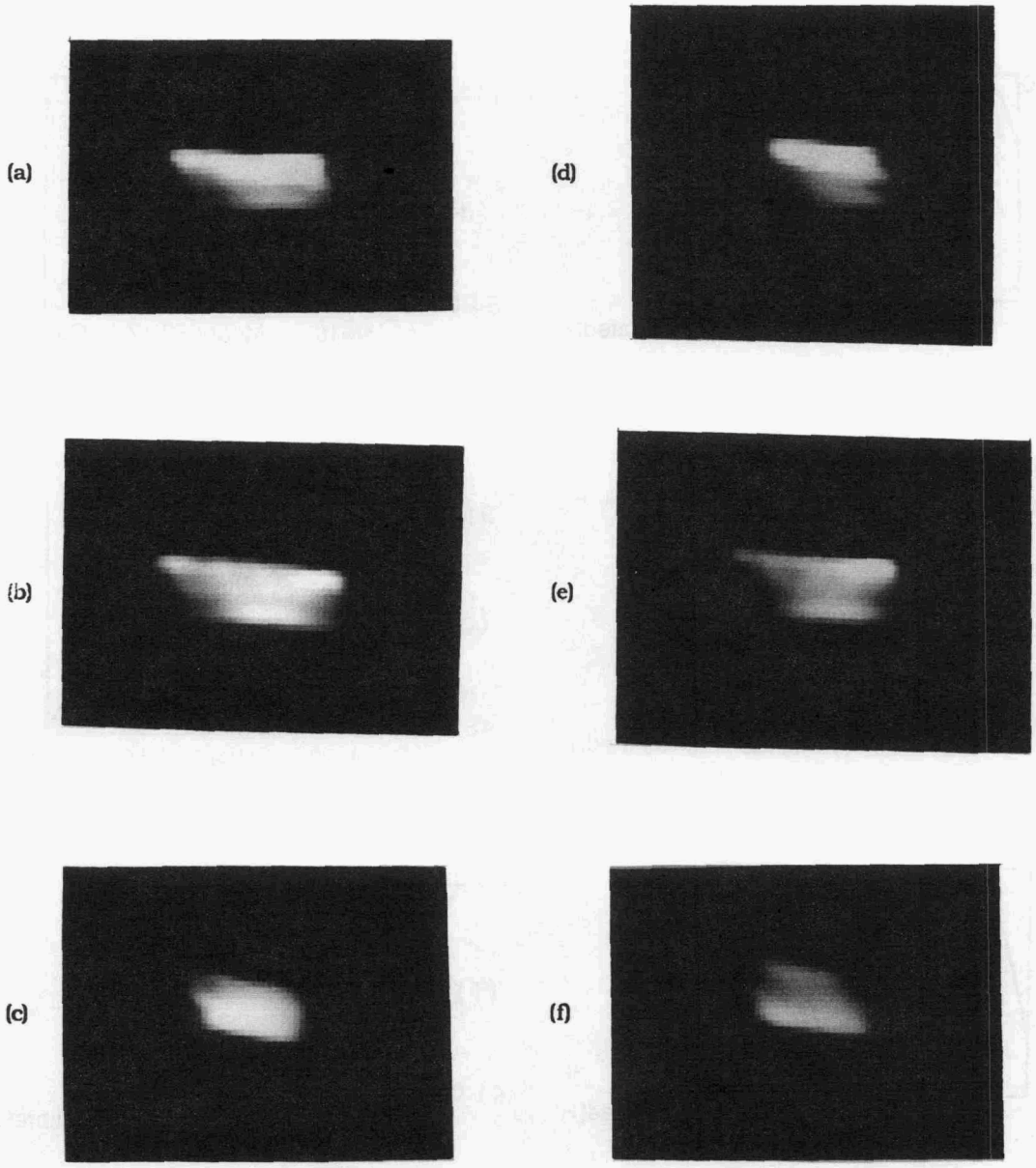

Fig. 4. Representative longitudinal sectional thin views "slices" of three-dimensional NMR imaging data obtained on the 20 (Fig. 1a - 1c) and 23 (Fig.1d - 1f) wt.% whisker-reinforced, as-cast composite imbibed with benzene. Images were acquired, reconstructed and displayed with 1 mm resolution in all three dimensions. The photos displayed are of slices from the side (2mm inside the specimen) (a&d), the exact specimen center (b&e) and 2 mm from the opposite side of the specimen (c&f).

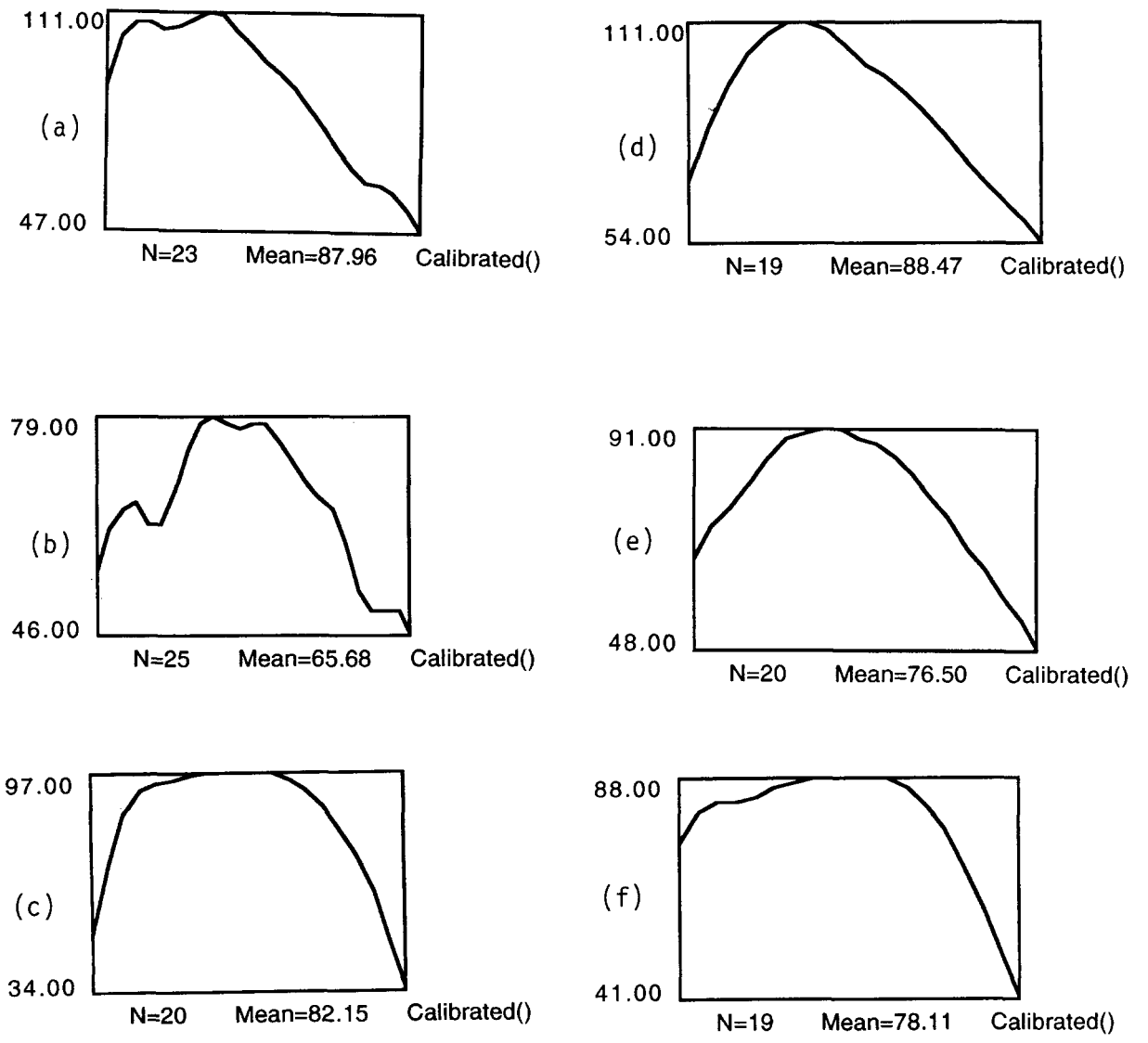

Fig. 5. Plots of longitudinal grey scale intensities taken from the corresponding photos in Fig. 4. Significant differences in distribution of image contrast agent are indicated in the plots.

Image intensity differences apparent in the photos result form variations in proton concentration within the specimen. It is postulated that these variations result from differences in porosity throughout the specimen. It is further postulated that the porosity variations result from the stratification in the buildup of ceramics on the wall of the mold during the molding process (see Fig. 6). In the top of the specimens much of the porosity remaining in the center of the specimen due to preferential buildup of ceramics on the wall as shown in Fig. 2(a-b), and Fig. 3(a-b). Image slices from the center and the bottom of the specimen suggest that there is a much more even distribution of porosity across the sample. Additionally it is worth noting that a significantly higher intensity (more protons) are observed near the top of the specimen. Comparison of data among the two specimen will be performed as the destructive testing results become available.

Work in phase three has begun with NMR imaging of Gelcast ceramic specimens. This work will be conducted in collaboration with Dr. Ogbemi O. Omatete, from the Materials and Ceramics Division, at Oak Ridge National Laboratory. The purpose of this work is to

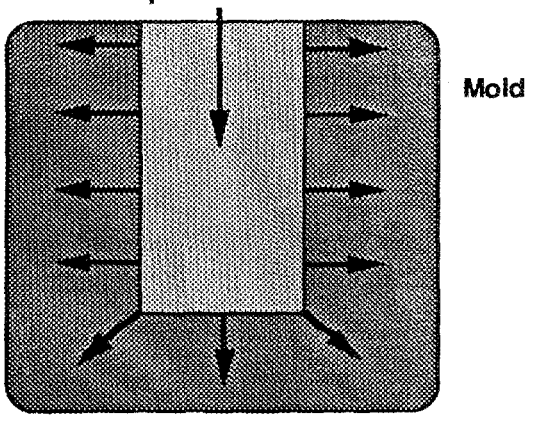

Fig. 6. Cross sectional diagram of a ceramic slip-cast specimen undergoing dewatering through transport of water into the porous mold.

evaluate to the potential of NMR imaging to 3D mapping of polymerization homogeneity, realtime imaging of polymerization process, nondestructive evaluation of voids and flaws in the resultant components, and correlation of NMR measured parameters (T_1, T_{1r}, and T_2) with physical parameters such as degree of polymerization, viscosity, and specimen strength. Both Dr. Omatete and myself feel that this phase of the imaging studies will produce invaluable information leading to a better understanding of and to further advances in the area of gelcast ceramic technology.

Status of Milestones

Milestone 3.5.1.6.08, the NMR imaging of two cast billets, has been met. Due to ES&H concerns, it is necessary to postpone milestone 3.5.1.6.09 until 6/31/92.

MILESTONE SCHEDULE (3.5.1.6)

3.5.1.6.08	Complete NMR Imaging of 2 slip cast billets	8/15/91.*
3.5.1.6.09	Submit initial report on correlation between NDE data and destructive testing.	12/15/91.
3.5.1.6.10	Complete NMR imaging of remaining billets	6/15/92.

* Milestone completed on schedule.

PHYSICOCHEMICAL CHARACTERIZATION AND SURFACE MODIFICATION OF SILICON NITRIDE CERAMIC POWDERS - Prof. Marc A. Anderson (University of Wisconsin - Madison)

Objective/scope

This project is designed to fulfill two primary objectives:

1. characterization of the aqueous surface chemistry of silicon nitride, which also requires the development of a standard for mobility measurements and participation in a round-robin characterization of this standard; and
2. spectroscopic characterization of aqueous suspensions of silicon nitride.

Technical progress

Since this project ended in February, most effort was devoted to documentation of the results. Experiments performed during the past six months were designed primarily to clarify effects noted during earlier experiments.

Round Robin Analysis of Mobility Measurements:

No further round robin studies were performed, although we had hoped to perform at least one study with industrial participation. A general discussion of the final round robin conducted with phosphated goethite suspensions has been submitted for publication. Detailed statistical analyses of all round robin studies are currently being evaluated by the participants at Rutgers University, with input from the other participants as needed. Researchers at the National Institute of Standards and Technology are starting to evaluate the use of aqueous suspensions of phosphated goethite as standards for calibrating particle electrophoresis instruments.

Aging of Aqueous Suspensions of Silicon Nitride:

Further studies of the kinetics of dissolution of "clean" Ube E-10 silicon nitride powder were conducted as a function of pH, ionic strength and solids concentration. ("Clean" powders were obtained by washing the Ube powder in alkaline solutions.) The dissolution rate of silicon nitride was measured by the amount of dissolved silica and free NH_4^+ in the suspension. The rate of dissolution of silicon nitride per m^2 (normalized by the surface area of powder present in the suspension) was found to increase with increasing pH (from 3.5 to 8.5) but to remain constant with solids concentration (over the range of 5 g solid/L to 60 g solid/L). However, the rate of dissolution decreased with increasing concentration of KCl.

Electrophoretic mobility measurements were performed to determine if the decrease in dissolution rate with increasing KCl concentration was due to specific adsorption of the Cl^- anion on the surface of Si_3N_4 or due to a general increase in ionic strength in the system. Measured isoelectric points were about pH 8.5 in both KCl and KNO_3 and agreed with the point of zero charge measured by potentiometric titration in KCl, as described in our last 6 month report. Thus, it appears that the decrease in dissolution rate is due solely to the effect of changing the ionic strength rather than formation of a surface complex with the anion. It is likely that this effect can be attributed to an increasing number of anions in the double layer around the particles that blocks the nucleophilic attack of OH^- or H_2O on exposed surface sites.

Ion chromatography studies of the speciation of the hydrolysis products of Si_3N_4 are continuing.

CIR-FTIR Spectroscopy of Silicon Nitride Suspensions:

No additional results.

Status of Milestones

1. Complete round robin characterization of "benchmark" colloid. Complete.
2. Complete initial round robin mobility testing of silicon nitride. Complete.
3. Complete round robin mobility testing of silicon nitride. Complete.
4. Complete peak assignments for CIR-FTIR spectra of aqueous suspensions of silicon nitride. Not conducted.

Publications

M.I. Tejedor-Tejedor, W.A. Zeltner and M.A. Anderson. "Surface Characterization of Ube Silicon Nitride Powders." submitted to J. Amer. Ceram. Soc.

W.A. Zeltner, J.-F. Wang, O.O. Omatete, M.A. Janney, M.I. Tejedor-Tejedor, M.A. Anderson, R.E. Riman, D.J. Shanefield and J.H. Adair. "Model Hydrous Oxide Colloids for Particle Electrophoresis." submitted for publication in Ceramic Transactions, "Characterization Techniques for Solid-Solution Interfaces in Ceramic Systems".

4.0 TECHNOLOGY TRANSFER

4.1 TECHNOLOGY TRANSFER

4.1.1 Technology Transfer

Technology Transfer
D. R. Johnson (Oak Ridge National Laboratory)

Technology transfer in the Ceramic Technology Project is accomplished by a number of mechanisms including the following:

Trade Shows - A portable display describing the program has been built and has been used at numerous national and international trade shows and technical meetings.

Newsletter - A Ceramic Technology Newsletter is published regularly and sent to a large distribution.

Reports - Semiannual technical reports, which include contributions by all participants in the program, are published and sent to a large distribution. Informal bimonthly management and technical reports are distributed to the participants in the program. Open-literature reports are required of all research and development participants.

Direct Assistance - Direct assistance is provided to subcontractors in the program via access to unique characterization and testing facilities at the Oak Ridge National Laboratory.

Workshops - Topical workshops are held on subjects of vital concern to the ceramics community.

International Cooperation - This program is actively involved in and supportive of the cooperative work being done by researchers in West Germany, Sweden, the United States, and, most recently, Japan under an agreement with the International Energy Agency. This effort is ultimately aimed at development of international standards and includes physical, morphological, and micro-structural characterization of ceramic powders and dense ceramic bodies, and mechanical characterization of dense ceramics.

IEA ANNEX II Management
V. J. Tennery (Oak Ridge National Laboratory)

Objective/scope

The purpose of this task is to organize, assist, and facilitate international research cooperation on the characterization of advanced structural ceramic materials. A major objective of this research is the evolution of measurement standards for key material properties. This task, which is managed in the United States by ORNL, now includes a formal IEA Annex agreement identified as Annex II between the United States, Germany, Sweden, and Japan. The original annex included four subtasks: (1) information exchange, (2) ceramic powder characterization, (3) ceramic chemical and physical characterization, and (4) ceramic mechanical property measurements. The research in Subtasks 2, 3, and 4 is now completed. For the new Subtasks 5 and 6, there are 35 and 45 laboratories participating, respectively. During CY 1990, agreements were reached for Japan to join the Annex and for research in two new subtasks to be initiated. These include Subtask 5, Tensile and Flexural Properties of Ceramics, and Subtask 6, Advanced Ceramic Powder Characterization.

The Amendment to Annex II, Ceramic for Advanced Engines and Other Conservation Applications (corrected March 5, 1991), was signed on March 5, 1991. A copy can be obtained from the author.

Technical progress

Subtask 5, Flexural and Tensile Properties of Ceramics

United States

As of March 31, 1992, all of the fractography measurements for the tensile and flexure specimens were completed, and these data were received from the U.S. participants. Analysis of the flexural strength data and tensile strength data is proceeding.

Future target dates for completion of reports from Subtask 5: Complete statistical analysis of flexure data (V. J. Tennery - 9/30/92); complete fractography analysis of flexure data (M. K. Ferber - 9/30/92); draft report on flexure results (VJT/MKF - 12/31/92); complete statistical analysis of tensile data (VJT - 9/30/92); complete fractography analysis of tensile data (M. G. Jenkins - 9/30/92); draft report of tensile results (VJT/MKF/MGJ - 12/31/92); and final reports printed and ready for exchange by 6/30/93.

Table 1 summarizes the status of all flexure and tensile specimens in this task with the participating countries as of the date shown.

Germany

All flexure-strength measurements have been completed in Germany, and data analyses are proceeding.

According to Dr. Hollstein's (Germany) letter of February 26, 1992, the Swedish specimens to be tested in Germany will be strain gauged in his laboratory, and the Swedish team will gauge the German specimens. Also,

Table 1. Status of exchange of flexure and tensile specimens with Germany, Sweden, Japan, and United States (March 1992)

Country	Flexure specimens	Tensile specimens
United States	Thirty specimens received: Germany (ESK), 10/15/91 Japan (SSN-H), 11/14/90 Sweden (ABB-Cerama), 10/15/91; All specimens were fractured at room temperature 3/3-4/92; Each country will provide 100% fractography on the exchange specimens; A report and the fractured specimens will be returned to each country.	Five specimens received: Germany (ESK) 1/9/92; Japan (SSN-H) 1/27/92. Japan--Specimens were returned (2/25/92) to Japan to be strain gauged again as the specifications had not been gauged according to specified guidelines. Sweden--Specimens are being strain gauged and will be sent by 6/92. The specimens will be fractured at room temperature, and 100% fractography will be performed when all are received. Each country will provide 100% fractography on the exchange specimens. When the measurements are completed, a report and the fractured specimens will be returned to each country.
Germany	V. J. Tennery delivered to German team 1/91, at meeting in Florida.	Sent to Germany--12/17/91. Specimens were received 1/10/92, due to error in handling by ORNL shipping department.
Sweden	V.J. Tennery delivered to Swedish team 1/91, at meeting in Florida.	Sent to Sweden--2/14/92 Received 2/19/92
Japan	Sent to Japan--10/90	Sent to Japan--11/17/91

Dr. Hollstein has informed me that each laboratory will test foreign tensile specimens according to the loading rates used in each participating country, and the Swedish and German Institutes will test/have tested the European specimens according to the CEN and DIN Standards, respectively.

Sweden

All flexure-strength measurements have been completed in Sweden, and data analyses are proceeding.

Japan

All flexure-strength measurements have been completed in Japan, and data analysis is proceeding. Some difficulty has been encountered with the strain-gauged tensile specimens from Japan, but it is expected that gauged specimens suitable for measurement will be at ORNL by the end of May 1992. Dr. Awaji informed V. J. Tennery that he would no longer be the Japanese Technical Leader in Japan for Subtask 5. Mr. Mineo Mizuno, JFCC, will now be the representative in this Subtask.

Subtask 6, Advanced Ceramic Powder Characterization

Major responsibility for this subtask in the United States is at NIST, and a detailed report of progress on this subtask is provided in the section of this report submitted by NIST for this program. Only a brief summary is provided here.

The preliminary results from the powder subtask, Subtask 6, were described at the Executive Committee meeting held in October 1991 in Japan. Some report-writing assignments were determined at this meeting.

Each technical leader reviewed all procedure writeups and provided any changes to NIST by December 31, 1991. A subset on surface analysis was included in these procedures. All "data set adjustments" were finalized by December 31, 1991. Each participant received a copy of their data as entered in the Data Compilation Report. The data compilation has been completed (the statistical data analysis activity is about 50% complete), and both will be submitted to the IEA Executive Committee for review and approval in early May 1992, with a request for early release approval to national standard-setting organizations for a report containing only the "procedures" used for ceramic powder characterization in Subtask 6. This approval is expected to form a basis for release of these procedures in the participating countries in advance of the release of the final report.

References

None

Status of milestones

Milestone No. 411510 was completed on October 1, 1991. Other milestones are on schedule.

Publications

V. J. Tennery, IEA Annex II Operating Agent Technical Representative, and Felicia M. Foust, IEA Annex II Recording Secretary, attended the Second IEA Annex II Executive Committee Meeting in Nagoya, Japan, on October 15, 1991.

V. J. Tennery and F. M. Foust attended a working group meeting for Subtask 5, U.S. participants, held during the DOE Contractor's Coordination Meeting in Dearborn, Michigan, on October 28, 1991.

Characterization of Ceramic Powders

S. G. Malghan, L.-S. Lum, J. F. Kelly, E. Begley and S. M. Hsu
(National Institute of Standards and Technology)

Objective/Scope

Ceramics have been successfully employed in engines on a demonstration basis. The successful manufacture and use of ceramics in advanced engines depends on the development of reliable materials that will withstand high, rapidly varying thermal stress loads. Improvement in the characterization of ceramic starting powders is a critical factor in achieving reliable ceramic materials for engine applications. The production and utilization of such powders require characterization methods and property standards for quality assurance.

The objectives of the NIST program are: (1) to assist with the division and distribution of ceramic starting powders for an international round-robin on powder characterization; (2) to provide reliable data on physical (dimensional), chemical and phase characteristics of powders; and (3) to conduct statistical assessment, analysis and modeling of round-robin data. This program is directed toward a critical assessment of powder characterization methodology and toward establishment of a basis for the evaluation of fine powder precursors for ceramic processing. This work will examine and compare by a variety of statistical means the various measurement methodologies employed in the round-robin and the correlations among the various parameters and characteristics evaluated. The results of the round-robin are expected to provide the basis for identifying measurements for which Standard Reference Materials are needed and to provide property and statistical data which will serve the development of internationally accepted standards.

Technical Progress

The technical progress covered in this report is on the data compilation, data analysis, preparation of procedures report, and ASTM activities.

Data Compilation. At present, data compilation activity is in the final stages of completion. A number of meetings of participants in each participating country were held to review data and identify outliers. In addition, a meeting of the technical leaders was held in Nagoya, Japan to review data and discuss inputs of participants.

The powders characterization data obtained from participants in Japan, Germany, Sweden and the U.S. were compiled. Specially developed computer programs were used for this purpose. Two different reports were produced as a result of this activity; 1) detailed tabulation of all data in as-received form, 2) detailed information provided by participants on the powder sample and changes made to the procedures. The first report was distributed to all participants, and second report was distributed only to technical leaders since it had a limited utility

to the participants. All data were included in this exercise, irrespective of suitability of their fit with the majority of data. During this phase, the participants met in the respective countries to discuss data obtained and problems encountered during analysis. These discussions were helpful in identifying problem areas in the data and procedures.

After receiving these reports, the participants met again to review data and identify outliers. In addition, specific details of the outliers were developed. Technical leaders held a meeting on October 14, 1992 to consolidate all inputs and discuss technical issues related to the data.

Data Analysis. Data analysis activity constituted calculation of preliminary statistical parameters and graphical presentation of summarized data. All data were analyzed to determine mean and standard deviation for each laboratory and for each method of analysis. A report containing tabulated data and graphical analysis was prepared, and distributed to all participants. This type of preliminary analysis was instrumental in identifying outliers. In addition, this analysis provided a rough idea of repeatability and reproducibility. By combining the information in these reports, we were able to identify not only the reasons for outliers, but also the influence of outliers on the rest of the data.

In general, most data showed improvement over the Subtask 2 data. This improvement is attributed to the use of recommended analysis procedures in Subtask 6. In some cases, the particle size distributions obtained by different techniques showed excellent agreement. The primary basis for this agreement is the use of recommended dispersion procedure. Data of participants using non-recommended practices showed lack of repeatability and reproducibility. Specific surface area of powders by single-point and multi-point BET method showed similar differences as in Subtask 2, i.e., higher values were obtained by the multi-point analysis than by the single-point analysis. In bulk chemical analysis, impurities analysis were affected by dissolution techniques. Data of bulk impurities, such as carbon and oxygen showed excellent reproducibility.

Preparation of Procedures Report. One of the major accomplishments of Subtask 6 is the development of approximately 25 procedures for analysis of powders. The use of these procedures has made a significant contribution towards improvement in the data. There is no single source of reference which contains such procedures. The procedures were compiled, edited and checked for technical accuracy by the participants. A special report was prepared to enable speedy distribution to the participants.

In the meantime, the standards setting bodies have been searching for procedures for powders analysis. To assist the standards development activities in the participating countries, an effort is being made to release this report to these activities. Currently, the procedures do

not contain supporting data. However, they are expected to serve as a starting point. At the time of writing of this progress report, the Executive Committee of IEA Annex II is considering to approve the release of this report to the standards setting bodies in Germany, Japan, Sweden, and the U.S.

ASTM Activities. Measurable progress is being made in the ASTM C-28.05.04 task group. This group is responsible for the development of standards for characterization of ceramic powders. NIST is providing vital assistance in the form of powder samples and leadership in the development of standards. A sample of silicon nitride powder has been prepared exclusively for the use of ASTM C-28 activities. This sample can be used for the development and/or confirmation of procedures for physical properties determination. Sufficient quantity of sample exists for subsequent round-robin studies. Since the beginning of 1992, S. G. Malghan, has been nominated to chair the C-28.05.04 sub-committee on characterization. Currently, there are five draft procedures under consideration of the sub-committee. These procedures will be submitted for ballot at the June 1992 meeting in Louisville, KY.

Status of Milestones

On target.

Ceramic Mechanical Property Test Method Development

George D. Quinn (National Institute of Standards and Technology)

Objective/Scope

This task is to develop mechanical test method standards in support of the Ceramic Technology for Advanced Heat Engines and Advanced Turbine Technology Applications Programs. The prime DOE contractors and subcontractors will be surveyed to assess their needs and capabilities. Test method development should also consider the general USA structural ceramics community as well as foreign laboratories and companies, but emphasis will be placed on the needs on the DOE community.

Draft recommendations for practices or procedures shall be developed based upon the needs identified above and circulated within the DOE ceramics heat engine community for review and modification. Round robins will be conducted as necessary, but shall be well-focussed, limited in scope and not interfere with ongoing IEA round robins. Procedures developed in this program shall be presented as ATTAP or CTAHE "standard procedures." Alternatively, (and eventually) these will be advanced for final standardization by ASTM or by the U.S. Army as possible MIL STD's.

Technical Highlights and Results

Previous work in this project has contributed to the following completed standards:

1. ASTM C-1198-91 "Dynamic Young's Modulus, Shear Modulus, and Poisson's Ratio for Advanced Ceramics by Sonic Resonance," by S. Gonczy, G. Quinn and J. Helfinstine.
2. ASTM C-1161-90 "Standard Test Method for Flexural Strength of Advanced Ceramics at Ambient Temperature,"
3. ASTM C-1211-92 "Standard Test Method for Flexural Strength of Advanced Ceramic at Elevated Temperature," by G. Quinn in cooperation with Mr. M. Foley, Norton; Mr. T. Richerson, Allied-Signal; Mr. L. Chuck, Univ. Dayton; and Dr. M. Ferber, ORNL.

During this six month period, the high-temperature flexure standard draft passed a concurrent main and subcommittee ballot without any negative ballots. Some editorial revisions were discussed at the C-28 meeting in Cocoa Beach in January and minor revisions were incorporated into the document. Professionally drawn figures were prepared, and a mistake in one figure (identified by M. Foley) was rectified. The document then passed a Society ballot in February and was accepted as ASTM standard C-1161 on 15 March, 1992.

Work has continued in this project on the following draft standards:

1. U. S. Army MIL HBK: "Standard Practice for Characterizing Fracture Origins Limiting Defects in Advanced Structural Ceramics", with M. Slavin and J. Swab of U. S. Army MTL.
2. ASTM draft standard: "Reporting Uniaxial Strength Data and Estimating Weibull Distribution Parameters for Advanced Ceramics," by S. Duffy and G. Quinn.

A draft of the standard for fractographic analysis of strength limiting defects in advanced ceramics was sent to over 100 reviewers. This was the second major review of a draft in this project. The new input received has led to some additional revisions and the document is nearing completion as a MIL HBK. The fractography standard has been strengthened and modified to make it more in harmony with the Weibull statistics standard under development in ASTM C-28. The following scheme has been adopted for the characterization of each fracture origin:

FLAW CHARACTERIZATION SCHEME

FLAW TYPE (identity, and how distributed)	FLAW LOCATION (specific location in a specimen)	FLAW SIZE (nominal diameter)
Pore, Volume distributed	Surface	120 μm
Inclusion, Volume distributed	Volume	50 μm
Machining Damage, Surface dist.	Surface	30 μm

In February 1992, G. Quinn visited MTL in Boston to work with M. Slavin and J. Swab in preparing a final draft. It is anticipated that it will be completed in May 1992. The document will be adopted at that time as a MIL HBK and copies will be brought to the next C-28 meeting at Louisville in mid-June. The flaw nomenclature list will be presented. A motion will be made to prepare a draft ASTM standard on the nomenclature.

Intensive work continued on the Weibull statistical analysis draft standard. Dr. Steven Duffy of NASA-Lewis has the lead in this initiative and draft 3 was presented at the DOE Contractors' Coordination Meeting in Dearborn in October. G. Quinn visited NASA-Lewis in December and assisted S. Duffy prepare draft 4 on the basis of the input from draft 3. Several dozen minor revisions were made. Draft 4 was presented at the ASTM C-28 meeting in Cocoa Beach in January. After this meeting, several long conference calls were held with C. Johnson of G.E.; J. Cuccio, Allied-Signal; S. Duffy, NASA; and G. Quinn, NIST. Draft 5 was prepared and submitted for a Subcommittee C-28.02 ballot in March 1992.

The draft standard utilizes maximum likelihood analysis to estimate the Weibull parameters and thus is able to assign confidence bounds to the estimates. Unbiasing factors are applied to the estimate of the Weibull modulus, but there is no need to do such for the characteristic strength (since the bias is small). A specific scheme of graphically depicting the data is recommended. For the case of a single flaw population, this draft standard will be completely consistent with, and will yield identical Weibull values and confidence intervals as a formal German DIN standard: DIN 51-110 Part 3. This is an important contribution to consistency in international standardization.

The USA standard is also very ambitious in that it also mandates that fractography be applied to establish whether or not multiple flaw populations are present. It has been the experience of nearly all DOE participants that multiple flaw populations are the norm, not the exception. Therefore, the USA standard incorporates censored statistics to permit a proper analysis of multiple flaw

populations (a procedure that the DIN standard does not include.) As a consequence, the statistical standard requires the existence of a fractography standard. The following standards are thus interrelated as shown in Figure 1.

FIGURE 1 Interrelated Standards

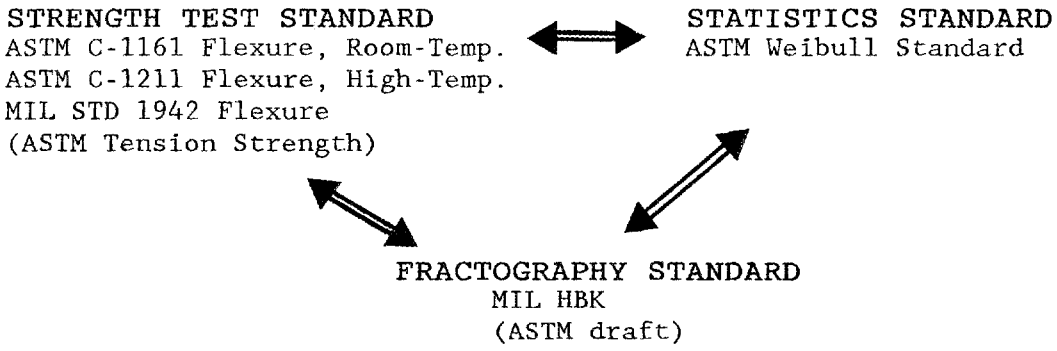

There are some trade-offs in the C-28 statistics draft standard, however. Unbiasing factors for the estimates, and the confidence bounds for these estimates are not known for multiple flaw population problems. Unidentified origins must be treated in some fashion as well. Fractures outside "gage lengths" must be propely dealt with. It is well known, and technically accepted that fractures outside the inner span should be included in flexure strength data, *and stresses should not be corrected when using Weibull analysis.* Regrettably, there seems to be confusion about this and a draft European standard has been prepared that strongly suggests that the stresses should be corrected for the location of fracture. *This is incorrect procedure. The maximum nominal stress must be used.* Detailed correspondence has been sent to the principals in Europe and it is hoped this can be corrected before a wrong analysis is codified in Europe. Similar problems can be anticipated to arise on how to treat failure in the taper of tension specimens.

In addition to the above standards and draft standards, work has commenced on fracture toughness and hardness.

Standardization of fracture toughness testing remains elusive. This is a very contentious issue since very strong preferences and opinions have developed over the years. There is at the moment, only a small amount of actual work ongoing on optimizing or refining the measurement of fracture toughness. The likelihood of standardizing a specific method within ASTM is hard to anticipate, but it may be a difficult process. The author has visited DOE contractors and subcontractors and assessed their needs and preferences.

During this six month period, final analysis was performed on the USA results on a VAMAS (Versailles Advanced Materials and Standards) round-robin exercise that used three fracture toughness tests as shown in Figure 2. The NIST testing and analysis of results were conducted by G. Quinn as part of this task. USA participants in the twenty-two laboratory international exercise are identified in Table I. Four of the five are DOE CTAHE program participants. Two materials,

INDENTATION FRACTURE (IF)

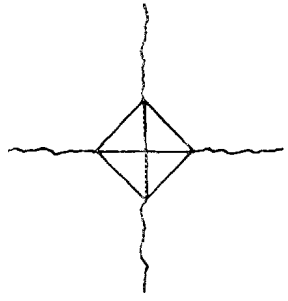

INDENT A POLISHED SURFACE,

MEASURE CRACK LENGTHS

INDENTATION STRENGTH (IS)

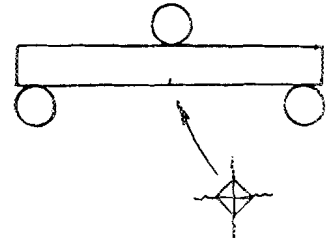

INDENT A SPECIMEN,

FRACTURE SPECIMEN IN FLEXURE

SINGLE EDGE PRECRACKED BEAM (SEPB)

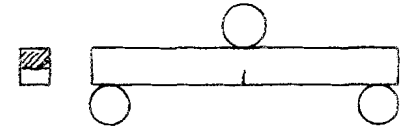

INDENT OR SAWCUT A SPECIMEN,

COMPRESSION LOAD IT IN A BRIDGE ANVIL UNTIL A PRECRACK POPS-IN,

FRACTURE SPECIMEN IN FLEXURE

FIGURE 2. The fracture toughness test methods in the VAMAS round-robin.

TABLE I
USA Participants

Laboratory	Points of Contact
NIST, Gaithersburg, MD	Dr. Edwin Fuller, Jr. Mr. George Quinn
Norton Company, Northboro, MA	Dr. Dennis Tracy Mr. Michael Foley
Allied-Signal/Garrett, Phoenix, AZ	Dr. James Wimmer Dr. Ho Fang
Worcester Polytechnic Institute Worcester, MA	Prof. Isa Bar-On Mr. Kyu Cho
NASA-Lewis, Cleveland, OH	Dr. John Shannon Dr. Jonathan Salem

a gas-pressure sintered silicon nitride and a sintered zirconia-alumina composite, were tested. Both were furnished by the Japan Fine Ceramic Center.

Figure 3 shows that very consistent results were obtained for the indentation strength (IS) method, although there is an trend of increased apparent toughness with indentation load, P. With one exception, the USA labs had very consistent fracture toughnesses from the single edge precracked beam method as shown in Figure 4. On the other hand, inconsistent results obtained for the zirconia-alumina composite by the indentation fracture (IF) method are illustrated in Figure 5. The latter scatter can be attributed to the difficulty in accurately measuring the crack lengths, and the dependency of the computed toughness upon such crack length raised to the 1.5 power. As a consequence, the IF method has been dropped from consideration as an ASTM standard. (The IF method is included as one method in the Japanese fracture standard, JIS R 1607!)

The successful results for the IS and SEPB methods have spurred a new initiative to standardize fracture toughness in ASTM. Dr. Edwin Fuller of NIST is the leader of the collaboration. A workshop was sponsored by NASA-Lewis in December, and a follow up meeting of the principals was held at NIST in February. It now appears that a fracture toughness standard will have to be a joint undertaking of ASTM Committees C-28, Advanced Ceramics, and E-24, Fracture Testing. E-24, a committee with limited ceramics representation, is insisting on jurisdictional control.

A final report on the USA VAMAS was prepared in December 1991 and was sent in April to the USA participants for review. The final report will be published in the NIST Journal of Research in 1992.

Work in this DOE project in 1992 will concentrate on refinement of the controlled surface flaw method. This is one of the five candidates for an ASTM fracture toughness standard as shown in Figure 6. The standard will undoubtedly include several of these configurations, and not be limited to one method.

An earlier VAMAS round robin revealed that there is inconsistency in measured hardnesses on advanced ceramics. A new initiative leading to an ASTM draft standard for microhardness will commence in this program in 1992.

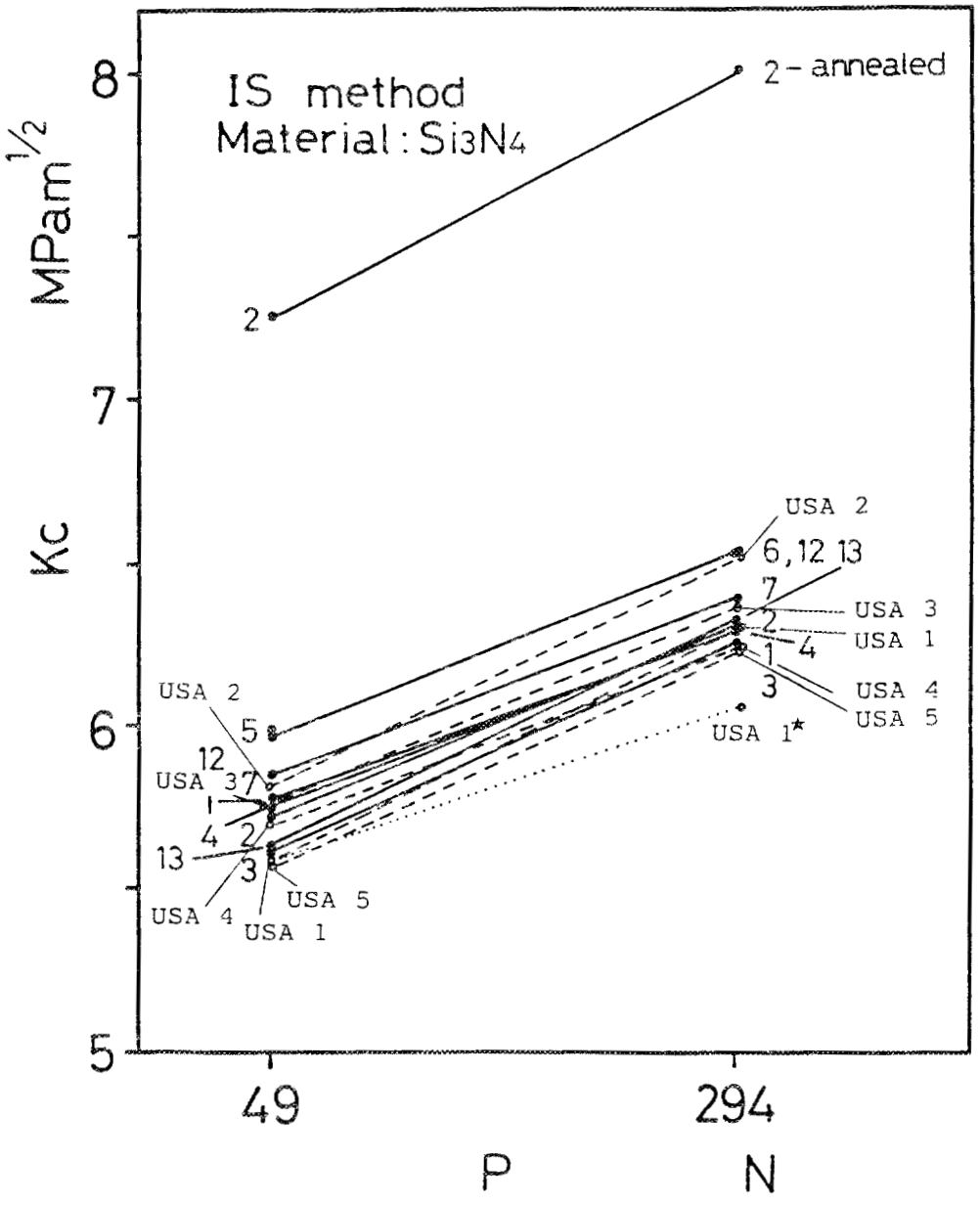

FIGURE 3. Fracture toughness results by the indentation strength (IS) method for silicon nitride.

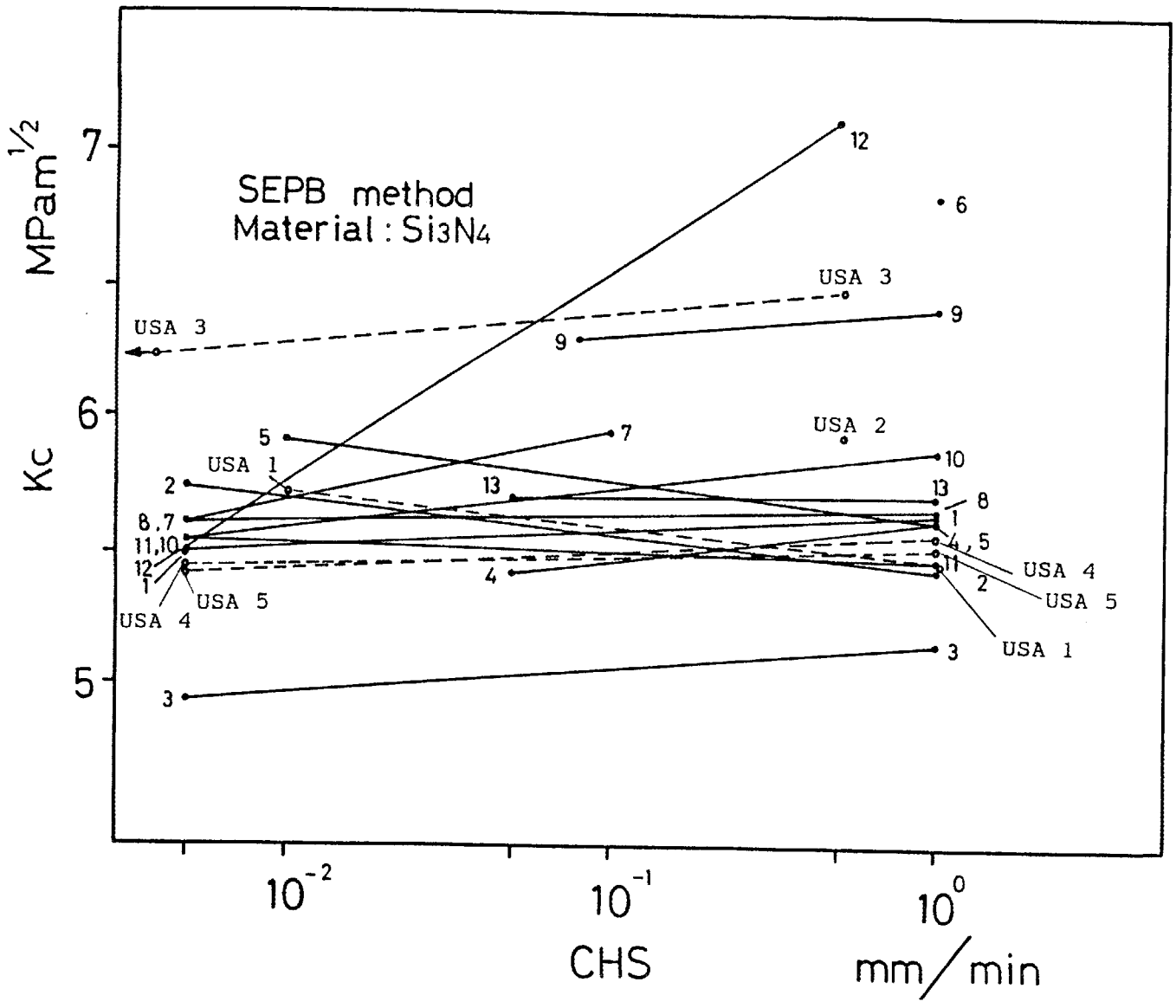

FIGURE 4. Fracture toughness results by single edge precracked beam (SEPB) for silicon nitride.

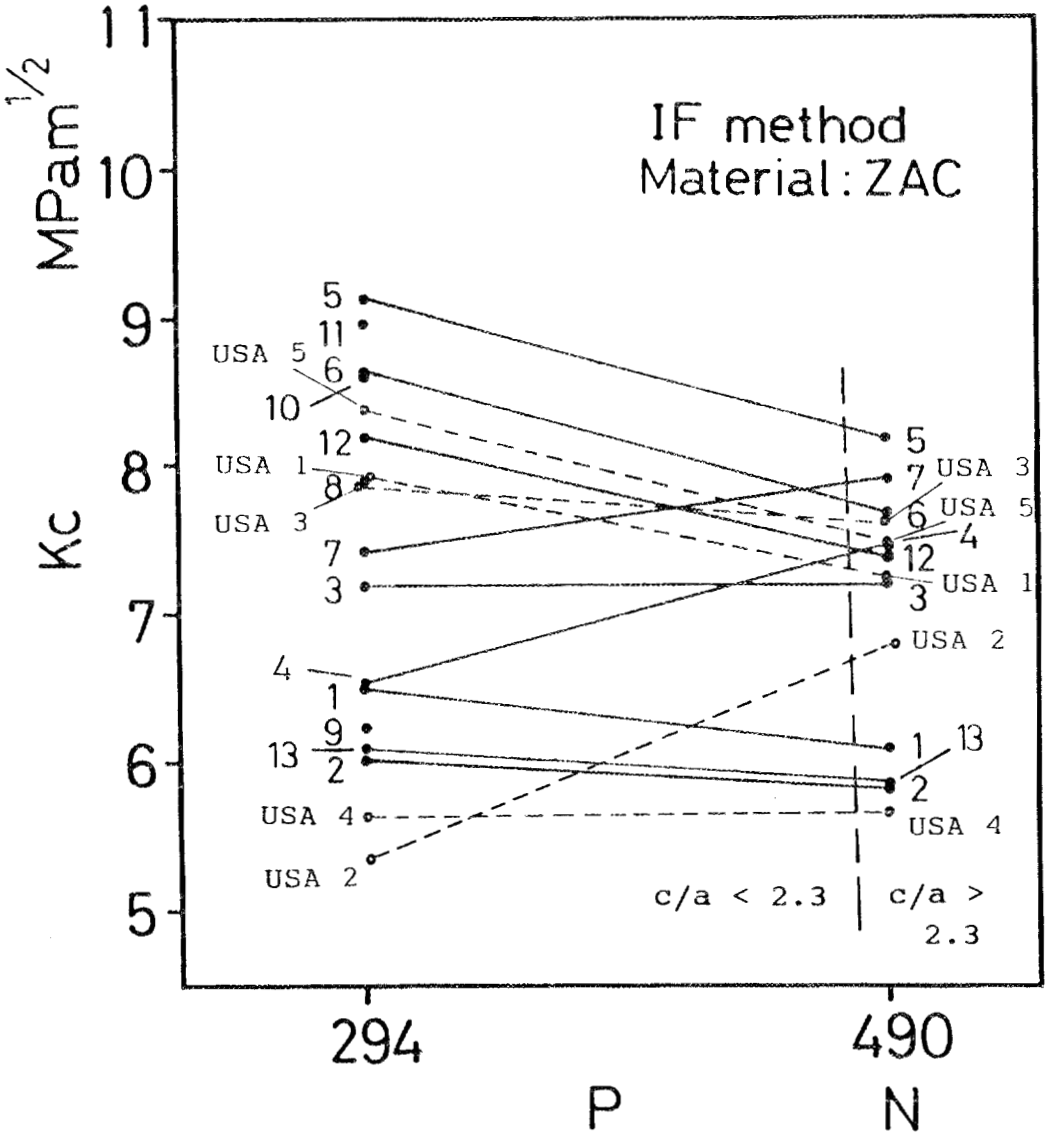

FIGURE 5. Fracture toughness results by indentation fracture (IF) for the zirconia-alumina composite (ZAC).

ADVANCED CERAMICS
FRACTURE TOUGHNESS CANDIDATES

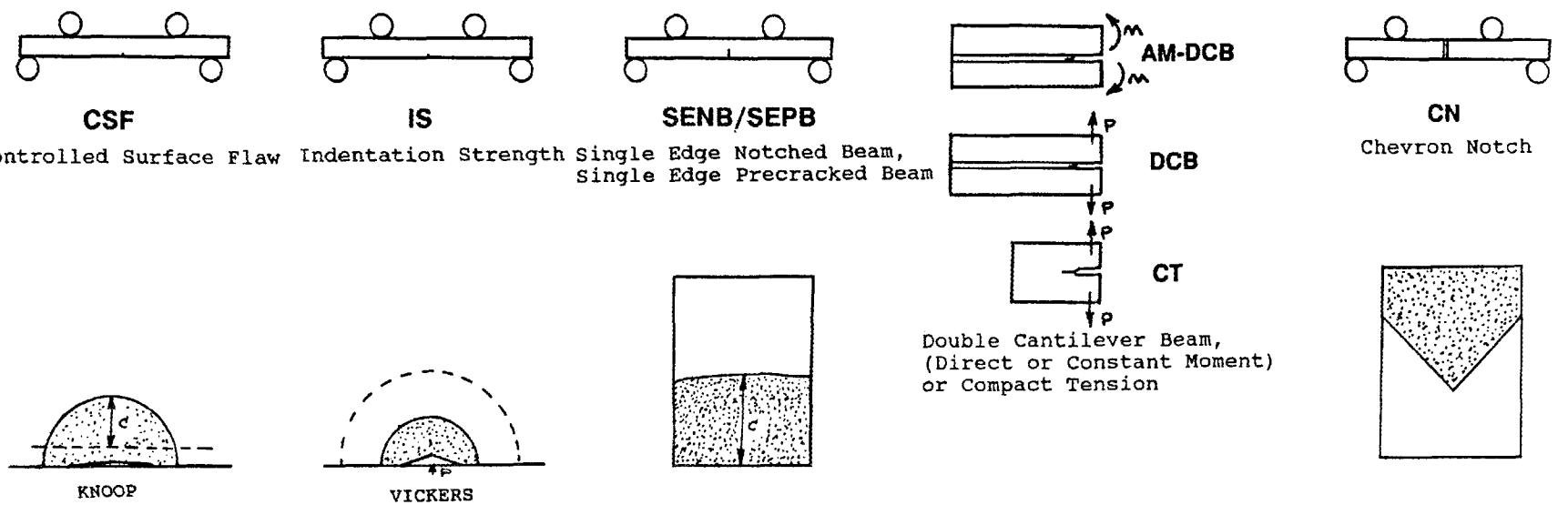

$K_{c,CSF} = Y\sigma_f\sqrt{c}$

Indent, remove indent and res. stress, measure σ_f and c

$K_{c,IS} = \eta(E/H)^{1/8}\ [\sigma_f P^{1/2}]^{3/4}$

Chantikul et al. 1981
Indent (Vickers, P)
then break.

$K_{c,NB} = (F_{max}/B\sqrt{W})\ Y$

Fatigue precracked,
or
Indentation or Sawcut
Bridge Precracked

K_c depends upon the specific loading configuration.

Loading by direct pulling
(CT or DCB)
or by constant moment
(CM)

$K_{c,CN} = (F_{max}Y_{min})\ /\ BW^{1/2}$

FIGURE 6. The candidate fracture toughness standard test methods under consideration by ASTM.

Finally, a definitive paper on the influence of twisting and friction errors, both at room and elevated temperature, in short and long duration tests, was presnted and submitted for publication at the ACS Cocoa Beach meeting in January 1992.

Status of Milestones

All milestones are on schedule.

Publications/Presentations

1. G. Quinn, "Strength and Proof Testing," in Ceramics and Glasses, Volume 4, Engineered Materials Handbook, ASM, Metals Park, OH, 1991, pp. 585-598.
2. G. D. Quinn and R. Morrell, "Design Data for Engineering Ceramics: A Review of the Flexure Test," J. Am. Ceram. Soc., 74 [9] (1991) 2037-66.
3. G. D. Quinn, "Refinements to Flexure Testing," presented at the second European Ceramic Society Conference, Augsburg, Germany, Sept. 1991.
4. ASTM Standard C-1211, "Standard Test Method for Flexural Strength of Advanced Ceramics at Elevated Temperature," ASTM Annual Book of Standards, Vol. 15.01, March 1992.
5. G. Quinn, "Twisting and Friction Errors in Flexure Testing," presented at the Engineering Ceramics Division meeting, American Ceramic Society, Cocoa Beach, January, 1992.

INTERNAL DISTRIBUTION

Central Research Library (2)
Document Reference Section
Laboratory Records Department (2)
Laboratory Records, ORNL RC
ORNL Patent Section
M&C Records Office
L. F. Allard, Jr.
L. D. Armstrong
D. L. Balltrip
R. L. Beatty
P. F. Becher
R. F. Bernal
T. M. Besmann
P. J. Blau
A. Bleier
E. E. Bloom
K. W. Boling
R. A. Bradley
C. R. Brinkman
V. R. Bullington
R. S. Carlsmith
P. T. Carlson
G. M. Caton
S. J. Chang
R. H. Cooper, Jr.
S. A. David
J. H. DeVan
J. L. Ding
M. K. Ferber
F. M. Foust
W. Fulkerson
R. L. Graves
D. L. Greene
M. R. Harris
E. E. Hoffman
C. R. Hubbard
M. A. Janney
M. G. Jenkins
D. R. Johnson (5)
F. W. Jones
D. Joslin
R. R. Judkins
M. A. Karnitz
B. L. Keyes
H. D. Kimrey, Jr.
T. G. Kollie
K. C. Liu
E. L. Long, Jr.
W. D. Manly
R. W. McClung
D. J. McGuire
J. R. Merriman
T. A. Nolan
A. E. Pasto
J. L. Rich
C. R. Richmond
J M Robbins
G. V. Rogers, Jr.
M. L. Santella
A. C. Schaffhauser
S. Scott
G. M. Slaughter
E. J. Soderstrom
D. P. Stinton
R. W. Swindeman
V. J. Tennery
T. N. Tiegs
J. R. Weir, Jr.
B. H. West
S. G. Winslow
J. M. Wyrick
C. S. Yust

EXTERNAL DISTRIBUTION

James H. Adair
University of Florida
Materials Science & Engineering
317 MAE Bldg.
Gainesville FL 32611-2066

Donald F. Adams
University of Wyoming
Mechanical Engineering Department
P.O. Box 3295
Laramie WY 82071

Jalees Ahmad
AdTech Systems Research Inc.
1342 North Fairfield Road
Dayton OH 45432-2698

Yoshio Akimune
NISSAN Motor Co., Ltd.
Materials Research Laboratory
1 Natsushima-Cho
Yokosuka 237
JAPAN

Mufit Akinc
Iowa State University
322 Spedding Hall
Ames IA 50011

Ilhan A. Aksay
University of Washington
Materials Science and Engineering
Department, FB-10
Seattle WA 98195

R. G. Alexander
BASE
26 Malvern Close
Kettering Northants NN16 AJP
UNITED KINGDOM

Richard L. Allor
Ford Motor Company
Material Systems Reliability Department
20000 Rotunda Drive
P.O. Box 2053, Room S-2031
Dearborn MI 48121-2053

Richard T. Alpaugh
U.S. Department of Energy
Advanced Propulsion Division
CE-322
Washington DC 20585

Joseph E. Amaral
Instron Corporation
Corporate Engineering Office
100 Royale Street
Canton MA 02021

Edward M. Anderson
Aluminum Company of America
North American Industrial Chemicals
Division
P.O. Box 300
Bauxite AR 72011

Norman C. Anderson
Ceradyne, Inc.
Ceramic-to-Metal Division
3169 Redhill Avenue
Costa Mesa CA 92626

Don Anson
BCL
Thermal Power Systems
505 King Avenue
Columbus OH 43201-2693

Thomas Arbanas
G.B.C. Materials Corporation
580 Monastery Drive
Latrobe PA 15650-2698

Frank Armatis
3M Company
3M Center
Building 60-1N-01
St. Paul MN 55144-1000

Everett B. Arnold
Detroit Diesel Corporation
Mechanical Systems Technology
13400 Outer Drive West
Detroit MI 48239-4001

Richard M. Arons
PA Consulting Group
279 Princeton Road
Hightstown NJ 08550

Bertil Aronsson
Sandvik AB
S-12680
Stockholm Lerkrogsvagen 19
SWEDEN

Dennis Assanis
University of Illinois
Department of Mechanical Engineering
1206 W. Green Street
Urbana IL 61801

William H. Atwell
Dow Corning Corporation
3901 South Saginaw Road, MS:540
Midland MI 48686-0995

V. S. Avva
North Carolina A&T State University
Department of Mechanical Engineering
Greensboro NC 27411

Patrick Badgley
Adiabatics, Inc.
3385 Commerce Drive
Columbus IN 47201

Sunggi Baik
Pohang Institute of Science & Technology
Department of Materials Science and Engineering
P.O. Box 125
Pohang 790-600
KOREA

John M. Bailey
Caterpillar Inc.
Technical Center, Building L
P.O. Box 1875
Peoria IL 61656-1875

Bob Baker
Ceradyne, Inc.
3169 Redhill Avenue
Costa Mesa CA 92626

Frank Baker
Aluminum Company of America
Alcoa Technical Center
Alcoa Center PA 15069

J. G. Baldoni
GTE Laboratories, Inc.
40 Sylvan Road
Waltham MA 02254

Clifford P. Ballard
Allied-Signal, Inc.
Ceramics Program
P.O. Box 1021
Morristown NJ 07962-1021

M. Balu
Amoco Performance Products Inc.
4500 McGinnis Ferry Road
Alpharetta GA 30202

B. P. Bandyopadhyay
Toyohashi University of Technology
School of Production Systems Engineering
Tempaku-cho Toyohashi 440
JAPAN

P. M. Barnard
Ruston Gas Turbines Limited
Metallurgical Laboratory
P.O. Box 1
Lincoln LN2 5DJ
ENGLAND

Harold N. Barr
Hittman Corporation
9190 Red Branch Road
Columbia MD 21045

Renald D. Bartoe
Vesuvius McDanel
510 Ninth Avenue
Box 560
Beaver Falls PA 15010-0560

David L. Baty
Babcock & Wilcox - LRC
P.O. Box 11165
Lynchburg VA 24506-1165

Donald F. Baxter, Jr.
ASM International
Advanced Materials & Processes
Materials Park OH 44073-0002

M. Brad Beardsley
Caterpillar Inc.
Advanced Materials Technology
Technical Center Bldg. E
P.O. Box 1875
Peoria IL 61656-1875

Robert Beck
Teledyne CAE
Materials Engineering/Programs
1330 Laskey Road
P.O. Box 6971
Toledo OH 43612

John C. Bell
Shell Research Limited
Thornton Research Centre
P.O. Box 1
Chester CH1 3SH
ENGLAND

Albert H. Bell, III
General Motors Technical Center
30200 Mound Road
Engineering Building/W3 Turbine
Warren MI 48090-9010

M. Bentele
Xamag, Inc.
259 Melville Avenue
Fairfield CT 06430

Larry D. Bentsen
BFGoodrich Company
R&D Center
9921 Brecksville Road
Brecksville OH 44141

Joseph C. Bentz
ENCERATEC
2525 Sandcrest Drive
Columbus IN 47203

Louis Beregszazi
Defiance Precision Products
P.O. Drawer 428
Defiance OH 43512

Tom Bernecki
Northwestern University
BIRL
1801 Maple Avenue
Evanston IL 60201-3135

Charles F. Bersch
Institute for Defense Analyses
1801 North Beauregard Street
Alexandria VA 22311

Ram Bhatt
NASA Lewis Research Center
21000 Brookpark Road
Cleveland OH 44135

Deane I. Biehler
Caterpillar Inc.
Engineering Research Materials
Technical Center, Building E
P.O. Box 1875
Peoria IL 61656-1875

John W. Bjerklie
Consolidated Natural Gas Service Co., Inc.
Research Department
CNG Tower
Pittsburgh PA 15222-3199

William D. Bjorndahl
TRW, Inc.
One Space Park
Building 01, Room 2040
Redondo Beach CA 90278

Keith A. Blakely
Advanced Refractory Technologies, Inc.
699 Hertel Avenue
Buffalo NY 14207

Edward G. Blanchard
Netzsch Inc.
119 Pickering Way
Exton PA 19341

Keith Blandford
Boride Products, Inc.
2879 Aero Park Drive
Traverse City MI 49684

Bruce Boardman
Deere and Company Technical Center
3300 River Drive
Moline IL 61265

Russell Bockstedt
Hoechst Celanese Corporation
150 JFK Parkway
Short Hills NJ 07078

M. Boehmer
DLR German Aerospace Research
Establishment
Postfach 90 60 58
D-5000 Koln 90
GERMANY

Lawrence P. Boesch
EER Systems Corp.
1593 Spring Hill Road
Vienna VA 22182-2239

Donald H. Boone
Boone & Associates
2412 Cascade Drive
Walnut Creek CA 94598-4313

Tom Booth
Allied-Signal Aerospace Company
AiResearch Los Angeles Division
2525 West 190th Street
Torrance CA 90509-2960

Tibor Bornemisza
Sundstrand Power Systems
4400 Ruffin Road
San Diego CA 92186-5757

J.A.M. Boulet
University of Tennessee
Department of Engineering Science and
Mechanics
310 Perkins Hall
Knoxville TN 37996-2030

H. Kent Bowen
Massachusetts Institute of Technology
77 Massachusetts Avenue
Room E40-434
Cambridge MA 02139

Leslie J. Bowen
Materials Systems
53 Hillcrest Road
Concord MA 01742

Steven C. Boyce
Air Force Office of Scientific Research
AFOSR/NA Bldg. 410
Bolling AFB DC 20332-6448

Gary L. Boyd
CEC
4901 South Calle Los Cerros #203
Tempe AZ 85282

Steve Bradley
UOP Research Center
50 East Algonquin Road
Des Plaines IL 60017-6187

Michael C. Brands
Cummins Engine Company, Inc.
P.O. Box 3005, Mail Code 50179
Columbus IN 47201

Raymond J. Bratton
Westinghouse Science and Technology
Center
1310 Beulah Road
Pittsburgh PA 15235

John J. Brennan
United Technologies Corporation
Research Center
Silver Lane, MS:24
East Hartford CT 06108

Jeff D. Bright
Ceramatec, Inc.
2425 South 900 West
Salt Lake City UT 84108

Terrence K. Brog
Coors Ceramics Company
Corporate Development and Technology
4545 McIntyre Street
Golden CO 80403

Gunnar Broman
317 Fairlane Drive
Spartanburg SC 29302

Al Brown
High-Tech Materials Alert
P.O. Box 882
Dayton NJ 08810

Jesse J. Brown
Virginia Polytechnic Institute and State University
Center for Advanced Ceramic Materials
Blacksburg VA 24061-0256

Sherman D. Brown
University of Illinois
Materials Science and Engineering Department
105 South Goodwin Avenue
204 Ceramics Building
Urbana IL 61801

S. L. Bruner
Ceramatec, Inc.
2425 South 900 West
Salt Lake City UT 84119

Adolfo Brusaferro
Keramont Corporation
4231 South Fremont Avenue
Tucson AZ 85714

Walter Bryzik
U.S. Army Tank Automotive Command
R&D Center, Propulsion Systems Division
Warren MI 48397-5000

S. T. Buljan
GTE Laboratories, Inc.
40 Sylvan Road
Waltham MA 02254

S. J. Burden
GTE Valenite
1711 Thunderbird
Troy MI 48084

Curt V. Burkland
AMERCOM, Inc.
8928 Fullbright Avenue
Chatsworth CA 91311

Bill Bustamante
AMERCOM, Inc.
8928 Fullbright Street
Chatsworth CA 91311

Oral Buyukozturk
Massachusetts Institute of Technology
77 Massachusetts Avenue
Room 1-280
Cambridge MA 02139

David A. Caillet
Ethyl Corporation
451 Florida Street
Baton Rouge LA 70801

Frederick J. Calnan
Heany Industries, Inc.
249 Briarwood Lane
P.O. Box 38
Scottsville NY 14546

Roger Cannon
Rutgers University
Ceramics Department
P.O. Box 909
Piscataway NJ 08855-0909

Scott Cannon
P.O. Box 567254
Atlanta GA 30356

Harry W. Carpenter
19945 Acre Street
Northridge CA 91324

David Carruthers
Kyocera Industrial Ceramics Company
P.O. Box 2279
Vancouver WA 98668-2279

Calvin H. Carter, Jr.
Cree Research, Inc.
2810 Meridian Parkway
Durham NC 27713

J. David Casey
35 Atlantis Street
West Roxbury MA 02132

Jere G. Castor
J. C. Enterprise
5078 North 83rd Street
Scottsdale AZ 85250

James D. Cawley
Case Western Reserve University
Materials Science & Engineering Department
Cleveland OH 44106

Thomas C. Chadwick
Den-Mat Corporation
P.O. Box 1729
Santa Maria CA 93456

Ronald H. Chand
Chand Kare Technical Ceramics
2 Coppage Drive
Worcester MA 01603

Robert E. Chaney
EG&G Idaho, Inc.
Idaho National Engineering Laboratory
P.O. Box 1625
Idaho Falls ID 83415-3525

Frank C. Chang
U.S. Army Materials Technology Laboratory
AMTL-EMM
405 Arsenal Street
Watertown MA 02172

Robert M. Chapman
Allied-Signal Aerospace Company
1001 Pennsylvania Avenue, N.W.
Suite 700 South
Washington DC 20004

William Chapman
Williams International Corporation
2280 West Maple Road
Walled Lake MI 48390-0200

Charlie Chen
LECO Corporation
P.O. Box 211688
Augusta GA 30917

Albert A. Chesnes
U.S. Department of Energy
Transportation Technologies
CE-30
Washington DC 20585

Kaiyin Chia
Carborundum Company
P.O. Box 832
Niagara Falls NY 14302

Frank Childs
EG&G Idaho, Inc.
Idaho National Engineering Laboratory
P.O. Box 1625
Idaho Falls ID 83415-3527

William J. Chmura
Torrington Company
59 Field Street
Torrington CT 06790-4942

Tsu-Wei Chou
University of Delaware
Center for Composite Materials
201 Spencer Laboratory
Newark DE 19716

R. J. Christopher
Ricardo Consulting Engineers
Bridge Works
Shoreham-By-Sea West Sussex BN43 5FG
ENGLAND

Joel P. Clark
Massachusetts Institute of Technology
Room 8-409
Cambridge MA 02139

Giorgio Clarotti
Commission of the European Communities
DGXII-C3, MO75, 1-53; 200 Rue de la Loi
B-1049 Brussels
BELGIUM

W. J. Clegg
ICI Advanced Materials
P.O. Box 11
The Heath, Runcorn Cheshire WA7 4QE
ENGLAND

Joseph Cleveland
GTE Products Corporation
Hawes Street
Towanda PA 18848-0504

Gloria M. Collins
ASTM
1916 Race Street
Philadelphia PA 19103

William C. Connors
Sundstrand Aviation Operations
Materials Science and Engineering
Department
4747 Harrison Avenue
P.O. Box 7002
Rockford IL 61125-7002

John A. Coppola
Carborundum Company
P.O. Box 156
Niagara Falls NY 14302

Normand D. Corbin
Norton Company
Advanced Ceramics
Goddard Road
Northboro MA 01532-1545

Douglas Corey
Allied-Signal Aerospace Company
2525 West 190th Street, MS:T52
Torrance CA 90504-6099

Keith P. Costello
Chand/Kare Technical Ceramics
2 Coppage Drive
Worcester MA 01603-1252

Ed L. Courtright
Pacific Northwest Laboratory
MS:K3-59
Richland WA 99352

Anna Cox
Mitchell Market Reports
P.O. Box 23
Monmouth Gwent NP5 4YG
UNITED KINGDOM

Art Cozens
Instron Corporation
3414 Snowden Avenue
Long Beach CA 90808

Robert C. Craft
American Ceramic Society, Inc.
757 Brooksedge Plaza Drive
Westerville OH 43081

Mark Crawford
New Technology Week
4604 Monterey Drive
Annandale VA 22003

Richard A. Cree
Markets & Products, Inc.
P.O. Box 14328
Columbus OH 43214-0328

Les Crittenden
Vesuvius McDanel
Box 560
Beaver Falls PA 15010

William J. Croft
U.S. Army Materials Technology
Laboratory
405 Arsenal Street
Watertown MA 02172

M. J. Cronin
Mechanical Technology, Inc.
968 Albany-Shaker Road
Latham NY 12110

Gary M. Crosbie
Ford Motor Company
1430 Culver Avenue
S-2079, SRL Building
Dearborn MI 48121-4036

Floyd W. Crouse, Jr.
U.S. Department of Energy
Morgantown Energy Technology Center
Collins Ferry Road
P.O. Box 880
Morgantown WV 26505

John Cuccio
Allied-Signal Aerospace Company
Garrett Auxiliary Power Division
P.O. Box 5227, MS:1302-2Q
Phoenix AZ 85010

Raymond A. Cutler
Ceramatec, Inc.
2425 South 900 West
Salt Lake City UT 84119

Charles D'Angelo
GTE Laboratories, Inc.
40 Sylvan Road
Waltham MA 02154

Stephen C. Danforth
Rutgers University
Ceramics Engineering Department
P.O. Box 909
Piscataway NJ 08855-0909

Sankar Das Gupta
Electrofuel Manufacturing Co., Ltd.
9 Hanna Avenue
Toronto Ontario MGK-1W8
CANADA

Charles Davis
Sverdrup Technology, Inc. MSFC
620 Discovery Drive
Huntsville AL 35806

Frank Davis
Allied-Signal Aerospace Company
7550 Lucerne Drive, #203
Middleburg Heights OH 44130

Robert F. Davis
North Carolina State University
Materials Engineering Department
229 Riddick Laboratory
P.O. Box 7907
Raleigh NC 27695

Thomas DeAngelis
Carborundum Company
Niagara Falls R&D Center
P.O. Box 832
Niagara Falls NY 14302

George DeBell
Ford Motor Company
Material Systems Reliability Department
20000 Rotunda Drive
P.O. Box 2053, Room S-2023
Dearborn MI 48121-2053

Michael DeLuca
AMP-AKZO
West Lane
Aquebogue NY 11931

Gerald L. DePoorter
Colorado School of Mines
Metallurgical and Materials Engineering Department
Golden CO 80401

J. F. DeRidder
Omni Electro Motive, Inc.
12 Seely Hill Road
Newfield NY 14867

Nick C. Dellow
Materials Technology Publications
40 Sotheron Road
Watford Herts WD1 2QA
UNITED KINGDOM

L. R. Dharani
University of Missouri-Rolla
224 M.E.
Rolla MO 65401

Douglas A. Dickerson
Union Carbide Specialty Powders
1555 Main Street
Indianapolis IN 46224

John Dodsworth
Vesuvius Research & Development
Technical Ceramics Group
Box 560
Beaver Falls PA 15010

B. Dogan
Institut fur Werkstofforschung
GKSS-Forschungszentrum Geesthacht GmbH
Max-Planck-Strasse
D-2054 Geesthacht
GERMANY

Jean-Marie Drapier
FN Moteurs S.A.
Material and Processing
B-4041 Milmort (Herstal)
BELGIUM

Kenneth C. Dreitlein
United Technologies Research Center
Silver Lane
East Hartford CT 06108

Robin A.L. Drew
McGill University
Department of Mining and Metallurgical Engineering
3450 University Street
Montreal Quebec H3A 2A7
CANADA

Winston H. Duckworth
BCL
Columbus Division
505 King Avenue
Columbus OH 43201-2693

Edmund M. Dunn
Texel Company
6 Third Street
Lexington MA 02173

Bill Durako
Sundstrand Aviation Operations
Department 789-6
4747 Harrison Avenue
P.O. Box 7002
Rockford IL 61125-7002

Ernest J. Duwell
212 Elm Street
Hudson WI 54016

Chuck J. Dziedzic
Coors Ceramics Company
Structural Products Group
17750 West 32nd Avenue
Golden CO 80401

Robert J. Eagan
Sandia National Laboratories
Engineered Materials & Processes Center
Org 1700
P.O. Box 5800
Albuquerque NM 87185-5800

Jeffrey Eagleson
Lanxide Corporation
1001 Connecticut Avenue, N.W.
Washington DC 20036

Harry E. Eaton
United Technologies Corporation
Research Center
Silver Lane
East Hartford CT 06108

Harvill C. Eaton
Louisiana State University
Office of Research & Economic Development
240 Thomas Boyd Hall
Baton Rouge LA 70803

Christopher A. Ebel
Carborundum Company
Technology Division
P.O. Box 337
Niagara Falls NY 14302

J. J. Eberhardt
U.S. Department of Energy
Office of Transportation Materials
CE-34
Washington DC 20585

Jim Edler
Eaton Corporation
26201 Northwestern Highway
P.O. Box 766
Southfield MI 48037

William A. Ellingson
Argonne National Laboratory
Materials Science & Technology Division
9700 South Cass Avenue
Argonne IL 60439

William S. Ellis
Machined Ceramics
629 N. Graham St., N. Industrial Park
Bowling Green KY 42101

Glen B. Engle
Nuclear & Aerospace Materials
Corporation
16716 Martincoit Road
Poway CA 92064

Jeff Epstein
Ceramic Technologies, Inc.
2107 Jamara Lane
Houston TX 77077

Kenneth A. Epstein
Dow Chemical U.S.A.
Ceramics and Advanced Materials
800 Building
Midland MI 48667

Art Erdemir
Argonne National Laboratory
Materials and Components Technology
Division
9700 South Cass Avenue
Argonne IL 60439

E. M. Erwin
Lubrizol Corporation
1819 East 225th Street
Euclid OH 44117

Kenji Esaki
Toyota Technical Center U.S.A., Inc.
2000 Town Center, Suite 500
Southfield MI 48075

John N. Eustis
U.S. Department of Energy
Industrial Energy Efficiency Division
CE-221
Washington DC 20585

Robert C. Evans
NASA Lewis Research Center
Terrestrial Propulsion Office
21000 Brookpark Road, MS:86-6
Cleveland OH 44135

W. L. Everitt
Kyocera International, Inc.
8611 Balboa Avenue
San Diego CA 92123

Gordon Q. Evison
332 South Michigan Avenue, Suite 1730
Chicago IL 60604

John W. Fairbanks
U.S. Department of Energy
Advanced Propulsion Division
CE-322
Washington DC 20585

Tim Fawcett
Dow Chemical Company
Central Research, Advanced Ceramics
Laboratory
1776 Building
Midland MI 48674

Robert W. Fawley
Sundstrand Power Systems
Division of Sundstrand Corporation
4400 Ruffin Road
P.O. Box 85757
San Diego CA 92186-5757

John J. Fedorchak
GTE Products Corporation
Hawes Street
Towanda PA 18848-0504

Jeff T. Fenton
Vista Chemical Company
900 Threadneedle
Houston TX 77079

Larry Ferrell
Babcock & Wilcox
Old Forest Road
Lynchburg VA 24505

Raymond R. Fessler
BIRL
Industrial Research Lab
1801 Maple Avenue
Evanston IL 60201

Michelle Finch
E. I. DuPont de Nemours & Company, Inc.
Experimental Station
Information Center E302/301
Wilmington DE 19898

Ross F. Firestone
Ross Firestone Company
188 Mary Street
Winnetka IL 60093-1520

Sharon L. Fletcher
Arthur D. Little, Inc.
15 Acorn Park
Cambridge MA 02140-2390

Thomas F. Foltz
Textron Specialty Materials
2 Industrial Avenue
Lowell MA 01851

Renee G. Ford
Materials and Processing Report
P.O. Box 72
Harrison NY 10528

John Formica
Supermaterials
2020 Lakeside Avenue
Cleveland OH 44114

Jennifer M. Fox
Dyson Refractories Limited
R&D Laboratory
Owler Bar
Sheffield S17 3BJ
UNITED KINGDOM

Edwin Frame
Southwest Research Institute
Division 2
P.O. Drawer 28510
San Antonio TX 78284

Armanet Francois
French Scientific Mission
4101 Reservoir Road, N.W.
Washington DC 20007-2176

R. G. Frank
Technology Assessment Group
10793 Bentley Pass Lane
Loveland OH 45140

David J. Franus
Forecast International
22 Commerce Road
Newtown CT 06470

Marc R. Freedman
NASA Lewis Research Center
21000 Brookpark Road, MS:49-3
Cleveland OH 44135

Douglas Freitag
LTV Missiles Division
P.O. Box 650003, MS:WT-21
Dallas TX 75265

Brian R.T. Frost
Argonne National Laboratory
9700 South Cass Avenue
Building 900
Argonne IL 60439

Lawrence R. Frost
Instron Corporation
100 Royall Street
Canton MA 02021

George A. Fryburg
Norton/TRW Ceramics
7A-4 Raymond Avenue
Salem NH 03079

Xiren Fu
Shanghai Institute of Ceramics
Chinese Academy of Sciences
1295 Ding-xi Road
Shanghai 200050
CHINA

John Gahimer
P.O. Box 1302
Dublin OH 43017

J. P. Gallagher
University of Dayton Research Institute
300 College Park, JPC-250
Dayton OH 45469-0120

Tom Garritano
University of Tennessee
Science Alliance
101 South College
Knoxville TN 37996-1328

Joy A. Garwood
Norton Company
Advanced Ceramics
Goddard Road
Northboro MA 01532-1545

H. Maury Gatewood
Reynolds Metals Company
Corporate R&D
Fourth and Canal Streets
P.O. Box 27003
Richmond VA 23261

L. J. Gauckler
ETH-Zurich
Sonneggstrasse 5
CH-8092 Zurich 8092
SWITZERLAND

Peter A. Gaydos
Battelle Columbus Laboratories
505 King Avenue
Columbus OH 43201

George E. Gazza
U.S. Army Materials Technology
Laboratory
Ceramics Research Division
405 Arsenal Street
Watertown MA 02172-0001

D. Gerster
CEA-DCOM
33 Rue De La Federation
Paris 75015
FRANCE

John Ghinazzi
Coors Technical Ceramics Company
1100 Commerce Park Drive
Oak Ridge TN 37830

Robert Giddings
General Electric Company
Research Laboratory
P.O. Box 8
Schenectady NY 12301

A. M. Glaeser
University of California
Materials Science and Mineral
Engineering
Lawrence Berkeley Laboratory
Hearst Mining Building
Berkeley CA 94720

Paul Glance
Concept Analysis
R&D
950 Stephenson Highway
Dupont Automotive Development Bldg.
Troy MI 48007-7013

Joseph W. Glatz
Naval Air Propulsion Center
Systems Engineering Division
P.O. Box 7176, PE24
Trenton NJ 08628

W. M. Goldberger
Superior Graphite Company
R&D
2175 East Broad Street
Columbus OH 43209

Allan E. Goldman
U.S. Graphite, Inc.
907 West Outer Drive
Oak Ridge TN 37830

Stephen T. Gonczy
Allied Signal Research
P.O. Box 5016
Des Plaines IL 60017

Jeffrey M. Gonzales
GTE Products Corporation
Hawes Street
Towanda PA 18848-0504

Robert J. Gottschall
U.S. Department of Energy
ER-131 MS:G-236
Washington DC 20545

Earl Graham
Cleveland State University
Department of Chemical Engineering
Euclid Avenue at East 24th Street
Cleveland OH 44115

William A. Graham
Lanxide Corporation
P.O. Box 6077
Newark DE 19714-6077

Robert E. Green, Jr.
Johns Hopkins University
Materials Science and Engineering
Department
Baltimore MD 21218

Lance Groseclose
General Motors Corporation
Allison Gas Turbine Division
P.O. Box 420, MS:W-5
Indianapolis IN 46206

Mark F. Gruninger
Union Carbide Corporation
Specialty Powder Business
1555 Main Street
Indianapolis IN 46224

Ernst Gugel
Cremer Forschungsinstitut GmbH&Co.KG
Oeslauer Strasse 35
D-8633 Roedental 8633
GERMANY

Donald L. Guile
Corning Glass Works
SP-DV-1-9
Corning NY 14831

Bimleshwar P. Gupta
Solar Energy Research Institute
Mechanical and Industrial Technology
Division
1617 Cole Boulevard
Golden CO 80401

John P. Gyekenyesi
NASA Lewis Research Center
21000 Brookpark Road, MS:6-1
Cleveland OH 44135

Nabil S. Hakim
Detroit Diesel Corporation
13400 Outer Drive West
Detroit MI 48239

Philip J. Haley
General Motors Corporation
Vehicular Engineering
P.O. Box 420, MS:T12A
Indianapolis IN 46236

Judith Hall
Fiber Materials, Inc.
Biddeford Industrial Park
5 Morin Street
Biddeford ME 04005

Y. Hamano
Kyocera Corporation
5-22 Kitainoue-Cho, Higashino
Yamashina-Ku Kyoto 607
JAPAN

Y. Harada
IIT Research Institute
Nometallic Materials and Composites
10 West 35th Street
Chicago IL 60616

R. A. Harmon
25 Schalren Drive
Latham NY 12110

Norman H. Harris
Hughes Aircraft Company
P.O. Box 800520
Saugus CA 91380-0520

Alan M. Hart
Dow Chemical Company
Advanced Ceramics Laboratory
1776 Building
Midland MI 48674

Pat E. Hart
Battelle Pacific Northwest Laboratories
Ceramics and Polymers Development Section
P.O. Box 999
Richland WA 99352

Stephen D. Hartline
Norton Company
Advanced Ceramics
Goddard Road
Northboro MA 01532-1545

Michael H. Haselkorn
Caterpillar Inc.
Engineering Research Materials
Technical Center, Building E
P.O. Box 1875
Peoria IL 61656-1875

N. B. Havewala
Corning Inc.
SP-PR-11
Corning NY 14831

John Haygarth
Teledyne WAA Chang Albany
P.O. Box 460
Albany OR 97321

Norman L. Hecht
University of Dayton Research Institute
300 College Park
Dayton OH 45469-0172

Peter W. Heitman
General Motors Corporation
Allison Gas Turbine Division
P.O. Box 420, MS:W-5
Indianapolis IN 46206-0420

Robert W. Hendricks
Virginia Polytechnic Institute and State University
Materials Engineering Department
210 Holden Hall
Blacksburg VA 24061-0237

Wynne Henley
Hertel Cutting Technologies Inc.
1000 Clearview Court
Oak Ridge TN 37830

Thomas L. Henson
GTE Products Corporation
Chemical & Metallurgical Division
Hawes Street
Towanda PA 18848

Thomas P. Herbell
NASA Lewis Research Center
21000 Brookpark Road, MS:49-3
Cleveland OH 44135

Marlene Heroux
Rolls-Royce, Inc.
2849 Paces Ferry Road, Suite 450
Atlanta GA 30339-3769

Robert L. Hershey
Science Management Corporation
1255 New Hampshire Ave., NW, Suite 1033
Washington DC 20036

Hendrik Heystek
Bureau of Mines
Tuscaloosa Research Center
P.O. Box L
University AL 35486

Wallace C. Higgins
Norwal Unlimited
Box 1258
Alfred NY 14802

Robert V. Hillery
GE Aircraft Engines
One Neumann Way, M.D. H85
Cincinnati OH 45215

Arthur Hindman
Instron Corporation
100 Royall Street
Canton MA 02021

Jon Hines
American Ceramic Society, Inc.
757 Brooksedge Plaza Drive
Westerville OH 43081-6136

Hans Erich Hintermann
CSEM
Materials and Micromechanics Division
Rue Breguet 2
Neuchatel 2000
SWITZERLAND

Shinichi Hirano
Mazda R&D of North America, Inc.
1203 Woodridge Avenue
Ann Arbor MI 48105

Tommy Hiraoka
NGK Locke, Inc.
1000 Town Center
Southfield MI 48075

John M. Hobday
U.S. Department of Energy
Morgantown Energy Technology Center
Collins Ferry Road
P.O. Box 880
Morgantown WV 26507

Greg Hoenes
Vista Chemical Company
900 Threadneedle
P.O. Box 19029
Houston TX 77079-2990

Clarence Hoenig
Lawrence Livermore National Laboratory
P.O. Box 808, Mail Code L-369
Livermore CA 94550

Thomas Hollstein
Fraunhofer-Institut fur
Werkstoffmechanik IWM
Wohlerstrabe 11
D-7800 Freiburg
GERMANY

Richard Holt
National Research Council of Canada
Structures and Materials Laboratory
Ottawa Ontario K1A 0R6
CANADA

Joseph Homeny
University of Illinois
Department of Materials Science and
Engineering
105 South Goodwin Avenue
Ceramics Building
Urbana IL 61801

A. T. Hopper
BCL
Metals and Ceramics Department
505 King Avenue
Columbus OH 43201-2693

Michael Horgan
Materials Engineering Magazine
1100 Superior Avenue
Cleveland OH 44114

Woodie Howe
Coors Technical Ceramics Company
1100 Commerce Park Drive
Oak Ridge TN 37830

Stephen M. Hsu
National Institute of Standards and
Technology
Gaithersburg MD 20899

Hann S. Huang
Argonne National Laboratory
9700 South Cass Avenue
Argonne IL 60439-4815

Gene Huber
Precision Ferrites & Ceramics
5576 Corporate Drive
Cypress CA 90630

M. L. Huckabee
GTE Laboratories, Inc.
40 Sylvan Road
Waltham MA 02254

Harold A. Huckins
Princeton Advanced Technology, Inc.
56 Finley Road
Princeton NJ 08540

Fred R. Huettic
Advanced Magnetics Inc.
45 Corey Lane
Mendham NJ 07945

Bill Huffman
Zircar
110 North Main Street
Florida NY 10921

Brian K. Humphrey
Lubrizol Petroleum Chemicals Co.
3000 Town Center, Suite 1340
Southfield MI 48075-1201

Robert M. Humrick
Dylon Ceramic Technologies
3100 Edgehill Road
Cleveland Heights OH 44118

Lorretta Inglehart
National Science Foundation
Division of Materials Research
1800 "G" Street, N.W., Room 408
Washington DC 20550

Michael S. Inoue
Kyocera International, Inc.
KII Library
8611 Balboa Avenue
San Diego CA 92123-1580

Osama Jadaan
University of Wisconsin-Platteville
General Engineering Division
1 University Plaza
Platteville WI 53818

Curtis A. Johnson
General Electric Company
Corporate R&D
Room MB-187
P.O. Box 8
Schenectady NY 12301

Sylvia Johnson
SRI International
333 Ravenswood Avenue
Menlo Park CA 94025

Thomas A. Johnson
Lanxide Corporation
1300 Marrows Road
P.O. Box 6077
Newark DE 19714-6077

W. S. Johnson
Indiana University
One City Centre, Suite 200
Bloomington IN 47405

W. F. Jones
Air Force Office of Scientific Research
AFOSR/NA
Bolling AFB DC 20332-6448

Jill E. Jonkouski
U.S. Department of Energy
9800 South Cass Avenue
Argonne IL 60439-4899

L. A. Joo
Great Lakes Research Corporation
P.O. Box 1031
Elizabethton TN 37643

A. David Joseph
SPX Corporation
700 Terrace Point
Muskegon MI 49443

Adam Jostsons
Australian Nuclear Science & Technology Organisation
Lucas Heights Research Laboratories
New Illawarra Road
Lucas Heights New South Wales
AUSTRALIA

Matthew K. Juneau
Ethyl Corporation
451 Florida Street
Baton Rouge LA 70801

Hartmut Kainer
Didier-Werke AG
Anlagentechnik Wiesbaden
Abraham-Lincoln-Str. 16
D-62 Wiesbaden
GERMANY

Tom Kalamasz
Norton/TRW Ceramics
7A-4 Raymond Avenue
Salem NH 03079

Lyle R. Kallenbach
Phillips Petroleum Company
R&D
Mail Drop:123AL
Bartlesville OK 74004

Nick Kamiya
Kyocera Industrial Ceramics Corporation
2700 River Road
Des Plaines IL 60018

Roy Kamo
Adiabatics, Inc.
3385 Commerce Park Drive
Columbus IN 47201

S. Kang
GTE Laboratories, Inc.
40 Sylvan Road
Waltham MA 02254

Chih-Chun Kao
Industrial Technology Research Institute
Materials Research Laboratories
195 Chung-Hsing Road, Sec. 4,
Chutung Hsinchu 31015 R.O.C.
TAIWAN

Keith R. Karasek
Allied-Signal, Inc.
Engineered Materials Research Center
50 East Algonquin Road
P.O. Box 5016
Des Plaines IL 60017-5016

Robert E. Kassel
Ceradyne, Inc.
3169 Redhill Avenue
Costa Mesa CA 92626

Allan Katz
Wright Laboratory
Metals and Ceramics Division
WL/MLLM
Wright-Patterson AFB OH 45433

R. Nathan Katz
Worcester Polytechnic Institute
Department of Mechanical Engineering
100 Institute Road
Worcester MA 01609

Tony Kaushal
Detroit Diesel Corporation
13400 Outer Drive West, Speed Code:L-04
Detroit MI 48239

Ted Kawaguchi
Tokai Carbon America, Inc.
375 Park Avenue, Suite 3802
New York NY 10152

Noritsugu Kawashima
TOSHIBA Corporation
Mechanical Engineering Laboratory
4-1 Ukishima-Cho
Kawasaki-Ku Kawasaki 210
JAPAN

Lisa Kempfer
Penton Publishing
Materials Engineering
1100 Superior Avenue
Cleveland OH 44114-2543

Frederick L. Kennard, III
General Motors Corporation
AC Rochester, Department 32-24, EB
1300 North Dort Highway
Flint MI 48556

David O. Kennedy
Lester B. Knight Cast Metals Inc.
549 West Randolph Street
Chicago IL 60661

George Keros
Photon Physics
3175 Penobscot Building
Detroit MI 48226

Pramod K. Khandelwal
General Motors Corporation
Allison Gas Turbine Division
P.O. Box 420, MS:W05
Indianapolis IN 46206

Jim R. Kidwell
Allied-Signal Aerospace Company
Garrett Auxiliary Power Division
P.O. Box 5227
Phoenix AZ 85010

Han J. Kim
GTE Laboratories, Inc.
40 Sylvan Road
Waltham MA 02254

Shin Kim
Korea Institute of Machinery & Metals
66 Sangnam-dong, Changwon
Kyungnam 641-010
KOREA

W. C. King
Mack Truck, Z-41
1999 Pennsylvania Avenue
Hagerstown MD 21740

Carol Kirkpatrick
MSE, Inc.
CDIF Technical Library
P.O. Box 3767
Butte MT 59702

Tony Kirn
Caterpillar Inc.
Defense Products Department, JB7
Peoria IL 61629

James D. Kiser
NASA Lewis Research Center
21000 Brookpark Road, MS:49-3
Cleveland OH 44135

Max Klein
Gas Research Institute
Thermodynamics
8600 West Bryn Mawr Avenue
Chicago IL 60631

Richard N. Kleiner
Coors Ceramics Company
4545 McIntyre Street
Golden CO 80403

Stanley J. Klima
NASA Lewis Research Center
21000 Brookpark Road, MS:6-1
Cleveland OH 44135

Chris E. Knapp
Norton Advanced Ceramics of Canada Ltd.
8001 Daly Street
Niagara Falls Ontario L2G 6S2
CANADA

Albert S. Kobayashi
University of Washington
Mechanical Engineering Department
Mail Stop:FU10
Seattle WA 98195

Shigeki Kobayashi
Toyota Central Research Labs, Inc.
Nagakute Aichi 480-11
JAPAN

Richard A. Kole
Z-Tech Corporation
8 Dow Road
Bow NH 03304

E. Kostiner
University of Connecticut
Chemistry Department, U-60
Storrs CT 06269-3060

Joseph A. Kovach
Eaton Corporation
Manufacturing Technologies Center
32500 Chardon Road
Willoughby Hills OH 44094

Kenneth A. Kovaly
Technical Insights Inc.
P.O. Box 1304
Fort Lee NJ 07024-9967

Ralph G. Kraft
Spraying Systems Company
North Avenue at Schmale Road
Wheaton IL 60189-7900

Saunders B. Kramer
U.S. Department of Energy
Advanced Propulsion Division
CE-322
Washington DC 20585

Arthur Kranish
Trends Publishing Inc.
1079 National Press Building
Washington DC 20045

A. S. Krieger
Radiation Science, Inc.
P.O. Box 293
Belmont MA 02178

Pieter Krijgsman
Ceramic Design International Holding B.V.
P.O. Box 68
Hattem 8050-AB
THE NETHERLANDS

Waltraud M. Kriven
University of Illinois
Materials Science & Engineering Department
105 South Goodwin Avenue
Urbana IL 61801

Edward J. Kubel, Jr.
ASM International
Advanced Materials & Processes
Materials Park OH 44073

Dave Kupperman
Argonne National Laboratory
9700 South Cass Avenue
Argonne IL 60439

Oh-Hun Kwon
Norton Company
Advanced Ceramics
Goddard Road
Northboro MA 01532-1545

W. J. Lackey
Georgia Institute of Technology
Materials Science and Technology
Atlanta GA 30332

Jai Lala
Tenmat Ltd.
40 Somers Road
Rugby Warwickshire CV22 7DH
ENGLAND

Hari S. Lamba
General Motors Corporation
Electro-Motive Division
9301 West 55th Street
LaGrange IL 60525

Richard L. Landingham
Lawrence Livermore National Laboratory
Ceramics, Corrosion, and Thermochemistry
P.O. Box 808, L-369
Livermore CA 94550

Charles J. Landry
Chand Kare Technical Ceramics
712 Flat Hill Road
Lumenburg MA 01462

James Lankford
Southwest Research Institute
Department of Materials Sciences
6220 Culebra Road
San Antonio TX 78228-0510

Stanley B. Lasday
Business News Publishing Co.
Manor Oak One
1910 Cochran Road, Suite 630
Pittsburgh PA 15220

Mark S. Laser
Solar Turbines, Inc.
2211 Erie Street
San Diego CA 92110

S. K. Lau
Carborundum Company
Technology Division
P.O. Box 832, B-100
Niagara Falls NY 14302

Edward A. Lauder
Advanced Composite Materials Corporation
1525 South Buncombe Road
Greer SC 29651-9208

J. Lawrence Lauderdale
Babcock & Wilcox
Contract Research Division
1850 "K" Street, Suite 950
Washington DC 20006

Harry A. Lawler
Carborundum Company
Technology Division
P.O. Box 832
Niagara Falls NY 14302

Jean F. LeCostaouec
Textron Specialty Materials
2 Industrial Avenue
Lowell MA 01851

Benson P. Lee
Interscience, Inc.
9718 Lake Shore Boulevard
Cleveland OH 44108

Burtrand I. Lee
Clemson University
Department of Ceramic Engineering
Olin Hall
Clemson SC 29634-0907

June-Gunn Lee
KIST
Structural Ceramic Lab
P.O. Box 131, Cheong-Ryang
Seoul 130-650
KOREA

Ran-Rong Lee
Ceramics Process Systems Corporation
155 Fortune Boulevard
Milford MA 01757

Stan Levine
NASA Lewis Research Center
21000 Brookpark Road, MS:49-3
Cleveland OH 44135

Alan V. Levy
Lawrence Berkeley Laboratory
One Cyclotron Road, MS:62-203
Berkeley CA 94720

Ai-Kang Li
Materials Research Laboratories, ITRI
195-5 Chung-Hsing Road., Sec. 4
Chutung Hsinchu 31015 R.O.C.
TAIWAN

Winston W. Liang
Hong Kong Industrial Technology Centre
Co. Ltd.
78 Tat Chee Avenue
4/F, HKPC Building
Kowloon
HONG KONG

Robert Licht
Norton Company
Advanced Ceramics
Goddard Road
Northboro MA 01532-1545

E. Lilley
Norton Company
Advanced Ceramics
Goddard Road
Northboro MA 01532-1545

Laura J. Lindberg
Allied-Signal Aerospace Company
Garrett Fluid Systems Division
1300 West Warner, MS:93-901-1207-4TT
P.O. Box 22200
Tempe AZ 85284-2200

Leonard C. Lindgren
General Motors Corporation
Allison Gas Turbine Division
P.O. Box 420, Speed Code:T-20A
Indianapolis IN 46206-0420

Hans A. Lindner
Cremer Forschungsinstitut GmbH&Co.KG
Oeslauer Strasse 35
D-8633 Rodental 8866
GERMANY

Ronald E. Loehman
Sandia National Laboratories
Chemistry & Ceramics Department 1840
P.O. Box 5800
Albuquerque NM 87185

Jeffrey C. Logas
Winona State University
Composite Materials Engineering
115 Pasteur Hall
Winona MN 55987

Bill Long
Babcock & Wilcox
P.O. Box 11165
Lynchburg VA 24506

William D. Long
Wacker Chemicals (USA), Inc.
ESK Engineered Ceramics
50 Locust Avenue
New Canaan CT 06840

L. A. Lott
EG&G Idaho, Inc.
Idaho National Engineering Laboratory
P.O. Box 1625
Idaho Falls ID 83415-2209

Raouf O. Loutfy
MER Corporation
7960 South Kolb Road
Tucson AZ 85706

Gordon R. Love
Aluminum Company of America
Alcoa Technical Center
Alcoa Center PA 15069

Lydia Luckevich
Ortech International
2395 Speakman Drive
Mississauga Ontario L5K 1B3
CANADA

James W. MacBeth
Carborundum Company
Structural Ceramics Division
P.O. Box 1054
Niagara Falls NY 14302

H. MacLaren
General Electric Company
Thomson Laboratory, Materials
Engineering 36807
1000 Western Avenue
Lynn MA 01910

George Maczura
Aluminum Company of America
Industrial Chemicals Division
670 One Allegheny Square
Pittsburgh PA 15212

David Maginnis
Tinker AFB
OC-ALC/LIIRE
Tinker AFB OK 73145-5989

Frank Maginnis
Aspen Research, Inc.
220 Industrial Boulevard
Moore OK 73160

Tai-il Mah
Universal Energy Systems, Inc.
Ceramics and Composites Research
4401 Dayton-Xenia Road
Dayton OH 45432

Kenneth M. Maillar
Barbour Stockwell Company
83 Linskey Way
Cambridge MA 02142

Lorenzo Majno
Instron Corporation
100 Royall Street
Canton MA 02021

S. G. Malghan
National Institute of Standards and Technology
I-270 & Clopper Road
Gaithersburg MD 20899

Lars Malmrup
United Turbine AB
Box 13027
Malmo S-200 44
SWEDEN

John Mangels
Ceradyne, Inc.
3169 Redhill Avenue
Costa Mesa CA 92626

Russell V. Mann
Matec Applied Sciences, Inc.
75 South Street
Hopkinton MA 01748

William R. Manning
Champion Aviation Products Division
Old Norris Road
P.O. Box 686
Liberty SC 29657

Ken Marnoch
Amercom, Inc.
8928 Fullbright Avenue
Chatsworth CA 91311

Robert A. Marra
Aluminum Company of America
Alcoa Technical Center
Advanced Ceramics Center - E
Alcoa Center PA 15069

Chauncey L. Martin
3M Company
3M Center, Building 60-1N-01
St. Paul MN 55144

Steven C. Martin
Advanced Refractory Technologies, Inc.
699 Hertel Avenue
Buffalo NY 14207

Kelly J. Mather
Williams International Corporation
2280 West Maple Road
P.O. Box 200
Walled Lake MI 48088

James P. Mathers
3M Company
3M Center
Building 201-3N-06
St. Paul MN 55144

Marshall Mayer
Instron Corporation
3815 Presidential Parkway, Suite 100
Atlanta GA 30340

Ron Mayville
Arthur D. Little, Inc.
15-163 Acorn Park
Cambridge MA 02140

F. N. Mazadarany
General Electric Company
Research Laboratory
Building K-1, Room MB-159
P.O. Box 8
Schenectady NY 12301

James W. McCauley
Alfred University
NYS College of Ceramics
Binns-Merrill Hall
Alfred NY 14802

Louis R. McCreight
2763 San Ramon Drive
Rancho Palos Verdes CA 90274

Colin F. McDonald
McDonald Thermal Engineering
1730 Castellana Road
La Jolla CA 92037

B. J. McEntire
Norton Company
TRW Ceramics
Goddard Road
Northboro MA 01532-1545

Chuck McFadden
Coors Ceramics Company
600 9th Street
Golden CO 80401

Henry McFadden
Magnetic Bearings, Inc.
Engineering Library
609 Rock Road
Radford VA 24141

Thomas D. McGee
Iowa State University
Materials Science and Engineering Department
110 Engineering Annex
Ames IA 50011

Carol McGill
Corning Inc.
Sullivan Park, FR-02-08
Corning NY 14831

T. C. McLaren
Cameron Forged Products Company
P.O. Box 1212
Houston TX 77251-1212

James McLaughlin
Sundstrand Power Systems
4400 Ruffin Road
P.O. Box 85757
San Diego CA 92186-5757

Matt McMonigle
U.S. Department of Energy
Improved Energy Productivity Division
CE-231
Washington DC 20585

Dennis McMurtry
EG&G Idaho, Inc.
Idaho National Engineering Laboratory
P.O. Box 1625
Idaho Falls ID 83415

J. C. McVickers
Allied-Signal Aerospace Company
Garrett Auxiliary Power Division
Bldg. 1303-206
P.O. Box 5227, MS:9317-2
Phoenix AZ 85010

D. B. Meadowcroft
National Power
Technology and Environmental Centre
Kelvin Avenue
Leatherhead Surrey KT22 7SE
ENGLAND

Jo Meglen
11004 Birdfoot Court
Reston VA 22091

Joseph J. Meindl
Reynolds International, Inc.
6603 West Broad Street
P.O. Box 27002
Richmond VA 23261-7003

Michael D. Meiser
Allied-Signal Aerospace Company
Garrett Ceramic Components Division
2525 West 190th Street
P.O. Box 2960, MS:T21
Torrance CA 90509-2960

George Messenger
National Research Council of Canada
Engine Laboratory
Building M-7
Ottawa Ontario K1A OR6
CANADA

D. Messier
U.S. Army Materials Technology Laboratory
SLCMT-EMC
405 Arsenal Street
Watertown MA 02172-0001

Gary L. Messing
Pennsylvania State University
Ceramic Science and Engineering Department
119 Steidle Building
University Park PA 16802

Arthur G. Metcalfe
Arthur G. Metcalfe and Associates, Inc.
2108 East 24th Street
National City CA 91950

R. Metselaar
Eindhoven University
Centre for Technical Ceramics
P.O. Box 513
Eindhoven 5600 MB
THE NETHERLANDS

David J. Michael
Harbison-Walker Refractories Company
P.O. Box 98037
Pittsburgh PA 15227

Ken Michaels
Chrysler Motors Corporation
Ceramics Development Metallurgical Processes
P.O. Box 1118, CIMS:418-17-09
Detroit MI 48288

Bernd Michel
Institute of Mechanics
Fracture and Micromechanics Department
P.O. Box 408
D-9010 Chemnitz
GERMANY

David E. Miles
Commission of the European Communities
rue de la Loi, 200
B-1049 Brussels
BELGIUM

John V. Milewski
Superkinetics, Inc.
2881 Tramway Pl NE
Albuquerque NM 87122

Carl E. Miller
AC Rochester
1300 North Dort Highway, MS:32-31
Engineering Building B
Flint MI 48556

Charles W. Miller, Jr.
Centorr Furnaces/Vacuum Industries
542 Amherst Street
Nashua NH 03063

R. Mininni
Enichem America
2000 Cornwall Road
Monmouth Junction NJ 08852

Michele V. Mitchell
Allied-Signal Aerospace Company
Garrett Ceramic Components Division
2525 West 190th Street
P.O. Box 2960, MS:T21
Torrance CA 90509-2960

Howard Mizuhara
GTE - WESGO
477 Harbor Boulevard
Belmont CA 94002

Helen Moeller
Babcock & Wilcox
P.O. Box 11165
Lynchburg VA 24506-1165

Francois R. Mollard
Concurrent Technologies Corporation
1450 Scalp Avenue
Johnstown PA 15904

Phil Mooney
Panametrics
NDE Division
221 Crescent Street
Waltham MA 02254

Thomas Morel
Ricardo North America
645 Blackhawk Drive
Westmont IL 60559

Geoffrey P. Morris
3M Company
3M Traffic Control Materials Division
Bldg. 209-BW-10, 3M Center
St. Paul MN 55144-1000

Jay A. Morrison
Rolls-Royce, Inc.
Engineering and Information Center,
Overlook 1
2849 Paces Ferry Road, Suite 450
Atlanta GA 30339-3769

Joel P. Moskowitz
Ceradyne, Inc.
3169 Redhill Avenue
Costa Mesa CA 92626

Brij Moudgil
University of Florida
Material Science & Engineering
Gainesville FL 32611

Christoph J. Mueller
Sprechsaal Publishing Group
P.O. Box 2962, Mauer 2
D-8630 Coburg
GERMANY

Thomas W. Mullan
Vapor Technologies Inc.
345 Route 17 South
Upper Saddle River NJ 07458

M. K. Murthy
MKM Consultants International
10 Avoca Avenue, Unit 1906
Toronto Ontario M4T 2B7
CANADA

Solomon Musikant
TransCon Technologies, Inc.
Materials Science and Engineering
1508 Waynesboro Road
Paoli PA 19301

David L. Mustoe
Custom Technical Ceramics
8041 West I-70 Service Road, Unit 6
Arvada CO 80002

Curtis V. Nakaishi
U.S. Department of Energy
Morgantown Energy Technology Center
Collins Ferry Road
P.O. Box 880
Morgantown WV 26507-0880

Yoshio Nakamura
Faicera Research Institute
2-5-8 Hiyakunin-cho Shinjuku-Ko
Tokyo
JAPAN

K. S. Narasimhan
Hoeganaes Corporation
River Road
Riverton NJ 08077

Samuel Natansohn
GTE Laboratories, Inc.
40 Sylvan Road
Waltham MA 02254

Robert Naum
Applied Resources, Inc.
P.O. Box 241
Pittsford NY 14534

Malcolm Naylor
Cummins Engine Company, Inc.
P.O. Box 3005, Mail Code 50183
Columbus IN 47202-3005

Jeffrey T. Neil
GTE Laboratories, Inc.
40 Sylvan Road
Waltham MA 02254

Fred A. Nichols
Argonne National Laboratory
9700 South Cass Avenue
MCT - Building 212
Argonne IL 60439

H. Nickel
Forschungszentrum Juelich (KFA)
P.O. Box 1913
Juelich 1-5170 BRD NRW
GERMANY

Dale E. Niesz
Rutgers University
Center for Ceramic Research
P.O. Box 909
Piscataway NJ 08855-0909

David M. Nissley
United Technologies Corporation
Pratt & Whitney Aircraft
400 Main Street, MS:163-10
East Hartford CT 06108

Richard D. Nixdorf
ReMaxCo Technologies, Inc.
11317 Snyder Road
Knoxville TN 37932

Bernard North
Kennametal, Inc.
P.O. Box 639
Greensburg PA 15601

Bruce E. Novich
Ceramics Process Systems Corporation
155 Fortune Boulevard
Milford MA 01757

Daniel Oblas
GTE Laboratories, Inc.
40 Sylvan Road
Waltham MA 02254

Don Ohanehi
Magnetic Bearings, Inc.
1908 Sussex Road
Blacksburg VA 24060

Robert Orenstein
General Electric Company
55-112, River Road
Schenectady NY 12345

Norb Osborn
Aerodyne Dallas
151 Regal Row, Suite 120
Dallas TX 75247

A. M. Paddick
BP International Limited
BP Research Centre, Main Library
Chertsey Road
Sunbury-on-Thames
Middlesex TW16 7LN
UNITED KINGDOM

Russell J. Page
Kanthal-Artcor
3001 Redhill Avenue, II-109
Costa Mesa CA 92705

Richard Palicka
Cercom, Inc.
1960 Watson Way
Vista CA 92083

Muktesh Paliwal
GTE Products Corporation
Hawes Street
Towanda PA 18848

Joseph E. Palko
General Electric Company
55-113, River Road
Schenectady NY 12345

Hayne Palmour, III
North Carolina State University
Materials Science & Engineering
Department
Raleigh NC 27605-7905

Joseph N. Panzarino
Norton Company
Advanced Ceramics
Goddard Road
Northboro MA 01532-1545

Pellegrino Papa
Corning Inc.
MP-WX-02-1
Corning NY 14831

E. Beth Pardue
MPC
8297 Williams Ferry Road
Lenoir City TN 37771

Soon C. Park
3M Company
3M Center
Building 142-4N-02
P.O. Box 2963
St. Paul MN 55144

Hartmut Paschke
Schott Glaswerke
Christoph-Dorner-Strasse 29
D-8300 Landshut
GERMANY

Marina R. Pascucci
GTE Laboratories, Inc.
40 Sylvan Road
Waltham MA 02254

James W. Patten
Cummins Engine Company, Inc.
Materials Engineering
P.O. Box 3005, Mail Code 50183
Columbus IN 47202-3005

Robert A. Penty
Eastman Kodak Company
KAD/D73 - 35612
901 Elmgrove Road
Rochester NY 14653

Robert W. Pepper
Textron Specialty Materials
2 Industrial Avenue
Lowell MA 01851

Peter Perdue
Detroit Diesel Corporation
Research Advanced Development Group
13400 Outer Drive West, Speed Code L-04
Detroit MI 48239-4001

Bruce Peters
Dow Chemical Company
Building 52
Midland MI 48667

John J. Petrovic
Los Alamos National Laboratory
Group MST-4, MS:G771
Los Alamos NM 87545

Frederick S. Pettit
University of Pittsburgh
Pittsburgh PA 15261

Ben A. Phillips
Phillips Engineering Company
721 Pleasant Street
St. Joseph MI 49085

Richard C. Phoenix
Ohmtek, Inc.
2160 Liberty Drive
Niagara Falls NY 14302

Bruce J. Pletka
Michigan Technological University
Metallurgical & Materials Engineering
Department
Houghton MI 49931

John P. Pollinger
Allied-Signal Aerospace Company
Garrett Ceramic Components Division
2525 West 190th Street
P.O. Box 2960, MS:T21
Torrance CA 90509-2960

P. Popper
High Technology Ceramics International
Journal
22 Pembroke Drive
Westlands Newcastle-under-Lyme Staffs
ST5 2JN
ENGLAND

F. Porz
Universitat Karlsruhe
Institut fur Keramik Im Maschinendau
Postfach 6980
D-7500 Karlsruhe
GERMANY

Harry L. Potma
Royal Netherlands Embassy
Science and Technology
4200 Linnean Avenue, N.W.
Washington DC 20008

Bob R. Powell
General Motors Research Laboratories
Metallurgy Department
30500 Mound Road
Box 9055
Warren MI 48090-9055

Stephen C. Pred
ICD Group, Inc.
1100 Valley Brook Avenue
Lyndhurst NJ 07071

Karl M. Prewo
United Technologies Research Center
411 Silver Lane, MS:24
East Hartford CT 06108

Peter E. Price
Industrial Materials Technology, Inc.
P.O. Box 9565
Andover MA 01810

Joseph M. Proud
GTE Laboratories, Inc.
Materials Science Laboratory
40 Sylvan Road
Waltham MA 02254

Vimal K. Pujari
Norton Company
Advanced Ceramics
Goddard Road
Northboro MA 01532-1545

George Quinn
National Institute of Standards and Technology
Ceramics Division, Bldg. 223
Gaithersburg MD 20899

Ramas V. Raman
Ceracon, Inc.
1101 North Market Boulevard, Suite 9
Sacramento CA 95834

Charles F. Rapp
Owens Corning Fiberglass
2790 Columbus Road
Granville OH 43023-1200

Dennis W. Readey
Colorado School of Mines
Department of Metallurgy and Materials Engineering
Golden CO 80401

Wilfred J. Rebello
PAR Enterprises, Inc.
12601 Clifton Hunt Lane
Clifton VA 22024

Harold Rechter
Chicago Fire Brick Company
R&D
7531 South Ashland Avenue
Chicago IL 60620

Robert R. Reeber
U.S. Army Research Office
P.O. Box 12211
Research Triangle Park NC 27709

K. L. Reifsnider
Virginia Polytechnic Institute and State University
Department of Engineering Science and Mechanics
Blacksburg VA 24061

Paul E. Rempes
McDonnell Douglass Aircraft Company
P.O. Box 516, Mail Code:0642263
St. Louis MO 63166-0516

Gopal S. Revankar
John Deere Company
Metals Research
3300 River Drive
Moline IL 61265

K. T. Rhee
Rutgers University
Mechanical Engineering
P.O. Box 909
Piscataway NJ 08854

James Rhodes
Advanced Composite Materials Corporation
1525 South Buncombe Road
Greer SC 29651

Roy W. Rice
W. R. Grace and Company
7379 Route 32
Columbia MD 21044

David W. Richerson
2093 East Delmont Drive
Salt Lake City UT 84117

Tomas Richter
J. H. France Refractories
1944 Clarence Road
Snow Shoe PA 16874

Michel Rigaud
Ecole Polytechnique
Campus Universite De Montreal
P.O. Box 6079, Station A
Montreal, P.Q. Quebec H3C 3A7
CANADA

R. E. Riman
Rutgers University
Ceramics Engineering Department
P.O. Box 909
Piscataway NJ 08855-0909

Barry Ringstrom
Superior Graphite Company
P.O. Box 2373
Smyrna GA 30081

John E. Ritter
University of Massachusetts
Mechanical Engineering Department
Amherst MA 01003

Frank L. Roberge
Allied-Signal Aerospace Company
Garrett Auxiliary Power Division
P.O. Box 5227
Phoenix AZ 85010

W. Eric Roberts
Advanced Ceramic Technology, Inc.
990 "F" Enterprise Street
Orange CA 92667

Martha Rohr
U.S. Department of Energy
Oak Ridge Operations
Building 4500N
P.O. Box 2008, MS:6269
Oak Ridge TN 37831-6269

Y. G. Roman
TNO TPD Keramick
P.O. Box 595
Einhoven 5600 AN
HOLLAND

Michael Rossetti
Arthur D. Little, Inc.
15 Acorn Park
Cambridge MA 01240

Barry Rossing
Lanxide Corporation
1300 Marrows Road
Newark DE 19714-6077

Steven L. Rotz
Lubrizol Corporation
29400 Lakeland Boulevard
Wickliffe OH 44092

Bruce Rubinger
Global Competitiveness, Inc.
One Devonshire Place, Suite 1011
Boston MA 02109

Robert Ruh
Wright Laboratory
WL/MLLM
Wright-Patterson AFB OH 45433

Robert J. Russell
17 Highgate Road
Framingham MA 01701

L. William Sahley
Supermaterials Company
24400 Highland Road
Richmond Heights OH 44143

Jon A. Salem
NASA Lewis Research Center
21000 Brookpark Road
Cleveland OH 44135

W. A. Sanders
NASA Lewis Research Center
21000 Brookpark Road, MS:49-3
Cleveland OH 44135

J. Sankar
North Carolina A&T State University
Department of Mechanical Engineering
Greensboro NC 27411

Yasushi Sato
NGK Spark Plugs (U.S.A.), Inc.
1200 Business Center Drive, Suite 300
Mt. Prospect IL 60056

Maxine L. Savitz
Allied-Signal Aerospace Company
Garrett Ceramic Components Division
2525 West 190th Street
P.O. Box 2960, MS:T21
Torrance CA 90509-2960

Ashok Saxena
Georgia Institute of Technology
Materials Engineering
Atlanta GA 30332-0245

David W. Scanlon
Instron Corporation
100 Royall Street
Canton MA 02021

Charles A. Schacht
Schacht Consulting Services
12 Holland Road
Pittsburgh PA 15235

James Schienle
Allied-Signal Aerospace Company
Garrett Auxiliary Power Division
2739 East Washington Street
P.O. Box 5227, MS:1302-2P
Phoenix AZ 85010

John C. Schneider
San Juan Technologies
P.O. Box 49326
Colorado Springs CO 80949-9326

Gary Schnittgrund
Rocketdyne, BA05
6633 Canoga Avenue
Canoga Park CA 91303

Mark Schomp
Lonza, Inc.
Corporate Headquarters
17-17 Route 208
Fair Lann NJ 07410

Joop Schoonman
Delft University of Technology
Laboratory for Inorganic Chemistry
P.O. Box 5045
2600 GA Delft
THE NETHERLANDS

John Schuldies
Industrial Ceramic Technology, Inc.
37 Enterprise Drive
Ann Arbor MI 48103

Robert B. Schulz
U.S. Department of Energy
Office of Transportation Materials
CE-34
Washington DC 20585

Murray A. Schwartz
Materials Technology Consulting, Inc.
30 Orchard Way, North
Potomac MD 20854

Peter Schwarzkopf
SRI International
333 Ravenswood Avenue
Menlo Park CA 94025

William T. Schwessinger
Multi-Arc Scientific Coatings
1064 Chicago Road
Troy MI 48083-4297

W. D. Scott
University of Washington
Materials Science Department
Mail Stop:FB10
Seattle WA 98195

Nancy Scoville
Thermo Electron Technologies
74 West Street
P.O. Box 9046
Waltham MA 02254-9046

Brian Seegmiller
Coors Ceramics Company
600 9th Street
Golden CO 80401

T. B. Selover
AICRE/DIPPR
3575 Traver Road
Shaker Heights OH 44122

J. H. Selverian
GTE Laboratories, Inc.
40 Sylvan Road
Waltham MA 02254

Charles E. Semler
Semler Materials Services
4160 Mumford Court
Columbus OH 43220

Thomas Service
Service Engineering Laboratory
324 Wells Street
Greenfield MA 01301

Kish Seth
Ethyl Corporation
R&D Laboratories
P.O. Box 341
Baton Rouge LA 70821

Karleen Seybold
Allied-Signal Aerospace Company
Garrett Auxiliary Power Division
P.O. Box 5227
Phoenix AZ 85010

William J. Shack
Argonne National Laboratory
9700 South Cass Avenue
Building 212
Argonne IL 60439

Peter T. B. Shaffer
Technical Ceramics Laboratories, Inc.
4045 Nine/McFarland Drive
Alpharetta GA 30201

Richard K. Shaltens
NASA Lewis Research Center
21000 Brookpark Road, MS:301-2
Cleveland OH 44135

Robert S. Shane
238 Hemlock Road
Wynnewood PA 19096

Daniel J. Shanefield
Rutgers University
Ceramics Engineering Department
P.O. Box 909
Piscataway NJ 08855-0909

Ravi Shankar
Chromalloy
Research and Technology Division
Blaisdell Road
Orangeburg NY 10962

Terence Sheehan
Alpex Wheel Company
727 Berkley Street
New Milford NJ 07646

Dinesh K. Shetty
University of Utah
304 EMRO, Dept. of Materials Science and Engineering
Salt Lake City UT 84112

Masahide Shimizu
Ceramic Society of Japan
2-2-503 Takiyama 6-chome
Higashikurume-Shi Tokyo 203
JAPAN

John Shipinski
Toyota Technical Center U.S.A., Inc.
Technical Research Department
2000 Town Center, Suite 500
Southfield MI 48075

Thomas Shreves
American Ceramic Society, Inc.
Library
757 Brooksedge Plaza Drive
Westerville OH 43081-2821

Jack D. Sibold
Coors Ceramics Company
Contracts for Corporate Technology
4545 McIntyre Street
Golden CO 80403

Johann Siebels
Volkswagen AG
Werkstofftechnologie
Postfach
3180 Wolfsburg 1
GERMANY

George H. Siegel
Point North Associates, Inc.
P.O. Box 907
Madison NJ 07940

Richard Silberglitt
Technology Assessment and Transfer, Inc.
133 Defense Highway, #212
Annapolis MD 21401

Mary Silverberg
Norton Company
Advanced Ceramics Library
Goddard Road
Northboro MA 01532-1545

Gurpreet Singh
Department of the Navy
Internal Combustion & Gas Turbine Engine Division
Code 56X31
Washington DC 20362-5101

Maurice J. Sinnott
University of Michigan
Chemical and Metallurgical Engineering
5106 IST Building
Ann Arbor MI 48109-2099

John Skildum
3M Company
3M Center
Building 224-2S-25
St. Paul MN 55144

David P. Smith
Hoskins, Rees & Smith
1910 Cochran Road
Manor Oak II, Suite 658
Pittsburgh PA 15220

Richard H. Smoak
Smoak & Associates
3554 Hollyslope Road
Altadena CA 91001-3923

Jay R. Smyth
Allied-Signal Aerospace Company
Garrett Auxiliary Power Division
2739 East Washington Street
P.O. Box 5227 MS:93-173/1303-207
Phoenix AZ 85010

Edward A. Snajdr
Premier Refractories and Chemicals, Inc.
P.O. Box 392
Bettsville OH 44815

Rafal A. Sobotowski
British Petroleum Company
Technical Center, Broadway
3092 Broadway Avenue
Cleveland OH 44115

A. G. Solomah
SAC International Ltd.
1445 Bonhill Road, #13
Mississauga Ontario L5T 1V3
CANADA

S. Somiya
Nishi Tokyo University
3-7-19 Seijo, Setagaya
Tokyo 157
JAPAN

Boyd W. Sorenson
DuPont Lanxide Composites
1300 Marrows Road
P.O. Box 6077
Neward DE 19707

Charles A. Sorrell
U.S. Department of Energy
Advanced Industrial Concepts Division
CE-232
Washington DC 20585

C. Spencer
EA Technology
Capenhurst Chester CH1 6ES
UNITED KINGDOM

Allen Spizzo
Hercules Inc.
Hercules Plaza
Wilmington DE 19894

Richard M. Spriggs
Alfred University
Center for Advanced Ceramic Technology
Alfred NY 14802

Charles Spuckler
NASA Lewis Research Center
21000 Brookpark Road, MS:5-11
Cleveland OH 44135-3191

M. Srinivasan
Material Solutions
P.O. Box 663
Grand Island NY 14702-0663

Gordon L. Starr
Cummins Engine Company, Inc.
Design & Technology
P.O. Box 3005, Mail Code 50182
Columbus IN 47202-3005

Jim Stevenson
Windrock, Incorporated
154 Fairbanks Plaza
Oak Ridge TN 37830

Tom Stillwagon
Allied-Signal Aerospace Company
Garrett Ceramic Components Division
2525 West 190th Street
P.O. Box 2960, MS:T21
Torrance CA 90509-2960

Harold L. Stocker
General Motors Corporation
Allison Gas Turbine Division
P.O. Box 420
Indianapolis IN 46206

H. M. Stoller
TPL Inc.
3754 Hawkins, N.E.
Albuquerque NM 87109

Paul D. Stone
Dow Chemical USA
1776 "Eye" Street, N.W., Suite 575
Washington DC 20006

Roger S. Storm
Carborundum Company
Technology Division
P.O. Box 337
Niagara Falls NY 14302-0337

Peter A. Stranges
4 Chittenden Lane
Owings Mills MD 21117

F. W. Stringer
Aero & Industrial Technology Ltd.
P.O. Box 46, Wood Top
Burnley Lancashire BB11 4BX
UNITED KINGDOM

Thomas N. Strom
NASA Lewis Research Center
21000 Brookpark Road, MS:86-6
Cleveland OH 44135

M. F. Stroosnijder
Institute for Advanced Materials
Joint Research Centre
21020 Ispra (VA)
ITALY

Karsten Styhr
30604 Ganado Drive
Rancho Palos Verdes CA 90274

T. S. Sudarshan
Materials Modification, Inc.
2929-P1 Eskridge Center
Fairfax VA 22031

M. J. Sundaresan
University of Miami
Mechanical Engineering Department
P.O. Box 248294
Coral Gables FL 33124

Patrick L. Sutton
U.S. Department of Energy
Advanced Propulsion Division
CE-322
Washington DC 20585

Willard H. Sutton
United Technologies Corporation
Research Center, MS:24
Silver Lane
East Hartford CT 06108

Ron Sviben
100 Indel Avenue
Rancocas NJ 08073

J. J. Swab
U.S. Army Materials Technology
Laboratory
Ceramics Research Division, SLCMT-EMC
405 Arsenal Street
Watertown MA 02172

Robert E. Swanson
Metalworking Technology, Inc.
1450 Scalp Avenue
Johnstown PA 15904

Scott L. Swartz
BCL
Metals and Ceramics
505 King Avenue
Columbus OH 43201

Steve Szaruga
Air Force Wright Aeronautical Laboratory
Materials Directorate
WL/MLBC
Wright-Patterson AFB OH 45433-6533

Yo Tajima
NGK Spark Plug Company, Ltd.
NTK Technical Ceramic Division
2808 Iwasaki
Komaki-shi Aichi-ken 485
JAPAN

Fred Teeter
5 Tralee Terrace
East Amherst NY 14051

Monika O. Ten Eyck
Carborundum Company
Technology Division
P.O. Box 832
Niagara Falls NY 14302

David F. Thompson
Corning Glass Works
SP-DV-02-1
Corning NY 14831

Merle L. Thorpe
Hobart Tafa Technologies, Inc.
146 Pembroke Road
Concord NH 03301

Eberhard Tiefenbacher
Daimler-Benz AG Abt. F1S
Mercedes-Strabe 136
Stuttgart 60
GERMANY

T. Y. Tien
University of Michigan
Materials Science and Engineering
Dow Building
Ann Arbor MI 48103

D. M. Tracey
Norton Company
Advanced Ceramics
Goddard Road
Northboro MA 01532-1545

Dick Trippett
General Motors Corporation
Allison Gas Turbine Division
P.O. Box 420, MS:W-16
Indianapolis IN 46206-0420

L. J. Trostel, Jr.
Box 199
Princeton MA 01541

W. T. Tucker
General Electric Company
Corporate R&D
Building K1-4C35
P.O. Box 8
Schenectady NY 12301

Masanori Ueki
Nippon Steel Corporation
Central R&D Bureau
1618 Ida
Nakahara-Ku Kawasaki 211
JAPAN

Filippo M. Ugolini
ATA Studio
Via Degli Scipioni, 268A
ROMA 00192
ITALY

Donald L. Vaccari
General Motors Corporation
Allison Gas Turbines
P.O. Box 420, Speed Code S49
Indianapolis IN 46206-0420

Carl F. Van Conant
Boride Products, Inc.
2879 Aero Park Drive
Traverse City MI 49684

Marcel H. Van De Voorde
Commission of the European Communities
Institute for Advanced Materials
Joint Research Centre
P.O. Box 2
1755 ZG Petten
THE NETHERLANDS

O. Van Der Biest
Katholieke Universiteit Leuven
Departement Metaalkunde en Toegepaste
de Croylaan 2
B-3030 Leuven
BELGIUM

Michael Vannier
Washington University, St. Louis
Mallinckrodt Institute of Radiology
510 South Kings Highway
St. Louis MO 63110

Stan Venkatesan
Southern Coke & Coal Corporation
P.O. Box 52383
Knoxville TN 37950

V. Venkateswaran
Carborundum Company
Niagara Falls R&D Center
P.O. Box 832
Niagara Falls NY 14302

Dennis Viechnicki
U.S. Army Materials Technology
Laboratory
405 Arsenal Street
Watertown MA 02172-0001

Ted Vojnovich
U.S. Department of Energy
Office of Energy Research, ER-42
Washington DC 20585

John D. Volt
E. I. Dupont de Nemours & Company, Inc.
P.O. Box 80262
Wilmington DE 19880

John B. Wachtman
Rutgers University
Ceramics Department
P.O. Box 909
Piscataway NJ 08855

Shigetaka Wada
Toyota Central Research Labs, Inc.
Nagakute Aichi 480-11
JAPAN

Janet Wade
Allied-Signal Aerospace Company
Garrett Auxiliary Power Division,
Department 93-772
P.O. Box 5227, MS:1303-2
Phoenix AZ 85010

Richard L. Wagner
Ceramic Technologies, Inc.
537 Turtle Creek South Drive, Suite 24D
Indianapolis IN 46227

J. Bruce Wagner, Jr.
Arizona State University
Center for Solid State Science
Tempe AZ 85287-1704

Daniel J. Wahlen
Kohler, Co.
444 Highland Drive
Kohler WI 53044

Ingrid Wahlgren
Royal Institute of Technology
Studsvik Library
S-611 82 Nykoping
SWEDEN

Ron H. Walecki
Allied-Signal Aerospace Company
Garrett Ceramic Components Division
2525 West 190th Street
P.O. Box 2960, MS:T21
Torrance CA 90509-2960

Michael S. Walsh
Vapor Technologies Inc.
2100 Central Avenue
Boulder CO 80301

Chien-Min Wang
Industrial Technology Research Institute
Materials Research Laboratories
195 Chung-Hsing Road, Sec. 4
Chutung Hsinchu 31015 R.O.C.
TAIWAN

Robert M. Washburn
ASMT
11203 Colima Road
Whittier CA 90604

Gerald Q. Weaver
Carborundum Specialty Products
42 Linus Allain Avenue
Gardner MA 01440-2478

Karen E. Weber
Detroit Diesel Corporation
Technology and Planning
13400 Outer Drive West
Detroit MI 48239-4001

J. K. Weddell
DuPont Fibers
Experimental Station, E302
Wilmington DE 19880-0302

R. W. Weeks
Argonne National Laboratory
MCT-212
9700 South Cass Avenue
Argonne IL 60439

Ludwig Weiler
ASEA Brown Boveri AG
Corporate Research
Eppelheimer Str. 82
D-6900 Heidelberg
GERMANY

James Wessel
Dow Corning Corporation
1800 "M" Street, N.W., Suite 325 South
Washington DC 20036

Robert D. West
Therm Advanced Ceramics
P.O. Box 220
Ithaca NY 14851

Thomas J. Whalen
Ford Motor Company
26362 Harriet
Dearborn Heights MI 48127

Ian A. White
Hoeganaes Corporation
River Road
Riverton NJ 08077

Alan Whitehead
General Electric Company
1 River Road, 55-111
Schenectady NY 12345

Sheldon M. Wiederhorn
National Institute of Standards and Technology
Building 223, Room A329
Gaithersburg MD 20899

John F. Wight
Alfred University
McMahon Building
Alfred NY 14802

D. S. Wilkinson
McMaster University
Materials Science and Engineering Department
1280 Main Street, West
Hamilton Ontario L8S 4L7
CANADA

James C. Williams
General Electric Company
Engineering Materials Technology Labs
One Neumann Way, Mail Drop:H85
Cincinnati OH 45215-6301

Janette R. Williams
Kollmorgen Corporation
PCK Technology Division
150 Motor Parkway, #262
Hauppauge NY 11788-5108

Steve J. Williams
RCG Hagler Bailly, Inc.
1530 Wilson Boulevard, Suite 900
Arlington VA 22209-2406

Craig A. Willkens
Norton Company
Advanced Ceramics
Goddard Road
Northboro MA 01532-1545

Roger R. Wills
TRW, Inc.
Valve Division
1455 East 185th Street
Cleveland OH 44110

David Gordon Wilson
Massachusetts Institute of Technology
Mechanical Engineering Department
77 Massachusetts Avenue, Room 3-455
Cambridge MA 02139

Matthew F. Winkler
Seaworthy Systems, Inc.
P.O. Box 965
Essex CT 06426

Gerhard Winter
Hermann C. Starck Berlin GmbH, Werk Goslar
P.O. Box 25 40
D-3380 Goslar 3380
GERMANY

W. L. Winterbottom
Ford Motor Company
Material Systems Reliability Department
20000 Rotunda Drive
SRL, Room E-3182
P.O. Box 2053
Dearborn MI 48121

David G. Wirth
Coors Ceramics Company
600 9th Street
Golden CO 80401

Thomas J. Wissing
Eaton Corporation
Engineering and Research Center
P.O. Box 766
Southfield MI 48037

James C. Withers
MER Corporation
7960 South Kolb Road
Building F
Tucson AZ 85706

Dale E. Wittmer
Southern Illinois University
Mechanical Engineering Department
Carbondale IL 62901

Warren W. Wolf
Owens Corning Fiberglass
2790 Columbus Road, Route 16
Granville OH 43023

Egon E. Wolff
Caterpillar Inc.
Technical Center
P.O. Box 1875
Peoria IL 61656-1875

George W. Wolter
Howmet Turbine Components Corporation
Technical Center
699 Benston Road
Whitehall MI 49461

James C. Wood
NASA Lewis Research Center
21000 Brookpark Road, MS:86-6
Cleveland OH 44135

Marrill Wood
LECO Corporation
Augusta Division
P.O. Box 211688
Augusta GA 30917-1688

Wayne L. Worrell
University of Pennsylvania
Department of Materials Science and Engineering
3231 Walnut Street
Philadelphia PA 19104

John F. Wosinski
Corning Inc.
ME-2 E-5 H8
Corning NY 14830

Ian G. Wright
Battelle Columbus Laboratories
505 King Avenue
Columbus OH 43201

Ruth Wroe
ERDC
Metals & Materials Industries Division
Capenhurst Chester CH1 6ES
ENGLAND

Bernard J. Wrona
Advanced Composite Materials Corporation
1525 South Buncombe Road
Greer SC 29651

Carl C. M. Wu
Naval Research Laboratory
Ceramic Branch, Code 6373
Washington DC 20375

John C. Wurst
University of Dayton Research Institute
300 College Park
Dayton OH 45469-0101

Neil Wyant
ARCH Development Corp.
9700 South Cass Avenue
Building 202
Argonne IL 60439

Roy Yamamoto
Texaco Inc.
P.O. Box 509
Beacon NY 12508-0509

John Yamanis
Allied-Signal, Inc.
Ceramics Program
P.O. Box 1021
Morristown NJ 07962-1021

Harry C. Yeh
Allied-Signal Aerospace Company
Garrett Ceramic Components Division
2525 West 190th Street
P.O. Box 2960, MS:T21
Torrance CA 90509-2960

Hiroshi Yokoyama
Hitachi Research Lab
4026 Kuji-Cho
Hitachi-shi Ibaraki 319-12
JAPAN

Thomas M. Yonushonis
Cummins Engine Company, Inc.
P.O. Box 3005, Mail Code 50183
Columbus IN 47202-3005

Thomas J. Yost
Corning Inc.
Technical Products Division, Main Plant
21-1-2
Corning NY 14831

Jong Yung
Sundstrand Aviation Operations
Department 789-6
4747 Harrison Avenue
Rockford IL 61125

A. L. Zadoks
Caterpillar Inc.
Technical Center, Building L
P.O. Box 1875
Peoria IL 61656-1875

Avi Zangvil
University of Illinois
Materials Research Laboratory
104 South Goodwin Avenue
Urbana IL 61801

Charles H. Zenuk
Transtech
6569 East Calle Cavalier
Tucson AZ 85715

Anne Marie Zerega
U.S. Department of Energy
Office of Energy Research, ER-42
Washington DC 20585

Carl Zweben
General Electric Company
P.O. Box 8555, VFSC/V4019
Philadelphia PA 19101

Klaus M. Zwilsky
National Research Council
National Materials Advisory Board
2101 Constitution Avenue
Washington DC 20418

Department of Energy
DOE Field Office, Oak Ridge
Assistant Manager for Energy
Research and Development
P.O. Box 2001
Oak Ridge, TN 37831-8600

Department of Energy (10)
Office of Scientific and
Technical Information
Office of Information
Services
P.O. Box 62
Oak Ridge, TN 37831

For distribution by microfiche as shown in DOE/OSTI-4500, Distribution Category UC-332 (Ceramics/Advanced Materials).